DOE/ER-0313/12

Fusion Reactor Materials

Semiannual Progress Report for Period Ending March 31, 1992

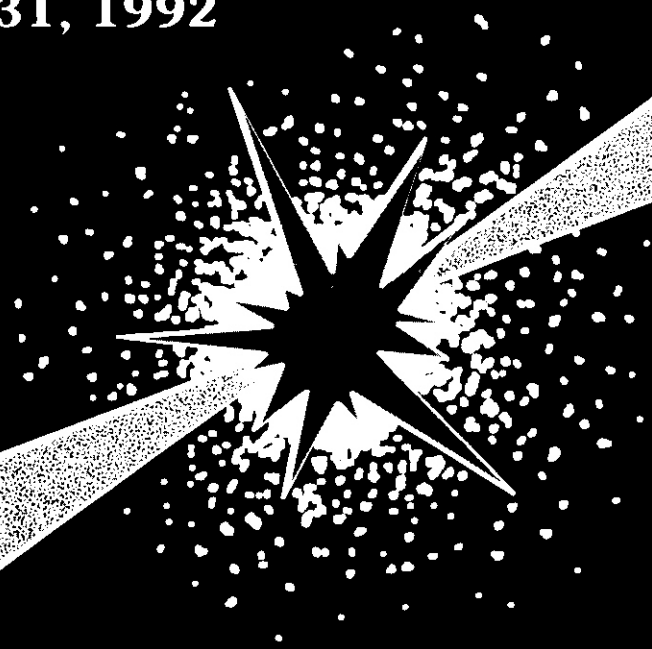

U. S. Department of Energy
Office of Fusion Energy

DOE/ER-0313/12
Distribution
Categories
UC-423, -424

FUSION REACTOR MATERIALS
SEMIANNUAL PROGRESS REPORT
FOR THE PERIOD ENDING
MARCH 31, 1992

Prepared for
DOE Office of **Fusion** Energy
(AT 15 02 03 A)

DATE PUBLISHED: JULY 1992

Prepared for
OAK RIDGE NATIONAL LABORATORY
Oak Ridge, Tennessee 37831
Managed by
MARTIN MARIETTA ENERGY SYSTEMS, INC.
for the
U.S. DEPARTMENT OF ENERGY
under contract DE-AC05-84OR21400

FOREWORD

This is the twelfth in a series of semiannual technical progress reports on fusion reactor materials. This report combines research and development activities which were previously reported separately in the following progress reports:

- Alloy Development for Irradiation Performance
- Damage Analysis and Fundamental Studies
- Special Purpose Materials

These activities are concerned principally with the effects of the neutronic and chemical environment on the properties and performance of reactor materials; together they form one element of the overall materials programs being conducted in support of the Magnetic Fusion Energy Program of the U.S. Department of Energy. The other major element of the program is concerned with the interactions between reactor materials and the plasma and is reported separately.

The Fusion Reactor Materials Program is a national effort involving several national laboratories, universities, and industries. The purpose of this series of reports is to provide a working technical record for the use of the program participants, and to provide a means of communicating the efforts of materials scientists to the rest of the fusion community, both nationally and worldwide.

This report has been compiled and edited under the guidance of A. F. Rowcliffe and Frances Scarboro, Oak Ridge National Laboratory. Their efforts, and the efforts of the many persons who made technical contributions, are gratefully acknowledged. F. W. Wiffen, Reactor Technologies Branch, has responsibility within DOE for the programs reported on in this document.

R. Price, Chief
Reactor Technologies Branch
Office of Fusion Energy

Reports previously listed in this series are **as follows:**

DOE/ER-0313/1	Period ending September 30, 1986
DOE/ER-0313/2	Period ending March 31, 1987
DOE/ER-0313/3	Period ending September 30, 1987
DOE/ER-0313/4	Period ending March 31, 1988
DOE/ER-0313/5	Period ending September 30, 1988
DOE/ER-0313/6	Period ending March 31, 1989
DOE/ER-0313/7	Period ending September 30, 1989
DOE/ER-0313/8	Period ending March 31, 1990
DOE/ER-0313/9	Period ending September 30, 1990
DOE/ER-0313/10	Period ending March 31, 1991
DOE/ER-0313/11	Period ending September 30, 1991

CONTENTS

The Fe-Cr-Mn alloy system is being studied as an alternative to the Fe-Cr-Ni system because of the need to reduce long-term radioactivation in fusion-power devices. In this study, four Fe-12Cr-XMn (X = 15, 20, 25, 30 wt %) alloys were irradiated in the Fast Flux Test Facility to 20 dpa at 643 K and 40 dpa at 679. 793, and 873 K to investigate the influence of manganese content on void swelling and phase stability. The results confirm and expand the results of earlier studies that indicate that the Fe-Cr-Mn system is relatively unstable compared lo that of the Fe-Cr-Ni system. with alpha and sigma phases forming as a consequence of thermal aging or high-temperature irradiation.

Additions of silicon and aluminum suppress the neutron-induced swelling of pure nickel but to different degrees. Silicon is much more effective initially when compared to aluminum on a per-atom basis, but silicon exhibits a non-monotonic influence on swelling with increasing concentration. Silicon tends to segregate toward grain boundaries while aluminum segregates away from these boundaries. Whereas the formation of the Ni_3Si phase is frequently observed in charged particle irradiation experiments conduted at much higher displacement rates. it did not occur during neutron irradiation in this study. Precipitation also did not occur in Ni-5Al during neutron irradiation. nor has it been reported to occur during ion irradiation.

A procedure for determining the Burgers vector anisotropy in irradiated ferritic steels is described. allowing identification of all a<100> and all (a/2)<111> dislocations in a region of interest. The necessary micrographs to apply the procedure have been taken of two pressurized tube specimens of JFMS. a duplex ferritic steel following irradiation in FFTF/MOTA at 407°C to 7.5 X 10^{22} n/cm^2 (E > 0.1 MeV) or 37.5 dpa. Preliminary analysis of one set of micrographs indicates large anisotropy in Burgers vector populations for an 86 MPa stressed condition.

Ferriticlmartensitic steels are candidate structural materials for fusion reactors because of their higher swelling resistance, higher thermal conductivity, lower thermal expansion, and better liquid-metal compatibility than austenitic steels. Irradiation effects will ultimately determine the applicability of these steels, and the effects of irradiation on microstructure and swelling and on the tensile, fatigue. and impact properties of the ferriticmartensitic steels are discussed. Most irradiation studies have been carried out in fast reactors. where little transmutation helium forms. Helium has been shown to enhance swelling and affect tensile and fracture behavior. making helium a critical issue, since high helium concentrations will be generated in conjunction with displacement damage in a fusion reactor. These issues are reviewed to evaluate the status of ferriticlmartensitic steels and to assess the research required to insure that such steels are viable candidates for fusion applications.

Reanalysis of an earlier data set derived from irradiation of long creep tubes in EBR-II at 550°C has shown that the creep-swelling coupling coefficient is relatively independent of temperature at approximately 0.6×10^{-2} MPa^{-1}, but falls with increases in the swelling rate especially at high stress levels. The action of stress-affected swelling and carbide precipitation exert different influences on the derivation of this coefficient.

Analysis of creep data for 20% cold-worked 316 stainless steel irradiated in FFTF/MOTA demonstrates that the creep-swelling coupling coefficient is not a strong function of temperature and can be assumed to be approximately 0.6 X 10^{-2} MPa^{-1} in the range 400-600°C. It appears, however, that the creep compliance B_o is a moderately strong function of displacement rate, especially at lower irradiation temperatures. It also appears to be a function of temperature and alloy composition. The latter dependency arises primarily because derived values of B_o unavoidably incorporate precipitation-related strains that cannot be easily separated from contributions arising from true creep. It has also been found that at approximately 550-600°C there is an upper limit on the total diametral strain rate at 0.33%/dpa. In contrast to the conclusion of an earlier experiment, this limitation does not arise initially from the total disappearance of creep, however. The creep rate first increases with the onset of swelling and then diminishes as the swelling rate increases, disappearing only when the swelling rate reaches its steady state value.

The austenitic stainless steel prime candidate alloy (PCA) is a titanium-modified alloy (14Cr-16Ni) developed for void swelling resistance at 400 to 600°C by the U.S. Fusion Reactor Materials (FRM) program. During irradiation in the High Flux Isotope Reactor (20-70 appm Heidpa) at 300-600°C, the PCA (and the closely related D9-type alloys) has been shown to be highly susceptible to void swelling at 500°C after 34-57 dpa. Generally such alloys show good void swelling resistance to higher doses during irradiation in fast-breeder reactors (FBRs, 0.5-1 appm Heidpa) in the 20-25% cold-worked condition. New multiply stabilized. phosphorus-modified PCA alloys have been dcvcloped, with specific amounts and combinations of minor alloy elements added for better MC formation and stability characteristics during irradiation. After HFIR irradiation at 300-500°C to 34-57 dpa, the multiply stabilized, phosphorus-modified PCA and phosphorus-modified D9 alloy showed better swelling resistance (by density-change measurements) than similar alloys without phosphorus, particularly at 500°C. Microstructural studies after 34 dpa at 500°C showed that void swelling resistance in the multiply stabilized, phosphorus-modified PCA alloys was directly related to the formation of ultrafine dispersions of MC precipitates during HFIR irradiation.

Disk specimens of the molybdenum alloy TZM that had been stress relieved at 1199 K (926°C) for 0.9 ks (15 min) were irradiated in the FFTF/MOTA 1F at 679, 793, and 873 K (406, 520, and 600°C) to a fast fluence of approximately 9.6 X 10^{22} n/cm^2. Microstructures were observed in a transmission electron microscope (TEM). Dislocation structures consisted of isolated loops, aggregated loops (rafts) and elongated dislocations. The size of the loops increased with the irradiation temperature. Void swelling was about 1 and 2% at 793 and 873 K (520 and 600°C), respectively. A void lattice was developed in the body centered cubic (bcc) structure with a spacing of 26 to 28 nm. The fine grain size (0.5 -2 μm) was retained following high-temperature irradiation, indicating that the stress relief heat treatment may extend the material's resistance to radiation damage up to high tluence levels. Microhardness measurements indicated that irradiation hardening increased with irradiation temperature. The relationship between the microstructure and the observed hardening was determined.

A commercial dispersion-slrcngthened Cu-Al_2O_3 alloy was irradiated with 750-MeV protons at 470 K to a damage level of about 2 displacements per atom. The density and size distribution of the Al_2O_3 particles was measured in nonirradiated and irradiated specimens using transmission electron microscopy. The mean primary knock-on atom (PKA) energy for 750-MeV protons in copper is 2.5 MeV, which is about 10 and 100 times higher than the average PKA energies in copper for fusion and fission neutrons. respectively. The irradiation caused only a slight decrease in the mean Al_2O_3 size, from 10.5 nm to 8.3 nm and a slight decrease in the particle density from 4 to $3 \times 10^{22}/m^3$. These results suggest that Cu-Al_2O_3 alloys. which are resistant lo radiation-induced microstructural changes during fission neutron irradiation, may also be microstructurally stable in a fusion neutron environment.

High purity copper containing approximately 100 appm helium was produced in two ways. In the first. helium was implanted by cyclotron at Harwell at 323 K. In the sewnd method, helium was produced as a transmutation product in 800 MeV proton irradiation at Los Alamos. also at 323 K. The distributions of helium prior to fission neutron irradiation were determined by a combination of transmission electron microscopy (TEM) and positron annihilation techniques (PAT). These specimens. together with pure copper. were then irradiated with fission neutrons in a single capsule in Fast Flux Test Facility (FFTF) at approximately 686 ±5 K to a dose level of approximately 48 dpa (7.7×10^{26} n.m.$^{-2}$; E > 0.1 MeV). Investigation of the void and dislocation microstructures in the three specimens by TEM showed large differences between the specimens in void size and swelling. The observed differences as well as the effect of the presence of other transmutation-produced impurity atoms in the 800 MeV proton irradiated copper will be discussed,

A variety of solute and precipitation strengthened copper base alloys have been irradiated to neutron-induced displacement levels of 34 to 150 dpa at 415°C and 32 dpa at 529°C in the Fast Flux Test Facility to assess their potential for high heat flux applications in fusion reactors. Several MZC-type alloys appear to offer the most promise for further study. For low fluence applications CuBeNi and spinodally strengthened CuNiTi alloys may also he suitable. Although Cu-2Be resists swelling, it is not recommended for fusion reactor applications because of its low conductivity.

Tensile tests and fractography were used to examine the radiation-induced evolution of Cu-5Ni and three commercially prepared precipitation-strengthened alloys after irradiation at 685 and 800 K (411 and 527°C). The addition of nickel to copper resulted in increased ductility prior to irradiation but decreased relative ductility after irradiation. The difference in behavior following irradiation appears to arise from the influence of nickel on void swelling. The precipitation-strengthened alloys in general exhibited a drop in yield strength after irradiation and an associated increase in ductility. The major effect in these alloys appeared to be related to overaging of the precipitates.

The results of this analysis suggest that H-induced crack growth of Type 316 SS is a definite concern for ITER first-wall applications. It was estimated that crack velocities as high as 2×10^{-6} m/s could result in Type 316 SS irradiated at 100°C to 10 dpa, while the threshold, K_{th}, for crack growth could be as low as 28 to 37 MPa$\sqrt{m}$ for hydrogen generated by (n,p) reactions. This crack velocity would propagate through a 4-mm-thick first wall in 33 min, and therefore these conclusions should be evaluated experimentally. Also, a K_{th} of 28 MPa$\sqrt{m}$ requires that the applied and residual stresses in the structure be limited to 500 MPa for a I-mm-long crack to avoid H-induced crack growth. Higher stress limits are possible for shorter cracks. These predictions are based on the assumption that all the H generated by (n,p) reactions would be contained within the material; however, some loss of H to the vacuum or water side of the first wall is expected. The extent of this loss will depend on engineering considerations such as coatings, etc.

Susceptibility of Types 316NG and sensitized 304 stainless steels (SS) to SCC was investigated at temperatures of 60-289°C in slow-strain-rate-tensile (SSRT) tests in oxygenated water that simulates important parameters anticipated in first-wall/blanket systems. Type 316NG SS exhibits good resistance to SCC under crevice and noncrevice conditions at temperatures <150°C in nominal ITER coolant chemistry that does not contain any short-lived radical species from radiolysis of water. Initial SSRT tests have been conducted on weldment specimens of Type 316NG SS with matching filler metal under crevice and noncrevice conditions in oxygenated water at 95°C. These specimens fractured in the base metal rather than in the weld or heat-affected zones.

In this work, we characterized radiation-induced grain-boundary segregation of commercial-purity (CP) and high-purity (HP) Type 304 SS irradiated in a fission power reactor at 288°C to 2×10^{21} n/cm^2 (E > 1 MeV) or about 1 dpa using both high-resolution AEM and Auger electron spectroscopy (AES). Both AEM and AES showed strong nickel and silicon enrichment along with moderate chromium depletion at grain boundaries in the CP material. Chromium and nickel segregation, measured both by AEM and AES, were less in the HP material. No statistically significant minor element segregation was measurable with either AEM or AES. Good agreement between AEM segregation profiles measured perpendicular to grain boundaries and AES sputter-depth profile results was obtained.

The electrochemical behavior and microstructural evolution of a solution-annealed. heavy-ion-irradiated. austenitic stainless steel (SS) have been investigated at temperatures above 600°C at doses of 1, 10, and 70 displacements per atom with concurrent helium injection of 0.2 at. ppm He per dpa. Changes in the electrochemical properties were measured by the single-loop electrochemical potentiokinetic reactivation (SL-EPR) technique using transmission electron microscopy disk specimens. Microchemical analysis has also been performed on some duplicate specimens in an AEM. Electrochemical results showed that the reactivation charge per unit etched area and Flade potential increased with increasing dose. In the case of the 70 dpa specimen, complete passivation of the specimen could not be obtained. AEM microanalysis showed changes in composition at both grain boundaries and faulted dislocation loops of chromium, iron, nickel, and silicon due to RIS.

Fe-Cr-Mn steels may possibly be used in conjunction with aqueous blankets or coolants in a fusion device. Therefore, standard chemical immersion (modified Strauss) tests were conducted to characterize the effects of compositional modifications on the thermal sensitization behavior of these steels. A good correlation among weight losses, intergranular (IG) corrosion, and cracking was found. The most effective means of decreasing their susceptibility was through reduction of the carbon concentration of these steels to 0.1%, but the sensitization resistance of Fe-Cr-Mn-0.1C compositions was still inferior to type 304L and other similar stainless steels (SS). Alloying additions that form stable carbides did not have a very significant influence on the sensitization behavior.

A method for removal of nitrogen from liquid lithium has been investigated that allows nitrogen purification to be done at temperatures below 500°C. The method utilizes the formation of an insoluble, ternary compound on chromium-plated stainless steel surfaces lo remove nitrogen. Capsule tests established the initial feasibility of the method and determined optimum warm-trapping parameters for a large-scale batch test. Favorable results from capsule tests were obtained with processing temperatures of 450°C and chromium surface area-to-lithium volume ratios greater than 100 m^{-1}. Nitrogen levels as low as 37 weight parts per million were achieved in less than 30 h at 450°C by using a staged. large-scale batch process. When used in conjunction with conventional cold trapping, the method allows lithium purification to be done in a single, inexpensive vessel with a higher degree of safety, as compared to higher temperature methods (e.g., hot gettering).

The BEATRIX-II irradiation experiment is an in-situ tritium release experiment lo evaluate the stability and tritium release characteristics of Li_2O under fast neutron irradiation to extended burnups. A thin annular ring specimen capable of temperature changes was irradiated in Phase I of the experiment to a lithium burnup of 5%. The primary emphasis of the test plan was to determine the effect and interrelationship of gas composition and temperalure on the tritium recovery from Li_2O. Temperature changes in the range from 500 to 650°C resulted in a decreasing tritium inventory with increasing temperature and a series of specific temperature changes were carried out at intervals throughout the experiment to characterize the effect of burnup. Decreasing the amount of hydrogen in the sweep gas resulted in an increase in the tritium inventory in the Li_2O specimen. The tritium recovery during startup and shutdown was observed to be strongly influenced by the composition of the sweep gas.

The results lrom recent studies on radiation-induced changes in the electrical conductivity, loss tangent. and thermal conductivity of ceramics are reviewed, with particular emphasis on in situ data obtained during irradiation. The in situ measurements have found that the physical property degradation during irradiation is generally much more severe than indicated by post-irradiation mcasurcments. In particular, permanent degradation in the clectrical resistivity may occur after irradiation to damage levels of $<10^{-3}$ displacements per atom (dpa) for temperatures near 450°C. This radiation-induced electrical degradation (RIED) is observed only if an electric field is applied during the irradiation.

Anticipated radiation fluxes in D-T burning machines such as BPX and ITER arc intense, and accumulated damage levels are moderate to severe. Thus materials used in diagnostic systems may suffer significant degradation of electrical. optical, and structural properties, either lrom transient or permanent damage effects. Of particular concern arc windows, optical fibers, reflectors, and insulators. However, materials design and modification based on results from an appropriate irradiation testing program, when combined with design optimization for location. shielding. and ease of replacement, should point the way to development of acceptable materials systems.

1.0 IRRADIATION FACILITIES, TEST MATRICES, AND EXPERIMENTAL METHODS

PREPARATION AND IRRADIATION OF FUSION MOTA 28 - M. L. Hamilton, R. M. Ermi (Pacific Northwest Laboratory)' and A. M. Ermi (Westinghouse Hanford Company)

OBJECTIVE

The purpose of this effort is to document the loading of the Fusion Materials Open Test Assembly (MOTA 28) into the Fast Flux Test Facility (FFTF) for irradiation in cycle 12.

SUMMARY

MOTA 28 was built to support the research and development efforts of three fusion materials programs: the U.S. DOE Neutron Interactive Materials (NIMs) program, the Japanese university fusion materials program, and the IEA-sponsored BEATRIX-II experiment. The MOTA was inserted into the FFTF for irradiation beginning in cycle 12. Irradiation has been completed successfully through cycle 128.2. Both the specimen loading and the history of cycle 12 to date are documented here.

PROGRESS AND STATUS

Introduction

The MOTA type of irradiation vehicle provides the U.S. and international materials community with the unique capability of performing instrumented, temperature controlled, fast neutron irradiation experiments in the FFTF. The first such vehicle devoted exclusively to the needs of the fusion materials community was referred to as MOTA 28; this is the second such vehicle. The same three partners participated in the irradiation of MOTA 28 as participated in MOTA 2A:[1] the U.S. NIMs program, the Japanese university fusion materials community (funded by the US/Japan Collaborative Program on Fundamental Studies of Irradiation Effects in Fusion Materials Utilizing Fission Reactors), and the IEA-sponsored BEATRIX-II program. The loading of the Fusion MOTA was tailored to meet the needs of each partner. The goal of the NIMS and the Japanese programs is to develop improved materials for use in many different components of proposed fusion devices and to facilitate the prediction of their performance limits in a fusion environment. These programs focus on metallic or ceramic specimens for post-irradiation determination of swelling, mechanical properties and microstructure. The goal of BEATRIX-II is to characterize the tritium release behavior of fusion-relevant solid breeder materials during fast neutron irradiation. It is primarily an in situ tritium recovery experiment that focuses on the irradiation behavior of Li_2O under a variety of temperature and purge gas conditions.

MOTA Loading

Canister Allocation. The canister matrix for MOTA 28 is shown in Table 1. The numbers given vertically indicate the axial level of the canister (below core through row 8), while the alphabetic designations refer to the radial position around the MOTA stalk (A through F). The box for each occupied canister indicates the irradiation temperature and the program using the canister. Two additional programs, the U.S. isotope production program and the Japanese breeder reactor materials program, utilized some of the unused IEA canisters. Specimens for the high heat flux program were also included where space was available. A "W" in the lower left corner of the box indicates that the canister is a weeper without temperature control; the absence of a "W" indicates that the canister is gas gapped to control temperature. Information relevant to the thermocouples, such as their absence or their offset location, is given in brackets.

Dosimetry Specimen Matrix. The dosimetry loaded into MOTA 28 is given in Table 2. Spectral sets, gradient sets and helium accumulation fluence monitors (HAFM) were used. Each entry in the table comprises the canister basket followed by a colon and the dosimetry specimen identification code, and the dosimetry type in parentheses. The relative physical location of the dosimetry specimen in a given canister is indicated by the relative placement of the entry in the box corresponding to the canister.

BEATRIX-II Specimen Matrix. The specimen matrix for BEATRIX-II is summarized in Table 3. The experiment includes the irradiation of two in-situ tritium recovery capsules containing either a Li_2O ring or a Li_2ZrO_3 sphere bed. The ring specimen is located in a vented canister (1B) capable of incrementally imposing large temperature changes. It is vented to allow the recovery of tritium via a sweep gas flowing through the canister. This specimen will provide data on the kinetics of tritium release through variations in temperature, burnup, and sweep gas flow rate and composition. The Li_2ZrO_3 sphere bed specimen is also located in a vented canister (2C) that operates under a large temperature gradient to investigate the thermal stability of Li_2ZrO_3. The Li_2ZrO_3 sphere bed irradiation is more prototypic of the conditions expected in a fusion blanket, with an initial centerline temperature approaching 1100°C. The nonvented

---

'Pacific Northwest Laboratory is operated for the U.S. Department of Energy by Battelle Memorial Institute under Contract DE-AC06-76RLO 1830.

Table 1. MOTA-2B Canister Matrix

[Rev. 13; January 15, 1991]

	A	B	C	D	E	F	Nominal Mid-Canister Fast Fluence (10^{22} n/cm^2)
8		440°C US/JPN					0.045
7		435°C US/JPN					0.17
6	430°C US (HHF) I [offset]	430°C US/JPN	430°C JPN (HHF) W [offset]	430°C US (HHF) W [offset]	430°C JPN (HHF) W [offset]	430°C US (HHF) W [No TC]	0.54
5	495°C PNC	600°C 3/4 US 1/4 PNC	600°C US/JPN (DHCE)	500°C US/JPN (DHCE)	425°C 1/2 JPN 1/2 US/JPN (DHCE) W	425°C 1/2 US(HHF) 1/4 JPN 1/4 IEA W [offset]	3.5
4	425°C ISOT (hhf) / [No TC]	425°C 1/4 JPN 1/4 PNC 1/2 Be	600°C 3/4 US 1/4 PNC	425°C 1/2 US/JPN (DHCE) 1/2 JPN W	520°C JPN	600°C US	6.3
3	420°C US /	670°C PNC	420°C IEA W [offset]	420°C US W	520°C JPN	600°C JPN	1.5
2	520°C US	550°C 3/4 Be 1/4 PNC	400-1000°C IEA-Solid (in situ) W [3 TCs]	800°C JPN	410°C JPN W	520°C US	6.8
1	390°C JPN W	500-650°C IEA-Ring (In situ) 13 TCs]	390°C US W	520°C US	600°C US	460°C JPN	3.9
IC	365°C 112 Be 1/2 ISOT W [No TC]	365°C IEA (hhf) [offset]	365°C US W	365°C US W	365°C JPN W	410°C JPN	1.2

; = U.S. Fusion Program
'N = Japanese HONBUSHO Program
A = I.E.A. BEATRIX-II Experiment
ICE = Dynamic Helium Charging Experiment
IF = High Heat Flux Program
If = High Heat Flux Type Subcapsule

Be = U.S. Beryllium Irradiation
PNC = Japanese PNC Program
ISOT = Isotopes Program
W = Weeper
[offset] = Offset Thermocouple

canisters (5F and 8B) contain a ceramic solid breeder in contact with beryllium specimens for the evaluation of chemical compatibility.

Dynamic Helium Charging Experiment (DHCE). The DHCE was developed jointly by the U.S. and Japanese MOTA partners to provide baseline irradiation data on the effects of concurrent helium production and neutron irradiation on the physical and mechanical properties of vanadium alloys.' Both mechanical and microscopy specimens were encapsulated in TZM capsules filled with lithium that was enriched in ^{6}Li. The use of 'Li in conjunction with the initial tritium present in a piece of doped vanadium was designed to produce a helium-to-dpa ratio that is both fusion-relevant and approximately constant over the course of the irradiation, As is shown in Table 1, the space allocated for the DHCE was shared jointly by the U.S. and Japanese MOTA partners. Details on the loading of the experiment are given in Reference 2.

U.S. NIMs Specimen Matrix. The objective of the U.S. NIMs program is to develop improved materials for use in fusion devices and predict their performance limits in a fusion environment. The long term effort focuses on providing an increased understanding of damage mechanisms through experiment, data analysis and

Table 2. Dosimetry Placement in Fusion MOTA-2B
[Basket: ID code (Type)]

	A	B	C			F
8		881:C01(SH) 8B4:C20(G)				
7		7B4:C14(S)				
6		6B4:C15(S)				
5	5A2:C23(G)	582:C03(SH)		5D1:C24(G)		5F2:C25(G)
4		483:c17(S)	4C2:C31(G)			4F3:C33(G)
3	3A4:C36(G)	382:C19(S)		3D6:C05(SH)		3F4:C35(G)
2	2A1:C29(G)	2B4:C18(S)		2D1:C30(G)	2E5:C32(G)	2F2:C34(G)
1	1A3:C38(G)		1C3:C04(SH)		1E1:C28(G)	
B C C			BCC1:C21(G) BCC5:C02(SH)	BCD5:C22(G)	BCE4:C16(S)	BCF4:C37(G)

(G) = 0.885" long gradient set
(S) = 0.885" long spectral set
(SH) = 0.993" long spectral t HAFM set
Cxx = dosimetry ID code

modelling. A short term effort is focussed on meeting the near-term materials needs for the International Thermonuclear Experimental Reactor (ITER).

A summary of the U.S. specimen matrix is shown in Table 4. The geometries of the U.S. and Japanese specimens are listed in Table 5. The U.S. specimen matrix contains specimens from four national laboratories: Pacific Northwest Laboratory (PNL), Oak Ridge National Laboratory (ORNL), Idaho National Engineering Laboratory (INEL) and Argonne National Laboratory (ANL). In addition, there are spetimens supplied by American, European, Russian and Japanese scientists engaged in collaborative research with U.S. staff.

The emphasis is primarily on (but is not limited to) alloys for first wall/blanket applications. Major areas include 1) supplying high fluence engineering data for current or potential fusion candidate heats of

Table 3. BEATRIX-II Specimen Matrix

MOTA Canister	Target Temperature (°C)	Vented	Material	Enrichment (%)	Purpose
1B	Variable (gas gapped)	Yes	Li_2O ring	95	T release, thermal conductivity
2t	Gradient (weeper)	Yes	Li_2ZrO_3 sphere bed	85	T release, thermal stability
5F	425 (weeper)	No	Be disks alternating with disks of Li_2O, Li_2ZrO_3, Li_4SiO_4, and $LiAlO_2$	0.2	Compatibility of Li ceramics and Be
8B	440 (weeper)	No	Be disks alternating with disks of Li_2O, Li_2ZrO_3, Li_4SiO_4, and $LiAlO_2$	0.2	Controls for compatibility study

ferritic and austenitic steels, 2) exploring reduced activation alloys of several types (austenitic and ferritic iron-based steels as well as vanadium alloys), 3) the development of copper alloys for high heat flux applications and an understanding of their fundamental radiation response, and 4) clarifying the role of helium. Smaller efforts are directed toward the development of beryllium for neutron multiplier or plasma interactive components and the development of composite materials for high heat flux and structural applications.

Monbusho Specimen Matrix. The Japanese university program for the development of fusion reactor materials is using the FFTF/MOTA as part of a larger program to attain an understanding of the various radiation responses that control materials' behavior. Specifically, their program is designed 1) to establish correlations between high and low exposure irradiations in fission and fusion neutrons and 2) to determine the mechanisms governing microstructural and microchemical evolution and their relation to property changes in materials.

Six sub-groups have been designated responsible for such efforts for different classes of materials:

a) Ferrous materials.
b) Refractory metals'and alloys, high heat flux materials,
c) Pure metals and model alloys for fundamental studies,
d) Isotopic tailoring experiments,
e) Ceramics and composite materials, and
f) Dosimetry.

A summary of the Japanese matrix is given in Table 6. Their program areas are somewhat similar to those of the U.S. Major areas include the characterization of candidate austenitic and ferritic alloys, the development of low activation alloys of several types, and a consideration of high heat flux materials, as well as a significant fundamental effort to provide a mechanistic understanding of radiation damage in many materials.

Cvcle 12 Operation

Figures 1a and 1b show the reactor's power history during cycles 12A and 128 in the form of a temperature history of the in-core coolant thermocouple c2 in level 3 of MOTA 28. Each cycle was nominally 100 days in duration, with each comprising two shorter 50-day segments referred to with the suffixes -1 and -2. Temperature histories for individual canisters mirror the reactor power history. The gas gapped canisters were placed under the control of the MOTA instrumentation when the reactor power level reached 75%.

The startup of cycle 12A-2 was slightly irregular due first to some transient tests performed at low temperatures and at up to 8% power, and second to the need to correct two problems that surfaced with other components during the startup. Passive safety tests at low power and reactivity calibrations were performed at low temperatures prior to the startup of cycle 12B-1. Gas gapped canister temperatures were maintained during the power coefficient test that was run several days into the start of each of the 50-day cycles; these tests entailed a brief drop to 85% power, during which time the temperature of the weeper canisters dropped slightly.

Tables 7 and 8 give the time-averaged temperature data for MOTA 28 during cycles 12A and 128. Time-averaged temperatures were calculated using only temperatures greater than or equal to 20°C below the target temperature. Since temperatures other than this usually indicated a reactor shutdown condition, the calculated values provide the average temperature at or near full power. Both the average temperature and the time at temperature are included for temperatures above (T_{target}-20°C) and below (T_{target}-20°C). The

latter is included since significant times can be realized at lower temperatures during startups, etc. Note that these averages do not include temperatures less than 300°C since temperatures below this value indicate a very low power or reactor shutdown condition.

Table 4. Summary of NIMs Specimens in MOTA 2B

ype of pecimen	Alloy	T_i (°C) 365	395	420	495	520	600	800
ensile	Ferritic:							
	HT9 - Very low dose	P[a]						
	- High dose	P		P		P	P	
	- TMT variations	O[a]		O		O	O	
	9Cr1Mo - TMT variations	O		O		O	C	
	Fe-Cr binaries	P		P				
	Low activation ferritic:							
	37xx series	O						
	GA#X series	P		P		P	P	
	F82H	P		P		P	P	
	Austenitic:							
	316	C		O		O	O	
	Low activation austenitic:							
	High Mn PCMA-x series	O		O		C	C	
	Russian Fe-Cr-Mn	O		O		O	C	
	Vanadium alloys:							
	DHCE			A[a]	A		A	
	Standard			A		A	A	
	Tritium tricked			O		O	O	
	JPCA/JFMS (Size effects)			P		P		
	Helium effects:							
	^{59}Ni						P	
	Nickel-doped ferritics		C					
	copper alloys	P	P	P				
	Copper brazer	P	P	P				
harpy[b]	Ferritic:							
	HT9 - Very low dare	P						
	- High dose	P	P	P		P		
	- TMT variations		O	O				
	- Size effects	C						
	9Cr1Mo - High dore					P		
	- TMT variations		O	O		O	O	
	2¼Cr	O						
	Low activation ferritic:							
	37xx series	O	C					
	GA#X series	P	P	P		P		
	F82H	P	P	P		P		
	Vanadium alloys:							
	Standard			A		A	A	
ompact Tension	Ferritic:							
	HT9 - High dare	P	P	P		P	P	
	Lou activation ferritic.							
	GAXX series	P	P	P		P	P	
	F82H	P	P	P		P	P	
ressurized Tube	Ferritic:							
	HT9, modified HT9	P		P	P	P	P	
	9Cr1Mo			P		P	P	
	FeCr binary			P		P		
	Low activation ferritic:							
	GAXX series			P	P	P		
	F82H			P	P	P		
	ODS			P		P		
	Austenitic							
	316			C		O		
	PCA			O,P	P	O	O	
	Low activation austenitic:							
	Russian Fe-Cr-Mn			P		P	P	

Continued on next page..

Table 4. Summary of NIMs Specimens in MOTA 28 - continued

Type of Specimen	Alloy	365	395	420	495	520	600	800
TLH	**Austenitic:**							
	PCA. 316	P	P	O		O	O	
	Low activation austenitic:							
	High Hn PCMA-x series	O		O		O	O	
	Russian Fe-Cr-Mn			O,P		O,P	O,P	
	AHCR variants			P		P	P	
	Fe-Cr-Mn			P		P	P	
	Ferritic.							
	HT9 - Low dose	P						
	- **High dose**[c]	P	P	P	P	P	P	
	9Cr1Mo - **High dare'**	P	P	P	P	P	P	
	FeCr binary	P		P		P	P	
	Low **activation ferritic:**							
	GAXX series	P	P	P		P	P	
	F82H	P	P	P		P	P	
	9Cr2W, Fel0Cr-X	P		P		P	P	
	ODS	P		P		P	P	
	Fe-XCr-W			O				
	V02xxx **series**	P	P					
	Capper alloys and brazes	P,O	P,O	P,O		P,O	P,O	
	Vanadium alloys:							
	OHCE			A	A		A	
	Standard			A		A	A	
	Tritium tricked			O		O	O	
	Helium effects:							
	^{58}Ni						P	
	Ceramics			O				O
	Dynamically compacted SS, W			P		P	P	
	Pure Ni	P		P		P	P	
Miscellaneous								
Bend bars	SiC/SiC							O
CCT	HT9, 9Cr1Mo		P				P	
Compression	Beryllium[d]	I[a]		I				
Density ring	316, PCA			O	O	O		
Disk	Graphite or C/C composites			P				
	Ceramics							O
Fibers	SiC			P,O				O
	C			P				
Punch	Low **activation ferritic.** HT9, **FeCr binary**	P				P	P	

[a] P: PNL, O: ORNL, A: ANL, I: INEL
[b] All specimens are 1/3 size except for those in size effects study, which included 1/2 size specimens
[c] Also at 670°C
[d] Also at 550°C

CONCLUSIONS

The second fusion MOTA (28) was successfully prepared and inserted into the FFTF **for** operation during cycle 12. The vehicle supports materials testing for the U.S. NIMs program, the comparable Japanese university fusion materials program and the IEA sponsored BEATRIX program, as well as the high heat flux, Japanese breeder, and U.S. isotope programs.

FUTURE WORK

Planning will continue for both post-irradiation testing of MOTA 2B specimens and the loading for MOTA 2C.

Table 5. U.S. and Japanese Fusion Specimen Geometries in MOTA 2B

Specimen Type	Geometry	Nominal Mass (gm)	Dimensions (in.)
0.256 in. Swelling lube	Open tube	0.90	0.256 dia. x 0.375 long
0.160 in. Creep Tube	Pressurized tube	0.63	0.180 dia. x 0.86 long
0.230 in. Creep Tube	Pressurized tube	2.05	0.230 dia. x 1.11 long
SS-3 Tenrile	Sheet	0.48	0.195 x 0.030 x 1.00
SS-3 Tensile Modified	Sheet	0.70	0.400 x 0.030 x 1.00
Miniature Tensile	Sheet	0.06	0.100 x 0.010 x 0.5
Japanese Tensile (S)	Sheet	0.056	0.157 x 0.010 x 0.630
Japanese Tensile (W)	Sheet	0.786	0.315 x 0.020 x 1.280
0.630 in. Compact Tension	Disc	3.50	0.630 dia. x 0.10 thick
ANL/PNL 113 Size Charpy	Block	2.10	0.131 x 0.121 x 0.930
ORNL 1/3 Size Charpy	Block	2.24	0.131 x 0.131 x 1.0
ORNL 1/2 Size Charpy	Block	5.06	0.197 x 0.197 x 1.0
Japanese 1.5 mm Charpy	Block	0.354	0.059 x 0.059 x 0.187
Japanese 1/3 Size Charpy	Block	1.97	0.130 x 0.130 x 0.906
Bend Bars	Block	0.4	0.074 x 0.01 x 1.375
Fibers	Fiber	--	10μm dia. x 1.2 long
Ceramic Squarer	Square sheet	0.1	0.035 x 0.25 x 0.25
Miniature CCT Fatigue	Sheet	1.56	0.5 x 1.0 x 0.024
TEM Disc	Disc	0.014	0.118 dia. x 0.01 thick
High Heat Flux	Disc	10.1	0.630 dia. x 0.25 thick
0.12 in. Packet (SS)	Capped weeper tube	1.09	0.144 dia. x 0.72 long
0.88 in. Packet (SS)	Capped weeper tube	1.25	0.144 dia. x 0.88 long
1.14 in. Packet (SS)	Capped weeper tube	1.12	0.144 dia. x 1.14 long
1.14 in. Packet (SS)	Sealed tube	1.94	0.144 dia. x 1.14 long
1.58 in. Packet (SS)	Capped weeper tube	2.59	0.144 dia. x 1.58 long
Punch Packet (SS)	Capped weeper tube	5.00	0.500 dia. x 0.34 long
1.75 in. Subcapsule (TZM)	ti-filled tube	14.0	0.375 dia. x 1.75 long
2.05 in. Subcaprule (TZM)	ti-filled tube	14.6	0.375 dia. x 2.05 long
2.25 in. Subcapsule (TZM)	ti-filled tube	17.2	0.315 dia. x 2.25 long
2.4 in. Subcapsule (TZM)	ti-filled tube	14.4	0.375 dia. x 2.4 long
2.5 in. Subcaprule (TZM)	ti-filled tube	14.6	0.375 dia. x 2.5 long
0.71 in. Subcapsule (SS)	He-filled tube	3.6	0.370 dia. x 0.70 long
0.80 in. Subcapsule (SS)	He-filled tube	5.0	0.370 dia. x 0.60 long
1.5 in. Subcapsule (SS)	He-filled tube	6.2	0.310 dia. x 1.5 long
2.05 in. Subcaprule (SS)	He-filled tube	10.9	0.370 dia. x 2.05 long

REFERENCES

1. M. L. Hamilton and R. M. Ermi, "Preparation and Irradiation of the MOTA (2A)," Fusion Reactor Materials Semiannual Progress Report for Period Ending March 31, 1990, DOE/ER-0303/8, p. 3.

2. O. L. Smith, B. A. Loomis, H. Matsui, M. L. Hamilton, K. L. Pearce, J. P. Kopasz, C. E. Johnson, R. G. Clemmer and L. R. Greenwood, "Status of the Dynamic Helium Charging Experiment (DHCE) in FFTF/MOTA", Fusion Reactor Materials Semiannual Progress Report for Period Ending March 31, 1991, DOE/ER-0303/10, p. 159.

Table 6. Summary of Japanese Specimens in MOTA 2B

Type of Specimen	Alloy	355'	390	405-430	410[a]	460	50	520	600	700	30-440[c]
Tensile	Ferritic:										
	JFMS	S[b]	S	S,W[b]		S					
	HT9	S	S	S,W		i					
	ODS							S			
	Misc Fe alloys	S		S		S					
	Low Activation Ferritic:										
	ASx series			S,W							
	JLFx series	S	S	S,W		S		i			
	F82H		0[b]	S		S					
	NLFx series	S	S	S,W		S		S			
	Fe-(9-12Cr)-W		S	S		i		S			
	Austenitic										
	PCA/JPCA			0,S							
	316F		0	0							
	316	i									
	Low Activation Austenitic										
	Fe-Cr-Mn-X	S	S	S				S			
	JHMx **series**	S	S	S		S		S			
	Copper	S		S		S					
	Vanadium alloys										
	DHCL			S							
	Standard			S				S			
	Refractories of Yo. W, Re			5				S			
	Nickel			S							
	Zirconium alloys	i									
Charpy[c]	Ferritic:										
	HT9		S								
	ODS			5				5			
	Low Activation Ferritic										
	JLFx **series**	5	5	5.3		5					
	NLFx series		5	5							
	F82H		5								
	Fe-(9-12)Cr-2W-X		5	5		5					
	Law Activation Austenitic										
	JHMx **series**		5	5				5			
	Fe-Cr-Mn-x		5	5				5			
Rod/	Mo-Re, TZM			X				X			
Disk/											
Wafer/	91 alloy			X							
Foil/	C/Al	X			X			X			
Fiber/	SiC/Al	X			X	X					
Block/	Carbon, C/C			X		X		X			
Plate/	SiC										
Wire/	Graphite			X		X		X			
Coupon	AlN	X				X					
	$MgAl_2O_4$										
	Cu Alloys	X		X							
	Pyro Graphite										
TEM	Low activation ferritic	X	X	X		X	X	X			
	Misc. ferritic	X	X	X	X	X		X			
	Iron + iron alloys	X	X	X	X	X	X	X			
	Low activation austenitic	I	X	X		X	X	X			
	Misc. austenitic	I	X	X	X	X		X			
	Vanadium alloys -										
	Standard	X	X	X	X	X	X	X			
	DHCE			X			X				
	Copper and copper alloys	X			X	X	X				
	Pure metals, model alloys		X	X	X	X		X			
	Refractories of Mo, W, Re							X			

Continued on next page...

Table 6. Summary of Japanese Specimens in MOTA 2B - continued

Type of Specimen	Alloy	365[a]	390	405-430	410[a]	460	500	520	600	800	430-440[d]
TEM - cont.											
	Zr Alloys	X									
	Ti Alloys	X		X	X	X	X	X	X		X
	Ni Alloys	X		X	X	X	X				X
Pressurized Tube	Low activation ferritic:										
	ASx series			X		X		X			
	JLFx series			X		X		X			
	F82H		X	X		X		X	X		
	Austenitic:										
	PCA/JPCA		X	X		X		X	X		
	316F		X	X							
	Low activation austenitic:										
	HMNx series			X		X					
	Fe-Cr-Mn		X					X	X		

[a] Below core
[b] Dimensions of "S" and "W" specimens are given in Table 5; W specimens are twice the size of S specimens in each dimension.
[c] "3" refers to 1/3 size charpy specimens and "5" refers to 1.5 mm charpy specimens. Dimensions of both types of charpies are given in Table 5.
[d] Above core

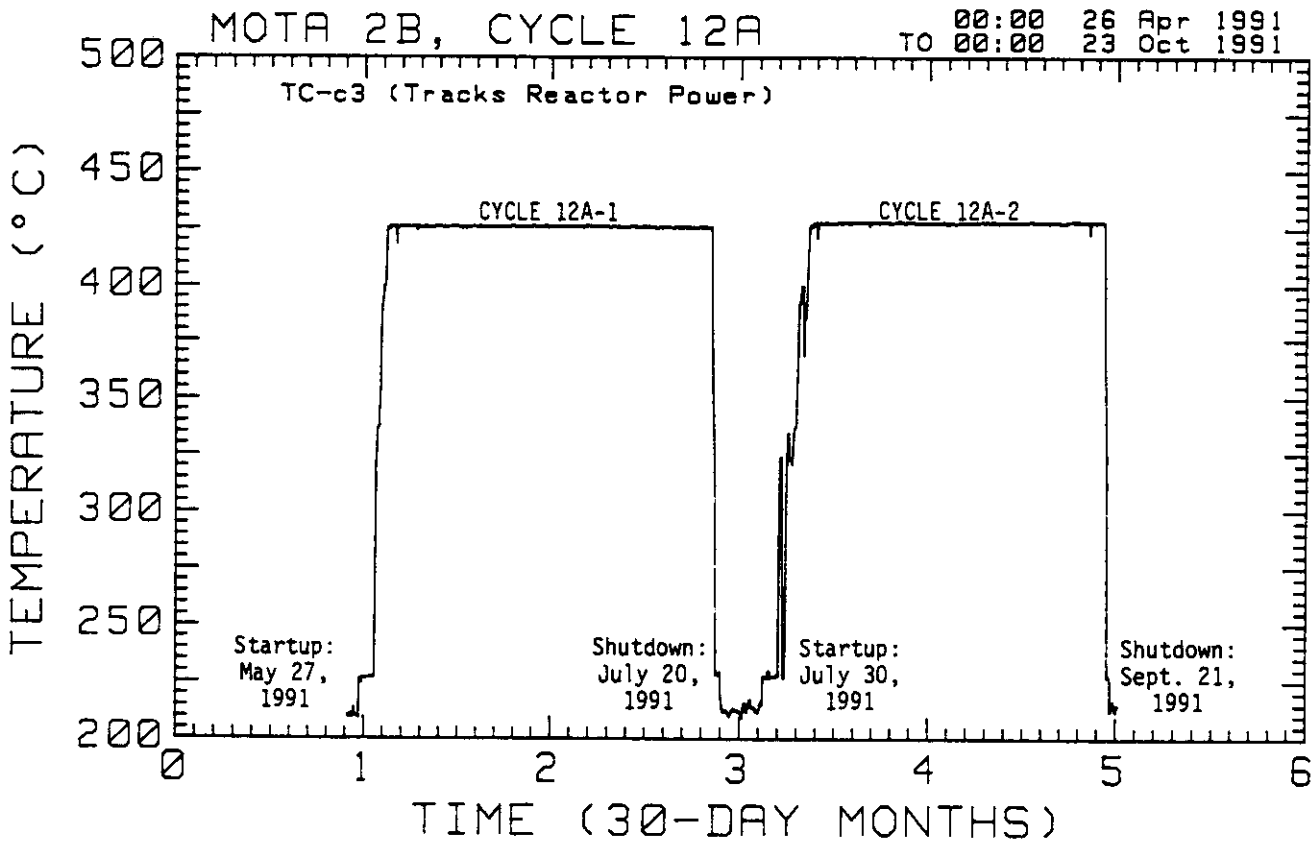

Figure 1a. Reactor's power history during FFTF cycle 12A.

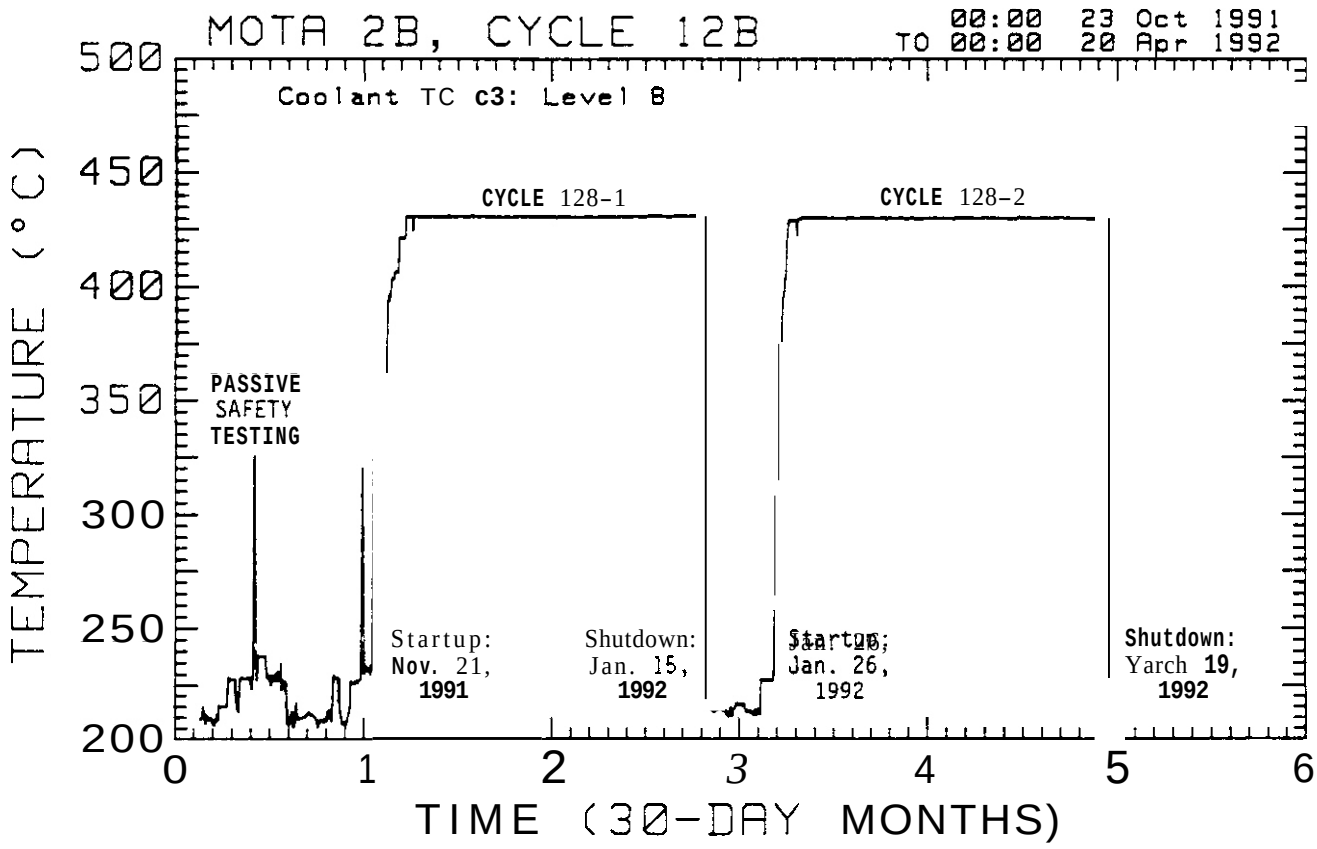

Figure lb. **Reactor's** power **history during** FFTF **cycle** 12B

Table 7. Temperature Data for MOTA 2B During Cycle 12A

27 May 1991 TO 21 Sep

anister r TC No	Type	Target Temp. (°C)+	Min. emp. °C)	Max. emp. °C)	Temp. < T_{targ}-20°C)* No. of Days	Temp. < T_{targ}-20°C)* Avg. Temp. (°C)	Ten T_{targ} No. of Days	> (°C) Avg. emp. °C)
la	Weeper	385	207	389	4.9	336	00.8	386
ıc	Weeper	395	207	400	5.2	338	00.5	392
Id	Gas-Gapped	520	209	534	5.8	365	00.0	519
le	Gas-Gapped	600	209	614	5.8	382	99.9	599
If	Gas-Gapped	460	208	471	5.7	356	00.1	461
1b	Gas-Gapped	35-645	208	654	**	**	**	**
1y	Outer lb	**	208	573	**	**	**	**
1z	Right lb	**	208	654	**	**	**	**
2c	Lower 2c	**	209	1074	**	**	**	**
2w	Outer 2c	385	207	386	4.2	330	101.5	383
2x	Nb-Mo TC	**	204	1116	**	**	**	**
2a	Gas-Gapped	520	209	532	5.8	373	100.0	519
2b	Gas-Gapped	550	210	563	5.8	379	99.9	549
2d	Gas-Gapped	800	210	816	5.9	432	99.9	800
2e	Weeper	405	207	410	5.6	345	100.2	406
2f	Gas-Gapped	520	209	533	5.8	372	100.0	519
3a	Weeper	435	208	440	6.2	357	99.5	432
3b	Gas-Gapped	670	210	684	5.9	400	99.9	670
3c	Weeper	400	208	399	6.1	346	99.6	397
3d	Weeper	425	208	430	6.2	355	99.5	426
3e	Gas-Gapped	520	210	533	5.8	375	99.9	519
3f	Gas-Gapped	600	210	613	5.8	385	99.9	601
4b	Weeper	430	209	430	6.2	355	99.5	425
4c	Gas-Gapped	600	210	614	5.8	392	99.9	599
4d	Weeper	430	209	432	6.2	357	99.5	429
4e	Gas-Gapped	520	210	532	5.8	375	99.9	520
4f	Gas-Gapped	600	210	614	5.8	394	99.9	599
5a	Gas-Gapped	495	210	509	5.8	371	99.9	495
5b	Gas-Gapped	600	210	615	5.8	387	100.0	600
5c	Gas-Gapped	600	210	615	5.8	387	99.9	599
5d	Gas-Gapped	500	210	514	5.8	370	99.9	500
5e	Weeper	435	209	438	6.3	358	99.4	434
5f	Weeper	425	209	425	6.2	354	99.5	422
6a	Weeper	435	210	431	6.3	357	99.4	428
6b	Weeper	435	209	429	6.3	357	99.4	427
6c	Weeper	425	209	422	6.2	354	99.1	420
6d	Weeper	425	209	423	6.2	354	99.5	421
6e	Weeper	425	209	426	6.3	355	99.4	424
7b	Weeper	440	210	434	6.3	359	99.4	432
8b	Weeper	450	210	440	6.3	360	99.4	437
bb	Weeper	370	206	372	4.1	328	101.6	370
bc	Weeper	380	207	379	4.2	330	101.5	377
bd	Weeper	380	207	380	4.1	329	101.6	377
be	Weeper	375	207	375	3.9	328	101.8	373
bf	Gas-Gapped	410	207	421	5.7	344	100.0	411
c1	Coolant TC	370	206	369	3.7	325	102.0	367
c2	Coolant TC	395	207	394	5.0	331	100.1	392
c3	Coolant TC	430	209	429	6.2	355	99.5	427

t Weeper and coolant TC target temperatures listed are the values used for the calculations of the average temperatures.

* Temperatures less than 300°C not included in calculation.

** Temperatures varied during the irradiation.

Table 8. Temperature Data for MOTA 28 During Cycle 128

21 Nov 1991 TO 19 Mar 2

Canister or TC No	Type	Target Temp. (°C)+	Min. Temp. (°C)	Max. Temp. (°C)	Ter (T_{tarc} No. of Days	< 0°C)* Avg. Temp. (°C)	Tem (T_{tarc} No. of Days	C) g. mp C)
la	Weeper	385	205	389	4.5	331	101.6	37
ic	Weeper	395	205	401	4.9	336	101.1	34
Id	Gas-Gapped	520	205	529	5.7	359	100.4	19
le	Gas-Gapped	600	205	609	5.7	373	100.4	99
If	Gas-Gapped	460	205	468	5.6	352	100.5	50
1b	Gas-Gapped	35-645	205	652	**	**	** +*	
1y	Outer 1b	**	205	565	**	**	**	
1z	Right 1b	**	205	650		**	**	
2c	Lower 2c	**	205	1066	**		**	
2w	Outer 2c	385	205	387	4.5	331	101.6	35
2x	Nb-Mo TC	**	226	1108	**	**	**	
2a	Gas-Gapped	520	205	528	5.7	366	100.4	19
2b	Gas-Gapped	550	206	559	5.8	372	100.4	19
2d	Gas-Gapped	800	206	810	5.9	416	100.4	39
2e	Weeper	405	205	412	5.7	344	100.4	19
2f	Gas-Gapped	520	205	528	5.7	365	100.4	19
3a	weeper	435	205	441	6.5	358	99.6	34
3b	Gas-Gapped	670	206	683	5.8	389	100.4	70
3c	Weeper	400	205	402	5.5	341	100.6	IO
3d	Weeper	425	205	433	6.5	356	99.6	28
3e	Gas-Gapped	520	206	530	5.7	369	100.4	19
3f	Gas-Gapped	600	206	608	5.8	377	100.4	01
4b	Weeper	430	206	434	6.3	356	99.8	30
4c	Gas-Gapped	600	206	609	5.8	383	100.4	39
4d	Weeper	430	206	436	6.9	360	99.2	32
4e	Gas-Gapped	520	206	528	5.8	368	100.4	19
4f	Gas-Gapped	600	206	613	5.8	384	100.4	39
5a	Gas-Gapped	495	206	504	5.7	367	100.4	35
5b	Gas-Gapped	600	206	608	5.8	378	100.4	39
5c	Gas-Gapped	600	206	610	5.8	380	100.4	39
5d	Gas-Gapped	500	206	510	5.7	365	100.4	IO
5e	Weeper	435	206	439	7.0	362	99.1	36
5f	Weeper	425	205	427	6.2	353	99.9	26
6a	Weeper	435	206	436	6.9	361	99.2	34
6b	Weeper	435	206	438	6.3	357	99.8	35
6c	Weeper	425	206	430	5.8	350	100.3	26
6d	Weeper	425	206	426	6.3	353	99.8	24
6e	Weeper	425	206	428	6.9	358	99.2	27
7b	Weeper	440	206	443	6.3	360	99.8	41
8b	Weeper	450	206	453	5.8	357	100.3	50
bb	Weeper	370	205	373	4.1	327	101.9	12
bc	Weeper	380	205	379	4.3	330	101.7	78
bd	Weeper	380	205	380	4.3	330	101.7	78
be	Weeper	375	205	376	4.2	328	101.8	74
bf	;as-Gapped	410	205	416	5.7	342	100.4	10
c1	Coolant TC	370	205	370	4.2	327	101.9	58
c2	Coolant TC	395	205	395	4.5	335	55.5#	94
c3	Coolant TC	430	206	431	6.3	355	99.8	10

t Weeper and coolant TC target temperatures listed are the values used for the calculations of the average temperatures.
* Temperatures less than 300°C not included in calculation.
# Indicates a bad thermocouple at some time during the cycle.
** Temperatures varied during the irradiation.

STATUS OF U.S./JAPAN COLLABORATIVE PROGRAM PHASE II HFIR TARGET CAPSULES - J. E. Pawel and R. L. Senn (Oak Ridge National Laboratory)

OBJECTIVE

The objective of this program is to determine the response of various U.S. and Japanese austenitic and ferritic stainless steels with different pretreatments and alloy compositions to the combined effects of displacement damage and helium generation at temperatures in the range of 300 to 600°C and doses of 18 lo 70 dpa.

SUMMARY

A complete description and details of the design, construction, and installation of capsules JP-9 through JP-16 has been previously reported.[1,2,3] The capsules were installed in the High Flux Isotope Reactor (HFIR) target July 20, 1990, for irradiation beginning with HFIR fuel cycle 289. The capsules were removed and stored in the reactor pool during HFIR cycle 292 (11/25/90 - 12/10/90) to provide room for required isotope production. They were reinstalled for HFIR cycle 293 for continued irradiation. Of these eight target capsules, JP-10, 11, 13, and 16 completed their scheduled number of cycles (11) and were removed from the reactor in September 1991. These four experiments were successfully disassembled in January 1992.

Three new capsules in this series, JP-20, 21, and 22, are presently being designed. These capsules were added to the program in order to complete the experimental matrix included in the JP-9 through 16 capsules. The new capsules will contain transmission electron microscope (TEM) disks and SS-3 flat tensile specimens at 300-600°C and will achieve doses of 8, 18 and 40 dpa, respectively.

PROGRESS AND STATUS

Caosules JP-9 throueh JP-16

The as-built specimen matrix for the JP-9 through JP-16 series capsules can be found in a previous report.[1] These capsules contain TEM disks, bar and flat (SS-3) tensile specimens, hourglass fatigue specimens, and sheet specimens. A wide variety of alloys and thermomechanical conditions are included. Many of the TEM disks were made from isotopically tailored alloys to produce a range of He/dpa ratios (<0.1, 10, 20, 70). The experiment addresses long-standing basic questions on the role of helium in microstructural evolution and will explore the high fluence swelling behavior of the most swelling-resistant materials currently available.

Capsules JP-10, 11, 13, and 16 were removed at the end of HFIR cycle 300 (9/19/91) after an irradiation of 20,270 MWd to a damage level of 17.7 dpa. Although originally scheduled for irradiation to 33 dpa, heavy experiment loading in HFIR resulted in a shorter fuel cycle time than was previously experienced, thus reducing total dpa for the agreed upon irradiation period. Consultation with both U.S. and Japanese participants in the program led to a reduction in the goal dpa levels for the experiments. Capsule JP-14 has been rescheduled for irradiation to about 40 dpa, and JP-9, 12, and 15 have been rescheduled for irradiation to about 70 dpa.

Capsules JP-9, 12, 14, and 15 continue under irradiation, having achieved an exposure of 29,973 MWd irradiation to a damage level of 25.7 dpa as of 2/27/92. Details of the irradiation history of these capsules is shown in Table 1.

Capsules JP-10, 11, 13, and 16 were successfully disassembled in January 1992. TEM disks from JP-10 (~600 disks) have been sorted in preparation for density measurements and electron microscopy. It is anticipated that mechanical property testing of the specimens from these capsules will begin in July 1992.

Capsules JP-20 throueh 22

Three new capsules have been added lo the US/Japan collaborative testing of Phase II HFIR target capsules, identified as JP-20, 21, and 22. A mutually agreed upon matrix for this subset of Phase II experiments is shown in Fig. 1. The individual subassemblies in the capsules hold TEM tubes, which contain approximately 120 disks each, or flat SS-3 tensile specimens in groups of two or four, designated as T(2) or T(4) in Fig. 1. Specimen material, design temperatures and the location of the various specimen holders with respect to the reactor mid-plane are shown. A notation for the previous capsule number and position of a similar subassembly at the same temperature is also shown on the figure.

Table 1. Irradiation History -- U.S./J Capsules JP-9, -10, -11, -12, -13, -14, -15, -16

HFIR OPERATION				JP-10, -11, -13, -16		JP-14		JP-9, -12, -15	
CYCLE NO.	START DATE	END DATE	MWd/ Cycle	IRR. TO 20 MWd		30 DPA dpa*		IRR. TO 70 DPA MWd	dpa*
289	07-20-90	09-07-90	1879	1879	1.64	1879	1.64	1879	1.64
290	09-19-90	10-11-90	1852	3731	3.26	3731	3.26	3731	3.26
291	10-17-90	11-13-90	1838	5569	4.86	5569	4.86	5569	4.86
292	11-25-90	12-10-90	1847	CAPSULES OUT OF REACTOR FOR THIS CYCLE.					
293	12-27-90	01-23-91	1965	7534	6 5 8	7534	6.58	7534	6.58
294	02-01-91	02-25-91	1906	9440	8 24	9440	8.24	9440	8.24
295	03-01-91	03-24-91	1909	11349	9 91	11349	9.91	11349	9.91
296	04-06-91	04-28-91	1874	13223	11 54	13223	11.54	13223	11.54
297	05-19-91	06-15-91	1835	15058	13 15	15058	13.15	15058	13.15
298	06-20-91	07-11-91	1747	16805	14 67	16805	14.67	16805	14.67
299	07-25-91	08-15-91	1741	18546	16 19	18546	16.19	18546	16.19
300	08-28-91	09-17-91	1724	20270	17.70	20270	17.70	20270	17.70
301	09-27-91	10-19-91	1851	JP-10, -11, -13, -16		22121	19.31	22121	19.31
302	10-27-91	11-21-91	1829	removed 9. .9/91 at		23950	20.91	23950	20.91
303	12-01-91	12-22-91	1821	end of HFIR Cycle 300.		25771	22.50	25771	22 50
304	12-31-91	01-24-92	1826			27597	24.09	27597	24 09
305	01-30-92	02-27-92	1876			29473	25.73	29473	25.73
306									
307									
308									
309									
310									
311									

* OPA levels based on achieving 0.000873 dpa/MWd.

Design and procurement of parts for these capsules is under way. The three new capsules have been carefully planned to use existing design parameters and drawings where possible. This will minimize costs and ensure that gas gaps, positioning, etc., will he comparable to the earlier capsules (JP-9 through 16). Parts that are the same as previous capsules in this series have been ordered and subassemblies have heen completed where possible. The minor design revisions required for the new specimens and new assembly drawings for each of the capsules are under way.

Specimen Matrix. These capsules are designed to complete the original alloy/thermomechanical conditionlfluenceitemperature matrix, to replicate previous irradiations, and tu irradiate new materials such as vanadium and TiAl. The majority of the U.S. specimens are TEM disks of isotopically tailored austenitic steels. Both flat tensile specimens and TEM disks will he included in the Japanese experiments.

Preliminary loading lists detailing the specimen type and material for each position are shown in Tables 2, 3, and 4 for capsules JP-20, 21, and 22, respectively. Alloy compositions are given in Tables 5 and 6. Material conditions include solution annealed **(SA),** cold worked (CW), strained, aged and recrystallized (SAR), and electron-beam welded (EB).

Irradiation Conditions. It is planned to irradiate the three capsules in inner target positions for 5, 11, and 22 cycles, respectively, to achieve peak doses of approximately 8, 18, and 35 dpa. Specimen temperatures in each capsule will be 300, **400.** 500, or 600°C, as shown in Fig. 1. Temperature and dosimetry monitors will he included in the capsules for post-irradiation analysis.

Thermal Analysis. The thermal analysis and design work for this set of experiments has been greatly reduced by choosing comparable positions and temperatures for specimen subassemblies of the same design from previous capsules. The aluminum spacers shown in Fig. 1 were incorporated to take full advantage of previous designs. Those analyses have already been completed. Additional thermal analysis for positions labelled "New Design" in Fig. 1 will he required. Calculations will he made for some of the TEM holders with major specimen material differences to determine if any gap changes will he required in order to achieve the design temperature.

ORNL-DWG 92-9395

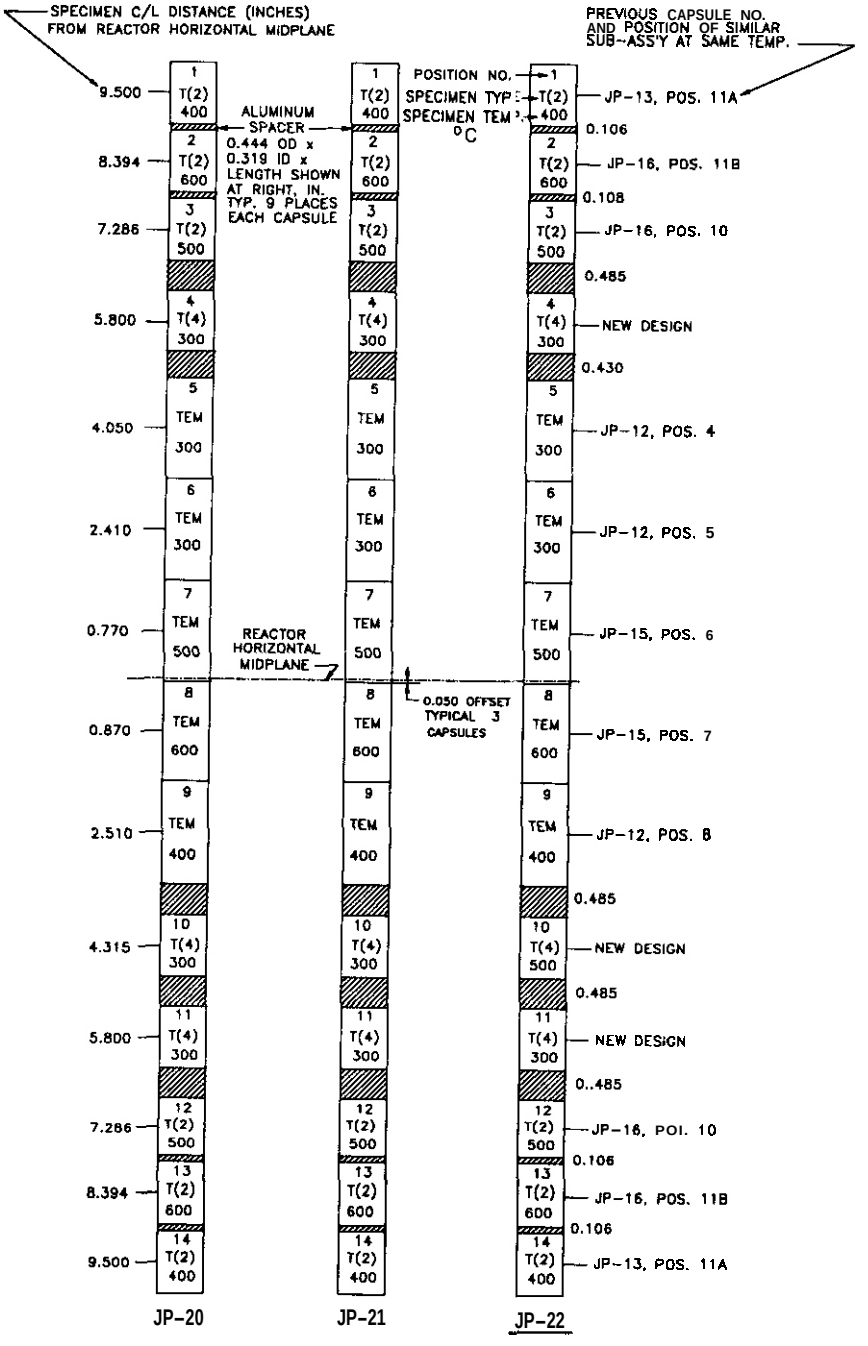

Figure 1. Matrix for HRR target capsules JP-20, 21, and 22.

Table 2. Preliminary loading list for IP-20.

Position No.	Program	Specimen Type, Design Temp., °C	Specimen Material, Condition (No. of Specimens)
1	Japan	T(2), 400	JPCA SA (1) JPCA CW (1)
2	Japan	T(2), 600	F82H (2)
3	Japan	T(2), 500	F3E *SAR* (1) FSE *SAR* (1)
4	US	T(4), 300	Vanadium (4)
5	US	TEM, 300	Vanadium (60) US IT* (60)
6	USiJapan	TEM, 300	US IT (96) DUPLEX (12) TiAl (12)
7	US/Japan	TEM, 500	US IT (84) FSE SA!! (2) F.I. SET (12) DUPLEX (8) TiAl (8) S.M.A. *(6)*
8	US/Japan	TEM, 600	US IT (108) TiAl (12)
9	USiJapan	TEM, 400	US IT (89) 316 *SAR* (5) F5E *SAR* (5) F.I. SET (12) S.M.A. (9)
10	Japan	T(4), 300	JPCA EB (2) F82H (2)
11	Japan	T(4), 300	JPCA SA (2) JPCA CW (2)
12	Japan	T(2), 500	F82H (I) TiAl (1)
13	Japan	T(2), 600	TiAl (2)
14	Japan	T(2), 400	JPCA EB (2)

* US isotopically tailored austenitic stainless steel

Table 3. Preliminary loading list for JP-21.

Position No.	Program	Specimen Type, Design Temp., °C	Specimen Material, Condition (No. of Specimens)
1	Japan	T(2), 400	F3E SAR (1) F5E SAR (1)
2	Japan	T(2), 600	TiAl (2)
3	Japan	T(2), 500	F3E SAR (1) F5E SAR (1)
4	US	T(4), 300	to be determined
5	US	TEM, 300	to be determined
6	US/Japan	TEM, 300	US IT* (77) 316 SAR (5) F5E SAR (3) F.I. SET (12) TiAl (12) DUPLEX (12)
7	US/Japan	TEM, 500	US IT (76) F3E SAR (5) F5E SAR (3) F.I. SET (12) TiAl (12) DUPLEX (12)
8	US/Japan	TEM, 600	US IT (120)
9	US/Japan	TEM, 400	US IT (82) F5E SAR (5) DUPLEX (12) S.M.A. (9) TiAl (12)
10	Japan	T(4), 300	JPCA SA (2) JPCA CW (2)
11	Japan	T(4), 300	JPCA EB (2) F82H (2)
12	Japan	T(2), 500	F82H (1) TiAl (1)
13	Japan	T(2), 600	TiAl (2)
14	Japan	T(2), 400	F82H (2)

* US isotopically tailored austenitic stainless steel

Table 4. Preliminary loading list for JP-22

Position No.	Program	Specimen Type, Design Temp., °C	Specimen Material, Condition (No. of Specimens)
1	Japan	T(2), 400	F3E SAR (1) F5E SAR (I)
2	Japan	T(2), 600	TiAl (2)
3	Japan	T(2), 500	F3E SAR (1) F5E SAR (1)
4	US	T(4), 300	to he determined
5	US	TEM, 300	to be determined
6	USiJapan	TEM. 300	US IT* (74) 316 SAR (5) F5E SAR (5) F.I. SET (12) TiAl (12) DUPLEX (12)
7	US/Japan	TEM, 500	US IT (103) F5E SAR (3) F3E SAR (2) TiAl (12)
8	US/Japan	TEM, 600	US IT (108) TiAl (12)
9	USiJapan	TEM, 400	US IT (108) TiAl (12)
10	Japan	T(4), 500	F82H (2) F82H-B (2)
11	Japan	T(4), 300	F3E SAR (1) F5E SAR (1) F82H (1) F82H-B (1)
12	Japan	T(2), 500	TiAl (2)
13	Japan	T(2), 600	TiAl (2)
14	Japan	T(2), 400	F82H (I) F82H-B (1)

US isotopically tailored austenitic stainless steel

Table 5. Alloy compositions for US isotopically tailored alloy.

Alloy	Fe	Cr	Ni^{N*}	^{60}Ni	Ti	C	N	Si	Nb	V	Mo	Mn	P	B
B12-1	bal.	14.0	-	15.0	0.2	0.04	0.01	0.8	-	-	-	-	0.05	-
B12-12	bal.	14.0	2.10	12.9	0.2	0.04	0.01	0.8	-	-	-	-	0.05	-
B12-70	bal.	14.0	15.0	-	0 2	0.04	0.01	0.8	-	-	-	-	0.05	-
1535-1	bal.	15.0	-	35.0		-			-	-	-	-	-	-
1535-4	bal.	15.0	0.35	34.65	-	-	-		-	-	-	-	-	-
1535-12	bal.	15.0	1.75	33.25	-	-	-		-	-	-	-	-	-
1535-130	bal.	15.0	35.0	-	-	-	-		-	-	-	-	-	-
316-1	bal.	17.5	0.0	13.7	-	0.05	-	0.53	-	-	2.3	1.7	-	-
316-4	bal.	17.5	0.7	13.0	-	0.05	-	0.53	-	-	2.3	1.7	-	-
316-12	bal.	17.5	2.06	11.63	-	0.05	-	0.53	-	-	2.3	1.7	-	-
316-70	bal.	17.5	13.7	0.0	-	0.05	-	0.53	-	-	2.3	1.7	-	-
PCA-1	bal.	14.0	0.0	16.0	0.25	0.05	0.01	0.40	-	-	2.3	1.8	-	0.01
PCA-12	bal.	14.0	2.08	13.92	0.25	0.05	0.01	0.40	-	-	2.3	1.8	-	0.01
PCA-70	bal.	14.0	16.0	0.0	0.25	0.05	0.01	0.40	-	-	2.3	1.8	-	0.01
1416 CP1-1	bal.	14.0	-	16.0	0.3	0.08	0.02	0.4	0.10	0.50	2.5	2.0	0.07	0.008
1416 CP1-12	bal.	14.0	2.08	13.92	0.3	0.08	0.02	0.4	0.10	0.50	2.5	2.0	0.07	0.008
1416 CP2-1	bal.	14.0	-	16.0	0.3	0.08	0.02	0.2	0.10	0.50	2.5	2.0	0.07	0.008
1416 CP2-12	bal.	14.0	2.08	13.92	0.3	0.08	0.02	0.2	0.10	0.50	2.5	2.0	0.07	0.008
1416 CP3-1	bal.	14.0	-	16.0	0.3	0.08	0.02	0.4	0.10	0.10	2.5	2.0	0.07	0.008
1416 CP3-12	bal.	14.0	2.08	13.92	0.3	0.08	0.02	0.4	0.10	0.10	2.5	2.0	0.07	0.008
1416 CP4-1	bal.	14.0	-	16.0	0.3	0.10	0.02	0.4	0.10	0.50	2.5	2.0	0.07	0.008
1416 CP4-12	bal.	14.0	2.08	13.92	0.3	0.10	0.02	0.4	0.10	0.50	2.5	2.0	0.07	0.008
1416 CP5-1	bal.	14.0	-	16.0	0.3	0.08	0.02	0.4	0.10	0.50	2.5	2.0	0.04	0.008
1416 CP5-12	bal.	14.0	2.08	13.92	0.3	0.08	0.02	0.4	0.10	0.50	2.5	2.0	0.04	0.008
RSP1-1	bal.	13	-	15	0.2	0.05	-	0.4	-	0.2	1.5	1.5	0.07	-
RSP1-12	bal.	13	2.1	12.9				0.4	-	0.2	1.5	1.5	0.07	-
RSP2-1	bal.	14	-	15				0.5	-	-	1.5	1.5	0.07	-
RSP2-12	bal.	14	2.1	12.9		0.05		0.5	-	-	1.5	1.5	0.07	-

* Ni^{N}: natural nickel

Table 6. Alloy compositions for Japanese alloys.

Material	JPCA	Duplex				Shape Memory Alloys						F.I. Set
		AF2	AF3	AF4	AF7	SM13	SM15	C8	F5E SAR	F3E SAR	316 SAR	F82H
Fe	bal.	bal.	bal.	bal.	bal.	bal.	bal.	bal.	bal.	bal.	bal.	bal.
C	.064	.02	.02	.02	.02	.017	.016	.006	.0016	.0012	.0042	.093
Si	.54	.48	.49	.50	.47	4.51	4.47	5.84	.038	.08	.61	.09
Mn	1.63	1.01	1.01	1.05	1.06	1.01	1.01	14.19	.016	.02	1.91	.49
P	.027	.02	.02	.02	.02	.017	.017	<.003	.002	.002	.004	.005
S	.0045	.003	.003	.003	.002	.002	.002	.002	.0008	.0025	.009	.001
Cr	14.27	25.2	21.3	19.3	20.9	18.2	18.1	5.1	17.7	16.8	19.96	7.65
Ni	15.95	5.8	9.0	11.0	8.9	14.8	14.9	8.9	35.1	25.1	13.7	.01
Mo	2.35	2.5	2.5	2.5	2.5	-	-	-	2.26	2.19	2.67	tr
Ti	.21	-	-	-	.22	-	-	-	.27	.25	<.01	.005
B	.0041	-	-	-	-	-	-	-	.003	.003	<.001	.0034
Co	.015	.004	.004	.004	-	.01	.01	<.01	.004	<.01	<.01	-
N	.003	.02	.01	.02	.01	.010	.009	.002	.0022	.0066	.0016	.0019
Sol.Al	-	-	-	-	-	.003	.003	.001	-	-	-	-
Nb	-	-	-	-	-	tr	.20	-	-	-	<.01	-
Al	-	-	-	-	-	-	-	-	-	-	.005	-
V	-	-	-	-	-	-	-	-	-	-	<.01	.18
Cu	-	-	-	-	-	-	-	-	-	-	.01	-
W	-	-	-	-	-	-	-	-	-	-	-	1.98
Ta	-	-	-	-	-	-	-	-	-	-	-	.038
T.Al	-	-	-	-	-	-	-	-	-	-	-	.01

PRESENT STATUS

Parts for JP-20, 21, and 22 that were the same as previous capsules have been received and subassemblies completed where possible. Thermal analysis for the new designs and subsequent drawing changes are under way. Loading lists are being finalized.

FUTURE WORK

The required drawing revisions must be completed and the balance of parts ordered so that capsule assembly can begin. Final loading lists and capsule assembly procedures will be developed. The goal is to have the capsules installed in HFIR during this fiscal year. Installation is planned for late August or early September 1992.

REFERENCES

1. R. L. Senn, "Status of U.S./Japan Collaborative Program Phase I1 HFIR Target Capsules," pp. 8-20 in Fusion Reactor Materials Semiann. Proe. Rep. April 30. 1987, DOE/ER-0313/3, U.S. DOE, Office of Fusion Energy.

2. R. L. Senn, "Status of U.S./Japan Collaborative Program Phase II HFIR Target Capsules." pp. 7-9 in Fusion Reactor Materials Semiann. Proe. Reo.. March 31, 1988, DOE/ER-0313/4, U.S. DOE, Office of Fusion Energy.

3. R. L. Senn. "Status of U.S./Japan Collaborative Program Phase II HFIR Target Capsules." pp.6-13 in Fusion Reactor Materials Semiann. Proe. Rep., Sept. 30. 1988, DOE/ER-0313/5. U. S. DOE Office of Fusion Energy.

FABRICATION AND IRRADIATION OF HFIR-MFE-JP-17, -18, AND -19 TARGET IRRADIATION CAPSULES

A. W. Longest, D. W. Heatherly, K. R. Thoms (Oak Ridge National Laboratory), and J. E. Corum (Midwest Technical, Inc.).

OBJECTIVE

The objective of this work is to fabricate and irradiate capsules for testing magnetic fusion energy (MFE) reactor candidate first-wall materials in the High Flux Isotope Reactor (HFIR) target positions. Japanese and U.S. test specimens are being irradiated to determine fracture toughness of austenitic stainless steels and a few chromium ferritic steels and high heat flux alloys after irradiation to 3 dpa at temperatures of 60-125 and 250-300°C.

SUMMARY

Fabrication and irradiation of three new uninstrumented HFIR target capsules for testing 12.5-mm-diam stainless steel fracture toughness specimens to a damage level of approximately 3 displacements per atom (dpa) at temperatures of 60-125 and 250-300°C were completed this report period. Two low temperature capsules of identical design, designated HFIR-MFE-JP-18 and HFIR-MFE-JP-19, each contained 32 fracture toughness specimens directly cooled by reactor cooling water. Irradiation of these two capsules was completed on October 19, 1991. A single helium-filled elevated temperature capsule, designated HFIR-MFE-JP-17, contained a stack of X6 fracture toughness specimen. Additional neutronic calculations were required for this experiment to insure that it would not cause unacceptable neutron flux shifting and hot spots in the HFIR fuel regions. Irradiation of this capsule was completed on February 27, 1992. Included in each capsule were companion transmission electron microscopy (TEM) and SS-3 tensile specimens for correlation of microstructural, tensile, and fracture toughness properties.

PROGRESS AND STATUS

Introduction

Three fracture-toughness-specimen irradiation capsules were fabricated and irradiated as part of the U.S./Japan collaborative program for testing fusion reactor candidate first-wall materials in mixed-spectrum fission reactors. The test specimens were irradiated in HFIR target capsules designed' for 60-125°C and 250-300°C specimen temperatures.

These capsules accommodate 12.5-mm-diam stainless steel Disk-Shaped Compact DC(T) specimens of standard proportions; also, companion TEM and SS-3 tensile specimens are accommodated to permit correlation of microstructural, tensile, and fracture toughness properties. The capsules were uninstrumented and were intended to provide early irradiation data on low-temperature fracture toughness properties of candidate first-wall alloys. Spectral tailoring of the neutron flux was deemed unnecessary for the planned two-cycle irradiation to a damage level of approximately 3 dpa. In the HFIR target region, the helium production-to-atom displacement ratio in austenitic stainless steels in a short irradiation of 1 to 2 cycles is reasonably close to the ratio (14 appm/dpa) expected in a fusion reactor first wall.

60-125°C Capsules

Irradiation of two uninstrumented low-temperature capsules of identical design, designated HFIR-MFE-JP-18 and HFIR-MFE-JP-19, was completed during this report period. Each capsule contained 31 12.5-mm-diam fracture toughness specimens directly cooled on their flat faces by downward-flowing reactor cooling water. Details of the test specimen loadings in these two capsules were given in the last progress report.' In addition to test specimens, each capsule contained six small melt-materials capsules for temperature monitoring and eight dosimetry capsules for neutron exposure and damage determination.

Capsules JP-18 and JP-19 were irradiated concurrently for two HFIR cycles in target positions B-1 and E-7, respectively. Irradiation began August 28, 1991, at the start of HFIR cycle 300 and ended October 19, 1991, at the end of HFIR cycle 301. Exposure for the two-cycle irradiation was 3575 MWd, or approximately 42.1 days at 85 MW reactor power.

250-300°C Cansule

A single uninstrumented helium-filled elevated-temperature capsule, designated HFIR-MFE-JP-17, was assembled and irradiated during this report period. Capsule JP-17 contained a stack of 86 12.5-mm-diam fracture toughness specimens (total of real specimens, blank specimens, and three dummy specimens holding TEM specimens and a few blank disks) and 12 SS-3 tensile specimens, all within a tight-fitting aluminum cladding tube. A few of the stainless steel fracture toughness specimens near the ends of the 50-cm test length were replaced by copper alloy and carbon specimens. Details of the test specimen loading are given in Table 1. In addition to test specimens, the JP-17 capsule contained 26 small melt-materials capsules and 3 small SiC rods for temperature monitoring and 8 dosimetry capsules for neutron damage determination. This capsule was of the shrouded type and was cooled by reactor cooling water flowing downward between the cladding tube and shroud tube.

Capsule JP-17 was irradiated for two HFIR cycles in peripheral target position G-4. Irradiation began December 31, 1991, at the start of HFIR cycle 304 and ended February 27, 1992, at the end of HFIR cycle 305. Exposure for the irradiation was 3702 MWd, or approximately 43.6 days at 85 MW reactor power.

FUTURE WORK

These irradiations of fracture toughness specimens to 3 dpa at temperatures of 60-125°C and 250-300°C have been completed.

REFERENCES

1. A. W. Longest, et al., "Design and Fabrication of HFIR-MFE-JP Target Irradiation Capsules," in Fusion Reactor Materials Semiann. Prog. Rep., March 31, 1991, DOE/ER-0313/10, U.S. DOE, Office of Fusion Energy.

2. A. W. Longest, et al., "Fabrication and Irradiation of HFIR-MFE-JP-17, -18, and -19 Target Irradiation Capsules," in Fusion Reactor Materials Semiann. Prog. Rep., September 30, 1991, DOE/ER-0313/11, U.S. DOE, Office of Fusion Energy.

Table 1. Test specimen loading in HFIR target capsule JP-17

Specimen Position Number	Specimen Type	Distance from Specimen Centerline to Reactor Core Midplane (cm)	Specimen Identification
		Top	
1	Fracture toughness	24.8	FC1
2	Fracture toughness	24.3	FA1
3	Fracture toughness	23.8	FB2
4	Fracture toughncss	23.4	FF4
5	Fracturr toughncss	22.9	FG3
6	Fracture toughncss	22.5	FD4
7	Fracture toughncss	22.0	FE2
8	Fracture toughness	21.5	FH2
9	Fracture toughness	21.0	FI1
10	Fracture toughness	20.6	FL1
11	Fracture toughness	20.1	FK5
12	Fracture toughness	19.7	FM1
13	Fracture toughness	19.2	FR1
14	Blank	18.7	(a)
15	Fracture toughness	18.3	FJ3 (Glidcop)
16	Fracture toughness	17.8	FJ2 (Glidcop)
17	Blank	17.3	(a)
18	Fracture toughness	16.9	FM4
19	Dummy fracture toughness holding TEM specimens. TEM-3	16.4	AF4 (2 Rods), AF5 (1 Rod), AF3 (5 disks), AF4 (5 disks). AF5 (5 disks), 7 blank disks
20	Fracture toughncss	15.9	FK9
21	Fracture toughncss	15.5	FR12
22	Fracturc toughness	15.0	R 2
23	Fracture toughness	14.5	FM2
24	Fracture toughncss	14.0	FR3
25	Fracture toughness	13.5	FKI1
26	Fracture toughncss	13.0	FL2
27	Fracture toughness	12.5	FH5
28	Fracture toughness	12.0	FE4
29	Fracture toughness	11.5	FD6
30	Fracture toughness	11.0	FG6
31	Fracture toughness	10.4	FF3
32	Fracture toughncss	9.9	FB5
33	Fracture toughness	9.4	FA9
34	Fracture toughness	8.8	FC2
35	Fracture toughness	8.3	FE7
36	Fracture toughness	7.1	FD10
37	Fracture toughness	7.1	FG11
38	Fracture toughness	6.6	FFI1
39	Fracture toughness	6.0	FB9
40	Fracture toughness	5.4	FA2
41	Fracture toughness	4.8	FC7
42	Fracture toughncss	4.2	FC10
43	Fracture toughncss	3.6	FA10
44	Fracture toughness	3.0	FB10

Table 1. **Test** specimen loading in **HFIR** target capsule JP-17 (Cont'd)

Specimen Position Number	Specimen Type	Distance from Specimen Centerline to Reactor Core Midplane (cm)	Specimen Identification
45	Fracture toughness	2.4	FF12
46-55	SS-3 Tensile	0.4	FA22T, FA25T, FD3T, FD5T, FF2T, FF5T
		Reactor Care Midplane	
	SS-3 Tensile	2.2	FE18T, FE19T, FH2T, FH7T, FI13, FI14
56	Fracture toughness	4.3	FG12
57	Fracture toughness	4.9	FD11
58	Fracture toughness	5.5	FE9
59	Fracture toughness	6.1	FC9
60	Fracture toughness	6.7	FA18
61	Fracture toughness	1.3	FB13
62	Fracture toughness	7.9	FF18
63	Fracture toughness	8.5	FG14
64	Fracture toughness	9.1	FD13
65	Fracture toughness	9.6	FEI1
66	Fracture toughness	10.2	FH6
67	Fracture toughness	10.8	FL5
68	Dummy fracture toughness holding TEM specimens, TEM-I	11.3	FL31,FL32,FL38,FL48.FK33,FK36,FK47, FK50.FA38,FA43,FA47.FA48.FA84,FA85, FA96,FA101,FA64,FA68,FA69, FA75,FC29,FC30,FC31,FC36,FD23,FD24,FD25,FD26, FF33,FF34,FF35,FF36,FE26.FE27,FE28, FE29,FG58,FG55,FG59,FG57,FI13,FI14, FI15,FI16,FI17,FI18,FI19,FI20,FM58, FM55,FM56,FM57,FN50,FN51, FN52,FN53,FN54,FN56,FN57,FN59
69	Fracture toughness	11.9	FK10
70	Fracture toughness	12.4	FR5
71	Blank	13.0	(a)
72	Blank	13.5	(a)
73	Fracture toughness	14.0	CX1 (Carbon-Carbon)
74	Blank	14.5	(a)
75	Blank	15.0	(a)
76	Fracture toughness	15.5	FI4
77	Fracture toughness	16.0	FR8
78	Fracture toughness	16.5	FK15

Table 1. Test specimen loading in HFIR target capsule JP-17 (Cont'd)

Specimen Position Number	Specimen Type	Distance from Specimen Centerline to Reactor Core Midplane (cm)	Specimen Identification
79	Dummy fracture toughness holding TEM specimens. TEM-2	17.0	FH32, FH39, FH45, FH46, AF4 (5 disks), AF3 (5 disks), AF5 (5 disks). AF3 (2 Rods), AF5 (1 Rod), 3 blank disks
80	Blank	17.5	(a)
81	Fracture toughness	18.0	cx2 (Carbon-Carbon)
82	Blank	18.5	(a)
83	Blank	18.9	(a)
84	Fracture toughness	19.4	FR14
85	Fracture toughness	19.8	FM6
86	Fracture toughness	20.3	FK13
87	Fracture toughness	20.8	f17
88	Fracture toughness	21.2	F16
89	Fracture toughncss	21.7	FH7
90	Fracture toughness	22.2	FE12
91	Fracture toughness	22.6	FD14
92	Fracture toughness	23.1	FG15
93	Fracture toughness	23.6	FF19
94	Fracture toughness	24.0	FB15
95	Fracture toughness	24.5	FA19
96	Fracture toughness	25.0 Bottom	FC14

'Stainless steel disk having the same external dimensions as a fracture toughness specimen and a central hole Cor gas communication.

FABRICATION AND OPERATION OF HFIR-MFE RB' SPECTRALLY TAILORED IRRADIATION CAPSULES -
A. W. Longest, D. W. Heatherly, E. D. Clemmer (Oak Ridge National Laboratory), and J. E. Corum (Midwest Technical, Inc.).

OBJECTIVE

The objective of this work is to fabricate and operate irradiation capsules for irradiating magnetic fusion energy (MFE) candidate first-wall materials in the High Flux **Isotope** Reactor (HFIR) removable beryllium (RB*) positions. Japanese and US. MFE specimens are being transferred to RB* positions following irradiation to 7.5 dpa at temperatures **of** 60, 200, 330, and 400°C in Oak Ridge Research Reactor (ORR) experiments ORR-MFE-6J and -7J.

SUMMARY

Fabrication and operation of four HFIR-MFE RB* capsules (60,200,330, and 400°C) to accommodate MFE specimens previously irradiated in spectrally tailored experiments in the ORR are proceeding satisfactorily. With the exception of the 60°C capsule, where the test specimens are in direct contact with the reactor cooling water, specimen temperatures (monitored by 21 thermocouples) are controlled by varying the thermal conductance of a thin gas gap region between the specimen holder and containment tube.

Irradiation of the 60 and 330°C capsules was started on July 17, 1990. **As** of March 31,1992, these two capsules had completed 17 cycles of their planned 22-cycle (formerly 28-cycle) irradiation to a damage level of approximately 17.5 displacements per atom (dpa). Assembly of the 200 and 400°C capsules is scheduled for completion in August, 1992; operation of these two capsules will follow the first two (60 and 330°C).

PROGRESS AND STATUS

Introduction

A series of spectrally tailored irradiation capsules are being fabricated and operated as part **of** the U.S./Japan collaborative program for testing MFE candidate first-wall materials in mixed-spectrum fission reactors. The test specimens are being irradiated in the RB' facility' of the HFIR.

Four HFIR-MFE RB* capsules were designed to accommodate Japanese and **U.S.** MFE specimens previously irradiated to 7.5 dpa at temperatures **of** 60, 200, 330, and 400°C in the ORR in spectrally tailored experiments ORR-MFE-6J and -7J. Details of these ORR experiments, including descriptions of the test matrix, mechanical property specimens, and techniques of spectral tailoring, have been reported elsewhere.[2,3] Hafnium liners are being **used** in the HFIR-MFE RB* experiments to tailor the neutron spectrum to closely match the helium production-to-atom displacement ratio **(14** appm/dpa) expected in a fusion reactor first wall.

The HFIR-MFE RB* capsules are being irradiated in pairs (first the 60 and 330°C capsules, then the 200 and 400°C capsules) to a damage level of approximately 17.5 dpa. The target exposure level was given as 20 dpa (28 HFIR cycles) in the last progress report'; however, in a recent review of the irradiation program, it was decided to end these four irradiations after accumulating 17.5 dpa **(22** HFIR cycles).

60°C Capsule

The 60°C capsule, designated HFIR-MFE-60J-1, **is** an uninstrumented capsule with the test specimens in contact with the reactor cooling water. Capsule design, assembly, and details of the specimen loading were described previously.'

Irradiation **of** this capsule began July 17, 1990, at the start of HFIR cycle 289. **As** of March 31, 1992, 17 cycles of its planned 22-cycle irradiation to a damage level of approximately 17.5 dpa had been completed. Specimen operating temperatures in this capsule are predicted to be within 10°C of 60°C.

330°C Capsule

The 330°C capsule, designated HFIR-MFE-330J-1, is an instrumented and singly contained capsule where the specimen temperatures are monitored by 21 thermocouples and controlled hy adjusting the thermal conductance of a thin gas gap region between the specimen holder outer sleeve and containment tube. This capsule is cooled with 49°C reactor cooling water flowing downward over the containment tube surface. Capsule design, assembly, and details of the specimen loading were described previously?'

Irradiation of this capsule began on July 17, 1990, at the start of HFIR cycle 289. As of March 31, 1992, 17 cycles of its planned 22-cycle irradiation to a damage level of approximately 17.5 dpa had been completed.

Typical thermal operating data for the 330J-1 experiment were presented in detail in the last progress report'. During this report period, measured temperatures in the aluminum alloy specimen holder continued to indicate specimen operating temperatures within about 25°C of 330°C, which satisfies the temperature criterion for these experiments.

200 and 400°C Capsules

The 200 and 400°C capsule designs were described previously* and are basically the same as that of the 330°C capsule. The main differences in the three capsule designs are associated with (1) the number and spacing of the specimen holder slots and holes to accommodate differences in the number of specimens of the various types, (2) the width of the temperature control gas gap region between the specimen holder outer sleeve and containment tube to obtain the desired specimen operating temperatures, and (3) the test piece included in the aluminum plug and holder above the test specimen holder to obtain extra information.

Assembly of both capsules is scheduled for completion in August, 1992. Operation of these two capsules will follow the first two (60 and 330°C).

FUTURE WORK

Assembly of the 200 and 400°C capsules is scheduled for completion in August, 1992. These two capsules are to be operated for 22 HFIR cycles.

REFERENCES

1. K. R. Thoms et al., "HFIR Irradiation Facilities Improvements - Completion of the HIFI Project," J. Nucl. Mater., 155-157 (1988) 1340-45.

2. J. L. Scott et al., pp. 12-20 in *ADIP Semiann. Prog. Rep.,* March *31, 1985,* DOE/ER-0045/14, U.S. DOE, Office of Fusion Energy.

3. J. L. Scott et al., *Second Annual Prog.* Rep. *on* United *States-Japan Collaborative* Testing in *the High Flux* Isotope Reactor *and the Oak* Ridge Research *Reactor,* Sept. *30, 1985,* ORNL/TM-10102.

4. A. W. Longest et al., "Fabrication and Operation of HFIR-MFE RB* Spectrally Tailored Irradiation Capsules," in Fusion Reactor Materials Semiann. Prog. Rep., Sept. 30, 1991, DOE/ER-0313/11, USDOE Office of Fusion Energy.

5. A. W. Longest et al., "Design and Fabrication of HFIR-MFE RB* Spectrally Tailored Irradiation Capsules," in Fusion Reactor Materials Semiann Prog. Rep., March 31, 1988, DOE/ER-0313/4, USDOE Office of Fusion Energy.

6. A. W. Longest et al., "Design and Fabrication of HFIR-MFE RB* Spectrally Tailored Irradiation Capsules," in Fusion Reactor Materials Semiann. Prog. Rep., Sept. 30, 1987, DOE/ER-0313/3, USDOE Office of Fusion Energy.

7. A. W. Longest et al., "Design and Fabrication of HFIR-MFE RB* Spectrally Irradiation Capsules," in Fusion Reactor Materials Semiann. Prog. Rep. Sept. 30, 1988, DOE/ER-0313/5, USDOE Office of Fusion Energy.

8. A. W. Longest et al., "Design and Fabrication of HFIR-MFE RB* Spectrally Tailored Irradiation Capsules," in Fusion Reactor Materials Semiann. Prog. Rep., March 31, 1989, DOE/ER-0313/6, USDOE Office of Fusion Energy.

STATUS OF AUTOMATED TENSILE MACHINE - M. Satou (Tohoku University), M. L. Hamilton (Pacific Northwest Laboratory[a]), S. Sato and A. Kohyama (University of Tokyo)

OBJECTIVE

The objective of this work is develop the Monbusho Automated Tensile machine (MATRON) and install and operate it at the Pacific Northwest Laboratory (PNL). The machine is designed to provide rapid, automated testing of irradiated miniature tensile specimens in a vacuum at elevated temperatures.

SUMMARY

The MATRON was successfully developed and shipped to PNL for installation in a hot facility. The original installation plan was modified to simplify the current and subsequent installations, and the installation was completed. Detailed procedures governing the operation of the system were written. Testing on irradiated miniature tensile specimens should begin in the near future.

PROGRESS AND STATUS

Introduction

Miniature tensile specimens are frequently used in the Japanese and U.S. materials testing programs to determine the mechanical properties of numerous materials in various conditions and the effect of irradiation on these properties. It is difficult, however, to perform tests at elevated temperatures on miniature specimens, particularly in a controlled environment. The MATRON was developed to enable such tests to be performed rapidly in either a vacuum or an inert gas. Typically, such tests are performed on one specimen at a time. The most time consuming steps in such testing are the vacuum pumping that must be performed prior to each test and the cooling that must occur before the vacuum can be released. The MATRON was designed to allow multiple specimens to be loaded into the test chamber that is evacuated only once yet allows each specimen to be tested. Only one specimen at a time is heated and tested, and each specimen can be tested at a different temperature. Thus only one evacuation cycle is required for multiple tensile tests. The data output from each test is recorded using an analog chart recorder. Analysis of the data can be computerized using a digitizer to input data from the chart.

As shown in Figure 1, the MATRON consists of two separate units, a tensile test frame and a specimen loading device. The frame comprises a heated vacuum chamber mounted on a standard tensile testing machine. The loading device pneumatically loads a specimen and all washers, screws, etc. into the fixture in which it is tested. The fixtures are transferred manually into the test chamber after the specimens are loaded. Both components were developed at the University of Tokyo, where successful operation of the machine was demonstrated using unirradiated tensile specimens. A more detailed description of the system is provided by Kohyama et al. [1]

Current Status

The MATRON was disassembled and shipped to PNL for reassembly and installation into a hot facility for the testing of irradiated tensile specimens. After the MATRON was received at PNL, it was reassembled and its successful operation was verified using unirradiated tensile specimens. Staff in the facility where it is being installed (the *321* building) were trained in its use. A number of minor components had corroded in transit and were replaced. Spare parts for numerous components were also procured.

A plan was developed to install the components into the hot cell facility. It was determined that the optimum installation would entail inserting the loading device into the hot cell and constructing a shielded "blister" to contain the tensile test frame; the latter will be butted up against the hot cell during a test series. Loaded specimen fixtures will be passed into the testing frame through a port in the cell wall. The controllers for the testing frame and the loading device will remain outside the hot cell and the blister, and will be connected to their respective components via electrical junction boxes.

The MATRON will not be installed in the hot facility permanently since the hot cell is also used for other work during periods that necessitates the temporary removal of the MATRON. Thus the installation plan was developed in such a way as to facilitate easy repeated installation and removal.

The electrical junctions for the installation were completed, as was the fabrication of the blister and the track along which the test frame will be moved. Both components of the MATRON were installed in the hot facility. After their successful operation is verified once again using unirradiated specimens, testing of

---

[a]Pacific Northwest Laboratory is operated for the U.S. Department of Energy by Battelle Memorial Institute under Contract DE-AC06-76RLO 1830.

irradiated miniature tensile specimens will begin. The majority of these specimens have already been sorted and are ready for shipment to the 327 building.

Detailed procedures were written for the operation of both the loading device and the tensile test machine. Since the automatic operation of the loading device is very sensitive and can require adjustment, the procedures for the loading device include instructions for manual operation in the event that problems develop while irradiated specimens are being loaded, making access to the loading device impossible. A draft copy of the procedures is being routed at PNL for the required approval signatures.

An additional device was developed to facilitate the manual disassembly of the test fixtures. This device can also be used to load the specimens into the test fixtures in the event that the loading device experiences problems.

It was originally envisioned that both the MATRON test frame and the loading device would be installed in the hot cell. While this plan would most likely have allowed the initial installation to proceed more rapidly, it would have been more expensive and more time consuming for each subsequent installation than the plan that was actually implemented. Development of the current installation plan required that anticipated radioactivity levels be calculated for a wide variety of specimens to verify that adequate shielding could be provided by the blister. While this led to some delays in the original installation of the MATRON, the modified installation will ultimately be more efficient and less costly, since it will frequently be possible to leave the loading device in the cell while other work is being performed, and insertion and removal of the testing frame will require only that it be rolled towards or away from the hot cell wall along a track.

CONCLUSIONS

The MATRON was successfully developed and shipped to PNL for installation in a hot facility. The original installation plan was modified and the installation was completed. Detailed procedures governing the operation of the system were written. Testing on irradiated miniature tensile specimens should begin in the near future.

FUTURE WORK

Tensile tests will be performed on miniature tensile specimens discharged from MOTA 2A. Consideration will be given to modifying the test fixtures to accommodate specimens that exhibit slightly different geometries due to such phenomena as swelling. A computerized data acquisition system will be installed. and appropriate data analysis procedures will be developed.

REFERENCES

1. A. Kohyama, S. Sato, and K. Hamada. "An Automated Tensile Machine for Small Specimens Heavily Neutron Irradiated in FFTF/MOTA," Proceedings of the ASTM Symposium on Small Specimen Test Techniques and Their Application to Nuclear Reactor Vessel Thermal Annealing and Plant Life Extension, held in New Orleans, LA on January 29-31, 1992

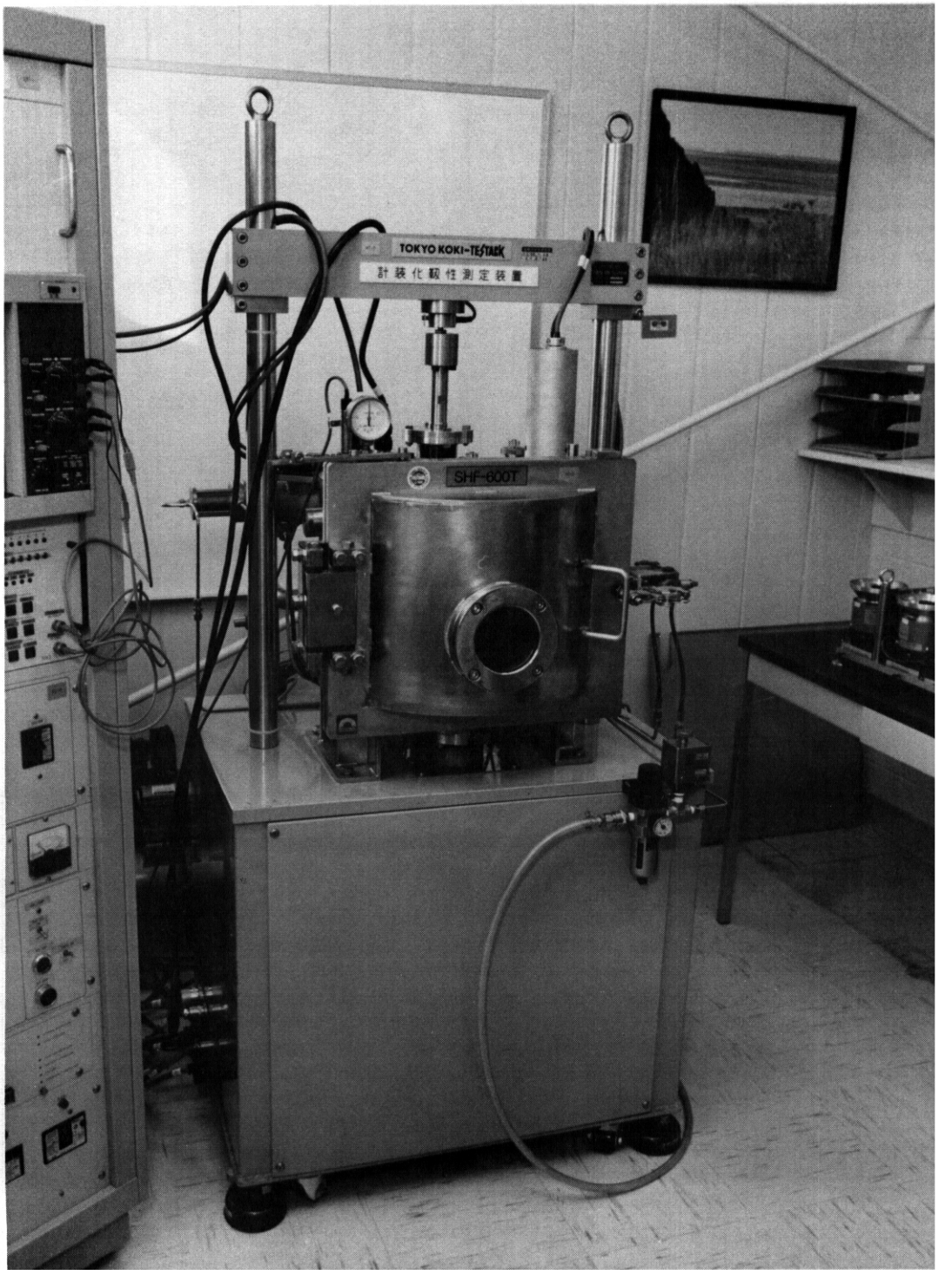

Fig. la. MATRON tensile test frame, showing the vacuum chamber mounted on a standard testing machine.

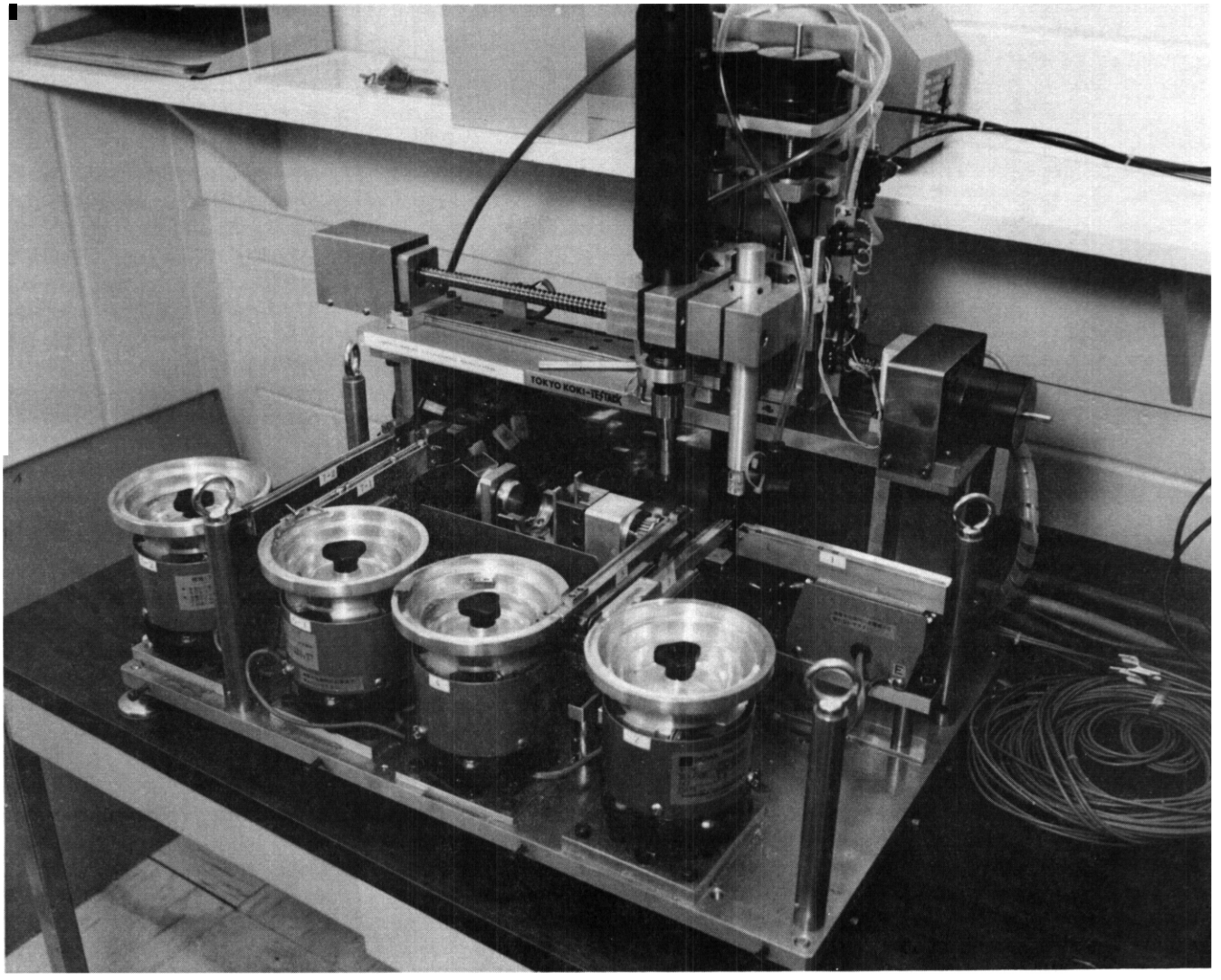

Fig. lb. MATRON specimen loading device. The bins at the front of the picture are the feeders from which the various parts of a specimen fixture **are** loaded.

FRACTURE TOUGHNESS MEASUREMENTS WITH SUBSIZE DISK COMPACT SPECIMENS - D. J. Alexander (Oak Ridge National Laboratory)

OBJECTIVE

Special fixtures and test methods are necessary to facilitate the fracture toughness testing of small disk compact specimens of irradiated candidate materials for first-wall fusion applications. New methods have been developed for the both unloading compliance and potential drop techniques of monitoring crack growth. Data generated with these methods must be compared to results from standard specimens to assure the usefulness of testing on subsize specimens.

SUMMARY

Special fixtures and test methods have been developed for testing small disk compact specimens (12.5 mm diam by 4.6 mm thick). Both unloading compliance and potential drop methods have been used to monitor crack extension during the J-integral resistance (J-R) curve testing. Provisions have been made to allow the necessary probes and instrumentation to be installed remotely using manipulators for testing of irradiated specimens in a hot cell. Laboratory trials showed that both unloading compliance and potential drop gave useful results. Both techniques gave similar data. and predicted the final crack extension within allowable limits. The results from the small disk compact specimens were similar to results from conventional compact specimens 12.7 mm thick. However, the slopes of the J-R curves from the larger specimens were lower, suggesting that the smaller disk compact specimens may have lost some constraint due to their size. The testing shows that it should be possible to generate useful J-R curve fracture toughness data from the small disk compact specimens.

PROGRESS AND STATUS

Introduction

Candidate materials are being evaluated for the first-wall structure in the International Thermonuclear Experimental Reactor (ITER). Current estimates of the operating temperatures indicate that the structure will operate below about 300°C. One of the materials proposed for the first wall is type 316 stainless steel. Very little information is available on the effects of irradiation at these low temperatures on the mechanical properties of austenitic stainless steels, particularly the fracture toughness.' Therefore, work is under way at Oak Ridge National Laboratory (ORNL) to measure the effect of irradiation on the fracture toughness of a variety of austenitic stainless steels. This paper describes some of the techniques that have been developed for this testing, and presents some preliminary results from unirradiated material and comparisons with larger conventional specimens.

The irradiations for these experiments are being conducted at the High-Flux Isotope Reactor (HFIR) at ORNL due to the reactor availability and the high fluxes present in the HFIR target region. However, achieving the necessary low irradiation temperatures (60 and 300°C) placed severe restrictions on the specimen geometry. The gamma heating from the high-flux irradiation and the limited cooling available from the reactor cooling water required a very small specimen size to attain the lowest irradiation temperature. To use the HFIR target region efficiently, it was necessary to adopt a circular specimen geometry for the fracture toughness specimens. Therefore, the disk compact specimen geometry was chosen. This is an accepted specimen geometry for K_{Ic} measurements (ASTM Standard Test Method for Plane-Strain Fracture Toughness of Metallic Materials, E 399-83), but is not yet included in the standards for J-integral or J-integral-resistance (J-R) curve testing (ASTM Standard Test Method for J, A Measure of Fracture Toughness, E 813-89, or ASTM Standard Test Method for Determining J-R Curves, E 1152-87, respectively). These standards presently allow only conventional rectangular compact specimens or bend bars: however, the disk and rectangular compact specimens are very similar in geometry, and J-R data can be correctly determined from each if the appropriate compliance expressions are used. Preliminary experiments' indicated that useful data could be generated in the laboratory from small disk compact specimens.

The heat transfer calculations performed at ORNL and the size limitations imposed by the HFIR target region characteristics resulted in the selection of the specimen diameter and thickness of 12.5 and 4.63 mm (0.492 and 0.182 in.), respectively. This very small specimen size would demand special techniques for testing.

There are two conventional methods employed in J-R testing for monitoring crack growth during the test: unloading compliance. and potential drop. Unloading compliance (UC) requires periodic partial unloadings of the specimen to determine the specimen compliance, from which the crack length and extension are calculated. This technique demands high accuracy for the measurement of the load-displacement data in order to determine the correct compliance values, and hence crack extensions. The second method, potential drop (PD). imposes a constant current across the specimen and measures the changing resistance of the unbroken ligament as the crack extends. Less accurate displacement measurements are necessary, since the calculation of the energy required for evaluating the fracture toughness is less sensitive to the displacement measurementthan are the compliance measurements. The UC measurements for irradiated specimens have been successfully done at ORNL, and much more experience had been accumulated in testing unirradiated material with UC than with PD. However, the small specimen size precluded conventional displacement measuring methods, and so it was decided to pursue both the UC and the PD techniques, in case one of the methods proved to be impractical for remote testing in a hot cell.

Test Methods

The UC technique requires accurate measurement of the specimen displacements. The usual technique for measuring the displacements along the specimen load line is to fabricate the specimen with a cutout that allows a clip gage to be inserted between the loading pin holes to the load line, where it seats on knife edges fastened along the load line on the sides of the notch cutout. An example of the resultant specimen geometry is shown in Fig. 1 for a compact specimen 12.7 mm (0.5 in.) thick (designated 0.5 T C(T)). However, the disk compact specimen is much smaller, with a thickness of only 4.6 mm (0.18 in.). (This disk compact specimen is thus designated 0.18 T DC(T)). As a result, there is not sufficient room between the loading holes for a cutout to allow a clip gage to be inserted to the load line. Therefore, grooves were machined on the outer edge of the specimen above and below the loading holes (see Fig. 1) so that the load line displacement could still be measured directly. but outside the loading holes rather than in between them. The grooves had an included angle of 60". with a depth of 0.5 mm (0.020 in.) and a root radius of 0.05 mm (0.002 in.). A robust and rugged yet highly accurate clip gage that could be handled by manipulators was designed. The gage included knife edges that would seat in the grooves. This clip gage, termed an "outboard gage since it was attached outside of the loading holes, contained a central flexural beam on which four strain gages were attached for a full-bridge measurement of the strains and hence the displacement. Figure 2 shows the outboard gage attached to one of the disk compact specimens.

There appeared to be only two drawbacks to the outboard gage: possible difficulties in remotely mounting the gage on the specimens using manipulators, and possible damage to the gage if the specimen fractured suddenly during testing. The manipulator operators indicated that the gage could be attached, perhaps with the aid of special fixtures. The problem of gage damage was addressed by providing overtravel stops on the back end of the gage. Hopefully, if the specimen did suddenly fracture and the servohydraulic test machine did not prevent a rapid separation of the grips and opening of the gage, the stops would prevent the central flexural beam from being permanently deformed and damaged. It was hoped that the knife edges would either slip out of the grooves, or perhaps break off where they are attached to the gage arms, thus preventing damage to the gage. Both of these possible problems have yet to be fully resolved.

The PD setup presented much greater difficulties. Four probes would have to be attached to each specimen: two for the constant current inputs. and two to monitor the changing voltage drop across the specimen ligament. Current input and output locations were chosen at the top and bottom of the specimen along the centerline, and the crack monitoring probes were located 15" above and below the crack plane. on the front edge of the specimen. It was decided to forgo two additional probes for a reference measurement, in part to reduce the number of necessary connections, and also because there was no obvious location for such probes. Instead, a second specimen would be connected in series with the test specimen, and the crack monitor signal from the dummy specimen would be used for a reference signal.

A PD calibration function was developed from measurements on thin aluminum mockups of the disk compact geometry. The calibration specimen diameter was 137.2 mm (5.4 in.) but the thickness was 3.2 mm (0.125 in.). Crack extension was simulated by slitting with a thin saw blade. The current and voltage readings were recorded at increments in the crack length to specimen width ratio (a/W) of about 0.05, for a/W values from 0.3 to roughly 0.9. These values were normalized by the value at a/W of 0.5, and then fitted with a third-order polynomial. This gave a correlation coefficient greater than 0.999.

Attaching the probes would be simple in the laboratory, but much more difficult remotely in the hot cell. A fixture and special tools were designed to assist the manipulator operators in this task (Fig. 3). The specimen would be located in a special fixture to align the predrilled and tapped holes in the specimen with the threaded probes. The fixture would prevent the probes from being cross-threaded. The initial prototype of the fixture was machined from clear Plexiglas simply for expediency; however, it was realized that the transparency of the plastic was helpful in the assembly and desirable. The stainless steel probes were machined with hex heads, and a nutdriver would be used to attach them. The sequence of

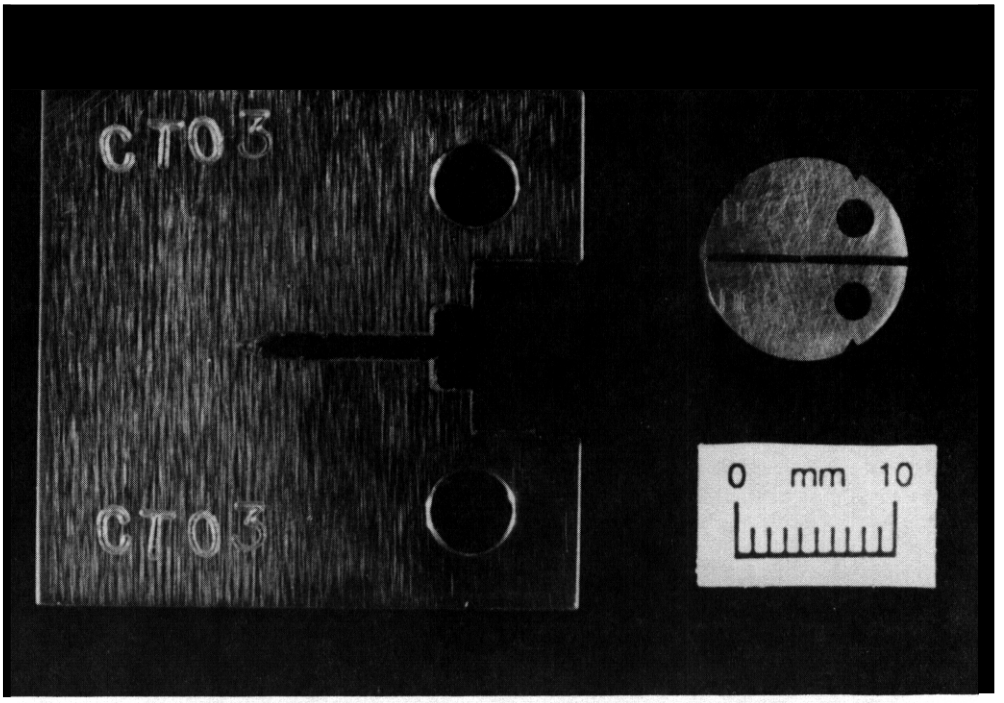

Fig. 1. A comparison of a conventional 1/2 T compact specimen (left) and the 0.18 T disk compact specimen (right). Note the cutout in the compact specimen to allow a clip gage to be inserted to the load line between the loading holes. The disk compact has notches outside the loading holes for the outboard clip gage.

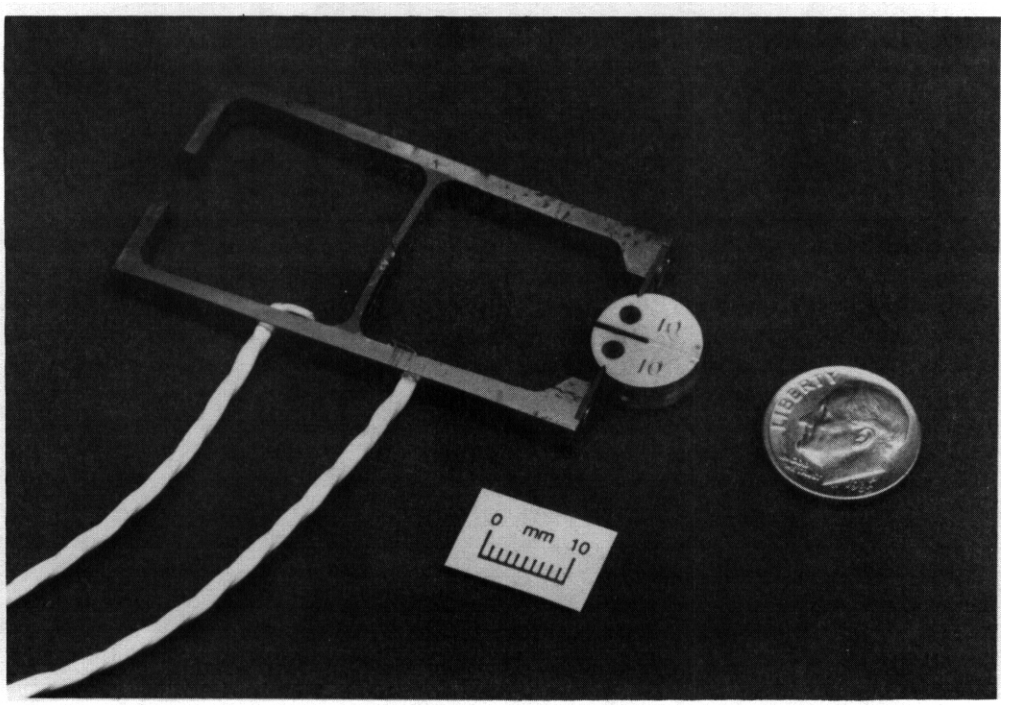

Fig. 2. The outboard clip gage seated on the disk compact specimen. The central flexural beam has four strain gages for the measurement of the displacements. The back end of the gage will allow handling with a manipulator. The gap at the rear of the gage is designed to provide overtravel protection if the specimen fractures suddenly during testing.

operations required to attach the probes is shown in Fig. 4. The top half of the fixture has been removed for clarity. The specimen would be placed in the central recess (Fig. 4a), and a thin piece of shim stock (omitted for clarity) would be inserted in the fixture slit and the specimen notch to properly align the specimen. The original proposal suggested that the probes be placed into the appropriate hole as shown in Fig. 4b. but it was realized that a better method would be to first load the probe into the shaft of the nutdriver, which was drilled out to allow the probe to slide into the nutdriver until the hex flats were engaged. The nutdriver would be inserted into the appropriate hole (Fig. 4c) and then rotated until the probe was secured. The process was repeated until all four probes were attached (Fig. 4d). The specimen and probes would then be removed from the fixture (Fig. 4e). The final step would be to attach the proper leads to the probes (Fig. 49. The leads would have fittings designed to slide onto the probes. The fittings on the leads were obtained by stripping the plastic coating from female banana plugs and soldering the internal connector to the lead wires. The probe diameters matched the corresponding male banana plugs. This provided an effective electrical connection that could be assembled with manipulators.

The nutdriver for attaching the probes is shown in Fig. 5. To facilitate handling the nutdriver. cross pieces were added to the handle by drilling through two offset holes 90° apart near the end of the handle, and pressing thin rods through these holes. These cross pieces prevent the nutdriver from rolling when it is laid down, and also hold the handle of the nutdriver up so that the manipulator can easily grasp the nutdriver. The primary function of the cross pieces is to allow the nutdriver to be rotated for screwing in the probes. An additional modification was the addition of a slip coupling with an adjustable torque setting to the shaft of the nutdriver (Fig. 5). The slip coupling was inserted by cutting the shaft of the nutdriver near the handle. A suitable torque level was determined by trial and error in the laboratory. The slip coupling would prevent inadvertent overtightening and twisting off of the fragile threaded probes as they were attached to the specimen. This would be very likely with the manipulators necessary for the attachment, as they do not transmit much "feel" back to the manipulator operator.

The completed assembly of the probes and clip gage on the specimen is shown in Fig. 6. This entire assembly would then be inserted into clevises for the fracture testing. The clevises would have a wider and deeper slot than normal, to facilitate assembly with manipulators. This would also reduce the likelihood of accidental contact of the leads with the legs of the clevises that would result in changes in the electrical signals, or rubbing of the clip gage against the clevis that would distort the displacement measurements. Using manipulators to insert the specimen and the instrumentation into the testing grips has not yet been attempted. it is expected that additional fixturing will be required to align the specimen assembly with the test grips so that the loading pins can be inserted. The pins will have one end tapered and an offset block on the other end for handling with the manipulator. The fixture that holds the grips and the specimen assembly will then be loaded into the load train of the test machine. The fixturing will be removed after the grips are pinned in place, again using tapered pins with handling blocks. This two-step procedure should reduce the possibility of accidentally overloading the small specimens before they were ready for testing.

Laboratory Trials and Discussion of Results

Several trials have been conducted in the laboratory to compare the UC and PD techniques on the 0.18 T DC(T) specimens, and to compare these results to UC data from 0.5 T C(T) specimens of the same material. Specimens of both geometries were machined from the same 14-mm-thick (0.55-in.) plate of annealed type 316 stainless steel from the National Fusion Reference Heat X15893. The specimens were oriented in the T-L orientation so that crack growth was in the rolling direction, All specimens were taken from the center of the plate thickness. The specimens were precracked at room temperature with a final maximum stress intensity of approximately 22 MPa√m (20 ksi√in.). A chevron notch was used for both specimens to assist crack initiation and maintain crack front straightness during precracking. The DC(T) and C(T) specimens were precracked to nominal a/W values of 0.5 and 0.6, respectively. The specimens were then side grooved 10% of their thickness on each side (20% total) with an included angle of 45" and a root radius of 0.25 mm (0.010 in.) or 0.10 mm (0.004 in.) for the C(T) and DC(T) specimens, respectively. The sidegrooves would suppress the development of slant shear fracture.

All tests were conducted at room temperature, and the manufacturer's values of 260 and 560 MPa (38 and 81 ksi) were used for the yield and ultimate tensile strengths, respectively, in calculating the blunting lines for the data analyses. Values of 193 GPa (28,000 ksi) and 0.3 were assumed for the elastic modulus and Poisson's ratio, respectively. Tests were conducted in general accordance with E 813-89 and E 1152-87 using a computer-controlled testing and data acquisition system described elsewhere? After completion of the test, the specimens were heat tinted by placing them on a hot plate and heating them until a noticeable color change was evident, The specimens were then cooled to room temperature and broken open. The initial and final crack lengths were measured with the aid of a measuring microscope, and the crack lengths were calculated by the nine-point average method.

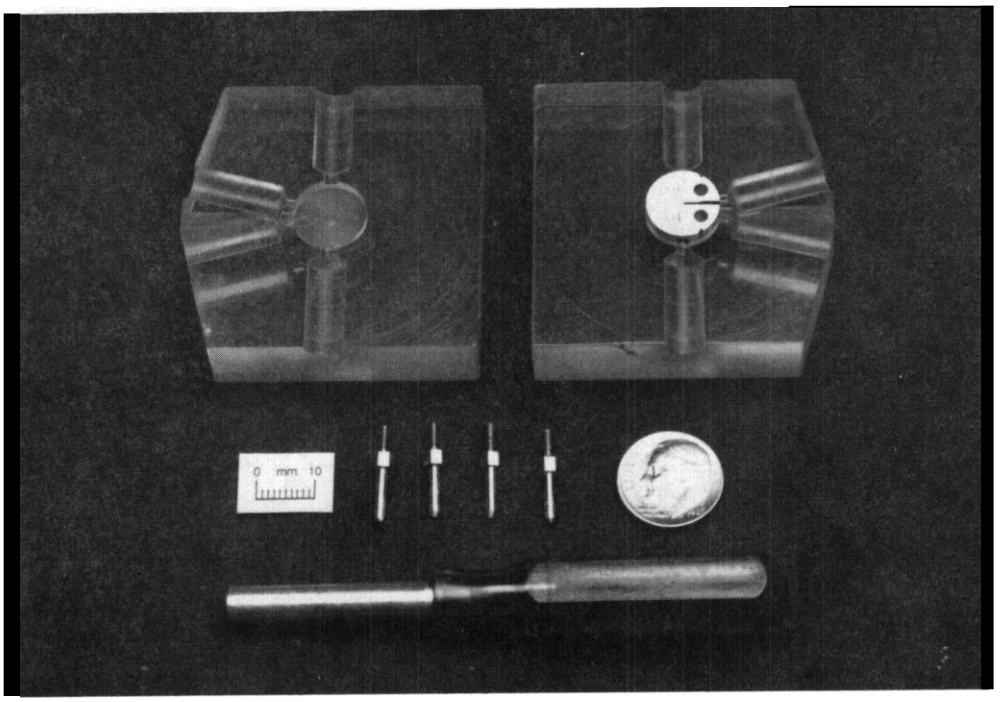

Fig. 3. The fixtures, probes, and tools **used for assembly of the potential drop setup.**

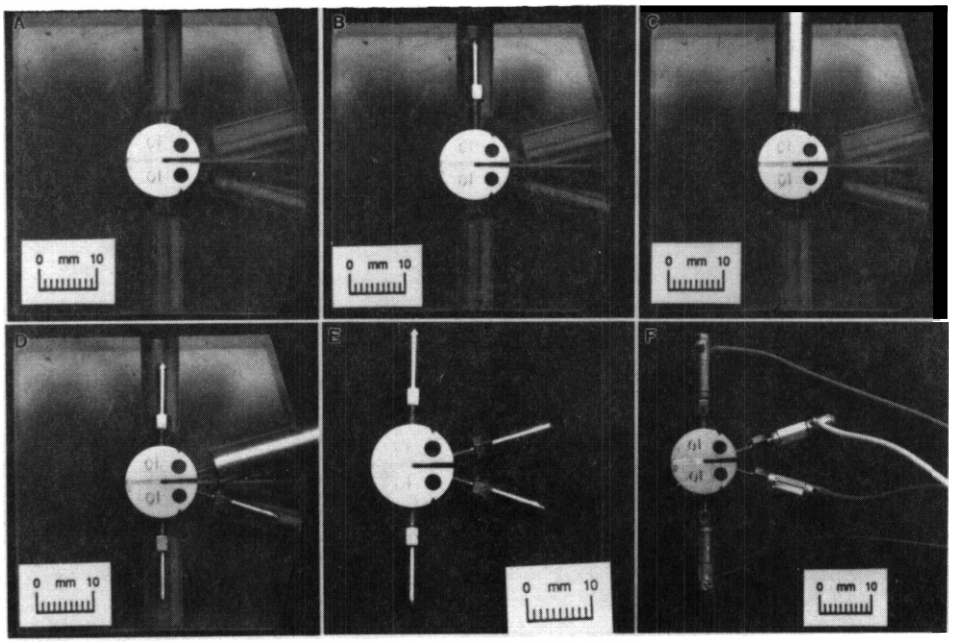

Rg. 4. The sequence of operations required for the attachment of **the potential drop probes to the disk** compact **specimen.**

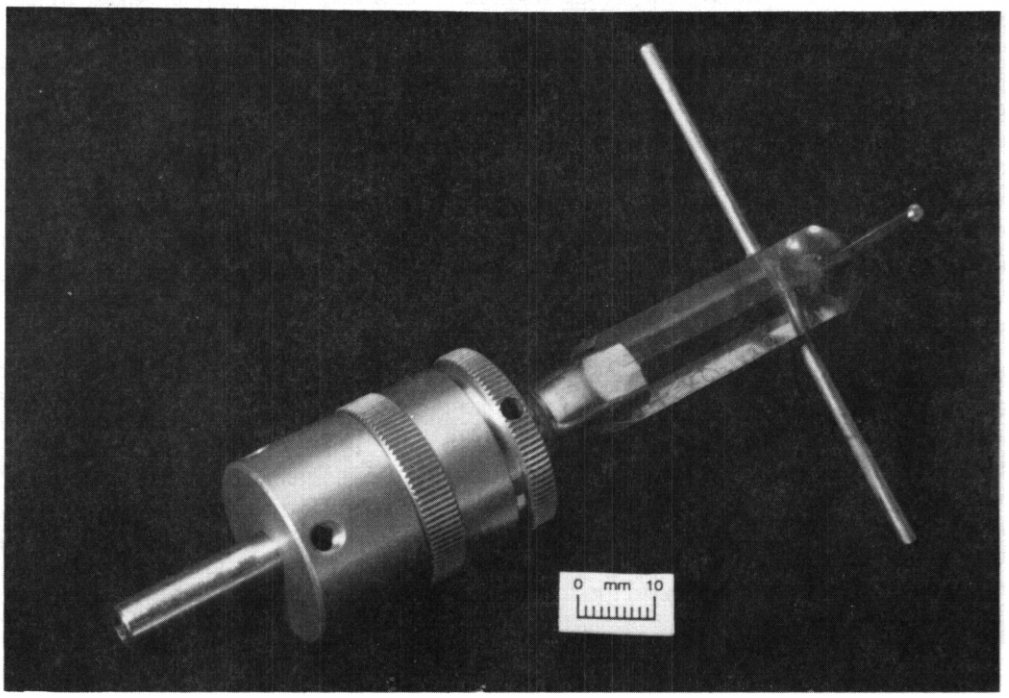

Fig. 5. The modified nutdriver used for attaching the probes to the disk compact specimen. **Note** the cross pieces at the end of the handle, and the slip coupling inserted on the shaft.

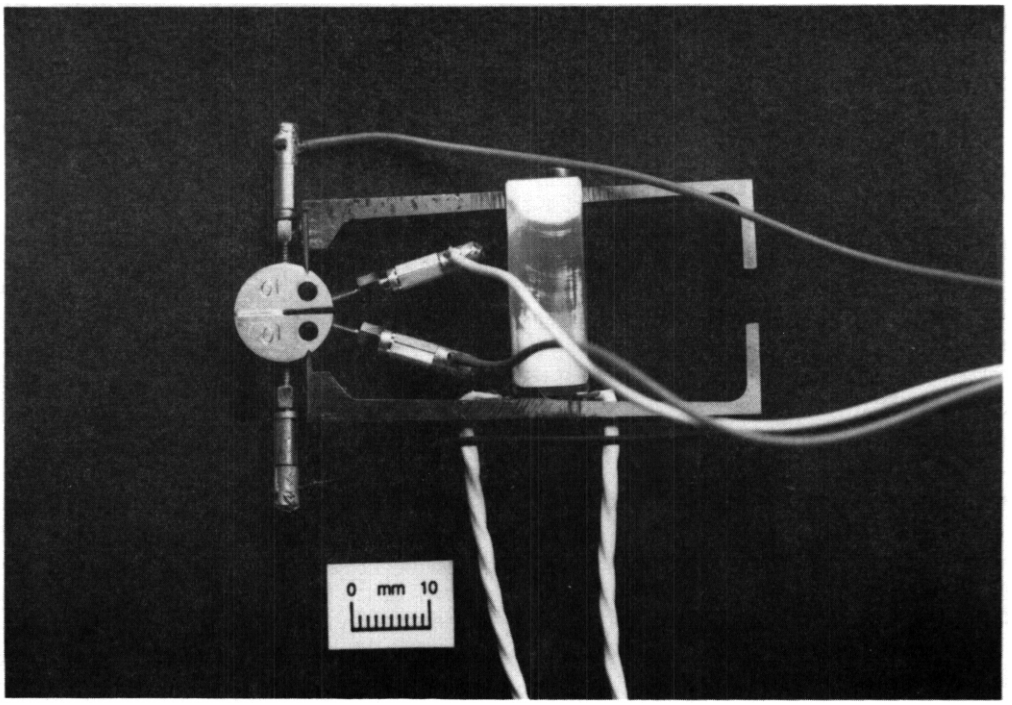

Fig. 6. A view of the complete assembly, showing the potential drop probes and lead wires, and the unloading compliance clip gage. The clip gage has a protective shield mounted over the middle flexural member, to protect the strain gages.

An electrical isolation grip was used in the top of the loading train to insure that the test machine would not provide an alternate current path for the potential during the testing. Measurements of the potential showed that attaching the clip gage resulted in a slight shift (about 2%) in the apparent crack length calculated from the potential drop, due to current travelling through the body of the clip gage. No correction was made for this small error, apart from normalizing the potential drop data to match the measured initial crack length at the beginning of the test.

A problem with the anaiysis of potential drop measurements is the determination of the initiation of crack growth. There may be significant changes in the potential drop signal prior to actual crack growth. In order to determine when crack growth begins, during the analysis routine the voltage ratio (the potential of the test specimen divided by the potential from the reference specimen) is plotted against the load line displacement. A typical example is shown in Fig. 7. There is an initial linear portion, with a subsequent deviation from this linearity. This deviation from linearii is taken as the beginning of crack extension." During the posttest analysis, the computer program allows the operator to interactively position a straight line through the data to assist in determining the initial deviation from linearii. The data prior to this point are assigned to the calculated blunting line, and crack extension is then calculated from this point on. As Fig. 7 shows, this material showed a sharp and distinct break, making the choice for the beginning of crack extension a simple one. The potential drop data shown in Fig. 7 are the average of sixty readings of the voltage taken during pauses in the test while the computer program performed calculations for the unloading compliance testing. Data were also taken continuously during the test, and showed excellent agreement with the data taken during the pauses.

The **UC** and **PD** data gave very similar results for the **DC(T)** specimens. An example of the results is shown in Fig. **8.** Both techniques show similar final crack extensions, and predicted the measured final crack extension to within the 15% allowed by ASTM E **813-89.** This excellent agreement between the *two* techniques provided further justification for the method used to determine the initiation of crack growth from the potential drop data. The load-displacement curves showed little or no hysteresis during the unload-load cycles until near the end of the test. The cause of this hysteresis late in the test is unclear. It may be caused by the knife edges contacting the sides of the grooves as the specimen opens, or to the rotation of the loading pins causing them to ride up the sides of the pin holes in the grips, although loading flats were provided in the clevises. Neither of these possibilities seems very likely, as the specimens fractured without gross changes of geometry. This problem will be examined with additional testing, although it does not seem to have harmed the quality of the data.

The material tested showed some scatter in the toughness, as is shown in Fig. **9.** These identical specimens show very different fracture behaviors. Specimen **DC9** shows a greater J_{Ic} value and a higher **J-R** curve than does specimen **DC2.** The fracture toughness and tearing modulus values from ail of the specimens tested are shown in Table 1. This table also includes the results from the 0.5 T **C(T)** specimens.

The thicker **C(T)** spedmens gave results similar to the low toughness DC(T) specimens. In general, the J_{Ic} values were similar, but the **J-R** curves for the thicker specimens were flatter, giving lower values of the tearing modulus (see Table **1).** A comparison of the results for the two specimens types is shown in Fig. 10.

The toughness values are surprisingly low for an annealed austenitic stainless steel. The tearing modulus values measured with the C(T) specimens are also very low. This low resistance to fracture resulted in very little distortion of the specimens. The fracture surfaces from two of the disk compact specimens are shown in Fig. **11.** The low toughness resulted in very flat fracture surfaces and very little lateral contraction of the specimens ahead of the crack front. This lack of change in the specimen geometry may have helped the agreement between the different specimen types. The low toughness favors fracture rather than the growth of a large plastic zone. A large plastic zone would have relieved the stresses ahead of the crack tip, and interacted more readily with the edges of the small disk compact than with those of the larger compact specimen, for similar levels of stress intensity. Thus, the good agreement between these two specimen types may not extend to tougher materials. Further trials are planned with a tougher material. However, the good agreement between the two specimen types is very encouraging for the planned irradiation program, as the irradiation is expected to result in higher strength and lower toughness for the stainless steels. Thus the small disk compact specimen should provide useful data.

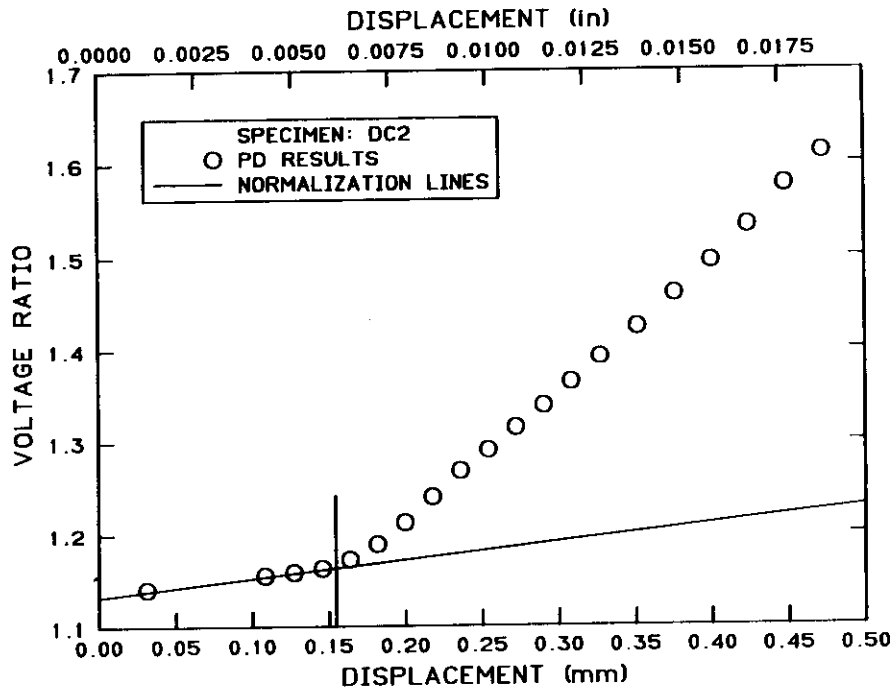

Fig. 7. A plot of the voltage ratio versus the load line displacement for one of the disk compact specimens. The straight line is used to assist in the selection of the point of initial deviation from linearity. The vertical line shows the point selected as the beginning of crack extension.

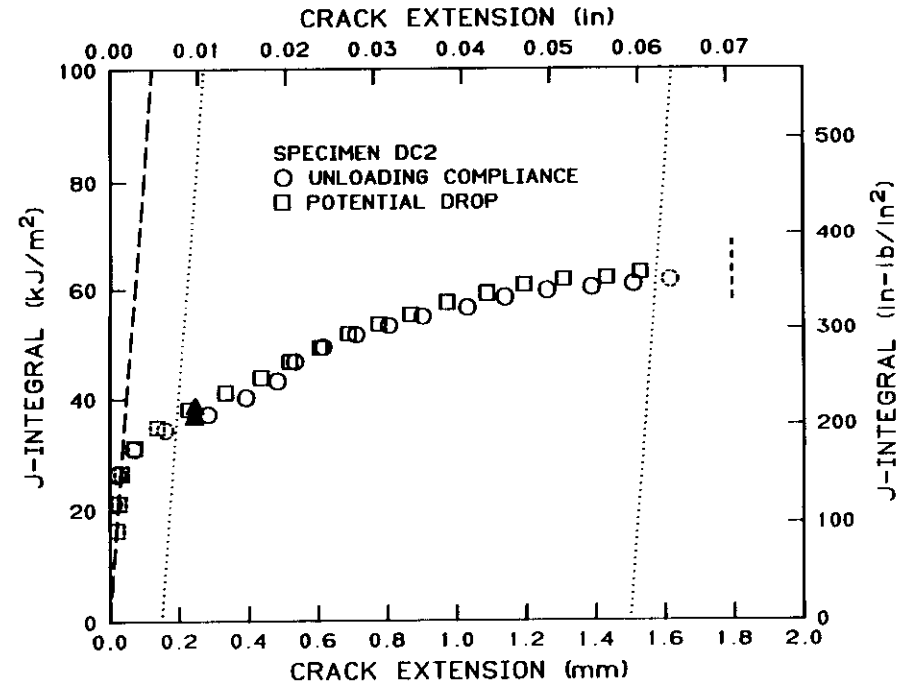

Fig. 8. An example of the J-R curve from a disk compact specimen, showing excellent agreement between the data from unloading compliance and that from potential drop. Both methods predict the measured final crack extension (vertical dashed line) quite well. The solid triangles show the calculated critical J values.

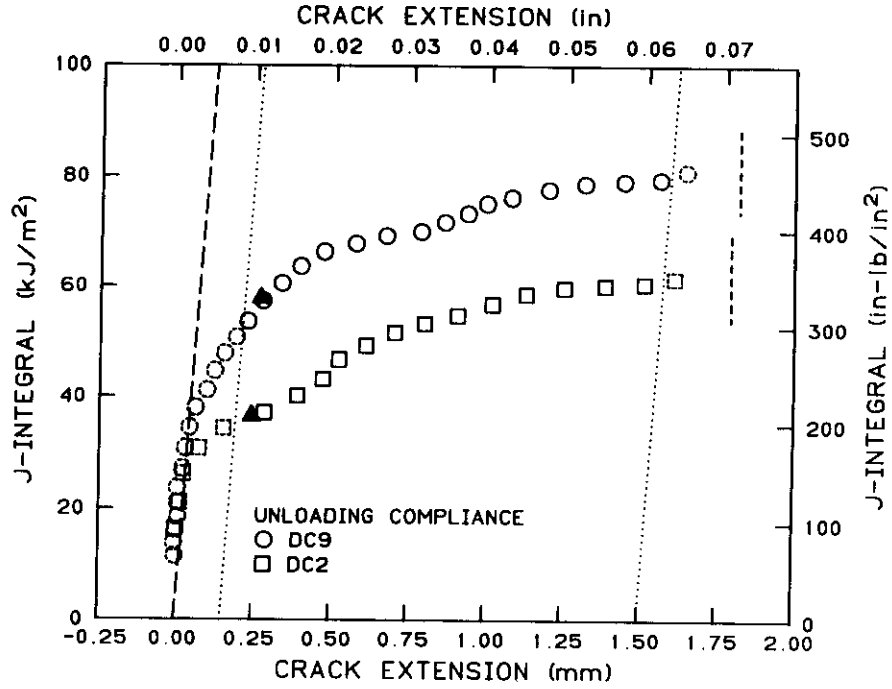

Fig. 9. J-R curves obtained by the unloading compliance technique from two apparently identical disk compact specimens, showing that some scatter was observed from replicate tests. Both tests showed good agreement between measured and predicted crack extensions.

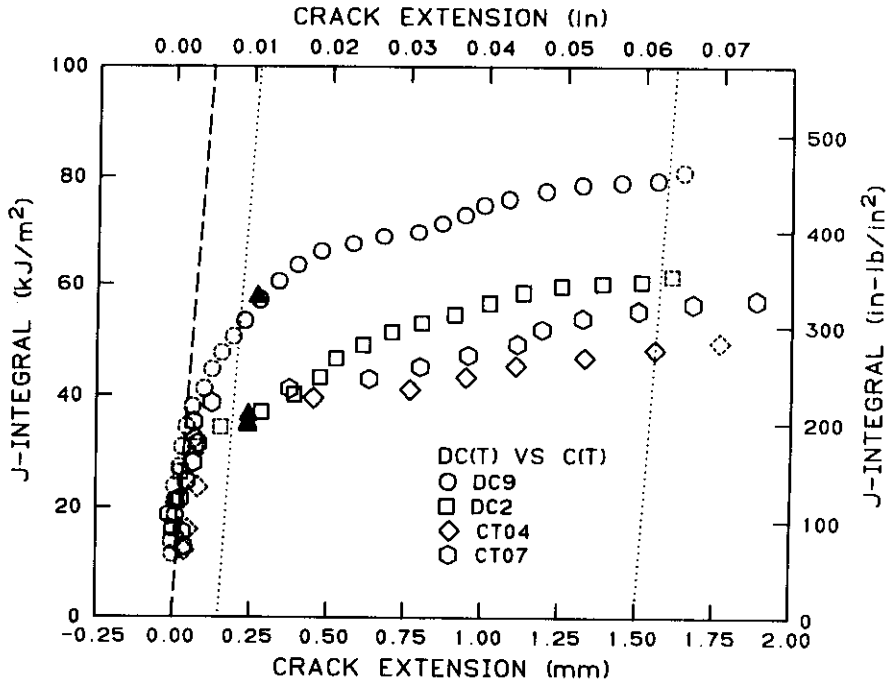

Fig. 10. A comparison between the J-R curves obtained by unloading compliance from 1/2 T compact specimens and the 0.18 T disk compact specimens. The compact specimens gave similar J_{Ic} values, but the J-R curves had lower slopes (lower tearing moduli).

Tabb 1. Fracture toughness results

Specimen number	Specimen type	Crack extension method[a]	J_Q		K_J		Tearing modulus	Crack extension agreement[b] (%)
			(kJ/m^2)	(in.-lb/in.^{2})	(MPa√m)	(ksi√in.)		
DC5[c]	Disk compact	UC	63	356	110	100	15	–9.0
DC9	Disk compact	UC	58	329	106	96	22	–9.6
DC2	Disk compact	UC	36	207	84	76	24	–10.0
	Disk compact	PD	38	218	86	78	23	–14.8
DC16	Disk comapct	UC	46	262	94	86	17	–13.4
	Disk compact	PD	44	254	93	84	21	–17.0
CT04	Compact	UC	36	203	83	75	10	–13.8
CT07	Compact	UC	34	196	81	74	18	–10.0

[a]UC = unloading compliance; PD = potential drop.
[b]Negative agreement indicates predicted crack extension was less than actual measured crack extension.
[c]Noticeable backup (apparent negative crack extension) reported at beginning of test.

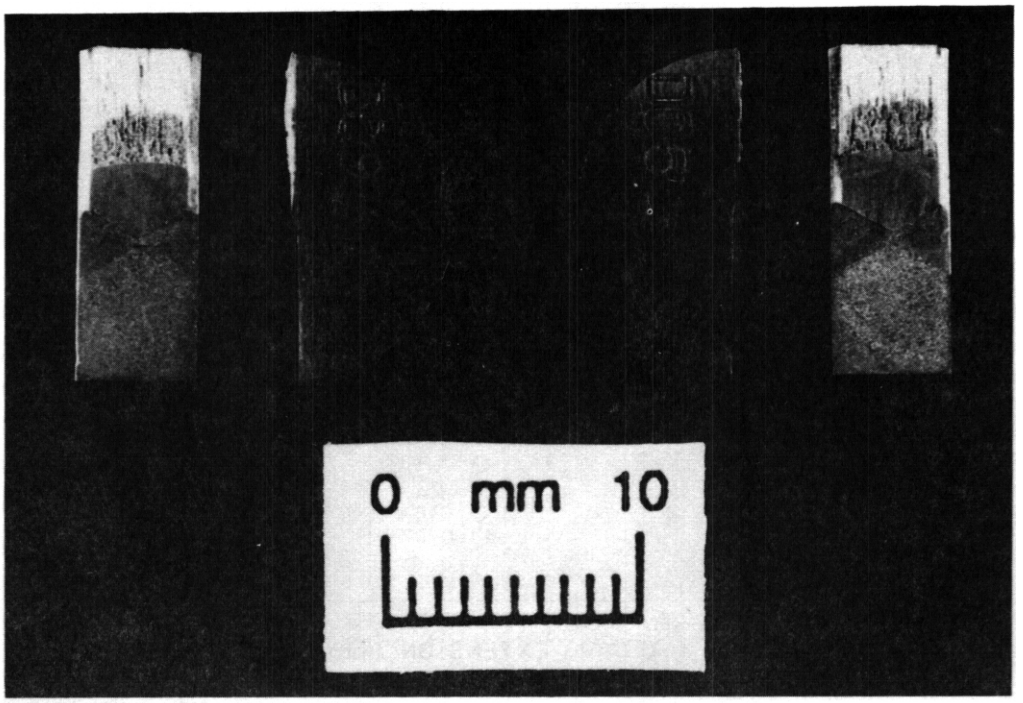

Fig. 11. Fracture surfaces from two of the disk compact specimens. Note the chevron notch to assist in precracking, and the side grooves added after precracking was finished. The fracture surface shows that crack growth occurred with slight tunneling, but there was little distortion of the specimens' shape.

CONCLUSIONS

Special tools, fixtures, and instrumentation have been developed to permit both UC and **PD** measurements to be made on small disk compact specimens. The techniques are apparently suitable for remote operation with manipulators. Laboratory trials have shown that both methods give similar results. In addition, these results are in good agreement with results from UC testing of larger conventional compact specimens. **These** methods will be used *to* determine the **effects** of low-temperature irradiation on the fracture toughness of candidate stainless **steel** alloys for the first wall of a fusion reactor.

FUTURE WORK

Additional trials will be conducted with a tougher material to determine if the small disk compact specimens will show similar agreement to standard specimens for tougher materials. Additional fixturing will **be** developed to facilitate the insertion of the disk compact specimen and the outboard clip gage in the load train of the servohydraulic testing machine in the hot cell. **The** ability of the servohydraulic testing machine to perform the fracture toughness testing will also be checked. The unloading compliance method will be used unless it is shown to give unsatisfactory results.

ACKNOWLEDGMENTS

Research sponsored by the Office of Fusion Energy, U.S. Department of Energy, under contract DE-AC05-84OR21400 with Martin Marietta Energy Systems, Inc. The clip gage was designed and fabricated by John Shepic, Lakewood, CO 80226. The slip coupling was purchased from Winfred M. Berg, Inc., East Rockaway, NY 11518. **We** would like to thank L. J. Turner and A. E. Parker for helpful suggestions for modifications to assist handling with the manipulators. The fracture toughness testing was performed by R. L. Swain, and M. J. Swindeman and J. J. Henry, Jr. performed the potential drop calibration experiments with a system assembled by D. L. Thomas from the Instrumentation and Controls Division. **The** manuscript was prepared by J. L. Bishop.

REFERENCES

1. G. **R.** Odette and G. E. Lucas. "Effects of Low Temperature Neutron Irradiation on the Properties of 300 Series Stainless **Steels,"** Fusion Reactor Materials Semiannual Progress *Report* for Period Ending March ***37,*** 7989, DOE/ER-0313/6, DOE Office of Fusion Energy, p. 313.

2. C. Elliot, **M.** Enmark, G. E. Lucas, G. **R.** Odette, and A. F. Rowcliffe. "Development of Disc Compact Tension Specimens and Test Techniques for HFIR Irradiations," Fusion Reactor Materials Semiannual Progress Report for Period Ending September ***30,*** *1990*, DOE/ER-0313/9, DOE Office of Fusion Energy, p. ***7.***

3. R. K. Nanstad. D. **J.** Alexander, **R.** L. Swain, **J.** T. Hutton, and D. **L.** Thomas, "A Computer-Controlled Automated Test System for Fatigue and Fracture Testing," Applications of Automation Technology to Fatigue and Fracture Testing, ***ASTM*** STP 7092. A. **A.** Braun, **N.** E. Ashbaugh, and F. M. Smith, Eds.. American Society for Testing and Materials. Philadelphia, 1990, p. ***7.***

4. J. **M.** Lowes and G. D. Fearnehough. *Eng. Frac.* Mech., Vol. 3, 1971, p. 103

5. M. G. Vassilaros and E. **M.** Hackett, "J-Integral R-Curve Testing of High Strength Steels Utilizing the Direct-Current Potential Drop Method,' Fracture Mechanics: 75th Symposium, ASTM STP 833, **R.** J. Sanford, Ed., American Society for Testing and Materials, Philadelphia, 1984, **p.** 535.

6. E. **M.** Hackett, M. T. Kirk, and **R.** A. Hays, An Evaluation of ***J-R*** Curve Testing of Nuclear Piping Materials Using the Direct-Current Potential Drop Technique, US. Nuclear Regulatory Commission NUREG/CR-4540, Washington, DC, August 1984.

2.0 DOSIMETRY, DAMAGE PARAMETERS, AND ACTIVATION CALCULATIONS

NEUTRON DOSIMETRY FOR THE MOTA-2A EXPERIMENT IN FFTF - L. R. Greenwood and L. S. Kellogg, Pacific Northwest Laboratory*

OBJECTIVE

To provide dosimetry and damage analysis for fusion materials irradiation experiments in the Materials Open Test Assembly (MOTA).

SUMMARY

Neutron fluence and spectral measurements and radiation damage calculations are reported for the MOTA-2A experiment in the Fast Flux Test Facility (FFTF). The irradiation was conducted from January 4, 1990 to March 19, 1991 for a total exposure of 299.7 EFPD. The maximum fluence was 15.8 x 10^{22} n/cm^2, 10.0 x 10^{22} above 0.1 MeV which produced 43.0 dpa in iron. This MOTA assembly contained the most comprehensive dosimetry to date with thirteen complete spectral measurements and twenty additional flux gradient measurements.

PROGRESS AND STATUS

Dosimetry for the MOTA-2A experiment was the most comprehensive to date with a total of thirty-three capsules positioned at different axial locations in the assembly. Each stainless steel capsule measured about 2.1 cm long by 0.48 cm o.d. and contained dosimetry wires for either spectral or gradient measurements. The thirteen spectral capsules contained Fe, Ti, Ni, Cu, Nb, 0.1% Co-A1 alloy, 0.825% ^{235}U in V, 0.936% ^{239}Pu in MgO, and 0.4% ^{237}Np in MgO monitors, whereas the twenty gradient capsules contained Fe and 0.1% Co-A1 alloy wires. The Co, U, Pu, and Np materials were separately encapsulated in vanadium. In addition, small amounts of Be, B, and LiF were included for helium analyses. Altogether, there were a total of 154 radiometric monitor wires.

Following irradiation each dosimetry capsule was opened in a hot cell and each individual monitor was identified and mounted for gamma analysis. The measured activities were then converted to saturated activities by correcting for the sample weight, atomic weight, isotopic abundance, gamma absorption, reactor power history, and fission yield, as needed. Neutron self-shielding effects were not significant since the Co, U, and Pu were dilute alloys and the FFTF neutron spectrum has few neutrons at lower neutron energies. For the U, Pu, and Np fission monitors, the gamma measurements detected four fission products, namely, ^{95}Zr, ^{106}Ru, ^{137}Cs, and ^{144}Ce. The standard deviation from the mean fission rate was generally less than 5% except for the ^{237}Np reactions at out-of-core locations, as discussed below.

Neutron burnup effects were found to be quite significant for the fission monitors and small corrections were necessary for the ^{59}Co(n,g) reactions. In the case of ^{59}Co this correction can be applied using an iterative procedure since the reaction itself is the sole source of the burnup, as described previously.[1] In the case of the ^{59}Co(n,g) reaction, the burnup effect varied from 0.4% at midplane to 2.5% in the below-core basket.

Neutron burnup effects were found to be much larger and more difficult to determine for the fission reactions. In all three cases, the fission reaction is not the sole source of the burnup since the (n,γ) cross section must also be included. Unfortunately, we have no measure of the (n,γ) reaction rates. However, we can readily calculate the rates using calculated neutron spectra. At each spectral location, neutron spectra were provided by R. Simons (Westinghouse Hanford) based on the cycle 9A irradiation. These spectra were used with the STAY'SL computer code[2] to determine reaction rates for both the fission and gamma reactions. Because the absolute measured fission rates were not known, we assumed that the ratios of gamma to fission were the same as the calculations and then determined the total burnup cross sections from the measured fission rates. Corrections were done separately for each fission product in order to account for the separate decay and burnup rates for each product isotope. The results were averaged to obtain a first order correction to the burnup effects. An iterative procedure was then used to determine a second order correction, which was found to be sufficient. The ^{235}U and ^{239}Pu burnup corrections were very similar and varied from 28% at midplane to only 2% at level 8.

The ^{237}Np burnup corrections were the most difficult to determine since we breed ^{238}Pu and ^{239}Pu from successive neutron capture reactions, especially at out-of-core locations. Both of these isotopes will then also contribute to the fission yields. At in-core positions, calculations show that the net effect is less than 5%. We also measured nearly identical fission rates for all four fission products for in-core positions, confirming our assumption that the Pu in-breeding effect is rather negligible. However, for the below-core basket, we calculate that Pu effects may be as large as 28%. Furthermore, we observed large variations in the four measured fission products. Due to such large and unpredictable effects, we did not include the Np data in the spectral analyses of the below-care basket and for the bottom of level 1.

---

* Pacific Northwest Laboratory is operated for the U.S. Department of Energy by Battelle Memorial Institute under Contract DE-AC06-76RLO 1830.

The corrected reaction rates are listed in Tables 1-3. All values are normalized to 291 MW operation and the values have an estimated absolute uncertainty of about 5%, although there is an additional uncertainty of about 5% for the fission reactions due to problems in determining the burnup rates. These rates appear to be inreasonable agreement with previous measurements[1-3] except for the fission reactions. Neither of the early experiments (MOTA-1A/1B or 1E) determined neutron burnup corrections for the fission reactions. Hence, our values are about 20-30% higher than previous measurements, allowing for differences in reactor power and core changes.

The measured activities were used as input to the STAY'SL computer code to adjust the calculated neutron spectra determined for cycle 9A.[2] STAY'SL performs a generalized least-squares adjustment of all measured and calculated values including the measured activities, calculated spectra, and neutron cross sections. Neutron cross sections and their uncertainties were generally taken from ENDF/B-V, although new data were available from ENDF/B-VI for the ^{46}Ti(n,p) and ^{63}Cu(n,a) reactions. The adjusted neutron fluence values are listed in Table 4. The neutron spectral adjustments for the thirteen positions are illustrated in Figure 1, which shows neutron spectra results at midplane, the edge of the core, and for the below-core basket. In comparisons with the calculated spectra, the agreement is reasonable (20-30%) for in-core positions. However, at out-of-core positions, the disagreement becomes progressively worse. At level 8 (+122 cm), the measured flux is about twice the calculated flux.

Damage calculations were also performed at all spectral positions using the SPECTER computer code.[5] Dpa rates for iron are also shown in Table 4 as well as the ratio of dpa per 10^{22} n/cm fast flux above 0.1 MeV. Damage parameters for other elements or compounds have been calculated and will be made available.

The flux and damage gradients at other positions can be found from the activity gradient data in Table 1 which are shown in Figure 2. Note that the ^{58}Fe and ^{59}Co(n,g) reactions peak outside of the core since they are sensitive to the lower-energy neutrons. The unusual behavior of the Co reaction is due to resonance effects. Fast fluence and dpa gradients from Table 4 are plotted in Figure 3. The apparent scatter is again due to the radial flux gradients, as discussed below.

Close examination of the activity data indicates the presence of radial flux and spectral gradients. The letters A to F under the position column in Table 4 indicates the radial position at the height indicated. The mota basket has six radial positions (A to F); hence, for example, A and D are the furthest apart while A and B or F are adjacent. The maximum radial flux differences are on the order of 10%; however, we also see clear indications of spectral differences in the ratio of the fast flux to the 54-Fe(n,p) activity rate. Such differences are complex and we are now studying these effects in order to construct a more complete flux and damage map of the entire MOTA assembly.

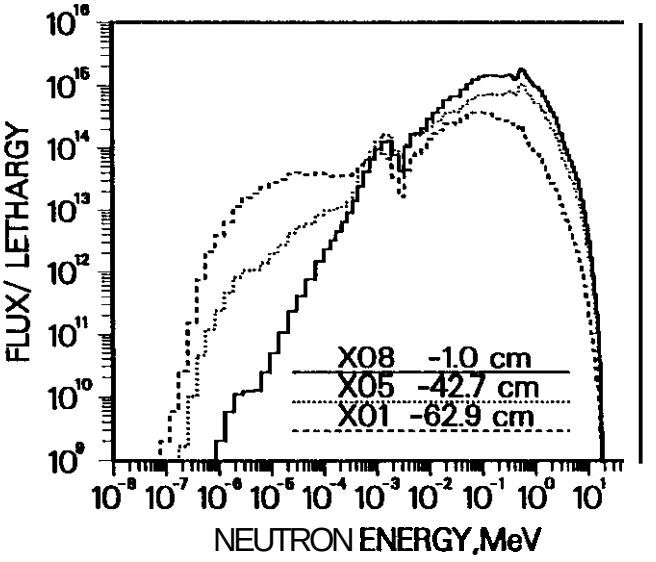

Fig. 1 Adjusted Neutron Flux Spectra are shown at Three Axial Locations in the MOTA-2A Assembly. The solid line is at -1 cm, the dotted line is at -42.1 cm, and the dashed line is at -62.9 cm. Note the drop in fast flux and increase in low-energy flux at out-of-core locations.

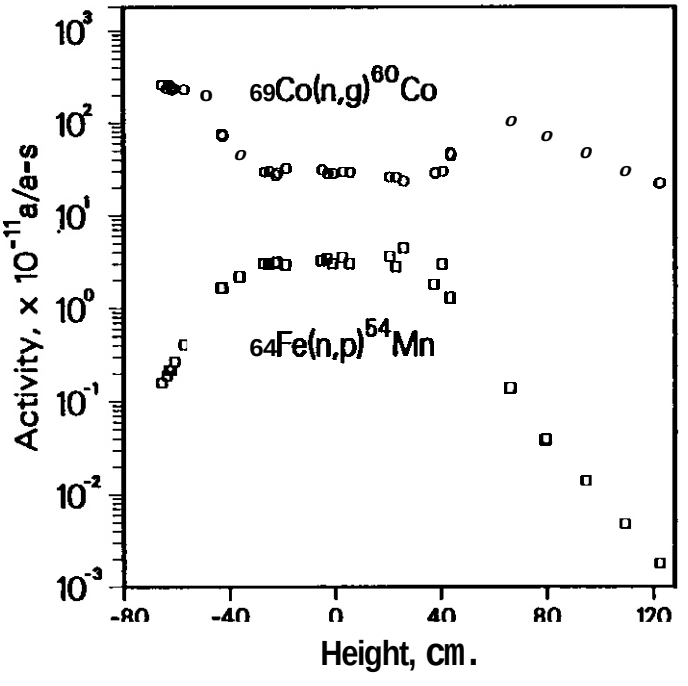

Fig. 2 Activities Values are Shown for the 54-Fe(n,p)54-Mn and 59-Co(n,γ)60-Co Reactions as a Function of Axial Location in the MOTA-2A Assembly. Some of the scatter is due to radial flux gradients.

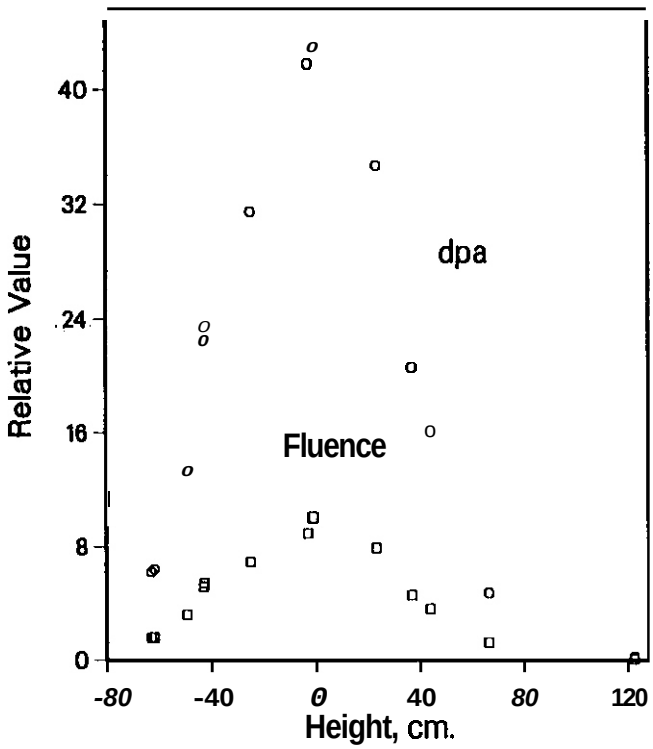

Fig. 3. Fast Flux (>0.1 MeV) and dpa in Iron are Shown as a Function of Axial Location in the MOTA-2A Assembly. The apparent scatter is indicative of the radial gradients.

FUTURE WORK

We plan to construct more detailed flux and damage maps for the entire MOTA-2A assembly. Damage parameters will also be provided for a variety of elements and alloys. These data will be used to help reanalyze previous data from MOTA-1A through 1E, especially to include burnup effects for the fission monitors. Dosimetry analyses are now in progress for MOTA-1G. The MOTA-2B irradiation had completed about 200 EFPO before the FFTF reactor was placed in a standby position. No decision has been reached about analysis of these dosimeters. Dosimetry has been provided for a variety of US/Japanese experiments in the High Flux Isotopes Reactor. Contracts are now being negotiated to commence the analyses for these experiments, many of which are now out of reactor.

REFERENCES

1. L. R. Greenwood and L. S. Kellogg, "Neutron Dosimetry for the MOTA-1F Experiment in FFTF", Fusion Reactor Materials Semiannual Prowess Report DOE/ER-0313/9, pp. 31-36 (1990).

2. F. G. Perey, Least Squares Dosimetry Unfolding: The Program STAY'SL, ORNL/TM-6062 (1977).

3. R. L. Simons, Damage Analysis and Fundamental Studies quarterly Progress Report, DOE/ER-0046/21, pp. 10-14, May 1985.

4. L. S. Kellogg, W. M. Mc Elroy, and W. Y. Matsumoto, FERRET-SAND II Physics-Dosimetry Analysis for the FTR MOTA-1E Experiments, PNL-NDC Report, December 1989.

5. L. R. Greenwood and R. K. Smither, SPECTER: Neutron Damage Calculations for Materials Irradiations, ANL/FPP-TM-197, January 1985.

PUBLICATIONS

The following papers have been approved for publication in the Journal of Nuclear Materials after the Fifth International Conference on Fusion Reactor Materials in November 1991.

1. L. R. Greenwood, F. A. Garner, and H. L. Heinisch, "The Impact of Spectral Effects in Fast Reactors on Data Analysis and Development of Fission-Fusion Correlations".

2. L. R. Greenwood, F. A. Garner, and B. M. Oliver, "Helium Generation Rates in Isotopically Tailored Fe-Cr-Ni Alloys Irradiated in FFTF/MOTA".

3. T. B. O'Hearn, A. S. Kumar, and L. R. Greenwood, "Comparison of Measured and Calculated Transmutation in Copper at Spallation Neutron Sources".

Table 1. Activity Measurements for MOTA-2A (atoms/atom-s)

Sample\ Level-Pin	Ht,cm	54Fe(n,p) (xE-11)	58Fe(n,g) (xE-11)	59Co(n,g) (xE-10)	93Nb(n,g) (xE-10)
X14 **8-BT**	122.4	0.0018	0.40	2.27	0.528
X34 8-BM	109.2	0.0048	**0.60**	3.10	
X33 7-BM	94.1	0.014	0.95	4.96	
X32 6-BT	79.8	0.040	1.47	7.48	
X13 6-BB	**66.6**	0.14	2.33	10.45	3.50
X31 5-EM	43.7	1.32	2.75	4.68	
X12 5-FTP	44.0	1.30	2.66	4.46	
X11 5-FBP	37.7	1.83	2.74	2.81	
X30 5-DMP	40.6	2.97	2.94	2.94	
X28 4-CMP	26.1	4.36	3.48	2.31	
X10 4-AMP	23.3	2.80	3.80	2.55	
X29 4-FMP	20.9	3.57	3.57	2.55	
X25 3-AT	5.3	3.02	4.59	2.95	
X27 3-EMP	2.7	3.50	4.34	2.97	
X08 3-AM	-1.0	3.01	4.68	2.86	9.81
X09 3-DM	-3.1	3.38	4.39	2.86	
X26 3-AB	-5.2	3.23	4.63	3.12	
X24 2-ET	-22.6	3.03	3.82	2.75	
X23 2-AMP	-18.7	2.94	4.28	3.25	
X22 2-BMP	-21.8	3.16	4.29	2.93	
X07 2-EM	-25.0	2.98	3.76	3.04	
X20 2-FMP	-26.8	3.04	3.78	2.99	
X21 1-DTP	-36.1	2.19	3.56	4.02	
X05 1-DMP	-42.7	1.64	3.67	7.17	
X06 1-FMP	-42.9	1.63	3.77	7.54	6.88
X04 1-DB	-49.2	0.00	0.00	14.22	7.15
X15 BC-AT	-57.2	0.41	**5.08**	23.12	
X17 BC-BM	-60.8	0.27	4.93	23.64	
X02 BC-EM	-61.7	0.00	0.00	23.04	
X18 BC-FM	-62.0	0.22	4.46	24.73	
X19 BC-DM	-63.7	0.19	4.26	23.85	
X01 BC-AM	-62.9	0.22	4.88	25.96	5.95
X16 BC-AB	-65.7	**0.16**	4.42	25.88	

Table 2. Activation Measurements for MOTA-2A (atoms/atom-s)

Sample\ Level-Pin	Ht,cm	46Ti(n,p) (xE-12)	58Ni(n,p) (xE-11)	60Ni(n,p) (xE-13)	58Ni-57Co (xE-14)	63Cu(n,a) (xE-13)
X14 8-BT	122.4	0.0018	0.0028	0.0061	0.0089	0.0009
X13 6-BB	**66.6**	0.16	0.19	0.33	0.40	0.074
X12 5-FT	44.0	1.65	1.83	3.09	3.62	0.76
X11 5-FB	37.7	2.25	2.56	4.45	5.12	1.08
X10 4-AM	23.3	3.50	3.83	6.68	7.96	1.63
X08 3-AM	-1.0	3.81	4.49	7.62	8.57	1.88
X09 3-DM	-3.1	3.93	4.42	7.94	8.76	1.90
X07 2-EM	-25.0	3.62	3.97	7.18	8.10	1.72
X05 1-DM	-42.7	2.00	2.22	4.11	4.35	1.56
X06 1-FM	-42.9	2.03	2.23	4.09	4.39	1.00
X04 1-DB	-49.2	1.18	1.23	2.15	2.52	0.53
X02 BC-EM	-61.7	0.25	0.30	0.54	0.61	0.12
X01 BC-AM	-62.9	0.24	0.29	**0.56**	0.63	0.12

Table 3. Fission Measurements for MOTA-2A (atoms/atom-s)

Sample\ Level-Pin	Ht,cm	239Pu (xE-9)	237Np (xE-10)	235U (xE-9)
X14 8-BT	122.4	0.80	0.079	0.84
X13 6-BB	66.6	4.46	2.25	4.84
X12 5-FT	44.0	4.74	9.52	5.97
X11 5-FB	37.7	5.35	12.30	6.49
X10 4-AM	23.3	8.43	20.90	9.14
X08 3-AM	-1.0	10.20	25.00	11.21
X09 3-DM	-3.1	8.80	30.00	10.58
X07 2-EM	-25.0	7.68	18.70	9.05
X05 1-DM	-42.1	7.09	14.30	8.17
X06 1-FM	-42.9	6.89	13.70	8.23
X04 1-08	-49.2	7.96		9.14
X02 BC-EM	-61.7	9.30		10.05
X01 BC-AM	-62.9	9.34		10.02

Table 4. Neutron Fluence and Displacement Damage for MOTA-2A

Ht,cm	Fast Fluence (>.1 MeV) xE+22 n/cm^2	Iron dpa	Ratio dpa/Fluence	Position
-62.9	1.58	6.2	4.0	A
-61.7	1.58	6.4	4.0	E
-49.2	3.18	13.3	4.2	D
-42.9	5.13	22.5	4.4	F
-42.7	5.41	23.5	4.3	D
-25.0	6.94	31.5	4.5	E
-3.1	8.93	41.8	4.7	D
-1.0	10.02	43.0	4.3	A
23.3	7.92	34.7	4.4	A
37.7	4.56	20.6	4.5	F
44.0	3.60	16.1	4.5	F
66.6	1.22	4.7	3.9	B
122.4	0.062	0.24	3.9	B

Calculation of Displacement Levels for Pure Elements and Most Multicomponent Alloys Irradiated in FFTF MOTA-1F - F. A. Garner and L. R. Greenwood, Pacific Northwest Laboratory' and A. M. Ermi, Westinghouse Hanford Company

OBJECTIVE

The objective of this effort is to ensure consistency in the displacement values reported by various experimenters involved in FFTF/MOTA irradiations.

SUMMARY

A simple method is presented for calculating displacement levels for most multicomponent alloys irradiated in FFTF/MOTA.

PROGRESS AND STATUS

Introduction

For each irradiation series conducted in FFTF/MOTA, the experimenters are provided the neutron fluences above 0.1 MeV and the displacement levels as shown in Tables 1 and 2, and Figure 1[1,2]. Table 2, however, is strictly valid only for Fe-18Cr-8Ni[b] and is not applicable to other metals (Cu and V, for instance). If a particular study involves a significant variation in composition within the specimen matrix, then the displacement level will also vary across that matrix.

In order to assist researchers involved in the FFTF Cycle 10 irradiation in MOTA 1F, spectral-averaged calculations of the displacements per neutron have been performed for the most common major elements employed in metal alloys.

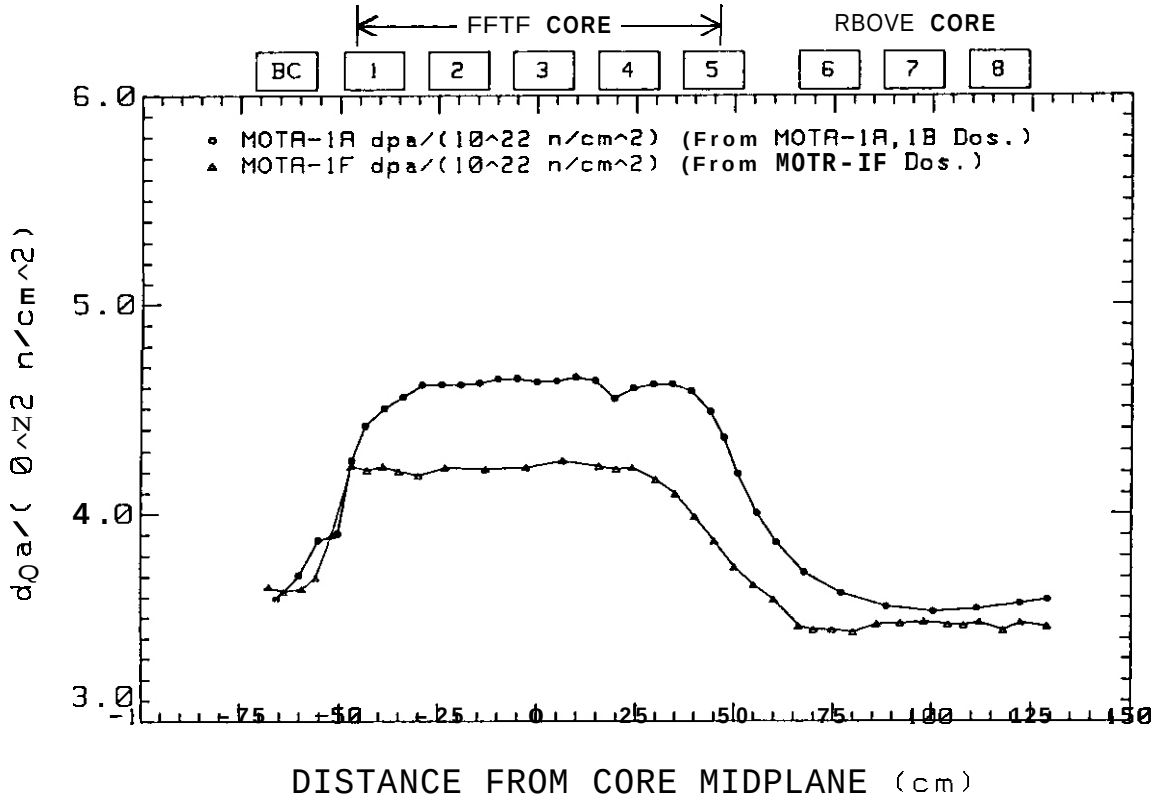

Figure 1. Comparison of dpa conversion factors for MOTAs 1A and 1F as a function of axial position.

'Pacific Northwest Laboratory is operated for the U.S. Department of Energy by Battelle Memorial Institute under Contract DE-AC06-76RLO 1830.

[b] Note that dpa values for MOTA-1A were calculated for Fe-18Cr-10Ni. The dpa difference between 8 and 10% Ni is less than I%, however.

Table 1. MOTA-1A FLUX. FLUENCE and OPA VALUES

BASED ON 202.0 EFPO FOR FFTF CYCLE(S) 2-3

DISTANCE FROM HOA. MIDPLANE (HMP)[cm]	FAST FLUX E>0.1 MeV [n/(cm^2-s)]	FAST FLUENCE E>0.1 MeV [n/cm^2]	Dpa per second	TOTAL Dpa	Dpa per (10^22 n/cm^2)
t129.00	1.95E+13	3.40E+20	7.00E-09	.122	3.59
+122.16	2.79E+13	4.87E+20	9.96E-09	.174	3.57
+111.22	4.77E+13	8.32E+20	1.69E-08	.295	3.54
t100.27	8.08E+13	1.41E+21	2.85E-08	.497	3.53
t88.33	1.41E+14	2.46E+21	5.01E-08	.874	3.55
t76.87	2.48E+14	4.33E+21	8.98E-08	1.567	3.62
t67.41	3.95E+14	6.89E+21	1.47E-07	2.566	3.72
t60.50	6.03E+14	1.05E+22	2.33E-07	4.067	3.86
t55.63	8.17E+14	1.43E+22	3.27E-07	5.707	4.00
t50.77	1.09E+15	1.90E+22	4.57E-07	7.976	4.19
t47.32	1.33E+15	2.32E+22	5.80E-07	10.123	4.36
t43.85	1.58E+15	2.76E+22	7.08E-07	12.357	4.48
t38.98	1.91E+15	3.33E+22	8.75E-07	15.271	4.58
t34.10	2.21E+15	3.86E+22	1.02E-06	17.802	4.62
t29.32	2.47E+15	4.31E+22	1.14E-06	19.896	4.62
+24.36	2.72E+15	4.75E+22	1.25E-06	21.816	4.60
t19.51	2.97E+15	5.18E+22	1.35E-06	23.561	4.55
t14.66	3.13E+15	5.46E+22	1.45E-06	25.307	4.63
+9.80	3.27E+15	5.71E+22	1.52E-06	26.528	4.65
t4.95	3.39E+15	5.92E+22	1.57E-06	27.401	4.63
t0.00	3.48E+15	6.07E+22	1.61E-06	28.099	4.63
-5.03	3.51E+15	6.13E+22	1.63E-06	28.448	4.64
-9.92	3.49E+15	6.09E+22	1.62E-06	28.274	4.64
-14.62	3.44E+15	6.00E+22	1.59E-06	27.750	4.62
-19.34	3.36E+15	5.86E+22	1.55E-06	27.052	4.61
-24.15	3.25E+15	5.67E+22	1.50E-06	26.179	4.62
-29.04	3.10E+15	5.41E+22	1.43E-06	24.958	4.61
-33.90	2.92E+15	5.10E+22	1.33E-06	23.212	4.55
-38.74	2.69E+15	4.69E+22	1.21E-06	21.118	4.50
-43.57	2.40E+15	4.19E+22	1.06E-06	18.500	4.42
-47.01	2.15E+15	3.75E+22	9.15E-07	15.969	4.26
-50.47	1.98E+15	3.46E+22	7.73E-07	13.491	3.90
-55.34	1.59E+15	2.77E+22	6.16E-07	10.751	3.87
-60.20	1.33E+15	2.32E+22	4.93E-07	8.604	3.71
-65.76	1.10E+15	1.92E+22	3.95E-07	6.894	3.59
-72.01	9.26E+14	1.62E+22	3.22E-07	5.620	3.48
-77.53	7.57E+14	1.32E+22	2.55E-07	4.450	3.37

Flux and dpa rates for Fe-18Cr-10Ni based on dosimetry from MOTA-1A and MOTA-1B[1].

Results

The calculated dpa conversion factors for many commonly irradiated elements are presented in Table 3 for both the core midplane and the top of the below-core basket (-59 cm). The units are dpa per 10^{22} n cm^{-2} (E>0.1 MeV]. Note that significant variations occur not only with elemental identity but also between the midplane and -59 cm. This reflects a softening of the spectrum outside the core, with only 56.7% of the neutrons above 0.1 MeV at -59 cm, compared to 74.8% at the midplane. These dpa calculations were performed with the SPECTER[3] computer code and are directly applicable only to pure elements. Calculations for multicomponent alloys require the use of the SPECOMP[4] computer code. For simple alloys, however, where all elements have similar masses and displacement thresholds, a linear sum is a reasonable approximation, as shown in detail below.

The suggested procedure for analysis and publication of MOTA data is to report not only the neutron fluence but also the alloy-specific dpa level, the latter defined by $\phi t\ [\Sigma_i C_i F_i]$, where ϕt is the neutron fluence (E>0.1 MeV) divided by 1 X 10^{22} n cm^{-2}, C_i is the fractional concentration of each major alloy component, and F_i is the number of displacements per 10^{22} n/cm^2 (E>0.1 MeV). The values reported for Fe-18Cr-8Ni were calculated by this method.

Table 2. MOTA-IF FLUX FLUENCE and OPA VALUES

BASED ON 335.4 EFPD FOR FFTF CYCLE(S) 10

DISTANCE FROM HOR. MIDPLANE (HMP)[cm]	FAST FLUX E>0.1 MeV [n/(cm^2-s)]	FAST FLUENCE E>0.1 MeV [n/cm^2]	Dpa per second	TOTAL Dpa	Dpa per (10^22 n/cm^2)
+129.00	5.18E+12	1.50E+20	1.79E-09	.052	3.46
t122.30	7.45E+12	2.16E+20	2.59E-09	.075	3.48
+118.00	9.63E+12	2.79E+20	3.31E-09	.096	3.44
t112.00	1.40E+13	4.06E+20	4.87E-09	.141	3.48
+108.00	1.84E+13	5.34E+20	6.38E-09	.185	3.46
+104.00	2.40E+13	6.95E+20	8.32E-09	.241	3.47
+98.00	3.62E+13	1.05E+21	1.26E-08	.365	3.48
t92.00	5.73E+13	1.66E+21	1.99E-08	.577	3.41
+86.00	9.08E+13	2.63E+21	3.15E-08	.913	3.47
+80.00	1.47E+14	4.26E+21	5.04E-08	1.461	3.43
t74.80	2.23E+14	6.45E+21	7.66E-08	2.220	3.44
t70.00	3.29E+14	9.53E+21	1.13E-07	3.280	3.44
+66.30	4.38E+14	1.27E+22	1.52E-07	4.390	3.46
+60.00	6.80E+14	1.97E+22	2.44E-07	7.071	3.59
t55.00	9.28E+14	2.69E+22	3.40E-07	9.850	3.66
t50.00	1.22E+15	3.55E+22	4.59E-07	13.301	3.75
t45.00	1.59E+15	4.60E+22	6.14E-07	17.799	3.87
t40.00	1.97E+15	5.72E+22	7.87E-07	22.800	3.99
t35.00	2.33E+15	6.76E+22	9.56E-07	27.701	4.10
t30.00	2.65E+15	7.68E+22	1.10E-06	31.992	4.17
t24.10	2.93E+15	8.50E+22	1.24E-06	35.904	4.22
t20.00	3.04E+15	8.80E+22	1.28E-06	37.093	4.21
t15.70	3.11E+15	9.01E+22	1.32E-06	38.107	4.23
+6.50	3.20E+15	9.28E+22	1.36E-06	39.498	4.26
-2.70	3.30E+15	9.56E+22	1.39E-06	40.396	4.23
-13.00	3.31E+15	9.58E+22	1.39E-06	40.396	4.22
-23.20	3.32E+15	9.61E+22	1.40E-06	40.599	4.22
-30.00	3.26E+15	9.46E+22	1.37E-06	39.585	4.19
-35.00	3.13E+15	9.06E+22	1.32E-06	38.107	4.21
-39.00	2.94E+15	8.51E+22	1.24E-06	35.991	4.23
-43.00	2.68E+15	7.76E+22	1.13E-06	32.688	4.21
-47.10	2.34E+15	6.78E+22	9.90E-07	28.700	4.23
-52.00	1.88E+15	5.44E+22	7.32E-07	21.201	3.90
-56.00	1.46E+15	4.22E+22	5.38E-07	15.599	3.70
-59.40	1.12E+15	3.24E+22	4.07E-07	11.800	3.64
-64.00	7.38E+14	2.14E+22	2.68E-07	7.760	3.63
-67.60	5.31E+14	1.54E+22	1.94E-07	5.619	3.65
-72.00	3.30E+14	9.56E+21	1.20E-07	3.480	3.64
-78.00	1.76E+14	5.10E+21	6.42E-08	1.860	3.65

Flux and dpa rates for Fe-18Cr-8Ni based on dosimetry from MOTA-1F[2]

As shown in Figure 1 and Table 2, the value of F_i within most of the core region in MOTA-IF does not change appreciably. Thus, the midplane value can he used throughout most of the core. This is not true, however, for level 5 and above. For alloys other than Fe-18Cr-8Ni, F values should be calculated individually for irradiations conducted in canisters 5 through 8, or for positions below -59cm.

Note also that the F_i values for MOTA-IF are smaller than those of MOTA-1A. This is a consequence of core changes (particularly in the reflector) associated with placement of the Core Demonstration Experiment in MOTA-1E and beyond. The values of F. for MOTA-IA and 1F are also significantly smaller than those involved in earlier irradiations conducted in EBR-II (5.0 ± 0.2 across the in-core region) as shown in Figure 2.[5] This difference between the two reactors reflects the greater neutron-moderating ability of oxide fuel in FFTF compared with that of metal fuel in EBR-II. Since EBR-II is a much smaller reactor than FFTF, it has more leakage of neutrons and this results in a larger variation of F_i across the EBR-II core. These distinctions are important when comparing data from the two reactors.

Experimenters should note that dpa levels may vary within an experiment as a function of composition. For example, in some ongoing experiments conducted in EBR-II and FFTF, nickel content is the primary variable. The Fe-15Cr-XNi (X=15 to 85) alloy used in these experiments have been described by Muroga, Garner and

Table 3. Dpa Conversion Factors (F_i) for MOTA 1F[a]

Element	Threshold Energy[b] (eV)	Value at Midplane dpa/10^{22}n cm^{-2} (E>0.1)	Value at -59 cm dpa/10^{22}n cm^{-2} (E>0.1)
Fe	40	4.12	3.56
Ni	40	4.77	4.39
Cr	40	4.60	3.97
V	40	5.44	4.98
Mn	40	5.05	4.59
Si	25	10.17	9.15
Ti	40	4.11	3.54
Cu	30	5.79	5.20
Nb	40	4.79	4.47
Mo	60	3.54	3.47
W	90	1.14	0.99
Ta	53	1.96	1.71

[a] Note: The dpa values in this table were derived from SPECTER calculations[3] and are strictly applicable only to pure elements. See text for recommendations on how to handle multicomponent alloys.

[b] Threshold values taken from ASTM Standard E521-83 "Neutron Radiation Damage Simulation by Charged Particle Irradiation."

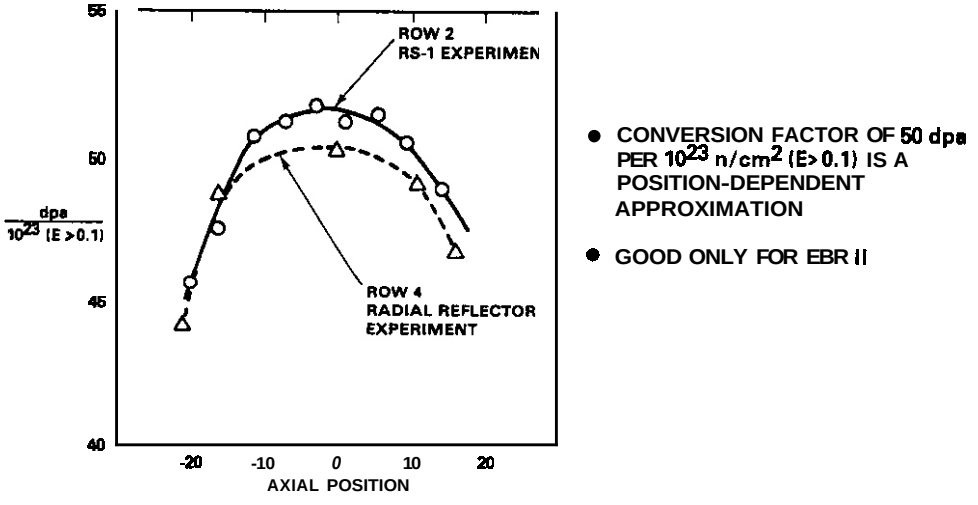

Figure 2. Opa conversion factors for two typical EBR-II experiments.[3] The axial position is given in cm.

McCarthy,[6]. At the midplane level of MOTA 1F the dpa level increases 9.3% from X=15 to 85. Comparable differences would have occurred in MOTA 1A and EBR-II. Note, however, that in reactors such as ORR or HFIR where the two-step $^{58}Ni(n, \gamma)^{59}Ni(n, \alpha)^{56}Fe$ reaction contributes strongly to the displacement rate, the difference can be much larger.[7,8]

When the primary material variable involves elements with significantly different atomic weights, displacement thresholds and PKA spectra from that of the host materials (FeCrW or FeSi alloys, for instance), the calculation becomes much more complicated. In this case, either the assumptions employed to calculate the displacement level should be clearly stated or a computer code such as SPECOMP[2] should be used. An alternate approach would be to quote the dpa level for the host material and mention that some variation will occur as a function of solute content.

CONCLUSIONS

The number of displacements experienced by a material irradiated in the FFTF depends on the total neutron exposure, the elemental composition, the location in the core, and the specific core employed. This requires that each experimenter determine the displacement levels for all alloys in their experiment and that they be careful to evaluate dpa values consistently when comparing data from different MOTAs or different reactors.

REFERENCES

1. R. L. Simons, "Analysis of Damage Exposure Rates in the Materials Open Test Assembly of the Fast Flux lest Facility" in Damage Analysis and Fundamental Studies Quarterly Progress Report DOE/ER-0046/21, 1985, pp. 10-16.

2. L. R. Greenwood and L. S. Kellogg, "Neutron Dosimetry for the MOTA-1F in FFTF" in Fusion Reactor Materials Semiannual Progress Report DOE/ER-0313/9, 1990, pp. 31-36.

3. t. R. Greenwood and R. K. Smither, SPECTER: Neutron Damage Calculations for Materials Irradiations, ANL-FPP/TM-197, Argonne National Laboratory, 1985.

4. I. R. Greenwood. "Radiation Damage Calculation for Compound Materials" in Effects of Radiation on Materials: 17th International Symposium (Vol. I), ASTM-STP 1046, N. H. Packan, R. E. Stoller and A. S. Kumar, Eds., American Society for Testing and Materials, Philadelphia, 1990, pp. 633-641.

5. F. A. Garner "Overview of the Swelling Behavior of 316 Stainless Steel" in Optimizing Materials for Nuclear Applications, F. A. Garner, D. S. Gelles and F. W. Wiffen, Eds., The Metallurgical Society, Inc., Warrendale, PA, 1985, pp. 111-139.

6. T. Muroga, F. A. Garner and S. Ohnuki, J. Nucl. Mater., 179-181 (1991) 546-549.

7. F. A. Garner and F. M. Mann, "The Impact of the $^{59}Ni(n,\alpha)^{56}Fe$ on Damage Calculations for HFIR" in Damage Analysis and Fundamental Studies Quarterly Progress Report DOE/ER-0046/9, 1982, pp. 41-49.

8. F. A. Garner and B. M. Oliver, "Helium Measurements for the MFE-4 Spectral Tailoring Experiment" in Fusion Reactor Materials Semiannual Progress Report, DOE/ER-0313/9, 1990, pp. 58-60.

3.0 MATERIALS ENGINEERING AND DESIGN REQUIREMENTS

IRRADIATION BEHAVIOR OF BONDED STRUCTURES: IMPACT OF STRESS-ENHANCED **SWELLING** ON IRRADIATION CREEP AND ELASTIC PROPERTIES - M. H. Hassan, J. P. Blanchard, and G. L. Kulcinski (Fusion Technology Institute, University of Wisconsin-Madison)

OBJECTIVE

To understand the factors that govern the adhesion of coatings on fusion reactor first walls which are subjected to neutron irradiation.

SUMMARY

Radiation damage will he a major key point in the design of the many duplex components in fusion reactors. There is a substantial amount of available data showing that stress plays a major role in the onset, and possibly the rate, of void growth in austenitic stainless steels. There is also strong support models which predict a coupling of swelling and creep through the stress environment. A parametric study for evidence to stress-enhanced swelling and its connection to creep is conducted for a typical fusion power demonstration reactor. Since microstructural changes are known to affect elastic moduli, the impact of stress enhanced swelling on these moduli are also evaluated.

PROGRESS AND STATUS

Introduction

Duplex structures (i.e., coatings or thin films on a substrate structure) are likely to he used in both near-term and commercial fusion reactors. The bonding of these structures leads to complicated stress fields which must he understood in order to evaluate the probability of failure for the device.' Radiation damage will be a major factor in the design of the different duplex components and the synergistic effectsof high heat fluxes, high dpa (displacement per atom) levels, and high primary stresses must he taken into consideration. While radiation-effects data on (as well as modelling for) fundamental phenomena can he correlated to structural effects, the uncertainty in the synergistic effects could jeopardize the success of the final design.?

The mechanisms of irradiation damage at the interface of bonded structures are not well understood although the damage mechanisms present in metallic materials should also apply to the damage in coatings (e.g., swelling or differential swelling). The properties of greatest concern are the fatigue/crack propagation properties and the effects of irradiation on swelling and embrittlement of the materials.[3]

Swelling due to radiation-induced voids is a major concern for the first wall of fusion devices at temperatures of 400°C and above, and has been the focus of considerable alloy development effort since 1970's.[4] Stress is also known to reduce the incubation period for swelling (see next section). Since one probable mechanism of failure of bonded structures is, in fact, the level of differential swelling,[6] it is obvious why an understanding of swelling (and the effect of stress on it) *is* critical to the design of **successful** duplex structures.

Since irradiation creep and swelling have a common **source,** an interrelationship between both phenomena existS.[7] There would be many practical consequences of such coupling. Flinn et al.[8] indicated that if no competing mechanism existed (swelling-enhanced creep for example), the residual stresses due to differential swelling could build up with exposure to a level where a component could yield or fracture, Thus, if irradiation creep and swelling are proportional to each other, many of the problems generated by differential swelling would he minimized through the relaxation mechanism of the swelling-enhanced creep. Daenner and Raeder[9] indicated that it would be dangerous to regard swelling and creep separately. They also proved that it is dangerous to see the stress/strain analysis isolated from the materials behavior. Figure 1 is a schematic of the interrelationships that exist between swelling, creep, and stress. The heavy lines indicate the areas that are examined in this paper.

For ITER and beyond, experimental data on the effect of stress on swelling, and the relationship between radiation creep and swelling are badly needed.'' For example, one of the major concerns for **316** SS is the differential swelling in the **400-500°C** range.'' This is the range where stress-enhanced swelling was first noticed. While extensive stress analyses have been carried out for high heat flux structures made of single materials such as 316 stainless steel, stress analysis for duplex structures is only in its early stages of development.[12] The major work in this area is mainly from Mattas,[10,13,14] Glasgow,[15] and Blanchard.[1,16] None of these previous works, as well as the few inelastic stress analyses that included radiation effects,[5,9,17–23] had incorporated the effect of stress on the swelling behavior of the structure. **As** for the interrelationship between creep and swelling, only Mattas'' took it into consideration.

Stress-Enhanced Swelling

The effect of stress on swelling was first recognized in 1967 when Cawthorne and Fulton[24] reported that "there is no doubt that stress and strain during irradiation will influence void growth." Since that time, the available data shows that stress plays a major role in the onset (and possibly) the rate of void growth in AISI 316 stainless steel in a variety of metallurgical conditions.[8,24,25–33] A more limited set of data on AISI 304[34] as well as nickel[35,36–39] shows that the effect of stress on void swelling is not limited only to the 316 stainless steel. A complete survey of the available data is presented in Ref. 40.

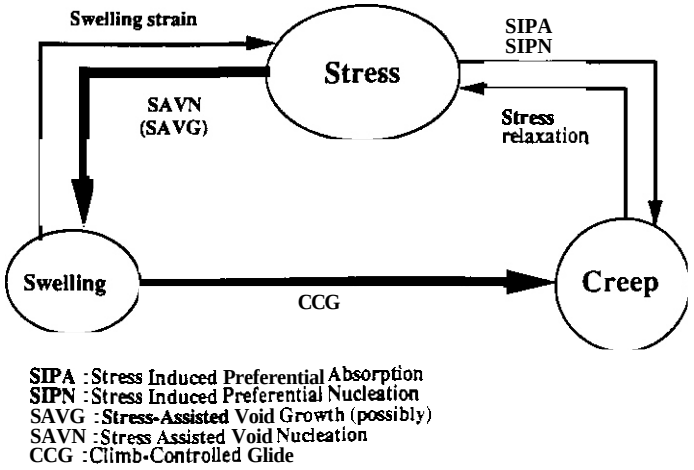

Fig. 1. Relationship between Swelling-Creep-Stress in a radiation environment.

1. Modelling of Stress-Enhanced Swelling

An empirical constitutive equation for the stress effect on swelling incubation dose is given as the larger of:[41]

$$\tau_e = \tau - q(T)\,\sigma_h \tag{1}$$

$$\tau_e = 0.5 \tag{2}$$

where τ_e is the incubation parameter in units of 10^{22} n $\cdot$ cm^{-2} ($E > 0.1$ MeV),

$q(T)$ expressed in the units of 10^{22} n $\cdot$cm$^{-2}\cdot$ MPa^{-1} is calculated'' from

$$q(T) = q_0 + \exp[a - Q'/(T + 273] \tag{3}$$

T is the temperature in units of °C,

σ_h is the hydrostatic stress in units of MPa, , $\sigma_h = \frac{1}{3}(|\sigma_x| + |\sigma_y| + |\sigma_z|)$,

where $q_0 = 0.013$, $a = 51.4$, $Q' = 50{,}000$ in units of °C^{-1}. Based on the observation that the compressive as well as tensile stresses enhance swelling,[33,42–45] the absolute values of the stresses are used in the calculation of the hydrostatic stress. The modified incubation dose is then used in conjunction with the swelling equation for 316 SS developed for the fuel pin cladding in fast reactors.'"

Straightforward use of the stress effect on incubation dose in fusion designs is complicated by the presence of time-varying stress histories. A formalism, the Incubation Averaged Fluence (IAF) technique:' has been developed so that the time-dependent stress can be included in calculations of the stress effect on incubation dose.

The IAF, $f(t)$, is defined as[27]

$$f(t) = \int_0^t \frac{\phi(t')}{\tau_e(t')}\,dt'. \tag{4}$$

In this equation the effective incubation fluence τ_e depends on time through the time variation of the hydrostatic stress σ_H. The value of σ_H is used to calculate τ_e from Equations 1 or 2. The condition for swelling to remain in the incubation phase is now $f(t) < 1$, while the condition for steady state swelling is $f(t) > 1$.

Coupling Between Irradiation Creep and Swelling

In a number of recent reports the creep-swelling relationship has been investigated for annealed AISI 304L[47,48] and various thermomechanical treatments of AISI 316 stainless steel.[49–55] These studies were conducted in EBR-II and showed a remarkable consistency in results. It was found that at most temperatures of interest, irradiation creep could be described as a combination of several minor contributions and two major contributions.[56] The major contributions were associated with the creep compliance, a quantity unrelated to void swelling, and a swelling-driven creep component. Other similar studies have also been conducted on the Prime Candidate Alloy (PCA) in FFTF[57] and for the ferritic/martensitic alloys HT9 and

9Cr1Mo [58] which showed the same trend. It has been proposed[56–60] that the creep rate at any relevant temperature is linearly dependent on stress and related to the swelling rate by the following relation:

$$\frac{\dot{\epsilon}}{\sigma} = B_0 + D_0\dot{S}. \tag{5}$$

The creep compliance B_0 has been shown to be approximately equal to 10^{-6} MPa^{-1} for a wide range of austenitic steels. The swelling-enhanced creep coefficient D_0 is likewise thought to be relatively constant ≈ 0.01 MPa^{-1} over a wide range of steels and temperatures. This relationship ignores the short transient usually observed in cold-worked alloys.[60] If we accept the proposed insensitivity of B_0 and D_0 to composition and starting microstructure, then the sensitivities of swelling will dominate the creep behavior at high fluence (where, as shown later, the effect of stress on swelling is more pronounced). Note that Equation 5 requires a swelling rate of greater than 0.01%/dpa (which is generally the case) to give dominance to the second term over the first one, i.e., to make the swelling behavior dominant over the irradiation creep behavior.[60] It is clear that due to the stress dependence of swelling, an apparent deviation from the linear stress dependence of the creep should be anticipated at high swelling rates (> 0.01% per dpa). This was reported for 1.4981 type stainless steel.[59]

Some research indicated that the creep rate in AISI 316 stainless steel declines as swelling approaches levels in excess of 5% for dpa < 50, and at 550°C.[49,62] It is not yet clear whether the cessation of creep arises as a direct consequence of large swelling levels or whether other late-term microstructural developments are responsible.[61] The increase in the stress-enhanced swelling with temperature as well as the observed cessation of irradiation creep may have deleterious effects on the performance of bonded structures.

Effect of Void Swelling on Elasticity

The behavior of bonded structures (especially along the interfaces) should be dependent on the inherent mechanical properties of both the substrate as well as the coating. Changes in microstructure, as well as microchemical changes, are also known to affect elastic moduli. For the design of a next step large fusion device the influence of neutron irradiation on elastic moduli is of particular interest! Also, a high value of the thermal strength factor $M = \lambda * G/\alpha * \sigma_u$ (λ = thermal conductivity, α = thermal expansion coefficient, σ_u = ultimate strength, G = elastic modulus) is an important parameter to indicate material suitability for heat sink materials in duplex structures.[63]

Hashin[64] has formulated an approach to calculate the elastic moduli of a two- phase, non homogeneous material, using elasticity theory and a concentric-spheres model. Using Hashin's approach, Christensen[65] has derived expressions for the bulk as well as lower and upper bounds for the shear moduli. Marlowe and Appleby[66] measured the reduction in Young's modulus due to swelling for 316 as well as 347 stainless steels using a dynamic resonance technique. For 316 stainless steel the following relation was reached:

$$(E/E_0)_{316} = [1.086 - 4.435S] \tag{6}$$

at the 95% confidence level for the coefficients, where the E_0's are the moduli of the fully dense materials, and S is the volume fraction swelling. Straalsund and Kay[67] also used an ultrasonic technique to measure the effect of swelling on the elastic constants of 403 stainless steel. Afzali and Nemat-Nasser[68] calculated, for 316 stainless steel irradiated in EBR-II, the reduction in both the shear and the bulk moduli. They found that the maximum reduction occurs at about 500°C which corresponds to the peak value for swelling. At lower temperatures, the reduction is low. For metals irradiated in fusion reactor environment, gas bubble production becomes a more dominant factor in the reduction of the elastic moduli.

Stress Analysis of Bonded Structures

The effect of stress history on the development of swelling in bonded structures and the role played by stress-enhanced swelling in irradiation creep calculations has been incorporated into the TSTRESS code[46] in its latest version GTSTRESS.[**] The code uses the method of the boundary integral method formulated for time dependent plastic deformation in one dimension, Four different sources of stress were initially considered: (1) membrane loads from internal coolant pressures, (2) temperature gradients through the wall caused by steady-state heat fluxes, (3) irradiation induced differential swelling gradients through the wall, and (4) residual stress gradients caused by both thermal and irradiation creep-induced stress relaxation.

The code was modified to incorporate models for the stress-enhanced swelling. The modification of the irradiation creep due to the stress-enhanced swelling was taken into consideration. The ability of the code to produce the swelling distribution throughout the thickness of the first wall (as well as in its coating) allows for the proper assessment of the swelling behavior especially near the interfacial area between the coating and the substrate. This gives an excellent chance to investigate the impact of differential swelling on the bonding of duplex structures.

Results

The behavior of 20% cold-worked 316 stainless steel plate free to expand but not to bend (an ideal simulation for first wall structures) and subject to different irradiation, stress, as well as thermal conditions was first investigated. The attempt was to determine an envelope for the behavior of the stress-enhanced swelling phenomena, and the impact of the swelling on the irradiation creep. The choice of 316 stainless steel was made since it is the only material on which the effect of stress on swelling has been studied and modeled, The upper temperature (525°C) was chosen since this is the temperature beyond which stress may have an impact on the swelling rate as well as the incubation period, Also, the effect of gas generation would become important above this temperature, Since the impact of stress on swelling is small below 400°C, most calculations were limited to above 400°C. In the following discussion, volumetric swelling is shown for three conditions of interest to the behavior of bonded structures: at the surface, using the average over the first millimeter, and using the average over the whole thickness. Also, in the following results, stress always refers to σ_z. It is apparent from the different results that the stress-enhanced swelling phenomena complicates the prediction of the irradiation behavior of bonded structures and will have a major role on their performance at the interfaces.

1. Parametric Study of the Stress-Enhanced Swelling Phenomena

Effect of plate thickness: Four different thicknesses were used in the calculations; 3, 5, 7, and 9 nun as shown in Figure 2. The same temperature range was maintained (400-525°C). In this case, varying the plate thickness had little effect on surface swelling and the average swelling along the whole thickness. Since the first mm has a different temperature gradient in each case, being hotter for the large thickness, the 9 nun plate experienced the largest increase in swelling.

Effect of damage rate: Three different cases were investigated (5.E-8, l.E-7, and 5.E-7 dpa/s) at an accumulated dose of 15.75 dpa as shown in Figure 3. The stress-enhanced phenomena played a major role as the damage rate increases. This has an impact for the DEMO as well as commercial reactors.

Effect of membrane stress: As shown in Figure 4, the stress-enhanced swelling is decreased with the increase in membrane stress. The trend will be reversed as the stress level increases. This is explained for a simple stress distribution in Figure 5. As the membrane stress increases, the stress on the surface as well as in the first millimeter will decrease in value, then it will increase once more, thus increasing the stress-enhanced swelling. We have to keep in mind that what is important is the absolute value of the stress. The importance of the membrane stress effect on swelling should be considered along with the future trends of using high temperature, high pressure coolants that generate high membrane stresses.

Effect of temperature range: As shown in Figure 6, the impact of the phenomena is high for high temperature ranges. It is important to note that this trend only reflects the increased stress levels rather than the promotion of the stress-enhanced swelling with temperature (in this temperature range, the stress-enhanced phenomena is an athermal process). This is also clear when considering that the reduction in stress-enhanced swelling as the temperature gets higher since the thermal creep began to be effective in reducing stress levels.

Swelling evolution with time: As shown in Figure 7, the stress-enhanced swelling will have a major role in the beginning of life (regardless of the low swelling value). This is expected since in the beginning, before the creep begins to redistribute the stresses, the stress levels will be high. This will have an impact on the the early performance of bonded structures.

Stress distribution: The time dependence of the stress distribution is shown in Figure 8. A remarkable deviation from linearity is observed, especially on the surface (i.e., at the coating). To investigate the roots of this behavior, both the swelling and the creep evolution were calculated. It is quite obvious from Fig. 9 that the evolution of stress-enhanced swelling is the key factor behind the resultant stress distribution, This is even more obvious when the stress-enhanced swelling with time is used to enhance the irradiation creep. The stress relaxation due to creep is more effective on the surface as a result of the dominant effect of the stress-enhanced swelling in this area.

Effect of Stress-Swelling-Creep Coupling

As shown in Figures 10 and 11, the creep-swelling coupling has a major impact on the swelling distribution, as well as on the stress evolution. As a result, the stress-enhanced swelling will be reduced (by as much as 40% in Figure 10). It is important to note that the creep relaxation of stress on the surface will have an important effect on the generation of intrinsic stresses along the interface if a coating is applied. It is thus obvious that the effect of stress-enhanced swelling should not he taken into design analysis without taking the impact of swelling on creep into consideration. Otherwise, an overestimation of swelling, especially along interfaces, may result. One complication is the cessation of irradiation creep at high values of swelling (5%) that was reported earlier.[49,62]

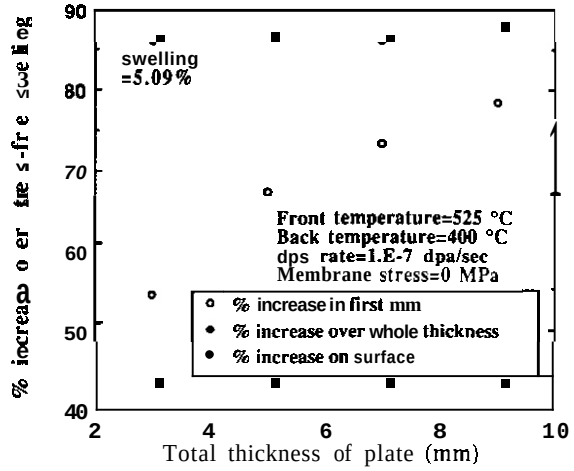

Fig. 2. Effect of plate thickness on the stress-enhanced swelling of 316 SS plate after 31.5 dpa.

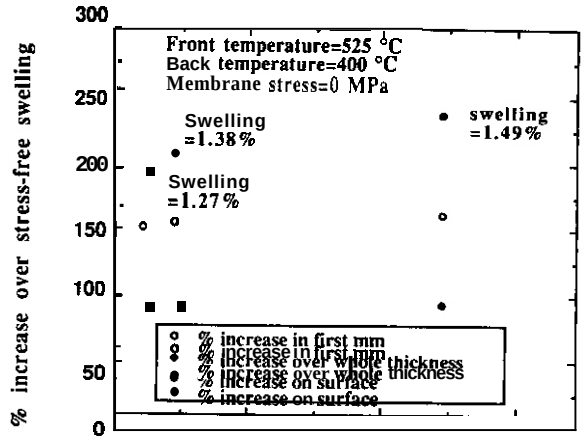

Fig. 3. Effect of dpa rate on the stress-enhanced swelling behavior of 5 mm 316 SS plate after 15.75 dpa.

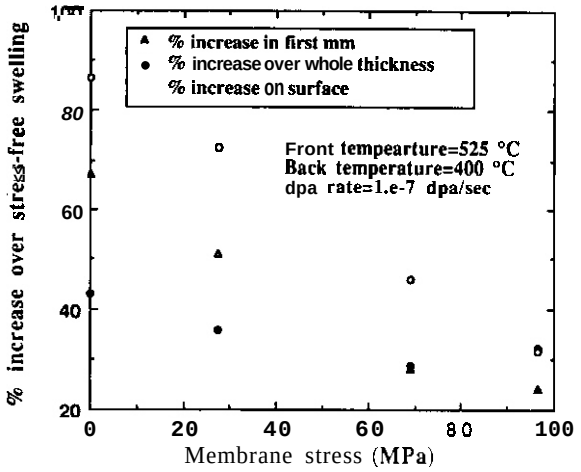

Fig. 4. Effect of membrane stress on the stress-enhanced swelling of a 5 mm 316 SS plate after 31.5 dpa.

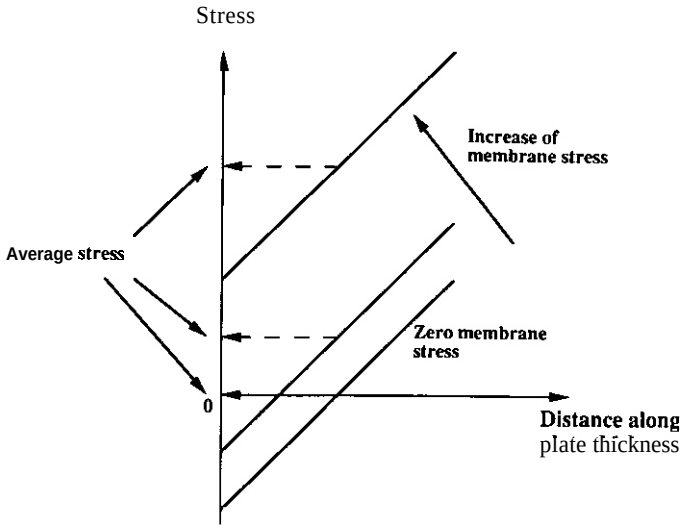

Fig. 5. Stress distribution in a plate subject to simple membrane stress. Initial stress distribution is assumed symmetric.

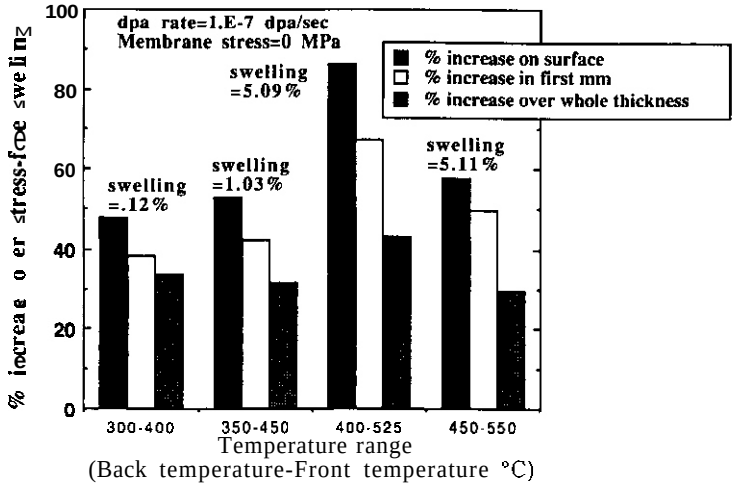

Fig. 6. Effect of temperature range on the stress-enhanced swelling behavior of 5 nun 316 SS plate after 31.5 dpa.

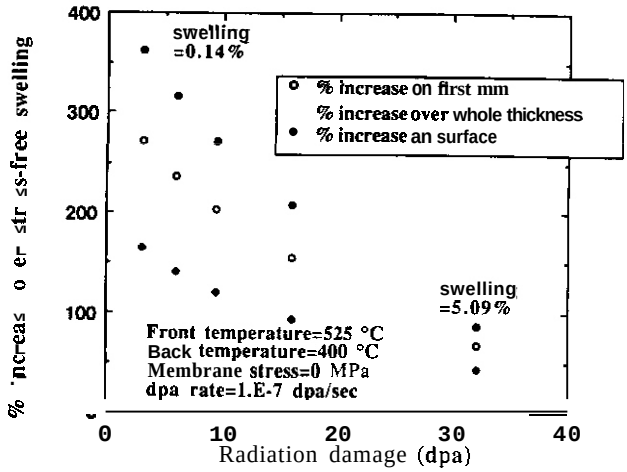

Fig. 7. Effect of stress on swelling behavior of a 5 mm SS plate as a function of radiation dose.

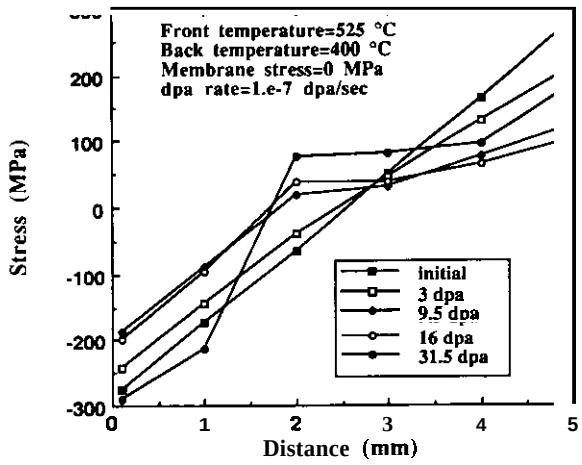

Fig. 8. Evolution of *stress* as a function of dpa for a **5** mm 316 SS plate.

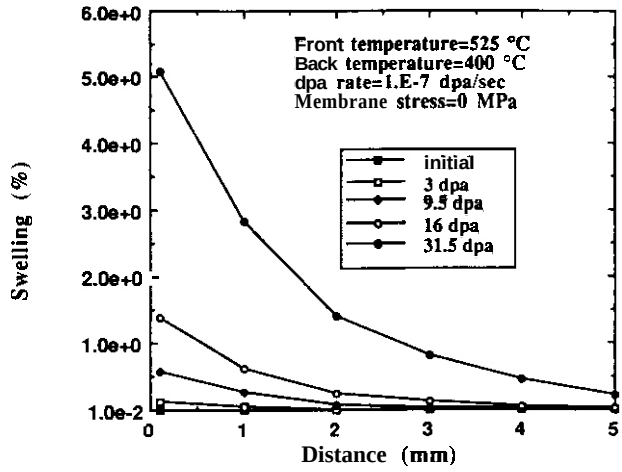

Fig. 9. Evolution of the stress-enhanced swelling distribution as a function of dpa for a 5 mm 316 SS plate.

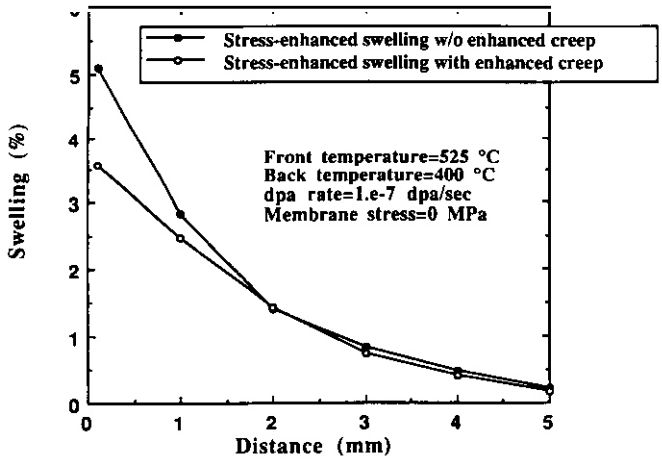

Fig. 10. Effect of (stress-enhanced swelling) enhanced creep on the swelling of a 5 mm 316 SS plate after 31.5 dpa.

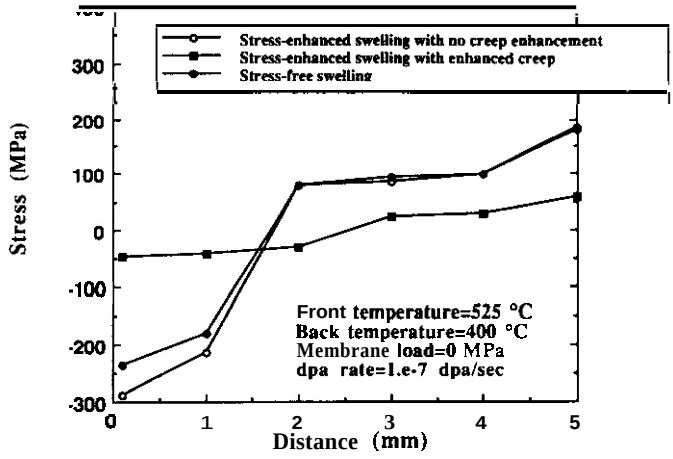

Fig. 11. Effect of stress-enhanced swelling with enhanced creep on the stress distribution in a 5 mm 316 SS plate after 31.5 dpa.

Effect of Swelling on the Elastic Modulus

As a result of the dependence of the elastic modulus on swelling, it is expected that the stress-enhanced swelling may reduce the modulus even further than in the stress free case. This is shown in Figure 12 where it is shown that the reduction io Young's modulus values may reach 15% on the surface (twice the reduction in case of stress-free swelling). A low value of Young's modulus indicates a greater elastic accommodation for the same stress level and smaller permanent damage. Also, this reduces the force required to develop the strain compatibility between the coating and the substrate.

Be/SS Structure for the DEMO Design To simulate an actual case of a duplex structure that uses stainless steel, the parameters of the first wall of a DEMO reactor were used.'' These were:

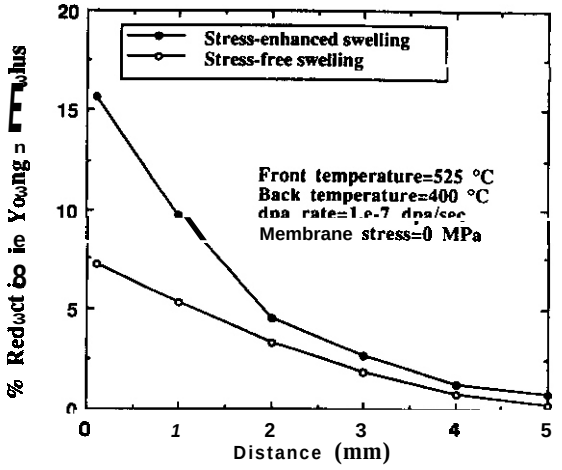

Fig. 12. Effect of stress-enhanced swelling on the Young's modulus in a 5 mm 316 SS plate after 31.5 dpa.

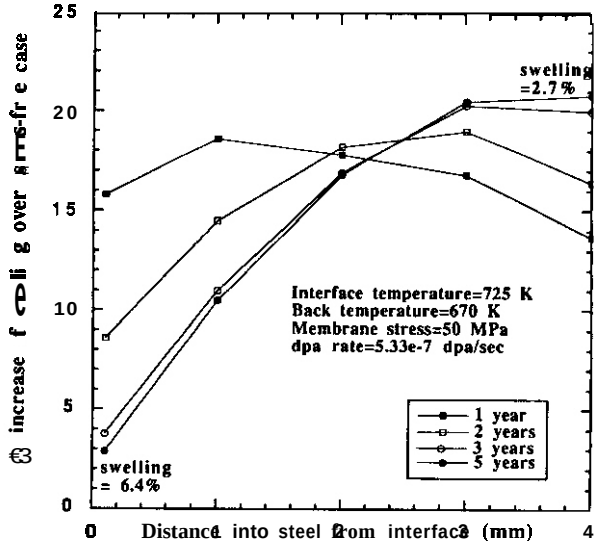

Fig. 13. Percentage increase in stress-enhanced swelling over the stress free case for a 20% CW 316 SS substrate coated with 2 mm of Be.

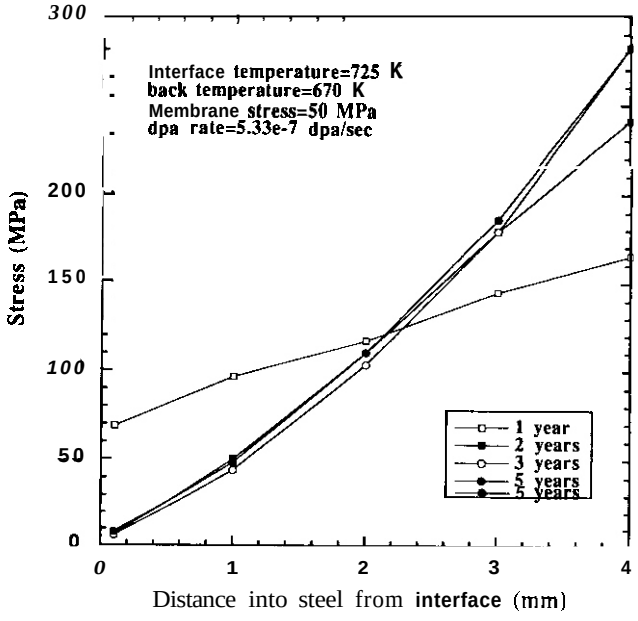

Fig. 14. Percentage increase in stress-enhanced swelling over the stress-free case for a 20% CW 316 SS substrate coated with 2 mm of Be.

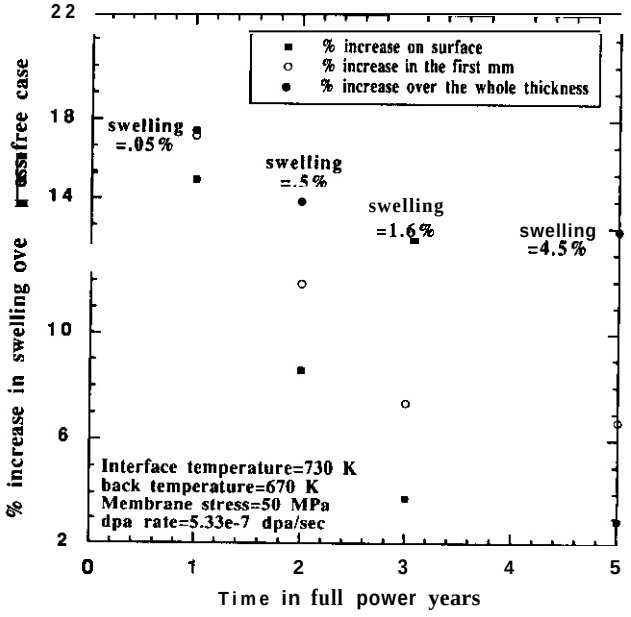

Fig. 15. Stress distribution in a 20% CW 316 SS substrate coated with 2 mm of Be.

Neutron wall loading	2.1
Thickness of Be (70% TD) tiles	2 mm
Thickness of 20% CW 316 SS	4 mm
Surface temperature	730 K
Interface temperature	725 K
Back temperature	670 K
Coolant temperature	653 K
Membrane load	50 MPa
Lifetime	10 years
Availability	50%
Damage level	84 dpa
Gas generation rate in Be	6405 appm/year

Since the stress-enhanced swelling phenomena is negligible below 300°C, all the temperatures used above are in fact 100 degrees higher than those in the original design. Recent data for[71] Be were taken into consideration to account for the gas induced swelling as well the irradiation creep. The percentage increase in swelling due to stress is shown in Figures 13 and 14 as a function of thickness **as** well as averaged over certain thicknesses Because of the way stress redistributed in steel (Figure 15), tending to peak at the hack end of the substrate, the increase in swelling is more pronounced there, eventually reaching a value of 20% over the stress free value. It should he noted that at the hack end of the substrate the low temperature should result in low swelling values. It is obvious that the stress-enhanced swelling increased the swelling level at the back of the substrate more than it affected the swelling level at the interface. Thus, the impact of stress-enhanced swelling should he evaluated in the relevant stress environment. Coupling between swelling and creep was not taken into consideration in the last three figures to single out the impact of stress-enhanced swelling. It is expected that if this coupling is taken into consideration, the increase in swelling at the back will be reduced since creep will he enhanced mnre there.

CONCLUSIONS

Radiation damage will he a key point in the design of the different components of fusion reactors hut unfortunately, the mechanisms of irradiation damage in bonded structures have not received much attention. The impact of stress on the incubation period for swelling should he taken into consideration for the analysis of both near and far term reactors, especially those experiencing high dose levels and using high temperature coolants and pressures (i.e., high primary stress levels). The interrelationship between (stress-enhanced) swelling and creep is a vital one in the proper assessment of the stress evolution in bonded structures. Failure to incorporate this effect may result in **an** overestimation of swelling. Whether or not creep ceases at high values of swelling will remain a key point in the assessment. The reduction in elastic moduli along the interfaces of bonded structures due to void swelling could he **as** high as 15% and has been shown to be another factor in the behavior of these structures.

Many questions concerning the stress-enhanced swelling phenomena are still to be answered. Further experimental, as well **as** theoretical, work is necessary to assess and model the effect of stress on cavity density, the observed enhanced void growth especially at high temperatures. The role played **by** the shear component of the stress, **as** well **as** the synergistic effects of temperature, damage rate, gas generation rate, and stress still need to be more fully understood before the influence of the different variables relevant to fusion applications can be assessed.

ACKNOWLEDGEMENT

Financial support for this work has been provided **by** the U.S. Department of Energy

REFERENCES

1. J. P. Blanchard and N. M. Ghoniem, J. Nucl. Mat. 172 (1990) **54.**

2. N. M. Ghoneim and J. B. Whitley, J. Fusion Energy 8 (1989) 157.

3. R. F. Mattas, et al., J. Nucl. Mat. 122&123 (1984) 66.

4. G. L. Kulcinski, Contemp. Phys. 20 (1979) 417.

5. J. P. Blanchard and N. M. Ghoneim, Nucl. Eng. Desi./Fusion 2 (1985) 19.

6. R. W. Conn, et **al.,** UCLA PPG-815 (1984).

7. H. R. Brager, et **al.,** J. Nucl. Mat. 66 (1977) 301.

8. A. E. Walter and A. B. Reynolds, Fast Breeder Reactor, Pergamon Press, New York, 1981, p. 290.

9. W. Daenner and J. Raeder, Proc. 3rd Top. Meeting on the Technology of Contr. Nucl. Fus., Santa Fe, New Mexico, May 1976, p. 347.

10. R. F. Mattas, Fusion Tech. 19 (1991) 1487

11. D. L. Smith, Blanket and Shield Design Meeting, ANL, November 6 (1991).

12. R. D. Watson, et al., J. Nucl. Mat. 103 (1981) 97.

13. R. F. Mattas, Fusion Tech. (1990) 637

14. R. F. Mattas, ANL/FPP/TM-160 (1982)

15. B. B. Glasgow and W. G. Wolfer, Fusion Tech. 8 (1985) 596

16. J. P. Blanchard, Analysis of Singular Stress Fields in Fusion Components, Thesis, 1988.

17. B. M. Ma, Nucl. Eng. Des. 28 (1974) 1.

18. W. Daenner and J. Raeder, J. Nucl. Mat. 85&86 (1979) 147.

19. **W.** Daenner, J. Nucl. Mat. 103&104 (1981) 121.

20. R. D. Watson, R. R. Peterson, and W. G. Wolfer, UWFDM-433 (1981).

21. R. D. Watson, R. R. Peterson, and W. G. Wolfer, J. Pressure Vessel Tech. 105 (1983) 144.

22. S. D. Harkness and B. Cramer, J. Nucl. Mat. 85&86 (1979) 135.

23. H. Oomura, et al., Fusion Tech. 8 (1985).

24. C. Cawthorne and E. J. Fulton, Nature 216 (1967) 576.

25. J. F. Bates and E. R. Gilbert, J. Nucl. Mat. 59 (1976) 95.

26. J. I. Bramman, et al., Proc. Intern. Conf. on Radiation Effects in Breeder Structural Materials, Scottsdale, Arizona, 1977, p. 479.

27. R. A. Weiner and A. Boltax, J. Nucl. Mat. 68 (1977)141

28. K. **Q.** Bagley, et **al.,** Proc. on Voids Formed by Irradiation of Reactor Materials, BNES, Harwell, 1971, **p.** 1

29. R. J. Jackson, et al., Trans. Am. Nucl. Soc. 22 (1975) 184.

30. R. A. Weiner and A. Boltax, Stress Effects on the Void Swelling Incubation Period, WARD-OX-3045-22, Westinghouse Advanced Reactors Division (1976).

31. J. F. Bates and E. R. Gilbert, J. Nucl. Mat. 71 (1978) 286

32. J. F. Bates and E. R. Gilbert, Proc. Int. Conf. on Structural Mechanics in Reactor Technology, Vol. C, Berlin, Germany, 1979, p. 4/1.

33. T. Lauritzen et al., **Proc.** on **Effects** of Radiation on Materials, **ASTM** 870, Williambsburg, Virginia, 1984, p. 221.

34. D. L. Porter, et al., Proc. on Effects of Radiation on Materials, ASTM 870, Williambsburg, Virginia, 1984, p. 212.

35. J. E. Harbottle, J. Nucl. Mat. 66 (1977) 258.

36. J. E. Harbottle, Proc. Intern. Conf. on Radiation Effects in Breeder Structural Materials, Scottsdale, Arizona, 1977, p. 455.

37. J. E. Harbottle and A. Silvent, Proc on Irradiation Behavior of Metallic Materials for Fast Breeder Reactors, France,1979, p. 391.

38. S. Ya. Lebedev, et **d.,** Phy. Met. Metall 54 (1982) 164.

39. P. J. Barton and P. H. Hunter, Proc. on Voids Formed by Irradiation of Reactor Materials, BNES, Harwell, 1971, p. 45.

40. M. H. Hassan, J. P. Blanchard and G. L. Kulcinski, Stress-Enhanced Swelling: Implication for Fusion Reactors, to be published.

41. F. A. **Garner,** et al., Proc. on Effects of Radiation on Materials, ASTM 725, Savanah, Georgia, 1980, p. 680.

42. H. Ullmaier, Rad. Eff. 101 (1986) 147.

43. H. K. Shau and P. Jung, J. Nucl. Mat. 136 (1985) 154.

44. T. Lauritzen, et al., DAFS Report, DOE/ER-0046/21, 1985, p. 83.

45. T. Lauritzen, et al., Proc. on Radiation Induced Changes in Microstructure, ASTM 955, Seattle, Washington, 1986, p. 101.

46. R. R. Peterson, University of Wisconsin Report UWFDM 382, 1980.

47. D. L. Porter, F. A. Garner and G. D. Hudman, DOE/ER-0313/7, 1989, p. 133.

48. J. P. Foster, et. al., J. Nucl. Eng. Desgn. 31 (1974) 117.

49. F. A. Garner, D. L. Porter and B. J. Makenas, J. Nucl. Mat. 148 (1987) 279.

50. D. L. Porter and F. A. Garner, Influence of Radiation on Material Properties, ASTM STP 956, Eds. F. A. Garner, C. H. Henager, Jr. and N. Igata, 1987, p. 11.

51. F. A. Garner and D. L. Porter, J. Nucl. Mat. 155-157 (1988) 1006.

52. D. L. Porter and F. A. Garner, J. Nucl. Mat. 159 (1988) 114.

53. D. L. Porter, E. L. Wood, and F. A. Garner, DOE/ER-0313/5, 1989.

54. F. A. Garner, DOE/ER-0313/8, 1990.

55. R. W. Clark, A. S. Kumar and F. A. Garner, J. Nucl. Mat. 155-157 (1988) 845.

56. M. B. Toloczko, F. A. Garner and C. R. Eiholzer, DOE/ER-0313/9, 1991, p. 160.

57. F. A. Garner and R. J. Puigh, DOE/ER-0313/7, 140.

58. F. A. Garner and R. J. Puigh, DOE/ER-0313/7, 114.

59. K. Ehrlich, J. Nucl. Mat. 100 (1981) 149.

60. F. A. Garner, J. Nucl. Mat., 122&123 (1984) 459.

61. D. L. Porter and F. Garner, ASTM 956 (1986) 11.

62. H. Nickel, Discussion session in Proc 4th Int. Conf. on Fusion Reactor Materials, ICFRM4, J. Nucl. Mat. 179-181 (1991) 1231.

63. G. M. Kalinin, J. Nucl. Mat. 179-181 (1991) 1193.

64. Z. Hashin, J. Appl. Mech. (1962) 143.

65. R. M. Christensen, J. Mech. Phys. Solids 17 (1969) 24.

66. M. O. Marlowe and W. K. Appleby, Trans. Am. Nucl. Soc. 16, (1973) 95.

67. J. L. Straalsund and C. K. Day, Nucl. Tech. 20 (1973) 27.

68. M. Afzali and S. Nemat-Nasser, Trans. 5th Int. Conf. on Structural Mechanics in Reactor Technology, Berlin, Germany, 1979, N2.5/2.

69. R. R. Peterson, personal communication, June 1989.

70. M. Abdou et al., A Demonstration Tokamak Power Plant Study (DEMO), ANL/FPP/82-1, 1982.

71. M. C. Billone and S. Majumdar, Thermomechanical Analysis of the U.S.-ITER Driver Blanket, ANL, 1990.

4.0 FUNDAMENTAL MECHANICAL BEHAVIOR

No contributions.

5.0 RADIATION EFFECTS, MECHANISTIC STUDIES, THEORY AND MODELING

TENSILE PROPERTY CHANGES OF METALS IRRADIATED TO LOW DOSES WITH FISSION, FUSION AND SPALLATION NEUTRONS -
H. L. Heinisch and M. L. Hamilton, Pacific Northwest Laboratory*, W. F. Sommer, Los Alamos National Laboratory and P. D. Ferguson, University of Missouri-Rolla

OBJECTIVE

The objective of this work is to investigate the effects of the neutron energy spectrum in low dose irradiations on the microstructures and mechanical properties of metals.

SUMMARY

Radiation effects due to low doses of spallation neutrons are compared directly to those produced by fission and fusion neutrons. Yield stress changes of pure Cu, alumina-dispersion-strengthened Cu and AISI 316 stainless steel irradiated at 36-55°C in the Los Alamos Spallation Radiation Effects Facility (LASREF) are compared with earlier results of irradiations at 90°C using 14 MeV D-T fusion neutrons at the Rotating Target Neutron Source and fission reactor neutrons in the Omega West Reactor. At doses up to 0.04 displacements per atom (dpa), the yield stress changes due to the three quite different neutron spectra correlate well on the basis of dpa in the stainless steel and the Cu alloy. However, in pure Cu, the measured yield stress changes due to spallation neutrons were anomalously small and should be verified by additional irradiations. With the exception of pure Cu, the low dose, low temperature experiments reveal no fundamental differences in radiation hardening by fission, fusion or spallation neutrons when compared on the basis of dpa.

PROGRESS AND STATUS

Introduction

The Los Alamos Spallation Radiation Effects Facility (LASREF) is a potential irradiation facility for fusion reactor materials testing, including ITER materials and components. Spallation neutron sources have not been utilized extensively in fusion materials research, primarily because there are no high flux sources, but also because of concerns about their suitability relative to fusion reactor neutron environments.

The primary question concerning the use of spallation neutrons for fusion materials testing is whether there are undesirable effects of the "high energy tail," i.e., the neutrons in the energy range from about 20 MeV to hundreds of MeV that occur in diminishing numbers with increasing energy. The effects of transmutations and displacement damage produced by these neutrons are largely unknown. The present experiment is the first step of a potentially broader study designed to investigate whether there are fundamental differences in displacement damage produced by spallation neutrons relative to damage produced in fission and fusion reactor neutron spectra.

Yield stress changes of metals and alloys due to low dose irradiations with spallation neutrons in LASREF are compared to results obtained on the same materials irradiated to similar doses at 90° C with fission reactor neutrons in the Omega West Reactor (OWR) and with 14 MeV D-T fusion neutrons in the Rotating Target Neutron Source (RTNS-II)[1,2,3]. In the earlier comparisons of OWR and RTNS-II it was found that, for all the alloys tested, the fission and fusion irradiation effects correlate well when compared on the basis of displacements per atom (dpa). However, in the case of pure Cu [1] and pure Nb [4] some differences between fission and fusion neutron irradiation effects were noted.

A limited examination of microstructures has been done by transmission electron microscopy (TEM) on the same Cu [5,6] and 316 SS [7] irradiated at 90°C in RTNS-II and OWR for the tensile tests. In general, the radiation-induced hardening scales with the visible microstructure. Comparative examinations of the microstructure of pure Cu specimens have recently been performed on specimens irradiated in LASREF, RTNS-II and OWR, and the results are reported in another paper in these proceedings [8].

ExDerimental Details

The LASREF irradiation contained miniature tensile specimens and TEM disks of 99.999% pure Cu (annealed at 450°C for 15 m), an alumina-dispersion-strengthened Cu alloy (CuAl25) with 0.25% Al in the form of Al_2O_3 (annealed at 982°C for 60 m) and AISI 316 stainless steel (annealed at 1000°C for 10 m). These three materials are a subset of the materials irradiated in the earlier OWR/RTNS-II comparisons [3] that includes the general range of behaviors observed in those studies.

---

*Operated for the U.S. Department of Energy by Battelle Memorial Institute under Contract DE-AC06-76RLO 1830.

The specimens were placed into four helium-filled capsules, which were placed into the LASREF facility through tubes also used for "fast" rabbit activation foil exposures [9,10]. The capsules were positioned at different distances from the center of the neutron-producing targets, exposing each capsule to a different flux level. The capsule temperatures were monitored with chromel-alumel thermocouples attached to each capsule. Details of the LASREF irradiations are given in Table 1.

Capsule ID	Distance from Target, m	Temp °C	Total Fluence 10^{15} n/m^2	Fluence E>0.1 MeV 10^{15} n/m^2	Fluence E>20 MeV 10^{15} n/m^2	DPA** in Cu
7	0.38	36	8.9	2.7	**0.47**	**0.0016**
5	0.27	37	27	9.5	**1.3**	0.0037
3	0.18	**44**	**40**	21	2.9	0.011
1	0.12	**55**	73*	--	--	0.020'

Each capsule contained activation foils of Cu, Ni, Co and Fe for neutron dosimetry. The gamma ray intensities of the radiation-induced ra 1 isotopes were measured at Los Alamos National Laboratory, and the results were analyzed with the STAY'SL " " 'spectral-fitting code. Both the neutron spectra and He/dpa ratios are documented in reference 12. The average fluence experienced by each capsule during the irradiation of 3.8 x 10^6 s duration is listed in Table 1 along with coarse spectral information. The fluences of two categories of high energy neutrons are listed: the fluence of neutrons with energies greater than 0.1 MeV, which produce most of the displacement damage, and the fluence of neutrons with energies greater than 20 MeV, the so-called "high energy tail."

The dosimetry foils in capsule 1 were badly corroded, and they were not useful for analysis. The total flux value for capsule 1 given in Table 1 was estimated from the relative fluxes at the four positions determined in previous work [9]. Neutron energy-dependent displacement cross sections [13] for Cu were used to calculate the dpa in Cu for each capsule. The dpa value for capsule 1 was estimated assuming the same neutron spectrum as capsule 3. Dpa values for 316 SS were estimated by multiplying the Cu dpa values by 0.75, the ratio of the displacement energies in Cu and Fe.

The test specimens in capsule 1 were also corroded, but not so badly that tensile tests and TEM could not be performed on them. The cause of the corrosion still eludes the experimenters. The tensile tests on specimens from capsule 1 appear to be unaffected by the corrosion, and the results are included in this paper. However, since the neutron dose for capsule 1 is also uncertain, the capsule 1 data should be viewed with caution.

Tensile tests were performed at room temperature at Pacific Northwest Laboratory on an apparatus designed specifically for testing miniature specimens [14].

Results

The results of the tensile tests are reported in Table 2.

Figure 1 shows the changes in 0.2% offset yield stress as a function of displacement damage for 316 SS irradiated in LASREF. Each point is the result of a single tensile test. The LASREF data are compared with earlier results from RTNS-II and OWR irradiations of the same material at 90°C [3]. The data are plotted against $dpa^{1/4}$ because the RTNS-II and OWR data are linear functions of that quantity. Dependence on the fourth root of dpa is typical for this dose range and temperature. It is consistent with the dispersed barrier model of irradiation hardening at doses where cascades interact but defect densities are not saturated. The error bar on the single point in the center of the graph indicates the minimum ±5% error in the value of the absolute yield stress, based on the estimated precision of the testing technique. The straight line through the data points was fitted to the RTNS-II and OWR data only. Overall, the agreement of data from all three neutron spectra is quite good. There are some minor systematic differences: the LASREF data exhibit somewhat greater scatter than the RTNS-II and OWR data, and they appear to lie along a line of slightly greater slope (the results from capsule 1 at the highest dose are suspect).

Table 2. LASREF TENSILE TEST DATA

Capsule ID	Yield Stress MPa	Ultimate Strength, MPa	Uniform Elongation, %	Total Elongation, %
cu				
unirrad	77	206	26.1	29.0
7	104	163	13.1	18.7
7	127	180	8.9	13.8
7	165	213	15.9	21.6
5	120	168	16.5	23.7
5	132	175	11.3	15.0
5	142	194	8.4	13.3
3	128	165	28.4	32.5
3	139	185	16.4	21.9
3	177	223	13.6	17.9
1	151	177	9.0	13.3
1	163	191	11.9	18.2
CuAl25				
unirrad	417	456	9.1	15.5
7	439	451	5.6	8.4
7	445	459	6.6	12.1
5	475	483	0.5	7.3
5	479	481	0.5	3.9
3	503	523	0.5	2.9
3	505	518	0.3	3.2
1	471	507	0.7	1.5
1	536	544	0.4	1.2
316 SS				
unirrad	269	648	57.2	61.7
7	334	608	50.1	55.6
7	347	633	50.0	55.3
7	356	655	50.9	55.8
5	354	564	34.0	37.7
5	382	619	47.1	51.9
5	401	651	47.1	52.9
3	459	673	36.7	43.3
3	468	687	39.7	43.9
3	486	715	32.3	37.7
1	491	675	37.2	42.9
1	491	679	32.3	40.7
1	530	703	21.7	25.9

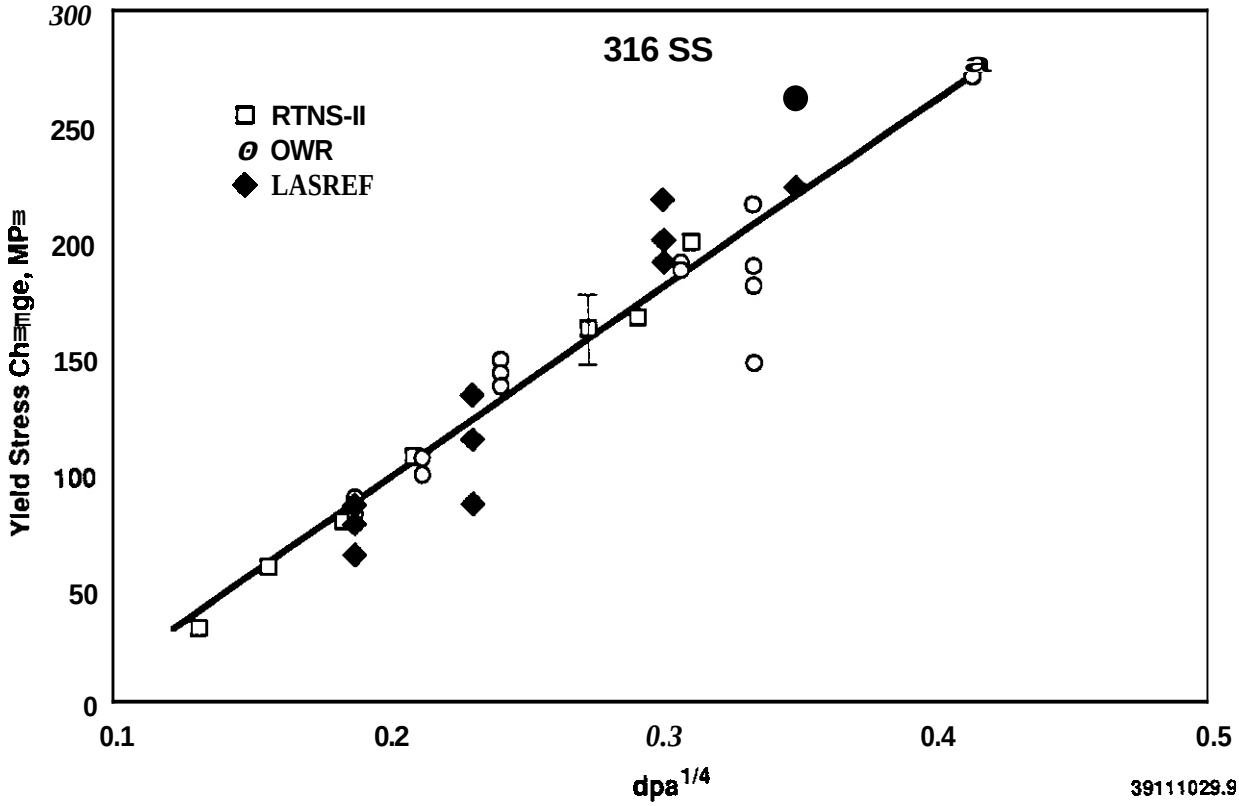

Figure. 1. The radiation-induced change in yield stress plotted against the fourth root of dpa for AISI 316 stainless steel irradiated in LASREF, RTNS-II and OWR. The straight line is fitted to the RTNS-II and OWR data onlv. The error bar near the center of the graph represents the estimated ±5% uncertainty in the absolute yield stress due to the precision-of'the measurements

Figure 2 compares LASREF data with earlier RTNS-II and OWR data for CuAl25 [2]. As in 316 SS, the yield stress changes are proportional to the fourth root of dpa. The line in the figure was fitted to only the RTNS-II and OWR data, and the error bar represents the 5% precision of the measurement of the absolute yield stress. There is good agreement among the results for LASREF, RTNS-II and OWR.

Figure 3 compares LASREF data for pure Cu with data from the earlier RTNS-II and OWR irradiations [3]. Both RTNS-II data and OWR data vary linearly with the fourth root of dpa, but the slope of the RTNS-II data is 1.4 times that of the OWR data. More than twice as many dpa are needed in OWR as in RTNS-II to produce a yield stress change of 200 Mpa in pure Cu. The LASREF data have considerably larger scatter than those of RTNS-II and OWR (although, if the two highest measured values of yield stress change are ignored, the scatter at each dpa value in the LASREF data is on the order of the f5% precision of the testing). The remarkable characteristic of the LASREF data is that the yield stress changes are considerably less than in RTNS-II and OWR.

Discussion

The yield stress changes of 316 SS and CuA125 irradiated with LASREF spallation neutrons correlate well with those measured on the same materials irradiated in RTNS-II and OWR, when compared on the basis of dpa. In Cu the yield stress changes due to the spallation neutrons are markedly lower than those due to the fission or fusion neutrons. They are too large and are in the wrong direction to be due to differences in temperature or dose rate.

Earlier irradiations of pure Cu in RTNS-II [3] at temperatures ranging from room temperature to 290°C demonstrated that radiation hardening is sensitive to the temperature, since defects in Cu have significant mobility in this temperature range. Increasing the temperature in Cu delays the onset of the transition fluence at which significant hardening begins to take place. If temperature were the only variable, then Cu irradiated at 36-55°C should have slightly higher yield stress values than when irradiated at 90°C.

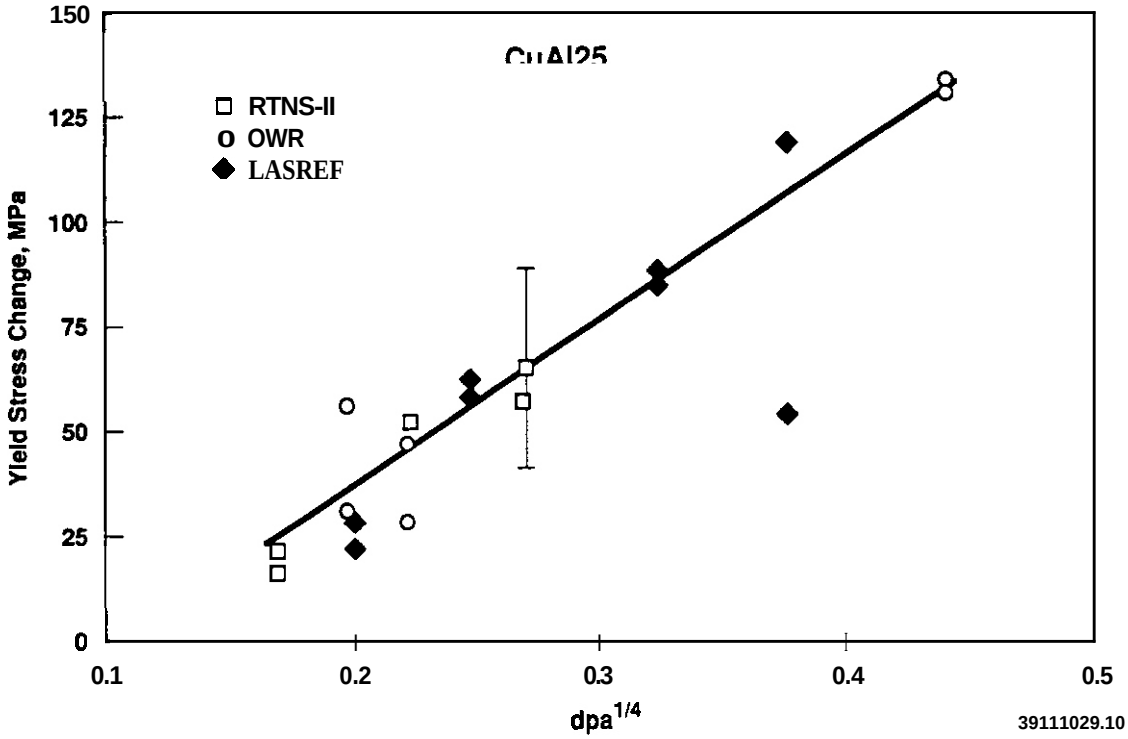

Figure. 2. The radiation-induced change in yield stress plotted against the fourth root of dpa for alumina-dispersion-strengthened Cu irradiated in LASREF, RTNS-II and OWR. The straight line is fitted to the RTNS-II and OWR data only. The error bar near the center of the graph represents the estimated ±5% uncertainty in the absolute yield stress due to the precision of the measurements.

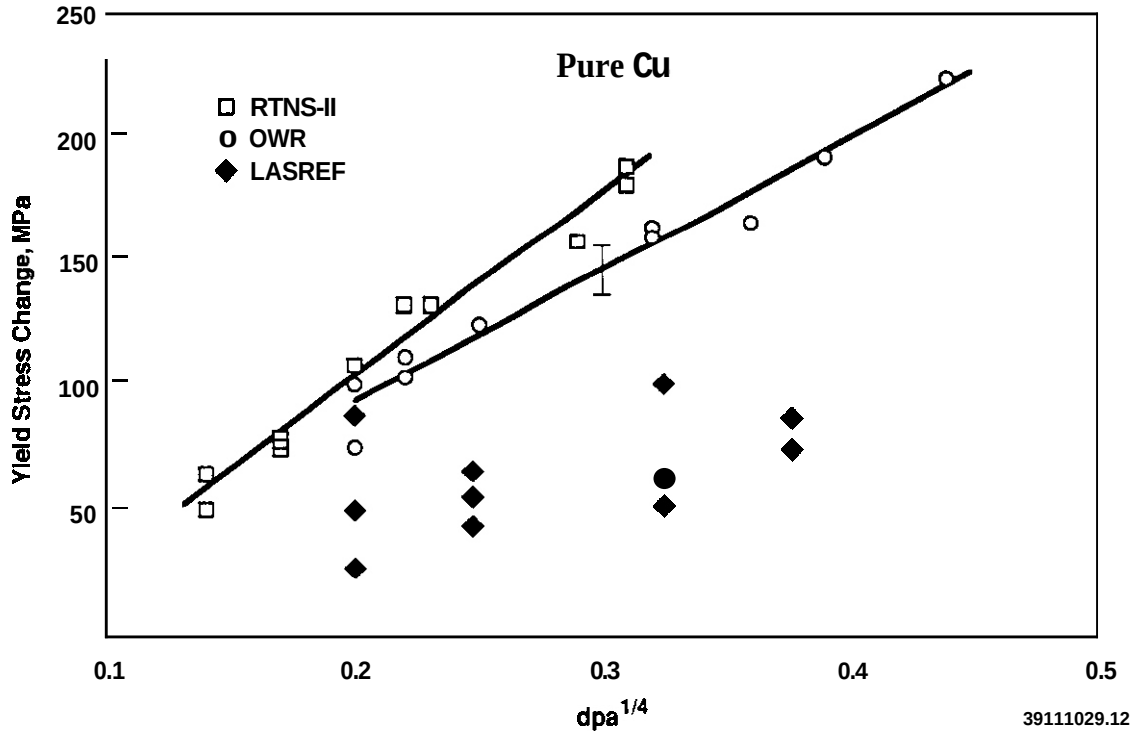

Figure. 3. The radiation-induced change in yield stress plotted against the fourth root of dpa for pure (99.999%) Cu irradiated in LASREF, RTNS-II and OWR. Straight lines are fitted to the RTNS-II and OWR data. The error bar near the center of the graph represents the estimated ±5% uncertainty in the absolute yield stress due to the precision of the measurements.

However, the yield stress changes due to irradiation in LASREF are about the same as those obtained in RTNS-II at 200°C. Thermocouples were attached to each LASREF capsule, and the specimens were tightly packed within each capsule. There is no indication that the specimens experienced temperatures greater than about ten degrees above the reported temperatures. If the LASREF capsules had been near 200°C, the yield stress changes in 316 SS should also have been smaller [3] than shown in Fig. 1.

Displacement rates in the LASREF irradiations varied with distance from the target over the range from 4.2 x 10^{-10} to 5.3 x 10^{-9} dpa/s, approximately three times the rates for comparable dpa values in RTNS-II. In OWR the displacement rate is much higher, 3.7 x 10^{-8} dpa/s. Earlier RTNS-II irradiations were also done in pure Cu at damage rates four times higher than those for the data plotted here. At the higher dose rates the yield stress changes were about 10% greater than at the lower dose rate. Thus, there is no evidence to support rate effects as the cause of the differences in yield stress changes of Cu irradiated in LASREF, RTNS-II and OWR.

In a companion paper in these proceedings [8] the microstructures of Cu specimens irradiated in LASREF are compared with those of Cu irradiated in RTNS-11 and OWR. The number densities of TEM-visible defects for specimens irradiated in all three neutron spectra correlate well when compared on the basis of DPA, and the visible defect size distributions are about the same. It is difficult to postulate a situation in which the visible microstructures are the same but the yield stresses are different. Perhaps the only possibility is that invisible defects are produced in RTNS-II and OWR that contribute to the hardening, but no invisible defects are produced in LASREF (or they were eliminated by an undetected temperature excursion). The search for a systematic error in the tensile tests of Cu specimens has been negative. As to whether there are spectral differences in irradiation effects in pure Cu, the evidence based on yield stress data is inconclusive.

CONCLUSIONS

In low-dose irradiations, the changes in tensile properties of 316 SS and CuAl25 produced by fission reactor neutrons, D-T fusion neutrons and LASREF spallation neutrons are the same when compared on the basis of dpa. The small yield stress changes measured for pure Cu irradiated in LASREF remain unexplained.

Excluding the Cu data, these low dose, low temperature experiments show that any fundamental differences in damage production at low doses by LASREF spallation neutrons and those of a fission or fusion reactor can be accounted for by comparing the test data on the basis of dpa.

REFERENCES

1. H. L. Heinisch, S. D. Atkin and C. Martinez, J. Nucl. Mater. 141-143 (1986) 807

2. H. L. Heinisch and C. Martinez, J. Nucl. Mater. 141-143 (1986) 883.

3. H. L. Heinisch, J. Nucl. Mater. 155-157 (1988) 121.

4. J. 8. Mitchell, R. A. VanKonynenburg, C. J. Echer and D. M. Parkin, Proc. Int. Conf. on Radiation Effects and Tritium Technology for Fusion Reactors, Gatlinburg, TN, Oct. 1-3, 1975, Vol. II, 172.

5. S. Kojima, S. J. Zinkle and H. L. Heinisch, J. Nucl. Mater. 179-181 (1991) 982.

6. A. Horsewell, 8. N. Singh, S. Proennecke, W. F. Sommer and H. L. Heinisch, J. Nucl. Mater. 179-181 (1991) 924.

7. N. Yoshida, H. L. Heinisch, T. Muroga, K. Araki and M. Kiritani, J. Nucl. Mater. 179-181 (1991) 1078.

8. T. Muroga, H. L. Heinisch, W. F. Sommer and P. D. Ferguson, J. Nucl. Mater. (this conference).

9. D. R. Davidson, R. C. Reedy, L. R. Greenwood, W. F. Sommer and M. S. Wechsler, ASTM STP 956 (1987) 730.

10. W. F. Sommer, W. Lohmann, K. Graf, I. K. Taylor and R. M. Chavez, ASTM STP 956 (1987) 718.

11. F. G. Perry, Oak Ridge National Laboratory Report, ORNL-TM-6062 (1977).

12. W.F. Sommer, F.A. Garner and 8.M. Oliver, Fusion Reactor Materials Semiannual Progress Report, DOE/ER-0313/11 (1991).

13. M. S. Wechsler, D. R. Davidson, L. R. Greenwood and W. F. Sommer, ASTM STP 870 (1985) 1189

14. N.F. Panayotou, S.D. Atkin, R.J. Puigh and B.A. Chin, ASTM STP 888 (1986) 201.

A COMPARISON OF MICROSTRUCTURES IN COPPER IRRADIATED WITH FISSION, FUSION AND SPALLATION NEUTRONS - T. Muroga, Kyushu University, H. L. Heinisch, Pacific Northwest Laboratory*, W. F. Sommer, Los Alamos National Laboratory and P. D. Ferguson, University of Missouri-Rolla

OBJECTIVE

The objective of this work is to investigate the effects of the neutron energy spectrum in low dose irradiations on the microstructure and mechanical properties of metals.

SUMMARY

The microstructures of pure copper irradiated to low doses at 36-90°C with spallation neutrons, fusion neutrons and fission neutrons are compared. The defect cluster densities for the spallation and fusion neutrons are very similar when compared on the basis of displacements per atom (dpa). In both cases, the density increases in proportion to the square root of the dpa. The difference in defect density between fusion neutrons and fission neutrons corresponds with differences observed in data on yield stress changes.

PROGRESS AND STATUS

Introduction

The effect of the neutron spectrum on microstructural evolution is a key issue in fission-fusion correlations. Detailed examination of low dose microstructures contributes to a mechanistic understanding of the fundamental aspects of spectral effects. Microstructures of pure copper irradiated with D-T fusion neutrons near room temperature have been examined by a number of groups[1-6], enhancing our understanding of defect cluster formation and its fluence dependence under fusion neutron irradiation. Direct comparisons of the effects of fusion neutrons and other particle irradiations on microstructures[5,6], and yield stress changes[7,8] have also been reported. It has been found that, in pure copper, displacements per atom (dpa) is not a sufficient correlation parameter.

Spallation neutron sources have been proposed as a radiation source for fusion materials testing[9,10]. Little is known about the effects on materials of the "high energy tail" of the neutron energy spectrum that extends from about 20 MeV to hundreds of MeV. There is concern with respect to both displacement damage and transmutations.

A scoping irradiation on a limited specimen matrix at the Los Alamos Spallation Radiation Effects Facility (LASREF) has provided the opportunity to investigate displacement damage produced by spallation neutrons at very low doses and determine its relationship to damage produced in other neutron spectra. The objective of the present study is to compare microstructures of pure copper irradiated with fission, fusion and spallation neutrons to comparable displacement levels and to investigate the relationship between the neutron spectrum and the resulting microstructures. This study enhances our overall understanding of neutron spectral effects and will aid in the evaluation of future fusion materials testing done with a spallation source.

Experimental

The spallation neutron irradiations with LASREF were carried out in small capsules placed into the facility through tubes also used for "fast" rabbit activation foil exposures[11,12]. Specimens were irradiated in four capsules placed 0.12, 0.18, 0.27 and 0.38 m from the center of the neutron-producing targets, resulting in a different flux level for each capsule. The capsule temperatures were actively measured by thermocouples attached to each capsule. The average flux in each capsule during the irradiation was determined by analysis of the measured gamma-ray intensities from the radiation induced radioisotopes in activation foils of Cu, Ni, Co and Fe included with each capsule and use of a spectral-fitting code, STAY'SL[13]. Energy dependent displacement cross sections for copper[14] were used to calculate the dpa values in each measured spectrum. Foils included with Capsule 1 were badly corroded and not useful for the gamma-ray analysis. Thus, data from specimens in Capsule 1 are not reported.

The fusion neutron irradiation and fission neutron irradiation were conducted at 90°C with the Rotating Target Neutron Source-I1 (RTNS-II) and the Omega West Reactor (OWR), respectively. The irradiation conditions of LASREF, RTNS-II and OWR are listed in Table 1.

The specimens used are TEM disks of MARZ (99.999%) copper annealed at 450°C for 15 m. After irradiation, the specimens were electropolished and observed with a JEM-2000FX electron microscope.

---

*Operated for the U.S. Department of Energy by Battelle Memorial Institute under Contract DE-AC06-76RLO 1830.

Table 1. Irradiation conditions of the present experiment.

Facility	Position	Temperature	Total Fluence ($x10^{23}/m^2$)	dpa	dpa/sec ($x10^{-9}$)
LASREF	Capsule 1	55°C	2.8[1,2]	NA[1]	NA[1]
	Capsule 3	44°C	1.5	0.011	2.9
	Capsule 5	37°C	1.0	0.0037	0.97
	Capsule 7	36°C	0.34	0.0016	0.42 .0
RTNS-II		90°C	0.60	0.022	2.0
		90°C	0.38	0.014	1.3
		90°C	0.27	0.0098	0.89
OWR		90°C	3.6	0.011	48

[1] Not available because activation foils were badly corroded.
[2] Expected value from previous work[11].

Results

A high density of defect clusters was observed in all cases. Most of the clusters observed were identified as stacking fault tetrahedra (SFT). A lower density of dislocation loops and unidentified small clusters was also observed. The density of these defects was below 30% of the total density.

Figure 1 shows weak beam dark-field images of defect clusters formed by the *LASREF* irradiation. High densities of triangular images are the SFT. Figure 2 shows the defect clusters produced by RTNS-II and OWR irradiations, whose images were taken in the same diffraction condition as that of Figure 1. In all cases the cluster density increases with increasing dose.

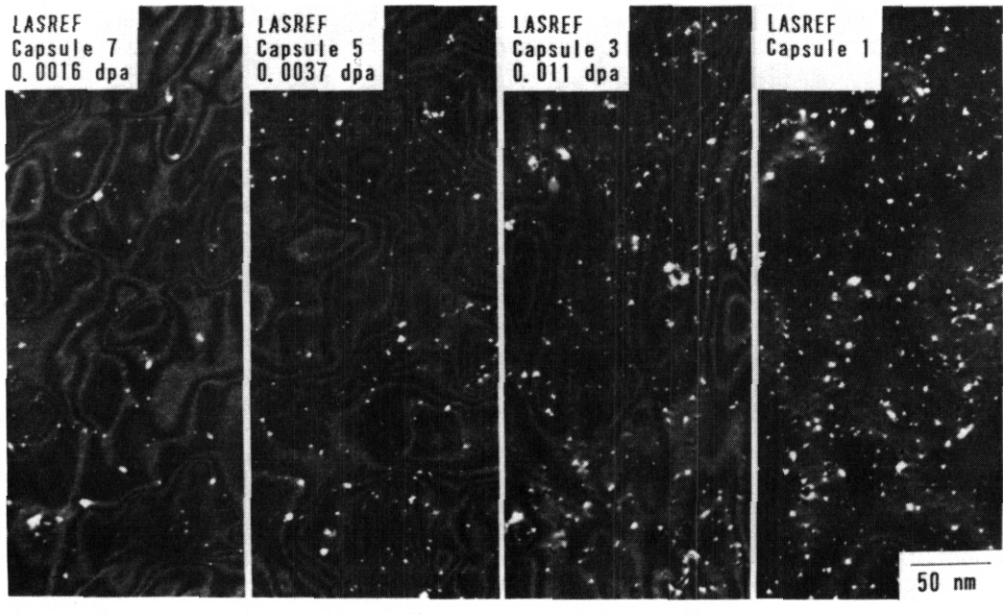

LASREF 36°C-55°C Annealed MARZ Copper

Fig. 1. Defect clusters formed in copper irradiated with spallation neutrons at 36 to 55°C.

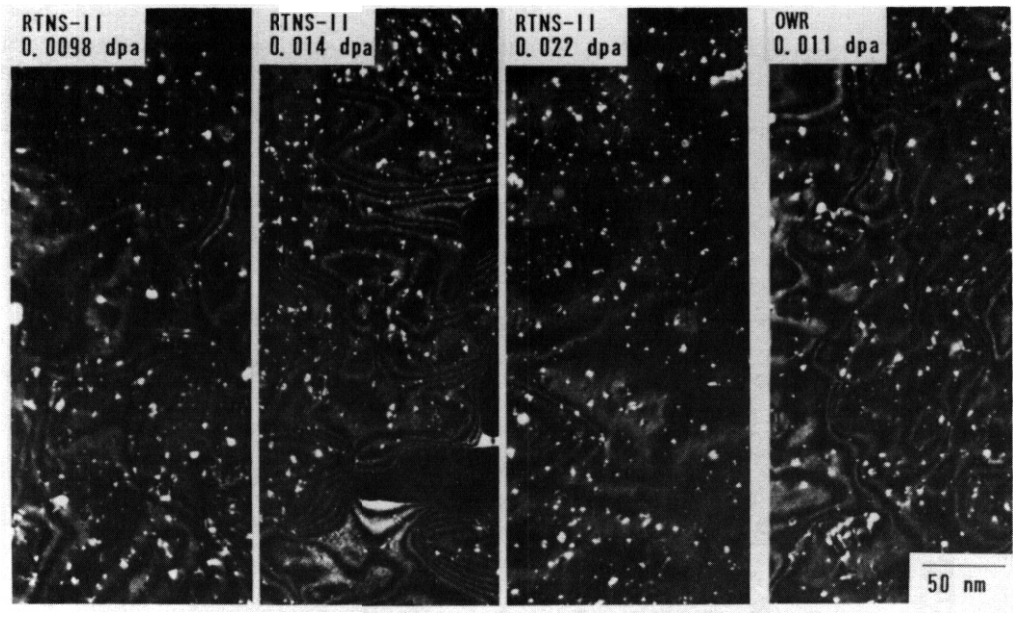

RTNS-II. OWR 90°C Annealed MARZ Copper

Fig. 2. Defect clusters formed in copper irradiated with fusion or fission neutrons at 90°C.

Figure 3 compares the sizes of defect clusters that were identified as SFT for the three irradiation cases at similar displacement dose. There are no drastic differences in type and size of defect clusters for fission, fusion and spallation neutron irradiations. However, the small differences in the size distribution of the three cases, e.g. the steep peak for RTNS-II and the peak at smaller sizes for OWR, may be due to differences in the neutron energy spectra. Figure 4 shows the defect cluster density as a function of dpa. The densities by LASREF and RTNS-II are very similar when compared on the basis of dpa. The densities in both cases vary proportionally to the square root of the dose.

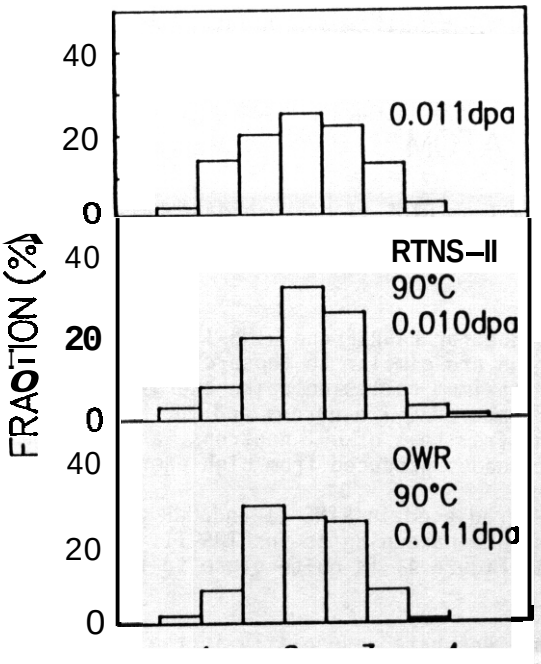

Fig. 3. Size distribution of defects that were identified as stacking fault tetrahedra for each spectrum.

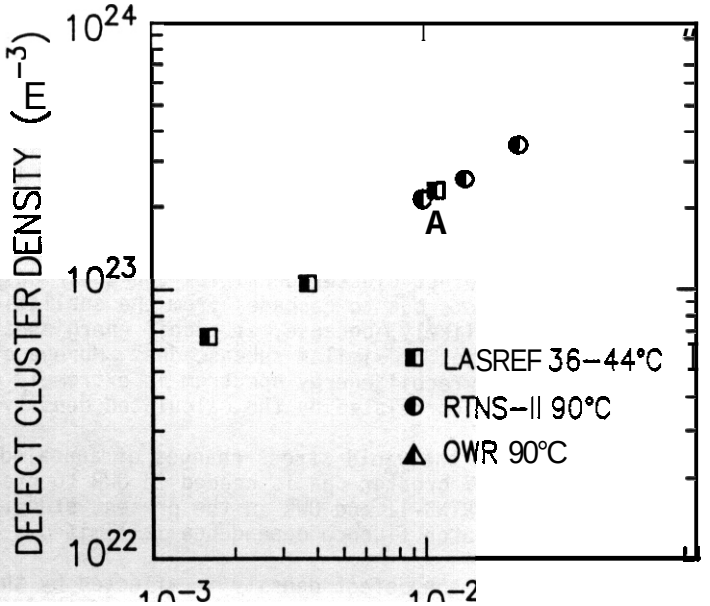

Fig. 4 The defect cluster density as a function of dpa.

Discussion

The defect cluster densities of copper irradiated with D-T neutrons at room temperature or at 90°C have been reported by several groups[1-6]. They are summarized in Figure 5 together with the present results. The data from OWR irradiations at 90°C by Horsewell et al.[5] are also shown. Analysis of very low dose data from RTNS-II[1,2] shows that the increases in defect cluster density are initially proportional to the dose and then proportional to the square root of the dose. The critical dose where the dose dependence changes from linear to square root is different in different studies or different specimen purities. According to Figure 5, the dose range of the present LASREF and RTNS-II irradiations is high enough that square root dependence is expected.

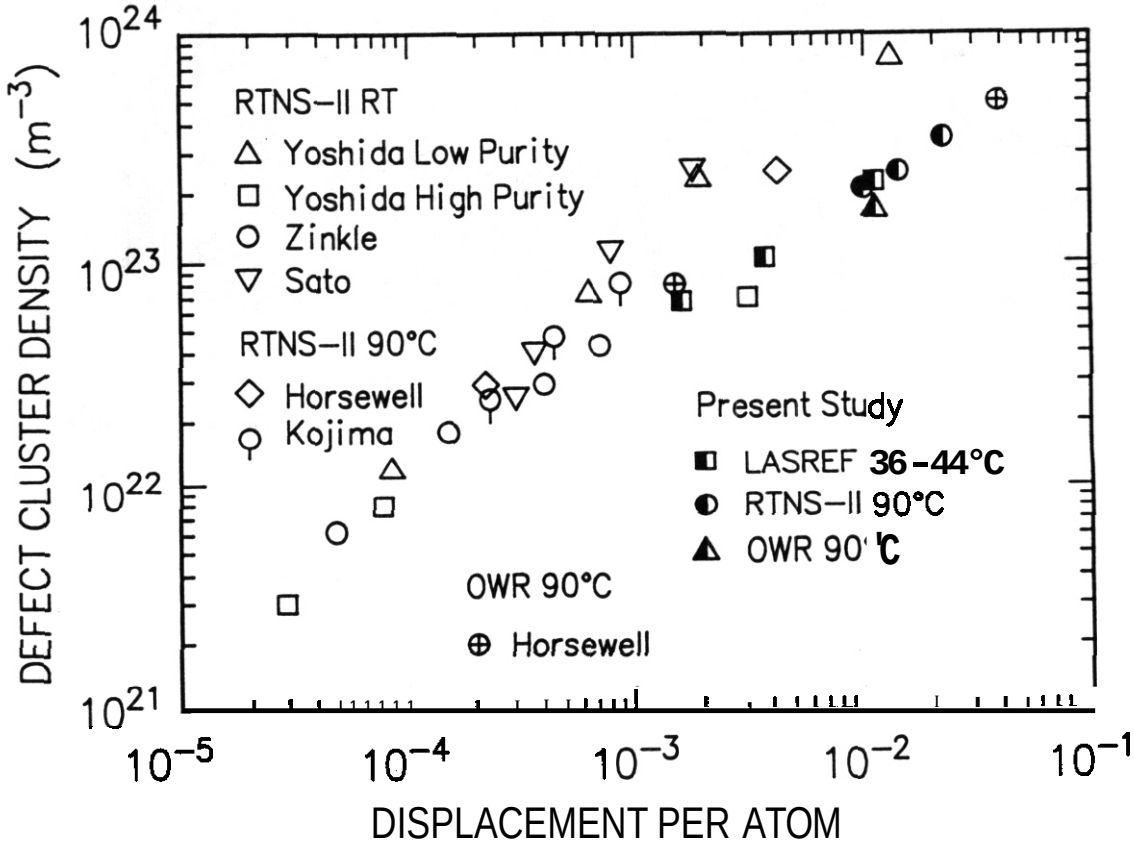

Fig. 5. The defect cluster density as a function of dpa. Data from RTNS-II by Yoshida et al.[1], Zinkle[2], Sato et al.[3], Horsewell et al.[5] and Kojima et al.[4] and from OWR by Horsewell et al.[5] are also shown for comparison.

The fact that the defect cluster densities and their dose dependence for LASREF and RTNS-II are similar may imply that the effects due to cascades from the spallation neutrons are similar to those of fusion neutrons. This is likely, because, at recoil energies above the maximum collision spike energy, cascades are formed as a series of similar subcascades. Muroga et al.[6] compared D-T neutrons and 100 MeV Ni ion irradiations, whose recoil energy spectrum is extremely different from that of D-T neutrons, and found that the density is well correlated by the calculated density of subcascades produced from high energy recoils.

Heinisch[7] compared the yield stress changes of annealed copper irradiated in RTNS-II and OWR at 90°C and found that about 1.7 greater dpa is needed in OWR to produce the same hardening as in RTNS-II. The difference between RTNS-II and OWR in the present study, shown in Figure 4, is quite close to the factor of 1.7, though the data on fluence dependence is limited.

It is expected that the defect density is affected by the displacement rate, especially in the region where the density is proportional to the square root of the dose. Heinisch et al.[8] compared the yield stress of copper irradiated in separate runs, R1 and R2, in RTNS-II. The displacement rate of R-1 is about four times higher than that of R-2. About 1.3 to 1.8 greater dpa in R-2 is needed to produce the same hardening as in R-1 at a dose of around 0.01 dpa (Figure 4 of ref.[8]). The defect density data from RTNS-II by Horsewell** shown in Figure 5 and the present RTNS-II data are from R-1 and R-2 runs, respectively. The difference in the equivalent dose between Horsewell's and the present data is a factor of 3.3, which is much greater than can be attributed to the difference in damage rates.

Interestingly, for OWR at 90°C, where all specimens are exposed at the same damage rate, there is a difference of a factor of 1.8 in the equivalent dose between Horsewell's data and the present data. Thus the difference between Horsewell's and the present data for RTNS-II in Figure 5 may be due to a systematic difference of about a factor of 1.8 in defect densities as well as the displacement rate effect. The origin of this systematic difference as not been identified.

Proper quantitative evaluation of spectral effects requires experiments with controlled variation of the displacement rate. Data at very low doses, where the density is proportional to the dose, may be useful because the density there appears to be insensitive to small variations in specimen purity and displacement rate.

CONCLUSIONS

Defect cluster densities in copper irradiated with spallation neutron (LASREF) and fusion neutrons (RTNS-II) are similar when compared on the basis of dpa. In both cases the density increases in proportion to the square root of the dose. Based on this limited evidence, there appears to be no fundamental difference in displacement damage at low doses between fusion and spallation neutrons. The difference in the density between fusion neutrons and fission neutrons (OWR) is close to what is expected from the previous data on the yield stress change. Further investigations, either at very low fluences or with systematic variation of the displacement rate, are needed in order to extend our understanding of neutron spectral effects and to evaluate the use of a spallation source as a tool for future fusion materials testing.

REFERENCES

1. N. Yoshida, Y. Akashi, K. Kitajima and M. Kiritani, N. Nucl. Mater. 133&134 (1985) 405.

2. S. J. Zinkle, J. Nucl. Mater. 150 (1987) 140.

3. Y. Satoh, I Ishida, T. Yoshiie and M. Kiritani, J. Nucl. Mater. 155-157 (1988) 443.

4. S. Kojima, S. J. Zinkle and H. L. Heinisch, J. Nucl. Mater. 179-181 (1991) 982.

5. A. Horsewell, B. N. Singh, S. Proennecke, W. F. Sommer and H. L. Heinisch, J. Nucl. Mater. 179-181 (1991) 924.

6. T. Muroga, M. Eguchi, N. Yoshida, N. Tsukuda and K. Kitajima, J. Nucl. Mater. 141-143 (1986) 865.

7. H. L. Heinisch, J. Nucl. Mater. 155-157 (1988) 121

8. H. L. Heinisch, S. D. Atkin and C. Martinez, J. Nucl. Mater. 141-143 (1986) 807

9. M. S. Wechsler and W. F. Sommer, J. Nucl. Mater. 122&123 (1984) 1078.

10. W. Kley, G. R. Bishop, A. Sinha and J. M. Perlado, ASTM STP 1046 (1990) 607.

11. D. R. Davidson, R. C. Reedy, L. R. Greenwood, W. F. Sommer and M. S. Wechsler, ASTM STP 956 (1987) 730.

12. W. F. Sommer W. Lohmann, K. Graf, 1. K. Taylor and R. M. Chavez, ASTM STP 956 (1987) 718

13. F. G. Perey, Oak Ridge National Laboratory Report, ORNL-TM-6062 (1977).

14. M. S. Wechsler, D. R. Davidson, L. R. Greenwood and W. F. Sommer, ASTM *STP* 870 (1985) 1189

MOLECULAR DYNAMICS AND BINARY COLLISION MODELING OF THE PRIMARY DAMAGE STATE OF COLLISION CASCADES

H. L. Heinisch, Pacific Northwest Laboratory[a] and B. N. Singh, RISØ National Laboratory

OBJECTIVE

The objective of this work is to determine the spectral dependence of defect production and microstructure evolution for the development of fission-fusion correlations.

SUMMARY

Quantitative information on defect production in cascades in copper obtained from recent molecular dynamics (MD) simulations is compared to defect production information determined earlier with a model based on the binary collision approximation (BCA). The total numbers of residual defects, the fractions of them that are mobile, and the sizes of immobile clusters compare favorably, especially when the termination conditions of the two simulations are taken into account. A strategy is laid out for integrating the details of the cascade quenching phase determined by MD into a BCA-based model that is practical for simulating much higher energies and longer times than MD alone can achieve. The extraction of collisional phase information from MD simulations and the correspondence of MD and BCA versions of the collisional phase is demonstrated at low energy.

PROGRESS AND STATUS

Introduction

To understand microstructure evolution it is important to understand the spatial and temporal characteristics of defect production in individual radiation events. Defects are produced in collision cascades in spatially discrete distributions of clustered and unclustered defects that are energy and temperature dependent. The primary damage state of a cascade strongly influences how the defects created in that cascade interact with each other and the existing microstructure.

Recent advances in molecular dynamics (MD) modeling of collision cascades are significantly adding to the quantitative knowledge of the primary damage state. MD cascades have been generated in significant numbers at energies up to 10 keV using realistic many-body interatomic potentials for copper.[1] Two cascades of 25 keV in copper[2] are the highest energy cascades ever simulated with MD. In one of those cascades, interstitial loop formation by collective atomic displacements or "punching" is demonstrated for the first time. The remarkable achievements in MD simulations of cascades are now providing a solid basis for understanding defect production in cascades.

MD simulations are limited in practice to the first few tens of picoseconds in the life of a cascade and to cascade energies on the order of the threshold for subcascade formation. Models not relying on many-body atomic interactions are required for simulating longer times and higher energies. Cascade simulations based on the binary collision approximation (BCA) have been successful in determining the overall structure of cascades, including the spatial distribution of subcascades.[3] Stochastic computer simulations[4] and methods based on the diffusion equation are being developed to deal with the intracascade and intercascade interactions of defects. The present paper describes a method for integrating MD simulations, BCA cascade simulations and stochastic annealing simulations into a description of the primary damage state of high energy cascades, which is necessary for a comprehensive, cascade-based model of microstructure evolution.

Binary Collision and Stochastic Annealing Simulations

A method for determining the primary damage state based on BCA cascade simulations was developed about ten years ago by Heinisch and coworkers.[4,6] Cascades in copper were generated with the BCA code MARLOWE[7] using a cut-off energy of only 5 eV. The other MARLOWE parameter settings were chosen to best represent low energy features of cascades observed in MD simulations, The low cut-off energy allows events such as replacement collision sequences to develop fully, resulting in BCA cascades with displaced atoms at more realistic positions. For example, some interstitials are displaced to the periphery of the cascade region, corresponding to those that escape being recombined during quenching.

To model the quenching stage and the subsequent defect interactions in the cascade region, the stochastic annealing simulation code ALSOME[6] was applied to the results of the MARLOWE simulations. The basic premise of the ALSOME code is that point defects and defect clusters are treated as entities that interact through thermally activated diffusion. The defects are associated with crystal lattice sites, and the mobile defects move by hopping stochastically from site to site. The hopping is governed by the numbers of the

---

[a]Pacific Northwest Laboratory is operated for the U.S. Department of Energy by Battelle Memorial Institute under Contract DE-AC06-76RLO 1830.

various types of defects and their relative jump frequencies. Interactions occur when two defects come within the critical reaction distance for their types.

Since ALSOME is designed to model defect diffusion, it should be applied to cascade defect configurations existing only after the quenching stage, However, because of a lack of information about atomic motion *in* the quenching phase, ALSOME was applied in the earlier work[4] to binary collision cascades that had undergone only the collisional phase. The effects of quenching were accounted for in ALSOME with a simple two-step approach: exaggerated values of defect mobilities and interaction parameters were used for the jumps occurring during the first 10^{-11} s, then normal parameter values were used for the subsequent intracascade annealing. Quenching parameter values were chosen to give the best agreement with available experimental information on the total number of defect pairs remaining after quenching[8] and the numbers of freely migrating defects[9,10,11] existing after the intracascade annealing.

Comparing MD and BCA Simulation Results

The recent MD simulations of cascades in copper',' make it possible to compare the earlier MARLOWE/ALSOME (MA) approach directly to cascade simulations in which the quenching phase is realistically portrayed. Three aspects of the primary damage state are vital to the course of microstructure evolution: the total number of point defects remaining, the number of residual defects that are mobile and escape the cascade region, and the sizes of the non-mobile defect clusters.

The MA results for cascades at 300 K are compared here to MD results for cascades at 100 K and 600 K. The total number of residual defects is about the same with each model, but they are partitioned between mobile defects and immobile clusters slightly differently. The numbers of freely migrating interstitials relative to the calculated number of displacements as a function of recoil energy for the MD simulations and the MA approach are compared in fig. 1.

In both cases single, di- and tri-interstitials are considered mobile. The MD cascades were run until very little was happening on the time scale practical for MD, up to about 10 ps. The ALSOME simulations were run until no mobile defects remained in the vicinity of the cascade, representing a considerably longer time and a somewhat greater chance for the mobile defects to annihilate or cluster than in the MD simulations. As a result, there are somewhat fewer mobile defects in the MA results than in the 100 K MD simulations. Because the vacancies are confined to a smaller volume in the center of the cascade, the mobile interstitials are more likelv to interact with the interstitial clusters. Thus, if the MD cascades were run for a much longer time, there should be fewer mobile defects and larger interstitial cluster;. Indeed, some coarseninq is observed in the MD cascades at 600 K where defect mobilities are greater.'

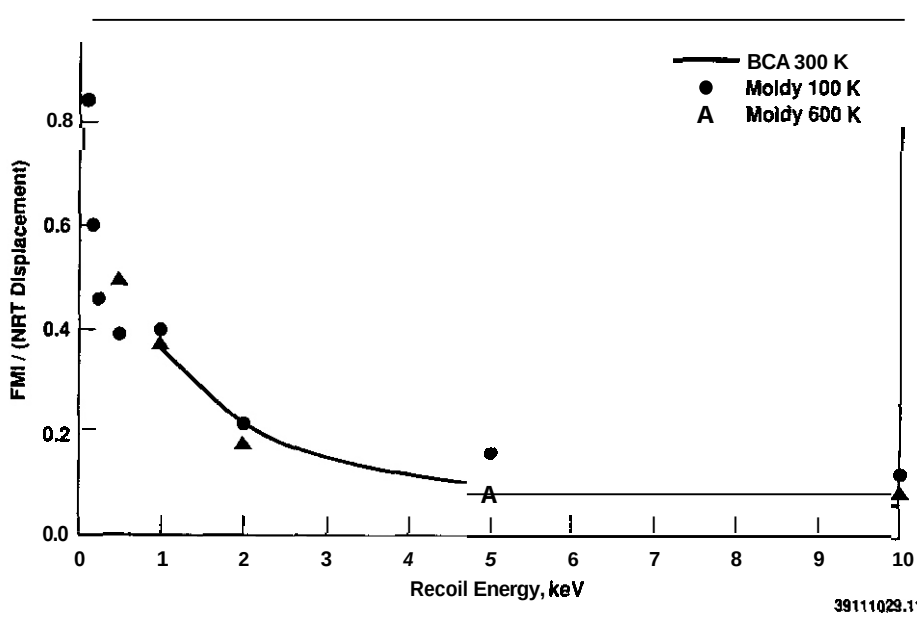

Fig. 1. The fraction of freely migrating interstitial defects relative to the calculated number of displacements per cascade as a function of recoil energy for MO and BCA cascades in copper. The points are for MD cascades at 100 K and 600 K [1]. The line represents a function fitted to results from BCA cascades at 1 keV and above [14].

The size distributions of interstitial clusters in the 100 K MD cascades and the MA cascades are compared in Fig. 2. The MD distributions are for only 5-15 cascades at each energy up to 10 keV,[1] while the MA distributions are for 100 cascades at each energy. The distribution for the two 25 keV MO cascades" is compared to that for forty 20 keV MA cascades.

The cluster size distributions compare very favorably, considering the small numbers of MO cascades and the simple ALSOME quenching model. There are more clusters per cascade by the MA approach because of the longer simulated times. The cluster of size 17 at 25 keV is the interstitial loop that was punched out,

and it is larger than any interstitial cluster obtained with ALSOME. No provision for loop punching presently exists in ALSOME.

The vacancy cluster size distribution of the 20 keV MA cascades is also consistent with the sizes of the few vacancy clusters in the 25 keV MD cascades. There is one vacancy cluster of size 14 in the MD results. while the

size 20.

The remarkably good agreement of defect production in copper by the MD and MA models may be somewhat fortuitous, given the simplicity of the MA model. On the other hand, it may be strong evidence that the spatial distribution of displaced atoms in the collisional phase has a major influence on the subsequent disposition of the defects. The distribution of displaced atoms in the collisional phase most certainly correlates with the cascade energy density. To be sure, what happens during the quenching stage depends on how the energy dissipates from the molten zone, which requires MO to model. But the formation of the molten zone does depend on the deposited energy density. The expulsion of interstitials to the periphery of the cascade region is a collisional effect that can be modeled with binary collisions, which may explain the success of the simple MA approach. Interstitial loop punching is an exception, because that phenomenon cannot be described in terms of binary collisions.

At the very least, the good agreement of MD and MA models of defect production indicates that even the simple ALSOME quenching model can be adjusted to give behavior very similar to that observed in the MD simulations. In the following section we outline how MD results can be integrated into the MA approach to produce a realistic model of defect production in cascades of all energies.

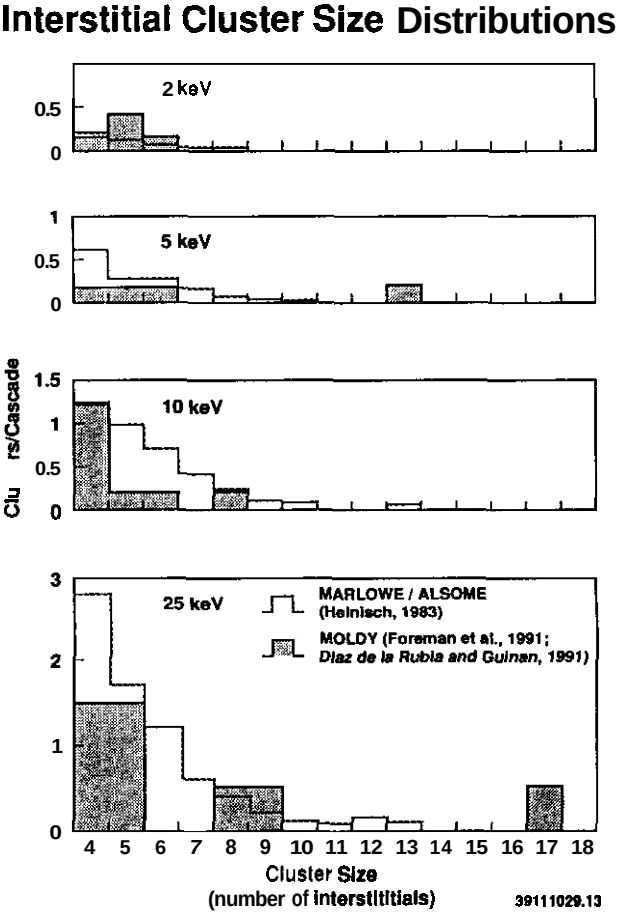

Fig. 2. A comparison of BCA and MD cluster size distributions for cascades in copper. The shaded bars are for 2-10 keV MD cascades at 100 K [1] and 25 keV MD cascades at 10 K [12].

The Integrated MD-MA Model

To model the primary damage state of high energy cascades, the MA approach will be calibrated with MD results obtained for cascades of the highest possible energies. It is not likely that any important cascade features observable only in MD simulations will occur at energies higher than the subcascade threshold energy, where at least two MD cascades have already been produced.

The MA formalism will be retained, but details such as the quenching stage parameter settings will be determined by calibration to the results of MD. It is possible that the quenching parameters will have to be functions of cascade energy density, especially to represent the clustering properly. For special circumstances such as interstitial loop punching, and perhaps for vacancy loop formation, correlations between aspects of the collisional phase (for example, localized areas of high energy density) and the MO results may need to be incorporated into the MA simulations of the quenching stage.

The MD simulations properly reflect the temperature dependence of the primary damage state, whereas the MA approach contains only indirect influences of the temperature. The MARLOWE cascades are produced in a crystal where the atoms have uncorrelated thermal displacements representative of the specified temperature, but the collisional phase is not strongly influenced by the temperature.[13] The concept of temperature enters into ALSOME in terms of the relative jump probabilities and the length of time of the simulation, since the annealing is modeled as a sequence of events without regard to the time between events. This is a serious shortcoming for ALSOME only when trying to model the quenching phase, for which it is not designed. Temperature effects (which are material dependent) will be incorporated into the MD-MA calibration, if necessary, once they are elucidated in the MD results.

The MD-MA calibration will be accomplished simply by choosing values for the existing MA parameters that will produce the same defect configurations as at the post-quenching stage in the MD simulations. The most rigorous way to develop and test the calibration is to perform the MA quenching on the collisional phase of MD simulations and compare the results to the quenching and post-quenching stages of the same cascades. The first step is to extract the collisional phase information from MD cascades and determine if the

collisional phase information is the same in both MD and MARLOWE cascades

Information on the collisional phase was extracted from five 500 eV cascades that were generated with the MOLDYCASK MD code. As each energetic atom in the MD cascade decreased in energy below the cut-off value, its original and final positions were noted. Fig. 3 shows the number of atoms above the-cut-off energy of 5 eV as a function of time. The collisional phase by this definition occurs in about 0.15 ps. The resulting list of displaced atoms and their original positions were analyzed as if they were output of the MARLOWE code. The results of the collisional phase of five 500 eV MD cascades are compared with that for 100 MARLOWE cascades of the same energy in Table 1.

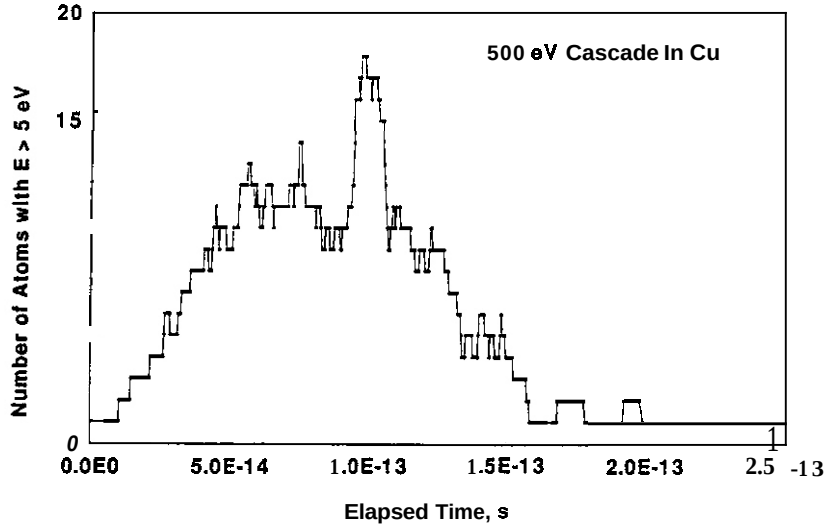

Fig. 3. The number of energetic atoms in the collisional phase of a 500 eV MD cascade in copper as a function of elapsed time.

Statistically, the results are quite similar, not only in the numbers of defects, but also in their spatial distribution. In Table 1 the cascade vacancy density is the density of vacancies within an enclosing rectangular volume. The average local vacancy density is an average of the fraction of lattice sites within three nearest neighbors about each vacancy that also contains a vacancy. It is a measure of the local defect density in the core of the cascade. The conclusion from this example is that, statistically, MARLOWE provides a good approximation to the collisional phase of a cascade. This comparison should be tested at higher energies, where the collisional phase is expected to last longer.

Table 1. The Collisional Phase of 500 eV Cascades in Copper by MD and BCA for a Cut-off Energy of 5 eV and Recombination Radius of 0.707 lattice parameters.

	MOLDYCASK	MARLOWE
Number of Cascades	5	100
Residual Defect Pairs	8.6 ± 0.9	8.0 ± 1.9
Cascade Volume	90 ± 71	44 ± 25
Cascade Vacancy Density	0.26 ± 0.32	0.22 ± 0.10
Average Local Vacancy Density, 3nn (%)	5.0	5.7

CONCLUSIONS

Based on the good agreement of earlier BCA-based modeling of defect production in copper displacement cascades with recent MD results, it appears that a BCA-based model, calibrated with information from MD simulations, can give a correct description of defect production in cascades of any energy.

Special consideration will have to be given in the model for the production of interstitial loops by the "punching" mechanism.

Comparison of MARLOWE results with collisional phase information extracted from MD cascade runs indicates that MARLOWE adequately represents the collisional phase. MD collisional and post-quenching information can be used to determine parameter values for the BCA-based model.

ACKNOWLEDGEMENTS

The authors are grateful to T. Diaz de la Rubia for providing the MOLDYCASK code and to A.J.E. Foreman and W. Phythian for access to their results prior to its publication.

REFERENCES

1. A.J.E. Foreman, W.J. Phythian and C.A. English, The Molecular Dynamics Simulation of Irradiation Damase Cascades Using Many-body Potentials, AEA-TRS-2031 (1991).

2. T. Diaz de la Rubia and M.W. Guinan, Phvs. Rev. Lett. **66,** 2766 (1991).

3. H.L. Heinisch and B.N. Singh, Phil. Mas. in press.

4. H.L. Heinisch, J. Nucl. Mater. 117, 47 (1983).

5. C.H. Woo, B.N. Singh and H.L. Heinisch, J.Nucl. Mater. **174,** 190 (1991).

6. H.L. Heinisch, D.G. Doran and O.M. Schwartz, ASTM STP 725, 191 (1981).

7. M.T. Robinson and I.M. Torrens, Phvs. **Rev. B9,** 5008 (1972).

8. R.L. Simons, J. Nucl. Mater. **141&143,** 665 (1986).

9. U. Theis and H. Wollenberger, J. Nucl. Mater. **88,** 121 (1980).

10. T.H. Blewitt, A.C. Klank, T. Scott and W. Weber, Proc. Int. Conf. on Radiation-induced Voids in Metals, Albany, NY, 1971, eds J.W. Corbett and L.C. Ianniello, 757 (1972).

11. J.A. Goldstone, D.M. Parkin and H.M. Simpson, J. Appl. Phys. **53,** 4189 (1982).

12. T. Diaz de la Rubia and M.W. Guinan, Fusion Reactor Materials Semiannual Progress Report, March 31, 1991, DOE/ER-0313/10, 29 (1991).

13. H.L. Heinisch, J. Nucl. Mater. **108&109,** 62 (1982).

14. H.L. Heinisch and F.M. Mann, J. Nucl. Mater. **122&123,** 1023 (1984)

ELEMENTAL INHOMOGENEITIES DEVELOPED IN STAINLESS STEELS BY RADIATION-INDUCED SEGREGATION -- E. A. Kenik (Oak Ridge National Laboratory)

OBJECTIVE

Analytical electron microscopy is being employed to study the origin of elemental inhomogeneities in several neutron-irradiated austenitic stainless steels stabilized with nickel or manganese. The similarity of radiation-induced segregation (RIS) to various point defect sinks is discussed. An alternate mechanism for matrix elemental inhomogeneities is proposed.

SUMMARY

Radiation-induced segregation (RIS) has been measured by analytical electron microscopy in a number of neutron-irradiated stainless steels stabilized with nickel or manganese. RIS to high angle grain boundaries, cavities, and dislocation loops was observed. Similar enrichment of nickel, silicon, and, in certain cases, phosphorus and depletion of chromium, iron, molybdenum, and manganese occurred at all three of these defect sinks. The origin of matrix composition fluctuations is discussed and an alternate mechanism, based on RIS to the initial dislocation loop microstructure. is suggested.

PROGRESS AND STATUS

Introduction

The motion of point defects in irradiated metals such as stainless steels can result in the transport of solute atoms and can produce elemental inhomogeneities in the material.',' Fluxes of point defects to defect sinks (e.g., grain boundaries, dislocation segments and loops, cavities, and precipitates) can result in radiation-induced segregation (RIS) of particular solute species toward or away from the sink. Interactions of solute atoms can occur with either the interstitial or the vacancy defect fluxes. The elemental inhomogeneities produced by RIS can result in phase instability of the matrix? precipitation,"' irradiation-assisted sensitization,"' embrittlement,[8] and strengthening.' RIS at grain boundaries can result in the first four effects, whereas RIS to dislocations, cavities, and precipitates may also result in matrix strengthening.

In many cases, RIS in irradiated stainless steels has been reported to produce chromium depletion at defect sinks.[6,7,10-12] This reduced chromium level can result in local instability of the protective passive film and in preferential attack. At grain boundaries, this preferential attack is associated with radiation-induced sensitization and irradiation-assisted stress corrosion cracking (IASCC).[6,7,10] The combination of electrolytic potentiostatic reactivation (EPR) and analytical electron microscopy (AEM) has demonstrated the association between chromium depletion at grain boundaries by RIS and preferential grain boundary attack." Optical and scanning electron microscopy of EPR tested specimens indicated both intergranular and intragranular preferential attack. The depletion of chromium and the enrichment of nickel and silicon were observed at both cavities and faulted dislocation loops.[14] Either defect sink may be the origin of the intragranular attack, though the loop density exceeded that of the cavities. Similar studies as a function of irradiation temperature indicated that preferential intergranular attack became negligible at temperatures $<300°C$, whereas intragranular attack continued to lower temperatures ($\sim 200°C$).[15]

Matrix elemental inhomogeneity has been reported in a number of neutron-irradiated stainless steels.[10,16] Such composition fluctuations have been attributed to either a spinodal-like decomposition of the austenite under irradiation" or segregation to cavities.[12] A third mechanism for matrix composition fluctuations should be considered: RIS to dislocation loops present in the early stages of irradiation. High resolution AEM has been employed to study RIS lo various defect sinks in both ion- and neutron-irradiated stainless steels.

Experimental Procedure

Table 1 gives the composition of two of the austenitic alloys studied; a solution-annealed titanium-modified stainless steel, USPCA, based on type 316 stainless steel and a 25% cold-worked, Russian manganese-stabilized steel, EP838. These two alloys were irradiated in the Fast Flux Test Facility (FFTF) to 15 displacements per atom (dpa) at 520°C. The other alloys in this study were commercial type 304 and type 316 alloys that were irradiated in two different light-water reactors at conditions specified below in the Results section.

	Fe	Ni	Cr	Mo	Mn	Si	Ti	C	Al
USPCA	65.0	15.4	15.1	1.3	1.8	0.80	0.28	0.23	--
EP838	67.4	3.9	12.3	0.5	13.5	0.8	<0.02	0.08	1.5

Analysis was performed in a Philips EM400T/FEG operated in the scanning transmission mode with a probe diameter of <2 nm (FWTM). The instrument is equipped with EDAX 9100170 energy dispersive X-ray spectrometry (EDXS) and Gatan 666 parallel detection electron energy loss spectrometry (PEELS) systems. A double-tilt, liquid-nitrogen-cooled specimen holder was employed for microanalysis to minimize contamination under the focussed probe. Subtraction of "in-hole" EDXS spectra from the measured spectra corrected for (1) the normal "in-hole" counts associated with uncollimated radiation from the microscope illumination system and (2) radiation associated with radioactivity of the specimen induced by neutron irradiation (predominantly Mn K X rays). All compositions are given in atomic percent, unless noted otherwise.

Results

Figure 1 illustrates the RIS profiles at a grain boundary in the nickel-stabilized USPCA after neutron irradiation in FFTF to 15 dpa at ***520°C.*** The local curvature of the boundary and the asymmetry of the dislocation density on either side of the boundary suggests that the boundary had migrated to the left during the irradiation. The volume swept out by the migrating boundary was enriched in nickel to ~20% and depleted in both chromium and molyhdenum. The chromium level in this region was <12%, below that required to maintain the corrosion resistance of the stainless steel. Molybdenum was depleted by a factor of three, whereas no significant difference in silicon was observed between the matrix and the volume swept out by the migrating boundary. A narrow (~70 nm wide) zone of reversed compositional change (i.e., nickel depletion and chromium enrichment) was present on the right, just ahead of the migrating boundary. Similar RIS of nickel, chromium, and molybdenum was observed at both cavities and Frank dislocation loops; the latter of which will be discussed later. Though both nickel and manganese are austenite stabilizing elements, their RIS behavior at boundaries and dislocation loops has been shown to be in the opposite sense in both ion- and neutron-irradiated stainless steels.[11,18]

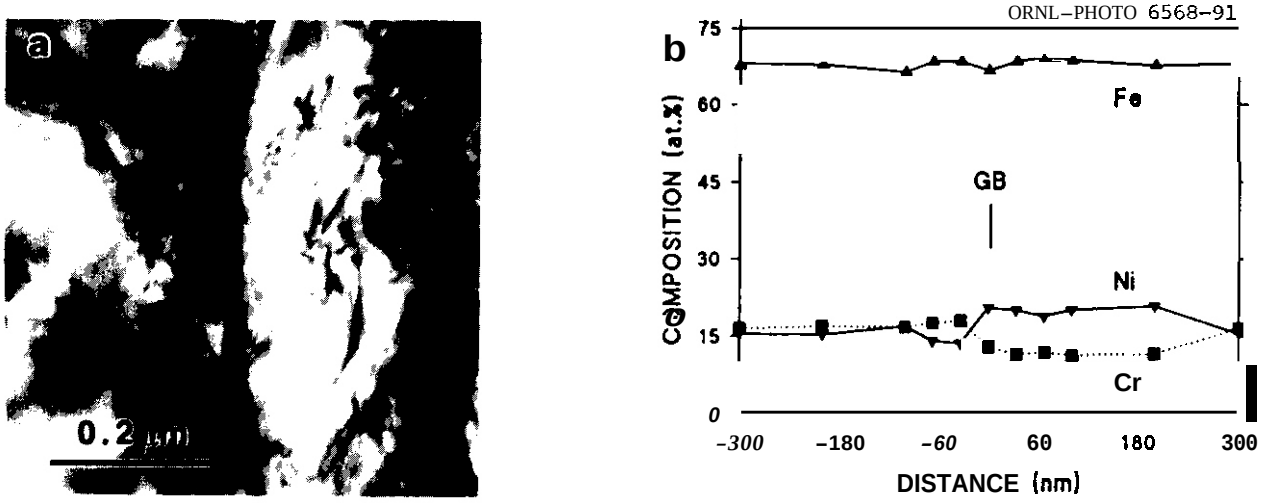

Fig. 1. RIS profiles measured by EDXS at a high angle grain boundary in USPCA after neutron irradiation to 15 dpa at 520°C. The boundary migrated to the left during irradiation.

Figure 2 compares the EDXS spectra for a high angle grain boundary and the adjacent matrix in a type 316 stainless steel irradiated to 3×10^{25} neutrons/m^2 at 300°C. Quantitative analysis of these spectra indicates that the grain boundary was enriched slightly in silicon, phosphorus, nickel, and molybdenum and depleted in iron relative to the matrix. Averaged over a number of spectra, the compositions are 3.2 Si, 0.6 P, 19.5 Cr, 61.4 Fe, 13.3 Ni, and 1.8 Mo for the grain boundary and 2.5 Si, 0.3 P, 19.4 Cr, 63.5 Fe, 12.7 Ni, and 1.3 Mo for the matrix. The enrichment of phosphorus and molybdenum and the attendant reduction in iron at the boundary were observed for all high angle boundaries analyzed in this material. Enrichment of silicon, chromium, and nickel was observed at more than 50% of the boundaries. Though enrichment of undersized solutes (e.g., Si and Ni) is consistent with RIS lo grain boundaries, the expected RIS depletion of oversized solutes (e.g., Mo and Cr) was not observed. The width of the segregation layer was very narrow, as the measured levels of phosphorus, molybdenum, and iron measured at ±3.3 nm from the boundary were essentially back to the matrix values. The absence of significant chromium depletion observed at this fluence was consistent with the results of post-irradiation, slow-strain-rate mechanical testing: material at this fluence did not exhibit IASCC, whereas materials with fluences $>3 \times 10^{25}$ neutrons/m^2 exhibited IASCC.

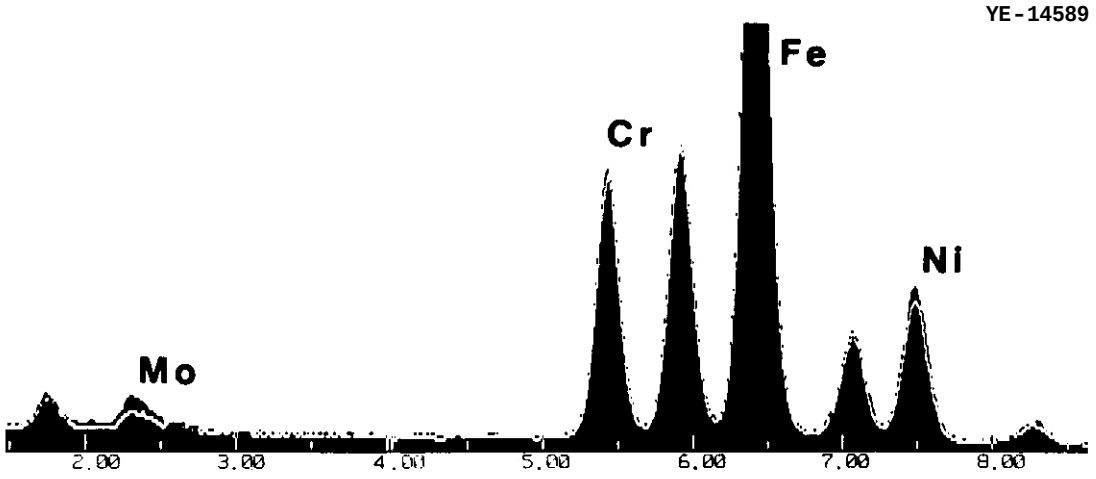

Fig. 2. EDXS spectra measured at a high angle grain boundary (solid) and the adjacent matrix (white line) in a type 316 stainless steel neutron irradiated to 3×10^{25} neutrons/m^2. The iron peaks are scaled to each other at twice full scale.

The absence of the expected radiation-induced depletion of chromium and molybdenum in the irradiated type 316 stainless steel, as described above, prompted the investigation of grain boundary compositions in the unirradiated control material. Figure 3 illustrates spectra typical of grain boundaries and matrix in the control material. Increased levels of phosphorus, chromium, and molybdenum and depletion of iron were observed at this and other analyzed boundaries. Average enrichment/depletion factors (boundary composition/matrix composition ratios) of 2, 1.04, 0.97, and 1.73 were observed for phosphorus, chromium, iron, and molybdenum. Similar cosegregation of chromium and molybdenum has been reported in conjunction with equilibrium segregation of phosphorus lo high angle grain boundaries in thermally-aged type 304L stainless steels." This equilibrium segregation in the type 316 stainless steel was also very narrow, with the segregants returning to the unperturbed matrix levels within <5 nm of the boundary. Therefore, the atypical segregation that was observed in the type 316 stainless steel irradiated to 3×10^{25} neutrons/m^2 is a modification of the equilibrium segregation profile by RIS.

In a further study of the differences in RIS behavior between nickel and manganese, the manganese-stabilized EP838 irradiated to the same conditions as the USPCA ahove (15 dpa, 520°C) was investigated. Figure 4 shows the elemental profiles at a similar high-angle grain boundary that appears to have migrated during irradiation. Manganese and molybdenum were strongly depleted, chromium was only slightly depleted, whereas silicon and nickel were enriched in both the volume swept by the boundary and that near to the boundary. As the chromium depletion in the Mn-stabilized EP838 was less than that observed in the Ni-stabilized USPCA, the EP838 may also be more resistant to radiation-induced sensitization and IASCC. The reduction of austenite stability associated with the manganese depletion at grain houndarirs may be offset by the concurrent nickel enrichment, especially as nickel is a more potent austenite stabilizer than manganese."

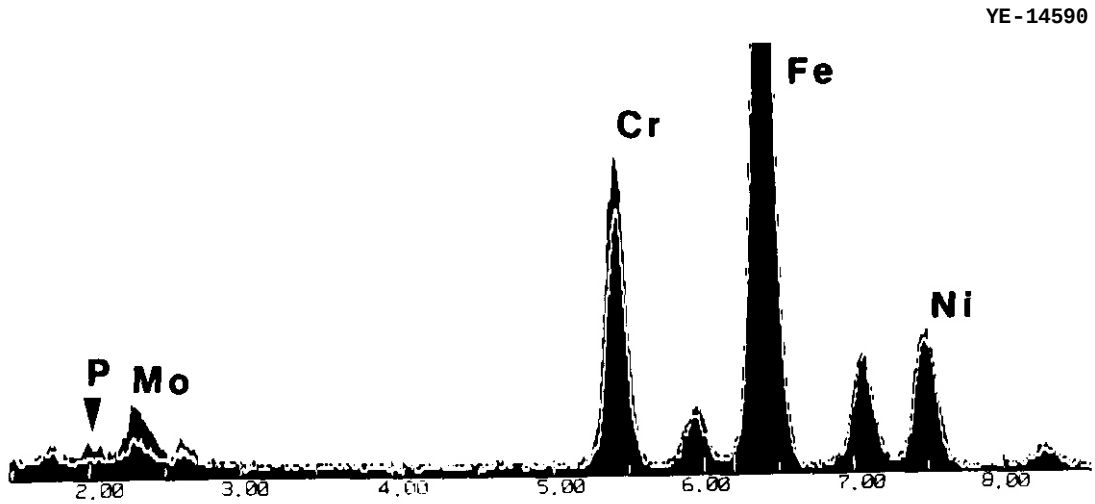

Fig. 3. EDXS spectra measured at a high angle grain boundary (solid) and the adjacent matrix (white line) in the unirradiated type **316** stainless steel control material. The iron peaks are scaled to each other at twice full scale.

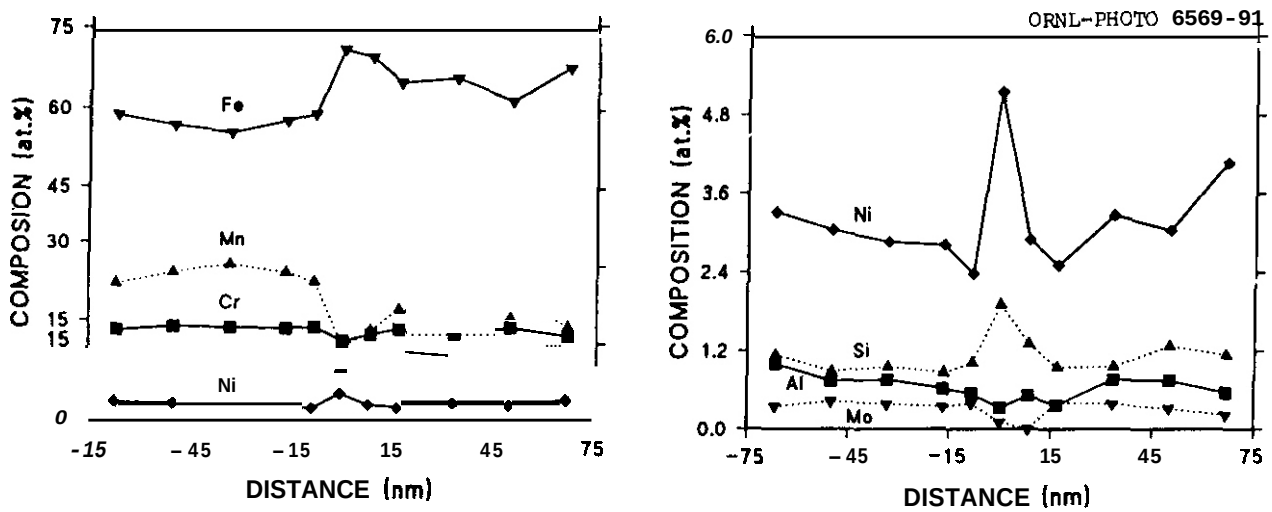

Fig. 4. RIS profiles measured by EDXS at a high angle grain boundary in EP838 after neutron irradiation to 15 dpa at **520°C.** The boundary migrated to the left during irradiation.

One of the first AEM measurements of RIS was made at faulted dislocation loops in an ion-irradiated, modified-type **316** stainless steel?' X-ray microanalysis indicated silicon and nickel were enriched in the vicinity of the fault plane, whereas chromium, and molybdenum were depleted. More recent work on the same material indicated that iron and manganese were also depleted at the dislocation loops." Similar RIS has been reported to dislocation loops in **USPCA** irradiated in FFTF to 15 dpa at 520°C.[22] Figure 5 shows the RIS profiles at a large (100-nm-diam) Frank dislocation loop in the neutron-irradiated material. The magnitude of the composition changes **is** striking; at the fault plane, nickel actually exceeds iron and becomes the dominant element. The dislocation loop **is** surrounded by a "microalloy" region" of significantly different composition from that of the matrix. The compositional changes decrease in magnitude the farther away from the fault plane. Beyond –40 nm the segregation reverses in sign as the species enriched at the fault plane are removed from the adjacent matrix. The opposite was true for species which are depleted at the fault plane. No indication of RIS **was** observed outside of the dislocation loop in the plane of the loop.

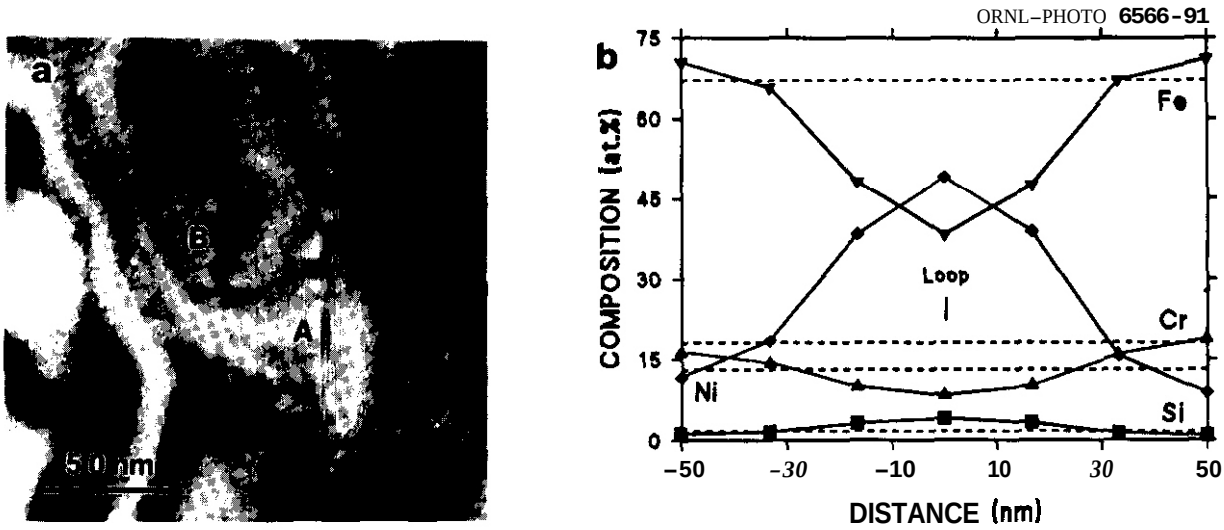

Fig. 5. (a) Large faulted dislocation loops (A,B) in USPCA after neutron irradiation to 15 dpa at 520°C. (b) RIS profiles measured by EDXS at large (100-nm-diam) dislocation loop A.

A very strong size dependence was measured for RIS at dislocation loops in USPCA neutron-irradiated to 15 dpa at 520°C. Roughly 80% of the dislocation loops >80 nm in diameter exhibited strong RIS similar to that in Fig. 5; whereas only 50% of the loops in the 40 to 80 nm size class exhibited strong RIS. In fact, only the larger loops in the upper half of the latter size class exhibited RIS. Dislocation loops in the lower half of that size class and those <40 nm in diameter did not exhibit any detectable RIS. It appears upon inspection, that some of the defects in the >80-nm-diam class that did not exhibit strong RIS were isolated dislocation segments rather than sessile faulted dislocation loops. This RIS behavior at dislocation loops is most likely the cause of the observed preferential matrix corrosion in materials with strong RIS.[13-15]

Similar segregation to faulted dislocation loops was observed in a commercial purity type 304 stainless steel neutron-irradiated to ~2 dpa at 288°C.[24] A moderate density of small faulted dislocation loops ranging from 8 to 40 nm in diameter was present in this material. Averaged over a number of dislocation loops with diameters ≥25 nm, RIS to the fault plane resulted in depletion of chromium by ~3% and enrichment of nickel and iron by ~1.5% each. In addition, there was indication of silicon segregation to some of the dislocation loops; however, X-ray microanalysis was hampered by problems associated with the induced radioactivity of the specimen. The magnitude of RIS to the dislocation loops was slightly less (45-75%) than that measured at high-angle grain boundaries in the same material. However, a portion of that difference may he explained on the basis of the lower RIS volume of a faulted dislocation loop relative to the surrounding matrix compared to that of a grain boundary which extends through the analyzed foil thickness.

Discussion

In all the cases of RIS reported in this work, the segregation has been caused by the flux of point defects to some defect sink; a grain boundary, a dislocation loop, or a cavity. In some cases, phase instability of the austenite matrix is related to RIS to defect sinks. It has been reported in ion-irradiated stainless steels that at low doses RIS at faulted dislocation loops results in pronounced enrichment of nickel and silicon and depletion of chromium, iron, molybdenum, and manganese.[11,21] In material irradiated to higher dose, precipitation of eta and G phase, both nickel-enriched silicides, occurs at number densities and sizes similar to those of the dislocation loops, suggesting that RIS zones at the loops eventually develop into precipitates. This sequence of events has been demonstrated in the case of ion-irradiated material." The degree of precipitation and austenite instability has been shown to increase with the level of silicon in the alloy.[10] As the silicon content is decreased, the tendency toward phase instability under irradiation decreases and eventually only elemental inhomogeneities or fluctuations are produced by RIS. Regions of high nickel and silicon alternate with regions of high chromium and iron.

In most of the reported work on composition fluctuations, no microstructural features were associated with the regions of differing composition[10,16,17] and in part led to the suggestion by Garner et al.[17] that the measured fluctuations may result from a spinodal-like instability of the austenitic matrix. Recently, an association between high nickel regions and clusters of cavities has been reported." Shepherd[26] demonstrated similar composition fluctuations by high spatial resolution X-ray mapping of an ion-irradiated stainless steel pre-injected with helium; he also noted that the high-nickel regions appeared to be associated with locally higher concentrations of cavities. In the absence of pre-injected helium, the only composition fluctuations noted were associated with dislocation loops and segments. Shepherd concluded that the pre-injected helium resulted in the nucleation of cavities which in turn produced the composition fluctuations.

However, there are several other results from that and related work that may indicate a different origin for the observed compositional inhomogeneities. It has been shown previously that pre-injection of helium prior to heavy-ion irradiation has a strong effect of the evolution of the dislocation loop structure,[27] enhancing loop nucleation and competition between the dislocation loops for point defects. Pre-injection of 14 appm helium, followed by ion irradiation to 1 dpa at 625°C, resulted in a high density ($> 2 \times 10^{21}$ m^{-3}) of small dislocation loops with average diameter of ~9 nm. This is at least a fourfold increase in loop density (with an attendant decrease in inter-loop spacing) and a fivefold decrease in loop size relative to that of the uninjected or simultaneously injected materials. As shown in both the current work and that of Shepherd,[26] there is strong RIS to dislocation loops. In the case of material pre-injected with helium (Shepherd), RIS to the high density of small dislocation loops may be the origin of the observed composition fluctuations. The large difference in the spatial extent of the composition fluctuations between the pre-injected and uninjected materials above would seem to argue against a spinodal decomposition mechanism for the formation of the fluctuations.

The inability in previous studies"." to link a microstructural feature with the composition fluctuations may be related simply to the high damage levels of the materials examined. As the dislocation loops grow, they unfault, glide, and interact to form the dislocation network normally observed at these high damage levels. As such, there is no identifiable defect at the original site of the dislocation loop and its associated RIS zone. The RIS zone may survive a long time after the dislocation loop is gone. A region with higher concentrations of nickel and silicon would he undersized relative to the unperturbed matrix and as such would continue to attract point defects in the absence of the dislocation loop. The possibility that composition fluctuations may indeed be self-perpetuating has been suggested previously."." In order to distinguish between the dislocation loop RIS and irradiation-induced instability mechanisms, the temporal and spatial evolution of both the dislocation loop microstructure and the composition fluctuations must be studied as a function of dose, especially at lower damage levels.

It is possible that the magnitude of RIS to dislocation loops may change during the evolution of the overall damage structure. Early in the irradiation of a solution-annealed material, the dislocation loops are the primary extended sink for point defects. However, as the dislocation network develops, the loops must compete with the network, which should reduce RIS to dislocation loops in the later stages of damage. In addition, there is an initial transient flux of excess interstitials that occurs prior to steady-state conditions being established. These excess interstitials may influence the RIS to dislocation loops produced during the point defect transient relative to that at loops formed under steady-state point defect fluxes. For these reasons, it is possible that dislocation loops present at high damage levels well beyond the initial loop nucleation and growth period might not exhibit any direct association with the observed composition fluctuations.

Conclusions

Radiation-induced segregation (RIS) in austenitic stainless steels occurs at a variety of point defect sinks, including grain boundaries, cavities, and dislocations loops. In the currently studied nickel-stabilized austenites, nickel and silicon are enriched at the defect sinks, whereas chromium, iron, molybdenum, and manganese are depleted. The depletion of chromium at grain boundaries reduces the stability of the passive film and can result in preferential intergranular attack and IASCC. Depletion at cavities and dislocation loops can produce enhanced general corrosion. In the manganese-stabilized EP838 alloy, manganese is the dominant element depleted at grain boundaries, leaving chromium only slightly depleted. As such, EP838 may be more resistant to radiation-induced sensitization and IASCC than a nickel-stabilized austenite. Possible origins of matrix composition fluctuations observed at high dose were discussed and an alternate mechanism was proposed. The mechanism was based on the observed RIS at dislocation loops and the survival of the RIS zone beyond the unfaulting and motion of the dislocation.

FUTURE WORK

In order to distinguish between dislocation loop RIS and irradiation-induced instability mechanisms, the temporal and spatial evolution of both the dislocation loop microstructure and the composition fluctuations must be studied as a function of dose, especially at lower damage levels. Such a study would require a range of specimens from low doses where the dislocation loop microstructure is first developing (< 1 dpa) through high doses where the matrix composition fluctuations are normally observed (> 10 dpa). However, it is not clear that such an assembly of specimens exists for a well-defined specimen temperature and material.

REFERENCES

1. R. A. Johnson and N. Q. Lam, Phys. Rev. B13 (1976) 4364.
2. A. D. Marwick, J. Phys. F 8 (1979) 1849.
3. D. L. Porter and E. L. Wood, J. Nucl. Mater. 83 (1979) 90.
4. E. H. Lee, P. J. Maziasz, and A. F. Rowcliffe, in: Phase Stability During Irradiation, eds. J. R. Holland, L. K. Mansur, and D. I. Potter (AIME, New York, 1981) p. 191.
5. T. M. Williams and J. M. Titchmarsh, J. Nucl. Mater. 98 (1981) 223.
6. D. I. Norris, C. Baker, and J. M. Titchmarsh, in: Proc. Symp. Radiation-Induced Sensitization of Stainless Steels, ed. D. I. R. Norris (Berkeley Nuclear Laboratory, CEGB, 1986) p. 86.
7. E. A. Kenik, J. Nucl. Mater. 187 (1992) 239.
8. W. Kesternich and R. V. Nandedkar, in: Effects of Radiation on Materials, 14th Inter. Symp., eds. N. H. Packan, R. E. Stoller, and A. S. Kumar (ASTM, Philadelphia, 1990) p. 284.
9. M. L. Grossbeck, P. J. Maziasz, and A. F. Rowcliffe, J. Nucl. Mater. (in press).
10. T. M. Williams, R. M. Boothby, and J. M. Titchmarsh, in reference 6, p. 116.
11. E. A. Kenik, in: Materials Problem Solving with the Transmission Electron Microscope, Mat. Res. Soc. Symp. Proc., 62, eds. L. W. Hobbs, K. H. Westmacott, and D. B. Williams (Materials Research Society, Pittsburgh, PA, 1986) p. 209.
12. C. M. Shepherd and S. M. Murphy, J. Nucl. Mater. 172 (1990) 143.
13. T. Inazumi, G. E. C. Bell, E. A. Kenik, and K. Kiuchi, Corrosion 46 (1990) 786.
14. E. A. Kenik, T. Inazumi, and G. E. C. Bell, J. Nucl. Mater. 183 (1991) 145.
15. T. Inazumi, G. E. C. Bell, P. J. Maziasz, and T. Kondo, J. Nucl. Mater. (in press).
16. H. R. Brager and F. A. Garner, in: Optimizing Materials for Nuclear Applications, eds. F. A. Garner, D. S. Gelles, and F. W. Wiffen (TMS-AIME, Warrendale, PA, 1984) p. 141.
17. F. A. Garner, H. R. Brayer, and J. M. McCarthy, Radiation-Induced Changes in Microstructure, 13th Inter. Symp. ASTM STP 955, eds. F. A. Garner, N. H. Packan, and A. S. Kumar (ASTM, Philadelphia, PA, 1987) p.775.
18. E. A. Kenik, N. D. Evans, and J. Bentley, in: Proc. Ann. EMSA Meeting 49 (1991) p. 443.
19. E.A. Kenik, Met. Trans. 22A (1991) 253.
20. R. L. Klueh, P. J. Maziasz, and E. H. Lee, Mat. Sci. & Eng. A 102 (1988) 115.
21. E. A. Kenik, Scripta Met. 10 (1976) 733.
22. E. A. Kenik and K. Hojou, J. Nucl. Mater. (in press).
23. P. J. Maziasz, J. Nucl. Mater. 169 (1989) 95.
24. E. A. Kenik, J. Nucl. Mater. (in press).
25. E. H. Lee and E. A. Kenik, J. Mater. Res. 3 (1988) 840.
26. E. A. Kenik, J. Nucl. Mater. 85&86 (1979) 659.
27. C. M. Shepherd, J. Nucl. Mater. 175 (1990) 170.
28. S. M. Murphy, Phil. Mag. A 58 (1988) 417.
29. G. Martin, Phys Rev. B 21 (1980) 2122.

A Microstructural Examination of the Mechanical Response of FeCrNi Alloys Irradiated at 365°C Using Isotopic Tailoring to Produce Different He/dpa Ratios - J. F. Stubbins (University of Illinois) and F. A. Garner (Pacific Northwest Laboratories')

OBJECTIVE

The objective of this effort is to determine the influence of helium on radiation-induced changes in microstructure and mechanical properties of alloys.

SUMMARY

A series of model Fe-15Cr-xNi-yP alloys with x = 25 or 45 and y = 0.001 or 0.04 wt.% were examined following irradiation to 10.3 dpa at 365°C. These alloys were irradiated both doped and undoped with the ^{59}Ni isotope to produce two levels of helium generation during irradiation. This latter variable produced average He/dpa values of approximately 1 and 16 appm He/dpa in the undoped and doped cases, respectively. Microscopy examination indicates that the major influence of a high He/dpa ratio is to induce a higher void number density and a lower average void size than in identical alloy conditions with low He/dpa. The total swelling is not substantially affected, however. Compositional and thermal mechanical treatment variables were found to influence the swelling behavior as much as the helium production rate. However, in all cases the swelling was low, and irradiation-induced microstructures were similar regardless of starting condition. This convergence in microstructure is reflected in the mechanical properties where similar room temperature tensile properties were measured on irradiated specimens regardless of material starting condition.

PROGRESS AND STATUS

Introduction

The role of helium in the nucleation and stabilization of irradiation-induced microstructure is of concern for fusion systems where sizable helium production in comparison to the atomic displacement levels is foreseen. Several studies are being carried forward to clarify this effect.[1-8] The effect of helium is most often considered in terms of the ratio of the helium production rate (appm He/s) to the atomic displacement rate (dpa/s), that is the He/dpa ratio. This ratio can change as a function of irradiation time due to the build-up of certain precursors to (n,α) reactions. This is well documented for the two stage reaction in nickle-bearing alloys where ^{58}Ni is transmuted to ^{59}Ni via the $^{58}Ni(n,\gamma)^{59}Ni$ reaction, then to Fe through the $^{58}Ni(n,\alpha)^{56}Fe$ reaction. The latter reaction produces helium, but the production is nonlinear with irradiation time due to the varying ^{59}Ni concentration, which must normally build up to significant levels from zero initial content, during irradiation. The most significant effect of this initial build-up period is that only minor amounts of helium are produced during the normal void incubation period, and thus the full effect of helium is not revealed. In the present series of experiments,[1-5,8] nickel-bearing Fe-Ni-Cr alloys were irradiated both with and without initial concentrations of ^{59}Ni. The ^{59}Ni dopant was extracted from previously irradiated nickle-bearing material. This technique produces a nearly constant helium/dpa ratio.

Previous studies in this series of experiments have shown that the role of helium in swelling and radiation-induced microstructural development, while identifiable, is modest when compared to the influence of other alloying and thermal mechanical treatment variables.

The present experiment deals with a higher irradiation exposure on a series of Fe-Ni-Cr alloys where lower dose (5.2 dpa) irradiation results have been reported previously by Kawanishi et al.[1] Results of other similar studies on the effects of He/dpa ratio at other temperatures on the irradiation performance on this class of alloys have also been reported previously.[2-5] Of particular interest are the results of mechanical properties measurements on this series of irradiations which indicate that, regardless of He/dpa ratio or thermal mechanical condition, tensile properties of these alloys converge to similar values after irradiation to relatively low dpa levels.[8] It is of interest to establish the microstructural origins of this convergent behavior,

ExDerimental

Fe-15Cr-xNi-yP (wt%) alloys were prepared with nickel concentrations of x = 25 and 45. For the Fe-15Cr-25Ni alloys, two phosphorus levels were prepared: y = 0.001 and 0.04. The Fe-15Cr-45Ni alloys were prepared with a phosphorus concentration of y = 0.001. In addition to variations in the alloying element concentrations, the alloys were irradiated in both the solution annealed (SA:1030°C for 30 min) and 20% cold worked (CW) conditions. In order to produce elevated helium production during irradiation, half of the specimens were produced with a high concentration of the ^{59}Ni isotope. The rest were fabricated with natural nickel.

'Pacific Northwest Laboratory is operated for the U.S. Department of Energy by Battelle Memorial Institute under Contract DE-AC06-76RLO 1830.

Irradiations of TEM discs and miniature tensile specimens were carried out in the Materials Open Test Assembly (MOTA) in the Fast Flux Test Facility (FFTF) at 365°C ± 5°C to a dose of first 6.1 dpa, then returned for an additional 4.2 dpa to yield a total of 10.3 dpa. This two part irradiation sequence produced average He/dpa ratios of 0.7 and 16.0 in the undoped and ^{59}Ni-doped 25Ni specimens, respectively.[5] For 45Ni, the average values are higher, 1.2 and 16.7, reflecting the greater production of ^{59}Ni in the higher nickel alloys.

Following irradiation, TEM discs were examined in a JEM JEOL 100CX scanning transmission electron microscope operated at 120kV. For one condition, CW Fe-15Cr-25Ni without ^{59}Ni, it was not possible to prepare specimens suitable for TEM examination.

Results

The results of the examination of void microstructure and swelling are shown in Fig. 1 and the data are presented in Table 1. A comparison of the void microstructures for the Fe-15Cr-25Ni cases with ^{59}Ni-doping at both phosphorus levels is shown in Fig. 2.

The effect of ^{59}Ni-doping, that is the role of He/dpa, is evident in both the average void diameters and in the void number density data. In every case, the void number densities are higher, and the average void diameters are smaller for the high helium conditions compared to the low helium conditions at the same composition and thermal mechanical treatment condition. These trends for number density and average void diameter with and without ^{59}Ni-doping are consistent with those found by Kawanishi et al.[1] at 5.2 dpa.

Table 1

Microstructural Data for Fe-15Cr Ni-yP Alloys Following Irradiation to 10.3 dpa at 365°C

Alloy	Void Density $10^{21}m^{-3}$	Mean Diameter nm	Swelling %	Dislocation Density $10^{14}m^{-2}$
CW/-	NM	NM	NM	NM
CW/He	4.50	8.00	0.200	1.88
SA/-	1.39	12.91	0.191	2.85
SA/He	3.28	6.90	0.161	2.99
CW/-/P	3.83	10.20	0,303	4.40
CW/He/P	4.61	6.30	0.128	4.16
SA/-/P	2.64	8.30	0.116	2.36
SA/He/P	12.40	6.90	0.302	4.40
CW/-/Ni	0.57	10.00	0.043	2.44
CW/He/Ni	3.80	7.00	0.040	3.94
SA/-/Ni	1.40	13.60	0.456	2.92
SA/He/Ni	3.60	8.60	0.225	3.38

NM = not measure

Oiscussion

The influence of He/dpa ratio on swelling in these alloys is small, and not uniform. This probably reflects the natural variability of the swelling process at low dpa levels rather than an effect of helium. Differences in swelling are less than a factor of 3 between ^{59}Ni-doped and undoped specimens in all cases with no specific tendency for either the doped or undoped case to show higher values. The levels of swelling at 10.3 dpa are uniformly larger than those reported by Kawanishi et al.[1] for the same alloys at 5.2 dpa. However, the swelling is low; it is only higher than 0.3% in one case.

The very low apparent swelling rate observed at 5.2 dpa for all alloy conditions at 365°C cannot be confidently ascribed to the effect of irradiation temperature alone. For the temperature range of 400 to 510°C, the incubation dose was found to he ~10 dpa, followed by swelling at a rate of ~1% per dpa.[9] Although swelling at 365°C has not been previously measured for ternary FeCrNi alloys, various stainless steels show a strong decrease from the 1% per dpa rate at temperatures below 400°C.[10-12] If the effect is related to an incubation difference rather than a change in the steady state swelling rate, nickel normally extends incubation,[9] whereas phosphorus normally shortens incubation at low temperature.[13,14] Apart from one data point, that of the SA Fe-15Cr-25Ni-0.04P doped case, void number densities are relatively insensitive to either phosphorus or nickel for otherwise identical compositions and thermal mechanical treatment condition. In addition, void number densities are generally comparable to those found by Kawanishi et al. at 5.2 dpa' indicating that the fast initial stage of void nucleation is over before 5.2 dpa. This, combined with the low swelling rates, indicates that a drop from an ~1%/dpa swelling rate has probably occurred at 365°C.

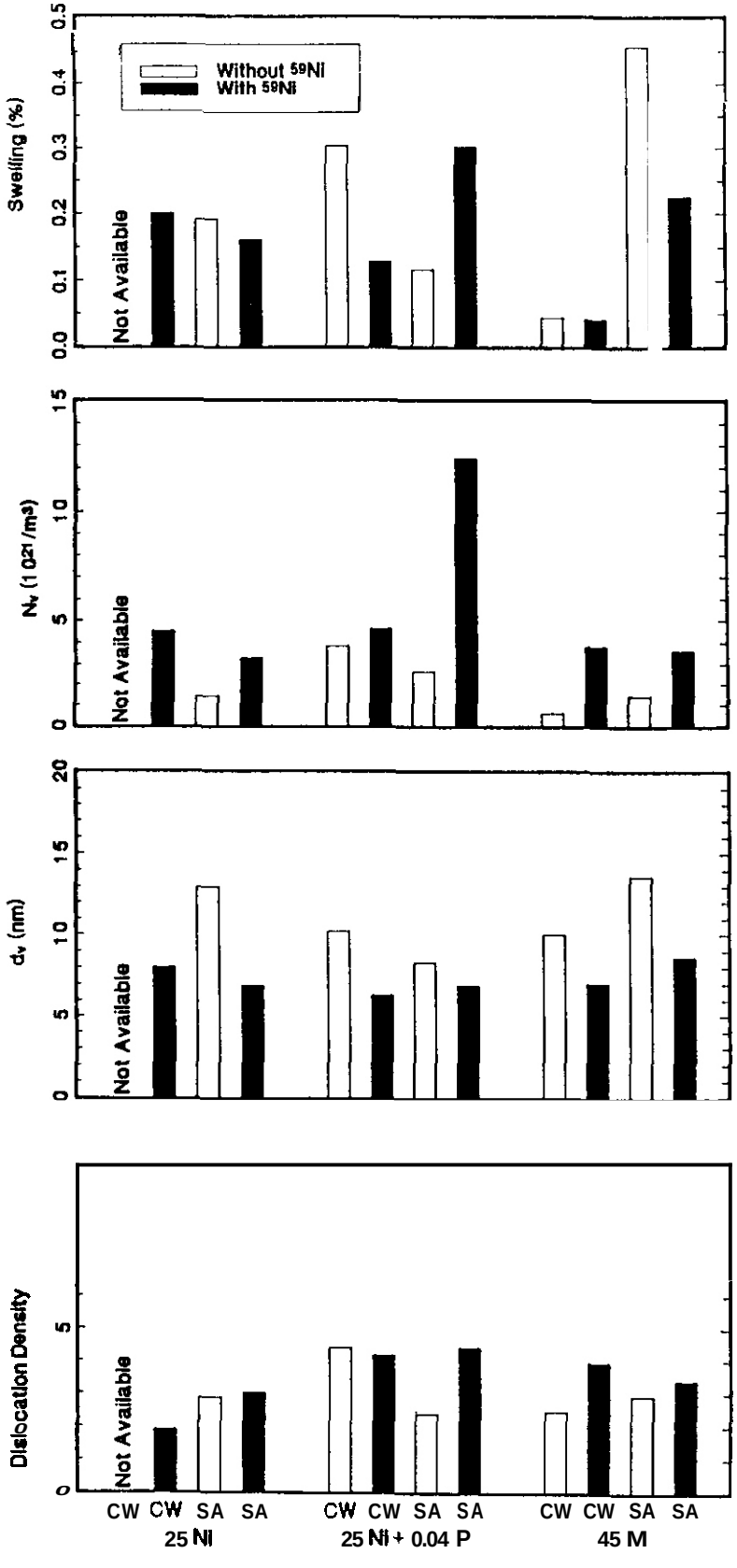

iq. 1. Swelling, void number density, average void diameter and total dislocation density as a function of alloy compositio and thermal mechanical treatment.

The influence of nickel content on void microstructure at this irradiation temperature and dose is not strong. A comparison of the void number densities, average diameter, swelling and dislocation densities for the three comparable cases at Fe-15Cr-xNi-0.001P (the CW Fe-15Cr-25Ni undoped case is not available) show that the numbers are nearly identical for the same condition at 25 and 45 Ni, and follow the same trend with thermal mechanical treatment and high and low helium conditions. This is consistent with other work that indicates that Ni influences swelling primarily at higher irradiation temperatures than examined in this study. There was no evidence of bimodal cavity structures in any of the cases studied here.

No evidence for the formation of phosphide precipitates was found in anv of the irradiation conditions examined here. Other studies on these alloys at 365, 495 and 600°C[1-5] have identified phosphide formation only at 600°C. This is consistent with the results of studies on other Fe-Cr-Ni-P alloys that show phosphide formation occurs onlv at higher irradiation temperatures.[14,15] Phosphorus also aooears *to play* no significant role in this relatively limited experiment in determining the total swelling.

There is no consistent difference in the influence of starting microstructure on void microstructure after 10.3 dpa. Dislocation densities as well as void microstructures are similar between similar alloy compositions, indicating that the influence of initial microstructure is nearly erased by 10.3 dpa. The highest observed dislocation densities were for three of the four alloy conditions with 0.04P, which indicates that P additions, even in the absence of phosphide formation, support a higher dislocation density at this irradiation temperature. However, the differences in dislocation number densities were not large.

For comparison to tensile data generated on this set of alloys,[8] an attempt was made to relate observed microstructure to measured yield properties.

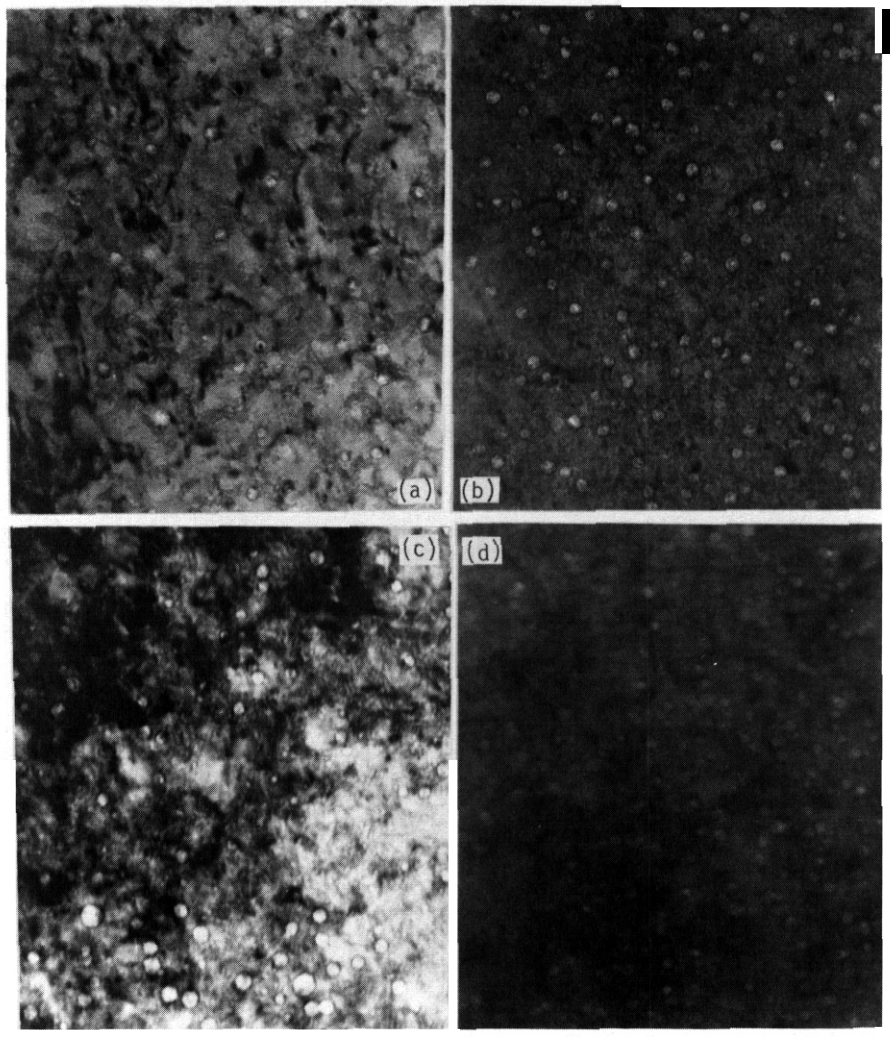

Fig. 2. Void microstructures for the four 59Ni doped alloy conditions at Fe-15Cr-25Ni: a) cold worked, low P; b) solution annealed, low P; c) cold worked, 0.04P; and d) solution annealed, 0.04P. 100 nm

examination are as follows:

1. Total swelling these alloys is low at 10.3 dpa and 365·C regardless of starting condition, helium generation rate, or composition.

2. Irradiation-induced microstructures are relatively independent of initial thermal mechanical treatment condition or helium production rate.

3. He/dpa levels comparable to those of fusion neutron spectra result in higher void number densities and lower average void diameters in comparison to the respective low He/dpa conditions. Bimodal cavity structures do not develop at 365°C with either the low or high helium generation rate.

4. The influence of nickel at 365°C and 10.3 dpa on microstructural development is minor.

5. The influence of phosphorous under these conditions is also minor, but slightly higher average dislocation densities are maintained at the higher phosphorous level.

6. Comparisons of measured yield strength values and those calculated from microstructural parameters show reasonable consistency. The convergence of strength values independent of He/dpa ratio and thermal mechanical condition are reflected in a similar convergence of microstructure.

This was done using a relationship for Fe-Cr-Ni alloys used successfully in an earlier study[16]:

$$\sigma_i = \sigma_o + \alpha G b \sqrt{\rho_d} + G b \frac{\sqrt{N_v d_v}}{P}$$

where the initial strength, σ_o = 180 MPa; the shear modulus, G = 200 GPa; the magnitude of the Burger's vector, b = 0.3 nm; α = 0.2; and β = 1.0. The dislocation density is that of both loops and free dislocations. The results of the calculations from the microstructural data and values measured from miniature tensile specimens[8] are compared in Fig. 3. The contributions to calculated yield strength are roughly the same for the void population and the dislocation density. The largest differences in the calculated and measured yield strength values are due primarily to variations in measured void number densities. Overall, the comparisons are reasonable, and show similar trends between the measure strengths and the irradiation-induced microstructure. The similarity in yield properties regardless of either initial microstructure or composition is quite remarkable.

CONCLUSIONS

Microstructural examination was carried out on three Fe-15Cr-xNi-yP alloys, where x = 25 and 45, y = 0.001 and 0.04 wt.% and doped or undoped with ^{59}Ni, irradiated to 10.3 dpa at 365°C. The general conclusions of the

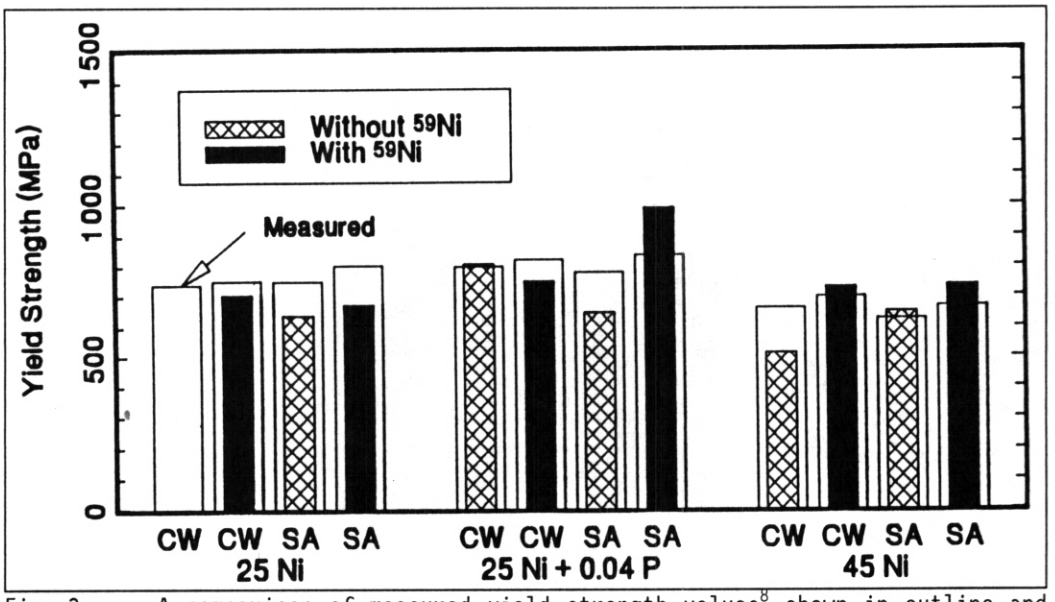

Fig. 3. A comparison of measured yield strength values[8] shown in outline and those calculated from microstructural parameters for the Fe-15Cr-xNi-yP alloy series irradiated to 10.3 dpa at 365°C shown in shaded bars.

ACKNOWLEDGEMENTS

This work was supported by the US Department of Energy under Contracts DE-AC06-76RLO 1830 and DE-FG06-89ER-75522.

FUTURE WORK

Microscopy examination will continue on specimens irradiated at other temperature and fluence levels.

REFERENCES

1. H. Kawanishi, F. A. Garner, and R. L. Simons, J. Nucl. Mater., 179-181 (1991) 511.

2. J. F. Stubbins and F. A. Garner, J. Nucl. Mater., 179-181 (1991) 523.

3. J. F. Stubbins, J. E. Nevling, F. A. Garner, and R. L. Simons, ASTM STP 1046, Vol. I (1990) 147.

4. F. A. Garner, M. L. Hamilton, R. L. Simons and M. K. Maxon, J. Nucl. Mater., 179-181 (1991) 554.

5. M. L. Hamilton, F. A. Garner and B. M. Oliver, Fusion Reactor Materials Semiannual Progress Report, DOE/ER-0313/9 (1990) 61.

6. L. Mansur and M. Grossbeck, J. Nucl. Mater., 155-157 (1988) 130.

7. P. Maziasz, accepted for publication in J. Nucl. Mater., proceeding of ICRFM-5.

8. M. L. Hamilton and F. A. Garner, accepted for publication in J. Nucl. Mater., proceeding of ICRFM-5.

9. F. A. Garner, J. Nucl. Mater., 122-123 (1984) 201.

10. F. A. Garner and D. L. Porter, J. Nucl. Mater., 155-157 (1988) 1006.

11. D. L. Porter, G. D. Hudman and F. A. Garner, J. Nucl. Mater., 179-181 (1991) 581.

12. F. A. Garner and R. J. Puigh, J. Nucl. Mater., 179-181 (1991) 577.

13. F. A. Garner and A. S. Kumar, ASTM STP 955 (1987) 289.

14. F. A. Garner, K. Miyahara, H. Kinoshita and J. W. Newkirk, accepted for publication in J. Nucl. Mater.,

proceeding of ICRFM-5.

15. T. Muroga, F. A. Garner, J. M. McCarthy, J. Nucl. Mater., 168 (1989) 109.

16. F. A. Garner, M. L. Hamilton, N. F. Panayotou and G. D. Johnson, J. Nucl. Mater., 103-104 (1981) 803.

Microstructures of Neutron-Irradiated Fe-12Cr-XMn (X=15-30) Ternary Alloys - K. Miyahara (Nagoya University), F. A. Garner (Pacific Northwest Laboratory') and Y. Hosoi (Nagoya University).

OBJECTIVE

The objective of this effort is to determine the factors which control the stability of irradiated alloys proposed for reduced activation applications.

SUMMARY

The Fe-Cr-Mn alloy system is being studied as an alternative to the Fe-Cr-Ni system because of the need to reduce long-term radioactivation in fusion-power devices. In this study, four Fe-12Cr-XMn (X = 15, 20, 25, 30 wt%) alloys were irradiated in the Fast Flux Test Facility to 20 dpa at 643K and 40 dpa at 679, 793, and 873K to investigate the influence of manganese content on void swelling and phase stability. The results confirm and expand the results of earlier studies that indicate that the Fe-Cr-Mn system is relatively unstable compared to that of the Fe-Cr-Ni system, with alpha and sigma phases forming as a consequence of thermal aging or high temperature irradiation.

PROGRESS AND STATUS

Introduction

Austenitic alloys based on the Fe-Cr-Mn system are being studied as alternatives to conventional Fe-Cr-Ni base alloys in an effort to reduce the long-term radioactivation generated by fusion neutron irradiation.[1-4] It has been shown by Garner and coworkers, however, that during irradiation Fe-Cr-Mn alloys are subject to a larger level of phase instability compared to that of alloys based on the Fe-Cr-Ni system.[4-10] Thermal aging studies conducted by several groups also indicate that phase instability is an important consideration even in the absence of irradiation.[2,3,7,11-15] This paper presents the results of microstructural examination of four Fe-Cr-Mn ternary alloys irradiated in the Fast Flux Test Facility (FFTF).

Experimental Procedure

As shown in Table 1, four Fe-12Cr-XMn alloys varying primarily in manganese content (15-30 wt%) were prepared in the solution-annealed condition (1373K for 3.6 Ks in vacuum, water quenched). Examination of these alloys before irradiation found that each alloy resided in the y-austenite regime. The alloys were irradiated side-by-side in the Materials Open Test Assembly (MOTA 1F) with temgeratures actively controlled to ±5K, reaching 5.0 x 10^{26} n/m^2 (E> 0.1 MeV) or ~20 dpa at 643 K and 9.5 X 10^{2} n/m^2 (E > 0.1 MeV) or ~40 dpa at 679, 793 and 873K. The specimens were in the form of microscopy disks 3.0 mm in diameter by 0.25 mm thick. After irradiation, the specimens were electropolished using 5% perchloric acid with 95% of either methanol or acetic acid. Examination of ten of the sixteen alloy/temperature combinations proceeded on a JEOLCO 2000ES electron microscope. The other six alloys have not yet been examined.

Table 1 Chemical Composition of Haterials Used (mass %)

Alloy	C	Cr	Mn	Si	P	S	N	W	O
Fe-12Cr-15Mn	0.006	12.33	14.74	0.009	<0.003	0.009	0.0015	(0.01	<0.001
Fe-12Cr-20Mn	0.004	12.28	18.98	0.010	(0.003	0.010	0.0010	<0.01	(0.001
Fe-12Cr-25Mn	0.003	12.23	25.31	0.030	<0.003	0.012	0.0024	<0.01	0.0045
Fe-12Cr-30Mn	<0.003	12.62	29.72	0.011	<0.003	0.013	0.0016	(0.01	0.011

Exoerimental Results

Voids were formed in all specimens examined at the 40 dpa level. Figs. 1-3 present typical void structures observed at 873, 793 and 679K, respectively. Relatively small voids (~15 nm average diameter) were also observed in the 20 Mn specimens at 643K and 20 dpa; the other manganese levels were not examined at this temperature. Fig. 4

'Pacific Northwest Laboratory is operated for the U.S. Department of Energy by Battelle Memorial Institute under Contract DE-AC06-76RLO 1830.

presents the void swelling observed at each of the four irradiation temperatures, as determined from microscopy measurements.

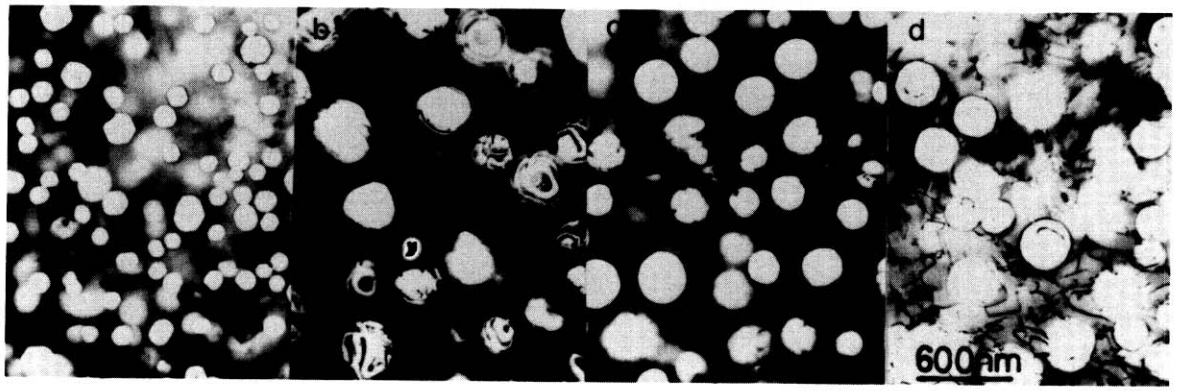

Fig. 1. Voids formed in Fe-12Cr-Mn alloys at 873K and 40 dpa. (From left to right: 15, 20, 25, 30 Mn).

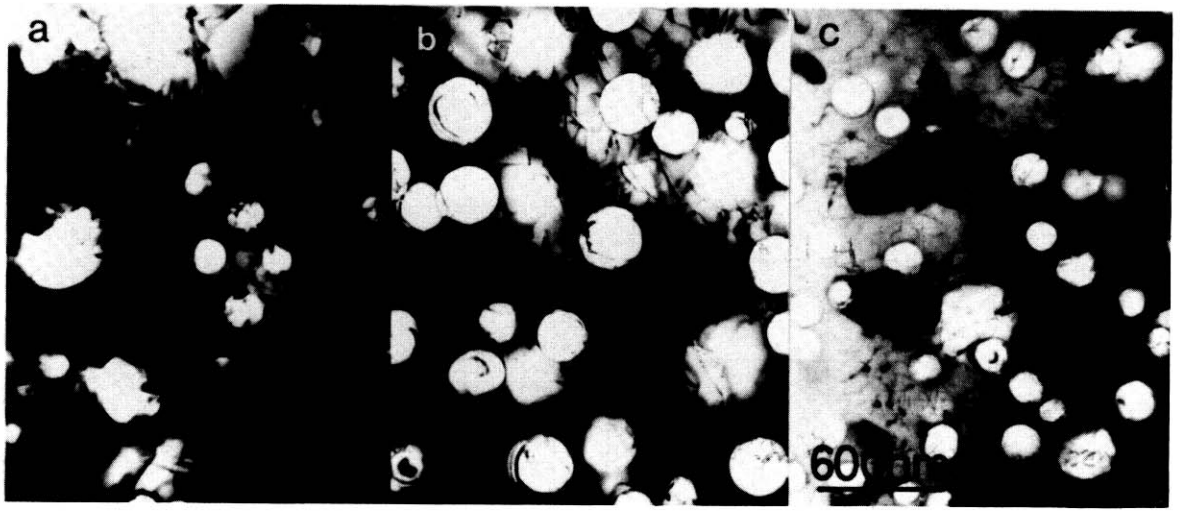

Fig. 2. Voids formed in the Fe-12Cr-Mn alloys at 793K and 40 dpa. (From left to right: 15, 20, 30 Mn).

Although no significant amount of precipitation was observed at 643 and 679K, Figs. 5 and 6 show that blocky alpha ferrite (α) phase precipitates formed in the 15 and 30 Mn alloys, but not in the 20 Mn alloy. The 25 Mn level was not examined. The α-phase precipitates often formed in association with voids. The α-phase was also observed in the 15 Mn alloy at 873K but was not found at 20, 25 or 30 Mn. Figs. 7 and 8 show that sigma (σ) phase formed at higher manganese levels (20-30 Mn) at 873K, however. The σ-phase precipitates were much larger and much less frequent than the α-phase precipitates found at other irradiation conditions. No voids were found to form in or in association with the σ-phase.

Discussion

The dependence of void swelling in Fe-12Cr-Mn alloys on manganese content shown in Fig. 4 is consistent, both in magnitude and in temperature dependence, with the trends observed in earlier studies conducted in FFTF/MOTA by Garner and coworkers on 10Cr and 15Cr alloys.[4,7] Those authors also reported the strong tendency toward ferrite formation in simple Fe-Cr-Mn alloys irradiated to 14 dpa in the annealed condition, especially at 793K. Sigma phase was not observed at 9-14 dpa in the 693-873K range, however.[6,8]

Ohnuki and coworkers found both α and σ to form in FFTF/MOTA at 730 and 820K (17 and 20 dpa, respectively) in annealed Fe-15Cr-15Mn. At 690K and 25 dpa, however, ferrite was just beginning to form.[16] In Fe-10Cr-

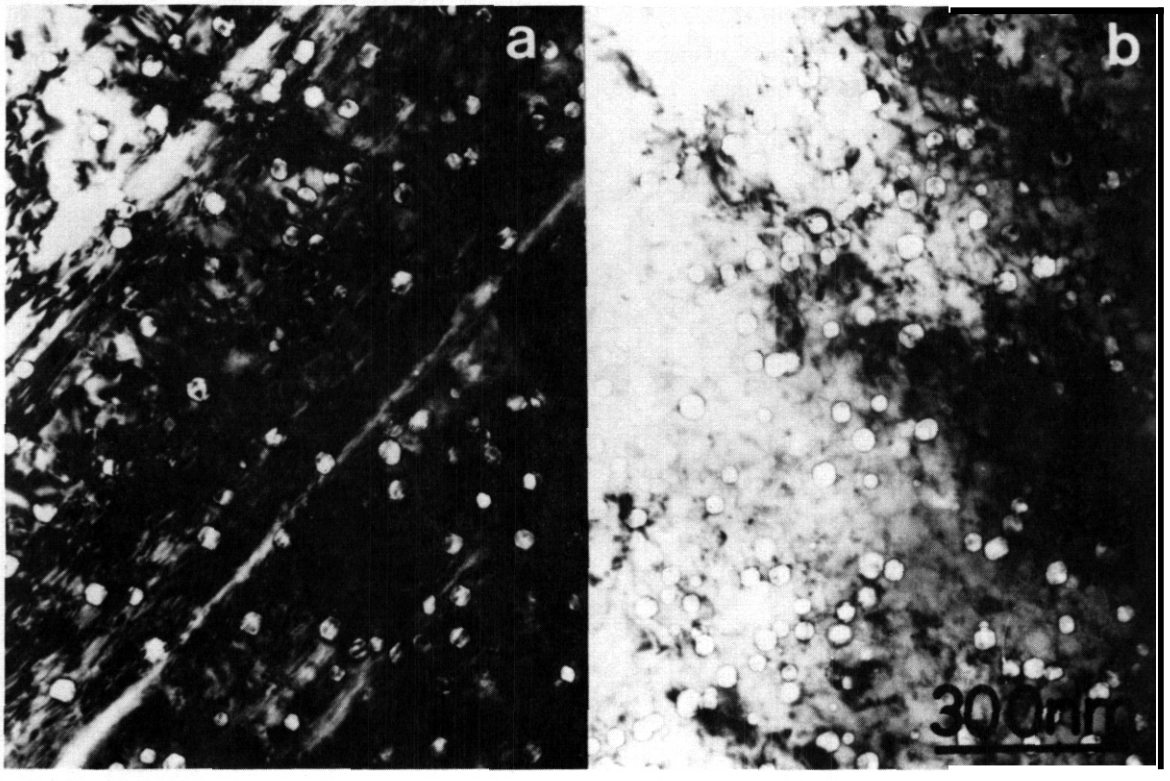

Fig. 3. Small voids formed in Fe-12Cr-Mn alloys at 679K and 40 dpa. (From left to right: 15, 25 Mn).

30Mn, Ohnuki found that the tendency toward α- and a-phase formation was reduced relative to that in Fe-15Cr-15Mn.[17] In Ohnuki's studies it was also noted that the a-phase often formed on grain boundaries and that the a-phase sometimes formed on the y-a boundary.

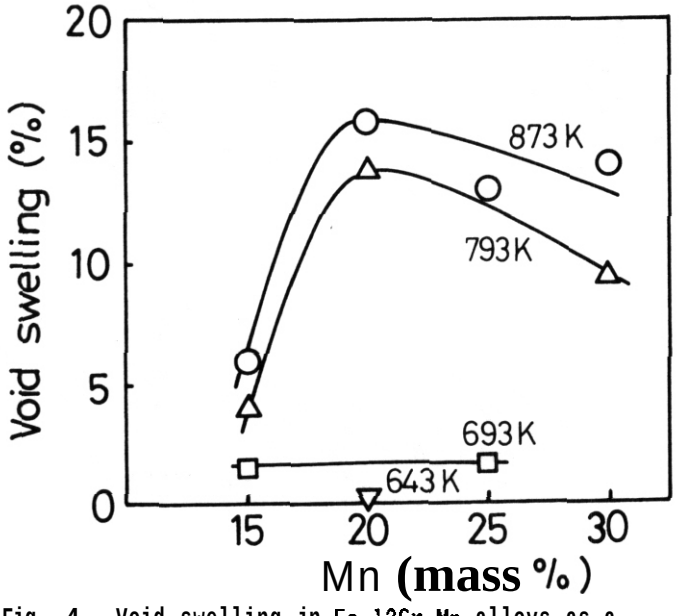

Fig. 4. Void swelling in Fe-12Cr-Mn alloys as a function of Mn content and temperature. Data at 643K obtained at 20 dpa. All other data at 40 dpa.

cold-worked ternary alloys would have yielded formation range of this study and the studies of Ohnuki. Garner,

Comparison of the results of the current study with those of Garner and Ohnuki indicates that the formation of a-phase in annealed Fe-Cr-Mn alloys depends on the alloy composition, irradiation temperature, and displacement level. Garner and coworkers showed that the enhanced formation of a-phase is a consequence of radiation-induced segregation of iron and concurrent outflow of manganese from voids, grain boundaries, and other microstructural sinks.[6,8] Takahashi and coworkers confirmed that iron indeed segregates at grain boundaries at the expense of manganese during electron irradiation of annealed Fe-Cr-Mn alloys, leading to an increased tendency toward both a- and a-phase formation.[18]

Garner and coworkers, however, did not observe σ-phase formation in annealed alloys in their relatively low fluence studies,[6,8] in contrast to the results of the current study and those of Ohnuki and coworkers.[16,17] Even in the higher fluence studies described in this paper, however, a-phase was not observed at all temperatures. It therefore appears that a-phase formation is very sluggish and requires a greater amount of diffusion and segregation than required for formation of α-phase.

It is quite likely, however, that irradiation of a-phase throughout the manganese and temperature Abe and Noda noted that grain boundaries,

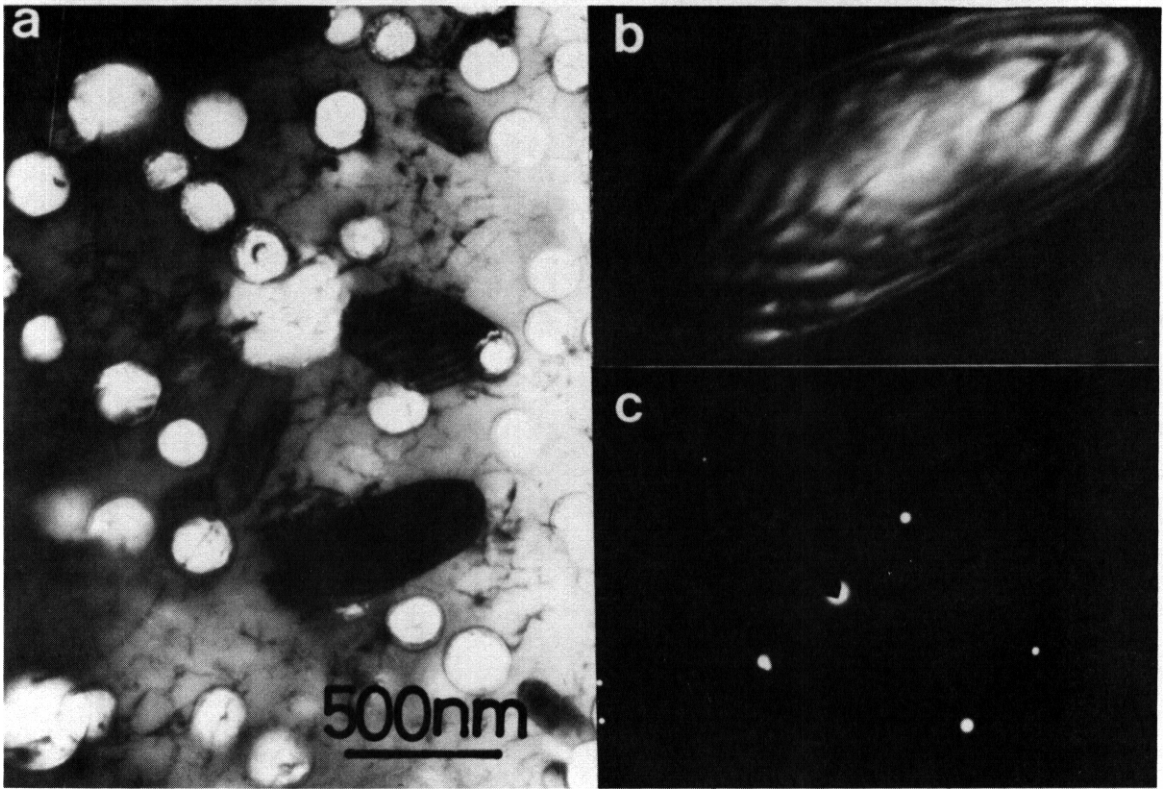

Fig. 5. Blocky particles of a-phase observed in Fe-12Cr-15Mn irradiated at 793K.

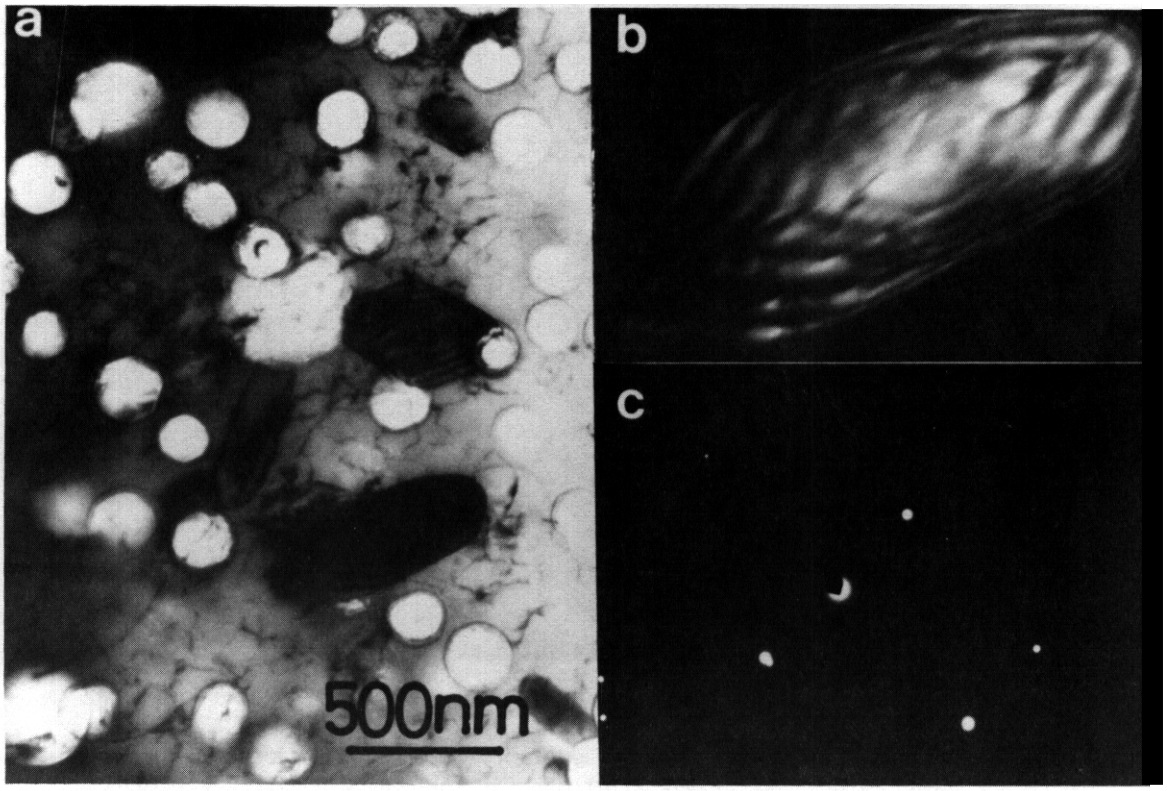

Fig. 6. Blocky particles of a-phase observed in Fe-12Cr-30Mn irradiated at 793K.

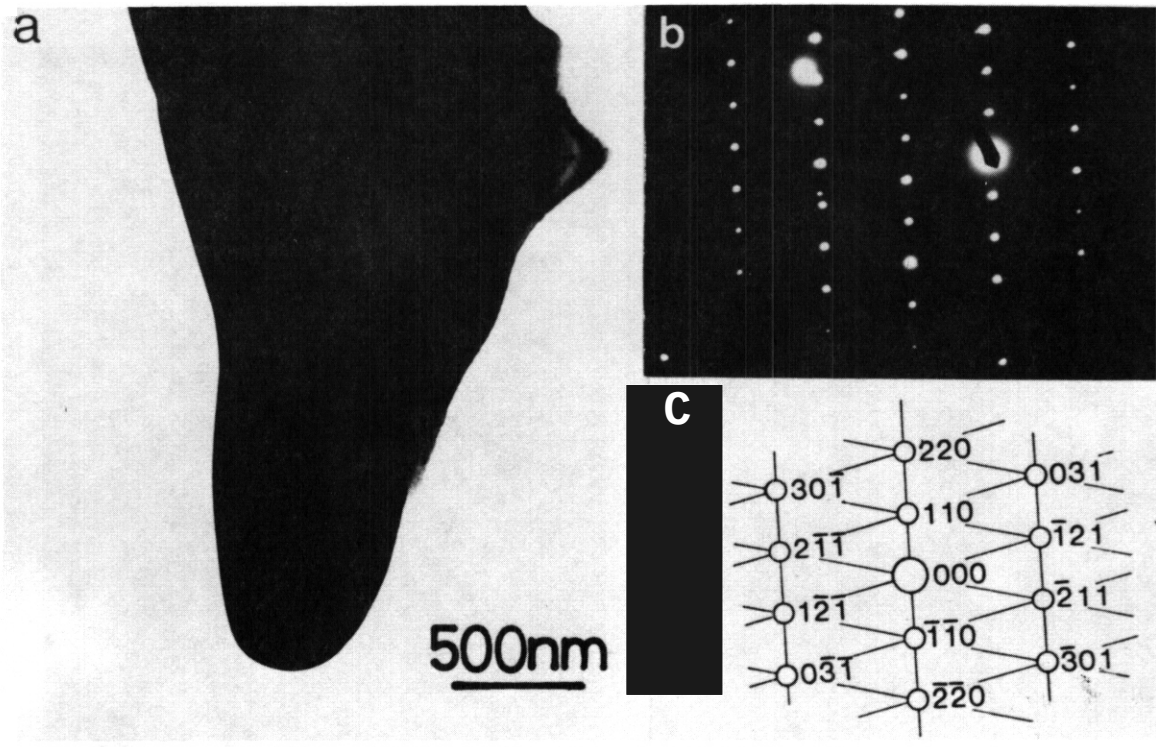

Fig. 7. o-phase formed in Fe-12Cr-20Mn irradiated at 873K.

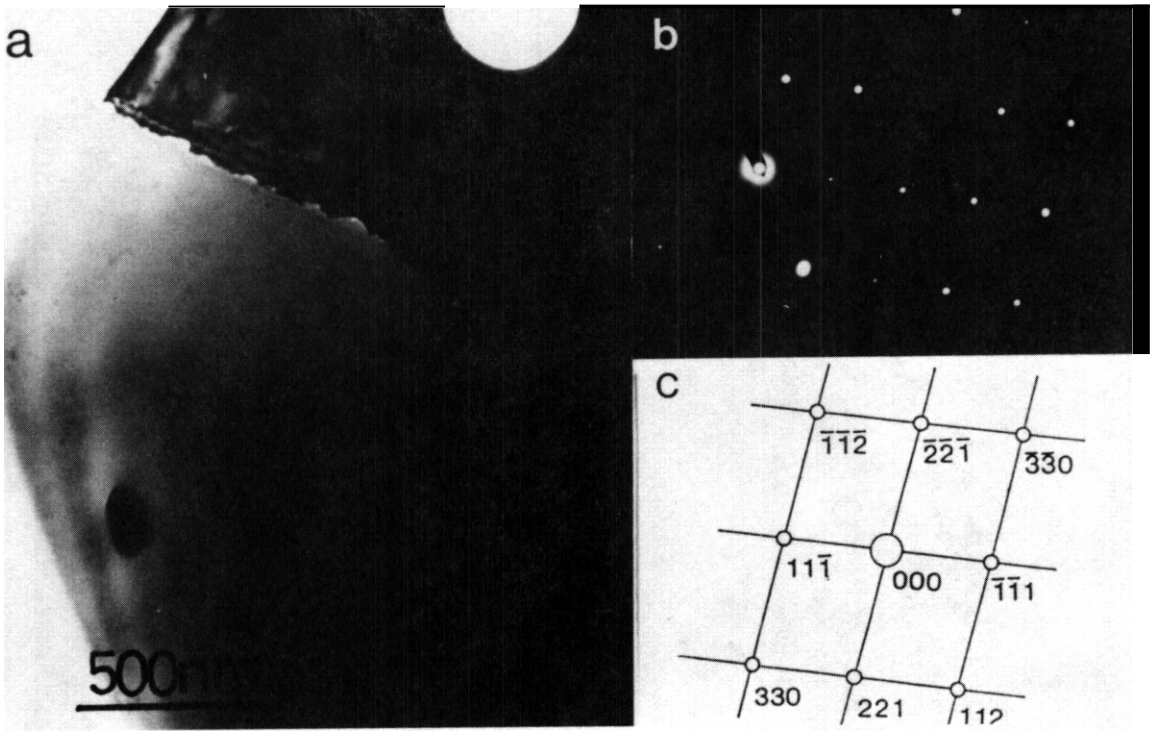

Fig. 8. o-phase formed in the Fe-12Cr-30Mn irradiated at 873K.

especially when they are moving in cold worked alloys during thermal aging, possess diffusion rates that are orders of magnitude larger than those of the alloy matrix, allowing o-phase to develop on grain boundaries even in the absence of radiation-induced diffusion.[7]

The thermal aging studies of three different groups have demonstrated that a-phase forms in simple Fe-Cr-Mn alloys throughout the compositional range of the current study, especially when the alloys were cold worked before aging.[12-15] An example relevant to this study is shown in Fig. 9. Abe and coworkers also observed the formation of a-phase in annealed Fe-10Cr-30Mn during creep rupture testing at 873K.[19]

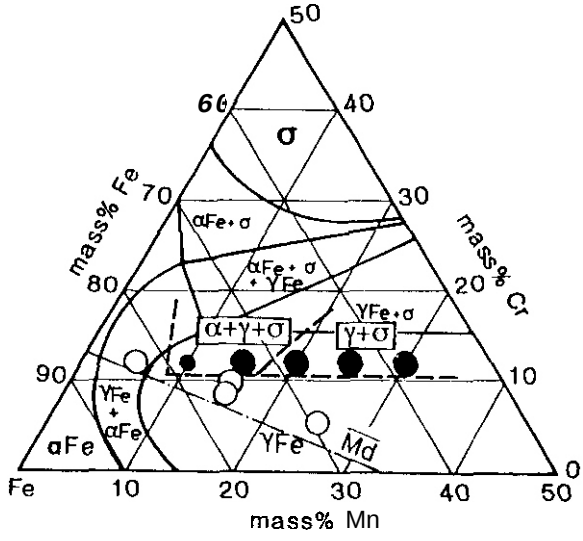

Fig. 9 Phase diagram of Schafmeister and Ergang[20] with superimposed phase boudaries determined in this and related studies. Solid circles denote a-phase formation found in 12Cr alloys by Okazaki and coworkers after the materials were aged at 773 to 923K.[11,12]

CONCLUSIONS

Eased on the results of this study and the results of other studies on either irradiated or thermally aged steels, it appears that Fe-(10-15)Cr-(15-30)Mn steels tend to decompose into the three phase ($\gamma + a + \sigma$) regime during irradiation at temperatures greater than 773K (see Fig. 9). The rate of phase evolution is sensitive to manganese level, temperature, and thermomechanical starting condition. The neutron-induced swelling observed in Fe-12Cr-XMn alloys is very consistent-with that observed earlier in 10Cr and 15Cr alloys.

ACKNOWLEDGEMENTS

This work was supported by Monbusho, the Japanese Ministry of Education, Science, and Culture and the U.S. Department of Energy under Contract DE-AC06-76RLO 1830.

REFERENCES

1. H. R. Brager, F. A. Garner, D. S. Gelles, and M. L. Hamilton, J. Nucl. Mater., 133 & 134 (1985), 907-911.

2. R. L. Klueh and E. E. Bloom, in Optimizing Materials For Nuclear Applications, F. A. Garner, D. S Gelles and F. W. Wiffen, Eds., the Metallurgical Society, Warrendale, PA, 1985, pp. 73-85.

3. R. L. Klueh and P. J. Maziasz in Reduced Activation Materials for Fusion Reactors, ASTM STP 1047, R. L. Klueh, D. S. Gelles, M. Okada and N. H. Packan, Eds., American Society for Testing and Materials, Philadelphia, 1990, pp. 7-18.

4. F. A. Garner and J. M. McCarthy, in ref. 3, pp. 19-29

5. F. A. Garner and H. R. Brager in Radiation-Induced Changes in Microstructure: 13th International Symposium, ASTM STP 955, F. A. Garner, N. H. Packan and A. S. Kumar, Eds., American Society for Testing and Materials, Philadelphia, 1987, pp. 195-206.

6. F. A. Garner, H. R. Erager, D. S. Gelles and J. M. McCarthy, J. Nucl. Mater., 148 (1987), 294-301.

7. F. A. Garner, F. Abe, and T. Noda, J. Nucl. Mater., 155-157 (1988), 870-876

8. J. M. McCarthy and F. A. Garner, in ref. 7, 877-882.

9. F. A. Garner, H. R. Erager, and H. Takahashi, J. Nucl. Mater., 179-181 (1991), 633-636

10. J. M. McCarthy, J. Nucl. Mater., in ref. 9, 626-628.

11. Y. Okazaki, K. Miyahara, Y. Hosoi, M. Tanino, and H. Komatsu, J. Japan Inst. Of Metals, 53 (1989) 512.

12. Y. Okazaki, Y. Mochizuki, K. Miyahara, and Y. Hosoi, in ref. 3, pp. 80-92.

13. F. Abe, H. Araki, and T. Noda, Mater. Sci. Technol., 4 (1988), 885.

14. H. Araki, F. Abe, and T. Noda, J. Japan Inst. Metals, 53 (19891, 964.

15. N. Yukawa, M. Morinaga, K. Nishiyama, Y. Matsumoto, Y. Murata, and H. Ezaki, in ref. 3, pp. 30-46

16. S. Ohnuki, F. A. Garner, H. Takahashi, and J. M. McCarthy, accepted for publication *in* J. Nucl. Mater..

17. S. Ohnuki, F. A. Garner, and H. Takahashi, "Effect of Nickel Content on Microstructural Evolution of Neutron-irradiated Fe-10Cr-30Mn-XNi Alloys, presented at ICFRM-5.

18. H. Takahashi, K. Shiba, S. Nakahigashi, S. Ohnuki, H. Kinoshita and F. A. Garner, in ref. 3, pp. 93-102.

19. F. Abe, S. Nakazawa, H. Araki and T. Noda, Proceedings of International Conference on Stainless Steels, Chiba, Japan, June 10-13, *1991,* pp. 610-617.

20. P. Schafmeister and R. Ergang, Arch. Eisen., 12 (1939) 507

MICROSTRUCTURAL EVOLUTION OF NEUTRON-IRRADIATED Ni-Si AND Ni-A1 ALLOYS - H. Takahashi, Hokkaido University and F. A. Garner, Pacific Northwest Laboratory[a]

OBJECTIVE

The objective of this effort is to provide data on the swelling and segregation response of alloys used in ongoing fission-fusion correlation efforts.

SUMMARY

Additions of silicon and aluminum suppress the neutron-induced swelling of pure nickel but to different degrees. Silicon is much more effective initially when compared to aluminum on a per-atom basis, but silicon exhibits a non-monotonic influence on swelling with increasing concentration. Silicon tends to segregate toward grain boundaries while aluminum segregates away from these boundaries. Whereas the formation of the Ni_3Si phase is frequently observed in charged particle irradiation experiments conducted at much higher displacement rates, it did not occur during neutron irradiation in this study. Precipitation also did not occur in Ni-5Al during neutron irradiation, nor has it been reported to occur during ion irradiation.

PROGRESS AND STATUS

Introduction

Nickel and various dilute nickel binary alloys are often studied in fundamental investigations of radiation damage. While most of these studies focus on phase stability and segregation [1,2], a recent emphasis has been placed on the influence of recoil spectra on these phenomena[3-7]. Since the majority of the irradiation data on nickel binary alloys have been derived from charged particle experiments, there is need for neutron irradiation data for comparison. Not only do neutron irradiation experiments proceed at much lower displacement rates compared with those of typical ion irradiations, but neutron experiments are free of perturbations from surface effects and displacement rate gradients that are typical of charged particle irradiations. This report presents data on the radiation response of pure nickel and several binary alloys often employed in charged particle studies.

Experimental Details

Pure nickel (99.999%) and Ni-5Si, Ni-8Si, and Ni-5Al, (all in at%), with very low levels of other solutes were prepared as 3 mm microscopy disks in three starting conditions: annealed (975°C/10 min/water quench), 30% cold worked, and 30% cold worked and aged (650°C/10 hr/water quench). Irradiation proceeded in EBR-II under static sodium at temperatures of 425, 500, and 600°C to doses of *12-14* dpa. Post-irradiation changes in density were determined using an automated immersion density technique known to be accurate to ±0.16% swelling. Microscopy proceeded on the binary alloys using a JEOL JEM 2000 ESII operating at 200 KeV.

Results

The microscopy results for the pure nickel were reported in an earlier paper[1]. The most significant observation of that study was that cold-working strongly increased the swelling of pure nickel at the higher irradiation temperatures, as shown in fig. 1. Fig. 2 shows that the swelling of nickel at each of the three irradiation temperatures and three starting conditions was reduced by additions of 5 at% Si, but often increased again at 8 at% silicon. Note, however, that in contrast to the behavior of pure nickel and Ni-5Si, the swelling of Ni-8Si is reduced by cold working at higher irradiation temperatures. A portion of the density change in

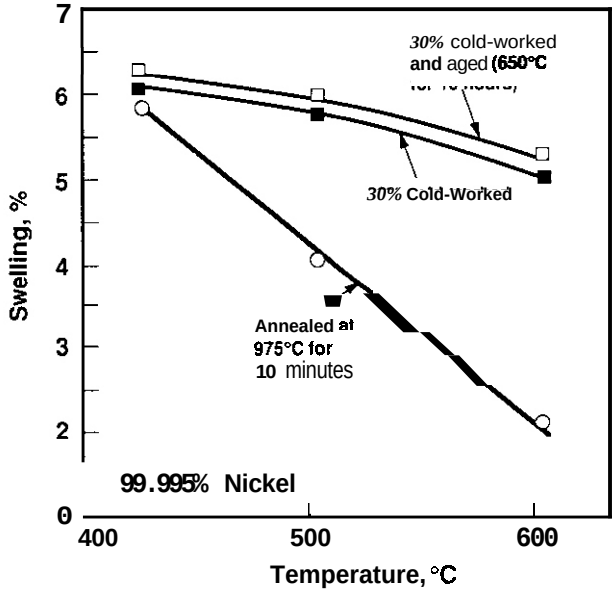

Fig. 1. Swelling of pure nickel in EBR-II at 12-14 dpa as a function of irradiation temperature and thermomechanical starting condition.[4,8] Swelling determined from measurements of density change.

---

[a]Pacific Northwest Laboratory is operated for the U.S. Department of Energy by Battelle Memorial Institute under Contract DE-AC06-76RLO 1830.

each alloy is assumed to result from segregation of silicon, since density measurements performed in this study show that the density of unirradiated, annealed, pure nickel falls from 8.88 g cm^{-3} to 8.65 g cm^{-3} with the addition of 5% silicon. Thus, segregation can lead to relatively large changes in density.

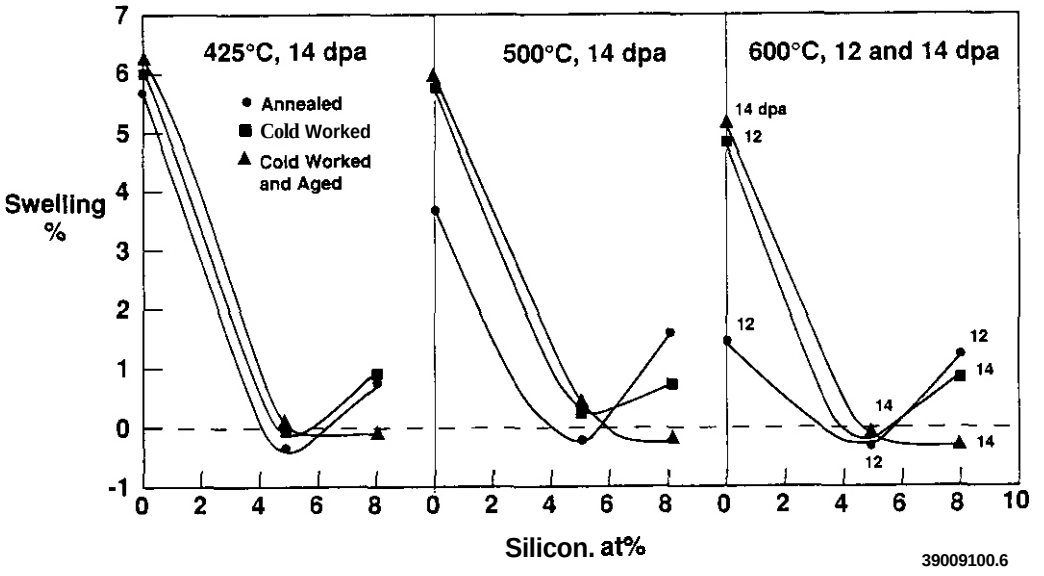

Fig. 2. The influence of silicon level, thermomechanical starting condition and irradiation temperature on the swelling of Ni-Si alloys at 12-14 dpa. Swelling determined from measurements of density change.

As shown in figs. 3-5, cavities were not found in the Ni-5Si alloy in any starting condition at irradiation temperatures of 500 and 600°C; a few cavities were found at 425°C in the annealed state but not in the cold worked state. At 8% silicon, however, small and very heterogeneously distributed amounts of cavities were observed at all temperatures, as shown in figs. 6-8. There was no precipitation of Ni_3Si observed, however, for any irradiation temperature, starting condition or silicon level. There was a tendency for silicon to segregate at grain boundaries, however. As shown in fig. 9, grain boundary segregation was most strong at 500°C, leading to silicon levels on the order of 9-10% in Ni-5Si. At 600°C the degree of segregation was smaller, usually only 1-2% higher than that of the matrix. Similar trends were also observed in Ni-8Si.

Fig. 10 shows that the addition of 5 at% Al also suppressed the swelling of nickel, but not as effectively as 5 at% Si. Note, however, that cold working suppresses swelling in Ni-5Al, in contrast to its effect on swelling in pure nickel. Figs. 11-12 show that cavities were always present to some degree, even at the lowest swelling levels. The negative density changes observed even in the presence of voids demonstrate that redistribution of the aluminum must have occurred. The density of Ni-A1 binary alloys is known to be a strong and decreasing function of aluminum content[9].

In contrast to the behavior exhibited by silicon, aluminum was found to segregate away from grain boundaries, as shown in fig. 13. Similar behavior was observed at void surfaces. Precipitation of Ni_3Al or other phases was not observed for any irradiation or material condition.

DISCUSSION

The suppression of swelling in nickel by silicon additions has been observed previously during ion irradiations[10,11] and neutron irradiations[12-14], although the increase in swelling above 5 at% Si has not been previously observed. Other experimenters have not explored swelling in this silicon range, and no explanation is currently available to explain this behavior.

Although Ni-Si alloys with Si≤10% exist in the single phase γ regime, numerous studies have shown that ion irradiation leads to the formation of the Ni_3Si γ'-phase, especially at the surface of the irradiated specimen[2,15-23]. The γ' phase has sometimes been observed in neutron irradiations, especially at higher silicon levels and lower irradiation temperatures[12-14]. The phase stability of Ni-Si alloys during irradiation has been reviewed by Russell[24], with general agreement that silicon segregates to microstructural sinks via an interstitial binding mechanism.

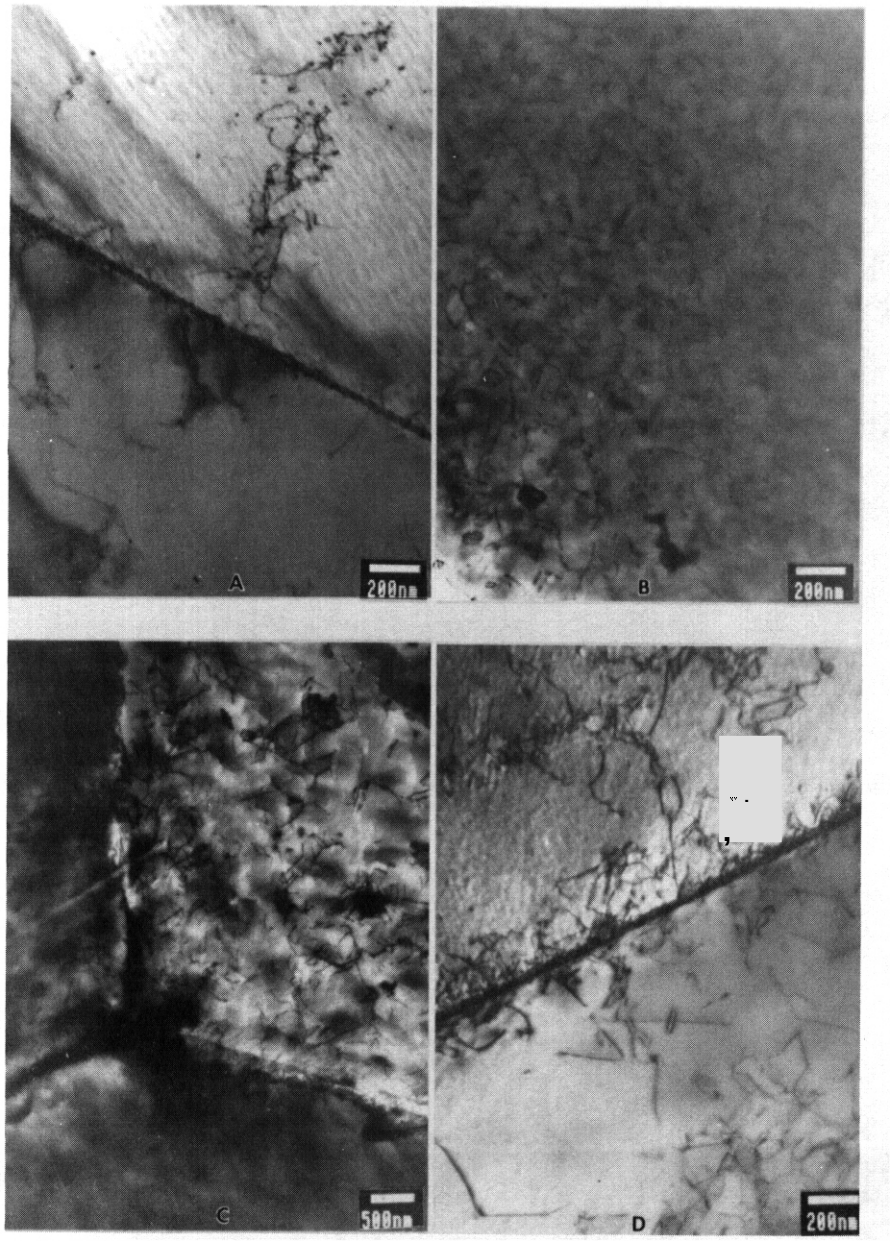

Fig. 3. Microstructures of annealed Ni-5Si (a) before irradiation and after irradiation at (b) 425°C, (c) 500°C, and (d) 600°C.

In agreement with the results of this study, aluminum additions to nickel have been found to reduce swelling during ion[11,25-28] and neutron[9] irradiation. As reviewed by Russell[29], substantial redistribution of existing γ' phase occurs in oversaturated Ni-A1 alloys during irradiation, but in undersaturated alloys aluminum segregates away from microstructural sinks and does not form the γ' phase[11,18,30]. This is also in agreement with the results of the current study.

The most interesting features of this experiment concern the differences observed between this and other studies. Whereas cold working increases the swelling of pure nickel[8], the behavior is reversed for the higher swelling Ni-8Si and Ni-5Al alloys. It was shown by Stubbins and Garner[8] that the collapse of the dislocation density that occurs in pure nickel during irradiation is a consequence of nickel's high stacking fault energy and leads to saturation of the swelling. Cold working retards, but does not eliminate, such a collapse. A similar collapse in dislocation density was not observed for the Ni-Si and Ni-Al alloys examined in this study. Pinizzotto and coworkers showed that the ion-induced dislocation density strongly increased with aluminum content in Ni-A1 alloys[11], noting that Al reduced the stacking fault energy[31].

The failure to observe γ' formation in the Ni-Si alloys in this study is in contrast to the results of many ion irradiation studies. Most of the ion studies were conducted at much higher displacement rates and involved segregation to free surfaces under the action of both gradients in displacement rate and the strong influence of the specimen surface as a sink for point defects. The segregation observed in this study at grain boundaries proceeded in the absence of displacement rate gradients and may also reflect a less efficient sink strength of grain boundaries compared to that of free surfaces. Even more importantly, however, several groups of researchers have shown experimentally and theoretically that the displacement rate plays a strong and temperature-dependent role in determining the stability of the γ' phase in various nickel binary alloys[32-37]. The latter paper of this series addresses the differences between the radiation response of phase stability in the Ni-Si and Ni-A1 systems and proposes phase diagrams for each system that are dependent on displacement rate[37].

Even at the lower disolacement rates tvoical of neutron irradiations. one would exoect that the γ' phase might form at lower irradiation temperatures. Muroga has indeed seen γ' formation in Ni-2% Si irradiated with fast neutrons in FFTF at 365 and 406°C but not at 520 and 600°C[14].

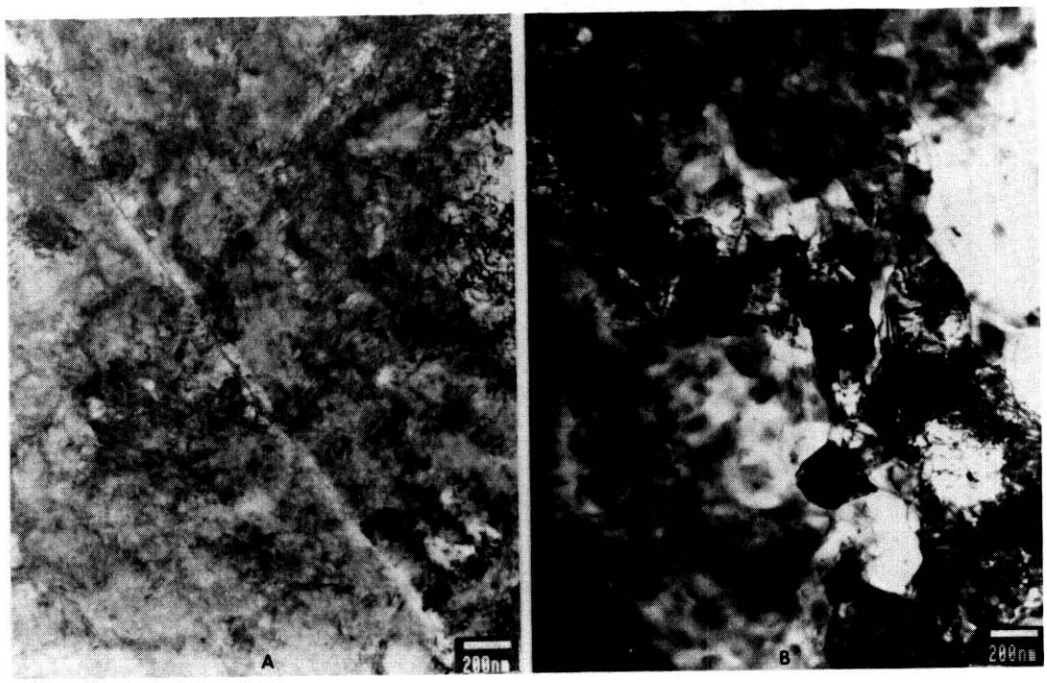

Fig. 4. Microstructures of cold worked Ni-5Si (a) before irradiation, and (b) after irradiation at 425°C.

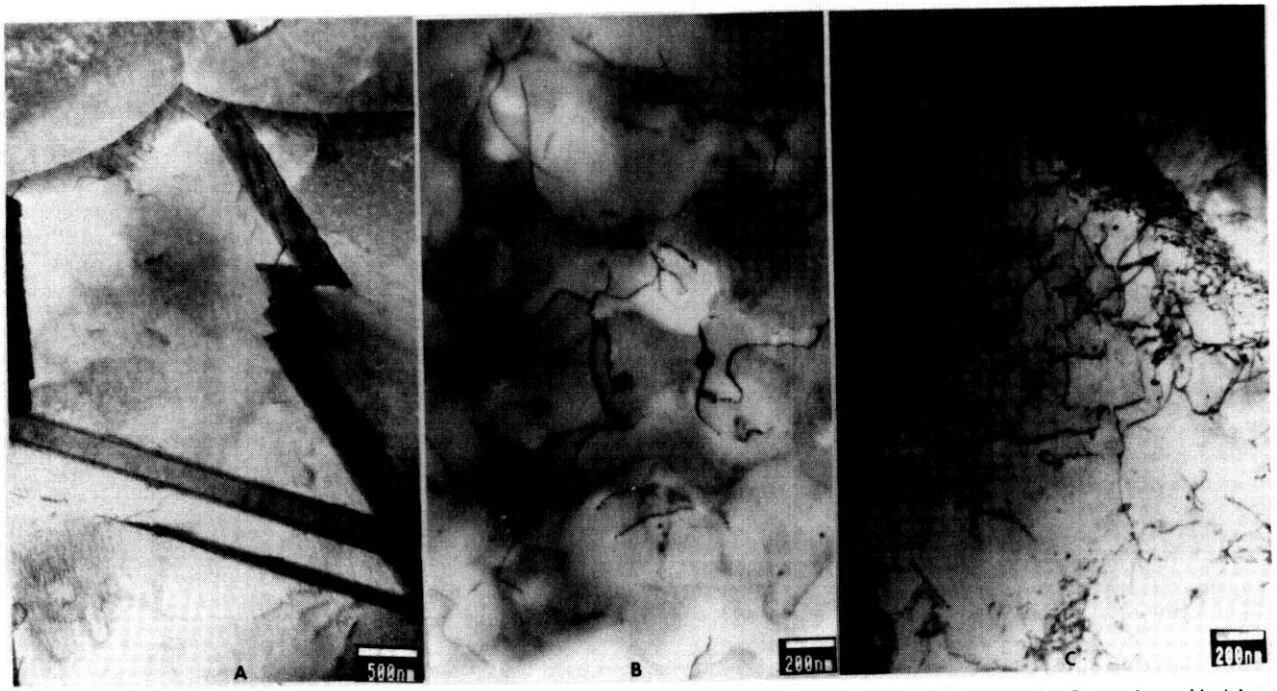

Fig. 5. Microstructures of cold worked and aged Ni-5Si (a) before irradiation and after irradiation at (b) 500°C, and (c) 600°C.

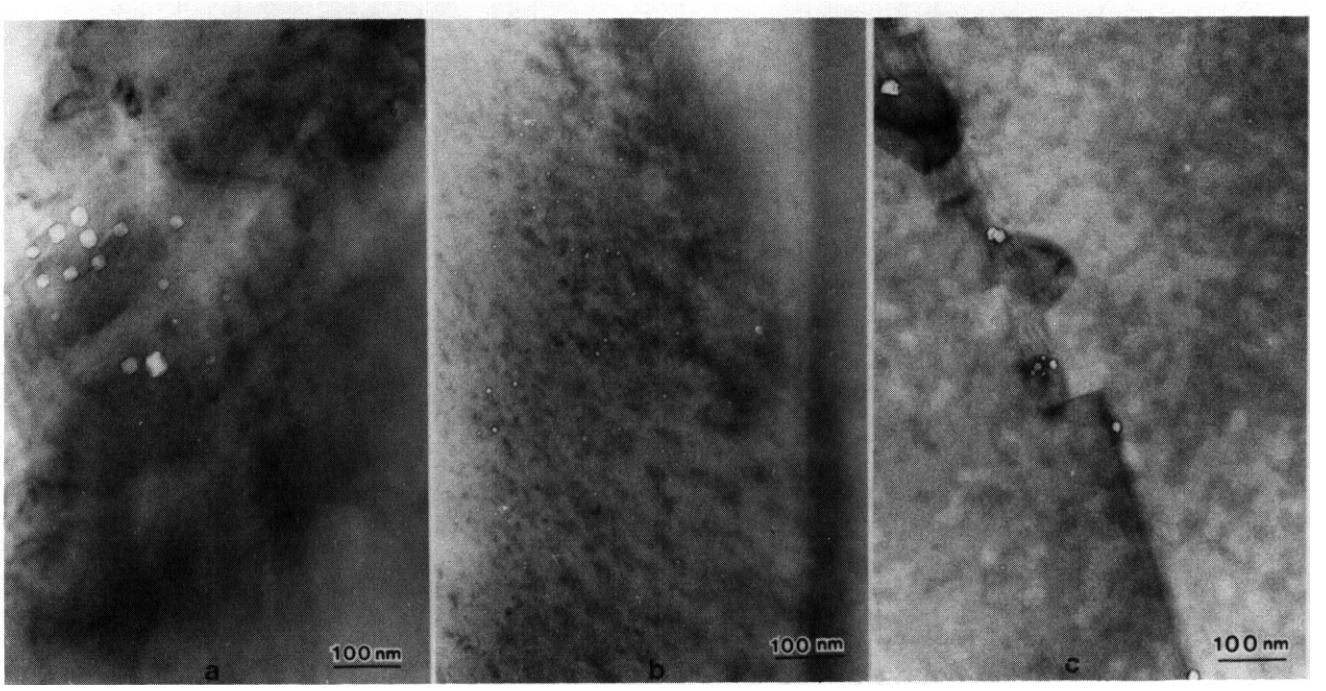

Fig. 6. Microstructures of annealed Ni-8Si after irradiation at (a) 425°C, (b) 500°C, and (c) 600°C.

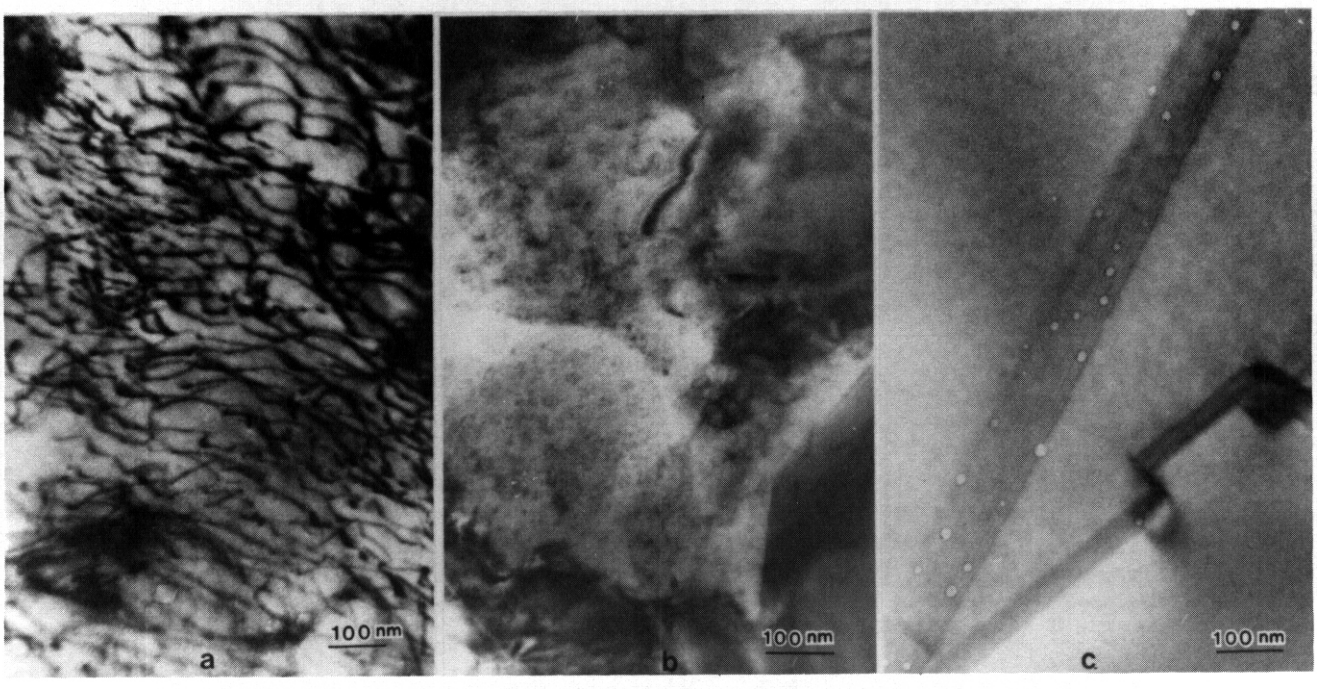

Fig. 7. Microstructures of cold worked Ni-8Si after irradiation at (a) 425°C, (b) 500°C, and (c) 600°C.

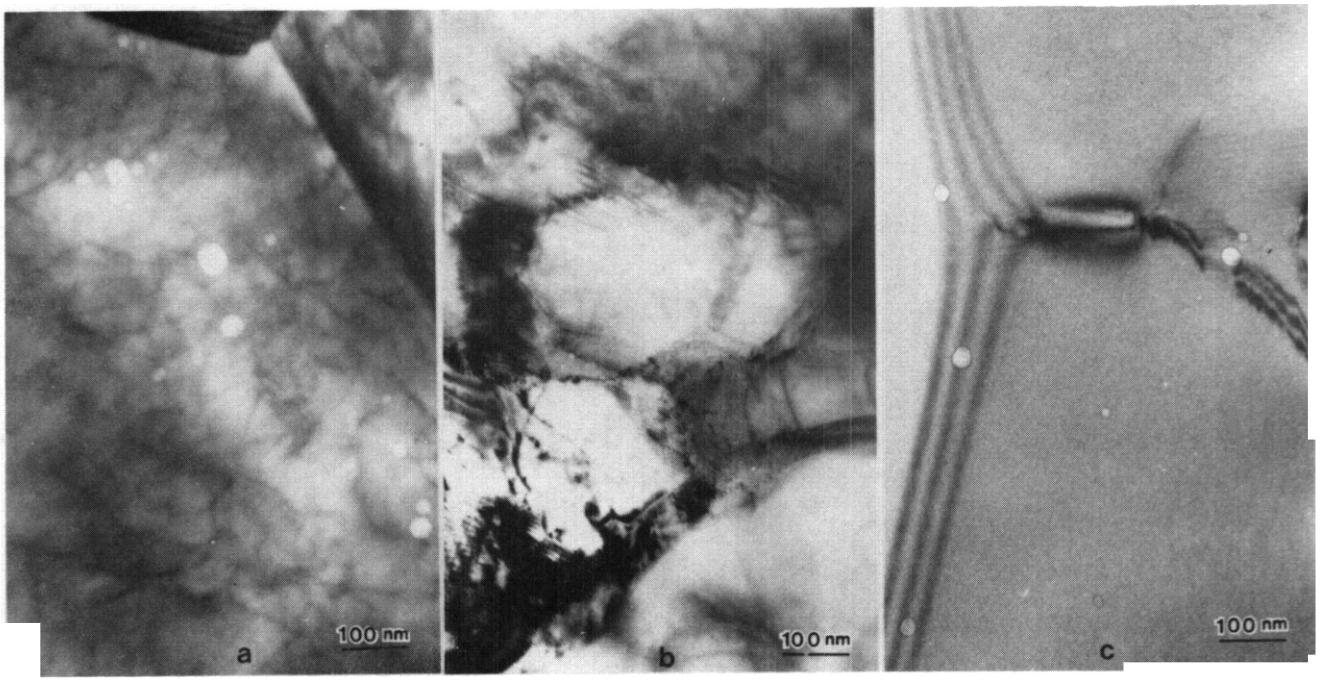

Fig. 8. Microstructures of cold worked and aged Ni-8Si after irradiation at (a) 425°C, (b) 500°C, and 600°C.

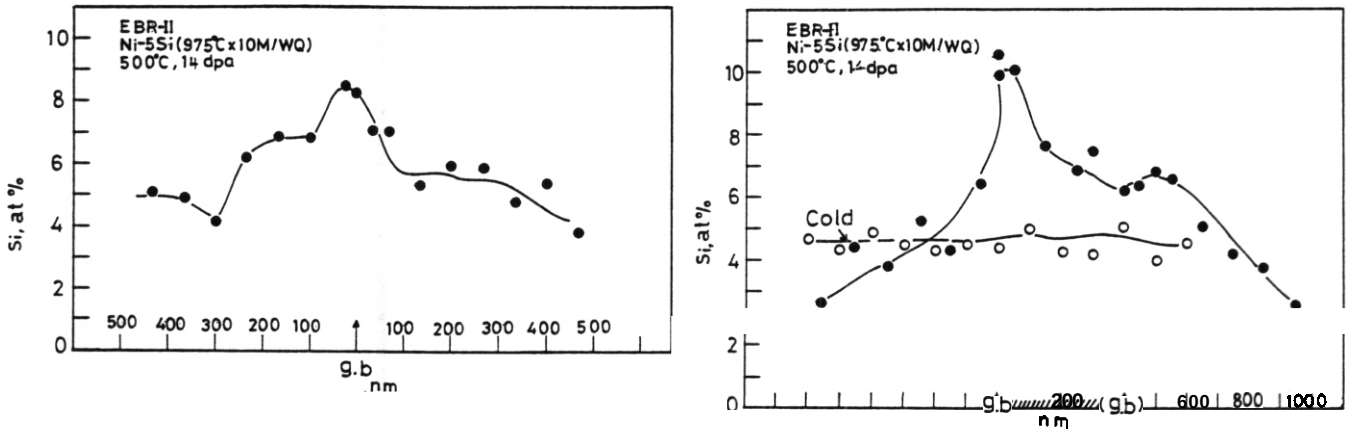

Fig. 9. Segregation of silicon on grain boundaries in annealed Ni-5Si after irradiation at 500°C. Two separate boundaries are shown.

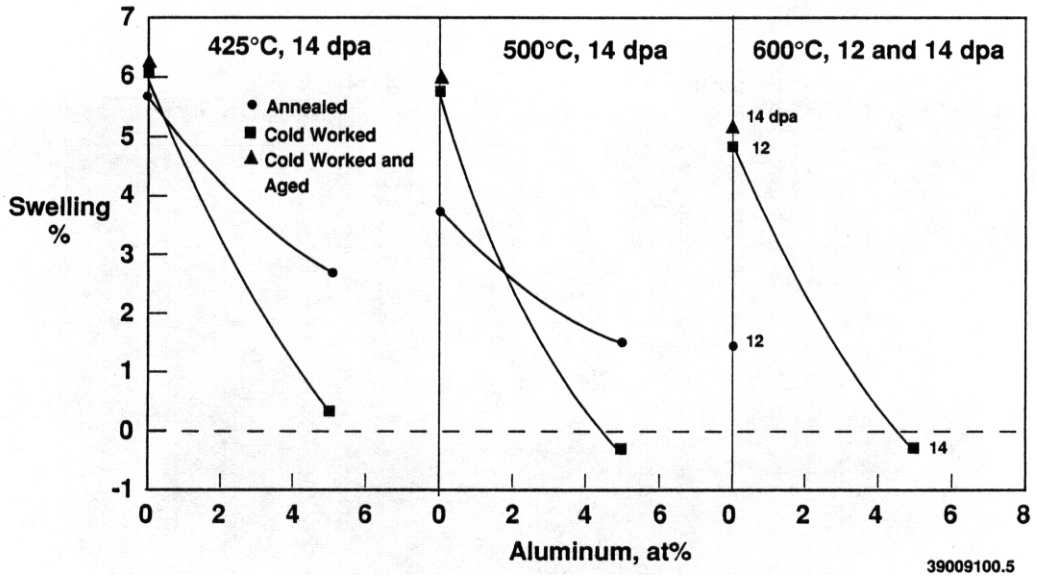

Fig. 10. The influence of aluminum, thermomechanical starting condition and irradiation temperature on the swelling of nickel at 12-14 dpa. Swelling determined from measurements of density change.

CONCLUSIONS

Both silicon and aluminum additions suppress void swelling in nickel-binary alloys initially, but it appears that the behavior is not necessarily monotonic, in that Ni-8Si swells much more than Ni-5Si and is dependent on the thermomechanical starting state. In agreement with other studies, silicon flows towards microstructural sinks during irradiation while aluminum flows away from sinks. In contrast to the behavior observed in ion irradiations conducted at much higher displacement rates, γ' formation did not occur in the matrix or at sinks in either Ni-5Si or Ni-8Si at 425-600°C. This difference is probably due to the lower displacement rate at which these irradiations were conducted. Since void swelling is also related to the silicon level and its distribution, this implies that comparison of neutron and ion irradiation results is not completely straightforward.

FUTURE WORK

No further work is planned.

REFERENCES

1. L. E. Rehn and P. R. Okamoto, in Phase Transformations During Irradiation, Frank V. Nolfi, Jr., Applied Science Publications Ltd., 1983, 247-290.

2. A. J. Ardell and K. Janghorban, pp. 291-329 in ref. 1.

3. F. A. Garner, H. L. Heinisch, R. L. Simons and F. M. Mann, Radiation Effects and Defects in Solids, 113 (1990) 229-255.

4. F. A. Garner, J. Nucl. Mater. 174 (1990) 229-239.

5. T. Muroga, H. Watanabe, M. Araki and N. Yoshida, J. Nucl. Mater., 155-157 (1988) 1290.

6. L. E. Rehn, P. R. Okamoto and R. S. Averback, Phys. Rev. 30B, (1984) 3073.

7. P. R. Okamoto, L. E. Rehn and R. S. Averback, J. Nucl. Mater., 133-134 (1985) 373.

8. J. F. Stubbins and F. A. Garner, accepted for publication in J. Nucl. Mater., proceeding of ICFRM 5.

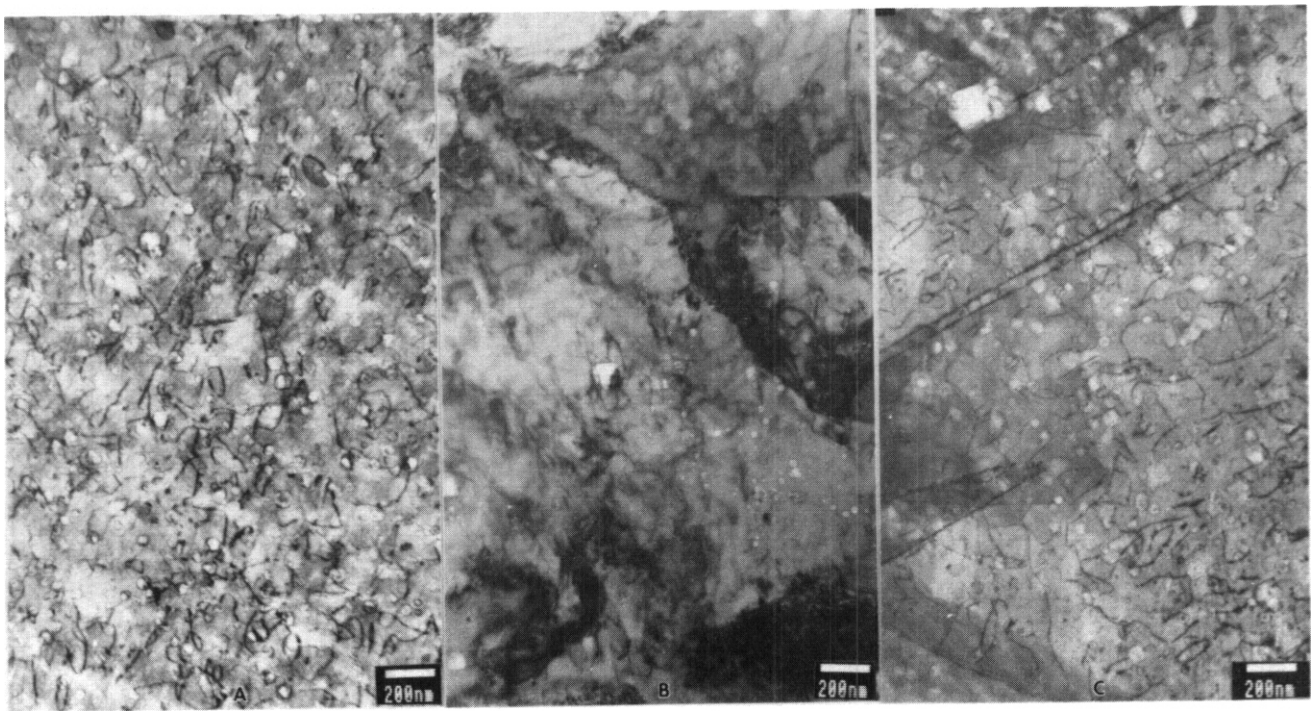

Fig. 11. Microstructures of Ni-5Al after irradiation at 425°C in the (a) annealed, **(b)** cold worked and (c) cold worked and aged conditions.

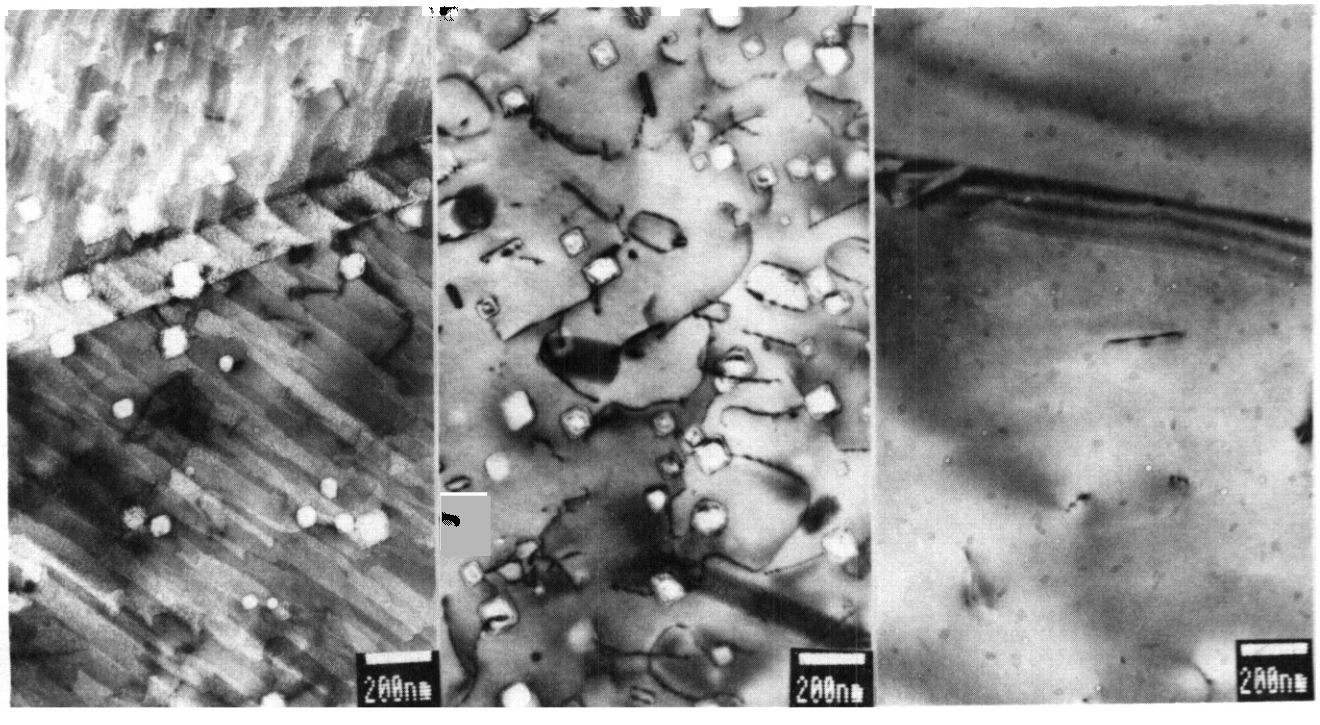

Fig. 12. Microstructures of Ni-5Al after irradiations in the following conditions: **(a)** cold worked, 500°C, (b) cold worked and aged, 500°C, and (c) annealed, 600°C.

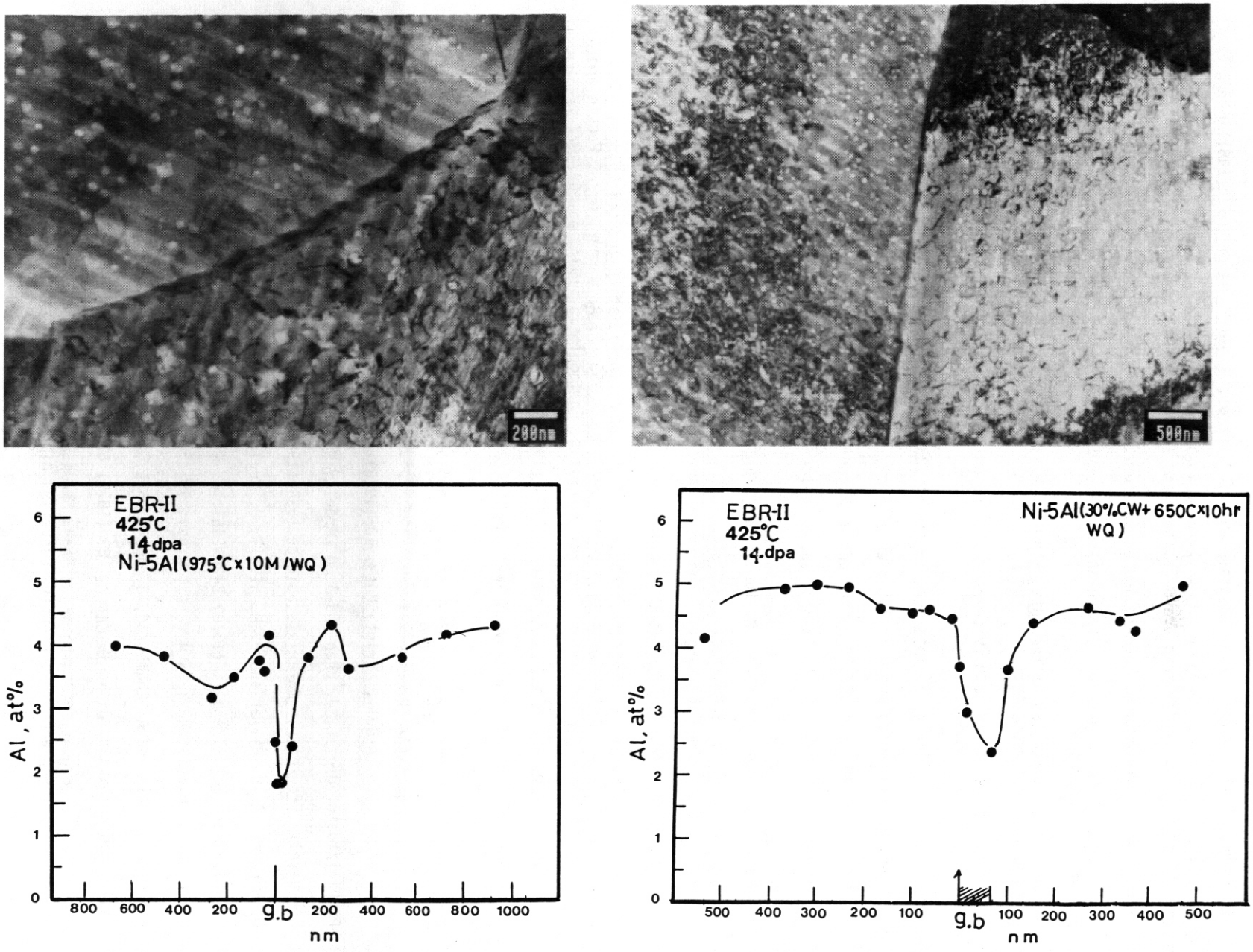

Fig. 13. Aluminum depletion at 425°C at grain boundaries in annealed Ni-5Al (left), and in cold-worked and aged Ni-5Al (right)

9. M. A. Mitchell and F. A. Garner, J. Nucl. Mater., 187 (1992) 103-108.

10. K. B. Roarty, J. A. Sprague, R. A. Johnson and F. A. Smidt, J. Nucl. Mater., 97 (1981) 67.

11. D. I. Potter, L. E. Rehn, P. R. Okamoto and H. Weidersich, in Radiation Effects in Breeder Reactor Structural Materials, M. L. Bleiberg and J. W. Bennett, Eds.. TMS-AIME, New York, 1977, pp. 377-386.

12. G. Silvestre, A. Silvent, G. Regnard and G. Sainfort, J. Nucl. Mater., 57 (1975) 125-135.

13. J. A. Sprague, K. B. Roarty and V. Provenzano, Report of NRL Progress, Naval Research Laboratory, Washington D.C., 8 (1978) 6.

14. T. Muroga, to be presented at the 16th ASTM International Symposium on Effects of Radiation on Materials, Denver, CO, June 1992.

15. D. I. Potter, P. R. Okamoto, H. Wiedersich, J. R. Wallace and A. W. McCormick, Acta Met., 27 (1977) 1175.

16. A. Barbu and A. J. Ardell, Scripta Met., 9 (1975) 1233.

17. L. E. Rehn, P. R. Okamoto and H. Wiedersich J. Nucl. Mater., BO (1979) 172.

18. L. E. Rehn, P. R. Okamoto, D. I. Potter and H. Wiedersich, J. Nucl. Mater., 74 (1978) 242

19. D. I. Potter, L. E. Rehn, P. R. Okamoto and H. Weidersich, Scripta Met., 11 (1977) 1095.

20. R. S. Averback, L. E. Rehn, P. R. Okamoto and R. E. Cook, in Ion Beam Modification of Materials, R. E. Benensen, E. N. Kaufmann, G. L. Miller and W. Scholz, Eds., North-Holland, New York, 1981 p. 79.

21. K. Janghorban and A. J. Ardell, in Phase Stability Durina Irradiation, J. R. Holland, L. K. Mansur and O. I. Potter, Eds., The Metallurgical Society of AIME, New York, 1981, p. 547.

22. A. Barbu and G. Martin, Scripta Met., 11 (1977) 771.

23. N. H. Packan, L. Heatherly, W. Kesternich and H. Schroeder, in Radiation-Induced Chanaes in Microstructure: 13th International Symposium (Part I) ASTM STP 955, F. A. Garner, N. H. Packan and A. S. Kumar, Eds., American Society for Testing and Materials, Philadelphia, 1987, pp. 617-627.

24. K. C. Russell, Prowess in Materials Science, 3-4 (1984) 371-374.

25. R. S. Nelson, "The Simulation of Void Swelling - A Critical Assessment After Ten Years," Harwell Report AERE-R-8826, July 1977.

26. J. A. Hudson, S. Francis, D. J. Mazey and R. S. Nelson, in Effects of Radiation on Substructure and Mechanical Properties of Metals and Alloys, ASTM STP 529, J. Moteff, Ed., American Society for Testing and Materials, 1973, pp. 326-333.

27. L. J. Chen and A. J. Ardell, Scripta Met., 10 (1976) 1047-1050

28. R. F. Pinizzotto, Jr., L. J. Chen and A. J. Ardell, Met. Trans. A, 9 (1978) 1715-1727.

29. K. C. Russell, Prowess in Materials Science, 3-4 (1984) 354-358.

30. A. D. Marwick, R. C. Pillar and P. M. Sivell, J. Nucl. Mater., 83 (1979) 35-41.

31. P. C. Gallagher, Met. Trans. 1 (1970) 2429-2461.

32. A. Barbu and G. Martin, Scripta Met., 11 (1977) 771-775.

33. A. Barbu, G. Martin and A. Chamberod, J. Appl. Phys., 51 (1980) 6192-6196.

34. R. Cauvin and G. Martin, J. Nucl. Mater., 83 (1979) 67-78.

35. G. Martin, J. L. Bocquet, A. Barba and Y. Adda, in Radiation Effects in Breeder Reactor Structural Materials, M. L. Bleiberg and J. W. Bennett, Eds., TMS-AIME, New York, 1977, pp. 899-915.

36. A. S. Bakay and A. A. Turkin, Phys. Met. Metall., 71 (1991) 64-73.

37. A. S. Bakay, A. A. Turkin and Yu. A. Turkin, Phys. Met. Metall., 71 (1991) 74-81.

6.0 DEVELOPMENT OF STRUCTURAL- ALLOYS

6.1 Ferritic **Stainless Steels**

ANALYSIS OF STRESS-INDUCED BURGERS VECTOR ANISOTROPY IN AN IRRADIATED FERRITIC - MARTENSITIC STEEL: JFMS

D.S. Gelles (Pacific Northwest Laboratory'), A. Kimura (Muroran Institute of Technology), A. Kohyama (University of Tokyo) and R. J. Puigh (Westinghouse Hanford Company)

OBJECTIVE

The objective of this effort is to improve understanding of the effect of fast neutron irradiation on microstructural evolution by examining the response of neutron irradiated pressurized tubes of a duplex ferritic/martensitic steel.

SUMMARY

A Drocedure for determining the Burgers vector anisotropy in irradiated ferritic steels is described. aliowing identification of all a<100> and all $\frac{a}{2}$<111> dislocations in a region of interest. The necessary micrographs to apply the procedure have been taken of two pressurized tube specimens of JFMS, a duplex ferritic steel following irradiation in FFTF/MOTA at 407°C to 7.5 x 10^{22} n/cm^2 (E > 0.1 MeV) or 37.5 dpa. Preliminary analysis of one set of micrographs indicates large anisotropy in Burgers vector populations for an 86 MPa stressed condition.

PROGRESS AND STATUS

Introduction

The opportunity to examine the effect of stress on microstructural evolution occurs rarely in FFTF/MOTA irradiation experiments because pressurized tubes are reirradiated until failure occurs in order to assess the consequences of increasing dose. However, in early Monbusho experiments in the FFTF/MOTA, a series of eight pressurized tubes of fhe Japanese duplex ferritic steel JFMS was irradiated for only one irradiation cycle and then was removed. JFMS is a Fe-10Cr-2Mo steel containing approximately 25% delta ferrite in martensite, with moderate carbon, high silicon and nickel, and intentional additions of vanadium and niobium. The series of specimens consisted of two sets of four tubes, one set irradiated at 407°C and the other irradiated at 520°C. Each set included one unstressed and three stressed conditions to maximum levels of about 90 MPa. Microstructural examination of these pressurized tubes was a part of the Monbusho experimental objectives.

Analysis of Buraers vector anisotropy in ferritic allovs

It has been shown that irradiation creep in Nimonic PE16, an austenitic superalloy, produces anisotropy in the populations of perfect dislocations as a function of the Burgers vectors.' Such an anisotropic response is to be expected if irradiation creep is controlled by dislocation motion. Orowan was the first to note that the plastic strain rate, $\dot{\epsilon}$, must be the sum of all dislocation motion[3]

$$\dot{\epsilon}=\sum_i \rho_i b_i \bar{v}_i \qquad (1)$$

where i defines each of the possible dislocation Burgers vectors, ρ is the dislocation density, b is the Burgers vector length, and $\bar{v}$ is the average dislocation velocity. Equation (1) shows that for irradiation creep caused by dislocation motion, anisotropy must exist in the Burgers vector populations (ρ) and / or in the dislocation velocities ($\bar{v}$), and anisotropy in $\bar{v}$ generally leads to anisotropy in ρ.

Procedures similar to those for Burgers vector analysis in austenitic microstructures' can be developed for ferritic alloys. It is presumed–that a straightforward procedure based on the standard approach requiring two no-contrast conditions ($\vec{g} \cdot \vec{b} = 0$) to identify each Burgers vector is impossible, and that the dislocations present are only of two types, either a<100> or $\frac{a}{2}$<111>. The procedure for ferritic alloys is based on a process of elimination.

Table 1 lists the contrast conditions for the three a<100> and four $\frac{a}{2}$<111> dislocation possibilities as a function of the low index imaging conditions possible near a (011) foil orientation as defined previously in reference 4. Figure 1 provides an indexed Kikuchi map showing the relationships of the g vectors given in Table 1. From Table 1, it can be noted that imaging with $\vec{g}$ = 200 shows all $\frac{a}{2}$<111> dislocations, but only a[100] dislocations, with a[010] and a[001] dislocations out of contrast, Also, a[100] 'dislocations should appear in much stronger contrast than $\frac{a}{2}$<111> dislocations because $\vec{g} \cdot \vec{b}$ is 2 instead of 1, a fact easily verified by experiment. If instead g = 011 contrast is used, then $\frac{a}{2}$[1$\bar{1}$1], $\frac{a}{2}$[111], a[100], and a[010] dislocations are visible but $\frac{a}{2}$[111], $\frac{a}{2}$[1$\bar{1}$1], and a[100] dislocations are not visible. Therefore, all dislocations of type $\frac{a}{2}$<111> and a<100> are imaged in a series of two such micrographs. Comparing the

---

'Pacific Northwest Laboratory is operated for the U.S. Department of Energy by Battelle Memorial Institute under Contract DE-AC06-76RLO 1830.

dislocation structure in micrographs taken with these contrast conditions reveals that images appearing only in $\vec{g}$ = 200 contrast must either be $\frac{a}{2}[111]$, $\frac{a}{2}[\bar{1}11]$ or a[100] dislocations (and the a[100] images are much stronger), and images that only appear in $\vec{g}$ = 011 contrast must be a[010] or a[001] dislocations. Thus, all the $\frac{a}{2}$<111> dislocqtions appearing in $\vec{g}$ = 200 contrast can be split intp two groups, $\frac{a}{2}[111]$ with $\frac{a}{2}[\bar{1}11]$ and $\frac{a}{2}[1\bar{1}1]$ with $\frac{a}{2}[11\bar{1}]$. When $\vec{g}$ = $\bar{1}$01 contrast is used, then $\frac{a}{2}[111]$, $\frac{a}{2}[\bar{1}11]$, a[100] and a[001] dislocations are visible and $\frac{a}{2}[11\bar{1}]$, $\frac{a}{2}[1\bar{1}1]$, and a[010] dislocations are invisible. A micrograph using $\vec{g}$ = 101 contrast will differentiate between the a[001] and a[001] images identified on the $\vec{g}$ = 011 micrograph because only a[001] is visible in both. With three micrography, all a<100> type dislocations can be identified and separated by Burgers vector. Furthermore, the g = 101 micrograph can also be used to differentiate between the two groups of $\frac{a}{2}$<111> dislocations appearing in $\vec{g}$ = 200 contrast and, therefore, all $\frac{a}{2}$<111> dislocations showing on the 200 image can be identified and separated by Burgers vector. A similar identification sequence can be defined if $\vec{g}$ = $\bar{1}$10 is used instead of 101.

Table 1. The $\vec{g} \cdot \vec{b}$ Imaging Criteria for Various bcc Imaging Conditions and Burgers Vector Combinations

	Burgers vector						
$\vec{g}$	$\frac{a}{2}[111]$	$\frac{a}{2}[\bar{1}11]$	$\frac{a}{2}[1\bar{1}1]$	$\frac{a}{2}[11\bar{1}]$	a[100]	a[010]	a[001]
200	1	1	1	1	2	0	0
020	1	1	1	1	0	2	0
002	1	1	1	1	0	0	2
01$\bar{1}$	0	0	1	1	0	1	1
$\bar{1}$10	0	1	1	0	1	1	0
101	0	1	0	1	1	0	1
10$\bar{1}$	1	0	1	0	1	0	1
11$\bar{2}$	0	1	1	2	1	2	1
121	0	1	2	1	2	1	1
2$\bar{1}$1	1	1	2	0	2	1	1
21$\bar{1}$	1	1	0	2	2	1	1
11$\bar{2}$	1	0	2	1	1	1	2
121	1	0	1	2	1	2	1

In practice, however, the large **tilt** angles required to obtain images using **g** = 200, 01$\bar{1}$, and $\bar{1}$01 sufficiently alter the dislocation configurations so that identification becomes difficult. Stereo pair images, taken for each contrast condition that is used, can greatly assist dislocation identification. Therefore, an optimum micrograph series to identify Burgers vector anisotropy in ferritic–alloys consists of six micrographs: a stereo pair using $\vec{g}$ = 200 contrast near (011), a stereo pair using-g = 011 contrast near (011), and a stereo pair using either $\vec{g}$ = 101 contrast between (010) and (111), or 110 contrast between (001) and (111).

ExDerimental Procedures

Eight pressurized tubes of JFMS steel were made from tubing fabricated from rod stock. The chemical composition of the rod stock is given in Table 2. Tube segments had dimensions of 0.57 mm outside diameter, 0.20 mm wall thickness, and were 19.8 mm in length. Endcaps of the same material were electron beam welded to both ends of the tubing segments. One endcap had a small (0.13 mm diameter) hole for pressurization *to* obtain the desired hoop stress at the design irradiation temperature. The pressurization gas was helium. Diameter measurements were made using a non-contacting laser measurement system before and after irradiation. Specimens were irradiated in level 2 of FFTF/MOTA 1F during cycle 10: four specimens at 407°C in canister 2C-3 and four at 520°C in canister 2A-2 for an accumulated exposure time of 335.4 equivalent full power days, over approximately 8050 h. The estimated accumulated damage in these creep specimens during irradiation was 7.5 x 10^{22} n/cm^2 (E > 0.1 MeV) or 37.5 dpa.

Table 2. Nominal Composition of JFMS (wt%).

Fe	Cr	Mo	C	Si	Mn	P	S	Ni	V	Nb	N
Bal.	9.85	2.3	0.05	**0.675**	0.58	0.009	0.006	0.94	0.12	**0.06**	>100 ppm

Following irradiation and diametral measurement, four specimens (RR00, RR03, RR04 and RR07), comprising zero and maximum stress conditions for the two irradiation temperatures, were selected for microstructural examination. Specimens were sectioned with a slow speed saw by first removing the end caps and then splitting each tube longitudinally. Curved disks 3 mm in diameter were then punched from the central region of each split tube using a punch designed for tubing specimens. The disks were mechanically ground flat and then thinned for transmission electron microscopy using standard procedures. Examinations were

performed using a JEDL 1200EX transmission electron microscope with a double tilting goniometer stage. Column realignment was found to be necessary after each change in specimen tilt.

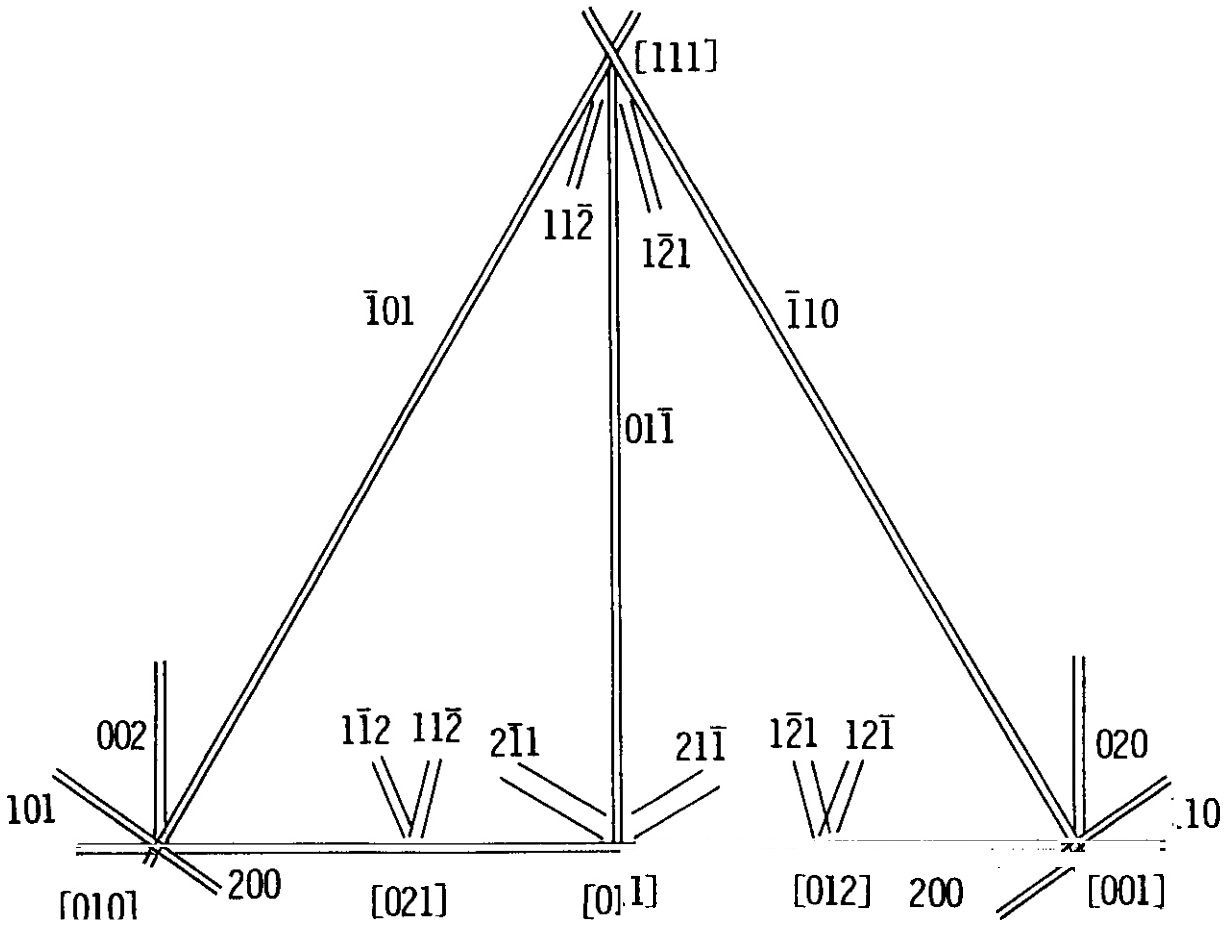

Figure 1. Definition of Notation as Represented on a Kikuchi Map for bcc Dislocation Imaging Conditions.

Results and Analysis

Diameter change measurements

Diameter change measures for the pressurized tube specimens of JFMS are given in Table 3, and the diametral creep strains are plotted using open symbols as a function of hoop stress in Figure 2, with measurements for HT-9 using closed symbols for comparison. From Figure 2, it can be shown that JFMS has better creep strength than does HT-9, and behavior in JFMS appears to be linear with stress, but with an offset due to apparent diametral change in the zero stress condition. Such offset response can be caused by void swelling or density change due to precipitation.

Microstructural examination

The effect of irradiation on microstructure was found primarily in the precipitate structure. No void swelling was observed. Following irradiation at 407°C, M_2C_6 was retained at prior austenite grain boundaries and martensite lath subboundaries, but a high density of equiaxed particles formed within grains. Particles on subgrain boundaries were larger than those in the matrix, and the decorated subgrain boundaries had adjacent regions denuded of particles. This precipitate has previously been characterized as G phase' or $M_6C(\eta)$.[6] The precipitate volume fraction appeared to be significantly higher than that found in HT-9, probably a result of the high levels of silicon and nickel in the alloy. Quantitative measurement showed the precipitate volume fraction was 1.14%, with a mean particle size of 6.6 nm and a number density

of $8.9x10^{16}$ cm^{-3}. Precipitate densities approaching 10^{17} cm^{-3} should produce high strength. Following irradiation at 520°C, significant rearrangement of precipitation at prior austenite grain boundaries and martensite lath subboundaries was found. Details of these microstructural changes will he published elsewhere

Table 3. Creep Data on JFMS Pressurized Tubes Irradiated in FFTF Cycle 10.

Specimen ID Code	Irradiation Temp. (°C)	Hoop Stress (MPa)	Average Diam. Change (mm)	Diametral Strain (%)
RR00	407	-0.1	0.0044	0.11
RR01	407	25.8	0.0042	0.03
RR02	407	51.3	0.0048	0.11
RR03	407	86.0	0.0067	0.15
RR04	520	-0.1	0.0004	0.01
RR05	520	26.6	0.0021	0.05
RR06	520	53.3	0.0057	0.12
RR07	520	90.5	0.0106	0.23

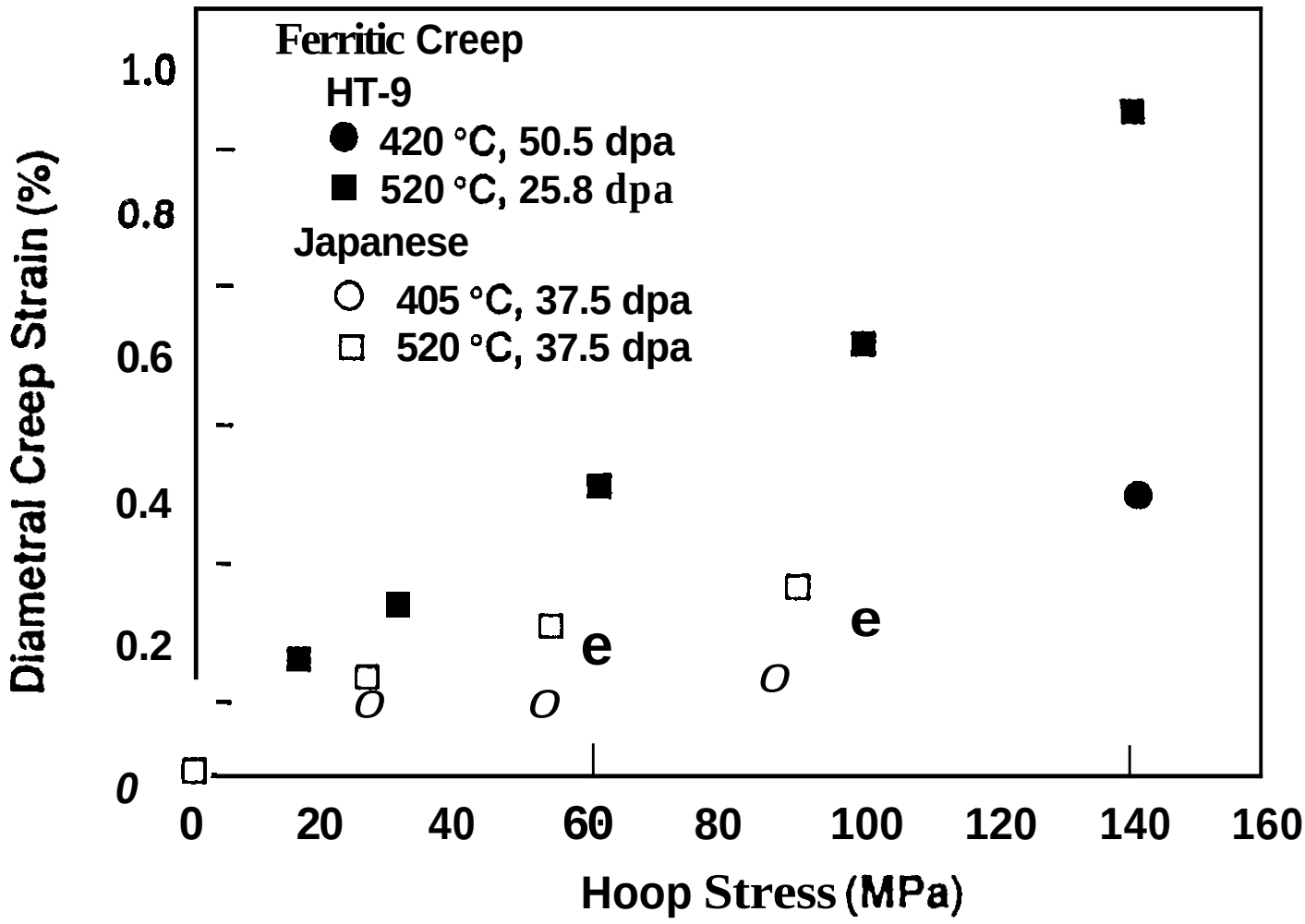

Figure 2. Irradiation Creep Response of JFMS in Comparison with HT-9 as a Function of Hoop Stress

Analysis of dislocation structures was limited to specimens irradiated at 407°C. Stress fields associated with precipitation complicated the analysis, hut it was found that imaging conditions approaching weak beam dark field were sufficient to unambiguously show $\frac{a}{3}$<111> dislocations using $\vec{g}$ = 200 contrast. Two types of regions were examined: martensite and delta ferrite, but the latter was easier to work with.

An example of the dislocation structure in a delta ferrite grain in specimen RR03 irradiated at 407°C at a stress level of 86 MPa is shown in Figures 3 and 4. The grain orientation is near [142]. In Figure 3,

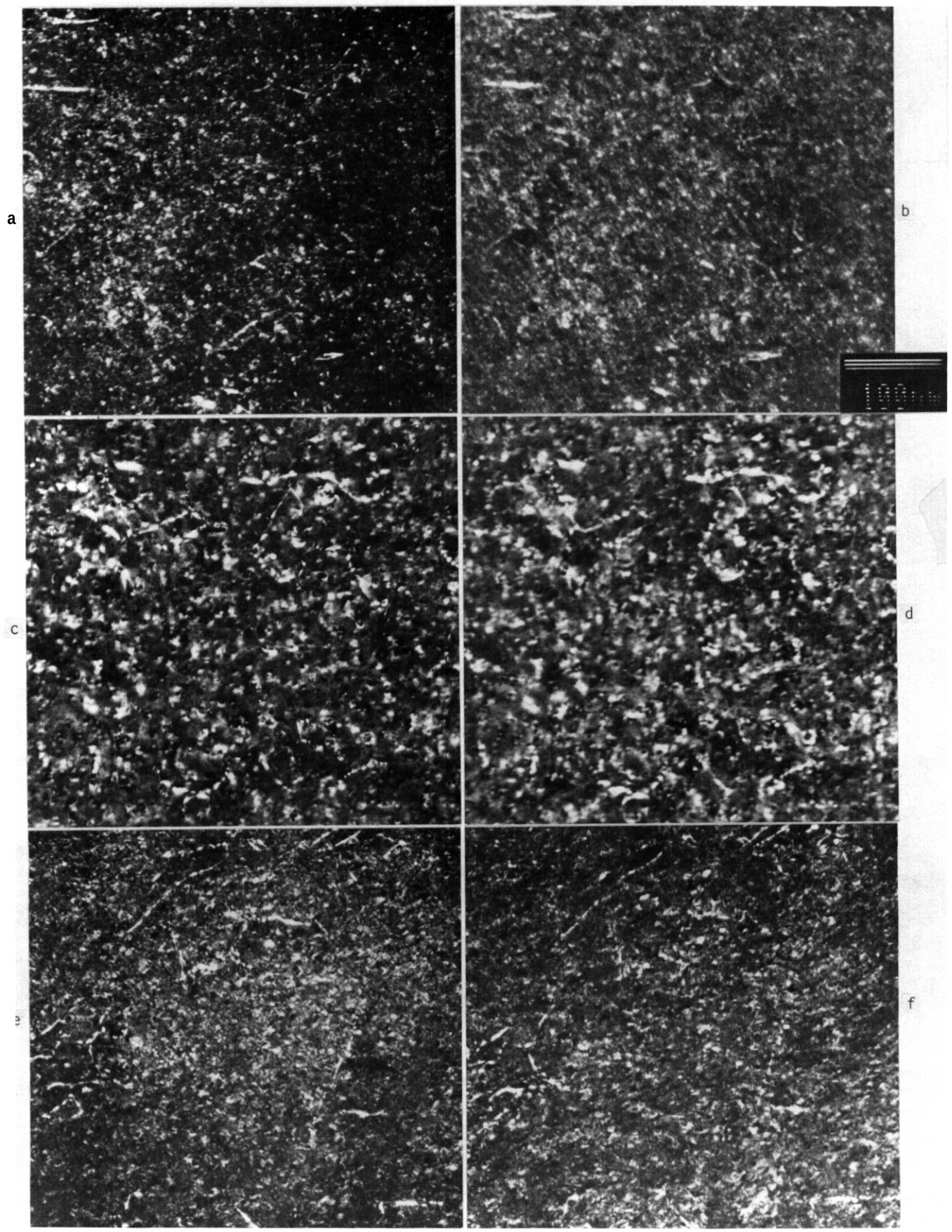

Figure 3. Weak Beam Dark Field Stereo Pair Micrographs of a Ferrite Grain in JFMS Pressurized Tube RR03 using 200 contrast in a) and b), 011 contrast in c) and d), and 110 contrast in 3) and f).

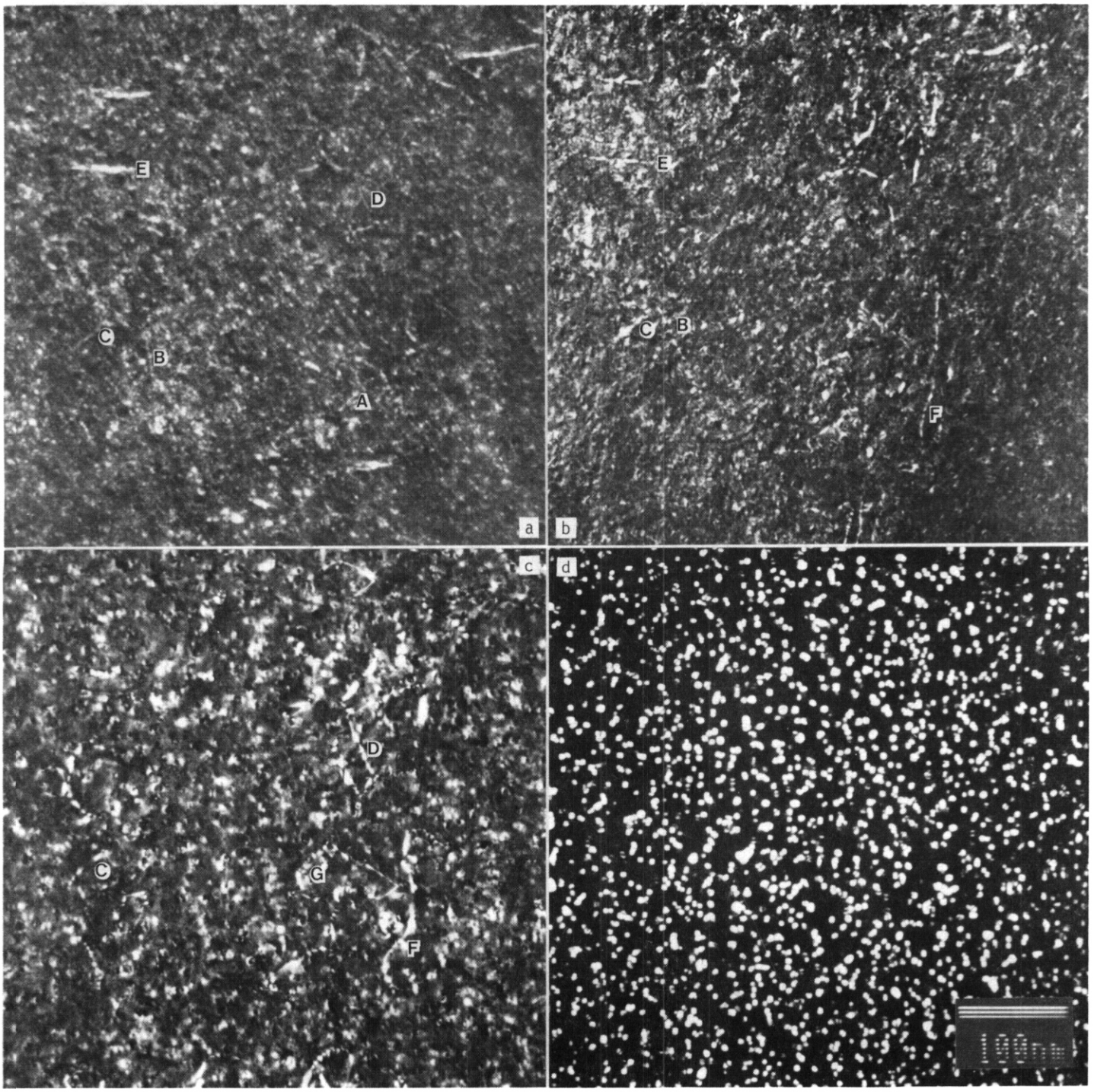

Figure 4. Weak Beam Dark Field Micrographs of the Same Area as Figure 3 Arranged for Comparison of Dislocation and Precipitate Structures using 200 contrast in a), 110 contrast in b), 011 contrast in c), and precipitate dark field contrast in d). The meaning of the various labels is described in the text.

stereo pair images in dark field using 200, $01\bar{1}$, and $\bar{1}10$ contrast are provided of the same area, but to show the stereo effect, it has been necessary to rotate the field of view. Figure 3a and b show the region using 200 contrast. Strong horizontal dislocation lines in the upper left and a smaller strong loop image towards the lower right correspond to a[100] dislocations and the remainder of the dislocation images correspond to $\frac{a}{2}$<111> dislocations. The $\frac{a}{2}$<111> dislocations are much weaker, often being difficult to distinguish from a background mottling arising from the strain fields of precipitate particles. However, for example, two weaker straight dislocation images can be seen on the central left. Figures 3c and d

provide a stereo pair using $01\bar{1}$ contrast, but the images have been rotated 90 degrees counter-clockwise so that the two weak $\frac{a}{2}$<111> images noted in figures 3a and b should appear at the lower center, but only one is visible. Again, the images are complicated by a background mottling from precipitate strain fields. Figures 3e and f provide stereo pair images using 110 contrast, with the images rotated a further 50 degrees counter-clockwise. Image contrast is again similar, complicated by precipitate strain fields. From this series of micrographs, it can be shown that dislocation images tend to be horizontal, and therefore perpendicular to the Burgers vector direction, indicating a strong tendency for edge dislocation character, rather than screw character.

Figure 4 is provided, using the same micrograph series without stereo pairs or rotation, so that the dislocation images can be compared more easily. Figure 4a, b and c use –200, $\bar{1}10$ and 011 contrast, respectively, and figure 4d gives a precipitate dark field image using g = ⅛ <222> for approximately the same area. Each of the dislocation image micrographs has been labelled to show a visible example of each of the types of dislocations, with $\frac{a}{2}[111]$ labelled A", $\frac{a}{2}[\bar{1}11]$ labelled "B", $\frac{a}{2}[\bar{1}\bar{1}1]$ labelled "C", $\frac{a}{2}[11\bar{1}]$ labelled "D", a[100] labelled "E", a[010] labelled "F", and a[001] labelled. "G". All labels are to the right of the respective dislocation images. Note that $\frac{a}{2}[111]$, $\frac{a}{2}[\bar{1}11]$, $\frac{a}{2}[\bar{1}\bar{1}1]$, $\frac{a}{2}[11\bar{1}]$ and a[100] dislocations can be identified in figure 4a, $\frac{a}{2}[\bar{1}11]$, f$[\bar{1}\bar{1}1]$, a[100] and a[010] can be identified in figure 4b, and $\frac{a}{2}[111]$, $\frac{a}{2}[\bar{1}11]$, a[010] and a[001] can be identified in figure 4c, based on the labels. Therefore, it is possible to differentiate between all of the dislocations present in this specimen area.

The area shown in Figures 3 and 4 has been analyzed to provide a quantitative estimate for Burgers vector anisotropy. The foil is approximately 67 nm thick, and the field of view for measurement is considerably larger than that shown in figures 2 and 3. Table 4 gives results of the dislocation density measurements. From Table 4, it can be shown that dislocation densities vary between 0.6 and 4.7×10^9 cm^{-2}, corresponding to nearly a factor of eight variation. Anisotropy develops in both the $\frac{a}{2}$<111> and a<100> populations with the populations smallest for those orientations in the tangential direction. Therefore, Burgers vector anisotropy can be measured using a process of elimination technique, and large Burgers vector anisotropy can develop in stressed duplex ferritic/martensitic steels.

Table 4. Dislocation Density Measurements, Showing Burgers Vector Anisotropy in Specimen RR03 Irradiated at 407°C with a Hoop Stress of 86 MPa.

Burgers vector	Dislocation density (10^9 cm/cm^3)
$\frac{a}{2}[111]$	1.94
$\frac{a}{2}[\bar{1}11]$	1.02
$\frac{a}{2}[1\bar{1}1]$	0.62
$\frac{a}{2}[11\bar{1}]$	4.50
a[100]	1.17
a[010]	4.28
a[001]	

Discussion

This work has provided an opportunity to extend Burgers vector anisotropy determination to the ferritic alloy class. Procedures have been established and tested, and results have been generated showing that a significant anisotropy can be generated in a ferritic/martensitic steel at 400°C for a stress level of 86 MPa. This discussion section is intended to cover two topics: limitations of the procedure and significance of the results.

JFMS is found to develop significant precipitation following irradiation. The precipitate is presumed to be due to high levels of silicon and nickel in the steel, resulting in G phase precipitation. The precipitate particles have a strain field associated with them that affects weak beam dark field imaging so that identification of $\frac{a}{2}$<111> dislocations using 200 contrast becomes very difficult, and the possibility for errors during analysis exists. A steel with less matrix precipitation, such as a low activation steel, is expected to provide images that are easier to identify.

The analysis given in Table 4 is based on measurements that may not be statistically significant. The specimen thickness was only 67 nm, and only about 40 dislocations were analyzed in the field of view. Dislocation motion may have occurred in such a thin foil, although evidence for such motion was not observed. No dislocation nodes could be found in the analyzed region to show that the Burgers vector identification did not violated energy balances. Also, dislocation density measurements have not yet been completed on an unstressed specimen.

The result that anisotropy as large as a factor of 8 between different Burgers vector populations is surprising, given the limited amount of total strain found in the specimen. The strain measured in specimen RR03 was 0.15%, whereas the unstressed specimen deformed 0.11% presumably due to precipitation. Therefore, the strain due to irradiation creep may have been as low as 0.04%. In comparison, results on austenitic steels provided similar levels of anisotropy in irradiated pressurized tubes, with deformations ranging between -0.02 and 1.255%. The lower value corresponded to a situation where the perfect dislocation population had only just been generated, and therefore the average dislocation velocity was very low. Therefore, it appears that the present results indicate that dislocation motion may have been very limited for the dose level achieved, about 40 dpa, possibly caused by the high precipitate density

found in the soecimen

CONCLUSIONS

Procedures have been developed to determine Burgers vector anisotropy in ferritic/martensitic steels containing both $\frac{a}{2}$<111> and a<100> Burgers vectors. The procedures have been tried on two irradiated pressurized tube specimens of JFMS steel irradiated in the FFTF/MOTA. Analysis of results for the specimen irradiated at a stress of 86 MPA indicates differences in Burgers vector anisotropy as large as a factor of 8.

FUTURE WORK

This work will be continued, concluding analysis of micrographs from the present study and examining irradiated oressurized tubes of other martensitic steels.

REFERENCES

1. A. Kohyama and R. J. Puigh, "Irradiation Creep Behavior of a Japanese Ferritic Steel," FFTF/MOTA Annual Proqress Report, Fusion Year 1988 (National Institute for Fusion Research, Nagoya, June 1989) 180.

2. D. S. Gelles in Effects of Radiation on Materials: Twelfth International Symposium, ASTM STP 870, Vol. I, F. A. Garner and J. S. Perrin, Eds. (ASTM, Philadelphia, 1985) 98.

3. E. Orowan in Proceedinss, Physical Society, Vol. 52 (1940) 8

4. D. S. Gelles in Radiation-Induced Changes in Microstructure: 13th International Symposium (Part I), ASTM STP 955, F. A. Garner, N. H. Packan and A. S. Kumar, Eds., (ASTM, Philadelphia, 1987) 560.

5. D. S. Gelles and L. E. Thomas in Alloy Development for Irradiation Performance Semiannual Progress Report for the Period Ending March 31, 1982, DOE/ER-0045/8, 343.

6. P. J. Maziasz, J. Nucl. Mater., V. 169 (1989) 95.

FERRITIC/MARTENSITIC STEELS: PROMISES AND PROBLEMS

(R. L. Klueh, Oak Ridge National Laboratory, K. Ehrlich, Kernforschungszentrum Karlsruhe, and F. Abe, Tsukuba Laboratories)

OBJECTIVE

The **goal** of this work is a review and evaluation of our present understanding of the status of ferritic steels as candidate materials for fusion reactors.

SUMMARY

Ferritic/martensitic steels are candidate structural materials for fusion reactors because of their higher swelling resistance, higher thermal conductivity, lower thermal expansion, and better liquid-metal compatibility than austenitic steels. Irradiation effects will ultimately determine the applicability of these steels, and the effects of irradiation on microstructure and swelling, and on the tensile, fatigue, and impact properties of the ferriticlmartensitic steels are discussed. Most irradiation studies have been carried out in fast reactors, where little transmutation helium forms. Helium has been shown to enhance swelling and affect tensile and fracture behavior, making helium a critical issue, since high helium concentrations will be generated in conjunction with displacement damage in **a** fusion reactor. These issues are reviewed to evaluate the status of ferriticlmartensitic steels and to assess the research required to insure that such steels are viable candidates for fusion applications.

PROGRESS AND STATUS

1. Introduction

Since the late 1970s, ferriticlmartensitic Cr-Mo steels have been considered alternate candidate structural materials to austenitic stainless steels for first wall and blanket structure applications for fusion reactors.[1,2] This choice followed irradiation studies in fast reactors that showed these steels to he more swelling resistant than austenitic steels. The steels **also** have higher thermal conductivity and lower thermal expansion than the austenitic steels, which provide improved resistance to thermal stresses for a reactor operating in a pulsed mode.'.'

An early concern for ferritic steels involved magnetostatic forces exerted on ferromagnetic components due to magnetic fields in the reactor. Field perturbations caused by the induced magnetic field of the ferromagnetic structure are also possible. Design studies indicated that stresses by magnetic forces must be accounted for, but can he managed.',' Attaya et al. showed that field perturbations in two conceptual designs for a tandem mirror reactor were end effects on the order of field ripples.' Magnetostatic loads were found to be small, but could not be ignored in the design of the blanket structure? Similar conclusions were reached for a tokamak design."

Compatibility **of** ferriticlmartensitic steels with potential breeder and coolant materials has been investigated. Liquid lithium and Pb-Li eutectic have received the most attention. Such studies indicate that ferritic steels corrode at rates ***5*** to 10 times slower than austenitic stainless steels.'

Work on ferriticlmartensitic steels for fusion has involved studies on the effect of irradiation on swelling, microstructure, and mechanical properties. Since no fusion test facility is available, irradiation studies are conducted in fission reactors or ion accelerators. Fission reactors can simulate displacement damage from neutrons in **a** fusion reactor. However, neutrons in a fusion reactor will have energies considerably higher than those in a fast reactor, and these high-energy neutrons will produce large amounts of transmutation helium in fusion reactor components. It is therefore necessary to investigate the effects of simultaneously produced displacement damage and transmutation helium on properties.

In this report, we will concentrate on irradiation effects on microstructure and mechanical properties, because these effects will determine whether ferriticlmartensitic steels are viable structural materials for fusion. We will not attempt to review all studies conducted, but rather, we will concentrate on the present understanding and indicate the research necessary to ensure that these steels meet the requirements for fusion.

2. Steels of interest

2.1. Cr-Mo steels

Various conventional Cr-Mo steels were considered in the late 1970s and early 1980s by the different research programs throughout the world? Although these steels contain alloying elements other than Cr and Mo, they will be referred to as Cr-Mo steels, because other elements, such as V, W, Nb, etc., are present in much smaller amounts. Steels with nominally 12% Cr, 0.5-1% Mo and **0.15-0.3%** V (all concentrations are wt %) included: DIN 1.4922/1.4923 in Germany, FV607 and CRM-12 in England, and Sandvik HT9 in the United States; steels with 9-12% Cr, 0.5-2% Mo, 0.15-0.3% V and 0.06-0.35% Nb included FV 448 in England, DIN 1.4914 in Germany, EM12 in France, JFMS (Japanese Ferritic Martensitic Steel) in Japan, 1KH12M2S2 in USSR, and modified 9Cr-1Mo (T91) in the United States.

In recent years, fusion research programs have concentrated on a more limited number of steels. Within the European Communities (EC) technology program, the martensitic DIN 1.4914 was chosen for study in 1983 and designated MANET (Martensitic Alloy for Next European Torus). Since then, an optimization program was initiated to improve the steel for fusion applications.6 Chromium and carbon were reduced to minimize radiation-induced precipitation and improve welding. Nitrogen was added to compensate for the **loss** of strength caused by the reduction of carbon. Low specification levels were set for phosphorous and sulphur to eliminate anisotropic impact properties, and zirconium was added to reduce the effect of sulphur on toughness.

Work in Japan has concentrated on JFMS, a 10Cr-2MoVNb steel, while U.S. work has been primarily on Sandvik HT9 (designated here as 12Cr-1MoVW) and modified 9Cr-1Mo (designated 9Cr-1MoVNb), with limited work on 2¼Cr-1Mo steel. The steels in the Japanese and U.S. programs were developed for elevated-temperature service in the fossil-fired and nuclear fission power applications. The USSR program is investigating several 9-12% Cr steels.' Table 1 lists compositions being considered by the various programs.

Table 1. Nominal Composition in Weight Percent of Conventional Ferritic/Martensitic Steels for Fusion Applications

Program	Designation	Cr	Mo	V	W	Nb	C	Si	Mn	Ni	N
EC	MANET (DIN 1.4914)	12	0.5	0.3		0.25	0.1	0.5	0.35	0.7	0.003
USSR	1KH12M2S2	12.5	1.5				0.15	1.8	0.4	0.2	
Japan	JFMS	10	2	0.1		0.06	0.05	0.7	0.6	1	0.01
U.S.	9Cr-1MoVNb	9	1	0.25		0.08	0.1	0.4	0.5		0.05
	12Cr-1MoVW (Sandvik HT9)	12	1	0.3	0.5		**0.2**	**0.4**	0.6	*0.5*	

2.2 Reduced-activation steels

In the mid 1980s, programs to develop reduced-activation ferritic steels began in Europe, Japan, the Soviet Union, and the United States?'' Calculations were made to determine which elements must he replaced in conventional Cr-Mo steels to obtain a rapid decay of induced radioactivity levels after irradiation in a fusion reactor.[8,9] Such calculations indicate that Mo, Nb, Ni, Cu, and N must be eliminated or minimized. Proposals for reduced-activation ferritic steels involved the replacement of molybdenum in conventional Cr-Mo steels by vanadium[10,15,18] and/or tungsten.[11,13-17]

Programs in Japan, the EC, and the United States have developed Cr-V and Cr-W-V steels,''.'' to which tantalum is sometimes added as a replacement for niobium.[11,13,14,17,19] Martensitic steels with 7-9% Cr have been favored over 12% Cr steels, because of the difficulty of eliminating 6-ferrite in a 12% Cr steel without increasing carbon or manganese for austenite stabilization. Delta-ferrite can lower toughness, and manganese promotes chi-phase precipitation during irradiation, which can cause embrittlement.[18] Low-chromium (2.25% Cr) bainitic steels are also being considered.[10,11,18,19] Table 2 lists compositions that have shown promise.

Table 2. Nominal Composition in weight percent of Selected Reduced Activation/Ferritic/Martensitic Steels for Fusion Applications

Program	Designation	Cr	V	W	Ta	C	Si	Mn	N	B
EC	LA12Ta	9.8	0.25	3	0.1	0.16	0.03	0.8	0.045	
	CETA[a]	9.6	0.6	0.8	0.5	0.18	0.07	1.4	0.015	0.008
Japan	F82H	8	0.2	2	0.04	0.1	0.2	0.5	0.002	0.003
	Mod. 9Cr-1W	9	0.2	1		0.1	0.13		0.003	0.005
	Mod. 9Cr-3W	9	0.2	3		0.1	0.17		0.003	0.007
	JLF-4	2.25	0.2	2	0.07	0.1	0.5	0.05	0.005	
U.S.	L5 (9Cr-1V)	9		1		0.1	0.3	0.5	0.002	
	L7 (9Cr-1W)	9		1		0.1	0.3	0.5	0.002	
	GA3X	7.5	0.02	2		0.17				
	2¼Cr-2WV	2.25	0.25	2		0.1	0.2	0.4		
	9Cr-2WVTa	9	0.25	2	0.07	0.1	0.25	0.4		

[a]Also contains 0.13 Ce.

3. Irradiation effects

3.1 Irradiation effects on microstructure and swelling

The 9-12% Cr steels are used in a normalized-and-tempered or quenched-and-tempered condition. Steels with up to 1%Mo and ≈0.1% C are essentially 100% tempered martensite, which retains the martensite lath Structure with the dislocation density determined by the tempering conditions. Steels with higher molybdenum concentrations andlor other ferrite stabilizers (e.g., tungsten) and without additional austenite stabilizers contain 6-ferrite (e.g., JFMS with 9% Cr and 2% Mo contains ≈25% δ-ferrite; HT9 with 1% Mo and 0.5% W contains 0.5% Ni and 0.2% C to eliminate δ-ferrite, although the steel sometimes contains small amounts of 6-ferrite).

Precipitate reactions that occur during tempering, thermal aging, and irradiation affect the properties.[20-28] Vitek and Klueh" showed that essentially all carbon in solution precipitates when normalized 9Cr-1MoVNb and 12Cr-1MoVW steels are tempered 1 h or more at 700-780°C, the tempering temperature range used for this type of steel. The major precipitate in the high-chromium Cr-MoV and Cr-MoVNb steels is $M_{23}C_6$, with lesser amounts of MC[20-28]; M_2X has been observed in tempered steels containing δ-ferrite.[22,23] Laves phase is the only new phase that forms during thermal aging between 300 and 650°C; it forms between 450 and 650°C in 10 000 h (refs. 21-24).

It is the disposition of the vacancies and interstitials formed by high-energy neutrons--the displacement damage--that is the major effect that irradiation has on the steels. There are few observations of dislocation structures formed below ≈300°C. Agueev et al.[22] observed that dislocation loop formation in a 13Cr-2MoVNbB steel depended on temperature for fast reactor irradiation to 10 to 40 dpa. For temperatures below 380°C, loop size remained constant at approximately 20 nm diameter. Loop size increased and loop number density decreased with increasing temperature. Loops were unstable above 520°C, and so the network dislocation density remained similar to that in the tempered condition or decreased with irradiation. Similar observations were made by Maziasz et al. for 9Cr-1MoVNb and 12Cr-1MoVW steels irradiated to ≈40 dpa at 300 to 600°C.[25]

In addition to displacement damage, precipitate changes caused by irradiation can also affect properties. There have been several studies of Cr-Mo steels irradiated in fast reactors or mixed-spectrum reactors at 300 to 650°C and up to 70 dpa (refs. 21,22,25,26). These studies indicate the formation of considerable irradiation-induced precipitation below ≈450°C. Precipitates identified include: G-phase (ref. 26), α′ (refs. 22, 26) M_6C (refs. 21, 25), and chi-phase.[25,26] Precipitation is superimposed on the as-tempered precipitates and the tempered martensite substructure, which generally remains stable, although the 9Cr-1MoVNb steel substructure was unstable and coarsened during irradiation at 300 to 500°C." Laves phase, which forms during thermal aging at 400 to 600°C[21-25] and can cause embrittlement,[23] does not form if the steels are irradiated below 600°C.[21,22,25,26]

One attraction of ferritic steels is their reduced tendency toward void swelling. Gelles and co-workers studied several steels irradiated in the Experimental Breeder Reactor (EBR-II) to 70 dpa at 400 to 650°C,[26,27,29] including 2¼Cr-1Mo, H-11 (5Cr-1.3Mo-0.9Si-0.5V-0.4C), 9Cr-1MoVNb, 12Cr-1MoVW (Sandvik HT9), AISI 416 (13Cr-0.25Mo-0.4Mn-0.3Ni-0.5Si-0.1C), AISI 430F (18Cr-0.4Mn-0.5Si-0.04C), and EM-12 (9Cr-2MoVNb). Voids were observed in only 2¼Cr-1Mo and EM-12 at 400 to

450°C (a few helium bubbles were observed at 650°C). The EM-12 was the only steel that showed significant swelling by densitometry, hut its swelling rate was one-twentieth that of austenitic steels.[26]

Although Gelles and Thomas observed no voids for 12Cr-1MoVW steel irradiated to 70 dpa in EBR-II,[26] a few scattered voids formed in another heat irradiated in the Fast Flux Test Facility (FFTF) at 420°C[27,29] in two different heat treatment conditions. After irradiation to 114 dpa at 420°C, voids were non-uniformly distributed, and swelling varied from 0.24 to 0.7% for one heat-treatment condition (four TEM measurements) and from 0.78 to 0.9% (two measurements) for the other condition. Heat treatment was considered a possible cause for the variation, but the precipitate distribution and dislocation structures were similar for the two conditions. A swelling rate of 0.015%/dpa was estimated between 50 and 114 dpa for the 0.9% change, a much lower rate than the 0.1-1%/dpa found in austenitic steels.

Maziasz and Klueh[30] investigated the effect of helium on swelling by irradiating 9Cr-1MoVNb and 12Cr-1MoVW steels and these steels with 2% Ni (9Cr-1MoVNb-2Ni and 12Cr-1MoVW-2Ni) in the High Flux Isotope Reactor (HFIR). Thermal neutrons in the mixed-neutron spectrum of HFIR react with ^{58}Ni to produce transmutation helium. (Irradiating a steel with 2% Ni in HFIR results in a Heidpa ratio similar to that expected in a tokamak.) By comparing microstructures of the nickel-doped steels irradiated at 400°C in HFIR (≈37 dpa, 400 appm He) with those irradiated at 407°C in FFTF (47 dpa, ≈5 appm He), it was concluded that increases in the He/dpa ratio enhanced the formation of large, bias-driven voids. Furthermore, after irradiation in HFIR, the extent of void formation depended on nickel concentration. an indication that helium affected void formation, since nickel had no significant effect on microstructure.'"

Gelles and Kohyama questioned this conclusion,[29] based on the observation that no voids formed after 70 dpa in EBR-II, but a few did form in a different heat after 34 dpa[27] and many formed after 114 dpa[29] in FFTF. They concluded that significant helium was not required for void formation and argued that the behavior appeared to be different even in different fast reactors (EBR-II vs. FFTF). Since different heats of 12Cr-1MoVW were irradiated in EBR-II[26] and FFTF[27,29] an alternate explanation might be differences in dissolved gas concentrations (e.g., O or N) in the two heats. Such gases can play a role similar to helium in nucleating voids."

Gelles and Kohyama" compared FFTF results for 12Cr-1MoVW steel irradiated to 114 dpa with dual ion-beam irradiations by Asano et al.[32] to 100 dpa and 15 appm He. The latter studies showed a density change of only 0.14%, compared to the high of 0.9% observed in FFTF. With 100 dpa and 5 appm He, only small cavities formed in the high-damage-rate ion-beam experiments. However, no cavities formed without helium, and Asano et al. concluded that helium was required for cavity formation." Despite these observations, Gelles and Kohyama implied helium might still not be a factor in FFTF by stating," "...in those materials where precipitation that formed during irradiation plays a role in microstructural development, care must be taken in interpreting the results of high-damage-rate irradiation." As stated above, other gases besides helium (or in addition to helium) can play a role in void formation.

A set of Cr-V, Cr-W, and Cr-W-V-Mn reduced-activation steels was examined by Gelles after irradiation to 114 dpa in FFTF.[18] Qualitatively, the precipitation and swelling behavior was similar to that for the Cr-Mo steels.

3.2. Mechanical properties after irradiation

Most work on effects of irradiation on mechanical properties has involved tensile, fatigue, and impact properties, and these properties will be discussed, Irradiation creep has been studied on 9Cr-1MoVNb and 12Cr-1MoVW steels," but will not be discussed because of space limitations.

3.2.1. Tensile properties

The effect of irradiation on the tensile behavior of ferriticimartensitic steels depends on temperature.[34-37] An increase in yield stress occurs at irradiation temperatures up to 425-450°C. This hardening is caused by the high density of dislocation loops and tangles that form from displacement damage, along with irradiation-induced precipitate changes.[21,22,25,26,30] Hardening saturates with increasing fluence, and saturation occurs by 10 dpa.[35] For irradiation above ≈425-450°C, properties are generally unchanged, hut there may be enhanced softening, depending on fluence.[34,35] At these temperatures, there is either little change in the microstructure, or precipitates begin to coarsen. Irradiation enhances diffusion and/or precipitate redistribution, which can enhance coarsening, and thus, enhance softening.

A limited number of reduced-activation steels have been irradiated in fast reactors, and the results are similar to those observed for the Cr-Mo steels.[18,38,39] Abe et al.[39] conducted recovety studies on 9Cr-3WVTa and 9Cr-1MoVNb steel that emphasize this behavior, After irradiation in the Japan Materials Test Reactor (JMTR) at 265°C to produce increases in yield stress of 109 and 159 MPa for 9Cr-3WVTa and 9Cr-1MoVNb, respectively, the irradiated specimens were annealed. With increasing annealing temperature, the yield stress first increased slightly up tu 400°C and then decreased abruptly from 400 to

600°C. The recovery of hardening correlated with the annealing out of irradiation-produced defects or defect clusters, and the recovery temperatures were similar to the irradiation temperatures at which the effects of irradiation change from hardening to softening.

To determine whether helium affects tensile properties, 9Cr-1MoVNb, 9Cr-1MoVNb-2Ni, 12Cr-1MoVW, 12Cr-1MoVW-1Ni, and 12Cr-1MoVW-2Ni steels were irradiated in HFIR.[36,37,40] Irradiation at ≈50°C to ≈25 dpa and 327 appm He indicated that helium affected the hardening.[36] Figure 1 shows the results for 12Cr-1MoVW and 12Cr-1MoVW-1Ni steels. The 12Cr-1MoVW-1Ni steel developed twice as much helium, and Fig. 1 indicates that both displacement damage and helium affect the yield stress increase. Above ≈5 dpa, the rate of strength increase with fluence decreased as the damage level increased, indicating that saturation is being approached.[36]

Evidence also exists that helium affects strength at 400°C (Table 3).[37,40] Specimens of the nickel-doped and undoped steels tested at 400°C after irradiation in HFIR at 400°C to 8-11 dpa (7-80 appm He)[37] showed a larger increase in strength after HFIR irradiation than after irradiation in EBR-II at 390°C to 16 dpa (<3 appm He).[41] Therefore, the saturation with fluence observed in EBR-II did not apply for HFIR irradiation. The largest increases occurred in the steels with 2% Ni, strongly suggesting that helium causes an increment of hardening,[37,40] in addition to the hardening caused by displacement damage alone.[41] Irradiation of the nickel-doped steels in HFIR to 37-72 dpa further supported the conclusion that helium affects strength.[40] When these data were compared with 8-11 dpa data, an increase in yield stress occurred for the 9Cr-1MoVNb and 12Cr-1MoVW steels irradiated to the higher dpa (Table 3). However, no further hardening occurred in the steels with 2% Ni. After the high-fluence irradiation, there was also no difference between the yield stress of the 12Cr-1MoVW and 12Cr-1MoVW-2Ni steels, but there was a difference between the 9Cr-1MoVNb and 9Cr-1MoVNb-2Ni steels.[40]

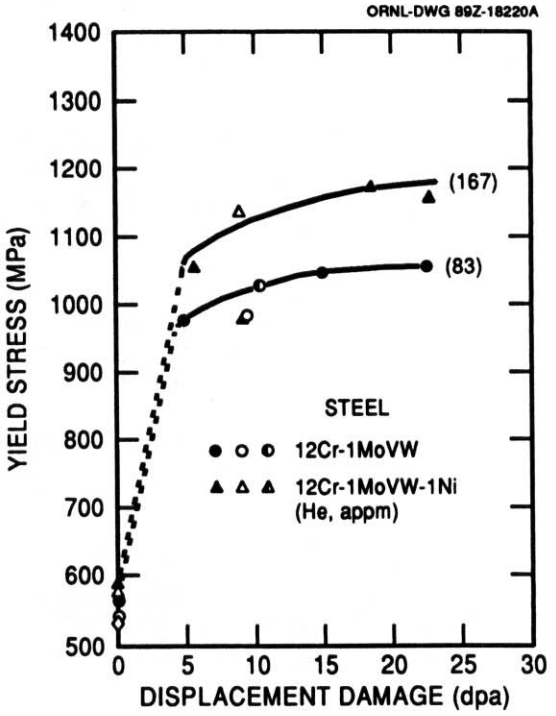

Fig. 1. The yield stress of 12Cr-1MoVW and 12Cr-1MoVW-1Ni steels as a function of fluence after irradiation in HFIR at ≈50°C (numbers in parentheses are helium concentrations for ≈25 dpa).

Table 3. Yield Stress of Steels Irradiated in HFIR

	9Cr-1MoVNb		9Cr-1MoVNb-2Ni		12Cr-1MoVW		12Cr-1MoVW-2Ni	
	He (appm)	YS (MPa)	He (appm)	YS (MPa)	He (appm)	YS (MPa)	He (appm)	YS (MPa)
EBR-II	<3	687	<3	729	<3	794	<3	808
HFIR (8-11 dpa)	7	881	77	1098	15	929	80	1056
HFIR (37-72 dpa)	37	937	456	1039	129	1070	598	1062

These data indicate that hardening due to helium saturates, and saturation occurs by 80 appm He. This follows because the 9Cr-1MoVNb-2Ni and 12Cr-1MoVW-2Ni contained ≈80 appm He after 8-11 dpa,[37] and there was no further increase in yield stress for these two steels during the high-dose (37-72 dpa) experiment.''' After the high-dose experiment, the 12Cr-1MoVW steel contained >80 appm He, and the yield stress was equivalent to that for 12Cr-1MoVW-2Ni steel, indicating that the steels with and without nickel ultimately saturate at the same strength level. The saturation to a common strength level for Steel with and without the 2% Ni addition also occurred during EBR-II irradiation, but at a lower strength (Table 3). The yield Stress of 9Cr-1MoVNb after the high-dose experiment was less than that for 9Cr-1MoVNb-2Ni. However, the 9Cr-1MoVNb contained only 37 appm He, less than the 80 appm required for saturation.

Irradiation hardening, therefore. saturates with tluence when hardening is due to displacement damage alone (EBR-II)[41] and Saturates at a higher level when displacement damage and helium are co-produced (HFIR).[40] Hardening caused by helium should saturate if it is due to helium atoms themselves or due to excess interstitial atoms caused by helium-vacancy cluster formation, which could present a harrier to recombination.'''

The effect of irradiation on tensile ductility, with and without helium, directly reflects the effect on strength.[34-41] Uniform and total elongation of the specimens irradiated at 55 to 400°C were slightly less than for unaged and aged controls. Above 450°C, there was little effect of irradiation on ductility. In all cases, ductile-transgranular fracture is observed, and strength and ductility changes caused by irradiation should not affect the use of these steels for fusion.

Certain irradiated alloys that contain helium develop large ductility decreases after irradiation at a temperature $T_t > 0.6T_m$, where T_m is the absolute melting temperature. This elevated-temperature helium embrittlement is caused by intergranular fracture, and the loss of ductility is caused by helium on grain boundaries.'' For austenitic stainless steels, the effect can occur with the presence of only a few appm He. All indications are that ferriticimartensitic steels are not seriously affected by helium embrittlement,'' even at slow strain rates (creep).[34]

Hydrogen will also he generated in a fusion reactor first wall. The effect of hydrogen on tensile properties is being investigated by ion implantation, but to date no drastic effects have been observed.[42,43]

3.2.2 Fatigue Properties

Isothermal fatigue behavior under strain-controlled conditions from 20 to 650°C has been investigated in the EC program.'''' Results indicate that the temperature dependence oithe number of cycles to failure, N_f, is not very pronounced. Also, in contrast to austenitic steels, there is only a small reduction of N_f with decreasing strain rate. The effect of hold time is presently being studied.

Initial results on thermal fatigue—the realistic form of loading in a tokamak—are now available!' Under thermal loading, the strain range is produced by a temperature variation between T_{min} and T_{max} and is not constant over the full length of the test. However, if the data of N_f^{Th} for a mean temperature of 375-450°C are compared with isothermal data at 450°C, they are over an order of magnitude lower than the latter values (Fig.2). If such a comparison is based on the maximum temperature (e.g. 650°C), the number of cycles to failure of thermally cycled samples is still lower than that of the isothermal data.

The effect of irradiation on the isothermal fatigue behavior in post-irradiation tests is being studied in push-pull tests.[47,49] Irradiations with alpha-particles and light ions with different energies in single- and dual-beam facilities are used to produce the appropriate He/dpa relation. The studies show that for damage levels of a few dpa and several-hundred appm He (<400 appm), the isothermal fatigue behavior is not essentially changed from 20-450°C. These simulation studies with light ions have illuminated the microstructural development of MANET. As is true for neutron irradiation, radiation hardening occurs below ≈400°C, where helium clusters play an important role.[46,49,50] At higher temperatures, irradiation enhances recovery. More recent investigations on the effect of hold times on isothermal fatigue of MANET preimplanted with high helium amounts confirm this general trend.[49]

The only fatigue data on neutron-irradiated steels was obtained on 12Cr-1MoVW steel with and without nickel additions irradiated at 55°C in HFIR to ≈25 dpa and up to 400 appm He (ref. 51). Low-cycle fatigue tests at room temperature indicated that there was an effect of helium, although the hehavior after irradiation still remained as good or better than unirradiated 20% cold-worked 316 stainless steel.

3.2.3. Impact properties

Irradiation effects on toughness are the greatest concern for fusion applications of ferriticimartensitic steels. The effect is observed in a Charpy impact test as an increase in ductile-brittle transition temperature (DBTT) and a decrease in upper-shelf energy (USE).[7,52-56] Figure 3 is an example from Wassilew and Ehrlich for MANET irradiated to 5 dpa in the High Flux Reactor (Petten) at 300, 400, and 475°C[52]; the magnitude of the shift varies inversely with irradiation temperature. The effect

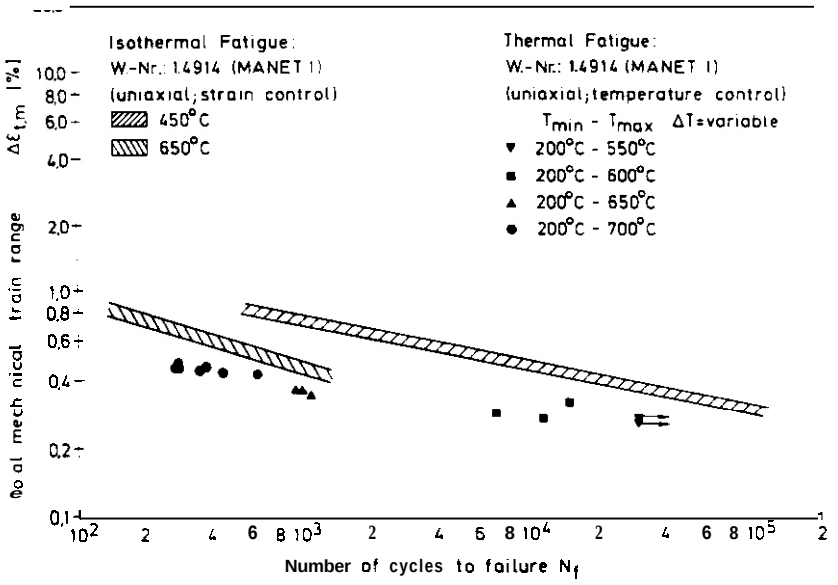

Fig. 2. Comparison of thermal fatigue data to isothermal strain-controlled fatigue for MANET steel.

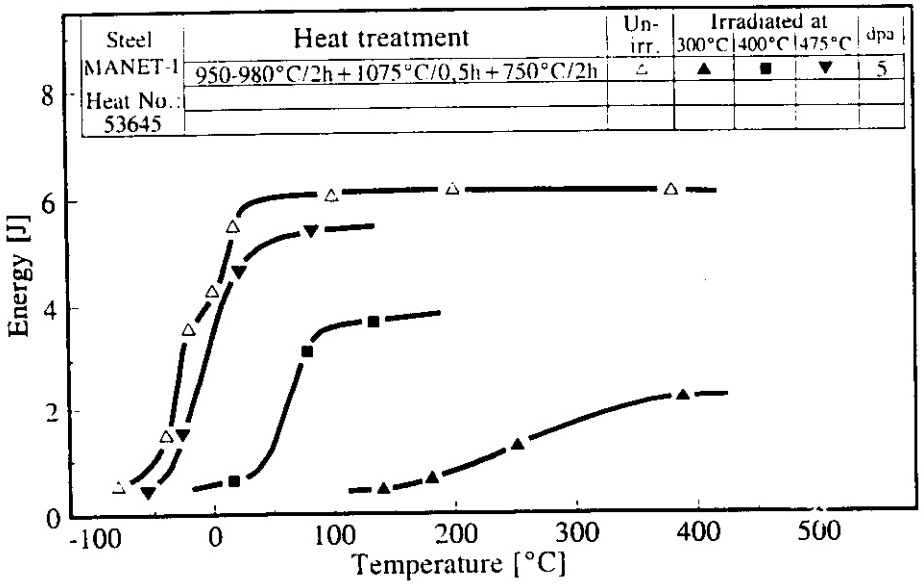

Fig. 3. Effect of irradiation temperature on the impact properties of **MANET** steel.

of irradiation can be affected by the normalizing-and-tempering treatment[11] and by the processing used on the steel during manufacture.[1] After irradiation at 300°C, part of the loss in USE was recovered by annealing for 0.5 h at 535°C.[11] Such an anneal would dissolve irradiation-induced defect structures (particularly tiny clusters and the dislocation component of the microstructure) that lead to hardening and cause the embrittlement.[22]

As shown by Hu and Gelles,[53] the shift in DETT (A DBTT) saturates with fluence. They irradiated 12Cr-1MoVW steel at 390°C in EBR-II to 13 and 26 dpa and observed $\Delta DBTT_S$ of 124 and 144°C, respectively; 9Cr-1MoVNb steel irradiated similarly developed shifts of 52 and 54°C, respectively.

Reduced-activation steels have been developed by optimizing compositions for strength and toughness,[1,2] in the hope that a low DBTI before irradiation would result in an adequately low DBTT after irradiation. Figure 4 shows the relationship between DBTI and 1000-h creep-rupture strength at 600°C in unirradiated Cr-WVTa and Cr-V reduced-activation steels developed in Japan.[3] For comparison, results on 9Cr-1MoVNb and 12Cr-1MoVW steels are shown. On the basis of optimized strength and toughness, the Cr-WVTa steels are improved significantly over the Cr-Mo and Cr-V steels.

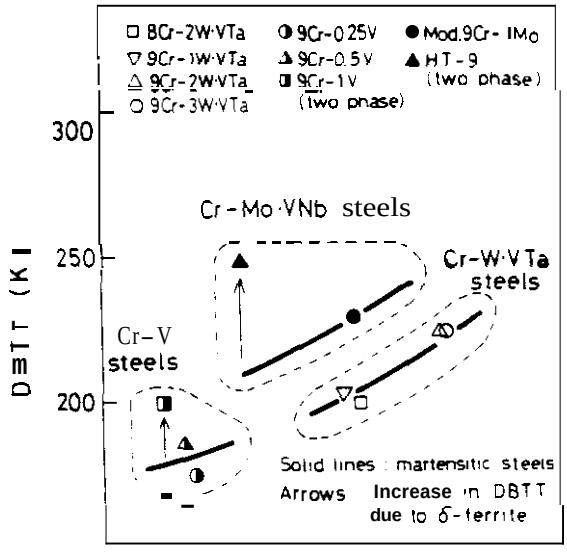

Fig. 4. Relationship between DBTT and creep-rupture strength for several reduced-activation ferriticlmartensitic Steels developed in Japan.

For reduced-activation steels with 2.25 to 12% Cr irradiated in a fast reactor to ≈10 dpa, steels with 7.5-10% Cr showed the smallest ΔDBTT.[18,58] A 9Cr-2WVTa steel irradiated to ≈7 dpa in FFTF had a ΔDBTT of only 4°C, one of the smallest shifts ever recorded for any ferriticlmartensitic steel for such irradiation conditions.[58] It compares with a shift of –160°C for 12Cr-1MoVW (HT9) for similar conditions. Tantalum plays a favorable role, presumably by refining the microstructure, because a 9Cr-2WV steel irradiated similarly had a ΔDBTT of 68°C.[58]

Helium appears to affect the impact behavior after irradiation. Irradiation of 12Cr-1MoVW in HFIR at 400°C to ≈9 dpa and ~25 appm He caused a ΔDBTT of 195°C.[54] When both 9Cr-1MoVNb and 12Cr-1MoVW steel were irradiated in HFIR at 400°C to ≈40 dpa. the ΔDBTT for the 9Cr-1MoVNb with ≈35 appm He was 204°C, while that for 12Cr-1MoVW with ≈110 appm He was 242°C.[3] Thus, the saturation with fluence of ≈54°C and 144°C for 9Cr-

Finally, a ΔDBTT of ≈350°C was observed for 9Cr-1MoVNb-2Ni and 12Cr-1MoVW-2Ni irradiated in HFIR to 40 dpa and ≈200 appm He. These differences between HFIR and EBR-II and between Ni-doped and undoped steels were attributed to helium.[54-56]

To obtain information on fracture mode, irradiated TEM specimens are being fractured after cooling in liquid nitrogen.[3] Such a fracture would presumably occur on the lower shelf of irradiated specimens. Preliminary observations on a 12Cr-1MoVW-2Ni disk irradiated in HFIR to ≈74 dpa and 760 appm He [Fig. 5(a)] indicated that over 50% of the fracture was intergranular, compared to a normalized-and-tempered specimen where there was no indication of intergranular fracture [Fig. 5(b)]. Thus, although hardening by helium saturates hy ≈80 appm He (ref. 40), a change in fracture mode determines the effect of helium on toughness. This implies that irradiation in HFIR lowers the fracture stress. Apparently, helium agglomerates on prior-austenite grain boundaries or lath boundaries to cause intergranular fracture. More fractography is required to verify this.

Such observations on helium effects are important for a fusion reactor first wall, where large amounts of helium will form. Therefore, the use of martensitic steels for fusion reactors will need to he reevaluated, particulary if a saturation in ΔDBTT does nut occur without a substantial further increase in the DBTT over that observed in the preliminary tests.[54-56]

4. Summary

Ferritic/martensitic steels are candidate structural materials for fusion applications because of their advantages over austenitic stainless steels. Conventional Cr-Mo steels have been studied for over ten years. Reduced-activation steels that do not contain molybdenum or niobium are being developed that have unirradiated and irradiated properties as good or better than those of conventional ferriticlmartensitic steels.

After irradiation to high dpa levels in the absence of large amounts of helium, the ferriticlmartensitic steels have low swelling rates and tensile and fracture properties remain adequate. Irradiation experiments where displacement damage and helium are simultaneously produced in the steel suggest that increased helium can negatively affect swelling, tensile behavior, and impact toughness. Even for high Heldpa ratios, swelling rates remain low, and tensile properties are adequate. However, helium markedly degrades fracture properties relative to displacement damage alone.

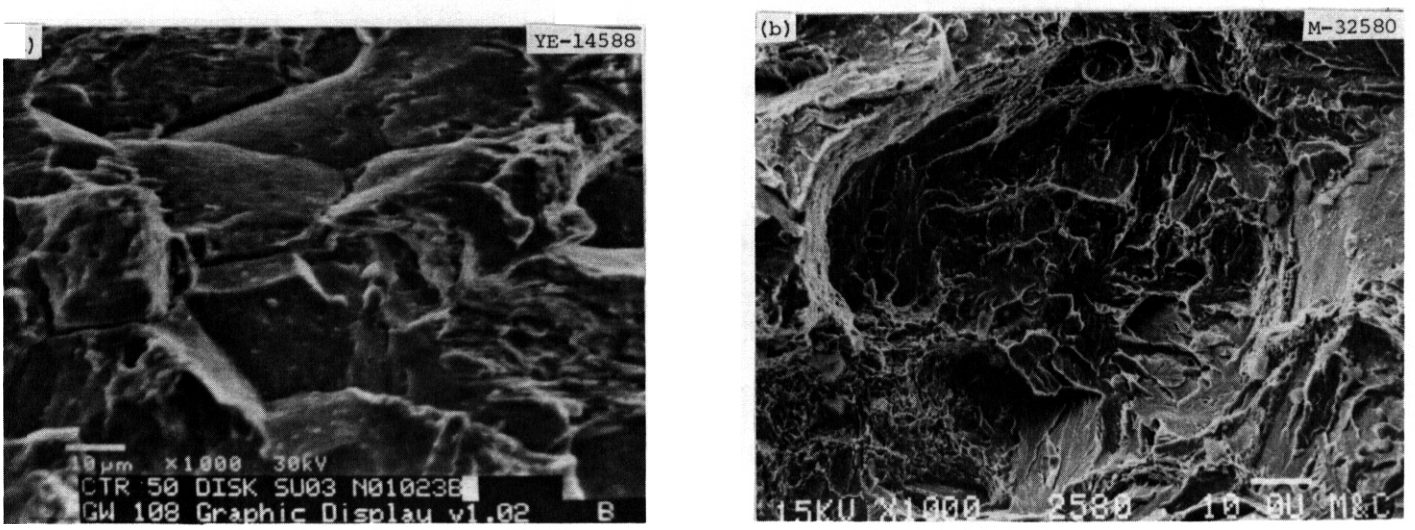

Fig. 5. Scanning electron micrographs of 12Cr-1MoVW-2Ni fractured after cooling with liquid nitrogen: (a) irradiated in HFIR at 400°C to 74 dpa and 760 appm He; (b) as normalized and tempered.

Future wnrk must be directed at understanding the effect of helium and He/dpa ratio, with emphasis on fracture properties. Steel compositions must be developed that maintain impact toughness during irradiation.

References

1. S. N. Rosenwasser et al., J. Nucl. Mater. 85 & 86 (1979) 177.

2. D. R. Harries, in: Proceedings of Topical Conference on Ferritic Steels for use in Nuclear Energy Technologies (The Metallurgical Society of AIME, Warrendale, PA, 1984) p. 141. This proceedings contains other papers on femtic steels for fusion; see: pp. 141-223, 291-329, and 551-631.

3. H. Attaya, K. Y. Yuan, W. G. Wolfer, and G. L Kulcinski, ibid, p. 169.

4. T. Lechtenberg, C. Dahms, and H. Attaya, ibid, p. 179.

5. H. S. Tas, F. Malang, F. Reiter, and J. Sannier, J. Nucl. Mater. 155-157 (1988) 178.

6. K. Anderko, et al., in: Proceedings of Topical Conference on Ferritic Steels for use in Nuclear Energy Technologies (The Metallurgical Society of AIME, Warrendale, PA, 1984) p. 299.

7. V. K. Shamardin et al., in: Proceedings of an International Conference on Radiation Materials Science (Kharkov Institute of Physics and Technology, Kharkov, 1990); also ORNL/TR 90/22.

8. R. W. Conn et al., Panel Report on Low Activation Materials for Fusion Applications, UCLA Report PPG-728, (University of California at Los Angeles, 1983).

9. G. J. Butterworth and O. N. Jarvis, J. Nucl. Mater., 122 & 123 (1984) 982.

10. N. M. Ghoniem, A. Shabaik, and M. Z. Youssef, in: Proceedings of Topical Conference on Femtic Steels for use in Nuclear Energy Technologies (The Metallurgical Society of AIME, Warrendale, PA, 1984) p. 201.

11. R. L. Klueh and E. E. Bloom, Nucl. Eng. Design/Fusion, 2 (1985) 383.

12. D. S. Gelles, in: Optimizing Materials for Nuclear Applications, Eds. F. R. Garner, D. S. Gelles, and F. W. Wiffen (The Metallurgical Society, Warrendale, PA, 1985) p. 63.

13. D. Dulieu, K. W. Tupholme, and G. J. Butterworth, J. Nucl. Mater., 141-143 (1986) 1097.

14. M. Tamura et al., ibid 1067.

15. T. Noda, F. Abe, H. Araki, and M. Okada, ibid 1102.

16. C. Y. Hsu and T. A. Lechtenberg, ibid 1107.

17. K. Anderko et al., Investigations on the Physical Metallurgy and Mechanical Properties of a LA-10% Cr steel CETA, KfK Report, Kernforschungszentrum Karlsruhe GmbH, to be published.

18. D. S. Gelles, in: Reduced Activation Materials for Fusion Reactors, ASTM STP 1047, Eds. R. L. Klueh,. D. S. Gelles, M. Okada, and N. H. Packan (ASTM, Philadelphia, 1990) p. 113.

19. H. Kayano et al., J. Nucl. Mater., 179-181 (1991) 425.

20. J. M. Vitek and R. L. Klueh, Met. Trans. A 14A (1983) 1047.

21. E. A. Little and L. P. Stoter, Effects of Radiation on Materials Proceedings of Eleventh International Symposium, ASTM STP 782, Eds. H. R. Brager and J. S. Perrin (American Society for Testing and Materials, Philadelphia, 1982) pp. 207.

22. V. S. Agueev et al., in: Effects of Radiation on Materials: 14th International Symposium, Vol. I, ASTM STP 1046, Eds. N. H. Packan, R. E. Stoller, and A. S. Kumar, (ASTM, Philadelphia, 1989) p. 98.

23. Y. Hosoi et al., J. Nucl. Mater. 141-143 (1986) 461.

24. P. J. Maziasz and V. K. Sikka, in: Alloy Development for Irradiation Performance, DOE/ER-0045/15, USDOE Office of Fusion Energy, Washington, DC (September 1985) p. 102.

25. P. J. Maziasz, R. L. Klueh, and J. M. Vitek, J. Nucl. Mater. 141-143 (1986) 929.

26. D. S. Gelles and L. E. Thomas, in: Proceedings of Topical Conference on Ferritic Steels for use in Nuclear Energy Technologies (The Metallurgical Society of AIME, Warrendale, PA, 1984) p. 559.

27. C. Y. Hsu, D. S. Gelles, and T. A. Lechtenberg, in: Radiation-Induced Changes in Microstructure, ASTM STP 955, Eds. F. A. Garner, N. H. Packan, and A. S. Kumar, (ASTM, Philadelphia, 1987) p. 545.

28. E. Materna-Morris, M. Schirra, and K. Ehrlich, in: Materials for Nuclear Reactor Core Applications (BNES, London, 1987) p. 263.

29. D. S. Gelles and A. Kohyama, in: Fusion Reactor Materials Semiannual Progress Report, USDOE ER/0313/6 (March 31, 1989), USDOE Office of Fusion Energy, Washington, DC, p. 193.

30. P. J. Maziasz and R. L. Klueh in: Effects of Radiation on Materials: 14th International Symposium, Vol. I, ASTM STP 1046, Eds. N. H. Packan, R. E. Stoller, and A. S. Kumar, (ASTM, Philadelphia, 1989) p. 35.

31. K. Farrell, Radiation Effects, 53 (1980) 175.

32. K. Asano et al, J. Nucl. Mater., 155-157 (1988) 912.

33. F. A. Garner and R. J. Puigh, J. Nucl. Mater. 179-181 (1991) 577.

34. C. Wassilew and K. Herschbach, in: Proceedings of Topical Conference on Ferritic Steels for use in Nuclear Energy Technologies (The Metallurgical Society of AIME, Warrendale, PA, 1984) p. 607.

35. R. L. Klueh and J. M. Vitek, J. Nucl. Mater. 182 (1991) 230.

36. R. L. Klueh and J. M. Vitek, J. Nucl. Mater. 161 (1989) 13.

37. R. L. Klueh and J. M. Vitek, J. Nucl. Mater. 132 (1985) 27.

38. R. L. Klueh, J. Nucl. Mater., 179-181 (1991) 728.

39. F. Ahe et al., J. Nucl. Mater., 191-194 (1992), in press.

40. R. L. Klueh and P. J. Maziasz, J. Nucl. Mater., 187 (1992) 43-54.

41. R. L. Klueh, P. J. Maziasz, and J. M. Vitek, J. Nucl. Mater. 141-143 (1986) 960.

42. H. Schroder and H. Ullmaier, J. Nucl. Mater., 179-181 (1991) p. 118.

43. K. K. Bae, K. Ehrlich, and A. Moslang, J. Nucl. Mater., 191-194 (1992). in press

44. W. Scheibe and R. Schmitt, KfK-Report 4944, Karlsruhe (October 1991).

45. P. Marmy, Y. Ruan, and M. Victoria, PSI-Report 37, Paul Scheerer Institute (August 1989).

46. C. Petersen et al., KfK Report 4944, Karlsruhe (October 1991).

47. A. Moslang, D. Preiniger, and K. Ehrlich, Proceedings All-Union Conf. on Effect of Irradiation on Materials for Fusion Reactors (Leningrad, USSR) to he published.

48. A. Marmy and M. Victoria, J. Nucl. Mater., 191-194 (1992), in press.

49. A. Moslang and R. Lindau, J. Nucl. Mater., 191-194 (1992), in press.

50. U. Stamm, KfK-Report, JUL-2225, Karlsruhe (1988).

51. M. L. Grossheck, J. M. Vitek, and K. C. Liu, J. Nucl. Mater., 141-143 (1986) 966.

52. C. Wassilew and K. Ehrlich, J. Nucl. Mater., 191-194 (1992), in press.

53. W. L. Hu and D. S. Gelles, in: Influence of Radiation on Material Properties: 13th International Symposium (Part 11), ASTM STP 956, F. A. Garner, C. H. Henager, Jr., and N. Igata, Eds. (American Society for Testing Materials, Philadelphia, 1987) p. 83.

54. J. M. Vitek, W. R. Corwin, R. L. Klueh, and J. R. Hawthorne, J. Nucl. Mater. 141-143 (1986) 948

55. R. L. Klueh and D. J. Alexander, J. Nucl. Mater., 179-181 (1991) 733.

56. R. L. Klueh and D. J. Alexander, J. Nucl. Mater., 187 (1992) 60.

57. F. Abe, Proceedings of the Workshop on Low Activation Materials, IEA Report EUR FU BRU/XII-6/91-MATIA 16 (June 1991).

58. R. L. Klueh, D. J. Alexander, and P. J. Maziasz, J. Nucl., 186 (1992) 185.

6.2 Austenitic Stainless Steels

INTERACTION OF IRRADIATION CREEP AND SWELLING IN THE CREEP DISAPPEARANCE REGIME - F. A. Garner, Pacific Northwest Laboratory' and M. B. Toloczko, University of California at Santa Barbara

OBJECTIVE

The objective of this effort is to determine the relationship between applied stresses and irradiation-induced dimensional changes in structural metals for fusion applications.

SUMMARY

Reanalysis of an earlier data set derived from irradiation of long creep tubes in EBR-II at 550°C has shown that the creep-swelling coupling coefficient is relatively independent of temperature at $\sim 0.6 \times 10^{-2}$ MPa^{-1}, but falls with increases in the swelling rate, especially at high stress levels. The action of stress-affected swelling and carbide precipitation exert different influences on the derivation of this coefficient.

PROGRESS AND STATUS

Introduction

In an earlier series of papers, it was shown that the irradiation creep rate per dpa and unit stress (ϵ/σ) is composed of two major contributions, one independent of swelling and another often larger component that is proportional to the instantaneous swelling rate.[1-5] These are referred to as the B_o and DS contributions respectively. The creep compliance B_o and the creep-swelling coupling coefficient D have been measured for a variety of steels. Although B_o is somewhat dependent on the steel and displacement rate, the coefficient D at ~400°C has been found to be remarkably independent of composition and thermomechanical starting condition at $\sim 0.6 \times 10^{-2}$ MPa^{-1}.

In another series of papers it was shown, however, that at ~550°C and high stress levels, the irradiation creep rate of AISI 316 in EBR-II first increases with the swelling rate as defined by DS, but then begins to decrease strongly and vanish as the swelling rate approaches its maximum value.[6-8] This in turn implies that the value of D must decrease at higher stress levels and higher swelling rates. The phenomenon has previously been defined as "creep disappearance".

Determination of the D-coefficient from most experiments is hampered somewhat by the action of several other phenomena. As the temperature increases, carbide precipitation leads to larger levels of matrix densification,[9] which produces an underestimate of the D-coefficient. On the other hand, stress-accelerated swelling, which increases with increasing temperature,[10] leads to an overestimate of the D-coefficient. A recent study showed, however, that this coefficient is still on the order of 0.6×10^{-2} MPa^{-1} for 20% cold worked 316 in the range 525-600°C.[5] This suggests that a design correlation for irradiation creep could assume that the D-coefficient is independent of temperature in this range.

With these various factors in mind, another previously published data set can be reanalyzed to confirm whether the D-coefficient at ~550°C is essentially the same as that found at ~400°C. These data (see Figures 1 and 2) were derived from side-by-side irradiation of two thermomechanical variations of the same 316 stainless steel.

ExDerimental Details

The steel employed was the V87210 reference heat of AISI 316 used in the U.S. Breeder Reactor Program. Its composition in wt.% was 13.57Ni, 16.36Cr, 2.88Mo, 1.42Mn, 0.47Si, 0.07C, 0.02P, 0.01S with <0.005B and the balance Fe. The two starting conditions analyzed in this report are the 20% cold worked and Heat Treat D (HTD) conditions. In the latter condition, the vendor-produced 20% cold worked version in the form of tubes was first aged 24 hours at 482°C and then aged again for 216 hours at 704°C to cause extensive and complete carbide precipitation. This two-step aging sequence is often called the Garafolo treatment. The HTD condition is known to begin swelling at a lower dose than does the 20% cold worked condition, as shown in Fig. 3.

The creep capsules produced from these tubes were 1.02 m long and had an outer diameter of 0.584 cm and a wall thickness of 0.038 cm, but only the top 0.28 m length of the capsules was pressurized with helium to yield hoop stress of 0, 103 and 206 MPa (0, 10, 15Ksi). The pressurized portion was welded to the lower portion of the capsule, which contained a tantalum rod to heat the reactor sodium to ~550°C as it flowed upward along the capsule. Irradiation proceeded in row 7 of EBR-II. The diameter measurements shown in Figs. 1 and 2 were made at the end of each irradiation period at the core center level, using a contact profilometer.

'Pacific Northwest Laboratory is operated for the U.S. Department of Energy by Battelle Memorial Institute under Contract DE-AC06-76RLO 1830.

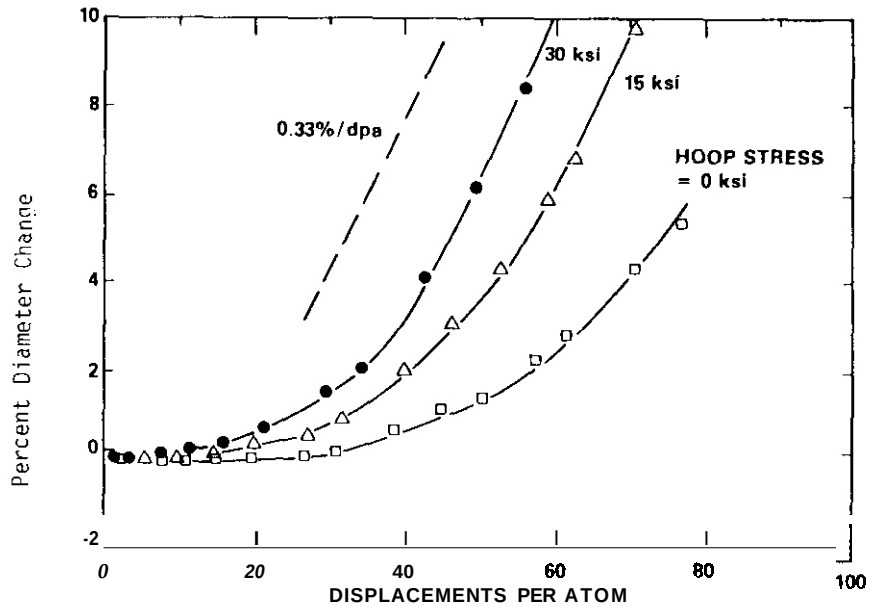

Fig. 1. Diametral strains observed in 20% cold worked AISI 316 irradiated in EBR-II at hoop stress levels of 0, 15, and 30 Ksi (0, 103, 206 MPa).

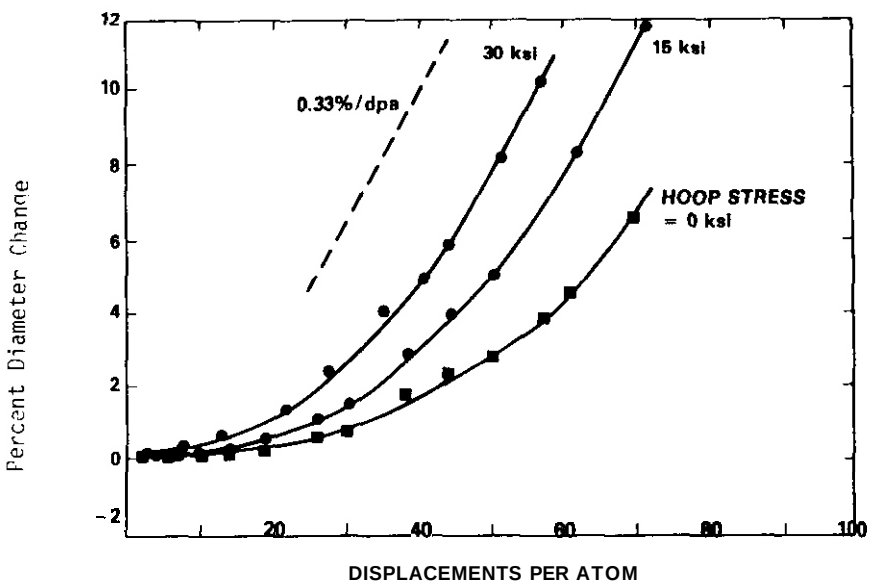

Fig. 2. Diametral strains observed in Heat Tread D condition of AISI 316 irradiated in EBR-II at hoop stress levels of 0, 15, and 30 Ksi (1, 103, 206 MPa).

Results

Assuming that creep obeys the following relationship

$$\bar{\epsilon}/\bar{\sigma} = C\frac{4}{3}\frac{\dot{\epsilon}}{\sigma_H} = B_o + DS_v,$$

then the creep-swelling coupling coefficient D is defined by

$$D = \frac{1}{3\dot{S}_L}\left(\frac{4C\dot{\epsilon}}{3\sigma_H} - B_o\right)$$

where $\dot{\epsilon}$ and $\dot{\bar{\epsilon}}$ are the diametral and effective creep strain rates, σ_H and $\bar{\sigma}$ are the hoop and effective stress levels, S_v and S_L are the volumetric and linear swelling rates ($S_v \approx 3S$), C is a geometric constant dependent on tube diameter and wall thickness (1.15 for this case) and B_o is the creep compliance.

The procedure employed to evaluate D was to measure the diameter change rates for both the 0 and 103 MPa tubes over a 10 dpa increment. Subtracting the rate of diameter change of the unstressed tube from that of the stressed tube yields a value for $\dot{\epsilon}/\sigma_H$. The 103 MPa tube was chosen instead of the 206 MPa tube to minimize the tendency toward creep disappearance in order to watch this phenomenon develop. A value of $B_o = 1 \times 10^{-6}$ MPa^{-1} dpa^{-1} was assumed based on earlier studies, although the analysis was found to be not too sensitive to this parameter.

As shown in fig. 4, there is a tendency for the D-coefficient to fall at higher swelling rates. The maximum swelling rate of austenitic steels is known to be ~1%/dpa. Note that the HTD curve in fig. 4 is initially somewhat higher than 0.6×10^{-2} MPa^{-1}, reflecting primarily the action of large stress levels to shorten the duration of the transient regime of swelling. This leads to an overestimate of the D-coefficient. This curve also does not contain any influence of carbide-related densification, which was probably concluded prior to irradiation as a result of the extended precipitation sequence. The 20% cold worked curve, however, reflects the influence of carbide densification, the presence of which generates lower total deformation rates in the early stages of irradiation than would arise from swelling and creep alone. Thus, as expected, the 20% cold worked curve represents an underestimate of the D-coefficient.

CONCLUSIONS

Based on the results of this sfudy and earlier studies, it appears that the creep-swelling coupling coefficient is $\sim 0.6 \times 10^{-2}$ MPa^{-1} over the temperature range of ~380 to ~600°C. At high stress levels and high swelling levels, however, this coefficient falls to much lower values. Applied stresses and carbide

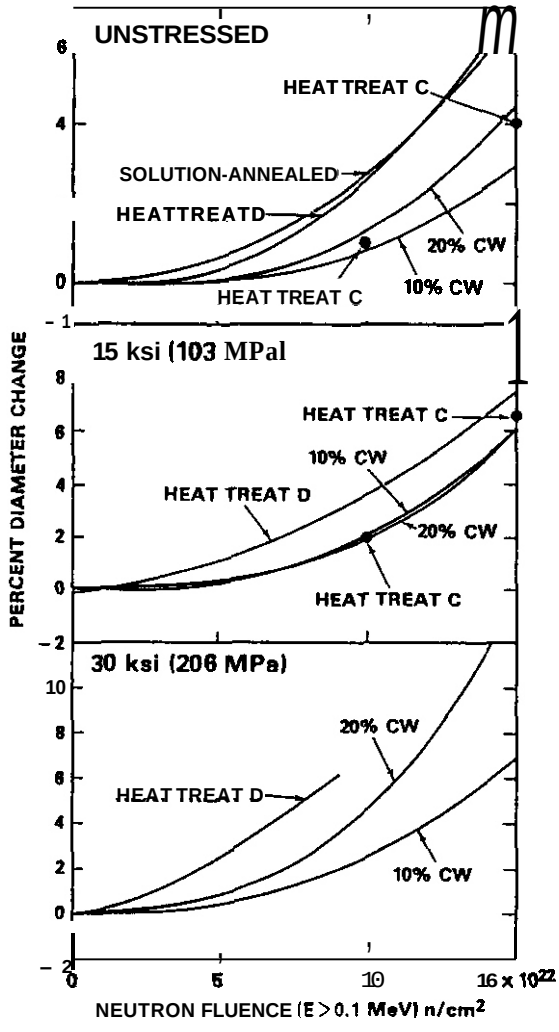

Fig. 3. Diametral strains of various conditions of AISI 316, showing that Heat Treat D swells prior to that of various cold work levels. The Heat Treat C condition represents the first step of the two-step aging treatment of Heat Treat D.

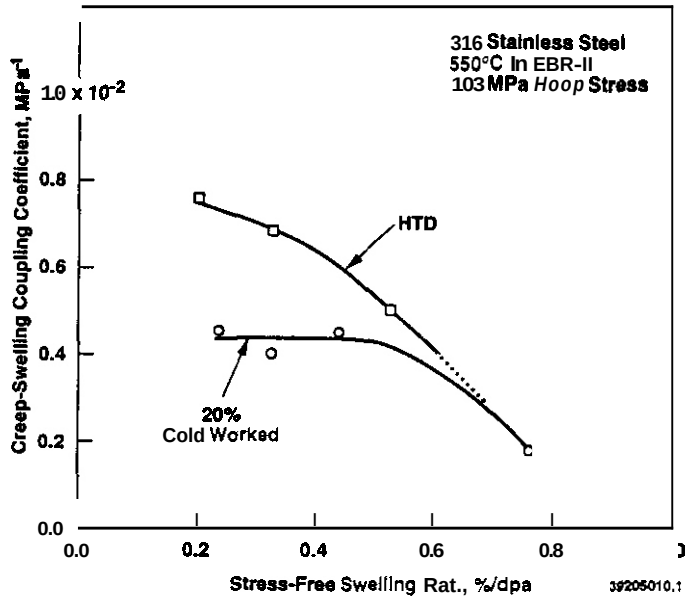

Fig. 4. Values of D-coefficient derived for HTD and 20% cold worked conditions of AISI 316 irradiated in EBR-II.

precipitation exert aifferent influences on tne deviation of tnis coefficient, yielding overestimates and underestimates, respectively.

FUTJRE WORK

A comparative analysis of ORR and **FFTF** data on irradiation creep of austenitic steels will be performed to **assess** the relative influence of displacement rate and helium/dpa ratio on irradiation creep.

REFERENCES

1. D. L. Porter, G. D. Hudman and F. A. Garner, J. Nucl. Mater. 179-181 (1991) 581-584.

2. F. A. Garner and R. J. Puigh, J. Nucl. Mater. 179-181 (1991) 581-584.

3. F. A. Garner and O. L. Porter, J. Nucl. Mater. 155-157 (1988) 1006-1013.

4. M. 8. Toloczko, F. A. Garner and C. R. Eiholzer, accepted for publication in J. Nucl. Mater., proceedings of ICFRM-5.

5. F. A. Garner, M. E. Toloczko and R. J. Puigh, in this semiannual report.

6. F. A. Garner, D. L. Porter and B. J. Makenas, J. Nucl. Mater., 148 (1987) 279-287.

7. D. L. Porter and F. A. Garner, in Influence of Radiation on Material Prouerties: 13th International Symposium (Part [(), ASTM STP 956, F. A. Garner, C. H. Henager, Jr., and N. Igata, eds., American Society for Testing and Materials, Philadelphia, 1987, pp. 11-21.

8. D. L. Porter and F. A. Garner, J. Nucl. Mater., 159 (1988) 114-121.

9. F. A. Garner, W. V. Cummings, J. F. Bates and E. R. Gilbert, Hanford Engineering Develoument Laboratory Report, HEDL TME 78-9, Richland, WA, June 1978.

10. F. A. Garner, E. R. Gilbert and D. L. Porter, in Effects of Radiation on Materials: Tenth Conference. ASTM STP 725, D. Kramer, H. R. Erager and J. S. Perrin, American Society for Testing and Materials, 1981, pp. 680-697.

Analysis of Creep Oata from MOTA Irradiation of 20% Cold Worked *316* Stainless Steel - F. A. Garner, (Pacific Northwest Laboratory*), M. B. Toloczko, (University of California at Santa Barbara), and R. J Puigh, (Westinghouse Hanford Company)

OBJECTIVE

The objective of this study is to provide insight into the relationship between void swelling, irradiation creep and applied stress. This insight will be used to develop irradiation creep correlations for fusion applications.

SUMMARY

Analysis of creep data for 20% cold worked *316* stainless steel irradiated in FFTF/MOTA demonstrates that the creep-swelling coupling coefficient is not a strong function of temperature and can be assumed to be ~0.6 x 10^{-2} MPa^{-1} in the range 400-600°C. It appears, however, that the creep compliance B_o is a moderately strong function of displacement rate, especially at lower irradiation temperatures. It also appears to be a function of temperature and alloy composition. The latter dependency arises primarily because derived values of B_o unavoidably incorporate precipitation-related strains that cannot be easily separated from contributions arising from true creep. It has also been found that at ~550-600°C there is an upper limit on the total diametral strain rate at 0.33%/dpa. In contrast to the conclusion of an earlier experiment, this limitation does not arise initially from the total disappearance of creeo. however. The creep rate first increases with the onset of swelling and then diminishes as the swelling rate increases, disappearing only when the swelling rate reaches its steady state value.

PROGRESS AND STATUS

introduction

In a series of recent reports[1-5] it was shown that irradiation creep of austenitic stainless steels in the EBR-II and FFTF fast reactors could be described in terms of a simple model in which the instantaneous creep rate possessed two major contributions, one independent of void swelling and another directly proportional to the instantaneous swelling rate. These contributions are referred to as the B_o and $D\dot{S}$ contributions to creep, where B_o is the creep compliance and $\dot{S}$ is the instantaneous swelling rate. The most recent of these studies involved the fusion PCA alloy and a group of D9 titanium-modified Type 316 stainless steels irradiated in FFTF-MOTA in the 20% cold worked condition at ~400°C.[4,5] It was clearly shown in that study that the creep-swelling coupling coefficient D at ~400°C is ~0.6 x 10^{-2} MPa^{-1}, in agreement with the results of earlier studies conducted on annealed 304 stainless steel and unmodified 316 stainless steels in the cold worked condition, both irradiated at ~400°C in EBR-II.[2,3]

Unfortunately, the MOTA data on the titanium-modified steels at temperatures above 400°C cannot be used to derive the temperature dependence of the creep-swelling coupling coefficient over the full temperature range of interest. The failure to complete this objective arises from both metallurgical and programmatic considerations. First, the addition of titanium to *316* stainless steel leads to earlier neutron-induced swelling at relatively low irradiation temperatures (i.e. 400°C) compared to that of unmodified 316 steels.[6] At higher irradiation temperatures (>500°C), however, swelling is delayed by titanium additions[6]. While it was possible to derive a value for the creep-swelling coupling coefficient at 400°C using data from the first four MOTA irradiation sequences, only data from the first three irradiation sequences were available at higher temperatures. This is due to a severe overtemperature event that occurred in the fourth irradiation sequence (MOTA-ID). This event resulted in the loss by rupture of many tubes, especially in canisters maintained at higher temperatures. This led to a programmatic decision to discontinue irradiation at these temperatures. When combined with the delay in swelling by titanium additions at these higher temperatures, an insufficient amount of swelling-enhanced creep was attained in D9-type steels to allow derivation of a confident value for the coupling coefficient.

Therefore, an alternative approach was used to derive the coupling coefficient for titanium-modified stainless steels at higher temperatures. This approach takes advantage of the fact that the coupling coefficient was found to be independent of composition for a wide range of stainless steels at ~400°C.[1-5] If the same independence of composition is assumed to apply at higher irradiation temperatures, then perhaps the creep data from the higher swelling titanium-free 316 steels in the first three MOTA sequences can be used to derive a value for the coupling coefficient.

These MOTA data can also be used to address a number of other questions that arose in previous studies conducted on AISI 316 stainless steel in the EBR-II fast reactor. Each of these issues has been considered to be controversial and unresolved, requiring additional data to confirm the existence of each phenomenon.

---

*Operated for the U.S. Department of Energy by Battelle Memorial Institute under Contract DE-AC06-76RLO 1830.

The first question concerns an earlier observation that at ~550°C the total diametral deformation rate during irradiation of AISI 316 could not exceed 0.33%/dpa.[7-9] In that experiment the irradiation creep rate of AISI 316 in various thermomechanical starting conditions always seemed to disappear as swelling approached its upper limit of 1% (volumetric) per dpa. Isotopic distribution of the strains associated with a 1%/dpa swelling rate yields a diametral strain rate of 0.33%/dpa, which implies that only swelling is occurring. Both the limiting strain rate and the observation of "creep disappearance" was considered to be controversial, however, and until this study no supporting data have become available.

The second question concerned the effect of temperature changes on creep and swelling.[10-14] Under some irradiation conditions a substantial enhancement of both swelling and creep was induced by abrupt or gradual changes in temperature, while in other conditions there was very little influence of temperature changes during irradiation. In the MOTA study reported here, one set of tubes was subjected to a series of temperature changes while others were irradiated in an isothermal manner. This experiment thus provided an opportunity to observe the creep-swelling relationship under a wider variety of environmental conditions.

A third question involved the observation in EBR-II that neutron irradiation under some conditions delayed the onset of high creep rates (and their associated failures) that arise from thermally activated processes.[15,16] This observation has not been reproduced in studies conducted on other steels employed in various liquid metal reactor programs.[17-18]

A fourth question concerns how to deal with problems associated with the measurement of the B_o component of irradiation creep, particularly when phase-related density changes occur early in the irradiation or when data are only available at relatively large increments of neutron exposure. Unfortunately, almost all steels develop temperature-dependent strains arising from formation of carbides[19] or intermetallic phases.[20]

Finally, although the B_o component of creep is thought to be relatively independent of irradiation temperature,[21-2] there is evidence provided by Lewthwaite and Mosedale from the OFR fast reactor that creep may be very sensitive to displacement rate at relatively low (240-360°C) irradiation temperatures where void swelling has not yet begun, with the creep rate per dpa increasing strongly with decreasing displacement rate.[23,24] Although the transient regime of swelling is known to be sensitive to displacement rate,[24] the sensitivity of creep to displacement rate in the absence of swelling has not yet been confidently confirmed in other studies, although Wassilew has provided some additional evidence that supports such a dependence.[25] Reviews of the data on this subject are found in references 24 and 26.

ExDerimental Details

Two heats of 20% cold worked AISI 316, designated FFTF Core 1 and Core 4 steels, were used to prepare 28.2 mm long gas-pressurized tubes with outer and inner diameters of 5.84 and 5.08 mm diameter, respectively. The construction of these tubes, their irradiation conditions and the measurement of their diameter change are described in detail in reference 5. The compositions of the two heats are presented in Table 1. These tubes were irradiated in the in-core region of MOTAs 1A, 1B, and 1C at temperatures between 400 and 670°C. Those tubes that had not failed in the usual manner were included in MOTA 10, but all of these were

Table 1. Composition (Weight Percent) of 316 Steels

Heat Oesisnation	Core 1	Core 4
Carbon	0.047	0.056
Manganese	1.77	1.53
Silicon	0.57	0.54
Phosphorus	0.004	0.002
Sulfur	0.006	0.005
Chromium	17.4	17.7
Nickel	13.7	13.7
Molybdenum	2.34	2.82
Copper	0.01	0.02
Boron	0.0005	0.0005
Cobalt	0.005	0.01
Aluminum	0.005	0.01
Vanadium	0.02	0.01
Niobium	0.005	0.01
Tantalum	0.015	0.01
Arsenic	0.005	0.005
Nitrogen	0.004	0.002
Oxygen	0.002	0.002

discarded without measurement after the overtemperature event in MOTA-1D caused many of them to fail and the others to develop atypically large strains.

While most of the tubes discussed in this report were irradiated to 50-70 dpa within the FFTF core, there were also some Core 1 tubes irradiated at much lower displacement rates in above-core canisters maintained at 475, 490 and 600°C. These tubes therefore attained relatively low total displacement levels, ranging from 4.5 to 8.6 dpa.

Results and Discussion

As shown in Figure 1, the diametral changes induced by swelling and creep in the cold worked 316 tubes during isothermal irradiation at 400 and 500°C increased with temperature but were relatively small, especially when compared to those of various titanium-modified steels irradiated in the same FFTF cycles.[5] Strains of these relatively small magnitudes do not allow a confident separation of the B_o and $D\dot{S}$ contributions to the creep rate.[5]

After subtracting the stress-free swelling strain, the resulting creep strains were divided by the stress levels that produced them. As shown in Figure 2 the stress-normalized creep rates were found to be essentially linear with applied stress. This in turn implies that the effect of stress on void swelling was rather small at these temperatures. This is important because applied stresses are known to shorten the incubation period of swelling[27-29] and thereby to complicate the derivation of the coupling coefficient.' The effect of stress on swelling of AISI 316 is known to be relatively small at lower temperatures but to increase as the temperature increases above ~550°C.[27]

At 550 and 575°C, larger values of swelling and creep developed, both in response to a shorter incubation period for stress-free swelling and to the larger dpa levels achieved in MOTA at these temperatures. As shown in Figure 3 the strain rates reached in these experiments increased with displacement level and stress level, but did not exceed the 0.33%/dpa limiting strain rate observed in earlier studies.'.' This limit was reached at stress levels ≤100 MPa and was not exceeded at higher stress levels. Also shown in Figure 3 are the strains of some tubes that appear to have reached the 0.33%/dpa limit and then failed and lost their pressure, continuing to swell thereafter, but not to creep. The post-failure strain rates of these tubes allow examination of the stress-affected swelling behavior at different displacement levels and different prior stress levels. The post-failure strains thus provide some insight on the partition of the creep and swelling strains at the time of failure. They also provide an opportunity to determine the creep-swelling coupling coefficient using the actual stress-affected swelling, rather than the usual procedure of using the stress-free swelling rate as a lower bound estimate.[5] An important conclusion drawn from the post-failure strains in Figure 3 (and also later in Figure 5) is that the 0.33%/dpa limit does not imply that the limiting deformation rate arises only from steady-state swelling, and that creep has "disappeared". Such an erroneous conclusion might have been drawn from the behavior observed in earlier studies whe e failure did not occur and the stress-free swelling rate approached 1%/dpa during the experiment.', [9] In this experiment the post-failure swelling rate falls far below the 0.33%/dpa rate observed prior to failure. It appears that the creep contribution to the strain rate first increases according to the $D\dot{S}$ relationship but then diminishes continually as the swelling rate increases.

Another indication of the increasing effect of stress on swelling at 550 and 575°C is shown in Figure 4, where the apparent nonlinearity of stress-normalized creep signals the onset of significant stress-affected swelling. This will tend to yield overestimates of both the D and B_o coefficient, especially at the higher stress levels.[5]

Figure 5 shows that at 600°C the incubation period of swelling has increased relative to that at 550 and 575°C, and the swelling at a given dpa level has therefore decreased. At 675°C the incubation period was even longer and the swelling was essentially zero for the displacement levels reached in this experiment. Although not as convincing as that observed at 550 and 575°C, Figure 5 also presents several strain curves that are consistent with a 0.33%/dpa maximum limit on deformation rate. As also shown in Figure 5, the tendency toward tube failure increased as the temperature increased. The failures presented in Figure 5 are fortunate in one sense, since they allow an opportunity to differentiate between stress-enhanced swelling and the onset of a significant rate of thermal creep at higher temperatures. If the post-failure strain rate is essentially zero (e.g. Core 4 alloy at 670°C and 31 MPa) then thermal creep was dominating the strain rate in the absence of swelling.

As shown in Figure 6, there is an increasingly nonlinear behavior of stress-normalized creep with stress at 600°C. This probably arises at least partially from the effect of stress in accelerating swelling and also from the onset of thermal creep. At 670°C, however, the stress-free swelling is either very low (Core 1) or nonexistent (Core 4), signaling that the large degree of nonlinearity of creep with stress at this temperature arises solely from the nonlinear dependence of thermal creep on stress.

Figure 7 presents the non-isothermal temperature history employed for another series of AISI 316 pressurized tubes. With one exception, the temperature was reduced in an irregular staircase fashion from 575 to 525°C by changing the ratio of MOTA cooling gases before or during a given irradiation cycle. The

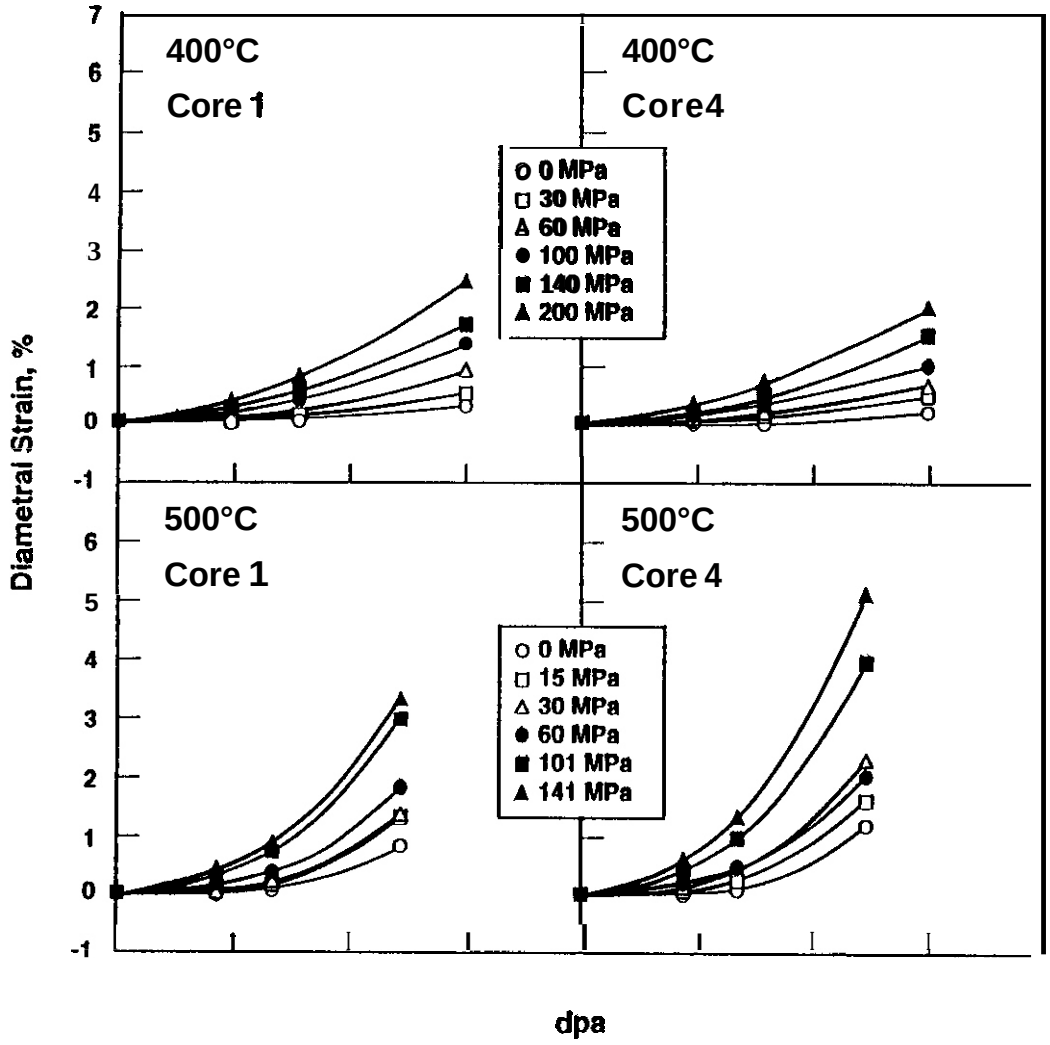

Fig. 1. Total diametral strains observed at 400 and 500°C.

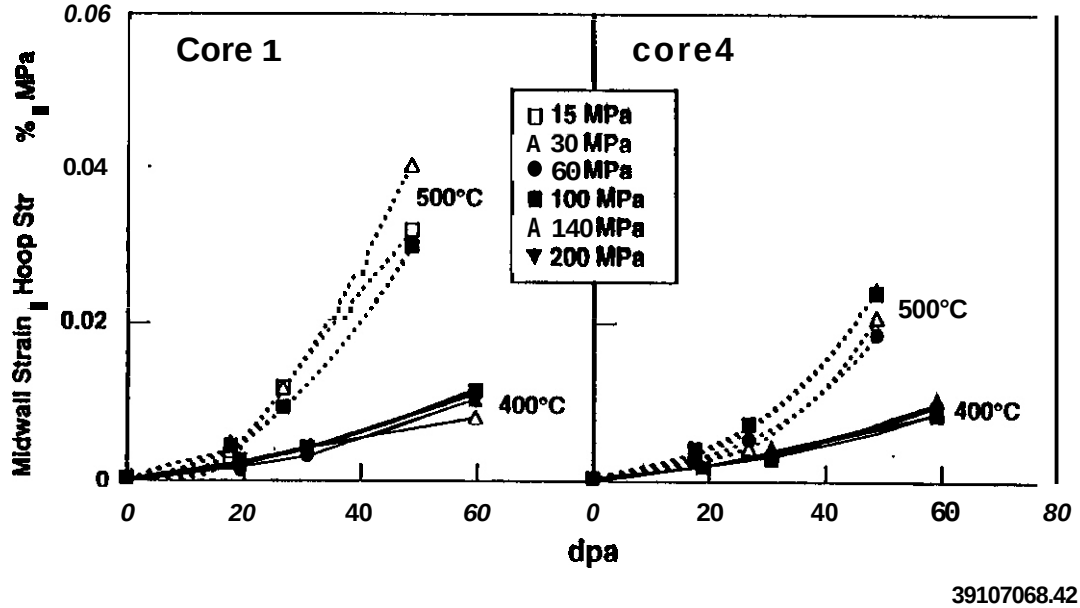

Fig. 2. Stress-normalized creep strains at 400 and 500°C.

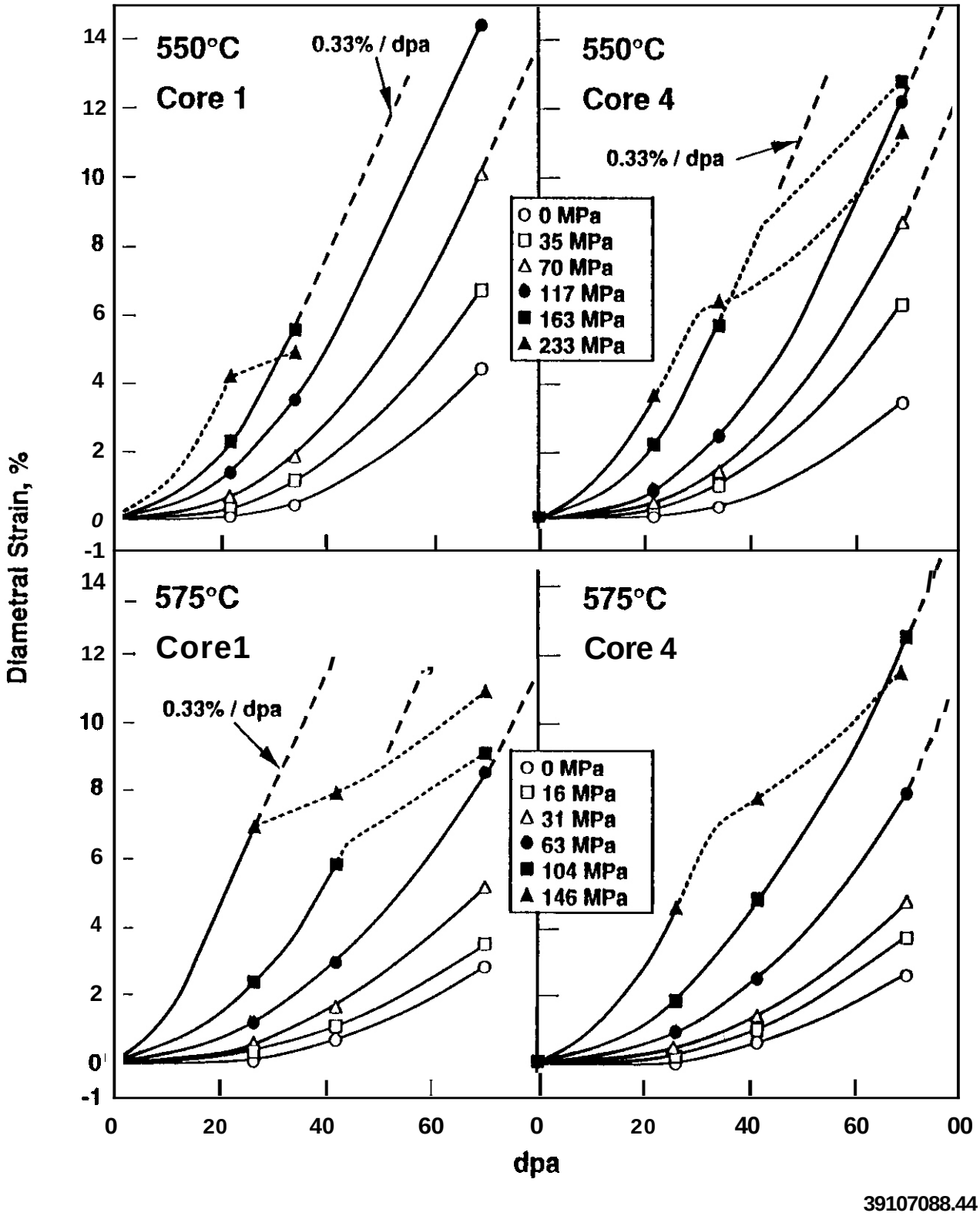

Fig. 3. Total diametral strains observed at 550 and 575°C

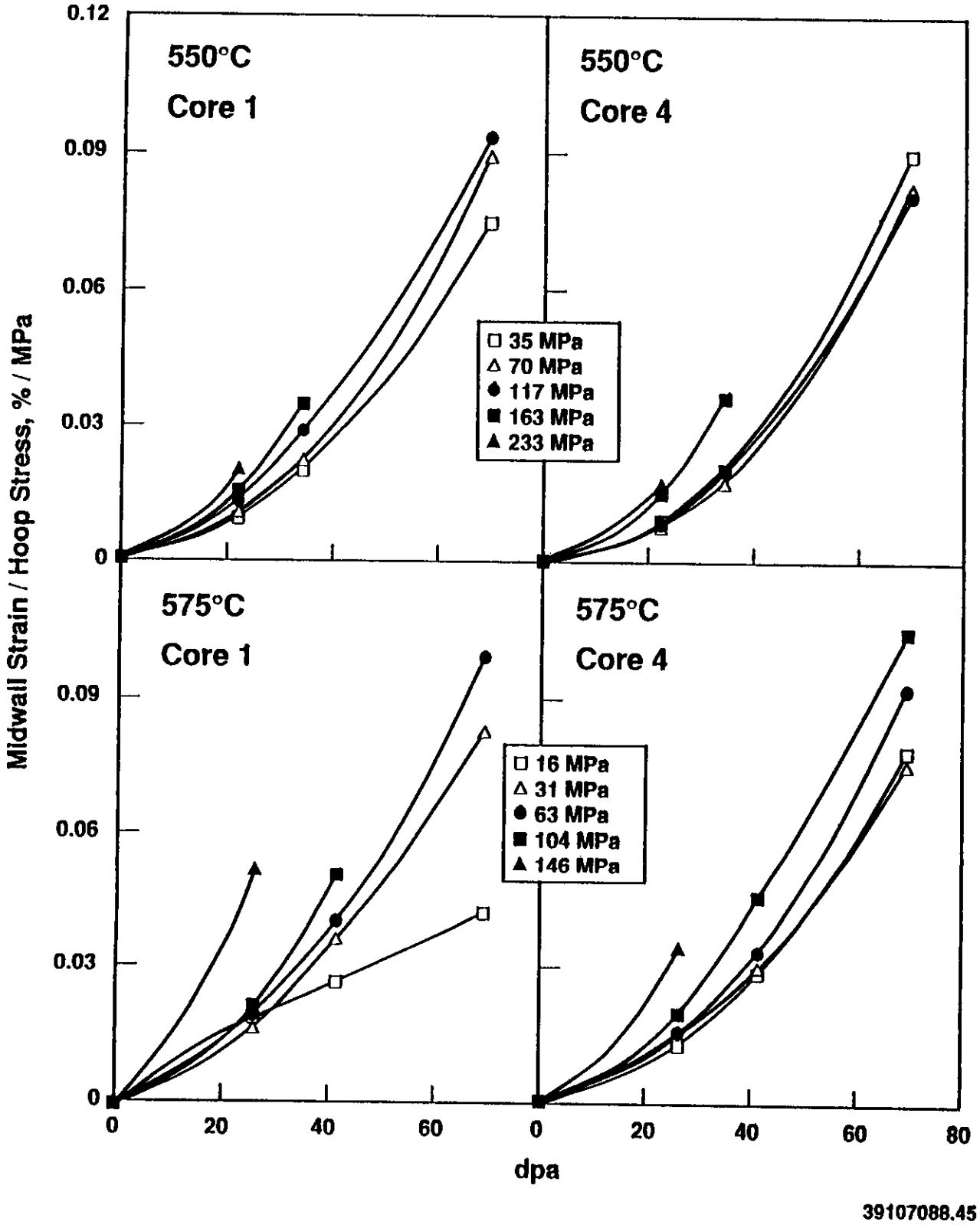

Fig. 4. Stress-normalized creep strains at 550 and 575°C.

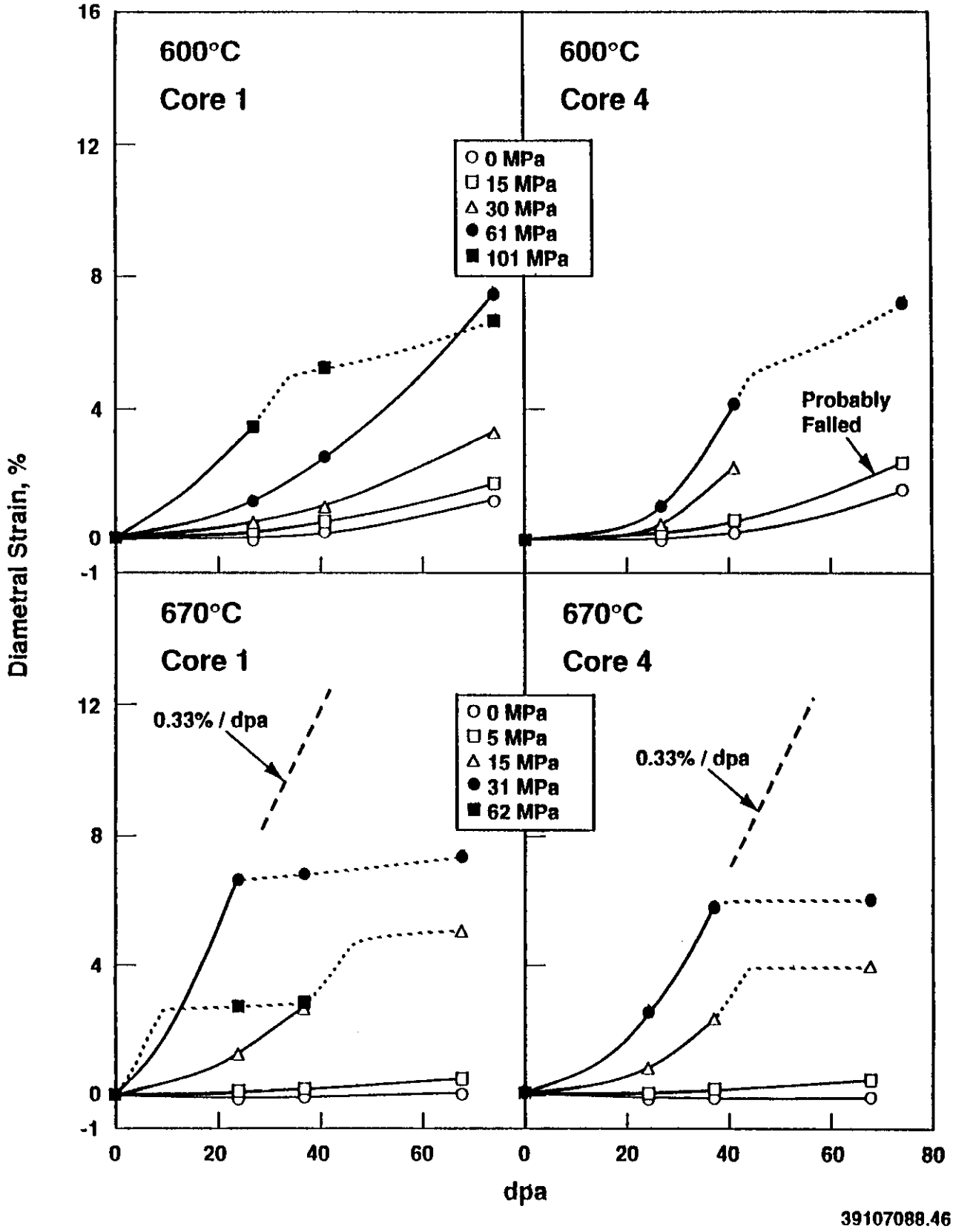

Fig. 5. Total diametral strains observed at 600 and 670°C.

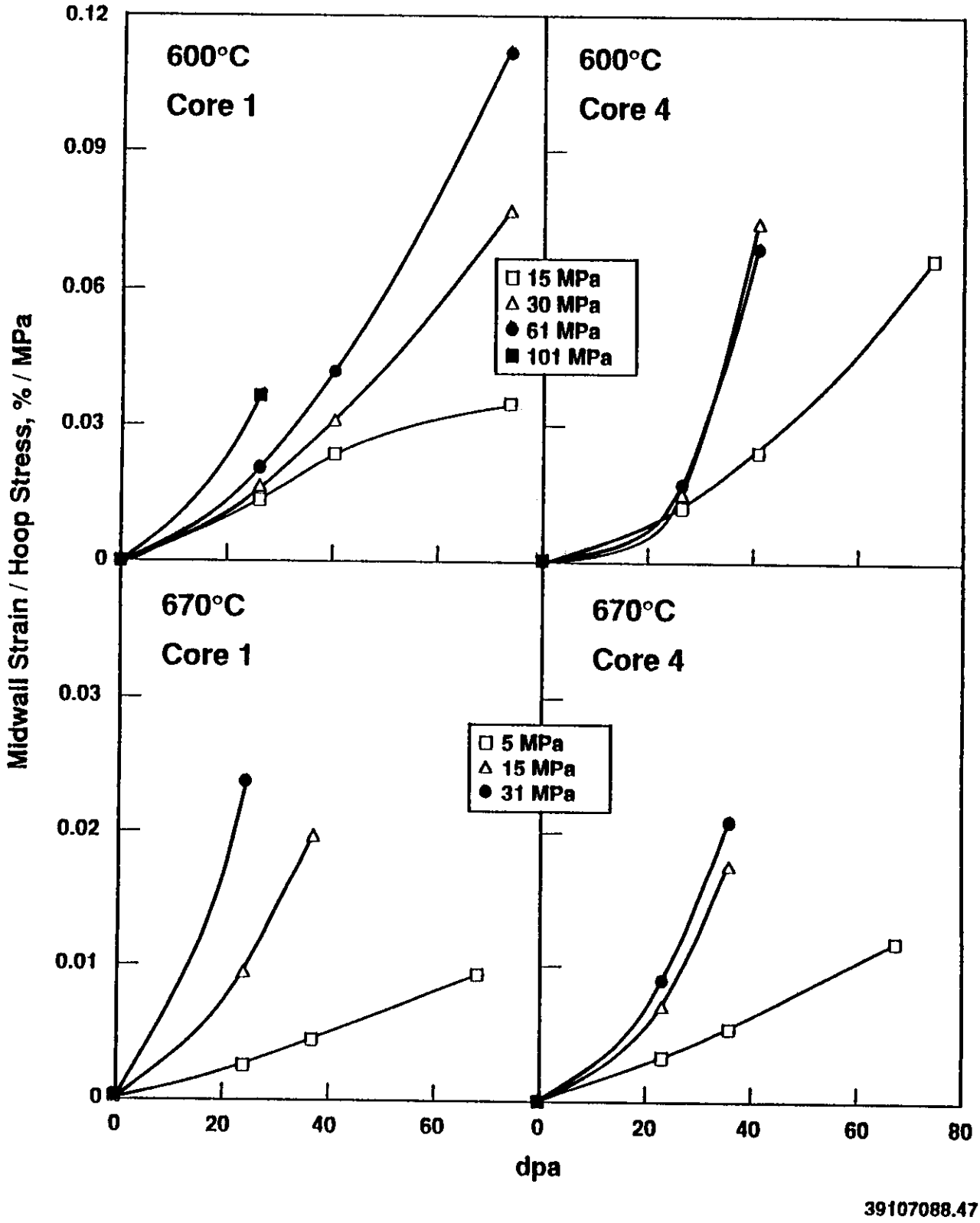

Fig. 6. Stress-normalized creep strains at 600 and 670°C.

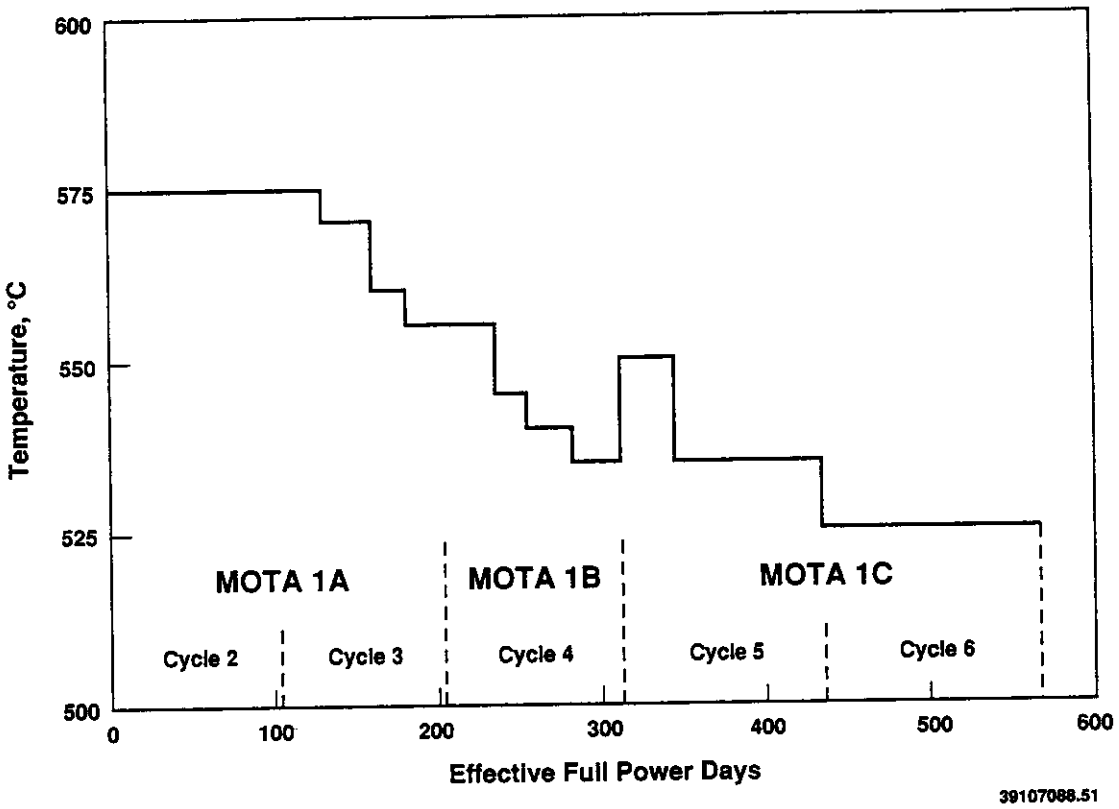

Fig. 7. Temperature history employed in the temperature change experiment in FFTF-MOTA.

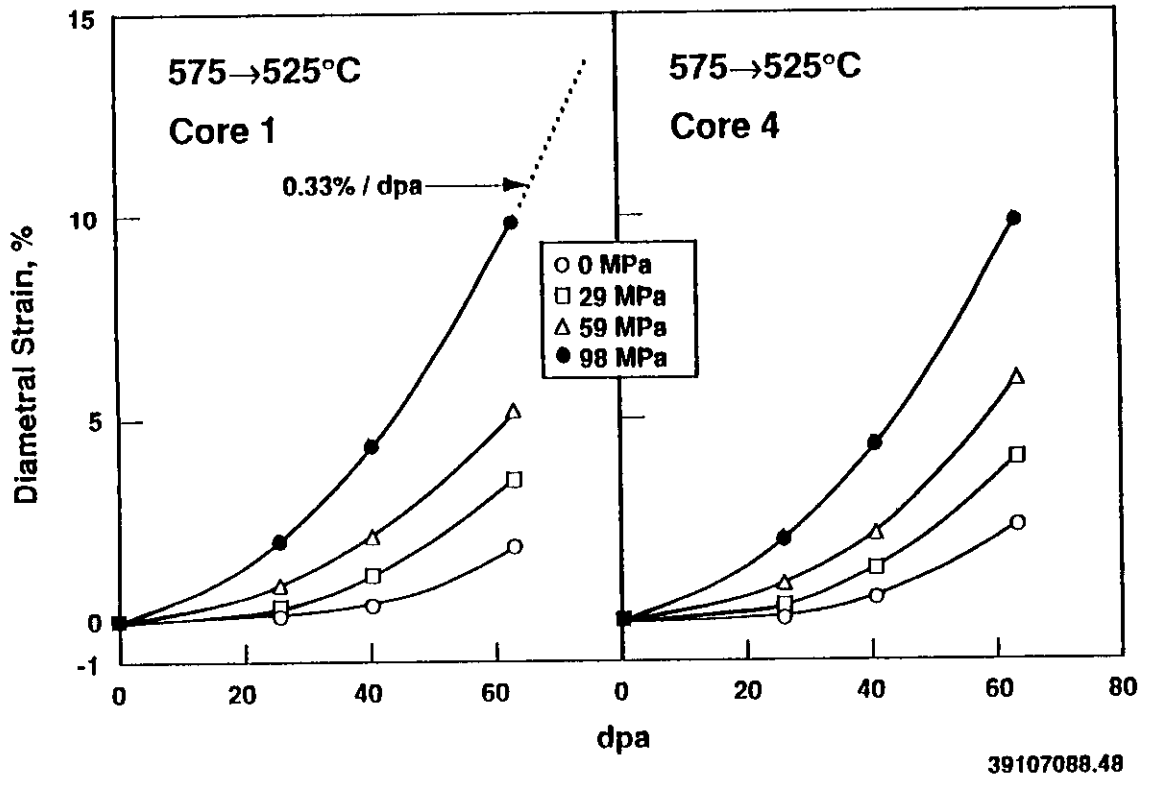

Fig. 8. Total diametral strains observed in the temperature change experiment.

resultant creep and swelling strains are shown in Figure 8. The strains observed were comparable, however, to those observed during isothermal irradiation at 550 and 575°C, indicating that the irregular temperature history had very little effect. This is thought to reflect the fact that the swelling incubation period for this steel under isothermal conditions is known from earlier studies to be relatively insensitive to temperature in the range 525-575°C.[6] This finding also agrees with an earlier study by Yang and Garner that abrupt temperature changes after the onset of swelling had very little effect on void swelling of similar steels.[13] It should also be noted that the tubes at the highest stress level have approached the 0.33%/dpa limit, but have not exceeded it. The stress-normalized creep strains shown in Figure 9 for the non-isothermal tubes were comparable to those observed at 550°C.

Woo, Garner, and Holt have modeled the 0.33%/dpa limitation as a predictable consequence of the stress-driven development of a highly anisotropic dislocation microstructure. This model predicts that the diametral strain rate cannot exceed the steady-state linear swelling rate, whether the swelling rate is relatively low[30] or at its maximum level.[31] It has been demonstrated experimentally that large and anisotropic stress states indeed lead to highly anisotropic distributions of dislocation Burger's vectors.[32] Garner and Toloczko have also shown that in an earlier EBR-II experiment[8,9] the creep-coupling coefficient initially approaches -0.6 x 10^{-2} MPa and declines as swelling approaches 1%/dpa and creep disappears.[33]

Using the procedures outlined in reference 5, the data in Figures 3, 5 and 8 were analyzed to determine estimates of the B_o and D creep coefficients. Remember that the presence of stress-affected swelling leads to overestimates of both these parameters. As shown in Table 2, some of the data at 500, 550, and 575°C reached high enough swelling levels to allow a reasonably confident separation between the B_o and DS contributions. The analysis indeed appears to have been complicated somewhat by the higher level of stress-affected swelling at higher temperatures but it appears, however, that the values of D at these temperatures (for both isothermal and non-isothermal histories) approach numbers close to -0.6 x 10^{-2} Mpa^{-1}, and are thus comparable to the value derived at 400°C. In cases where convergence was clearly reached, the calculated values of B_o ranged from 3 to 10 x 10^{-6} $MPa^{-1}dpa^{-1}$, somewhat larger than the 1 to 3 x 10^{-6} observed for a variety of other steels.[5] Titanium-modified steels at ~400°C in the current experiment were found to have values of 1-2 x 10^{-6}.[5] The variability of this parameter is thought to arise not only from the action of stress-affected swelling but also because B_o is small and comparable in magnitude to the varying levels of precipitation-related strain that occur in different austenitic steels.

Figure 10 presents the strain data from the pressurized tubes irradiated in the above-core positions to much smaller increments of exposure. Negative strains arising from carbide formation are clearly evident in the stress-free tubes and are commonly observed in austenitic steels during irradiation.[6] Once void swelling begins, this densification cannot always be observed, especially when data are taken at the larger increments of dpa attainable in the in-core positions of MOTA.

As shown in Figure 11, when the absolute value of the observed densification of the stress-free tubes was added to the stress-affected strains and then divided by the stress, the creep strains were found to be almost but not quite linear with stress, with the divergence increasing slightly at higher temperatures. This approach assumes that densification is independent of stress and is completed in the first exposure interval. Table 3 lists the values of B_o obtained from the above-core tubes.

As shown in Figure 12, the creep compliance, B_o, measured for the Core 1 tubes appears to be dependent on the irradiation temperature, although this may be an artifact of the increasing level of stress-affected swelling with increasing temperature. More importantly it appears that B_o increases with decreasing displacement rate in the range of 475 to 600°C. There is therefore some support in this study for the previously proposed inverse dependence of B_o on displacement rate, although the dependence on displacement rate appears to diminish at higher temperatures. Such a temperature-dependent rate effect was predicted by Lewthwaite and Mosedale earlier, using a model based on the rate dependence of point defect recombination.[23]

Lewthwaite and Mosedale also suggested that the inverse flux dependence may have arisen from some aspect of the softer neutron spectrum (involved in their below-core experiment) that was not adequately described by standard displacement models. This latter possibility has been explored recently by Greenwood, Garner and Heinisch who showed that such behavior might be contributing to the enhancement of radiation damage in the out-of-core regions of FFTF.[34]

CONCLUSIONS

It appears from this and other studies that the creep-swelling coupling coefficient, D, is not a strong function of irradiation temperature, temperature history, composition, or thermomechanical treatment in various 300 series stainless steels. The coefficient can be assumed to be 0.6 x 10^{-2} MPa^{-1} for irradiation below 600°C providing that some provision be made in design calculations to incorporate the effect of stress on swelling. Above 600°C, thermal creep will begin to overwhelm irradiation creep and the DS model will seriously underpredict the creep strain.

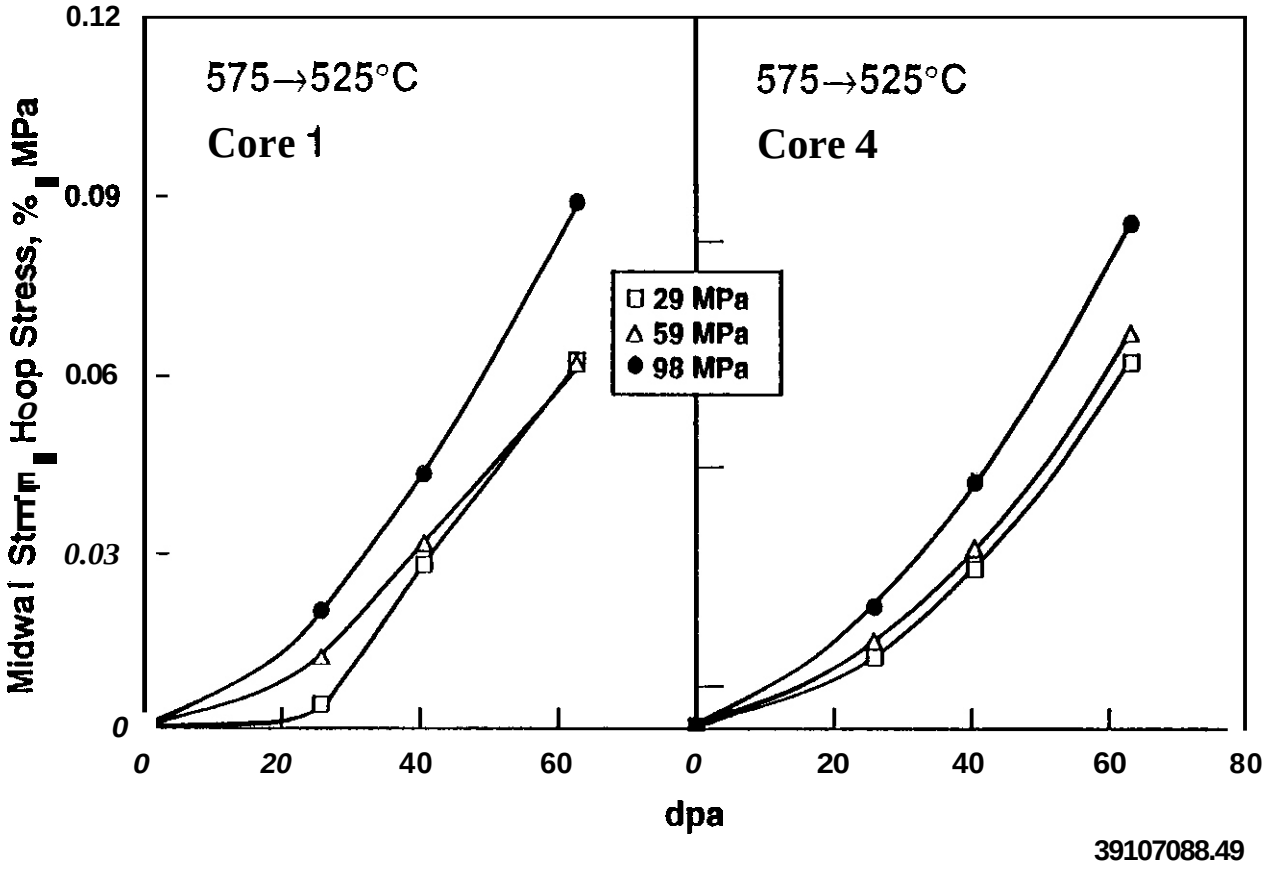

Fig. 9. Stress-normalized creep strains in the temperature change experiments

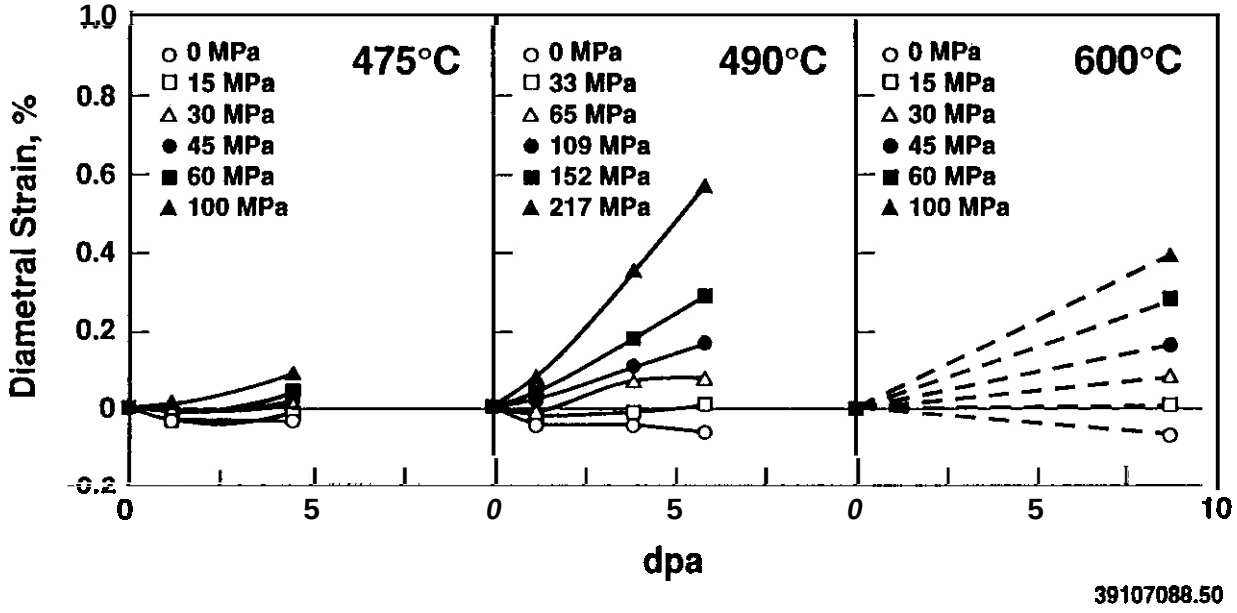

Fig. 10. Diametral strains observed in the above-core experiment

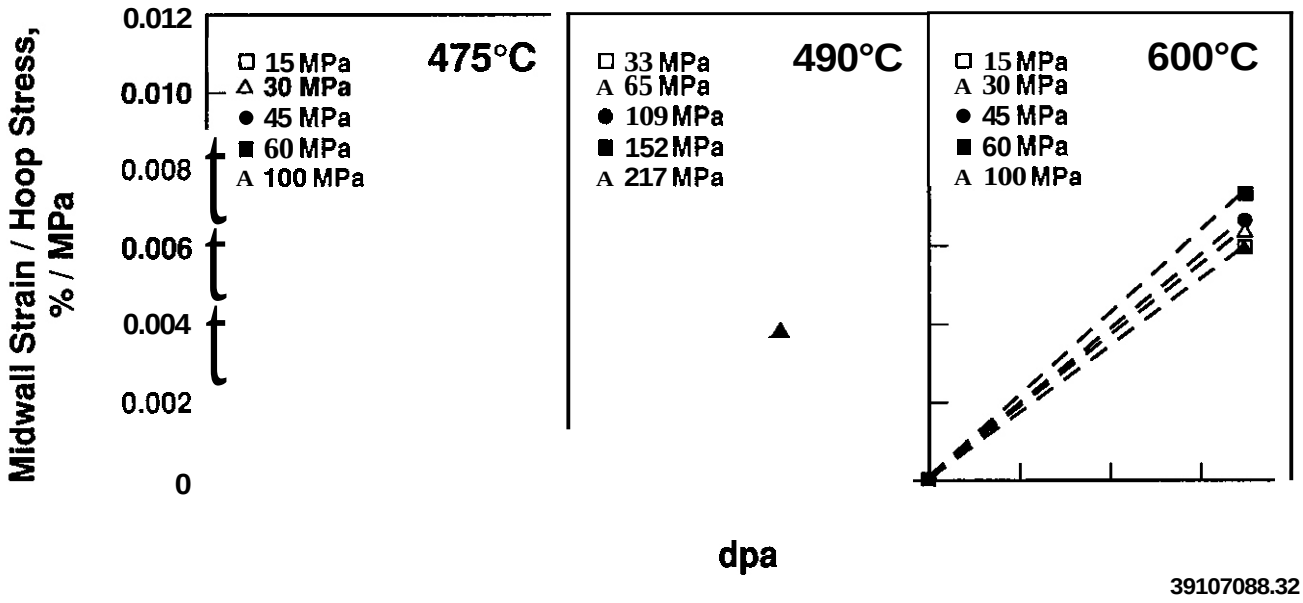

Fig. 11. Stress-normalized creep strains in the above-core experiment

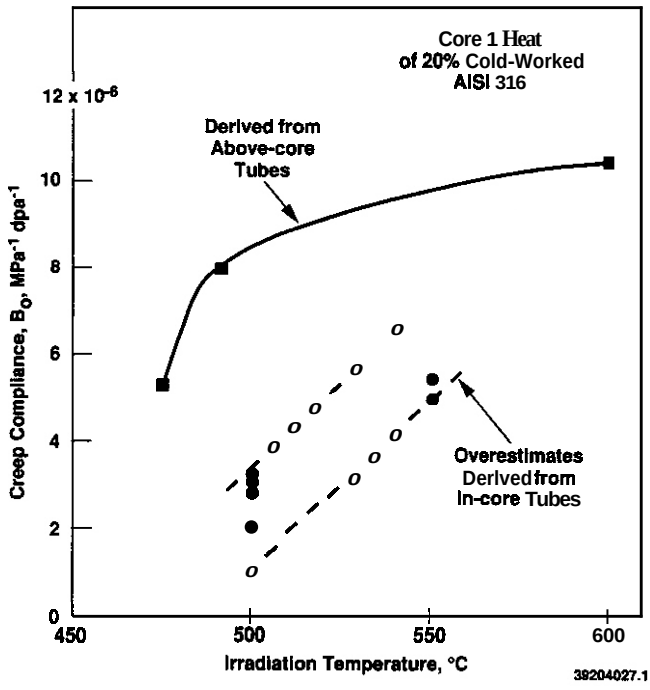

Fig. 12. Comparison of estimated B_o values derived from Core 1 tubes irradiated at various positions in the FFTF core. The neutron flux ($E>0.1MeV$) of the in-core tubes at 500°C is ~70% of those at 550 and 575°C. The fluxes of the out-of-core tubes vary from 6.4 to 12.3% of that of the in-core tubes at 550 and 575°C. The influence of stress-affected swelling leads to overestimates of the B_o coefficient for in-core tubes, especially at higher temperatures.

Table 2. Estimates of Creep Coefficients Derived from In-Core Canisters

Temperature °C	Heat	Stress Level MPa	B_o $10^{-6}MPa^{-1}dpa^{-1}$	D $10^{-2}MPa^{-1}$	Approaching Convergence?
500	Core 1	15	2.1	1.20	
		30	**2.8**	1.26	
		101	3.1	0.73	J
		141	3.2	0.73	✓
550	Core 1	35	5.1	0.51	f
		70	5.5	0.63	f
		117	7.4	0.59	✓
550	Core 4	35	4.6	0.86	J
		70	**4.0**	0.80	✓
		117	**4.4**	0.77	✓
575	Core 1	16	8.4	0.16	
		31	7.5	0.68	J
		63	8.7	0.81	✓
575	Core 4	16	5.6	0.78	✓
		31	6.6	0.66	f
		63	6.6	0.93	✓
		104	8.8	0.99	✓
600	Core 1	15	6.8	0.3	
		30	8.1	**1.26**	
		61	10.0	2.19	
575->525	Core 1	29	0.003	1.72	
		59	4.9	1.06	
		98	7.8	1.37	
575->525	Core 4	29	5.9	0.67	✓
		59	7.2	0.63	J
		98	10.4	0.70	J

Table 3. Estimated Values* of Creep Compliance Derived from Above-Core Canisters.

Temverature, °C	Creep Comvliance. $MPa^{-1}dpa^{-1}$
475°C	5.3×10^{-6}
490°C	8.0×10^{-6}
600°C	10.6×10^{-6}

* Values were derived as the average behavior exhibited by the stress-normalized strains in Figure 11

The creep compliance B_o appears to vary with alloy composition, primarily because it unavoidably contains strains arising from precipitation, a process which varies with both composition and temperature. Unless very small increments of exposure are studied, these strains cannot be observed and separated from the true creep strains. The creep compliance also appears to exhibit an inverse dependence on displacement rate that diminishes with increasing irradiation temperature, in agreement with a recombination-dominated creep model advanced by Lewthwaite and Mosedale. There is another possibility, however, that the observed enhancement of creep rate at lower displacement may arise in whole or part as a consequence of a concurrent softening of the neutron spectrum in the out-of-core regions of the reactor.

In agreement with the results of an earlier study it was shown that at 550 to 600°C, there appears to be a 0.33%/dpa limitation on the maximum deformation rate that develops from the combined action of swelling and creep. This limitation, however, does not always involve an immediate and total "disappearance" of creep associated with attainment of steady-state swelling. The creep rate gradually diminishes as the swelling rate increases, with the sum never exceeding 0.33%/dpa.

Expected Achievements in the Next Reporting Period

The irradiation creep data in this report will be compared with thermal creep data derived from identical tubes to determine whether a previous observation of delayed high temperature creep during irradiation can be confirmed.

ACKNOWLEDGEMENTS

M. Toloczko's participation was supported by the Northwest College and University Association for Science (Washington State University) under grant DE-FG06-8AER with the U.S. Department of Energy. The tubes were fabricated and irradiated under U.S. DOE Contract DE-AC05-76FF02170. The analysis was supported by U.S. DOE contract DE-AC06-76RLO 1830.

REFERENCES

1. F. A. Garner and R. J. Puigh, Journal of Nuclear Materials, 179-181 (1991) 577-580.

2. D. L. Porter, G. D. Hudman and F. A. Garner, Journal of Nuclear Materials, 179-181 (1991) 581-584

3. F. A. Garner and D. L. Porter, Journal of Nuclear Materials, 155-157 (1988) 1006-1011.

4. F. A. Garner, M. L. Hamilton, C. R. Eiholzer, M. B. Toloczko and A. S. Kumar, in Fusion Reactor Materials Semiannual Progress Report, DOE/ER-0313/11 (1992) in press.

5. M. B. Toloczko, F. A. Garner and C. R. Eiholzer, Fusion Reactor Materials Semiannual Progress Report, DOE/ER-0313/9 (1991) 160-166, also in DOE/ER-0313/11 (1992) in press.

6. F. A. Garner in Optimizing Materials for Nuclear Applications, F. A. Garner, D. S. Gelles and F. W. Wiffen, Eds., The Metallurgical Society, 1985, pp. 111-139.

7. F. A. Garner, D. L. Porter and B. .J. Makenas, J. Nucl. Mater., 148 (1987) 279-287

8. D. L. Porter and F. A. Garner in Influence of Radiation on Material Properties. ASTM STP 956, F. A. Garner, C. H. Henager, Jr., and N. Igata, Eds., American Society for Testing and Materials, 1987, pp. 11-21.

9. D. L. Porter and F. A. Garner, J. Nucl. Mater., 159 (1988) 114-121.

10. B. A. Chin and J. L. Straalsund, Journal of Nuclear Materials, 74 (1978) 260.

11. J. F. Bates and D. S. Gelles, Journal of Nuclear Materials, 71 (1978) 365.

12. F. A. Garner, E. R. Gilbert, D. S. Gelles and J. P. Foster, Effects of Radiation on Materials: Tenth Conference. ASTM STP 725, D. Kramer, H. R. Brager and J. S. Perrin, Eds., American Society for Testing and Materials, 1981, pp. 698-712.

13. W. J. S. Yang and F. A. Garner, Effects of Radiation on Materials: Eleventh Conference. ASTM STP 982, H. R. Brager and J. S. Perrin, Eds., American Society for Testing and Materials, 1982, pp. 186-206.

14. B. A. Chin and E. R. Gilbert in Effects of Radiation on Materials: Twelfth International Symposium, ASTM STP 870, F. A. Garner and J. S. Perrin, Eds., American Society for Testing and Materials, 1985, pp. 38-51.

15. A. J. Lovell, B. A. Chin and E. R. Gilbert, Journal of Materials Science, 16 (1981) 870.

16. E. R. Gilbert, B. A. Chin and D. R. Duncan, Metallurgical Transactions 18A (1987) 79-84

17. C. Wassilew, K. Ehrlich and H. J. Bergmann in Influence of Radiation on Material Properties: 13th International Symposium (Part II), ASTM STP 956, F. A. Garner, C. H. Henager, Jr. and N. Igata, Eds., American Society for Testing and Materials, Philadelphia, 1987, pp. 30-53.

18. R. J. Puigh and R. E. Schenter, in Effects of Radiation on Materials: Tenth Conference. ASTM STP 725, D. Kramer, H. R. Brager and J. S. Perrin, Eds., American Society for Testing and Materials, Philadelphia, 1981, pp. 795-802.

19. F. A. Garner, W. V. Cummings, J. F. Bates and E. R. Gilbert, Hanford Engineering Development Laboratory Report HEDL-TME 78-9, Richland, WA, June 1988.

20. R. J. Puigh, A. J. Lovell and F. A. Garner, J. Nucl. Mater., 122 & 123 (1984) 242-245

21. K. Ehrlich, J. Nucl. Mater. 100 (1981) 149

22. M. L. Grossbeck and J. A. Horak, J. Nucl. Mater. 155-157 (1988) 1001-1005.

23. G. W. Lewthwaite and D. Mosedale, J. Nucl. Mater., 90 (1980) 205-215

24. F. A. Garner, H. L. Heinisch, R. L. Simons and F. M. Mann, Radiation Effects and Defects in Solids, 113 (1990) 229-255.

25. C. Wassilew, Bestrahlungsinduriertes Kriechen und Schwellen-Experimentelle Ergebnisse, Phanomenologische Modelle und Modellgleichungen Fur Metalle, KfK Report 4668, Kernforschungsrentrum Karlsruhe (1989).

26. M. L. Grossbeck, K. Ehrlich and C. Wassilew, J. Nucl. Mater., 174 (1990) 264-281

27. F. A. Garner, E. R. Gilbert and D. L. Porter in Effects of Radiation on Materials: Tenth Conference. ASTM STP 725, D. Kramer, H. R. Brager and J. S. Perrin, Eds., American Society for Testing and Materials, 1981, pp. 680-697.

28. D. L. Porter, M. L. Takata and E. L. Wood, J. Nucl. Mater., 116 (1983) 272-276.

29. T. Lauritzen, S. Vaidyanathan, W. L. Bell and W. J. S. Yang, in Radiation-Induced Changes in Microstructure. Thirteenth International Symposium (Part I) ASTM STP 955, F. A. Garner, N. H. Packan and A S. Kumar, Eds., American Society for Testing and Materials, Philadelphia, 1987, pp. 101-103.

30. C. H. Woo and F. A. Garner, "A SIPA-based Theory of Irradiation Creep in the Low Swelling Regime," accepted for publication in J. Nucl. Mater.

31. C. H. Woo, F. A. Garner and R. A. Holt, "Irradiation Creep Due to SIPA in the Peak Swelling Regime," to be presented at the 16th International Symposium ON Effects of Radiation on Materials, Denver, CO, June 1992.

32. F. A. Garner and D. S. Gelles, J. Nucl. Mater. 159(1988)256.

33. F. A. Garner and M. B. Toloczko, in this semiannual report.

34. L. R. Greenwood, F. A. Garner and H. L. Heinisch in Fusion Reactor Materials Semiannual Prowess Report DOE/ER-0313/11, in press; also accepted for publication by J. Nucl. Mater., proceedings of ICFRM-5.

VOID SWELLING RESISTANCE OF PHOSPHORUS-MODIFIED AUSTENITIC STAINLESS STEELS DURING HFIR IRRADIATION TO 57 dpa AT 300 TO 500°C

-- P. J. Maziasz (Oak Ridge National Laboratory)

OBJECTIVE

The objective of this work is to develop advanced austenitic alloys that retain their swelling resistance under irradiation conditions that lead to high helium generation rates.

SUMMARY

The austenitic stainless steel prime candidate alloy (PCA) is a titanium-modified (14Cr-16Ni) alloy developed for void swelling resistance at 400 to 600°C by the US. Fusion Reactor Materials (FRM) program. During irradiation in the High Flux Isotope Reactor (HFIR) (20-70 appm He/dpa) at 300 to 600°C, the PCA (and the closely related D9-type alloy) has been shown to be highly susceptible to void swelling at 500°C after 34 to 57 dpa. Generally such alloys show good void swelling resistance to higher doses during irradiation in fast breeder reactors (FBRs, 0.5-1 appm He/dpa) in the 20 to 25% cold-worked (CW) condition. New multiply stabilized, phosphorus-modified PCA alloys have been developed, with specific amounts and combinations of minor alloy elements added for better MC formation and stability characteristics during irradiation. After HFIR irradiation at 300 to 500°C to 34 to 57 dpa, the multiply stabilized, phosphorus-modified PCA and phosphorusmodified D9 alloy showed better swelling resistance (by density-change measurements) than similar alloys without phosphorus, particularly at 500°C. Microstructural studies after 34 dpa at 500°C showed that void swelling resistance in the multiply stabilized, phosphorus-modified PCA alloys was directly related to the formation of ultrafine dispersions of MC precipitates during HFIR irradiation.

PROGRESS AND STATUS

1.0 Introduction

The austenitic stainless steel prime candidate alloy (PCA) is a titanium-modified 14Cr-16Ni-2.5Mo-2Mn alloy developed for void swelling resistance at 400 to 600°C by the U.S. Fusion Reactor Materials (FRM) program in 1977-78.[1] It was derived from the closely related D9 type steel (Ti- and Si-modified 15Cr-15Ni alloy) developed for void-swelling resistance in a fast-breeder reactor (FBR) environment (0.5 to 1 appm He/dpa) several years earlier.[2] Earlier FRM program studies of void swelling behavior of the PCA steel during irradiation in the HFIR showed good void swelling resistance at 400°C and at 600°C to 44 dpa, hut showed void swelling susceptibility at 500°C.[3] Subsequent spectrally tailored experiments in the Oak Ridge Research Reactor (ORR), with better controlled and more fusion-relevant helium/dpa ratios (12-18 appm Heidpa), again showed significant void swelling after only 11 to 13 dpa at 500°C.[4] Both the HFIR and ORR experiments confirmed that void swelling at 500°C was much worse in solution-annealed (SA) than in 20 to 25% cold-worked (CW) PCA. By contrast, irradiations of CW PCA in the Experimental Breeder Reactor-II (EBR-II) showed excellent void swelling resistance after almost 70 dpa at 500°C.[5] Microstructural studies have confirmed that helium-enhanced void swelling in SA or CW PCA in HFIR and ORR coincides with the lack of fine MC formation during irradiation.[3,4,6] Conversely, void swelling suppression related to helium effects in such steels, including the Japanese-PCA (slightly higher P and B than U.S.-PCA), almost always coincides with the formation of fine, stable, and associated dispersions of helium bubbles and MC precipitates.[7-9] Studies of CW JPCA irradiated in HFIR at 500°C consistently show that the eventual development of voids between 34 and 57 dpa coincides with the dissolution of radiation-produced MC precipitates?

Studies of thermomechanical pretreatments of PCA and JPCA steels have indicated that MC formation and stability during HFIR irradiation is best in CW material?,' MC precipitates developed by prior aging in CW PCA tend to dissolve during irradiation.' A new, modified version of the original PCA alloy composition, containing Ti, V, Nb, C, and P, has been developed based on the synergistic effects of these elements in enhancing formation and stability of fine MC during thermal aging.'' Compositionally modified versions of the D9 alloy containing phosphorus have also been developed, and these alloys have significantly better void swelling resistance than alloys without phosphorus during FBR irradiation.[11-13] Microstructural studies have related this void swelling resistance to the formation of fine phosphide precipitates during FBR irradiation, not MC.[11,12] The purpose of this work was to test the void swelling resistance of the new modified PCA alloy during HFIR irradiation, and to directly compare its behavior with many different alloys, all irradiated in the same experiment.

EXPERIMENTAL PROCEDURE

Standard transmission electron microscopy (TEM) disk (3 mm diam x 0.25 mm thick) specimens of various austenitic stainless steels were irradiated near reactor-midplane in HFIR peripheral target positions at 300 to 500°C to 34 dpa (2500 appm He) and 57 dpa (4300 appm He) in the HFIR JP-l through JP-8 experiments conducted collaboratively between the U.S. and Japan.'','' Chemical compositions of the various US. steels and the JPCA steel examined in these experiments are given in Table 1. U.S. steels were irradiated in the *25%* CW condition (this is termed A3; a closely related thermomechanical treatment - aging for 8 h at 800°C to produce only grain-boundary MC precipitates followed by 25% CW - is termed B3), while JPCA was irradiated in the SA and 15 to 20% CW conditions. Swelling was determined from density change measurem'ents made on duplicate disks of unirradiated control and irradiated material using the ORNL precision densitometer.'' Swelling measurements are accurate to ±0.1%.[17] Following densitometry, TEM observations were made on selected disks irradiated at 500°C to 34 dpa using a JEM 2000FX (LaB_6, 200 kV) analytical electron microscope. More details on the HFIR experiments, alloy preparation, and pretreatments, dosimetry, densitometry, and TEM techniques can be found elsewhere.[8,9,14-19]

Table 1. Chemical Compositions of Various U.S. and Japanese Steels

Alloy	Content,[a] wt %									
	Cr	Ni	Mo	Mn	Si	Ti	Nb	V	C	P
PCA	14.0	16.2	2.3	1.8	0.4	0.24			0.05	0.01
PCA-1	14.0	16.0	2.5	2.1	<0.01	0.13	0.12	<0.01	0.04	<0.001
PCA-3	14.3	15.8	2.5	2.0	0.4	0.13	0.11	<0.01	0.056	<0.001
PCA-6	14.0	16.0	2.4	1.9	0.4	0.23	0.01	<0.01	0.083	<0.001
PCA-8	13.9	16.0	2.7	2.1	<0.01	0.17	0.14	<0.01	0.081	<0.001
PCA-9	13.8	16.0	2.5	2.0	0.4	0.25	<0.01	<0.01	0.073	0.03
PCA-10	13.8	15.9	2.5	1.9	0.4	0.3	0.1	0.02	0.04	0.002
PCA-11	13.8	16.0	2.5	1.9	0.4	0.3	0.1	0.5	0.04	0.002
PCA-12	13.8	15.9	2.4	1.9	0.4	<0.01	0.47	0.01	0.044	0.002
PCA-13	13.8	15.9	2.5	1.9	0.4	0.3	0.1	0.5	0.063	0.002
PCA-19	13.8	19.9	2.44	2.1	0.44	0.28	0.1	0.5	0.076	0.030
PCA-20	13.8	16.1	2.5	2.1	0.42	0.28	0.1	0.5	0.083	0.07
PCA-21	15.8	15.8	2.44	3.4	0.4	0.27	0.1	0.5	0.077	0.06
PCA-22[b]	13.8	15.9	2.3	2.5	0.4	0.28	0.1	0.5	0.078	0.03
D9-697	14.4	16.2	1.5	1.9	0.5	0.25	0.01	0.02	0.035	0.003
D9-A7	13.7	16.3	2.5	2.0	1.42	0.18	<0.01	0.023	0.045	0.075
D9-F	14.3	14.3	2.2	2.1	1.0	0.3			0.05	
JPCA[b]	14.22	15.60	2.28	1.77		0.24			0.06	0.027

[a] Balance iron.

[b] 0.003 B (other alloys contain ≤ 0.001 B).

RESULTS

1. Swelling

Swelling at 300°C after 34 dpa was low (0.1-0.5%) in all U.S. steels, but then increased slightly after 57 dpa (0.2-0.9%); swelling at 300°C and 57 dpa was highest in the 25% CW (B3) PCA steel (1.3-1.9%; see Fig. 1). The phosphorus-modified PCA-9 steel showed the lowest swelling (<0.5%) among the compositionally modified PCA steels irradiated at 300°C to 57 dpa. Swelling was low in all U.S. and Japanese steels (0.1-0.9%) at 400°C after 34 and 57 dpa, and showed the least sensitivity to alloy composition observed over this temperature range (Fig. 1).[19] By contrast, swelling was generally higher in most steels at 500°C, and showed large dependencies on alloy composition, pretreatment condition, and dose (Figs. 1 through 3).[19]

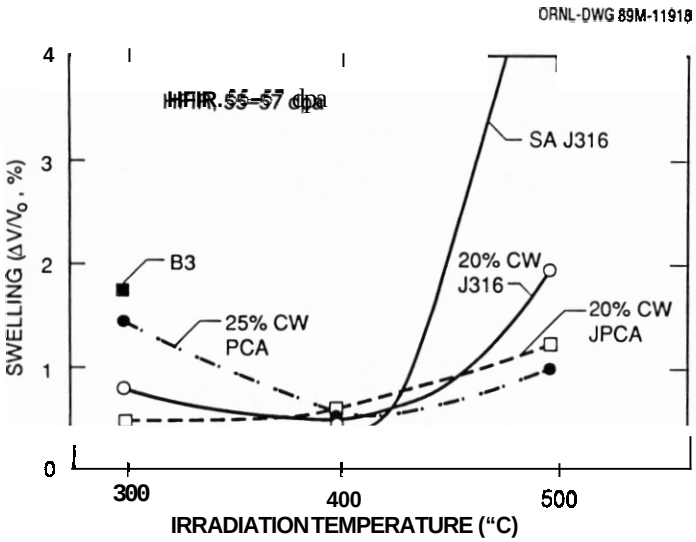

Fig. 1. Swelling measured by densitometry on TEM disks versus temperature for several austenitic stainless steels irradiated in HFIR to 55 to 57 dpa.

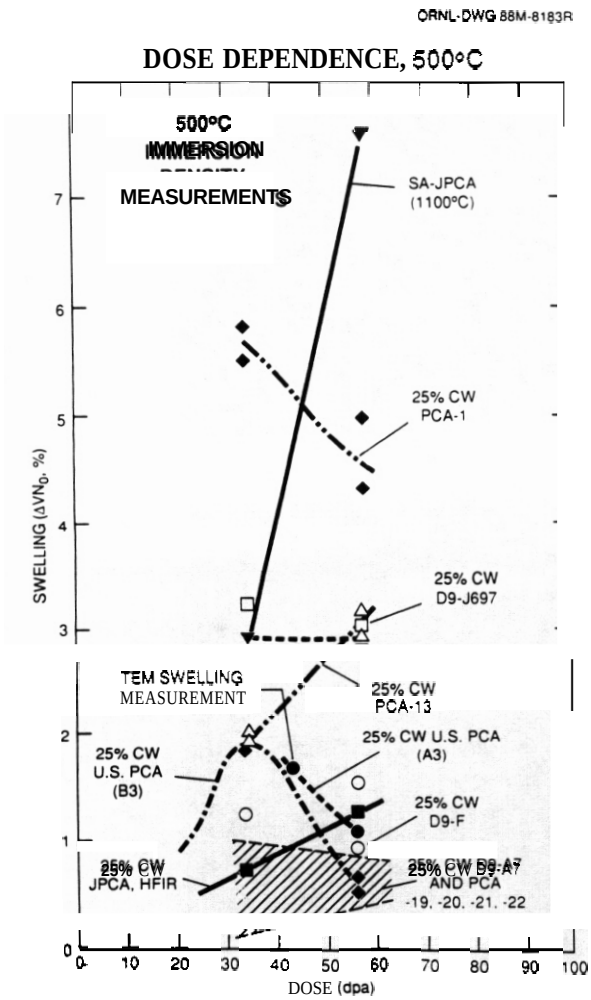

Fig. 2. Swelling as a function of dose for several austenitic stainless steels irradiated in HFIR at 500°C. Data for JPCA alloys are also reported elsewhere.[19]

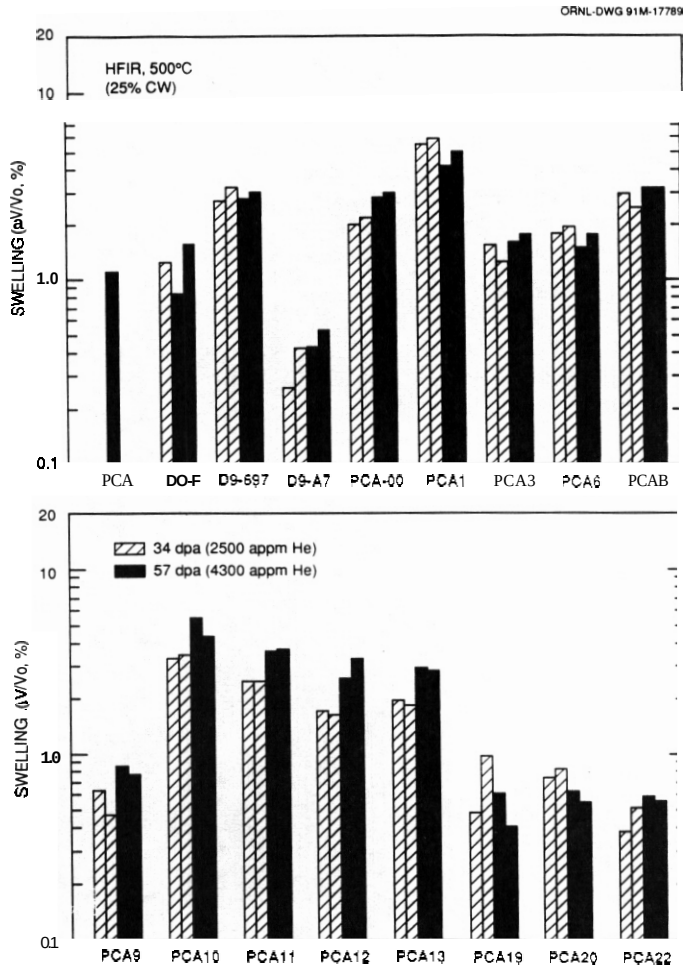

Fig. 3. Swelling of CW D9, PCA, and various modified alloys irradiated in HFIR at 500°C to 34 and 57 dpa. Alloy compositions are listed in Table 1. Each histogram bar represents a densitometer measurement of one TEM disk (PCA-B3 disk data," shown in Fig. 2, was not included here).

Swelling is plotted as a function of dose for several U.S. and Japanese alloys after irradiation in HFIR at 500°C in Fig. 2. Swelling data from each individual disk specimen of the U.S. steel (PCA, D9, and modified PCA/D9) irradiated at 500°C in the 25% CW condition are shown in Fig. 3. After 34 dpa, CW PCA and D9 steels had 1 to 2% swelling and CW PCA had slightly less (0.7%). whereas SA JPCA had about 3% swelling. CW D9-J697 had about 3% swelling and PCA-1 was the worst of the modified PCA alloys with >5.5% swelling (Figs. 2 and 3). Swelling of the other CW compositional variants of PCA without phosphorus ranged from 1.5 to 3.5%. The phosphorus-modified D9-A7, PCA-9 and PCA-19 through -22 steels all exhibited consistently low swelling after 34 dpa at 500°C (0.2 to 0.9%).

After 57 dpa at 500°C, some steels showed the expected increase in swelling with dose, while others showed either little change or an actual decrease in swelling with increasing dose (Figs. 2 and 3). The

highest swelling rate was found in SA JPCA (0.2%/dpa). CW JPCA showed a much smaller but positive welling rate (0.02%/dpa). Several alloys showed little or no change in swelling with increased dose (D9-F and -J697, PCA-3, -6, and -8), while two other alloys actually showed less swelling as dose increased (PCA and PCA-1). Swelling in CW PCA declined from 1.8% to 0.6 to 1.2% as dose increased from 34 to 57 dpa, while CW PCA-1 with more total swelling also showed a similar relative reduction in swelling over that same dose interval (Fig. 2). Despite the more complicated behavior of alloys with higher swelling values, the PCA/D9 steels containing phosphorus (D9-A7, PCA-9, -19, 20, -21, -22) all consistently continued to show very low swelling **(0.4-0.8%)** after 57 dpa.

2. Microstructure

Microstructures of PCA, D9-F, D9-J697, D9-A7, PCA-20 and PCA-22 steel specimens irradiated in HFIR at 500°C to 34 dpa were examined." The PCA, D9-F, and D9-J697 steels all contained bimodal cavity microstructures that were mixtures of small (2-6 nm diam) bubbles and larger (8-25 nm diam) voids (Figs. 4 and 5). Helium bubble concentrations were in the

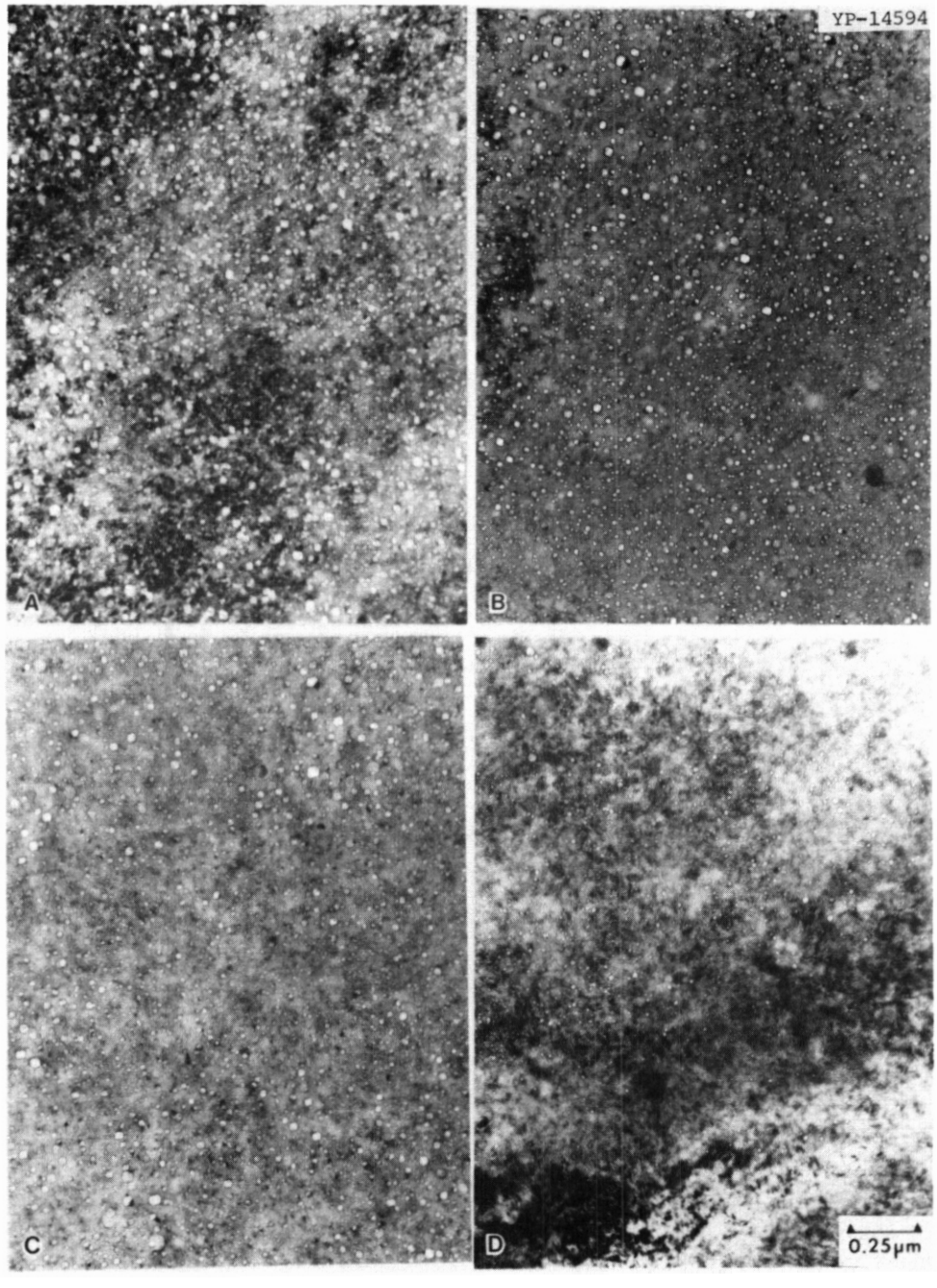

Fig. 4. Lower magnification TEM of cavity microstructures in (a) 25% CW D9-697, (b) 25% CW D9-F, (c) 25% CW PCA, and (d) 25% CW PCA-20, irradiated in HFIR at 500°C to 34 dpa.

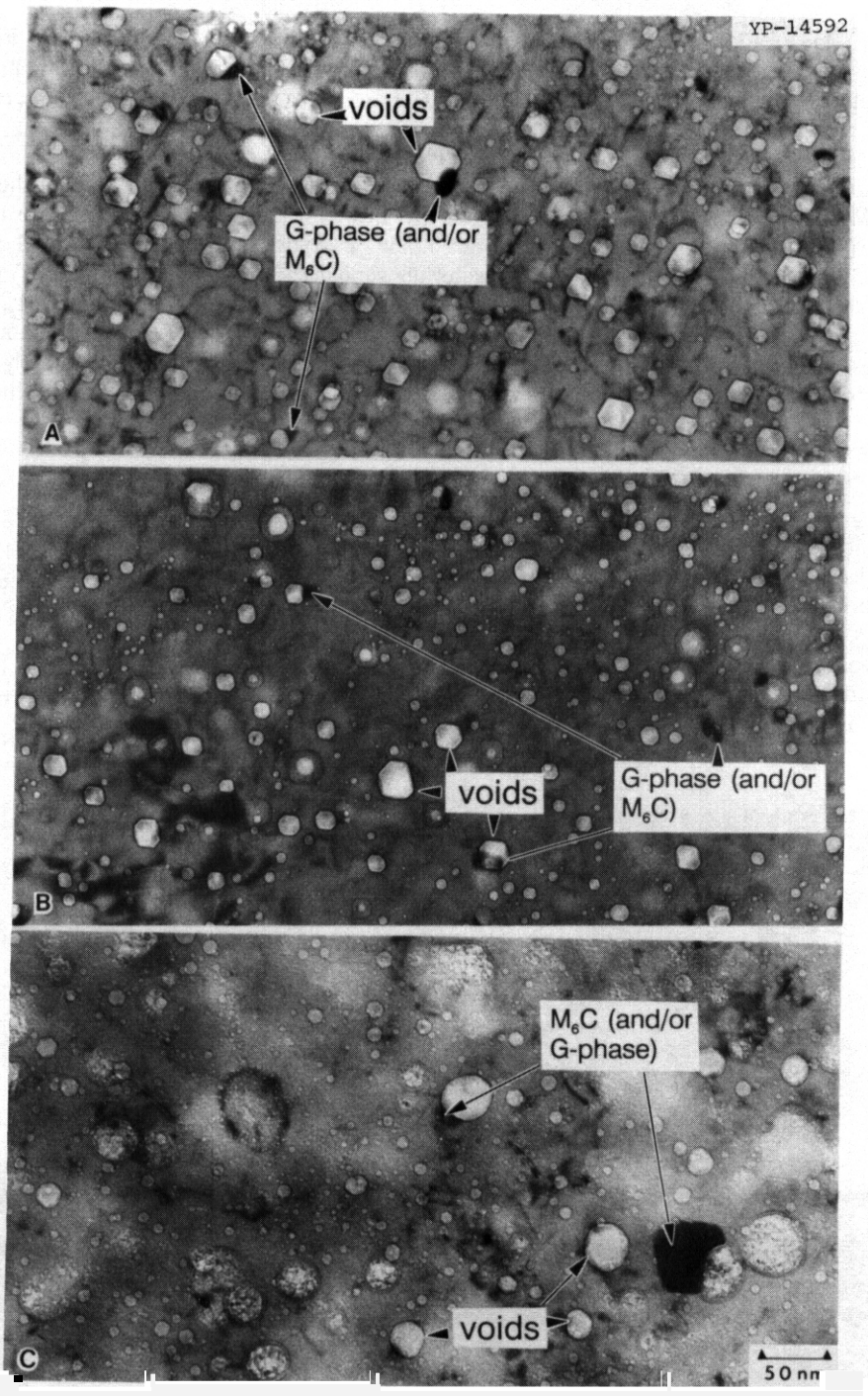

Fig. 5. Higher magnification TEM of cavity microstructures in (a) 25% CW D9-697, (b) 25% CW D9-F, and (c) 25% CW PCA, irradiated in HFIR at 500°C to 34 dpa. Note mixture of larger voids (some associated with coarse precipitates) and ultrafine helium bubbles. Rubble concentrations are in the <1 *to* 2 x 10^{22} m^{-3} range.

< 1 to 2 × 10^{22} m^{-3} range. Dislocation structures consisted of networks with many large Frank loops. Fine MC precipitation was not detectable in any of the three PCA/D9 type alloys; the two D9 type alloys (with significantly more Si than the PCA alloys; see Table 1) did, however, contain coarser M_6C and/or G-phase precipitates, most of which were associated with the largest voids (Fig. 5).

In contrast with the unmodified alloys, the phosphorus-modified D9 alloy (D9-A7) and the multiply stabilized, phosphorus-modified PCA alloys (PCA-20 and -22) examined by TEM all had very uniform, dense (>1 to 2 x 10^{22} m^{-3}) dispersions of ultrafine (2-3 nm diam) helium bubbles with no large voids in the matrix (Figs. 4 and 6). Dislocation microstructures of these phosphorus-modified alloys were generally similar (network plus Frank loops) to those found in the unmodified alloys. The PCA-20 and -22 alloys definitely contained copious dispersions of ultrafine MC particles throughout the matrix, which were easily detectable using the high-resolution moire fringes visible under dynamical-contrast imaging conditions (Fig. 7). These ultrafine dispersions of MC precipitates and helium bubbles were intimately associated with each other [Fig. 7(b)]. Fine precipitates were not detected in the CW D9-A7 alloy, neither MC nor phosphide phases.

DISCUSSION

The discussion will focus on three general areas: (a) the void swelling behavior found during HFIR irradiation of alloys not containing phosphorus, (b) void swelling resistance of the phosphorus-modified alloys irradiated in HFIR, and (c) mechanisms related to both of these.

The decrease in void swelling with increasing dose during HFIR irradiation at 500°C in several of the CW PCA/D9 alloys without phosphorus seems surprising and intuitively contrary to the general understanding of void swelling behavior during

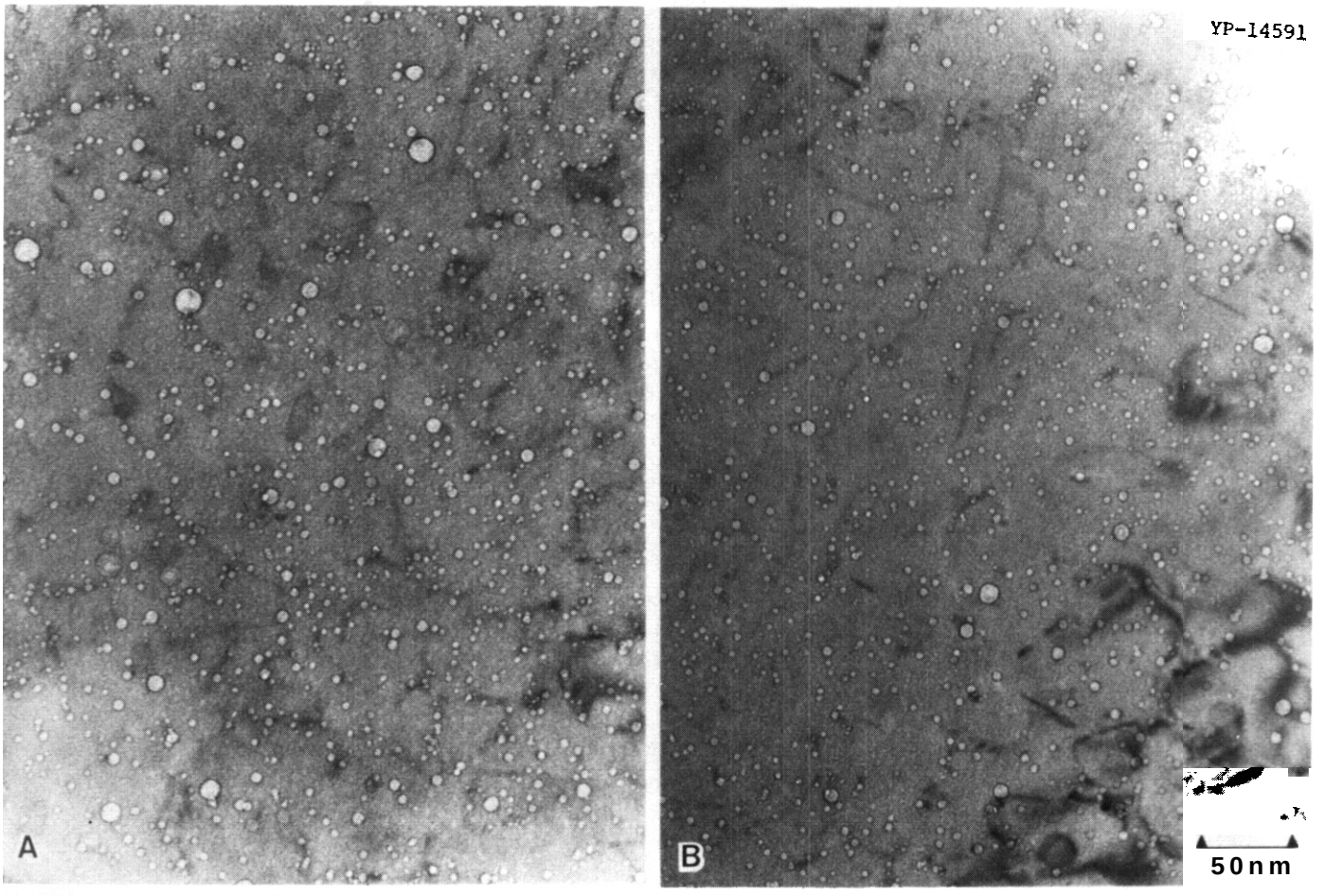

Fig. 6. Higher magnification TEM of ultrafine, subcritical helium bubble microstructures in (a) 25% CW PCA-20 and (b) 25% CW PCA-22, irradiated in HFIR at 500°C to 34 dpa.

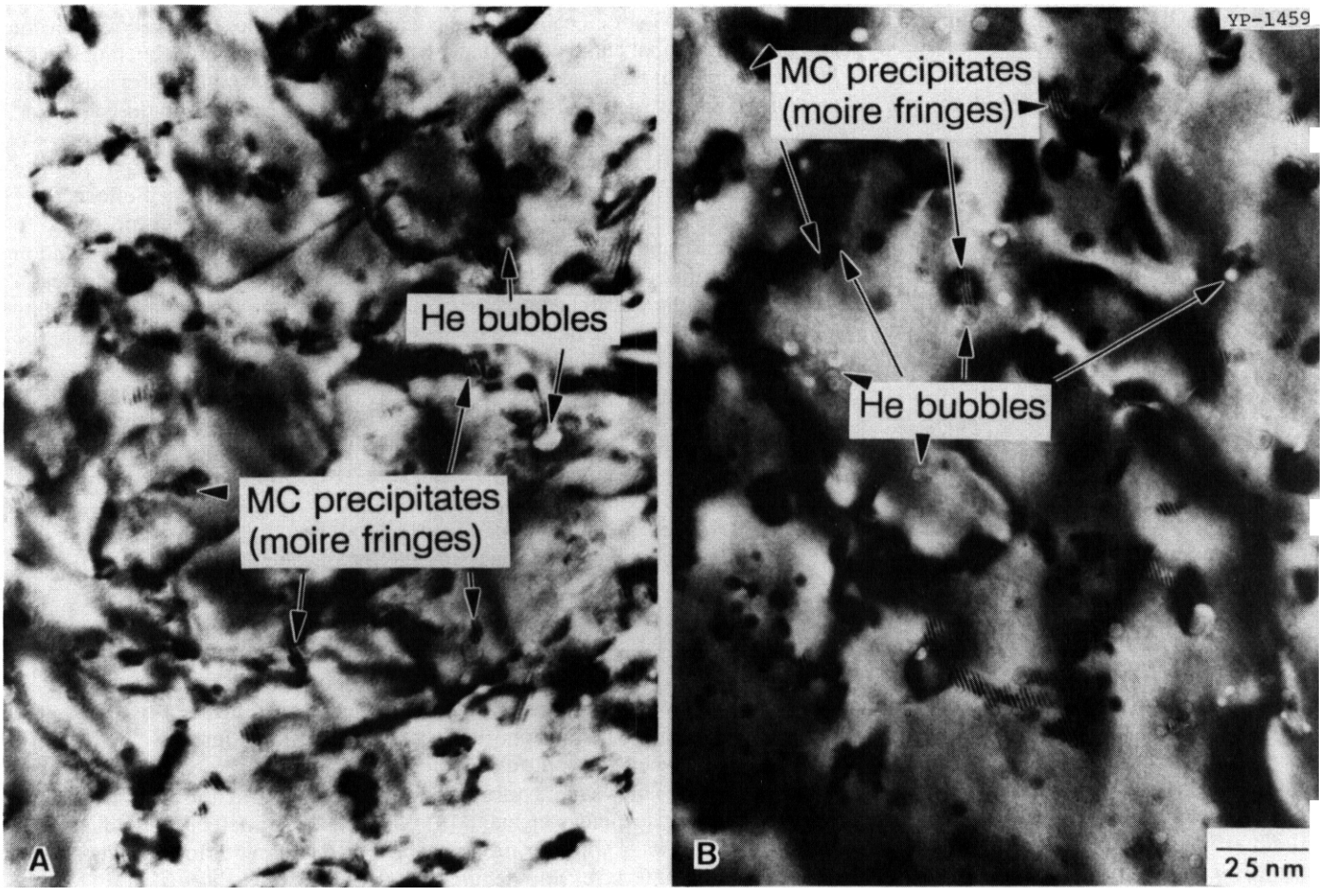

Fig. 7. High-resolution TEM showing moire fringe images [using dynamical contrast (g_{200}, s = 0) conditions] of ultrafine MC formed in (a) 25% CW PCA-20 and (b) 25% CW PCA-22, irradiated in HFIR at 500°C to 34 dpa. Most MC particles are associated with one or more ultrafine helium bubbles in both specimens, but that association is best shown in (b).

neutron irradiation. In most cases, after an initial low-swelling transient period, metals begin a period of linear swelling with dose at a high rate (0.1-1%/dpa) that does not abate until swelling saturates at some high dose and high level of swelling.[7,20-22] Experimentally, this describes the "regular" swelling behavior most often observed in FBR-irradiated austenitic steels and alloys.[21] There have, however, been several unusual observations of decreased swelling and void shrinkage with increased dose during HFIR irradiation of type 316 stainless steel noted previously.[23] Such unusual swelling behavior during HFIR irradiation has also coincided with dramatic changes in other components of the radiation-produced microstructure (disappearance of Frank loops, precipitate dissolution, or increased fine bubble nucleation)? Data from these present experiments provide definite confirmation that such "irregular" swelling behavior with dose is indeed real, because density was measured with a much more accurate technique and apparatus, and duplicate disks were measured. Moreover, the fact that many of the alloys irradiated in the same capsule exhibited "regular" swelling behavior means that such behavior can be blamed on strange irradiation conditions. Despite years of research on radiation-induced swelling behavior, there is still so little high-dose data, particularly at high Heldpa ratios, that void swelling under such conditions is still not well known.

As with previous work, the decrease in macroscopic swelling from 34 to 57 dpa in CW PCA irradiated in HFIR at 500°C observed in this work also may correlate with dramatic changes in microstructural evolution, if we include TEM data from Maziasz and Braski' on CW PCA irradiated in HFIR at 500°C to 44 dpa.[19] While no MC precipitates were found after 34 dpa, many fine MC particles and a slightly higher population of fine, subcritical helium bubbles were observed after 44 dpa in the CW PCA.[19] These observations can be easily understood within the existing theoretical/mechanistic framework used to describe microstructural evolution and void swelling in terms of radiation-induced point defect behavior.[20,23-25] Such microstructural changes could upset the balance between dislocation and cavity (and precipitate) sink strengths, so that cavities (together with the MC precipitate particles) now become the dominant neutral sinks for both vacancies and interstitials. The loss of "steady-state" biased defect partitioning at this advanced stage of microstructural evolution then would cause increased mutual defect recombination to reduce or eliminate the vacancy supersaturation. Dramatic enough changes in overall microstructure and in the point-defect partitioning/recombination behavior could, even at these high doses, cause the critical radius io increase enough so that existing voids whose growth was previously bias-driven would now become unstable. The loss of bias-driven growth

conditions would then cause existing voids to either stop growing or begin shrinking with increasing dose, as well as prevent further void nucleation. Consistent, but opposite effects of global changes in the evolving microstructure, have been observed in CW JPCA irradiated in HFIR at 500°C at **34** and 57 dpa. In this case, when the MC particles dissolved and previously fine dispersions of bubbles coarsened, voids developed in the microstructure and macroscopic swelling increased with dose (Fig. **3)?**

While there have been a number of examples of phosphorus-modified steels and alloys exhibiting void swelling resistance during dual-ion or FBR irradiation relative to similar alloys without phosphorus,[11-13,26-30] the present data on such effects after reactor irradiation at a high He/dpa ratio are unique. Furthermore, several underlying mechanisms have been proposed to explain the effects of phosphorus on void swelling resistance, ranging from phosphorus-vacancy interactions (a solid solution effect)'' to interfacial trapping of helium as fine bubbles at the interfaces of fine needle-phosphide (Fe_2P-type) precipitates (a direct precipitation effect).[26] However, these did not include the possibility of phosphorus enhancing the formation and stability of fine MC precipitates (an indirect precipitation effect), which was actually one of the effects of phosphorus anticipated in the design of the multiply stabilized, phosphorus-modified PCA steels.''

Beneficial effects of phosphorus on void swelling resistance during FBR irradiation have been shown **by** Lee and coworkers in the D9-A7 steel'' and in simpler alloys'' by Garner and Brager in type **316** steels modified with titanium and zirconium,''.'' by Hamilton and coworkers in D9I,[13] and by Dubuisson and coworkers in type **316** modified with titanium or the combination of titanium, niobium and vanadium.'' Phosphorus addition is particularly effective in 20 to 25% CW material, and appears to be far more effective in multiply stabilized alloys (i.e., Ti+Nb+V) than in alloys stabilized only with titanium.[30] The intentional addition of phosphorus has also been part of the Japanese alloying strategy for developing advanced FBR fuel cladding,'' hut their additions have been in the 0.025 to 0.04 wt % range, whereas phosphorus effects have been explored by additions in the **0.03** to 0.15 wt % range in both the **U.S.** and the French work.

While there is clear consistency on the experimental data that establishes the effects of phosphorus on void swelling resistance in various irradiation environments, there is some divergency in the underlying mechanisms invoked to explain that effect. The most frequently discussed mechanisms have been (a) the phosphorus-vacancy interaction effect[13,21,28,29,31,32] and (b) the phosphide precipitate effects.[11,12,25,26] Strong binding between phosphorus dissolved in solution and vacancies to enhance mutual point-defect recombination and reduce the matrix vacancy supersaturation during irradiation is the basis of the first effect. Several mechanisms involved in the effects of needle-phosphides include: (a) enhanced point-defect recombination at the matrix-precipitate interfaces when these act as sinks and their concentration is high,'' (b) increased critical cavity size for the conversion of helium bubble to voids when the precipitate interfaces trap helium such that fine, stable dispersions of bubbles nucleate,[11,24-26] (c) precipitate pinning of dislocations to stabilize the radiation-produced network.' and (d) phosphide phase formation itself preventing the formation of coarse, radiation-induced G phase particles, which directly enhance the formation and growth of attached voids.[27,34] Most of the microstructural analyses in support of studies of the swelling behavior of phosphorus-modified alloys indicate abundant formation of mainly M_2P precipitates during FBR irradiation at **400** to 600°C.[34,35] Indeed, direct TEM analysis by Yang'' showed abundant phosphide formation in the same phosphorus-modified D9-type steels irradiated in EBR-II (MV-III experiment) that were included as part of a larger study of trace element effects on macroscopic swelling by Garner and Brager.[28,29] While Garner and Brager[28] explain swelling resistance of the phosphorus-modified steels in terms of a mechanism based on strong binding between phosphorus atoms and vacancies, it is difficult to see how that single mechanism alone would explain the persistent effects of phosphorus during irradiation. The abundant dispersions of FeTiP phosphides formed during FBR irradiation would significantly (if not almost completely) deplete the matrix of phosphorus dissolved in solution and should promote void swelling if vacancy binding is the dominant effect of phosphorus. However, to the contrary, such fine, dense dispersions of phosphides almost always coincide with microscopic resistance to void formation and growth, as well as macroscopic swelling resistance during FBR irradiation, in support of the models relating the beneficial effects of phosphorus to phosphide formation.[11,12,25,26]

However, while phosphide precipitate effects dominate the microstructures of both FBR and dual-ion irradiated (the latter including a wide range of He/dpa ratios) phosphorus-modified austenitic stainless steels, their absence during HFIR irradiation at high He/dpa ratios means that some other explanation for the effects of phosphorus on void swelling resistance in the D9 type steel is needed. In the multiply stabilized, phosphorus-modified PCA alloys, phosphorus appears to play a role in the enhanced formation and stability of MC carbides during HFIR irradiation. Once formed, the fine, stable dispersions of MC particles then act directly to impart void swelling resistance by mechanisms similar to those invoked for the phosphide precipitates, with interfacial trapping of helium to nucleate fine dispersions of bubbles attached to those particles being the dominant effect at high He/dpa ratios.[7,10,36] However, as with the phosphorus-modified D9 steel (D9-A7), Dubuisson et al. find only FeTiP phosphides to form with no MC during irradiation of multiply stabilized, phosphorus-modified **type 316** steels irradiated in Phenix (FBR, < 1 appm He/dpa) at **400** to 550°C to 80 to 100 dpa.'' Details of whether FeTiP or MC precipitates form in a particular alloy irradiated in different reactors are related to the larger and more complicated issue of phase formation and stability during irradiation, which at least includes such factors as: (a) phase nature, (b) effects of helium of radiation-induced segregation (RIS) of solutes, and (c) effects (including synergisms) of alloying elements on precipitation.

With regard to phase nature, the MC carbides are a radiation-enhanced or -retarded thermal phase, with a negative coupling to RIS,[7,10,22,37-39] whereas the phosphide phases (MP, M_2P, M_3P) can be a radiation-induced or a radiation-modified/enhanced thermal phase with a positive RIS coupling, depending mainly on alloy composition.[7,10,22,34,35,37-39] The MC phase couples negatively to RIS because it is inherently titanium-rich (ultrafine MC can also be very rich in molybdenum and/or chromium') and contains little or no nickel and silicon, while RIS causes nickel and silicon enrichment and molybdenum and chromium depletion.[11,22] MC is a dominant precipitate phase in titanium- or niobium-modified austenitic stainless steels thermally aged at 550°C or above.[40-42] In CW 316 + Ti, D9, PCA or 15-15Ti steels, MC formation has been observed during FBR irradiation at 500 to 540°C and above, but not at lower temperatures for doses up to 100 dpa.[7,34,37,38,43,44] By contrast, thermal MC formation is enhanced by irradiation at 300°C and above in ORR (13 dpa) or in HFIR (10-56 dpa) in CW 316 + Ti, PCA and JPCA steels.[3,4,7-10,40,45]

Given the negative coupling of MC to RIS, differences in MC phase formation between FBRs (1 appm He/dpa) and mixed-spectrum reactors (12-70 appm He/dpa) have been explained in terms of the effects of helium bubble microstructures on dilution of RIS.[7,10,46] When helium bubble concentrations are sufficiently dense and are the dominant sinks for point defects, RIS effects can be diluted or suppressed due to enhanced recombination at too many sinks, analogous to the effect such sinks have on suppressing bias-driven void growth. In this case, thermal MC formation is enhanced during irradiation. Conversely, when RIS is intense, thermal MC does not form during irradiation. The trade-off between such opposing effects can be seen in the temperature dependence of MC formation in CW PCA irradiated in ORR at 11 to 13 dpa,[4,45,46] or in HFIR at 33 to 44 dpa.[3,8,9] MC is definitely observed in both reactors at 300 to 400°C and at 600°C when no voids or radiation-induced phases (G, M_6C) form, but MC is absent at *500°C* when both voids and G phase do form. The formation of fine MC in CW JPCA irradiated in HFIR at 500°C to 34 dpa is attributed to the enabling effects of higher levels of boron and phosphorus relative to the CW PCA,[8,9] but the eventual instability of titanium-rich MC at higher doses is at least partially attributed to the onset of RIS and its negative compositional coupling.[9]

Phosphides are radiation-induced phases that can form in solution-annealed (SA) type 316 and PCA steels (<0.03 wt % P) during FBR irradiation at 400 to 650°C lo <20 dpa.[35] The positive RIS coupling is apparent from the fact that the radiation-induced phosphides are highly enriched in silicon and/or nickel." Generally, the radiation-induced phosphides are also often attached to large voids. Consistently, when either CW or helium preinjection (bubble dilution) suppress RIS (and void formation) during FBR irradiation, radiation-induced phosphides do not form.[22,35] In titanium-modified D9 or PCA alloys with more than 0.04 wt % P added, FeTiP phosphides form thermally at about 700 to 800°C,[10,34,35,47] so that the phase is no longer induced by irradiation. The M_2P phosphide needles form abundantly in such steel in both the SA and CW conditions during FBR irradiation at 400 to 600°C, so their formation is radiation-enhanced unpublished work by Lee[10] shows that the FeTiP phase becomes much richer in nickel and silicon during ion irradiation, so this phase is also compositionally modified during irradiation. The positive RIS coupling together with helium bubble dilution of RIS may partly explain why such phosphides are not observed in the CW D9-A7 alloy irradiated in HFIR at 500°C.

Finally, the effects of minor alloying elements on the thermal formation of the FeTiP and MC phases also helps to explain why MC rather than phosphides form in the multiply stabilized, phosphorus-modified PCA steel during HFIR irradiation." Without phosphorus, comparison of SA PCA-10, -12, and -13 after aging for 166 h at 800°C showed much finer MC formation in the PCA-13 alloy, indicating that the triple addition of titanium, vanadium, and niobium was much better at producing ultrafine MC particles than single or double additions of titanium and niobium." Moreover, in the multiply stabilized PCA alloy (PCA-13) the ultrafine MC precipitate particles contain more Ti + Nb + V and less Mo + Cr, which appears to be an important factor in affecting microstructural stability (resistance to coarsening or dissolution) of the MC by controlling its phase composition. Similar aging comparison of PCA-9 and PCA-19 (both with 0.03 wt % P) showed that FeTiP formation was also enhanced by the addition of Ti + Nb + V relative to titanium alone." Both Maziasz[10] and Dubuisson et al.[30] show that niobium is enriched in the thermal FeTiP phase, but that vanadium is not, so that each element appears to have a different role in enhancing phosphide formation. However, there also appears to be an interference effect between the MC and FeTiP phases that most likely stems from their competition for common solutes (Ti and possibly Nb).[10,46] In PCA-19 through -22 aged for 166 h at 800°C, FeTiP needles form abundantly with some MC in SA material, whereas only ultrafine MC forms in CW material." The multiply stabilized, phosphorus-modified PCA alloys (PCA-19 through -22) generally contain more carbon than the phosphorus-modified 316 + Ti (ref. 30) or the phosphorus-modified D9 alloys (D9-A7, D9I),[11-13] which should also favor MC formation. Previous studies have also shown that phosphorus (<0.04 wt %) or phosphorus plus boron additions appear to enhance MC formation and stability.[13,48] In summary, the combined (and synergistic) compositional effects of minor alloying elements MC and FeTiP formation and stability are consistent with the formation of MC rather than phosphides in the PCA-20 and -22 steels during HFIR irradiation at 500°C, and also help explain why these steels have better MC formation/stability characteristics than the PCA base alloy or phosphorus-modified D9 alloys. Such microstructural effects were anticipated in the design of these new steels.[10,46]

From a practical point of view, the new HFIR data showing variable swelling behavior reinforce the need for swelling-resistant alloys for fusion applications. Void swelling is a stochastic phenomenon, difficult to predict and accommodate in design. The multiply stabilized, phosphorus-modified PCA alloys show swelling resistance at 300 to 500°C that is good to at least 57 dpa in HFIR. The MC-stabilized helium bubble microstructures found in the multiply stabilized, phosphorus-modified PCA alloys at 500% could remain stable to significantly higher doses *if* bubble dilution prevents RIS so that the ultrafine MC remains stable, *and* the associated MC precipitates prevent bubble coalescence and coarsening so that voids do not develop.'''' Coarsening and coalescence of bubbles during irradiation (aided by radiation-enhanced diffusion and radiation-driven dislocation evolution)[22] appear to he critical steps in destroying the dominant-sink effect of a fine dispersion of helium bubbles.'' The instantaneous decrease in critical size coupled with sudden, large jumps in size of the actual helium buhbles moves the *microstructure* in a situation where void formation becomes easy.[10,25] Not only do the ultrafine MC precipitates act as multipliers for bubble nucleation to push the microstructure into the cavity-sink dominant regime, they also act to keep the microstructure in that regime by pinning the bubbles to retard or prevent coalescence and coarsening. This special aspect of MC-bubble interaction was part of the general strategy for managing the effects of helium to produce void-swelling resistance in austenitic stainless steels for fusion reactor application in 1984.[7]

Spectral- and isotopically-tailored HFIR experiments to test these alloys at fusion-relevant Heidpa ratios (10-12 appm He/dpa) and higher doses are currently in progress (HFIR-JP9 through -13 and HFIR-RB* experiments). Although current near-term. water-cooled fusion reactor concepts, like the International Thermonuclear Experimental Reactor (ITER) with first-wall temperature of <350°C and total lifetime damage levels of 30 to 35 dpa, would not require advanced steels like the modified PCA that are void-swelling resistant.'' advanced blanket modules may. If the water coolant is replaced by helium, first-wall temperatures would likely be higher than 500°C, so that void swelling and possibly grain-boundary helium embrittlement could become life-limiting issues that would necessitate application of an advanced, radiation-resistant austenitic Stainless steel. Turning from fusion and the effects of helium, there is good evidence that the phosphorus-modified D9 and PCA steels have the potential for longer low-swelling transient periods and much lower swelling at 400 to 500°C (which seems a most difficult regime to control'') for FBR applications relative to unmodified steels.[13,44] TEM disks of these small heats of multiply stabilized, phosphorus-modified PCA steel, together with larger heats of the same steel produced commercially, have been included in FFTF experiments irradiated at 400 to 600°C to > 120 dpa. Renewed interest in FBRs in the form of inherently sate modular systems [i.e., the Power Reactor, Inherently Safe Module (PRISM) designed by General Electric''.'') could present an opportunity for application of these steels in the United States not seen since the early 1980s. These steels have been patented,[52] and represent a transferable-technology available from the Oak Ridge National Laboratory.[53,54]

CONCLUSIONS

1. Cold-worked, phosphorus-modified D9 (D9-A7) **and** multiply stabilized, phosphorus-modifed PCA alloys all show better void-swelling resistance after HFIR irradiation at 300 to 500°C to 34 to 57 dpa than similar alloys without phosphorus. At 500°C after 57 dpa, swelling of most alloys without phosphorus ranged from 1 to 5.5%, while the alloys with phosphorus showed only 0.4 to 0.8% swelling.

2. The CW phosphorus-modified alloys maintained swelling-resistant behavior over the dose interval from 34 to 57 dpa. Most other alloys without phosphorus showed increased swelling with increased dose ("regular" behavior), while a few alloys showed either no change in swelling (D9-J697, PCA-3, PCA-6) or decreased swelling (PCA, PCA-1) with increased dose at 500°C ("irregular" behavior).

3. Microstructurally, the swelling-resistant multiply stabilized, phosphorus-modified PCA alloys (PCA-19 through -22) had dense (>1 to 2 **x** 10^{23} m^{-3}) dispersions of very fine (2-3 nm diam) helium bubbles associated with similar dispersions of ultrafine MC precipitates, and virtually no large voids after 34 dpa at 500°C. The phosphorus-modified D9 (DY-A7) alloy had a similar ultrafine bubble structure, hut had no detectable precipitates. The CW D9 and PCA steels had significantly fewer fine bubbles, no fine MC precipitates, and many larger **voids.**

REFERENCES

1. E. E. Bloom et al., Third Topical Meeting on the Technology of Controlled Nuclear Fusion, CONF-780508, USDOE, Vol. 1 (1978), p. **554.**
2. J. J. Laidler, J. J. Holmes, and J. W. Bennett, Nucl. Eng. Int. (July 1980), p. 31.
3. P. J. Maziasz and D. N. Braski. J. Nucl. Mater. 122&123 (1984) 311.
4. R. E. Stoller, P. J. Maziasz, A. F. Rowcliffe, and M. P. Tanaka. J. Nucl. Mater. 155-157 (1988) 1328.
5. R. J. Puigh, J. Nucl. Mater. 141-143 (1986) 954.
6. P. J. Maziasz, R. L. Klueh, and **A.** F. Rowcliffe, MRS Bull. 14 (July 1989) 36.

7. P. J. Maziasz, J. Nucl. Mater. 122&123 (1984) 472.
8. M. P. Tanaka, S. Hamada, A. Hishinuma, and P. J. Maziasz, J. Nucl. Mater. 155-157 (1988) 801.
9. M. Suzuki et al., Effects of Radiation on Materials: 14th Int. Symo., Vol. 1, ASTM STP 1046, Philadelphia, PA (1989), p. 160.
10. P. J. Maziasz, MiCon 86 Optimization of Processing, Properties, and Service Performance Through Microstructural Control, ASTM STP 979, Philadelphia, PA (1988), p. 116.
11. E. H. Lee, L. K. Mansur, and A. F. Rowcliffe, J. Nucl. Mater. 122&123 (1984) 299.
12. E. H. Lee and N. H. Packan, Effects of Radiation on Materials: 14th Int. Symn.. Vol. 1, ASTM STP 1046, Philadelphia, PA (1989), p. 133.
13. M. L. Hamilton et al., Residual and Unspecified Elements in Steel, ASTM STP 1042, Philadelphia, PA (1989), p. 124.
14. J. L. Scott et al., Oak Ridge National Laboratory Report, ORNL/TM-10102 (August 1986).
15. A. F. Rowcliffe, M. L. Grossbeck, and S. Jitsukawa, ADIP Semiann. Proe. Rent.. DOE/ER-0045/12, USDOE Office of Fusion Energy (July 1984), p. 38.
16. R. A. Buhl and L. J. Turner, Oak Ridge National Laboratory Report, ORNL/TM-10378 (to be published).
17. H. Kanazawa, T. Sawai, and L. J. Turner, FRM Semiann. Proe. Rent.. DOE/ER/0313/8, USDOE Office of Fusion Energy (Sept. 1990), p. 17.
18. L. R. Greenwood, ADIP Semiann. Proe. Rent.. DOE/ER-0045/16, USDOE Office of Fusion Energy (Sept. 1986), p. 17.
19. P. J. Maziasz et al., FRM Semiann. Proe. Rent., DOE/ER-0313/2, USDOE Office of Fusion Energy (Sept. 1987), p. 188.
20. L. K. Mansur, Nucl. Technol. 40 (1978) 5.
21. F. A. Garner, J. Nucl. Mater. 122&123 (1984) 459.
22. P. J. Maziasz and C. J. McHargue, Int. Mater. Rev. 32 (1987) 190.
23. R. E. Stoller and G. R. Odette, in Radiation-Induced Changes in Microstructure: 13th Int. Symp. (Part I), ASTM STP 955 (1987), pp. 358 and 371.
24. L. K. Mansur and W. A. Coghlan, J. Nucl. Mater. 119 (1983) 1.
25. L. K. Mansur, E. H. Lee, P. J. Maziasz, and A. F. Rowcliffe, J. Nucl. Mater. 141-143 (1986) 633.
26. E. H. Lee and L. K. Mansur, J. Nucl. Mater. 141-143 (1986) 695.
27. M. Itoh, S. Onose, and S. Yuhara, in Radiation-Induced Chances in Microstructure: 13th Int. Symn. (Part 1), ASTM STP 955 (1987), p. 114.
28. F. A. Garner and H. R. Brager, J. Nucl. Mater. 133&134 (1985) 511.
29. F. A. Garner and H. R. Brager, J. Nucl. Mater. 155-157 (1988) 833.
30. P. Dubuisson et al., in 15th Int. Symo. Effects of Radiation on Materials, ASTM STP 1125, Philadelphia, PA; to be published in 1992.
31. H. Watanabe et al., J. Nucl. Mater. 155-157 (1988) 815.
32. T. Muroga, F. A. Garner, and J. M. McCarthy, J. Nucl. Mater. 168 (1989) 109.
33. L. K. Mansur, M. R. Hayns, and E. H. Lee, in Phase Stability During Irradiation, eds., J. R. Holland, L. K. Mansur, and D. I. Potter, TMS-AIME, New York (1981), p. 359.
34. W.J.S. Yang, in Radiation-Induced Changes in Microstructure: 13th Int. Symn. (Part 1). ASTM STP 955 1987), p. 628.
35. P. J. Maziasz, J. Nucl. Mater. 169 (1989) 95.
36. P. J. Maziasz, in Phase Stability Durine Irradiation. eds., J. R. Holland, L. K. Mansur, and D. I. Potter, TMS-AIME, New York (1981), p. 477.
37. E. H. Lee, P. J. Maziasz, and A. F. Rowcliffe, ibid., p. 191.
38. W.J.S. Yang, H. R. Brager. and F. A. Garner, ibid., p. 257.
39. P. J. Maziasz, J. Nucl. Mater. 108&109 (1982) 359.
40. P. J. Maziasz, J. A. Horak, and B. L. Cox, in Phase Stability Durine Irradiation, eds., J. R. Holland, L. K. Mansur, and D. I. Potter, TMS-AIME, New York (1981), p. 271.
41. T. M. Williams, J. M. Titchmarsh, and P. R. Arkell, J. Nucl. Mater. 107 (1982) 222.
42. G. Brun, J. LeNaour, and M. Vouillon, J. Nucl. Mater. 101 (1981) 109.
43. D. Gilbon, L. LeNaour, C. Rivera, and H. Lorant, in Effects of Radiation on Materials: 12th Int. Symp., ASTM STP 870 (1985). p. 115.
44. J. L. Seran et al., in 15th Int. Symn., Effects of Radiation on Materials, ASTM STP 1125, Philadelphia, PA; to be published in 1992.
45. P. J. Maziasz, to be published in J. Nucl. Mater. in 1992 (proc. of ICFRM-5).
46. P. J. Maziasz, R. L. Klueh, and A. F. Rowcliffe, MRS Bull. 24 (July 1989) 36.

47. J. **A.** Todd and J. ***C.*** Ren, in New Alloys for Pressure Vessels and Pining, PVP-Vol. 201, Am. Soc. Mech. Eng., New York (1990), p. 189.

48. M. Fujuwara et al., in Radiation-Induced Chances in Microstructure: 13th Int. Symp. (Part 1), ASTM STP ***955*** (1987), **p.** 127.

49. P. J. Maziasz et al., Fusion Technol. 19 **(May** 1991) **1571**

50. World News: USA. Nucl. Eng. Int., 33 (Sept. 1988) 2.

51. PRISM. Nucl. Eng. **Int.** 33 (Nov. 1988) 19.

52. P. J. Maziasz, D. N. Braski, and A. F. Rowcliffe, "Radiation Resistant Austenitic Stainless Steel Alloys," U.S. Patent 4,818,485 **(April** 4, 1989).

53. L. L. Horton, Mech. Eng. (Sept. 1988) 44.

54. P. J. Maziasz and R. W. Swindernan. in Proc. 1990 Int. Coneress on Technology and Technolow Exchanee, Int. Technol. Institute, Pittsburgh, PA (1990), **p.** 144.

6.3 Refractory Metal Alloys

NEUTRON IRRADIATION DAMAGE OF A STRESS RELIEVED TZM ALLOY - K. Abe, T. Masuyama, and M. Satou (Tohoku University), and M. L. Hamilton (Pacific Northwest Laboratory)'

OBJECTIVE

The objective of this work is to study defect microstructures and irradiation hardening in a stress relieved TZM alloy after irradiation in the Fast Flux Test Facility (FFTF) using the Materials Open Test Assembly (MOTA).

SUMMARY

Disk specimens of the molybdenum alloy TZM that had been stress relieved at 1199 K (926°C) for 0.9 ks (15 min.) were irradiated in the FFTF/MOTA 1F at 679, 793 and 813 K (406, 520 and 600°C) to a fast fluence of ~9.6 x 10^{22} n/cm^2. Microstructures were observed in a transmission electron microscope (TEM). Dislocation structures consisted of isolated loops, aggregated loops (rafts) and elongated dislocations. The size of the loops increased with the irradiation temperature. Void swelling was about 1 and 2% at 793 and 873 K (520 and 600°C), respectively. A void lattice was developed in the body centered cubic (bcc) structure with a spacing of 26 - 28 nm. The fine grain size (0.5 ~ 2 μm) was retained following high temperature irradiation, indicating that the stress relief heat treatment may extend the material's resistance to radiation damage up to high fluence levels. Microhardness measurements indicated that irradiation hardening increased with irradiation temperature. The relationship between the microstructure and the observed hardening was determined.

PROGRESS AND STATUS

Introduction

Molybdenum alloys such as TZM are candidate materials for high heat flux components in fusion reactors due to their high temperature strength, good thermal properties and their low sputtering yields.[1] The ductile-to-brittle transition temperature (DBTT) of the alloys, however, increases with neutron irradiation. Previous work showed that the embrittlement of molybdenum after high temperature neutron irradiation depended strongly on the pre-irradiation heat treatment of the material. A stress relief treatment, far example, conferred improved resistance to radiation-induced embrittlement at low dpa levels. It was therefore of interest to investigate the resistance to irradiation damage at high dpa levels conferred by a pre-irradiation stress relief.

Experimental Procedures

TEM disks 0.25 mm (0.010 in) in thickness were punched from an arc melted AMAX TZM sheet of composition 0.48% Ti, 0.10% Zr, 0.013% C, *0.0004%* O and 0.0002% N, where elemental levels are given in weight percent. The specimens were stress relieved at 1199 K (925°C) for 0.9 ks (15 min.) and were irradiated in the FFTF/MOTA cycle 10 at 679, 793 and 873 K (406, 520 and 600°C) to a fast fluence of ~9.6 x 10^{22} n/cm^2. Specimens were irradiated in lithium-filled capsules to prevent the pickup of interstitial contaminants from the reactor sodium.

Thin foils were prepared for microscopy by twin jet electropolishing and microstructures were observed in a 200kV TEM. Void size distributions and swelling levels were estimated using a personal computer coupled to a digitizer. Irradiation hardening was estimated using Vickers microhardness measured with both 200 and 500 gf loads after surface layers were removed by electropolishing.

Results and Discussion

MICROSTRUCTURE

Figure 1 demonstrates in low magnification micrographs that the fine grain size, ranging from about 0.5 to 2 μm, was retained following irradiation at all three temperatures. Since a fine grain structure was maintained duriny irradiation at a temoerature as hiah as 873 K (600°C), it may be surmised that a pre-irradiation stress relief may impart significant resistance to radiatian damage in TZM irradiated to even higher fluence levels than were achieved in the current experiment.

Voids were observed in stress relieved specimens irradiated at 793 and 873 K (520 and 600°C), but not in specimens irradiated at 679 K (406°C). Void swelling was caused primarily by voids located in the void lattice that developed during irradiation, examples of which are given in Figure 2; the lattice has a bcc structure with a lattice parameter of 27 and 28 nm for the 793 and 873 K (520 and 600°C) irradiations, respectively. These parameters are smaller than those determined for the void structures that developed in

---

'Pacific Northwest Laboratory is operated for the U.S. Department of Energy by Battelle Memorial Institute under Contract DE-AC06-76RLO 1830.

recrystallized Mo-0.5Ti after irradiation in the Exoerimental Breeder Reactor-11 (EBR-II) at 585 and 790 K (312 and 517°C) to 2.5 x 10^{22} n/cm^2 (E > 0.1 MeV).[3] 'Thus the void lattice parameter is smaller in stress relieved TZM than in recrystallized TZM, while the swelling level itself is comparable or larger.

The void distribution in the lattice is shown at higher magnification in figure 3. The void structures are summarized in Table 1. The mean void diameter after irradiation at 793 and 873 K (520 and 600°C) was 4.4 and 5.4 nm, respectively. It is significant that the lattice exhibited some irregularity with respect to void location and that there was a distribution in void sizes present (Figure 4). This figure shows that the irregularly positioned voids were relatively small in size. The fact that many smaller voids were present in irregular lattice sites may indicate that the interaction between the voids increases with void diameter. Zones denuded of voids were observed at both TiC precipitates and grain boundaries (Figure 5). The size of the denuded zone was typically several times the void lattice parameter.

It has been stated that voids were not observed in stress relieved TZM specimens irradiated at 679 K (406°C), although void swelling levels of about 0.7 and 1.6% were present in specimens irradiated at 793 and 873 K (520 and 600°C), respectively. In comparison, swelling levels of ≤0.4 and 3.8% were observed in recrystallized TZM specimens irradiated in the EBR-II at 667-791 and 839 K (394-518 and 566°C) to 2.5 x 10^{23} n/cm^2.[4] The temperatures given here are corrected irradiation temperatures based on the analyses presented in references 5 and 6. The current swelling data are compared in Figure 6 to those given in references 4 and 7; the current data are reasonably consistent with Gelles' data, although it could be argued that swelling appears to start slightly sooner in stress relieved TZM than in recrystallized TZM.

The dislocation structures that evolved during irradiation are illustrated in Figure 7, which shows dislocation loops and rafts (aggregates of loops) at 679 and 193 K (406 and 520°C) and elongated dislocations at 873 K (600°C). Microstructural data are given in Table 2. It is evident from this table that the size of the dislocation loops increased with irradiation temperature.

MICROHARDNESS

The microhardness data are listed in Table 3 and plotted in Figure 8. The smaller 200 gf load was used initially in an effort to compensate for the small size of the TEM disk specimens, but the hardness value obtained in the unirradiated condition was not consistent with the known hardness value and a large amount of scatter was observed in the data. Since the specimen thickness was well in Excess of ten times the indentation depth for both values of load, however, the data appear acceptable.

Figure 8 shows the irradiation-induced shifts in Vickers microhardness values that were obtained using both the 200 and 500 gf loads. The hardening produced by irradiation increased with irradiation temperature. Since the dislocation density decreased significantly as the irradiation temperature increased, the hardening is evidently due to the void lattice structure. The temperature dependence of the data appears to be slightly influenced by load, however. The data obtained at the lower load level probably include a load-dependent contribution and, based on comparison with the hardness values obtained at the higher load, are probably not completely valid.

CONCLUSIONS

Irradiation hardening in stress relieved TZM was observed to increase with irradiation temperature up to 793 K (520°C), and then decrease slightly at 873 K (600°C). The latter is attributed to a decrease in dislocation density in conjunction with the evolution of a void lattice during irradiation. The retention of a fine grain size following high temperature irradiation implies that a stress relief treatment may impart to the alloy significant resistance to radiation damage.

FUTURE WORK

TEM observations are in progress on single crystals of molybdenum that were also irradiated in MOTA 1F. Mechanical property measurements will be obtained using miniature tensile specimens irradiated in MOTA 2A. The deformation and fracture mechanisms will be of particular interest in this material with void lattice structures.

REFERENCES

1. J. B. Whitley, K. L. Wilson and D. A. Buchenauer, J. Nucl. Mater., 155-157 (1988) 82.

2. K. Abe, M. Kikuchi, K. Tate and S. Morozumi, J. Nucl. Mater., 122-123 (1984) 671.

3. F. W. Wiffen, "Radiation-Induced Voids in Metals," US-AEC Symp. Ser. No. 26 (1972) p. 386, USAEC

4. D. S. Gelles, J. Nucl. Mater., 122-123 (1984) 207

5. R. W. Clark, "Dimensional Change Correlations for 20% Cold-Worked AISI 316 Stainless Steel for Fusion Applications", Master's Thesis, University of Missouri, Rolla (1986).

6. F. A. Garner, H. L. Heinisch, R. L. Simons and F. M. Mann, Rad. Effects and Defects in Solids, 113 (1990) 229.

7. D. S. Gelles, D. T. Peterson and J. F. Bates, J. Nucl. Mater., 103-104 (1981) 1141.

8. K. Abe, T. Masuyama, M. Satou and M. L. Hamilton, to be published in J. Nucl. Mater. as the proceedings of the Fifth International Conference on Fusion Reactor Materials, held in Clearwater, Florida, on November 14 - 18, 1991.

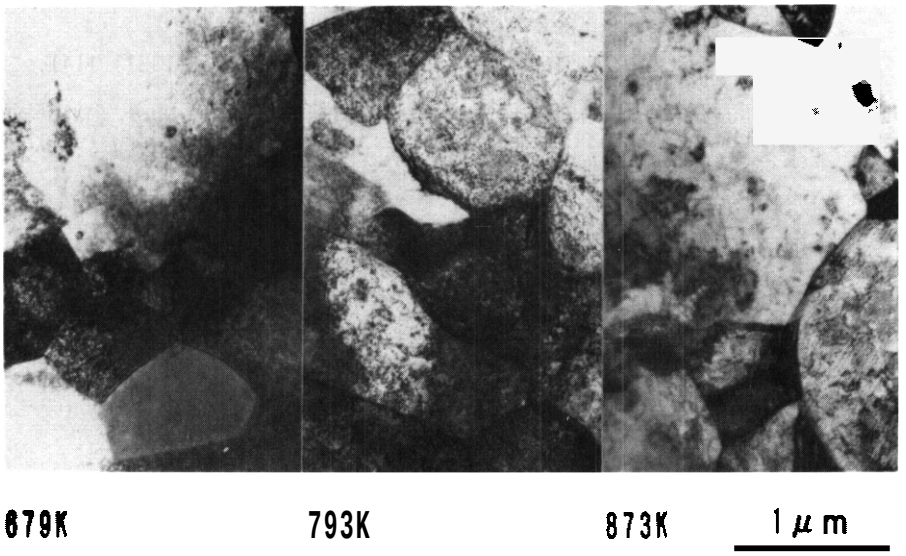

Fig. 1. Microstructure of stress relieved TZM after neutron irradiation at (a) 679 K (406°C), (b) 793 K (520°C), and (c) 873 K (600°C).

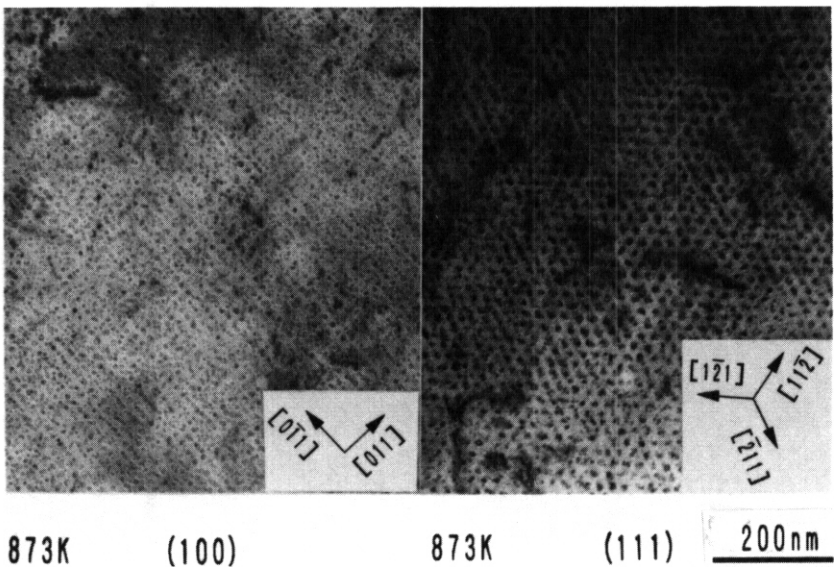

Fig. 2. Void lattice in stress relieved TZM after neutron irradiation at (a) 793 K (520°C) and (b) 873 K (600°C).

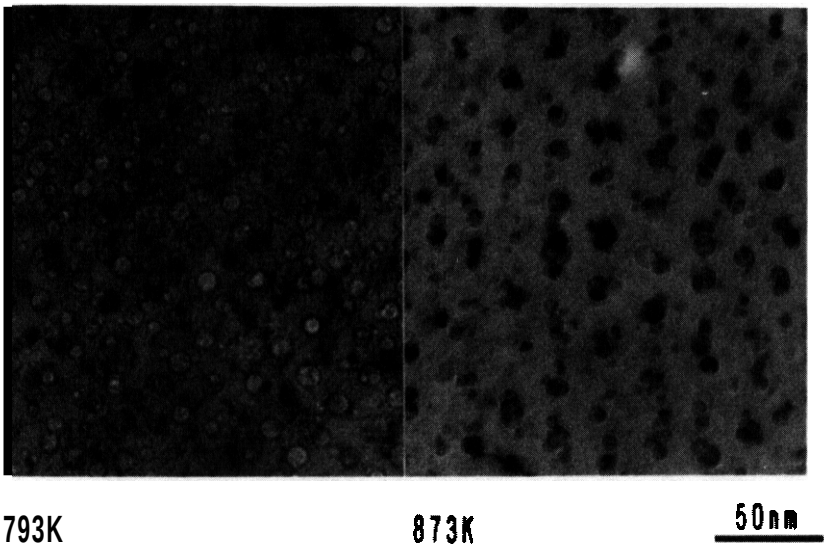

Fig. 3. Structure of the void lattice in stress relieved TZM after neutron irradiation at (a) 793 K (520°C) and (b) 873 K (600°C).

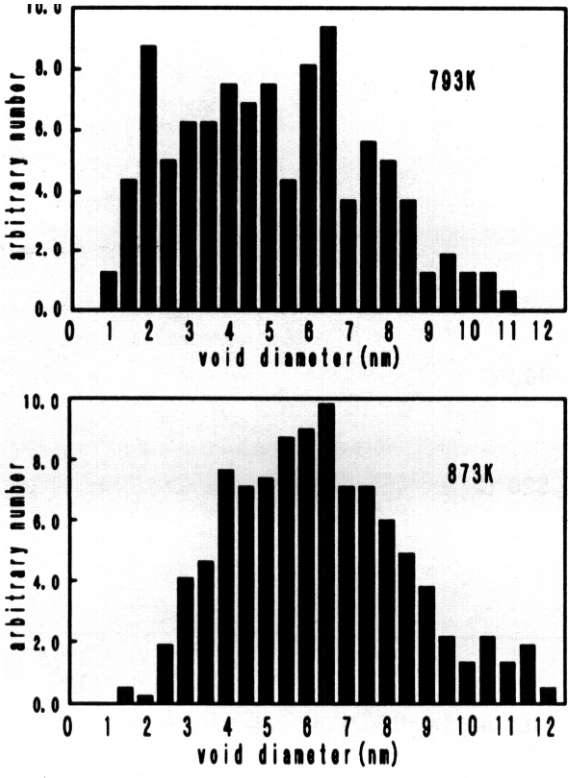

Fig. 4. Void size distribution in stress relieved TZM after neutron irradiation at (a) 793 K (520°C) and (b) 873 K (600°C).

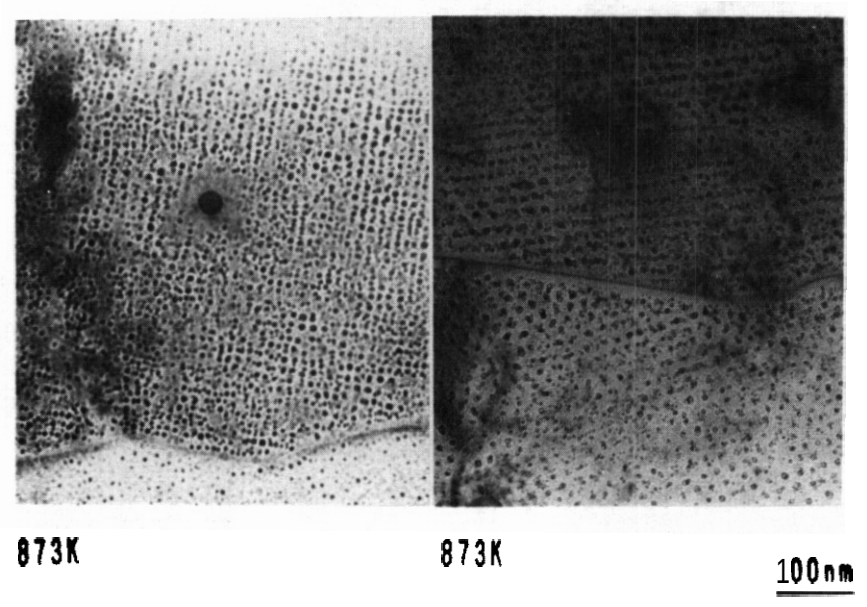

Fig. 5. Denuded zone around (a) precipitate and (b) grain boundary in stress relieved TZM after neutron irradiation at 873 K (600°C).

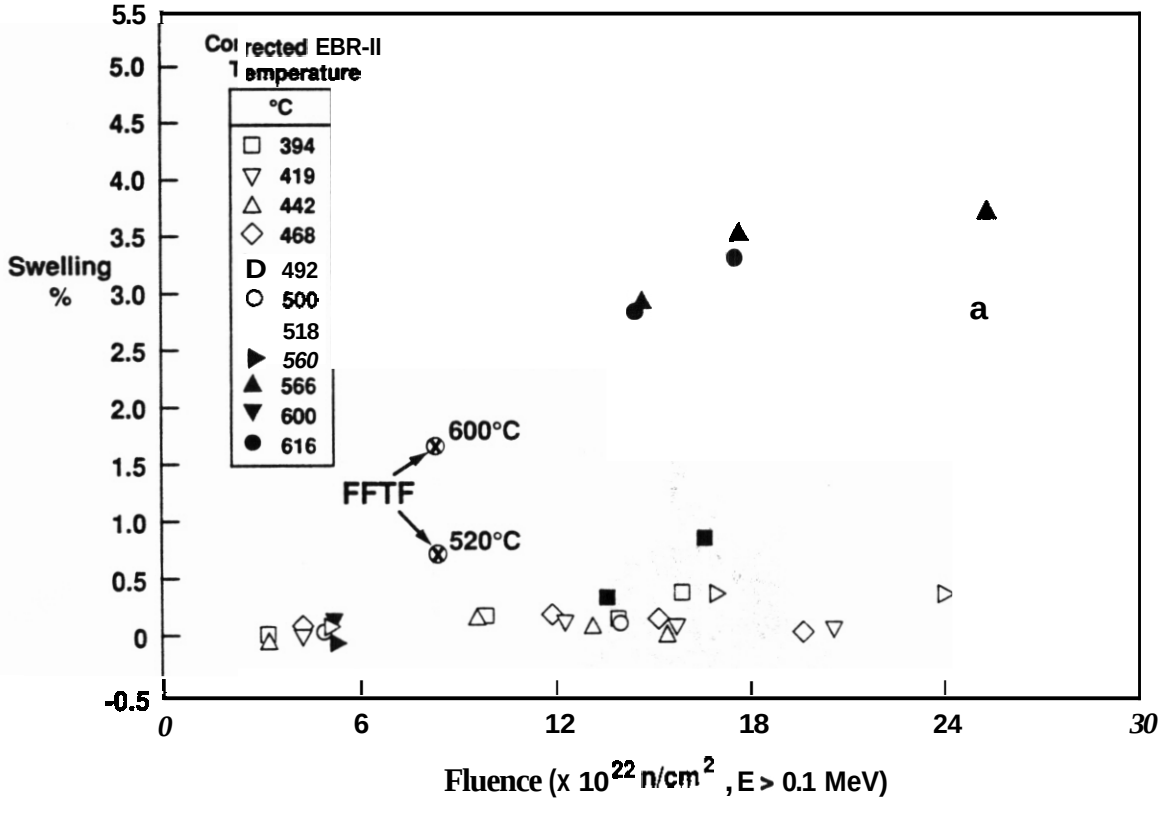

Fig. 6. Swelling data from the current work in FFTF compared to data from references 4 and 7.

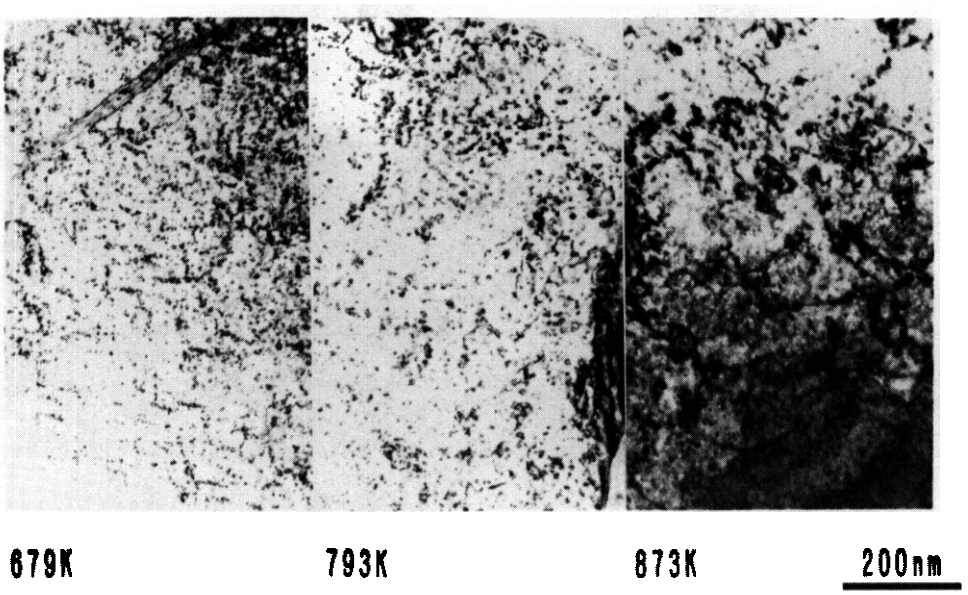

Fig. 7. Dislocation structures in stress relieved TZM after neutron irradiation at (a) 679 K (406°C), (b) 793 K (520°C), and (c) 873 K (600°C).

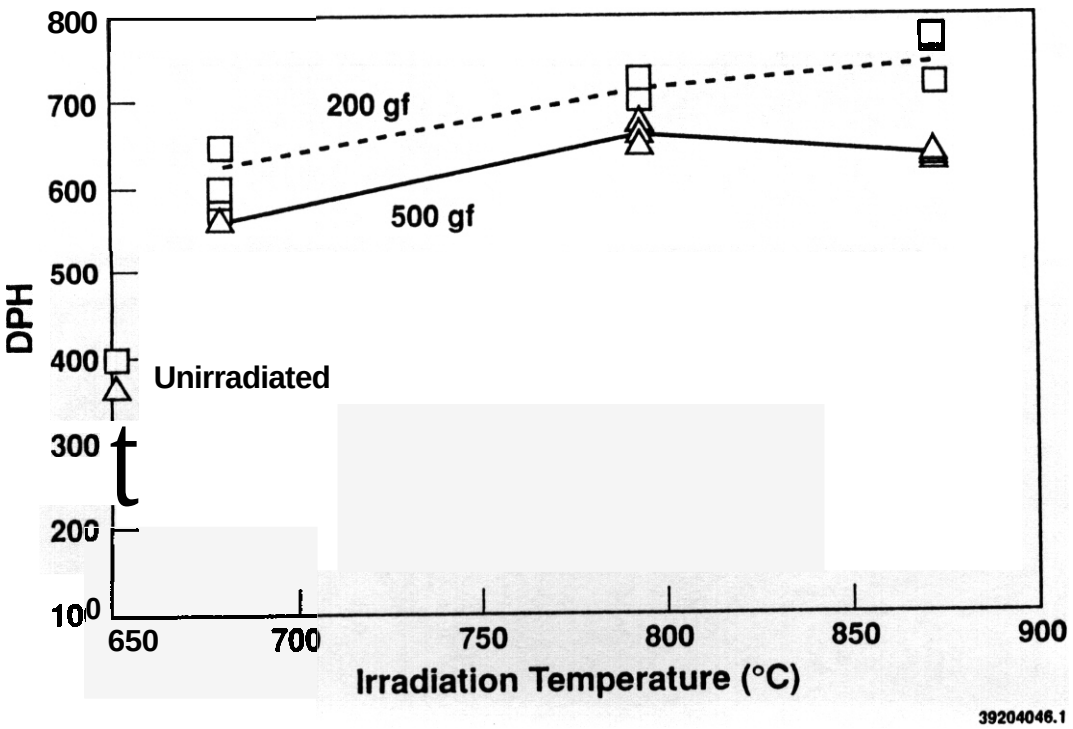

Fig. 8. Microhardness data on irradiated TZM.

Table 1. Void structures in stress relieved TZM after neutron irradiation.

Irradiation temperature	793 K (520°C)		873 K (600°C)	
Void structure	void lattice		void lattice	
Mean diameter (nm)	4.4		5.4	
Density (10^{16} cm^{-3})	10.0		9.4	
Swelling (%)	0.68		1.6	
Void lattice constant (nm)	26.7		28.0	
	In lattice	At random	In lattice	At random
Mean diameter (nm)	5.6	2.7	7.3	2.9
Density (10^{16} cm^{-3})	7.3	2.2	7.3	2.1
Swelling (%)	0.66	0.02	1.59	0.01

Table 2. Dislocation microstructures in stress relieved TZM after neutron irradiation.

Irradiation temperature	679 K (406°C)	793 K (520°C)	873 K (600°C)
Grain size (μm)	~2	~2	~2
Dislocation structure	loops, rafts	loops, rafts	elongated
Loop diameter (nm)	5.0	7.7	
Loop density (cm^{-3})	6.0 x 10^{16}	2.2 x 10^{16}	
Dislocation density (cm^{-3})			6.1 x 10^{9}

Table 3. Hardness values in stress relieved TZM after neutron irradiation.

Condition	Irradiation Temperature	Hardness (DPH), 500 g load	Hardness (DPH), 200 g load
Unirradiated		377	402
Irradiated	679 K (406°C)	577	618
	793 K (520°C)	657	707
	873 K (600°C)	633	749

6.4 **Copper** Alloys

DISPERSOID STABILITY IN A $Cu-Al_2O_3$ ALLOY UNDER ENERGETIC CASCADE DAMAGE CONDITIONS

S. J. Zinkle, (Oak Ridge National Laboratory), A. Horsewell and B. N. Singh, @is$ National Laboratory), and W. F. Sommer (Los Alamos National Laboratory)

OBJECTIVE

The objective of this study was to examine the stability of small Al_2O_3 particles in dispersion-strengthened copper under highly energetic displacement cascade conditions.

SUMMARY

A commercial dispersion strengthened $Cu-Al_2O_3$ alloy was irradiated with 750-MeV protons at 470 K to a damage level of about 2 displacements per atom (dpa). The density and size distribution of the Al_2O_3 particles was measured in nonirradiated and irradiated specimens using transmission electron microscopy. The mean primary knock-on atom (PKA) energy for 750-MeV protons in copper is 2.5 MeV, which is about 10 and 100 times higher than the average PKA energies in copper for fusion and fission neutrons, respectively. The irradiation caused only a slight decrease in the mean Al_2O_3 size, from 10.5 nm to 8.3 nm and a slight decrease in the particle density from $4 \times 10^{22}/m^3$ to $3 \times 10^{22}/m^3$. These results suggest that $Cu-Al_2O_3$ alloys, which are resistant to radiation-induced microstructural changes during fission neutron irradiation, may also be microstructurally stable in a fusion neutron environment.

PROGRESS AND STATUS

Introduction

Dispersion-strengthened copper alloys are of technological interest due to their combination of high thermal and electrical conductivity with high mechanical strength.[1] These alloys are processed by introducing a low volume fraction (typically 51%) of a chemically inert particulate phase into a pure copper matrix. High strength is achieved by heavy cold working, which produces a dense dislocation structure that is effectively pinned by the dispersoid particles. Dispersion-strengthened copper alloys have been shown to be resistant to recrystallization for annealing temperatures that approach the melting temperature of the copper matrix.[2,3] Conventionally processed high-conductivity precipitation-strengthened copper alloys, in contrast, generally begin to lose their strength following annealing above 0.5 T_M (680 K) due to precipitate overaging effects.[4]

The high density of dispersoid particles and dislocations present in dispersion-strengthened copper suggests that it should he microstructurally stable during irradiation, since most of the mobile defects produced by the irradiation would he annihilated at these defect sinks. Indeed, recent ion[5,6] and fission neutron[3,7-9] irradiation studies have shown that dispersion-strengthened copper alloys such as $Cu-Al_2O_3$ retain their high strength and are resistant to radiation-induced cavity swelling even at high doses (100 dpa) and high temperatures. The radiation stability at high temperature is particularly significant since most precipitation-strengthened copper alloys suffer radiation-enhanced recrystallization during irradiation at temperatures above 573 K, with an accompanying dramatic decrease in mechanical strength.[5,9-11] Dispersion-strengthened copper, in contrast, is generally resistant to radiation-enhanced recrystallization.[3,5,6,8,9]

For fusion energy applications, one underlying concern is the stability of the dispersoid particles against ballistic dissolution due to the highly energetic displacement cascades associated with fusion neutrons?[1] This would allow radiation-enhanced recrystallization (and subsequent void swelling) to occur since the dislocation structure would no longer he securely pinned by the dispersoid particles. The metastable dispersoid size during irradiation is determined by the relative balance between shrinkage via cascade recoil resolution events, and growth via radiation enhanced diffusion of the ejected solute hack to the particles. The amount of recoil resolution is dependent on the primary knock-on atom (PKA) energy, along with other experimental variables such as temperature, damage rate, and damage level.[12,13] Since the average recoil energy due to fission neutrons is substantially less than that due to 14-MeV fusion neutrons (~30 keV vs. ~300-keV in copper), fission reactor studies cannot directly determine if energetic fusion neutron cascades would cause significantly enhanced recoil resolution. One way to study the effect of very energetic PKA energies on dispersoid stability is to utilize high energy proton beams. Due to nuclear reactions, the mean PKA energy in copper for 750-MeV protons is 2.5 MeV.[16]

In the present study, transmission electron microscopy (TEM) has been used to study the dispersoid stability of a commercially available $Cu-Al_2O_3$ dispersion-strengthened alloy following irradiation with 750-MeV protons.

Experimental Procedure

The material chosen for this investigation was Glidcop *AT-25,* a commercial Cu-Al_2O_3 dispersion strengthened alloy produced by SCM Metal Products (Cleveland, USA) that contains *0.25* wt % Al in the form of Al_2O_3 particles. The alloy was prepared using a proprietary internal oxidation procedure that produced a nearly uniform distribution of cubic Al_2O_3 particles with a mean diameter of about 10 nm. Fast neutron irradiation studies performed on this same alloy heat have found that it is very resistant to radiation-induced microstructural modifications."'

A transmission electron microscopy (TEM) disk of dimensions 3 mm diam x 0.2 mm thickness was irradiated with 750 MeV protons at the Los Alamos Meson Physics Facility (LAMPF) using a water-cooled target chamber. The LAMPF proton beam operates in a pulsed mode, with an "on-time" of 0.5 to 0.8 ms during each 8.3 ms cycle period. The irradiation temperature was near 470 *K* and the proton fluence was 4×10^{24} p/m^2 during the 9-week irradiation, which corresponds to a calculated damage level of about 2 dpa.

Following the irradiation, the specimen was jet-electropolished at room temperature and examined at Risø National Laboratory in a JEOL-2000FX electron microscope operated at 200 kV. The dispersoid size distribution was determined from centered dark field (CDF) micrographs using prints with a total magnification of 3×10^5. The CDF imaging used reflections from a precipitate diffraction ring with an interplanar spacing of 0.14 nm; this corresponds to the *{440}* interplanar spacing for cubic Al_2O_3.[17] This precipitate ring is sufficiently separated from the matrix copper diffraction spots to allow exclusive imaging of the dispersoid particles without interference from strain contrast in the copper matrix. Additional photographs of the dispersed phase were taken in bright field using kinematical, low-contrast conditions with a small amount of underfocusing, (i.e. "void contrast"). The bright field imaging was convenient for analyzing the particle density and spatial distribution, but did not allow clear imaging of the smallest particles (d < 5 nm) due to the high dislocation density that was present in the alloy before and after irradiation.

Results

Figure 1 shows the general bright-field microstructure of Glidcop Al *25* prior to irradiation. A high density of dislocations, due to cold-working during fabrication, $\rho_d > 5\ 10^{15}/m^2$, is visible in the top photograph. The bottom photograph shows the nonirradiated microstructure at higher magnification. Here, the small triangular-shaped cubic-Al_2O_3 particles are visible. The measured particle size distribution was sharply peaked at an edge length near 10 nm. Two different Al_2O_3 phases were identified in the nonirradiated specimen from an analysis of electron diffraction patterns, in agreement with Ernst et al.[17] Large particles (L ~ 100 nm), which occurred with very low density and were preferentially located along subgrain boundaries, were identified as rhombohedral *a*-Al_2O_3. The high density ($\sim 4.5 \times 10^{22}/m^3$) of smaller particles had a cubic lattice structure with a lattice parameter near 0.795 nm and are presumably η-Al_2O_3.[17] The cubic Al_2O_3 particle morphology (determined from CDF micrographs) consisted of triangular-shaped platelets, in agreement with previous work." The measured aspect ratio of the particle edge length (L) to thickness (t) varied between 2 and 4. A small fraction of the cubic Al_2O_3 particles exhibited a hexagonal platelet morphology instead of the more common triangle platelet. The total Al_2O_3 precipitate density was about $4.5 \times 10^{22}/m^3$. The point defect sink strength" of the Glidcop Al *25* prior to irradiation was hence $C_i > 2 \times 10^{-5}$ (atomic concentration), with roughly equal contributions from the dislocations and Al_2O_3 precipitates.

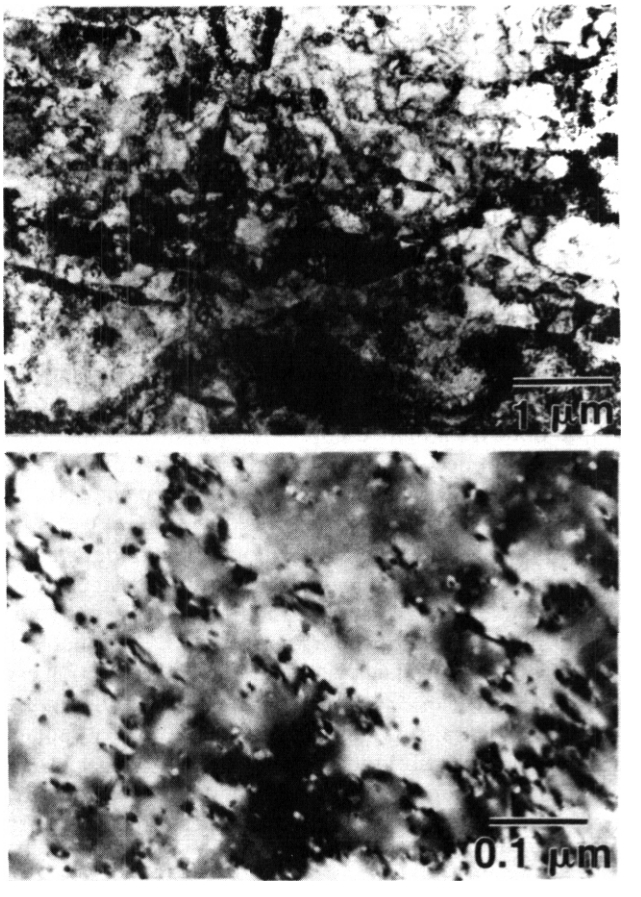

Fig. 1. Bright field microstructure of nonirradiated Glidcop Al 25 Cu-Al_2O_3 alloy showing the high dislocation density (tap) and high density of small triangular Al_2O_3 particles (bottom).

The general microstructure following irradiation was similar to the preirradiation microstructure. Figure 2 shows typical microstructures (dislocation contrast) before and after irradiation. There was no evidence of any recovery or recrystallization in the irradiated specimen. A detailed microstructural analysis at high magnification identified a high density ($\sim 2 \times 10^{23}/m^3$) of small cavities and point defect clusters. The geometry, size, and density of the defect clusters were comparable to that observed in pure copper irradiated at similar conditions.

A cursory examination of the dispersoid particle size and morphology indicated that there were no dramatic changes induced by the irradiation. Figure 3 shows typical dark field images of the Al_2O_3 particles before and after irradiation. A detailed examination of numerous irradiated panicles revealed occasional evidence of particle fracture, but the frequency of this complete particle break-up event was very low (<1% of examined particles). The particle number density following irradiation was $\sim 3 \times 10^{22}/m^3$ (i.e. slightly less than the non-irradiated density).

The particle size distribution of the irradiated and non-irradiated specimens was determined by measuring the dark-field image width of about 200 particles for each condition. As shown in Fig. 4, the irradiation caused a slight shift in the size distribution toward smaller sizes. The most probable particle size before and after irradiation was 10 nm and 8 nm, respectively. The root mean cube size, $\left(\overline{L^3}\right)^{\frac{1}{3}}$, showed a similar irradiation-induced shift from 11.7 nm to 9.6 nm. Using the measured aspect ratio for the particles of $Ut \approx 3$, the visible Al_2O_3 volume fraction was 1.0% and 0.4% before and after irradiation, respectively.

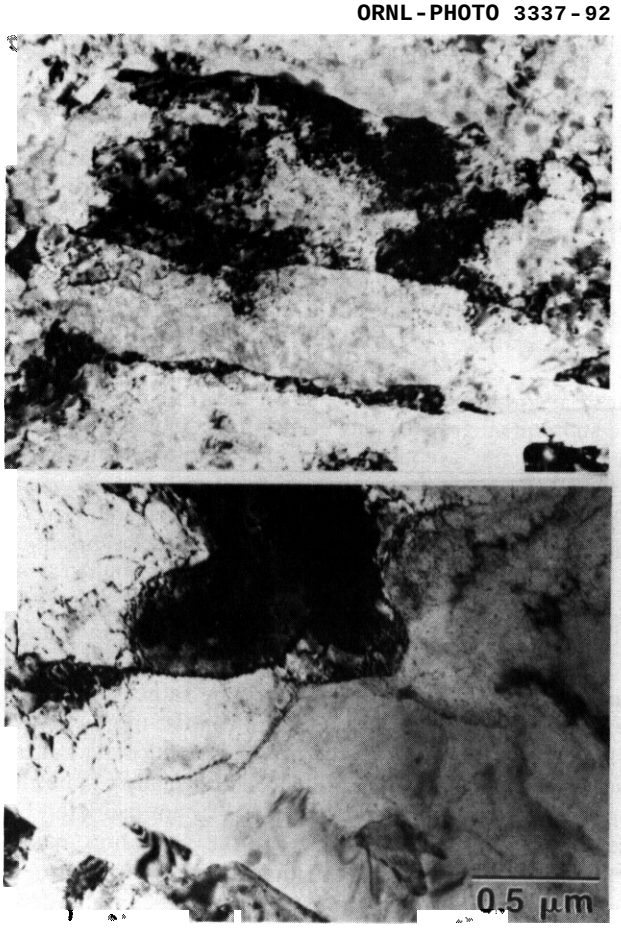

Fig. 2. Comparison of the dislocation structure in Glidcop Al 25 Cu-Al_2O_3 alloy before (top) and after (bottom) irradiation.

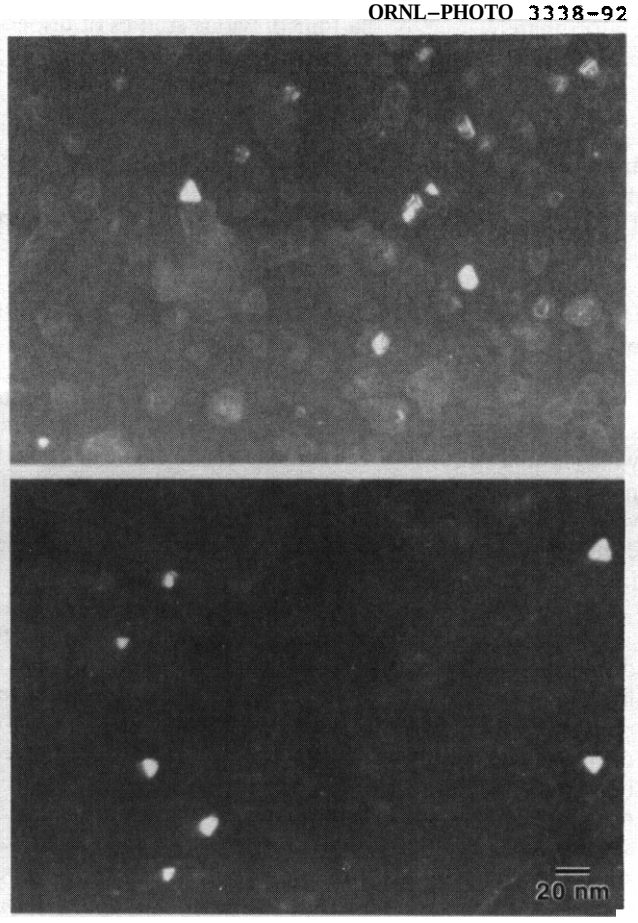

Fig. 3. Centered dark field images showing the Al_2O_3 particle dispersion before (top) and after (bottom) irradiation.

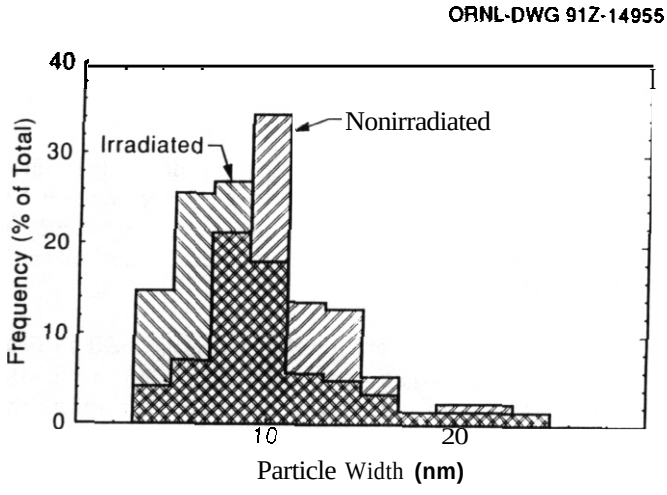

Fig. 4. Measured size distribution of Al_2O_3 particles in Glidcop Al 25 Cu-Al_2O_3 alloy before and after irradiation.

Discussion

Previous studies of dispersoid stability in Cu-Al_2O_3, employing lower energy PKAs than the present work, have produced mixed results regarding the importance of recoil resolution. Spitznagel and coworkers' reported direct TEM evidence of recoil resolution in isolated Al_2O_3 particles following 28-MeV Si ion irradiation to damage levels greater than 10-dpa at 523 to 623 K. On the other hand, Barabash and coworkers[6] reported that the Al_2O_3 particles in a Cu-Al_2O_3 alloy (average diameter of 7 nm) were unaffected by 3-MeV Ar ion irradiation to 88 dpa at 623 K. Livak and coworkers' used an extraction replica technique to examine the Al_2O_3 panicle morphology in two Cu-Al_2O_3 alloys before and after neutron irradiation to 3 and 15 dpa at 660 K. There was no noticeable effect of irradiation on the Al_2O_3 particles in their study. More recently, Anderson and coworkers' presented indirect evidence that recoil resolution had refined the particle size in several dispersion-strengthened copper alloys following fission neutron irradiation to 50 dpa at 690–K. The evidence for recoil resolution' was mostly confined to the larger particle sizes (d ≥ 100 nm) which is difficult to understand since on a theoretical basis[13,14] small particles with sizes less than or equal to the displacement cascade dimensions are most strongly affected by recoil resolution; large precipitates should be relatively unaffected by recoil resolution since the displacement cascade is usually completely contained within the precipitate and cannot induce solute ejection into the matrix. Unfortunately, none of the four previous studies of dispersoid stability in Cu-Al_2O_3 published the irradiated vs. non-irradiated particle size distribution. Hence, it is not possible to compare their conflicting conclusions on a more quantitative basis.

Wanderka et al.[19] recently reported TEM results on the size distribution and density of Al_2O_3 particles in Cu-Al_2O_3 before and after a high-flux 300-keV Cu^+ ion irradiation to a dose of 30 dpa at room temperature. Their measurements suggested that extensive refinement had occurred in the particle size, with a most probable particle diameter after irradiation of ~5 nm. The volume fraction of observable Al_2O_3 particles after irradiation was reduced to about half of the pre-irradiation value.

As reviewed by Russell," the recoil resolution process should generally produce a shift in the precipitate size distribution toward small sizes. This effect was observed in the present study (Fig. 4) and by Wanderka et al.,[19] although the magnitude of the shift was rather slight in our study.

The fate of solute atoms ejected from a precipitate by ballistic recoil processes depends on the (radiation-enhanced) solute diffusivity and solubility. Nucleation of the ejected solute (and subsequent growth) may occur under some circumstances, which would produce a refinement in the mean particle size while maintaining a constant precipitate volume fraction. The measurements of the present study and by Wanderka et al.[19] indicate that the mean particle size and observable Al_2O_3 particle volume fraction in Cu-Al_2O_3 were both reduced after irradiation. This suggests that at least some of the ejected solute remains either in solution or in submicroscopic precipitates for these irradiation conditions (i.e., there is not sufficient solute mobility in copper at irradiation temperatures of 20 to 200°C to produce observable redeposition of all of the ejected solute).

The present results suggest that the influence of recoil resolution in Cu-Al_2O_3 is rather modest, even for very energetic displacement cascades. The Al_2O_3 particle density and size were both reduced by only ~20% after the 750 MeV proton irradiation. As noted by Wollenberger," the dependence of recoil resolution on PKA energy should be rather small at high recoil energies due to subcascade formation. The morphology of a high energy displacement cascade consists of geometrically distinct highly damaged subcascade zones, separated by relatively large undamaged lattice regions." The calculated distance between subcascades associated with an energetic displacement cascade in copper is 14 nm." Hence, it is usually geometrically possible for only one subcascade from a given displacement cascade to interact with a precipitate of ~10 nm diameter. Since subcascade formation begins to occur in copper for PKA energies above about 25 keV (ref. 20), the preceding reasoning suggests that fission neutron studies (E, ~30 keV) may be directly applicable for estimating the importance of recoil resolution processes in a fusion neutron environment. On the other hand, the influence of irradiation spectra (mobile defect concentrations) on solute migration and reprecipitation needs further investigation.

It would be useful to irradiate specimens with 750 MeV protons to higher damage levels than the present study (2 dpa) to verify whether the steady-state particle size distribution has been attained. According to Russell,[12] the damage level required to reach steady state can be as high as 10 to 100 dpa. On the other hand, a simple calculation indicates that each Al_2O_3 particle (10 nm "diameter") has been at least partially struck by about 100 subcascades during the 2 dpa proton irradiation (each 2.5 MeV PKA generates ~15 subcascades, which each induce ~300 calculated displacements).

Conclusions

Irradiation of Cu-Al_2O_3 to a damage level of 2 dpa with very energetic (2.5 MeV PKA energy) cascades produced only a slight shift in the mean dispersoid size, from 10.5 nm to 8.3 nm. These results suggest that recoil resolution studies on Cu-Al_2O_3 performed with medium-energy ions or fission neutrons (E_{PKA} ~30 keV) may be directly applicable for determining dispersoid stability under fusion neutron conditions (E_{PKA} ~300 keV). Higher dose irradiations with 750 MeV protons would be useful for verifying that the Al_2O_3 dispersion remains stable.

References

1. A.V. Nadkarni, in "High Conductivity Copper and Aluminum Alloys," E. Ling and P.W. Taubenblatt, Eds. (TMS-AIME, New York, 1984) p. 77.
2. J.J. Stephens, R.J. Bourcier, F.J. Vigil, D.T. Schmale, Sandia National Laboratory, Report SAND 88-1351 (Sept. 1988)
3. O.K. Harling, N.J. Grant, G. Kohse, M. Ames, T-S Lee, and L.W. Hobbs, J. Mater. Res. 2 (1987) 568
4. S.J. Zinkle, D.H. Plantz, A.E. Bair, R.A. Dodd, and G.L. Kulcinski, J. Nucl. Mater. 133&134 (1985) 685
5. J.A. Spitznagel, N.J. Doyle, J.G. Greggi, W.J. Chyke, J.N. McGruer, J.T. Townsend, and J.W. Davis, Nucl. Instr. Meth. B 16 (1986) 279
6. V.R. Barabash, A.V. Naberenkov, E.V. Nesterova, V.V. Rybin, and S.A. Fabritsieff, Proc. Int. Conf. on Radiation Materials Science, Alushta, USSR, May 1990
7. F.A. Garner, H.R. Brager, and K.R. Anderson, J. Nucl. Mater. 179-181 (1991) 250
8. K.R. Anderson, F.A. Garner, M.L. Hamilton, and J.F. Stubbins, 15th Int. Symp. on Effects of Radiation on Materials, Nashville, TN, June 1990 (ASTM, Philadelphia)
9. R.J. Livak, T.G. Zocco, and L.W. Hobbs, J. Nucl. Mater. 144 (1987) 121
10. S.J. Zinkle, G.L. Kulcinski, and L.K. Mansur, J. Nucl. Mater. 141-143 (1986) 188
11. M. Appello and P. Fenici, J. Nucl. Mater. 152 (1988) 348
12. K.C. Russell, Prog. Mater. Sci. 28 (1984) 229
13. S.P. Chou and N.M. Ghoniem, Nucl. Instr. Meth. Phys. Res. B 42 (1989) 145
14. H. Wollenberger, J. Nucl. Mater. 179-181 (1991) 76
15. P. Bellon and G. Martin, Rad. Eff. Def. Solids 113 (1990) 165
16. S.L. Green, W.V. Green, F.H. Hegedus, M. Victoria, W.F. Sommer and B.M. Oliver, J. Nucl. Mater. 155-157 (1988) 1350
17. F. Ernst, P. Pirouz and A.H. Heuer, Phil. Mag. A 63 (1991) 259
18. A.D. Brailsford and R. Bullough, J. Nucl. Mater. 44 (1972) 121
19. N. Wanderka, Y. Yuan, L. Jiao, R.P. Wahi, and H. Wollenberger, 5th Int. Conf. on Fusion Reactor Materials, Clearwater, FL, Nov. 1991
20. H.L. Heinisch and B.N. Singh, J. Nucl. Mater. 179-181 (1991) 893; also Phil. Mag. A, in press.

FISSION NEUTRON IRRADIATION OF COPPER CONTAINING IMPLANTED AND TRANSMUTATION PRODUCED HELIUM · B. N. Singh, A. Horsewell and M. Eldrup (RISØ National Laboratory) and F. A. Garner (Pacific Northwest Laboratory*)

OBJECTIVE

The objective of this effort is to determine the factors which control the radiation-induced evolution of microstructure in copper.

SUMMARY

High purity copper containing approximately 100 appm helium was produced in two ways. In the first, helium was implanted by cyclotron at Harwell at 323K. In the second method, helium was produced as a transmutation product in 800 MeV proton irradiation at Los Alamos, also at 323K. The distributions of helium prior to fission neutron irradiation were determined by a combination of transmission electron microscopy (TEM) and positron annihilation techniques (PAT). These specimens, together with pure copper, were then irradiated with fission neutrons in a single capsule in Fast Flux Test Facility (FFTF) at ~686 ± 5K to a dose level of ~48 dpa (7.7×10^{26} n.m.$^{-2}$; E>0.1MeV). Investigation of the void and dislocation microstructures in the three specimens by TEM showed large differences between the specimens in void size and swelling. The observed differences as well as the effect of the presence of other transmutation-produced impurity atoms in the 800 MeV proton irradiated copper will be discussed.

PROGRESS AND STATUS

Introduction

It is well known that radiation damage at elevated temperatures can lead to, apart from void swelling, other interesting phenomenon such as void lattice formation (see ref. 1 for a review). However, the problem of void lattice formation, particularly in fcc metals, is still not properly understood. It is noteworthy that there exists practically no definite experimental evidence for the formation of void lattices in fcc metals under fast neutron irradiation. So far, there has been only one investigation in which the possible existence of void lattices in fcc aluminum irradiated with fast neutrons has been suggested.[2] It is not at all clear, for example, whether it is the high dose or high cavity density which is a prerequisite for the onset of the void lattice formation. In 1987 we reported the observation of a void hyperlattice in high purity aluminum irradiated with fast neutrons.[3] In this experiment the lattice formation took place even when the void density was relatively low.

Thus, in order to investigate whether or not it is at all possible to obtain void lattices in fcc metals, a number of pure fcc metals were irradiated with fast neutrons in FFTF to a relatively high dose of ~48 dpa. In order to enhance the possibility of void lattice formation, Cu specimens containing about 100 appm helium were also irradiated.

There were two additional interests in carrying out these investigations. First, the role of irradiation in cavity coarsening is not fully understood' and it was hoped that the irradiation of helium implanted specimens would provide some interesting information. Secondly, very little is known about the effect, if any, of the transmutational impurities produced during irradiation on the swelling behavior of materials. For this reason, Cu pre-irradiated with 800 MeV protons were further irradiated with fast neutrons in the FFTF.

ExDerimental procedure

In the present investigation three types of specimens were used. All specimens were in the form of 3 mm diameter discs. Thickness of the discs was ~ 0.1 mm. Type one specimens were of OFHC copper with an oxygen content of ~10 appm. Prior to irradiation in FFTF, these specimens were annealed at 823K for 2 h in a vacuum of ~10^{-6} torr. The second type of specimens were of 99.999% Cu implanted with 100 appm of helium at ~323K by cyclotron (VEC) at Harwell. The third type of specimens were also of 99.999% Cu and contained ~90 appm of helium; helium was produced as a transmutation product in 800 MeV proton irradiation at ~323K at Los Alamos in the Meson Physics Facility (LAMPF). The oxygen contents of the last two types of Cu are not known. The helium concentration of 90 appm was achieved by a proton fluence of 1.78×10^{24} p$^+$/m^2. A proton fluence of 3.94×10^{24} p$^+$/m^2 produces 201.5 appm of helium.[3] Some of the specimens implanted with 100 appm helium and irradiated at LAMPF were investigated by TEM as well as positron annihilation techniques prior to irradiation in the FFTF.

The TEM discs were separated by 0.001 inch thick molybdenum spacers and were encapsulated in a sealed 20% cold worked 316 stainless steel canister (1.12 inches long, 0.144 inches O.D. with wall thickness 0.007 inches)

---

* Pacific Northwest Laboratory is operatred for the U.S. Department of Energy by Battelle Memorial Institute under Contract DE-AC06-76RLO 1830.

under a room temperature pressure of 0.4 atm helium. This canister was placed in contact with the reactor sodium coolant in a weeper basket at level 2C-2 of the Materials Open Test Assembly (MOTA) and irradiated in FFTF in Richland, Washington, USA, operating at 291 megawatts thermal energy for 341.8 effective full power days. The temperature of the coolant in contact with the canister was 678 ± 5K during full power operation, the specimens are calculated to have experienced approximately 8K higher temperature (686 ± 5K) due to gama heating within the packet. Somewhat lower temperatures were experienced during the ascent to power stages of the various segments of the irradiation. The specimens were exposed to 1.1 x 10^{26} n/m² (E>0.1 MeV) which produced ~48 dpa in pure copper.

Irradiated specimens were electropolished in a solution of 25% H_3PO_4, 25% ethylene glycol and 50% water at 11 volts for about 15 seconds. Examinations were performed in a JEOL 2000FX electron microscope at Risø National Laboratory, Denmark.

Results

The defect microstructures of the specimens in the as-implanted and as-irradiated with 800 MeV protons (i.e. pre-MOTA irradiation) states are shown in Fig. 1. The total cluster density in the 800 MeV proton irradiated specimen was found to be 1.1 x 10^{24} m^{-3} of which 2.7 x 10^{23} m^{-3} were stacking fault tetrahedra (SFT).[6] Very few loops were observed in this specimen and there was no indication of either network dislocations or helium bubbles. The cluster density in the 100 appm implanted (at Harwell) specimen was found to be ~6x10^{22} m^{-3} and practically no SFT's were observed. A close examination of this specimen showed, on the other hand, the presence of small (1-2 nm) bubbles although in a relatively low concentration (≤ 10^{21} m^{-3}).

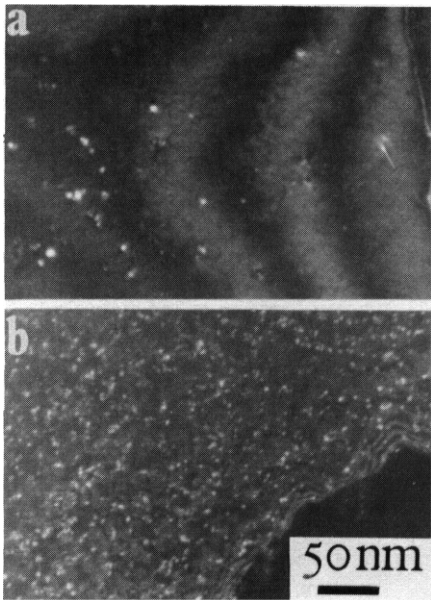

Fig. 1. Defect microstructures of copper specimens (a) in the as-implanted (with 100 appm helium) and (b) as-irradiated (with 800 MeV protons) conditions. The irradiation with 800 MeV protons is expected to have generated about 90 appm helium.

The positron lifetime measurements carried out on the 100 appm implanted Cu specimens showed the presence of submicroscopic clusters of vacancy type. The helium content of the clusters (i.e. helium bubbles) was estimated to be 0.3-1 times the number of vacancies. The cluster density was estimated to be roughly 3x10^{23} m^{-3} of an average size of ~1 nm diameter.

The void and void plus dislocation microstructures of the post-FFTF/MOTA irradiation of copper and copper containing 100 and 90 appm helium are shown in Fig. 2. The void distribution in all three specimens was reasonably uniform. It is interesting, though somewhat surprising, to note that even after a displacement dose of ~48 dpa, the dislocation densitv in the pure comer specimen remained'very low and that there was-no indication of'i'rradi'ation - induced dislocation network formation. In copper specimens containing 100 and 90 appm helium, on the other hand, the beginning of dislocation network formation was evident. Furthermore, unlike in pure copper, 10-20% of the clusters in these specimens were loops of sizes up to 20 nm. Fig. 3 shows the cluster densities, as seen in the TEM investigations, for the specimens that were implanted as well as for those that were irradiated with 800 MeV protons. The size distribution of voids observed in the three different conditions (i.e. no helium, helium implanted and helium produced via nuclear reactions) are shown in Fig. 4. The void size, density, swelling and the cluster density values determined from TEM investigations are quoted in Table 1. The TEM based swelling rate in Cu (without helium) in the present experiment (Table 1) is not very different from the one reported in Ref. 7 (based also on the TEM results) but is noticeably lower than the swelling rate obtained from the density change measurements.[8]

It should be pointed out that all three specimens were investigated for the existence of void lattices. However, TEM examinations provided no evidence of void ordering in any of the three specimens.

Discussion

The absence of void lattice formation in the present experiment may have resulted due to the high irradiation temperature which yielded rather low void densities. Even pre-implantations of 100 and 90 appm of helium in copper did not cause increases in void densities.

It is somewhat surprising that the void density in all three types of copper specimens turned out to be very similar. In other words, the pre-implantation of helium up to 100 appm had practically no influence on the final void density. Similar observations have been reported for neutron-irradiated Cu and Cu-B irradiated at

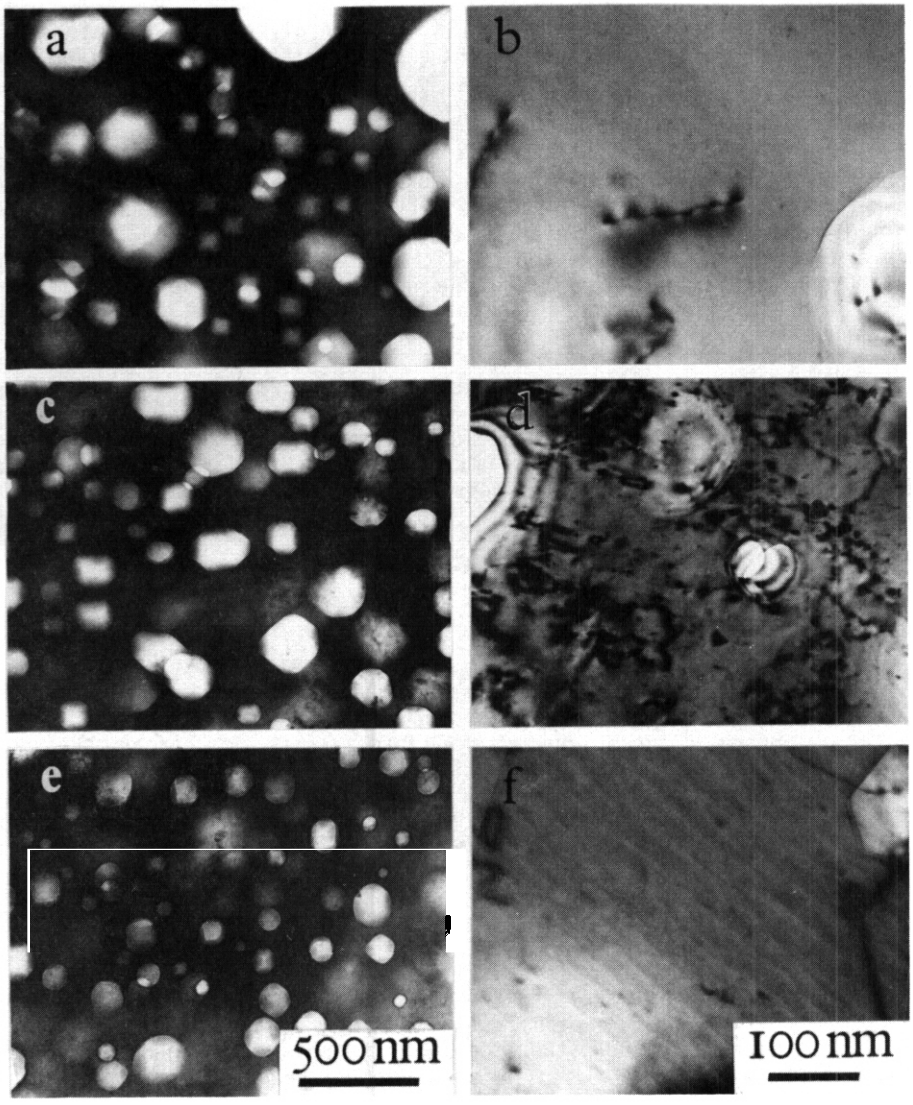

Fig. 2. Void and dislocation microstructures of specimens irradiated in FFTF/MOTA at 686K to a dose level of -49 dpa: (a,b) Cu, without helium, (c,d) cu containing 100 appm of implanted helium and (e,f) Cu containing about 90 appm of helium generated during irradiation with 800 MeV protons.

673K: althouoh in Cu-B helium was generate; continuously at a rate of 1.5×10^{18} at./m³/s, yet the void density in Cu and Cu-B was very similar.[9,10] Recently, Horsewell and Singh (unpublished work) have investigated copper irradiated with 600 MeV protons at 673K; the production rate of helium in this experiment was about 100 appm per dpa. Here too, the high helium generation rate did not cause any increase in void density.

The fact that the void densities in pure copper and copper containing helium are found to be about the same, does not mean that the same nucleation mechanism has been operative in the two cases. In pure Cu, for instance, the dominating driving force for the nucleation must have been the available vacancy supersaturation and the residual gas atoms during very early stages of irradiation. The void nucleation in Cu under neutron irradiation conditions may terminate already, for example, at about 10^{-2} dpa at 523K.[11] Since the nucleation time/dose is expected to be even lower at higher temperatures," in the present experiment at 686K, the void nucleation in pure Cu might have saturated at a very low dose. It should be noted, however, that the neutron irradiation of pure Cu to a dose of ~ 48 dpa is likely to have produced about 15 appm of helium.[13] Thus, it is possible that some of these helium atoms might have caused additional void nucleation. This may be one of the reasons for the higher void density in the present experiment than that reported for Cu[9] and Cu-B[10] irradiated at 673K to a dose of only 1 dpa.

A quantitative analysis of the cavity nucleation in copper specimens containing 100 or 90 appm of helium is complicated and is beyond the scope of the present paper. Qualitatively, however, it is worthwhile to note the following:

(i) Prior to FFTF/MOTA irradiation, the sink density in these specimens is very high. Consequently, the build-up of the vacancy supersaturation is likely to be slow and hence the nucleation might have been delayed.

Material	Void			Cluster density (m^{-3})
	size (nm)	density (m^{-3})	swelling (%)	
cu	182.8	3.3×10^{19}	10.6	2.5×10^{21}
cu + 100 appm He	142.0	4.6×10^{19}	6.8	4.4×10^{21}
cu + 90 appm He	137.5	2.9×10^{19}	3.9	1.8×10^{21}

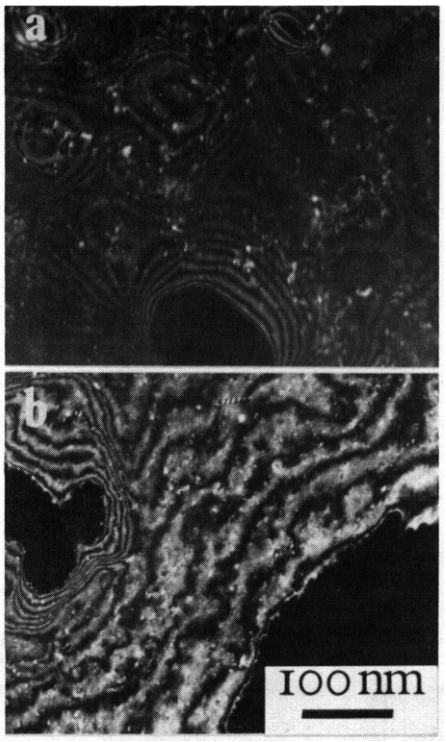

Fig. 3. Defect clusters in copper containing (a) 100 appm of implanted helium and (b) 90 appm of helium produced during 800 MeV proton irradiation following irradiation in FFTF/MOTA at 686K to a dose level of ~48 dpa.

(ii) Helium atoms in both types of specimens must be present (as shown by the PAT measurements in the implanted specimen) in the form of clusters. The coarsening of these clusters leading to the nucleation and growth of cavities may occur via Brownian-like motion, radiation resolution by cascade impingement and thermal resolution. At an appropriate vacancy supersaturation level, the bubbles would transform to voids that will continue to grow.

(iii) The presence of small bubbles in these specimens even after a dose of ~48 dpa would suggest that a secondary nucleation of bubbles must be taking place primarily via radiation resolution of helium atoms.

It is interesting to note here that the present results showing practically no effect of implanted or irradiation-induced helium on the final density of voids, are contrary to results obtained by 1MeV electron irradiation of helium-implanted copper.[14] In these experiments, pre-implantation with helium increases the void density, reduces the void growth as well as the swelling rate at irradiation temperatures up to 623K; at 723K the swelling rate is not affected. These differences between the results of neutron and electron irradiations cannot be rationalized easily.

Table 1 shows that the void swellina in Cu containina 100 and 90 appm helium is noticeably reduced and that this reduction occurs exclusively by a substantial reduction in the void size (Figs. 2 and 4). This reduction in the void size may arise due to the following reason: The pre-irradiation microstructure of the helium containing specimens contains a very high density of very small helium bubbles. These bubbles will coarsen during MOTA irradiation and the growth rate of the cavities is likely to be very low because of very high sink density. The growth rate would remain low until the bubbles have coarsened and grown into voids and the cavity sink density has reached a certain low value. This means that the voids in the specimens containing helium, must have had shorter time period (smaller dose) for fu11 growth and hence at smaller size.

In Cu containing 90 appm of helium introduced by 800 MeV proton irradiation a further decrease in the void swelling is noted. This decrease in swelling (with respect to the swelling in the Cu containing 100 appm of implanted helium), however, seems to be caused primarily by a reduction in the void density. It is possible that the production of additional impurity atoms, particularly nickel, via mutational reactions during irradiation with 800 MeV protons might be responsible for this reduction. This would be consistent with the recent observations that the presence of Ni drastically reduces the void density in Cu.[7]

CONCLUSIONS

No void lattices were observed in the neutron irradiated copper and copper containing up to 100 appm of helium to a dose level of ~48 dpa.

The void densities in pure copper as well as in copper containing helium up to 100 appm were found to be very similar after neutron irradiation in FFTF/MOTA to a displacement dose level of ~48 dpa. The nucleation in pure copper may be controlled by the available vacancy supersaturation and the concentration of residual gas atoms. In the helium containing copper, on the other hand, the cavity nucleation might occur via coalescence of clusters of gas atoms, thermal resolution and radiation resolution.

The additional reduction in swelling in copper irradiated with 800 MeV protons (prior to irradiation in FFTF/MOTA) may occur via nucleation poisoning by transmutational impurities, particularly nickel.

The effects of pre-implanted helium on the final void density in copper irradiated with 1MeV electrons are quite different from what has been observed in the present irradiation experiments with fission neutrons. This difference is not fully understood and needs further study.

REFERENCES

1. K. Krishan, Rad. Effects 66, (1982) 121.

2. A. Risbet and V. Levy, J. Nucl. Mater. 50 (1974) 116.

3. A. Horsewell and B,N, Singh, Rad. Effects 102 (1987) 1.

4. B.N. Singh and H. Trinkaus, J. Nucl. Mater., in press.

5. S.L. Green, W.V. Green, F.H. Hegedus, M. Victoria, W.F. Sommer and R.M. Oliver, J. Nucl. Mater. 155-157 (1988) 1350.

6. A. Horsewell, B.N. Singh, S. Proennecke, W.F. Sommer and H.L. Heinisch, J. Nucl. Mater. 179-181 (1991) 924.

7. B.N. Singh, A. Horsewell, D.S. Gelles, W.F. Sommer and F.A. Garner, Fusion Reactor Materials Semiannual Progress Report DOE/ER/0313/10, 1991, p. 167.

8. F.A. Garner, H.R. Brager and K.R. Anderson, J. Nucl. Mater. 179-181 (1991) 250.

9. S.J. Zinkle and K. Farrell, J. Nucl. Mat. 168 (1989) 262.

10. S.J. Zinkle, K. Farrell and H. Kanazawa, J. Nucl. Mat. 179-181 (1991) 994.

11. B.N. Singh and A.J.E. Foreman, Phil.Mag., in press.

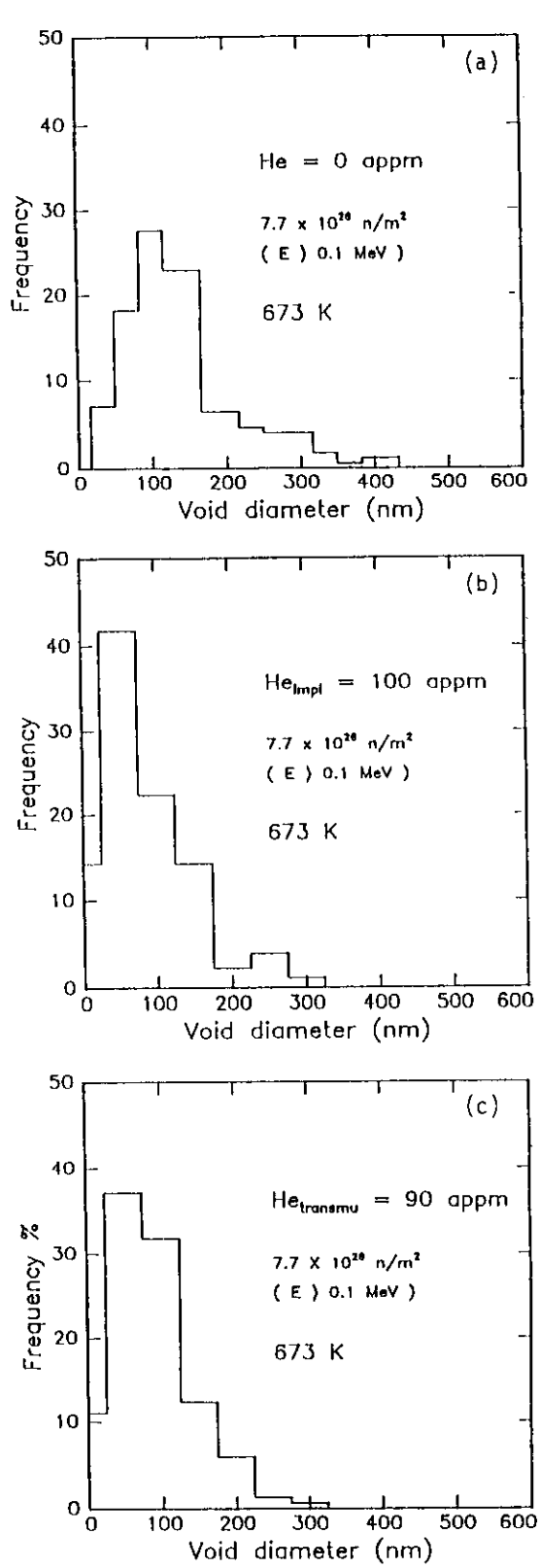

Fig. 4. Void size distribution for (a) copper without helium, (b) copper with 100 appm of helium and (c) with 90 appm of helium following irradiation in FFTF/MOTA at 686K to a dose level of ~48 dpa.

12. A.J.E. Foreman and B.N. Singh, in "Dimensional Stability and Mechanical Behavior of Irradiated Metals and Alloys", British Nuclear Energy Society, London 1983, p. 95.

13. H.R. Brager, J. Nucl. Mater. 141-143 (1986) 79.

14. P. Barlow, D.Phil. Thesis, University of Sussex, 1977.

Response of Solute and Precipitation Strengtheneti Copper Alloys at High Neutron Exposure - F. A. Garner and M. L. Hamilton, Pacific Northwest Laboratory*, T. Shikama, Tohoku University, D. J. Edwards and J. W. Newkirk, University of Missouri

OBJECTIVE

The objective of this study is to provide design-relevant data on copper-base alloys for high heat flux applications in fusion reactors.

SUMMARY

A variety of solute and precipitation strengthened copper base alloys have been irradiated to neutron-induced displacement levels of 34 to 150 dpa at 415°C and 32 dpa at 529°C in the Fast Flux Test Facility to assess their ootential for high heat flux aoolications in fusion reactors. Several MZC-type alloys appear to offer the most promise for further study'.' For low fluence applications CuBeNi and spinodally strengthened CuNiTi alloys may also be suitable. Although Cu-2Be resists swelling, it is not recommended for fusion reactor applications because of its low conductivity

PROGRESS AND STATUS

Introduction

Capper-based alloys have been suggested as candidaces for fusion ipplicationi as first wall, limiter and diverter components, with the latter application of most rurrent interest [1]. The attractiveness of copper arises primarily from its verv hiah thermal conductivitv compared to rtainless steel. allowina it to serve in high heat flu; applications-wit6 reduced levels of thermal' fatigue. Until recently, however, there have been little data available on the response of copper alloys to radiation at levels greater than 1 dpa. This paper outlines the major conclusions of a series of studies conducted at 411-430°C to doses as large as 150 dpa and at 539°C to 32 dpa

These studies were conducted in the. Fast Flux Test Facility (FFTF) employing controlled temperature (±5°C) irradiation in the Materials Open Test Assembly (MOTA). The experimental program involved three generations of irradiations, with the third generation currently in reactor. The first generation experiment (Generation 1) was exploratory in nature and was completed after reaching 1.6 x 10^{27} n m^{-2}, which corresponds to ~96 dpa for pure copper in FFTF.

Earlier publications described the results of this experiment at damage levels of 16, 41, 63 and 98 dpa [2-6]. The results of this experiment led to the initiation of the Generation 2 experiment where various copper alloys were irradiated to 34, 50, 104, and 150 dpa at 411-430°C. Generation 2 also included specimens of some alloys irradiated to 32 dpa at 529°C. These experiments focused on the alloy classes that exhibited promise in the Generation 1 experiment. This paper describes the results at the two higher fluence levels for all alloys except the oxide dispersion strengthened alloys, which are presented in a companion report [7]. Data for the lower fluence two levels were presented in earlier papers [8-10] and are also included in this report.

Exuerimental Details

Table 1 lists the compositions and heat treatments for the various classes of alloys examined in this study. Alloys in the first class are referred to as MZC alloys containing additions of Cr, Zr, and in some cases, Mg. Additions of Cr and Zr form precipitating phases that strengthen the matrix while magnesium acts as an oxygen scavenger to protect the zirconium additions [11]. The AMAX MZC alloy was produced by AMAX Base Metals Research and Development, Inc.

The two MIT alloys were supplied by N. J. Grant of the Massachusetts Institute of Technology (MIT). The fourth MZC-type alloy, CuCrZr, was supplied by G. Piatti of the Joint Research Center (JRC) in Italy. It is included here as an MZC-type alloy although it contains no magnesium. The AMAX-MZC alloy, the MIT #2 MZC alloy, and the JRC CuCrZr alloy were processed using conventional ingot metallurgy practices. The MIT #3 MZC alloy was produced using rapid solidification powder metallurgy (RSPM) techniques that introduced a sniall volume fraction of ZrO_2 and Cr_2O_3 particles arising from surface oxidation of the RS particles.

The second class of alloys consists of a high strength Cu-2Be alloy and a high conductivity CuNiBe alloy. The high nickel content and lower beryllium content of the latter yield moderate electrical conductivities (50 to 60% IACS) yet allow relatively high strengths to be obtained [12].

---

*Operated for the U.S. Department of Energy by Battelle Memorial Institute under Contract DE-AC06-76RLO 1830.

The third class of alloys are spinodally strengthened CuNiTi alloys. These alloys are of interest because they are easily heat treated to high strengths and are not as susceptible to overaging as are most precipitation strengthened alloys[13]. The high strength and phase stability, however, are obtained at the expense of the electrical and thermal conductivity. The MIT CuNiTi alloy, also obtained from N. J. Grant, is a RSPM product incorporating Zr and a TiO_2 dispersion to provide additional strengthening, the former acting as a precipitate phase[13]. The AMAX CuNiTi alloy was provided by R. Livak of Los Alamos National Laboratory as rolled sheet.

Pure copper (MARZ grade) was included in all irradiations as a standard reference material. Changes in density, electrical conductivity and tensile properties were measured using either transmission electron microscopy (TEM) disks or miniature tensile specimens. Electrical conductivity is more easily measured than thermal conductivity on these highly radioactive specimens and can be used to estimate changes in thermal conductivity. The techniques employed in making these measurements are described in detail elsewhere [8,13]. All measurements at 411-414°C have been completed. Data acquisition and analysis are still in progress for specimens irradiated at 529°C.

TABLE 1 Description of Generation 1.5 and 2.0 Copper Alloys

ALLOY	Composition (wt%)	Condition
MZC allovs		
AMAX HTA"	Cu-0.9Cr-0.1Zr-0.05Mg	90% CW[b], A[b]: 475°C/0.5 hr/AC[b]
AMAX HTB[a]	Cu-0.9Cr-0.1Zr-0.05Mg	90% CW, A: 500°C/1 hr/AC
MIT #2	Cu-0.6Cr-0.13Zr-0.05Mg	15% CW, A: 500°C/1 hr/AC
MIT #3	Cu-0.5Cr-0.5Zr-0.05Mg	SA[b]: 950°C/1 hr/WQ[b], A: 500°C/1 hr/AC
JRC	Cu-0.65Cr-0.08Zr	SA: 1000°C, 44% CW, A: 460°C
Be-containina allovs		
CuBe HTA	Cu-1.96Be	SA: 765°C/1 hr/WQ, 20% CW, A: 320°C/3 hrs/AC
CuBe HTB	Cu-1.96Be	SA: 765°C/1 hr/WQ, A: 320°C/3 hrs/AC
CuNiBe HTA	Cu-1.8Ni-0.3Be	SA: 900°C/1 hr/WQ, 20% CW, A: 482°C/3 hr/AC
CuNiBe HTB	Cu-1.8Ni-0.3Be	SA: 955°C/30 min/WQ, A: 482°C/3 hr/AC
CuNiBe HTC[a]	Cu-1.8Ni-0.3Be	SA: 900°C/1 hr/AC, 20% CW
Spinodal CuNiTi allovs		
MIT	Cu-5.0Ni-2.1Ti t 0.8% TiO_2 t 0.22% Zr	SA 950°C/20 min/WQ, A: 500°C/1 hr/AC
AMAX	Cu-5.0Ni-2.5Ti	SA 900°C/1 hr/WQ, A: 525°C/1 hr/AC
Reference Material		
MARZ Cu	99.999% pure Cu	Annealed: 450°C/15 min/AC

[a] HTA = heat treatment A
HTB = heat treatment B
HTC = heat treatment C

[b] CW = cold work
A = age
SA = solution annealed
AC = air cooled
WQ = water quenched

Results

MARL copper irradiated at 411-430°C exhibited a relatively reproducible behavior as shown in Figure 1, swelling at ~0.5%/dpa without evidence of saturation up to 150 dpa. Its electrical conductivity fell with both void swelling and transmutation, which forms nickel, zinc, and cobalt in order of decreasing formation rate [14]. Nickel formed by transmutation reaches 1.3 wt% in pure copper at 150 dpa in FFTF.

MARL tensile specimens were included only at the 34 and 50 dpa levels in the Generation 2.0 experiment at 411°C. The tensile and fracture behavior of pure copper containing large swelling levels were found to be rather unusual and was described by Anderson and coworkers [15].

Since pure copper did not swell as much at 529°C (1.8% at 32 dpa), the decrease in conductivity was smaller than at 411-430°C, resulting primarily from transmutation. Addition of 5 wt% Ni prior to irradiation has been shown not to affect the swelling of copper during neutron irradiation, but it did substantially reduce its pre-irradiation conductivity however

As shown in Figure 2, the beryllium-bearing alloys exhibited somewhat more complex behavior in response to solute redistribution as well as transmutation and void swelling. The conductivity of the CuNiBe alloys in Generation 1 initially increased in response to overaging and radiation-induced solute redistribution at 400°C, and then declined with continuing transmutation and swelling [10]. Althougli the early response depended somewhat on the alloy's initial thermomechanical treatment (TMT), the conductivities of the CuNiBe alloys in various TMT conditions converged at higher fluence levels. The three TMT conditions of CuNiBe irradiated to 34 dpa at 414°C in Generation 2 exhibited an increase in conductivity, in agreement with the Generation 1 results. The swelling and conductivity reached at 539°C and 32 dpa were lower than that reached at a comparable dpa levels at 411-430°C.

The conductivitv of the Cu-2Be alloy appears to be indeoendent of TMT in both the Generation 1 and 2 experiments, with a slight initial increase in conductivity probably caused by solute redistribution and overaging, followed by a plateau, as shown in Figure 2. The Cu-2Be alloy did not swell at either temperature in the Generation 2 experiment, in contrast to its behavior at 430°C in Generation 1. This difference is attributed to a progressive contamination of the Generation 1 specimens with aluminum,[3,4] which was used as a spacer material between specimens. Aluminum is known to accelerate the onset of swelling in copper [5,6]. The loss of strength shown in Figure 2 for the CuBe alloys is thought to be related primarily to overaging and was also observed in thermal aging studies [2].

Figure 3 shows the results of tests on the MZC-type alloys. While exhibiting some variability in pre-irradiation conductivity, the post-irradiation behavior of the conductivities for the various alloys was similar. The two TMTs of the AMAX MZC alloy swelled much more than the two MIT alloys or the JRC alloy. The reason for the swelling difference has not been ascertained but is thought to be related to differences in Cr content. The MIT alloys exhibited excellent strength retention up to 150 dpa, as shown in Figure 3, but unfortunately no strength data are available for the JRC alloy. It was shown previously that the yield strength of the AMAX MZC alloy in the HTA condition decreased significantly after irradiation to 16 dpa at 430°C [2].

The spinodally strengthened CuNiTi alloys also exhibited some complexity in their response to irradiation at 411-414°C [13,16], as shown in Figure 4. The conductivity initially increased for both alloys, then began to decrease after ~50 dpa. The conductivity of the AMAX alloy appeared to reach a plateau after ~100 dpa, while the conductivity of the MIT alloy continued to decline. The MIT alloy exhibited considerably less void swelling than the AMAX alloy, most likely due to the added dispersoid and the Zr precipitates in the MIT alloy. The conductivity loss appears to be less at 539°C and 32 dpa. The strength of both spinodal alloys was shown in other studies to increase during irradiation to 34 dpa at 411°C, a phenomenon not found in any of the other alloys studied [13 16].

Discussion

Based on the results of a companion study[7], internally oxidized, dispersion strengthened GlidCop™ alloys have been recommended as leading candidate materials for high heat flux service in fusion reactors. The MIT and JRC MZC alloys, however, exhibited sufficient promise to justify their consideration as back-up candidates. The higher swelling of the AMAC MZC disqualifies it from further consideration. CuBeNi may also be applicable for low fluence applications. Although Cu-2Be exhibited the smallest property changes under irradiation, its low conductivity may preclude its use. The spinodal CuNiTi alloys, particularly the MIT alloy, may be of value because of the stability of their conductivity, and tensile properties during irradiation.

Copper and its alloys exhibit a variety of responses to neutron irradiation, depending on alloy composition, TMT, irradiation temperature, and neutron spectra. The dependence on spectra is expressed in its strong influence on the rates of formation of solid transmutants, which can airectly or indirectly affect electrical and thermal conductivity. The influence of transmutation is not always reflected in all property measurements, however, as illustrated by ?he lack of influence of nickel on the swelling of pure copper.

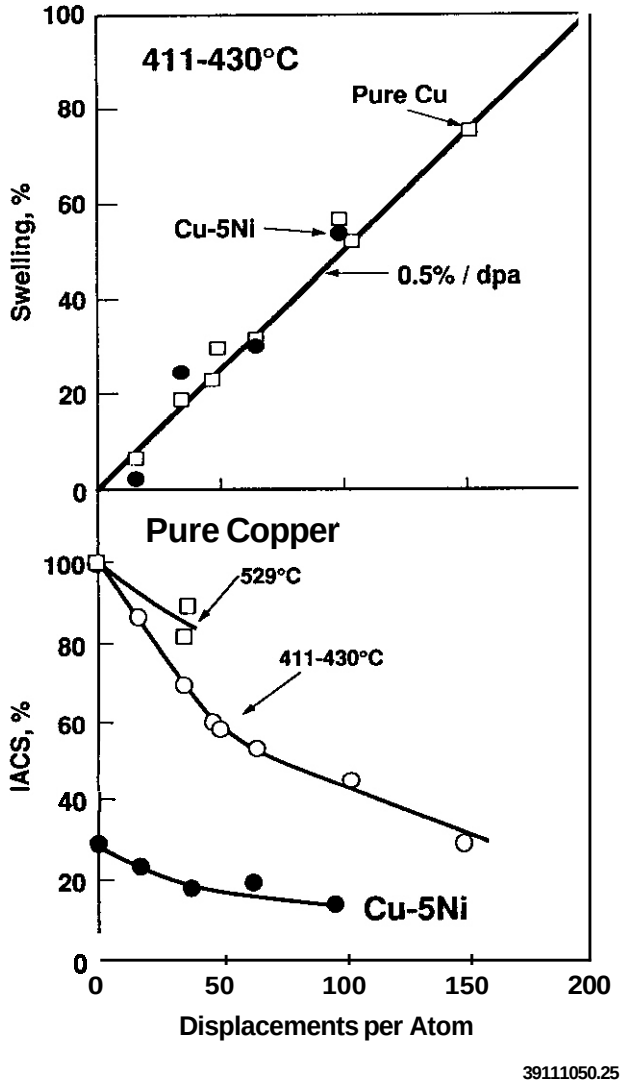

Figure 1. Swelling and conductivity changes observed in pure copper (411-430°C and 539°C) and tu-5 wt% Ni (430°C) during irradiation in FFTF-MOTA.

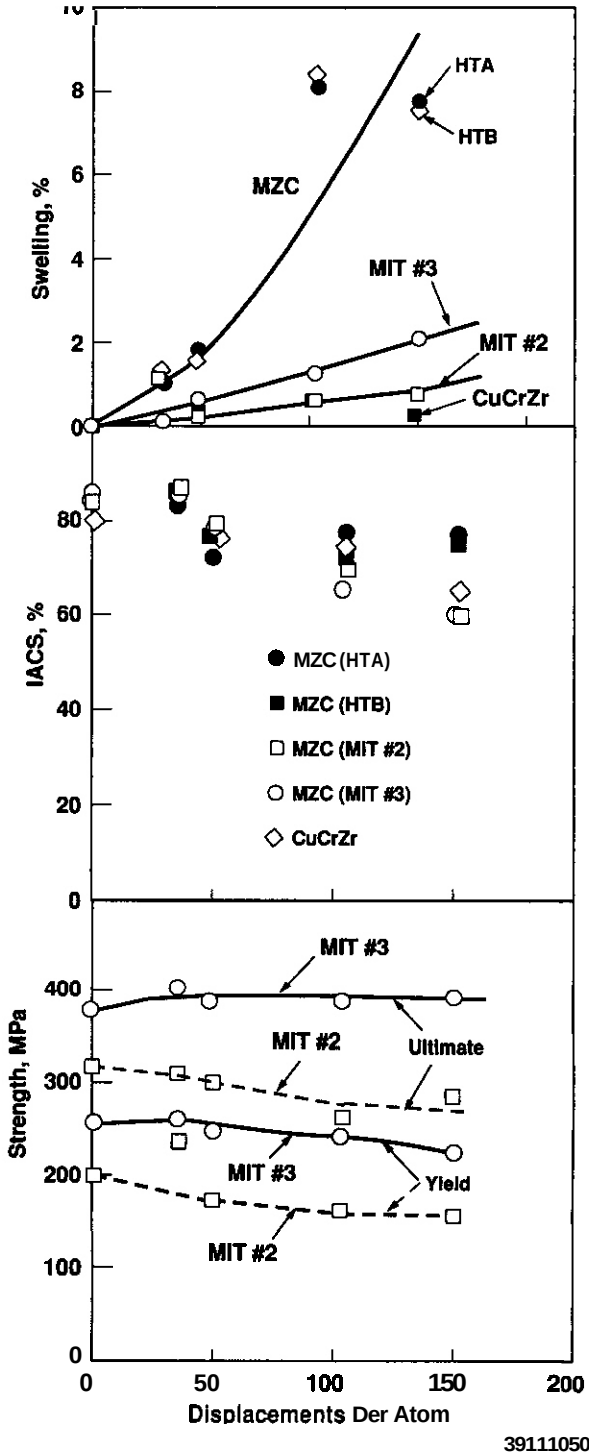

Figure 2. Swelling, conductivity and tensile strength measured in beryllium-containing alloys after irradiation at 411-430°C.

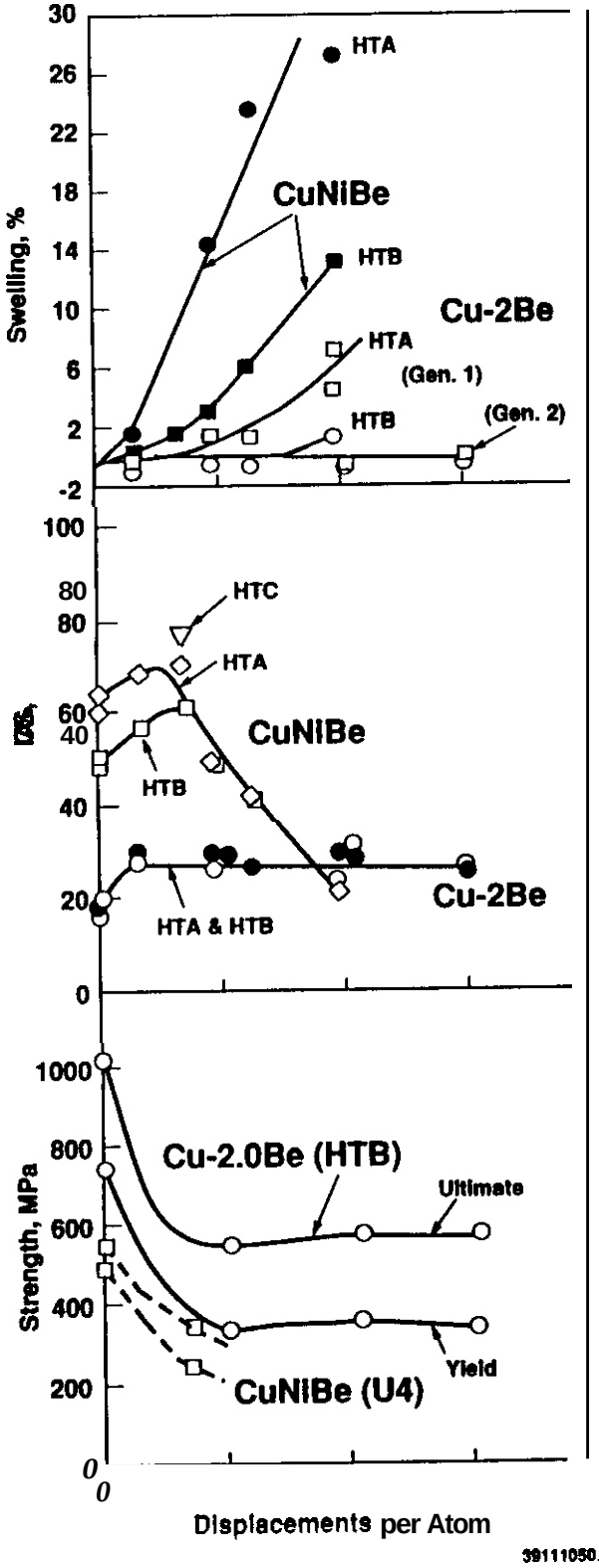

Figure 3. Swelling, conductivity and tensile strength measured in MZC-type alloys after irradiation at 411-414°C.

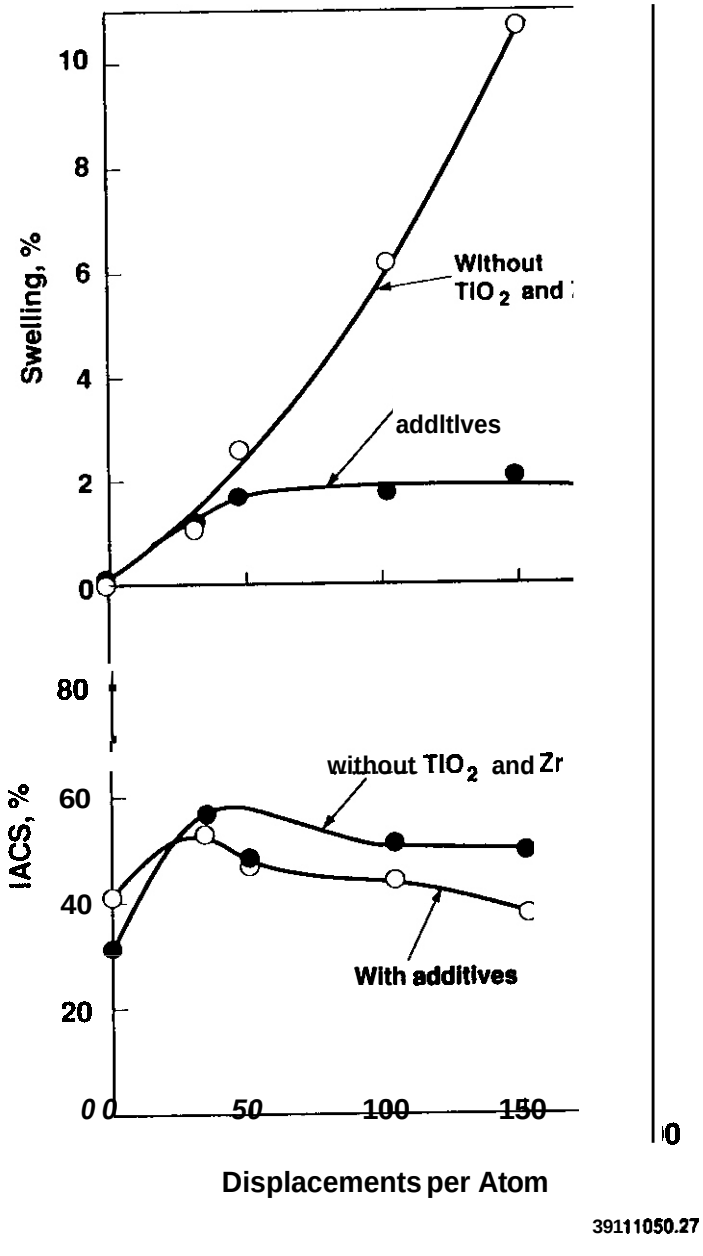

Figure 4. Swelling and conductivity changes observed in spinodally strengthened CuNiTi alloys after irradiation at 411-414°C.

The increase in nickel, zinc and cobalt due to transmutation appears to cause no degradation of electrical conductivity in Cu-2Be. This is thought to arise from the formation of (Cu,Ni,Co)Be beryllide precipitates[17]. The removal of beryllium from solution counteracts the influence of the added transmutants. In CuNiBe most of the beryllium was already out of solution prior to irradiation, and the full effect of both swelling and transmutation is exerted on the conductivity.

Judging from the conductivity and swelling data for the Cu-2Be alloy, the change in composition caused by transmuted nickel does not appear to alter the properties significantly, at least in the FFTF spectrum. It must be cautioned, however, that using the conductivity data from FFTF without corrections for spectrum will most likely underestimate the changes expected in a fusion environment, since nickel will form at much higher rates [14]. The production of helium from the $^{9}Be(n,2\alpha)$ reaction will aiso increase strongly in fusion spectra. These data should therefore be corrected for spectral influence, especially for conductivitv, as part of the extrapolation process to a fusion envircnment.

The MZC class of alloys provides another example of the complex behavior that occurs in irradiated materials. In general, the conductivities of the various MZC alloys fell within a limited range, regardless of compositional and TMT differences. Although their conductivities were similar, the AMAX MZC alloy exhibited much larger swelling than either the MIT or JRC MZC alloys. The decline in conductivity for the MZC class of alloys with irradiation is attributed primarily to transmutation, since the AMAX MZC alloys have roughly the same conductivity response despite their higher void swelling.

The temperature range in which swelling occurs in pure copper at ~1 dpa was determined by Zinkle and Farrell in the Oak Ridge Research reactor (ORR) to be 180-500°C [18,19], although ~1.8% swelling was observed in the current study at 529°C and 32 dpa. If it is assumed that pure copper exhibits the greatest tendency toward swelling, then the combined results of the ORR and FFTF experiments suggest that swelling for a given alloy is possible anywhere in the range of 180-530°C and perhaps at even higher temperatures at sufficiently large displacement levels. The largest steady-state swelling rate observed in pure copper and several other alloys at high fluences in Generation 1.0 was ~0.5%/dpa. It is uncertain, however, whether this rate also applies at the peak swelling temperature of 300-350°C determined by Zinkle and Farrell, or at temperatures above 430°C, where the post-transient swelling rate has not yet been determined. Swelling appears to be only slightly sensitive to helium content below the peak swelling temperature [18,19], but the presence of relatively large amounts of oxygen may lead to a pronounced change in swelling response [7,20,21].

It is thought by the authors that if a given copper alloy survived irradiation in this study to displacement levels on the order of 100 dpa or greater at ~400°C, then it could confidently be applied at lower doses and temperatures since the rate of solute redistribution probably declines strongly with decreasing temperature. The single exception to this otherwise confident assertion lies in the possible response of fatigue properties to the higher microstructural densities that will arise at lower irradiation temperatures.

CONCLUSIONS

The precipitation hardened MIT and JRC MZC alloys appear to offer promise as back-up candidates for high heat flux service in fusion reactors based on their relative resistance to swelling and to changes in conductivity and tensile properties. The CuNiBe alloy may be of interest for low fluence applications, but Cu-2Be is not recommended because of its low electrical conductivity. The spinodally strengthened CuNiTi alloys merit further study based on the limited data presented in this paper.

FUTURE WORK

This effort will continue, focusing primarily on microscopy analysis of various copper alloys.

ACKNOWLEDGEMENTS

The contributions of D. J. Edwards and J. W. Newkirk were performed under the auspices of the Northwest Association for Colleges and Universities for Science (NORCUS), administeriny contract DE-FG06-89ER-75522 for the U.S. Department of Energy. F. A. Garner and M. L. Hamilton were supported by the U.S. DOE Office of Fusion Energy under contract DE-AC06-76RLO-1830. T. Shikama's participation was funded by Monbusho, the Japanese Ministry for Education, Science and Culture.

REFERENCES

1. W. B. Gauster, Nuclear Fusion, 30, no. 9 (1990) 1897.

2. H. R. Braqer, H. L. Heinisch, and F. A. Garner, J. Nucl. Mater., 133 & 134 (1985) 676

3. H. R. Brager, J. Nucl. Mater. 141-143 (1986) 79.

4. H. R. Brager, J. Nucl. Mater. 141-143 (1986) i63

5. H. R. Brager and F. A. Garner, ASTM STP 1046 (1990) 599.

6. F. A. Garner, H. R. Brager, and K. R. Anderson, J. Nucl. Mater., 179-181 (1991) 250

7. D. J. Edwards, K. R. Anderson, F. A. Garner, M. L. Hamilton, J. F. Stubbins, and A. S. Kumar, these proceedings, 5th Int. Conf. on Fusion Reactor Materials, Clearwater, Florida, Nov. 17-22, 1991.

8. K. R. Anderson, F. A. Garner, M. L. Hamilton, and J. F. Stubbins, 15th ASTM International Symposium of Effects of Radiation on Materials, ASTM STP 1125, (in press).

9. T. Shikamr, F. A Garner, M. L. Hamilton, and K. R. Anderson, Proceedings of the 15th ASTM International Symposium on Effects of Radiation on Materials, ASTM STP 1125 [in press).

10. F. A. Garner and S. J. Zinkle, Intl. Conf. on Effects of Radiation on Materials, June 17-21, 1990, ASTM STP, 1125.

11. T-S. Lee, L. W. Hobbs, G. Kohse, M. Ames, O. K. Harling, and N. J. Grant, J. Nucl. Mater., 141-143 (1986) 179.

12. P. Robinson, ASM Metals Handbook, vol. 2, 10th ed., ASM International (1990) 289

13. K. R. Anderson, Doctoral Thesis, University of Illinois at Urbana-Champaign (1990).

14. F. A Garner, H. L. Heinisch, R. L. Simons. and F. M. Mann. Radiatiun Effects and Defects in Solids (1990) 229.

15. K. R. Andersun, F. A. Garner, and J. F. Stubbins, 15th ASTM International Symposium of Effects of Radiation on Materials, ASTM STP 1125, [in press).

16. K. R. Anderson, J. F. Stubbins, and F. A. Garner, accepted for publication in Nuclear Science and Engineering (1991).

17. J. C. Harkness, W. D. Spiegelberg, and W. R. Cribbs, ASM Metals Handbook, vol. 2, 10th ed., ASM International (1990) 403.

18. S. J. Zinkle and E. H. Lee, J. Nucl. Mater., 168 (1989) 262.

19. S. J. Zinkle and E. H. Lee, J. Nucl. Mater., 179 (1991) *994.*

20. S. J. Zinkle and E. H. Lee, Met. Trans., 21A, May (1990) 1037.

21. O. K. Harling, N. J. Grant, G. Kohse, M. Ames, T-S. Lee, and L. W. Hobbs, J. Mater. Research, 2 (1987) 568.

TENSILE AND FRACTURE BEHAVIOR OF Cu-5Ni AND VARIOUS PRECIPITATION-STRENGTHENED COPPER ALLOYS AFTER HIGH FLUENCE IRRADIATION - T. Shikama, Tohoku University, F. A. Garner, M. L. Hamilton, Pacific Northwest Laboratory[a] and K. R. Anderson, University of Illinois

OBJECTIVE

The objective of this effort is to determine the radiation response of copper alloys proposed for fusion service.

SUMMARY

Tensile tests and fractography were used to examine the radiation induced evolution of Cu-5Ni and three commercially prepared precipitation-strengthened alloys after irradiation at 685 and 800K (411 and 527°C). The addition of nickel to copper resulted in increased ductility prior to irradiation but decreased relative ductility after irradiation. The difference in behavior following irradiation appears to arise from the influence of nickel on void swelling. The precipitation strengthened alloys in general exhibited a drop in yield strength after irradiation and an associated increase in ductility. The major effect in these alloys appeared to be related to overaging of the precipitates.

PROGRESS AND STATUS

Introduction

Recent advances in the development of fusion reactors rely upon efficient heat removal from the plasma facing components. Copper alloys appear to be a viable choice for transporting such a high heat flux without thermal damage due to their high inherent thermal conductivity. However, acceptable copper alloys must also maintain their mechanical properties during their service life under the severe neutron exposure and stresses associated with electromagnetic and thermal interactions with a high temperature plasma.

Irradiation effects on copper and its alloys have been studied extensively, but the effects of very large levels of damage on copper and its alloys have only recently been studied. Recent experiments yielded promising results for the oxide dispersion-strengthened (ODS) copper alloys.[1-5] However, the ODS copper alloys have some shortcomings, such as poor weldability and poor properties in the welded and heat affected zones.[5] Precipitation-strengthened copper alloys have been widely used for many years as well as solution-strengthened alloys and their reliability is well known. This paper reports the effects of high levels of irradiation on the mechanical properties of commercially prepared, precipitation-strengthened alloys and a solution-strengthened Cu-5Ni alloy.

Exoerimental Procedures

A variety of commercially-prepared copper alloys (described in Table 1) were irradiated along with pure copper in the Materials Open Test Assembly (MOTA) in the Fast Flux Test Facility (FFTF), a sodium cooled fast reactor in Richland, WA. One of the precipitation-strengthened alloys, CuBeNi, was irradiated in two heat treatment conditions. Three different MZC alloys were also irradiated. The irradiation temperatures and the calculated dpa levels were 34 and 50 dpa at 684K (411°C) and 30 dpa at 800K (527°C). The tensile specimens measured 5.1 mm x 1.0 mm x 0.025 mm in the gauge section. They were tensile tested at room temperature and the fracture surfaces were examined in a scanning electron microscope (SEM). The Cu-2Be (CuBe) irradiated to 50 dpa at 684K (411°C) could not be examined by SEM due to the high level of induced

Table 1. Copper alloys studied in the present experiment

Designation	Composition (wt%)	Heat Treatment
MARZ	99.99%	annealed
5Ni-Cu	Cu-5%Ni	annealed
CuBe	Cu-2%Be	annealed and aged (2h at 590K)
CuNiBe-aa	Cu-1.8%Ni-0.3%Be	annealed and aged (3h at 750K)
CuNiBe-ca	Cu-1.8%Ni-0.3%Be	20% cold worked & aged (3h at 750K)
MZC (AMAX)	Cu-0.9%Cr-0.1%Zr-0.05%Mg	90% cold worked & aged (0.5h at 740K)
MZC (MIT#2)	Cu-0.9%Cr-0.1%Zr-0.05%Mg	annealed and aged
MZC (MIT#3)	Cu-0.9%Cr-0.1%Zr-0.05%Mg	annealed and aged

'Pacific Northwest Laboratory is operated for the U.S. Department of Energy by Battelle Memorial Institute under Contract DE-AC06-76RLO 1830.

radioactivity. Density changes were also determined using disks 3 mm in diameter and 0.2 mm thick. Additional details of the present experiment are given in references 1-5. The results of the irradiation of pure copper were described in reference 4.

Results and Discussion

Cu-5Ni

The tensile data and density determinations on the Cu-5Ni alloy are tabulated in Table 2 in comparison with those of MAR2 copper (zone refined, highly pure copper).[4] The yield strength of Cu-5Ni was smaller than that of MARZ Cu in the unirradiated condition, while the ultimate strength was larger. The work hardening coefficient of Cu-5Ni was therefore much larger than that of MARZ Cu. The elongation observed in unirradiated Cu-5Ni was much larger than that of MARZ Cu, although the fracture surfaces of both alloys were knife edges and the reduction in area in both alloys was nearly 100%, indicating that both were very ductile.

Table 2. Results on Cu-5Ni in comparison with MAR2 pure copper,[4] both irradiated 34 dpa at 864K

	Cu-5Ni		MAR2	
	Pre-irrad.	Post-irrad.	Pre-irrad.	Post-irrad.
Swelling (%)	0	22.9	0	15.1
Y.S.[1] (MPa)	50	86	13	64
U.T.S. (MPa)	208	124	171	116
U.E. (%)	34.2	5.4	20.0	9.7
T.E. (%)	38.1	5.5	25.0	10.1

1) Y.S.: Yield stress; U.T.S.: Ultimate tensile strength; U.E.: Uniform elongation; T.E.: Total elongation

Irradiation at 684K (411°C) resulted in a slight decrease in the yield strength of MARZ Cu, while an increase was clearly observed in that of Cu-5Ni. Irradiation decreased the ultimate tensile strength of both alloys, however, down to about the same level, and both specimens fractured without necking just after they reached this stress level.

SEM fractographs are shown in Figure 1 for a fracture surface of Cu-5Ni, which is covered by voids on the order of 1 micron in diameter. The fracture occurred primarily transgranularly by coalescence of the irradiation induced voids, although a small amount of intergranular fracture was observed as steps at grain boundaries. The distribution of the voids is quite uniform in the Cu-5Ni alloy, in contrast to the MAR2 Cu where the voids clearly coarsen in the vicinity of grain boundaries.[4] As indicated by the density measurements given in Table 2, Cu-5Ni exhibited a large amount of swelling (over 20%). even more than did MARZ Cu.

These results indicate that nickel addition exerts a substantial influence on the post-irradiation behavior of copper. The effects observed could result from changes in stacking fault energy that accompany the addition of nickel.

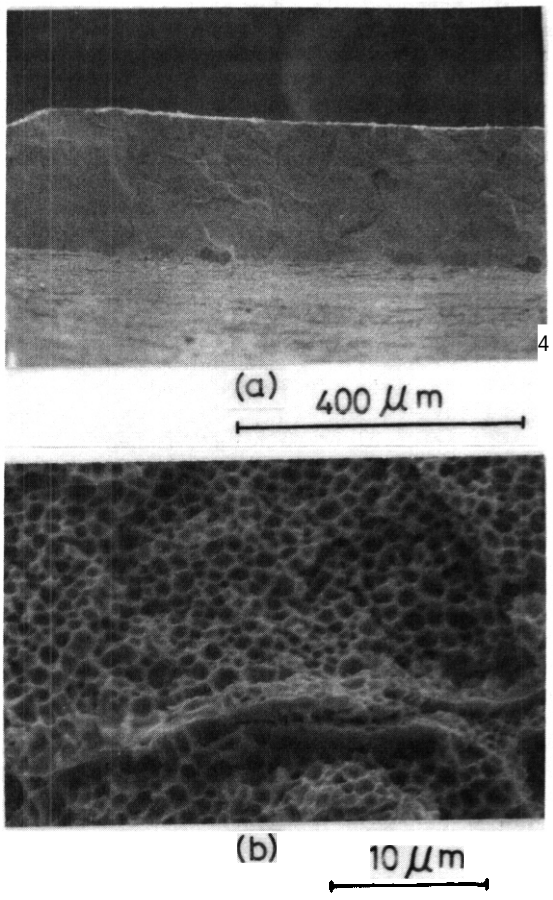

Fig. 1. SEM micrograph of fracture surface of Cu-5Ni after irradiation to 34 dpa at 684K. (a) low magnification (b) high magnification.

Precipitation-Strengthened Alloys

The tensile and density data for the precipitation-strengthened alloys are given in Table 3. While the AMAX MXC and MIT #2 alloys are typical precipitation-strengthened ingot metallurgy alloys, the MIT #3 alloy was produced using rapid solidification powder metallurgy that introduced small ZrO_2 and Cr_2O_3 particles by surface oxidation of the powder particles. Irradiation generally caused the strength to decrease and the ductility to increase, particularly at 800K (527°C). The exception to this was the MIT-MZC alloy in the two annealed and aged heat treatments after exposure at 684K (411°C), which showed virtually no effect of irradiation at 684K (411°C). While cold work imparted an initial benefit to the MZC, as shown in Figure 2, this benefit disappeared after irradiation at elevated temperature. The post-irradiation strength of the cold worked and aged MZC lay between that of the two annealed and aged MZC conditions, which exhibited a similar response to irradiation at all three conditions, maintaining the difference in behavior produced by the pre-irradiation heat

Table 3. Results on precipitation-strengthened copper alloys

		Swelling (%)	Y.S. (MPa)	U.T.S. (MPa)	U.E. (%)	T.E. (%)
CuBe	Unirradiated	0.	807	1040	7.0	7.6
	50 dpa, at 684K	0.68	331	541	12.1	12.5
CuNiBe -aa	Unirradiated	0.	575	770	9.5	9.5
	34dpa, at 684K	-0.04	508	531	1.1	1.1
CuNiBe -ca	Unirradiated	0.	501	553	2.5	3.0
	34dpa, at 684K	1.66	240	349	8.7	9.2
	30dpa, at 800K	-	111	248	19.8	21.9
MZC (AMAX)	Unirradiated	0.	520	542	3.7	5.9
	34dpa, at 684K	1.11	231	335	16.7	19.3
	30dpa, at 800K	0.42	124	256	23.0	26.7
MZC (MIT#2)	Unirradiated	0.	198	315	13.1	16.2
	34dpa, at 684K	1.12	231	307	11.7	14.2
	50dpa, at 684K	0.19	169	295	14.1	16.7
	30dpa, at 800K	0.53	93	221	28.9	32.4
YZC (MIT#3)	Unirradiated	0.	256	379	14.4	17.6
	34dpa, at 684K	0.26	264	403	13.2	16.2
	50dpa, at 684K	0.66	248	388	15.1	18.7
	30dpa, at 800K	0.21	166	314	18.9	22.8

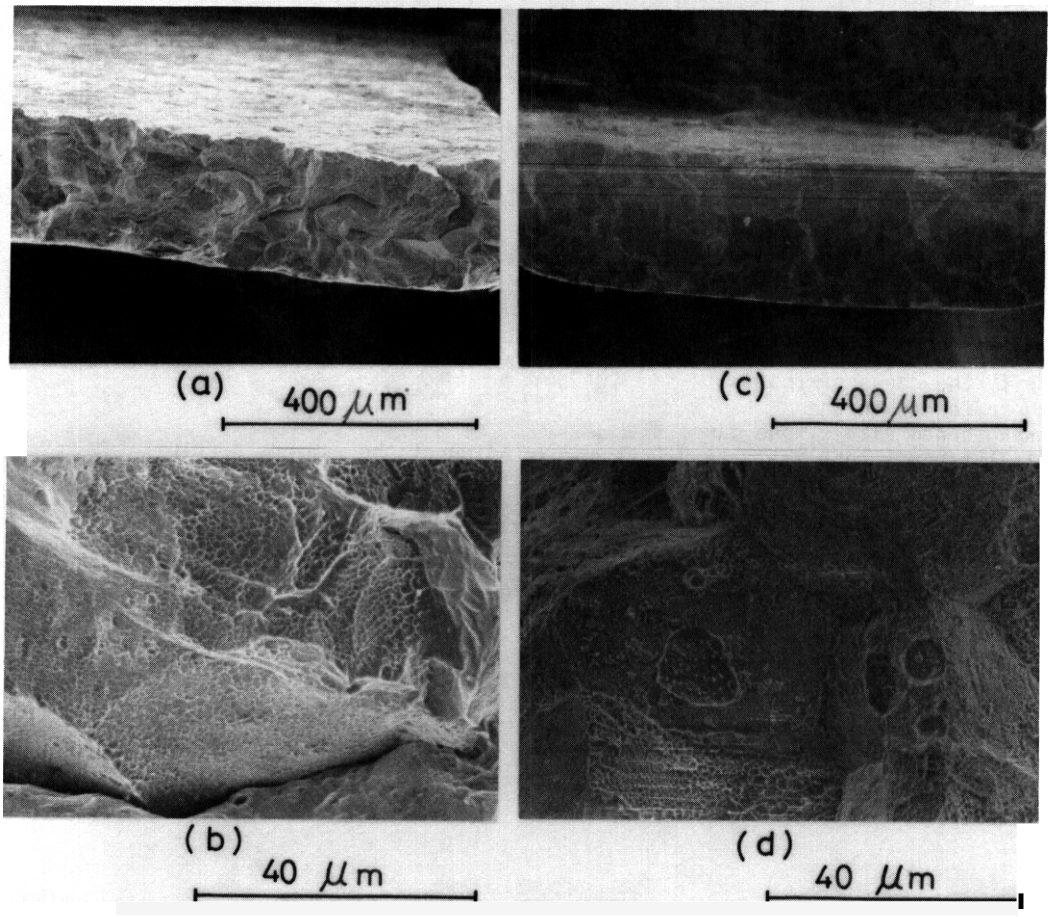

Fig. 2. SEM micrograph of fracture surface of annealed and aged CuNiBe before and after irradiation to 34 dpa at 684K. (a) before irradiation, low magnification (b) before irradiation, high magnification, (c) after irradiation, low magnification, (d) after irradiation, high magnification.

treatment. These results are consistent with previous observations that the microstructures of MZC were stable during thermal aging at 673K (400°C) for 1000 hours.[2]

Cold working CuNiBe prior to aging did not produce the same improvement in pre-irradiation tensile behavior as was observed in MZC. The relative degradation observed in the cold worked and aged CuNiBe compared to that of the annealed and aged CuNiBe was similar to the relative degradation observed in the MZC, i.e., the cold worked and aged alloy exhibited a larger degradation in behavior with irradiation. The significant decrease in strength observed in the annealed and aged alloy is not consistent with previous observations [2] that the microstructure of CuNiBe is stable during thermal aging at 673K (400°C) for 1000 hours, suggesting that irradiation is responsible for some microstructural evolution in addition to that which would be expected thermally

The fracture mode of the precipitation-strengthened alloys did not appear to be affected by irradiation at 684 or 800K (411 or 527°C). The CuBe and the MZC specimens failed in a ductile fashion, exhibiting transgranular fracture surfaces both before and after irradiation. CuNiBe (in the cold worked and aged condition) exhibited a mixture of intergranular and transgranular failure prior to irradiation, with some degree of deformation near the fracture as shown in Figure 3a and b. Irradiation enhanced the intergranular fracture and decreased the deformation in the vicinity of the fracture (Figure 3c and d). CuNiBe (in the annealed and aged condition) failed intergranularly both before and after irradiation.

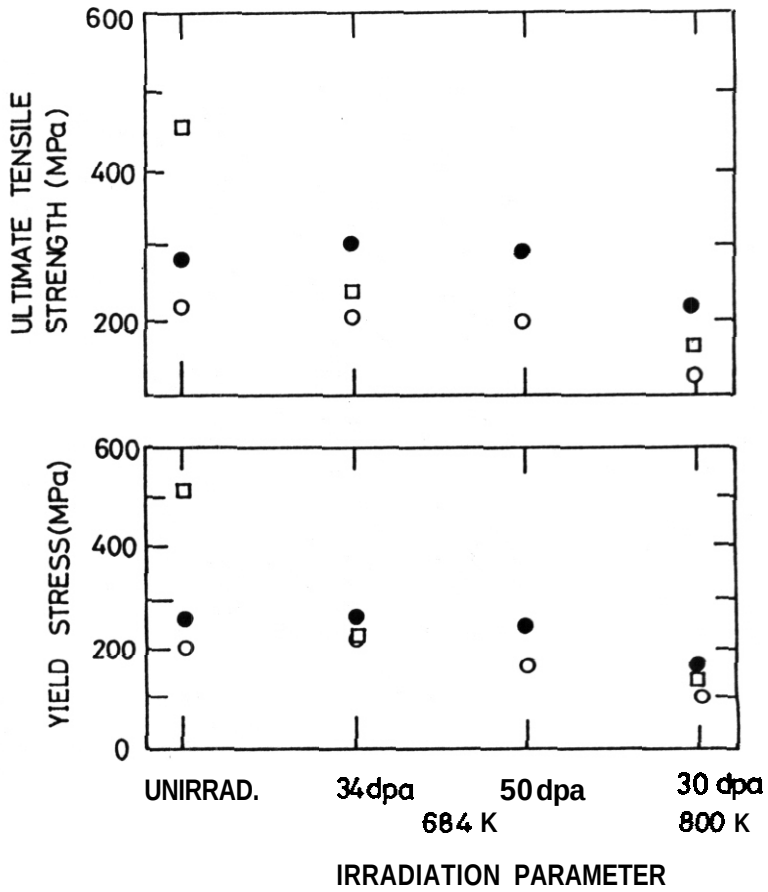

Fig. 3. Tensile properties of MZC alloys (open squares: 90% cold worked and aged), (open circles: annealed and aged [MIT#2]), (closed circles: annealed and aged [MIT#3]).

In the absence of transmission electron microscopy to verify the cause of the radiation-induced softening in the precipitation-strengthened-alloys, one can only surmise that it is most likely the result of an overaging of the various precipitates involved, particularly at 800K (527°C). Nonetheless, these alloys retained a reasonable fraction of their pre-irradiation strength. In addition, they exhibited only very small amounts of swelling (less than 2%), consistent with the absence of visible voids in the SEM fractographs.

CONCLUSIONS

Tensile testing, density determinations and SEM fractography were used to investigate the effects of irradiation at 684 and 800K (411 and 527°C) on the behavior of Cu-5Ni and three commercially prepared precipitation-strengthened copper alloys. The addition of nickel caused both an increase in swelling and a degradation in tensile behavior relative to pure copper. The precipitation-strengthened alloys exhibited far less swelling and generally less degradation in tensile properties than Cu-5Ni or pure copper, demonstrating their potential viability as fusion reactor materials.

ACKNOWLEDGEMENTS

T. Shikama wishes to express his gratitude to R. M. Ermi and E. M. Oieffenbacher for their kind assistance during his stay at PNL.

REFERENCES

1. H. R. Brager, H. L. Heinisch and F. A. Garner, J. Nucl. Mater., 133&134 (1985) 676-679.

2. H. R. Brager, J. Nucl. Mater., 141&143 (1986) 79-86

3. H. R. Brager, J. Nucl. Mater., 141&143 (1986) 163-168

4. K. R. Anderson, F. A. Garner and J. F. Stubbins, accepted for publication in proceedings of 15th ASTM International Symposium on Effects of Radiation on Materials, ASTM STP 1125, in press.

5. F. A. Garner, M. L. Hamilton, T. Shikama, D. J. Edwards and J. W. Newkirk, accepted for publication in J. Nucl. Mater., proceedings of ICFRM-5.

6.5 Environmental Effects on Structural Materials

Assessment of H-Induced Crack Growth of Type 316 SS at ITER Conditions- R.H. Jones, Pacific Northwest Laboratory*

OBJECTIVE

The purpose of this study was to evaluate the potential for H-induced crack growth of Type 316 SS at ITER relevant conditions.

SUMMARY

The results of this analysis suggest that H-induced crack growth of Type 316 SS is a definite concern for ITER first-wall applications. It was estimated that crack velocities as high as 2 x 10^{-6} m/s could result in Type 316 SS irradiated at 100°C to 10 dpa, while the threshold, K_{th}, for crack growth could be as low as 28 to 31 MPa$\sqrt{m}$ for hydrogen generated by (n,p) reactions. This crack velocity would propagate through a 4-mm-thick first wall in 33 minutes, and therefore these conclusions should be evaluated experimentally. Also, a K_{th} of 28 MPa$\sqrt{m}$ requires that the applied and residual stresses in the structure be limited to 500 MPa for a 1-mm-long crack to avoid H-induced crack growth. Higher stress limits are possible for shorter cracks. These predictions are based on the assumption that all the H generated by (n,p) reactions would be contained within the material; however, some loss of H to the vacuum or water side of the first wall is expected. The extent of this loss will depend on engineering considerations such as coatings, etc.

PROGRESS AND STATUS

Introduction

Environment-induced crack growth of Type 316 stainless steel may occur at ITER conditions if the incorrect design and material-processing parameters are utilized. Jones (1) noted that austenitic stainless steels will crack at temperatures of 100°C and below if they are allowed to become thermally sensitized or if the O or impurity concentrations in the water are allowed to exceed established limits. Austenitic stainless steels may become susceptible to intergranular stress-corrosion cracking (IGSCC), even if they are not thermally sensitized, by a process called irradiation-assisted stress-corrosion cracking (IASCC). Whether IASCC will occur at temperatures of 100°C and below has not been determined, although recent model-based predictions by Simonen, Jones and Bruemmer (2) suggest that 10 dpa at 150°C is sufficient to produce a grain boundary microchemistry that could produce IGSCC. Experimental verification of these predictions is needed. Radiolysis of water from neutron and gamma radiation has been shown to increase the oxidizing potential of water (3) such that stress-corrosion cracking is more likely. However, Jones and Henager (4) concluded that even with impure water and mildly sensitized Type 316 SS, radiolysis did not accelerate crack growth at 100°C.

H-induced crack growth is another environment-induced crack growth mechanism that must be considered in material selection and reactor design. Most materials experience some form of H-induced crack growth with a characteristic crack velocity-stress intensity curve as shown in Figure 1. Subcritical crack growth induced by aqueous environments also follows a similar subcritical crack growth curve. However, for unirradiated austenitic stainless steels, the threshold, K_{th} for H-induced crack growth is usually very high, so that H-induced crack growth is not a problem. The crack velocity in stage II for ferritic steels has been thoroughly documented to exhibit the temperature dependence shown in Figure 2 where the maximum crack velocity occurs at 25 to 100°C and the velocity drops off rapidly at temperatures above this peak. The temperature of the peak velocity is a function of material properties, environment, etc. The temperature at the peak velocity is not well known for austenitic stainless steels but has generally been considered to be higher than for ferritic steels.

H-induced crack growth of solution-annealed Type 316 SS, the reference ITER material, is possible for the following reasons:

> H-induced crack growth has been observed in a stable Type 310 SS for bulk H concentrations similar to the concentration generated by (n,p) reactions following a dose of 45 dpa (2255 appm).

*Operated for the U.S. Department of Energy by Battelle Memorial Institute under Contract DE-AC06-76RLO 1830.

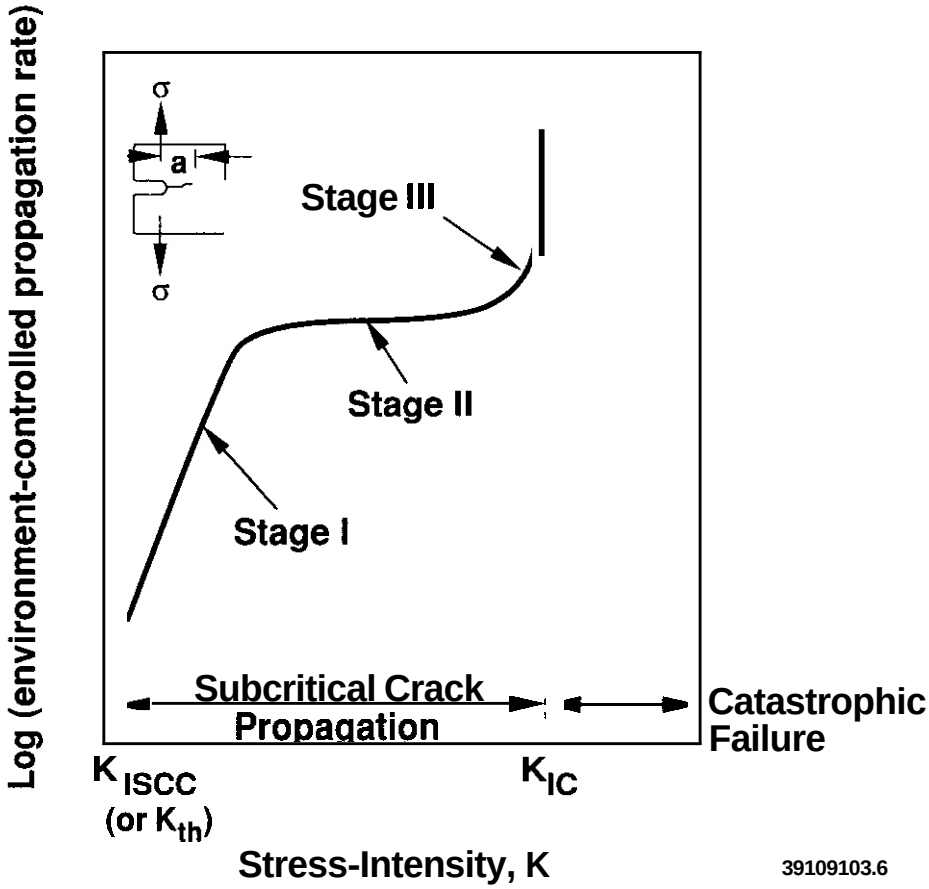

Figure 1. Schematic of da/dt vs stress intensity curve for H-induced subcritical crack growth

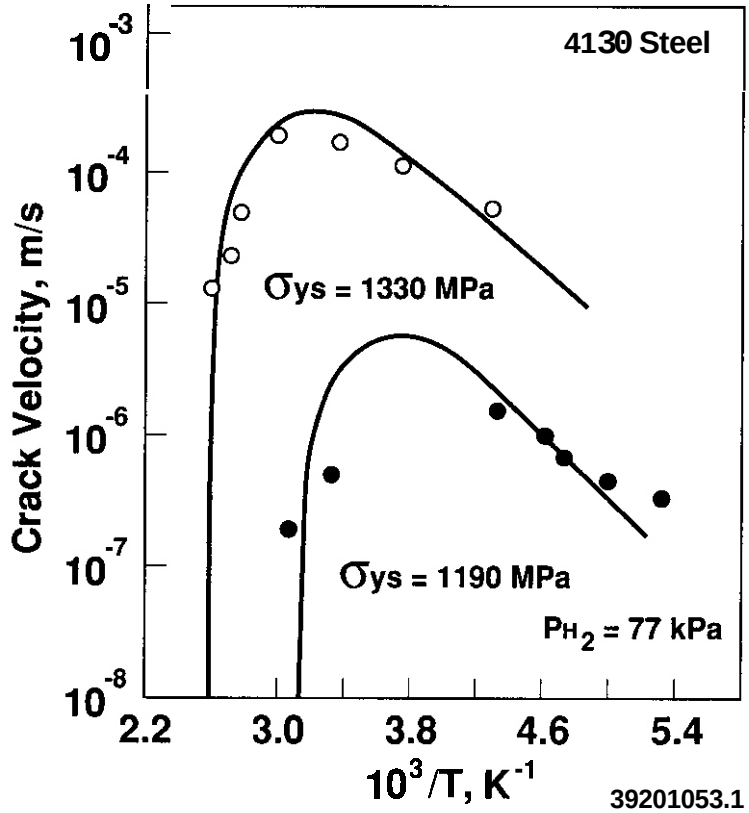

Figure 2. Fit of Equation 1 to the H-induced subcritical crack velocity data from two 4130 steels with different strength levels.

K_{th} is known to decrease and da/dt increase with increasing hardness and the yield strength of Type 316 SS will be increased from about 300 MPa to 900 MPa by irradiation in ITER (5).

A da/dt versus 1/T curve for austenitic stainless steels was recently shown to have a maximum velocity at 130°C for tests in water which is similar to H-induced crack growth peaks observed in ferritic steels (6).

It has been shown that the da/dt versus 1/T curve for ferritic steels was similar for internal H and external H derived from cathodic corrosion.

Radiation has been shown to increase the diffusivity of H in austenitic stainless steels (7) and since the crack velocity is a function of H diffusivity, the crack velocity would be increased during reactor operation.

Therefore, this assessment was undertaken to help identify the likelihood that H-induced crack growth occurs under ITER reactor conditions. Estimates of both the temperature dependence of the crack velocity and the K_{th} have been undertaken since both a low K_{th} and a high crack velocity are necessary before H-induced crack growth is a concern.

Crack Velocity

Calculational Approach

The temperature dependence of the crack velocity for both Type 304 SS and Type 316 SS was estimated by combining experimental and theoretical analysis as summarized in the following steps. Both Type 304 and 316 SS were evaluated because the database on Type 304 SS is considerably greater than it is for Type 316 SS. Therefore, a more complete analysis was possible with Type 304 SS which is useful for interpreting the Type 316 SS results. The following calculational steps were followed:

- Assume that the temperature dependence of da/dt for austenitic stainless steels is similar to ferritic steels, as shown in Figure 2. (Evidence to support this assumption is shown in Figure 3.)
- Assume that the model by Gerberich et al. (8), which was developed to describe the da/dt versus 1/T behavior of ferritic steels, is also valid for austenitic stainless steels.
- Utilize the data of Altstetter et al. (9) to establish the low temperature crack velocity of unirradiated material with a known H concentration (500 appm corresponding to 10 dpa).
- Utilize known H diffusion activation energy for H in austenitic stainless steels for the slope of the low temperature portion of the da/dt vs 1/T curve of the unirradiated material. [This is consistent with equation 1.)
- Determine the crack velocity at T_{max} (100°C) by extrapolation of the curve from the da/dt at low temperature.
- Calculate the increase in crack velocity at T_{max} resulting from radiation-enhanced diffusivity of H and radiation hardening using the model by Gerberich.
- Plot the curve for the irradiated material based on the activation energy for diffusion of H during irradiation.

The temperature dependence of the crack velocity for a sensitized austenitic stainless steel is shown in Figure 3. The low temperature peak is assumed to be the result of H-induced crack growth and the increase in crack growth rate with increasing temperature above 136°C is considered to be aqueous stress-corrosion cracking. While these data are for sensitized Type 304 SS, it was concluded that the presence of the peak in the crack velocity at around 100°C is a general phenomenon, as it has been shown to be for ferritic steels, and that a similar da/dt vs 1/T dependence would occur for H-induced crack growth of nonsensitired austenitic stainless steels. Recent calculations by Simonen et al. (2) suggest that Cr depletion may occur at ITER relevant temperatures such that the grain boundary Cr depletion *in* an ITER first wall material could approach that of a sensitized material. If this occurs, the data shown in Figure 3 could be very representative of the ITER condition. The T_{max} and $T_{\emptyset}$ for the data shown in Figure 3 are about 100 and 136°C, respectively and they were assumed to be independent of irradiation.

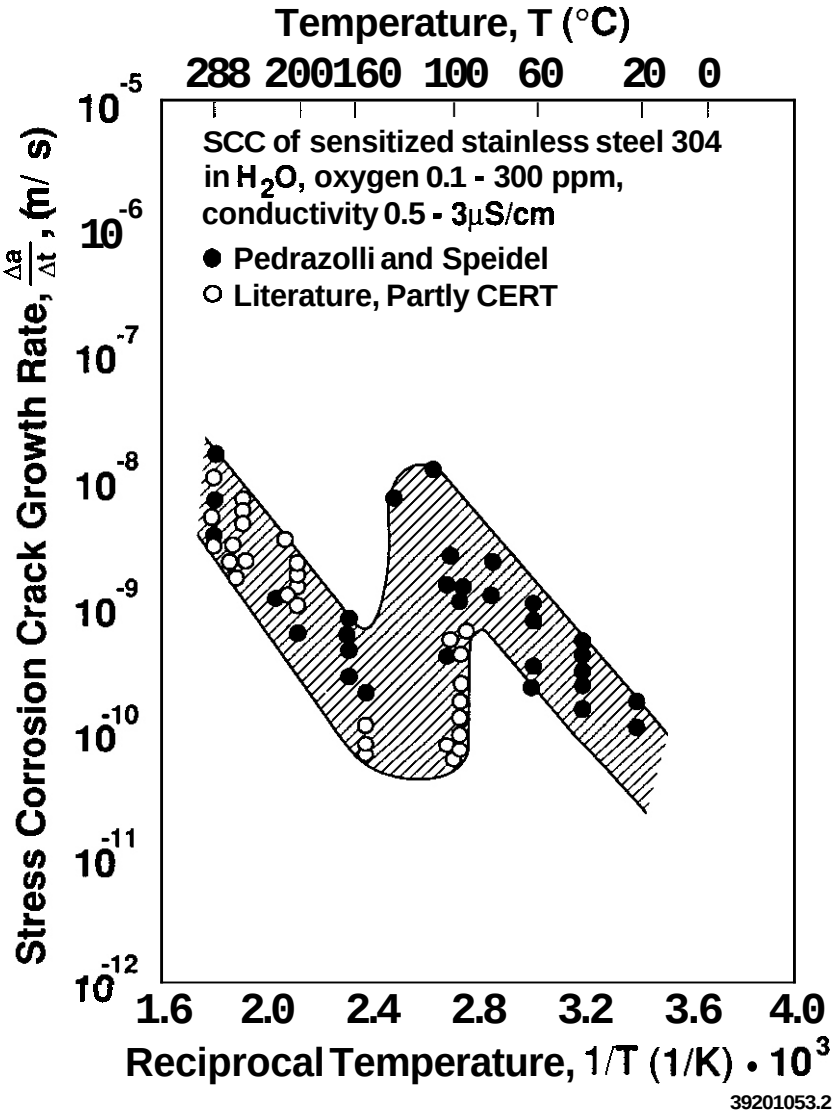

Figure 3. Crack velocity results versus 1/T for a sensitized Type 304 SS (6).

Examples of H-induced crack growth of Type 304 SS are shown in Figure 4a (9). There is a clear decrease in K_{th} and increase in da/dt with increasing H concentration; however, these data were obtained with thin samples in which there was considerable α' formation. The K_{th} was higher and the crack velocity was lower in Type 310 SS (10), in which there was no α' transformation, for an H concentration of 2255 appm, Figure 4b.

The crack velocity model used in this assessment is that described by Gerberich et al. (8) and given below:

$$\frac{da}{dt} = \frac{4D_0 \exp(-Q^{eff}/RT)}{X^{CR}} \times \left[1-\exp\left\{\frac{(\frac{1+\pi}{2})\sigma_y \overline{V}_H (T-T_0)}{RTT_0}\right\}\right]^2 \quad (1)$$

where $\overline{V}_H$ is the partial molar volume of H in austenitic stainless steel (2×10^{-6} m^3/mol), Q_{eff} is the activation energy for H diffusion, T is temperature, T_o is the upper temperature cut-off for crack growth (136°C), σ_y is yield strength and R is the gas constant. It was not necessary to define the magnitudes of D_o or X^{cr} since the model was used only to determine the relative velocities of irradiated to unirradiated material. The value for V_H was obtained from Moody et al. (11) and Baranowski et al. (12). Activation energies for diffusion were taken from the data shown in Figure 5 for unirradiated and irradiated

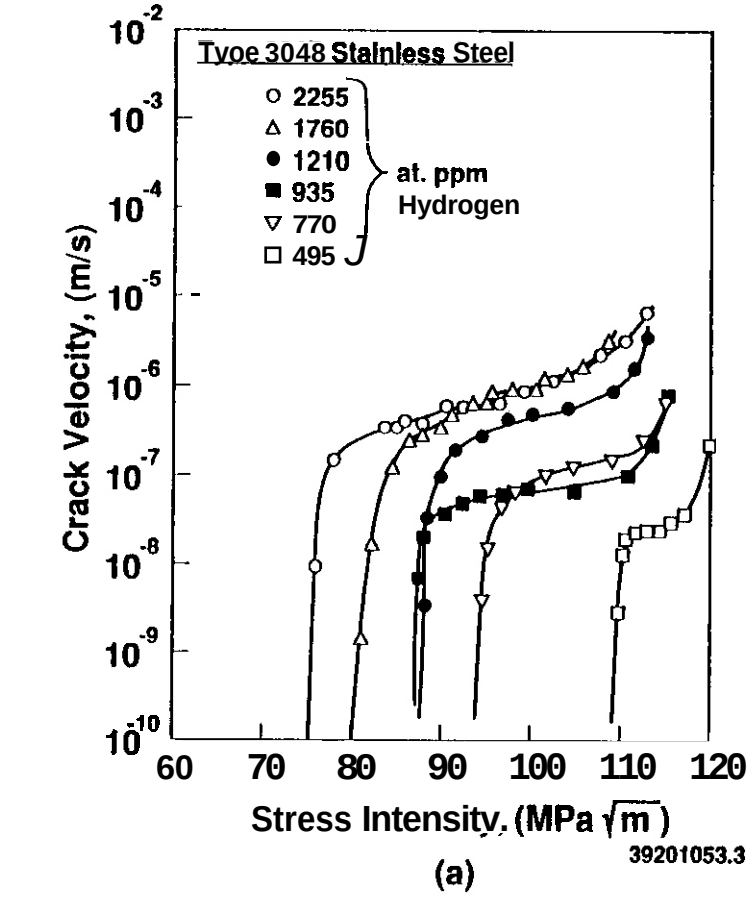

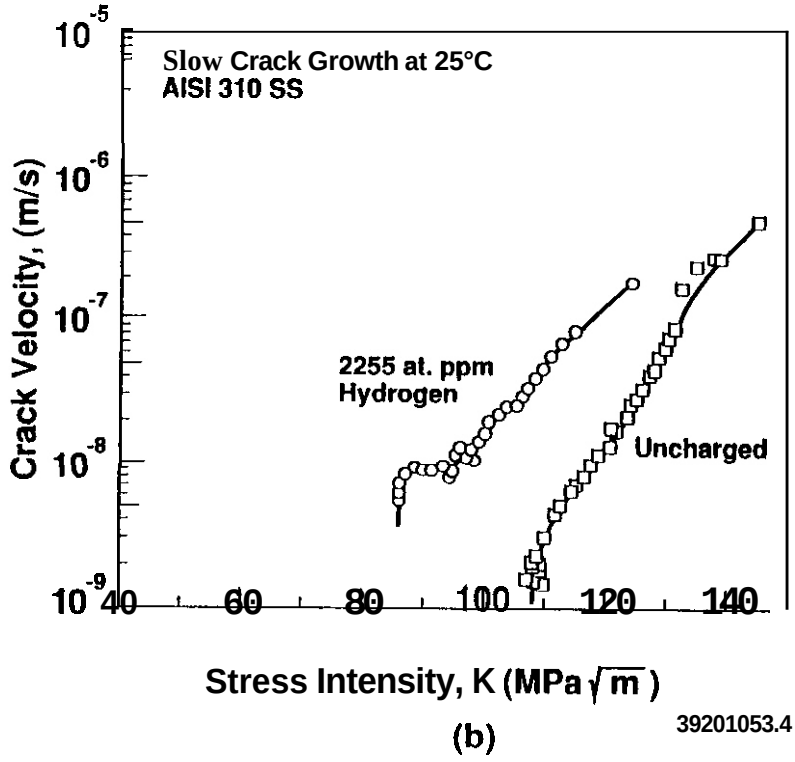

Figure 4. Crack velocity versus stress intensity for H-induced subcritical crack growth of a) Type 304 SS and b) Type 310 SS (9,10).

austenitic stainless steel (7). The Q^{eff} values were 55.9 and 22.6 kJ/mol for out-of-reactor and in-reactor conditions, respectively, for a Type 304 SS. The Q^{eff} value of Type 316 SS without irradiation was assumed to be equal to that of Type 304 SS, while the in-reactor value was estimated from the ratio of the activation energy for permeability of irradiated to nonirradiated Type 316 SS and activation energies for permeability and diffusivity of Type 304 SS (7). This estimation approach was needed because an activation energy for irradiated Type 316 SS was not reported (7).

The following assumptions were made in applying Equation 1 to the analysis of H-induced crack growth of ITER materials:

- that all the H produced by (n,p) reactions remains in the material,

- that the irradiation-enhanced diffusion data shown in Figure 5 can be extrapolated to the lower temperature range of interest,

- that the Altstetter et al. (10) data for the stable Type 310 SS are prototypic of Type 316 SS,

- that irradiation increases the velocity component of the da/dt vs I/T curve but does not shift the temperature component; i.e., T_o is constant and equal to 136°C, and T_{max} is constant and equal to 100°C,

- that there is no correction for flux dependence between the radiation enhanced diffusion data and the flux in ITER,

- that there is no correction for cyclic stress and temperature,

- that the critical concentration of hydrogen required at the crack tip to drive subcritical cracking is not a function of radiation damage or He generation, i.e., that there are no other embrittlement processes.

The H diffusion data shown in Figure 5 does not exhibit the expected temperature dependence for an irradiation enhanced process. For austenitic stainless steel, the irradiation enhanced and thermally activated processes should merge at temperatures above 650°C, between 400 to 650°C a weakly temperature dependent stage is expected, while below 400°C a well defined Arrhenius dependence related to the vacancy migration energy is expected. Eventhough this data doesn't display all the expected features, it is the only data available on irradiation effects on H diffusion; therefore, it was utilized in this analysis. A more accurate crack growth analysis requires irradiation-enhanced H diffusion data obtained at 50 to 350°C.

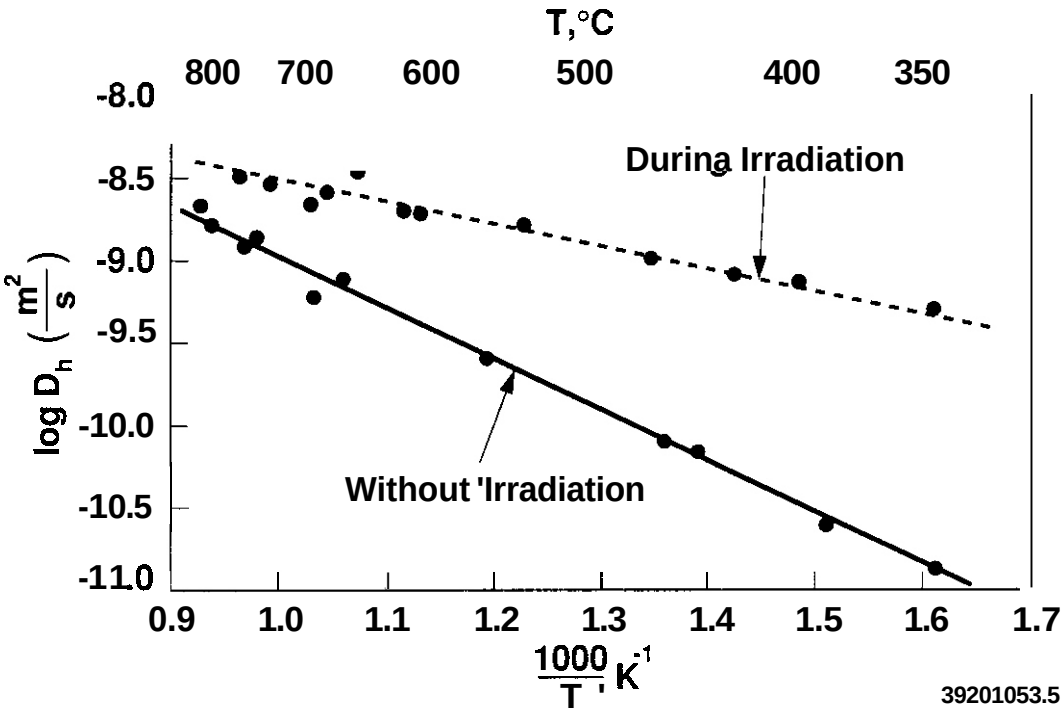

Figure 5. Diffusivity of H versus I/T for a 16Cr10NiTi austenitic stainless steel with and without irradiation.

Crack Growth Rates

The estimated crack velocity versus 1/T results are given in Figure 6a and 6b for Type 304 SS and 316 SS, respectively. The H-induced crack-growth data were obtained from Type 304 SS and Type 310 SS (9) (prototypic of Type 316 SS) while the irradiation-enhanced diffusion data were from Type 304 and 316 SS's with the addition of Ti (7). The maximum velocity for Type 304 SS with 495 at. ppm H (9 dpa) is predicted to be 3 x 10^{-5} m/s without irradiation and 3 x 10^{-4} m/s with irradiation. These are stage II crack velocities with applied stress intensities of 115 MPa$\sqrt{m}$. Since stage II is K independent, the velocities would be essentially the same at stress intensities down to K_{th}. Estimates of K_{th} for ITER relevant conditions have also been made and are presented in the next section. Increasing the H concentration to 770 at. ppm (14 dpa) increases the maximum crack velocities to 2 x 10^{-4} and 2 x 10^{-3} m/s with and without irradiation, respectively. Since the goal fluence in the technology phase of ITER ranges from 10 to 50 dpa and the H generation rate is 52 appm/dpa, both of these H concentrations are within the end-of-life range for the first-wall material (520 to 2600 at. appm H). These values also fall within the range of H concentrations in materials tested by Altstetter et al. (9) as given in Figure 4.

Estimates of the H-induced crack-growth rate for Type 316 SS were based on data for Type 310 SS because of the lack of an adequate database on Type 316 SS. The H diffusivity data for the irradiated material was for a steel with 16% Cr, 11% Ni, 3% Mo, *0.04%* C and some Ti. The results of these estimates are shown in Figure 6b, where it can be seen that the estimated crack velocities at 100°C range from 2 x 10^{-6} m/s to 4 x 10^{-5} m/s for irradiation doses of 10 and 45 dpa, respectively. The curve for 550 at. ppm H (10 dpa) was estimated from the H concentration dependence of the crack velocity of irradiated Type 304 SS curves. While these crack velocities are slower than for an unstable austenitic stainless steel, they are still faster than could be tolerated in an ITER structure.

Stress Intensity Thresholds for Crack Growth

The crack-growth threshold, K_{th} of austenitic stainless steel has clearly been demonstrated to be a function of yield strength and hydrogen concentration (C_H), as demonstrated by the results in Figures 7a-c. The decrease in K_{th} of austenitic stainless steels reaches a minimum with increasing C_H and appears to be relatively temperature independent within the temperature range of 0 to 50°C. The trend is the same between internal and external H as shown by comparison between Figures 7a and 7b. However, results by Moody et al. (13) for IN 903, presented in Figure 8, suggest that the threshold continues to decrease with increasing hydrogen concentration. In ferritic steels, the K_{th} was shown to be a function of -log P_H without the minimum at high pressures (14). Clearly, the absence of a minimum in K_{th} with increasing C_H will result in lower predicted values of K_{th} but these differences occur at relatively high C_H values and may have a small effect on the K_{th} predicted for ITER conditions. For instance, the plateau in K_{th} shown in Figure 7a, occurs at about 10 wt ppm (550 at. ppm or 10 dpa) which is near the end-of-life fluence for the ITER structural material. A decrease in K_{th} with increasing yield strength is also noted for a variety of fcc alloys as demonstrated in Figure 7c.

The effect of C_H T and yield strength on K_{th} is needed to estimate its value at ITER conditions; however, such a model does not exist. Therefore, it was necessary to estimate K_{th} of ITER first-wall materials from existing data. Using the Altstetter data, the K_{th} of a stable austenitic stainless steel, with 2255 at. ppm of H is 85 MPa$\sqrt{m}$. The threshold at 550 at. ppm (10 dpa) is estimated to be 113 MPa$\sqrt{m}$ based on the relative effect of C_H on K_{th} in Type 304 SS. Using the relative effect of temperature on K_{th} of Type 301 SS, as shown in Figure 7a, the K_{th} at 100°C and 10 dpa (550 appm) would be 68 MPa$\sqrt{m}$. This value would be further decreased by the yield strength increase from 300 MPa to 900 MPa, as suggested by the data in Figure 7c, but the magnitude of this change is unknown. If the slope of the data in Figure 7c is utilized, it suggests that K_{th} of Type 316 SS at 100°C and 10 dpa would be zero but K_{th} is not expected to decrease this much.

Another method to estimate the K_{th} is to use known K_{th}/K_{Ic} ratios such as those shown in Figure 9 (15). These data indicate that the ratio of K_{th}/K_{Ic} increases with decreasing fracture toughness. The fracture toughness is shown as a ratio of $K_c/K_{Ic}(o)$ where K_{Ic}, for the present case, is that for irradiated material and $K_{Ic}(o)$ is that for unirradiated material. The data in Figure 9 indicate that as the toughness decreases, the relative effect of hydrogen (i.e., the K_{th}) decreases. Using data from Hamilton et al. (16), the value of K_{Ic} (irr)/K_{Ic} (unirr) for solution-annealed Type 316 SS is 0.44 which results in a K_{th}/K_{Ic} ratio of between 0.5 to 0.68 based on Figure 9. The K_{Ic} after irradiation to 10 dpa at 250 C is 55 MPa$\sqrt{m}$ which yields a K_{th} of 28 to 31 MPa$\sqrt{m}$. These values for K_{th} are sufficiently low that H-induced crack growth could occur in an ITER first-wall with modest flaw lengths and stresses. This estimate does not consider the possible effect of H on K_{Ic} which would result in a ratio of K_{Ic} (irr t H)/K_{Ic} (unirr) less than that for irradiation only. There is some suggestion in the data shown in Figure 4 that H reduces the transition from stage II to stage III presumably because of a reduction of K_{Ic}; however, the extent of this reduction cannot be determined from these data. If H does reduce K_{Ic} (irr), the concept presented in Figure 9 would

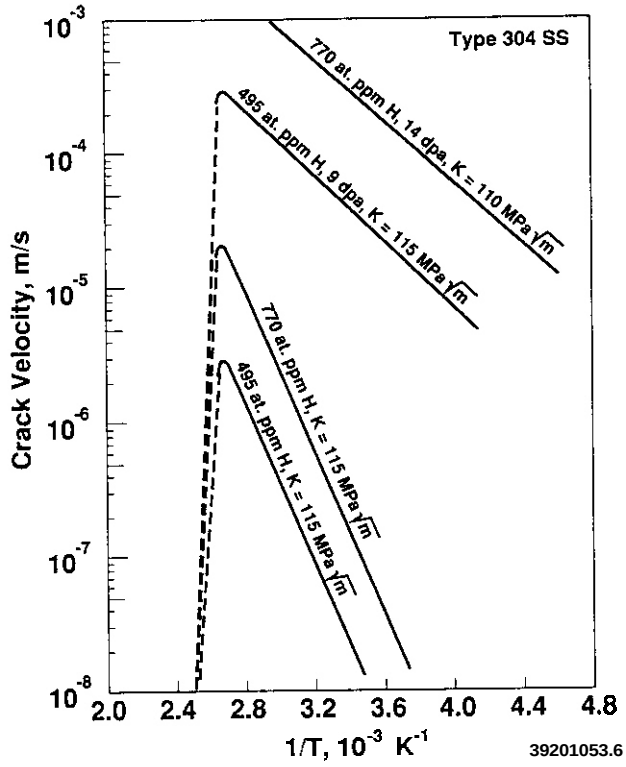

(a)

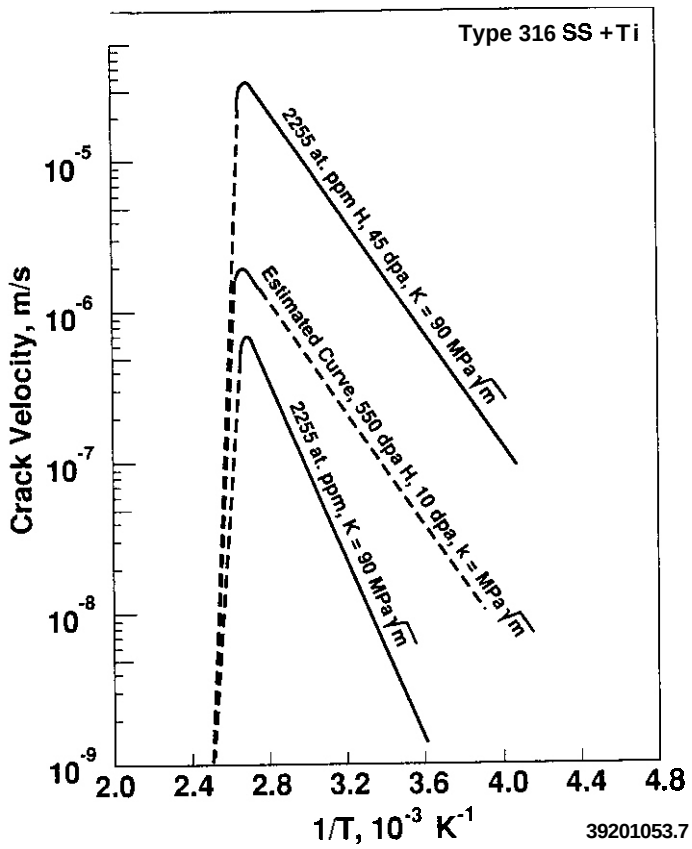

(b)

Figure 6. Estimated da/dt versus 1/T for H-induced subcritical crack growth of a Type 304 SS and Type 316 SS at ITER relevant conditions.

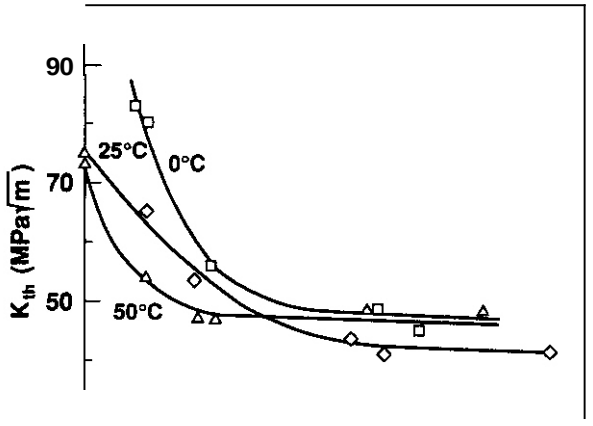

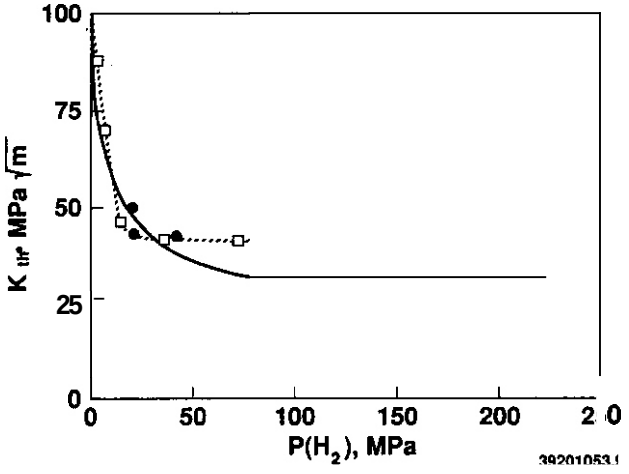

(b)

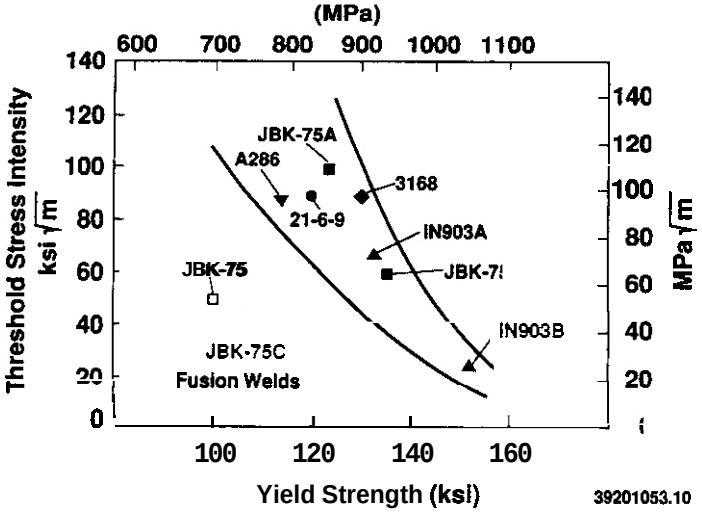

(c)

Figure 7. Stress intensity threshold for H-induced subcritical crack growth, a) effect of H concentration on Type 301 SS, b) effect of H pressure on IN 718 and IN 903 and c) effect of material yield strength.

predict a further decrease in K_{th}. For instance, for values of K_{Ic} (irr)/K_{Ic} (unirr) of 0.4, 0.2 and 0.1, the K_{th} of Type 316 SS would be approximately 33, 22 and 12 MPa$\sqrt{m}$. Clearly, the low values of K_{th} predicted by this analysis indicate a concern about the possibility that H reduces the K_{Ic} of Type 316 SS.

Implications to ITER

These results indicate that H-induced crack growth of Type 316 SS is a definite possibility under ITER conditions. However, the quantity of hydrogen needed to induce significant crack velocities will only exist after substantial radiation damage; i.e., about 10 dpa and any loss of H to the plasma or coolant would reduce the probability of crack growth. A crack velocity of 2×10^{-6} m/s is predicted after 10 dpa at 100°C which would produce a through-wall crack in a matter of hours. Because failure could occur so rapidly at 10 dpa, further evaluation is necessary since any error in this analysis could prove disastrous for ITER.

Subcritical crack growth could lead to through-wall leaks that allow coolant into the plasma chamber or tritium leakage into the coolant or reactor containment. Jones, Conn and Schafer (17) estimated that 6-8 mm long flaws would allow sufficient water leakage into the plasma to overwhelm the plasma clean-up systems resulting in serious degradation of plasma performance. Subcritical crack growth can also produce critical sized flaws and rupture of the coolant containment. This would be a very catastrophic event; however, it is more likely that a leak-before-break process will occur.

Hydrogen is very mobile at 100°C in Type 316 SS, so it is very likely that a build-up of (n,p) generated H to concentrations necessary for subcritical crack growth will not occur. With an irradiation induced diffusivity of 3×10^{-6} cm^2/s, H will diffuse 2 mm in 3000 s (about 1 hr) or in about 30 h during reactor shut-down without irradiation-enhanced diffusion. Therefore, if the surface concentration is low, as it would be on both the plasma and coolant sides, and the surfaces are uncoated, the H generated by (n,p) reactions will merely diffuse out of the material during reactor operation. However, if the surfaces are coated *to* protect them from the plasma or corrosion on the coolant side, then large H concentrations and subcritical crack growth could result. Maintaining the stress-intensity of flaws within the first wall below the threshold stress-intensity for H-induced crack growth is another method to mitigate this possible problem. However, for a 1 mm length flaw and for practical minimum flaw sizes detectable by non-destructive testing, stresses less than 500 MPa would be needed to assure stress intensities less than the predicted threshold of 28 MPa$\sqrt{m}$. Applied stresses could possibly be maintained less than 500 MPa in a low pressure ITER; however, local stresses due to thermal stresses could easily exceed this value. local stresses would not be likely to cause critical flaw growth but could induce through-wall cracking and coolant leaks.

FUTURE WORK

Verification of these predictions is clearly needed. Approximate effects can be determined by charging irradiated materials with H and measuring subcritical crack velocities. A more quantitative determination requires an in situ measurement with dynamic radiation effects and H generation or implantation. Methods for performing this type of experiment will be assessed.

REFERENCES

1. R.H. Jones, S.M. Bruemmer and C.H. Henager, Jr., J. of Nucl. Mater., Vol. 179 (1991) p. 607.

2. E.P. Simonen, R.H. Jones and S.M. Bruemmer, "Radiation Effects on Grain Boundary Chemistry and Stress Corrosion Cracking of Stainless Steel," Fusion Reactor Materials Semiannual Report for Period Ending Sept. 30, 1991, DOE/ER-0313/11.

3. N. Saito, N. Ichikawa, Y. Hemmi, A. Sudo, M. Itow and T. Okada, Corrosion, Vol. 46 (1990) p. 531.

4. R.H. Jones and C.H. Henager, Jr., "Effect of Gamma Irradiation on Stress-Corrosion Behavior of Austenitic Stainless Steel Under ITER-Relevant Conditions", Fusion Reactor Materials Semiannual Report for Period ending Sept 30, 1991, DOE/ER-0313/11.

5. P.J. Maziasz, A.F. Rowcliffe, M.L. Grossbeck, G.E.C. Bell, E.E. Bloom, O.C. lousteau, A. Hishinuma, T. Kondo, R.F. Mattas and D.L. Smith, Fusion Technology, Vol 19 (1991) p. 1571.

6. R. Pedrazzoli and M.O. Speidel, "Effect of Temperature on Stress Corrosion Crack Growth in Austenitic Steels Exposed to Water", Corrosion/90, Paper 491.

7. B.G. Polusuhin, A.P. Zyryanov, E.P. Baskakov, M.G. Golovachev, G.M. Kalinin, Yu. S. Strebkov, Yu. S. Shestakov, A.G. Dobrynskih and A.V. Sidorenkov, PM-90, Conference on Radiation Damage, Alushta, USSR, May 22-25, 1990.

8. W.W. Gerberich, T. Livne and X. Chen in: Proc. Symp. on Modeling Environmental Effects on Crack Initiation and Propagation, R.H. Jones and W.W. Gerberich, Eds., Toronto, Canada, 1985, TMS-AIME, Warrendale, PA.

9. S. Singh and C. Altstetter, Metall. Trans., Vol 13A (1982) p. 1799.

10. J-H. Huang and C.H. Altstetter, Metall. Trans., Vol 21A (1990) p. 2605

11. N.R. Moody, M.W. Perra and S.L. Robinson, Scripta Metall., Vol. 22 (1988) p. 1261

12. B. Baranowski, S. Majchrzak and T.B. Flanagan, J. Phys. F: Metal Physics, Vol 1 (1971) p. 258

13. N.R. Moody, S.L. Robinson and M.W. Perra, "Internal Hydrogen Effects on Thresholds for Crack Growth in the Iron-Based Superalloy IN 903", Sandia Report, SAND90-8466, Oct. 1991.

14. R.A. Oriani and P.H. Josephic, Acta Met. vol 22 (1974) p. 1065

15. R.H. Jones, "Grain Boundary Segregation and Environmentally Induced Fracture of Materials" in Mechanical Properties and Phase Transformations in Engineering Materials, S.D. Antolovich, R.O. Ritchie and W.W. Gerberich, eds, The Metallurgical Society of AIME, Warrendale, PA, 1986.

16. M.L. Hamilton, "Mechanical Properties and Fracture Behavior of 20% Cold-Worked 316 Stainless Steel Irradiated to Very High Neutron Exposures," in Influence of Radiation on Materials Properties: 13th International Symposium (Part 11), ASTM STP 956, Philadelphia, PA, p. 245, 1987.

17. R.H. Jones, R.W. Conn and R.F. Schafer, Nuclear Engineering and Design/Fusion, 2 (1985) p. 175

AQUEOUS STRESS CORROSION OF CANDIDATE AUSTENITIC STEELS FOR ITER STRUCTURAL APPLICATIONS - A. B. Hull, P. R. Luebbers, M. R. Fox, W. K. Soppet. and T. F. Kassner (Argonne National Laboratory)

OBJECTIVE

The corrosion resistance of the structural material to be used in an aqueous environment characteristic of candidate first-wall/blanket systems in the International Thermonuclear Experimental Reactor (ITER) has never been quantified. Information on the stress corrosion cracking (SCC) susceptibility of several candidate stainless steels under ITER-relevant conditions will help to identify an optimal combination of structural materials, coolant chemistry, and operational conditions for ongoing ITER design work. The objective of the task described in this reportis to provide baseline information on SCC susceptibility of candidate stainless steels in high-purity oxygenated water that simulates many important parameters anticipated in ITER first-wall/blanket systems. SCC tests will also be conducted under off-normal water chemistry conditions and at higher temperatures to establish the performance limits of the materials.

SUMMARY

Susceptibility of Types 316NG and sensitized 304 stainless steels (SS) to SCC was investigated at temperatures of 60-289°C in slow-strain-rate-tensile **(SSRT)**tests in oxygenated water that simulates important parameters anticipated in first-wall/blanket systems. Type 316NG SS exhibits good resistance to SCC under crevice and noncrevice conditions at temperatures <150°C in nominal ITER coolant chemistry that does not contain any short-lived radical species from radiolysis of water. Initial **SSRT** tests have been conducted on weldment specimens of Type 316NG SS with matching filler metal under crevice and noncrevice conditions in oxygenated water at 95°C. These specimens fractured in the base metal rather than in the weld or heat-affected zones.

PROGRESS AND STATUS

Research and development needs' of the ITER with respect to aqueous corrosion include establishing a reliable data base on reference materials (viz., Types 316, 316L, and 316NG SS in the solution-annealed, cold-worked, and welded conditions). The nominal ITER water chemistry will most likely be high-punty water containing stable radiolysis/electrolysis products, e.g., dissolved O_2, H_2O_2, H_2 at ppm levels, and ionic species at ppb levels, namely, soluble corrosion products and impurities in the makeup water and from release by ion-exchange resins in water-purification systems. Higher concentrations of ionic impurities (e.g., Cl^-, SO_4^{2-}, H^+. etc.) in the coolant may be present during off-**normal** operating and extended lay-up conditions of the system.

Although the nominal ITER coolant operating temperature is -60°C. periodic increases to 150°C might occur. Mechanical loads and temperature gradients across the first-wall structure will produce both static and cyclic stresses, which when coupled with residual tensile stresses associated with welds, can exceed the yield strength of the material. Tensile stresses above yield under cyclic operation (ITER $=10^4$ cycles) are conducive to crack propagation under corrosion fatigue conditions. Coolant channel geometry and material microstructure in the heat-affected zone of weldments [both diffusion and fusion welds) can lead to crevice conditions that increase susceptibility of the materials to SCC.

Radiation dose (gamma, electron. neutron) causes radiolysis of the aqueous coolant and produces short-lifetime radical species (e.g., H. OH. HO_2, e_{aq}^-, etc.), as well as stable molecular species (O_2, H_2O_2, H_2) that participate in corrosion reactions. In addition, fast-neutron fluence causes radiation hardening, radiation-induced segregation (RIS) of alloying elements at grain boundaries, and transmutation reactions (n,p, and n,α) that yield up to 2500 appm hydrogen and 250 appm helium. These phenomena can influence environmentally assisted cracking of materials by different mechanisms.

Previous work[2,3] focused on developing criteria to define the simulated ITER water chemistry and establishing experimental methods for SSRT tests on noncrevice and crevice specimens. Results from experiments to evaluate SCC susceptibility from SSRT tests on Types 316NG, 316. and 304 SS have been reported previously.[4-7] No indication of SCC was observed in tests on noncrevice specimens of Type 316NG SS in oxygenated water containing 0.1-1.0 ppm SO_4^{2-} at temperatures of 95 and 150°C and a strain rate of 3×10^{-7} s^{-1}.[7] Predominantly ductile fracture (a minor amount of transgranular cracking, TGSCC) was observed in crevice specimens of Type 316NG SS. The failure behavior of Type 304 SS crevice specimens. heat treated to yield sensitization values of 2 and 20 $C \cdot cm^{-2}$ by electrochemical potentiokinetic reactivation (EPR), demonstrated that the degree of sensitization had a dramatic effect on susceptibility to intergranular stress corrosion cracking (IGSCC).[7] Type 304 SS specimens sensitized to a higher value exhibited shorter failure times, lower maximum stresses, and lower reduction in area than did less-sensitized Type 304 SS or Type 316NG SS specimens. Scanning electron microscopy (SEM) showed minimal evidence of SCC in Type 316NG and solution-annealed Type 316 SS, but clear evidence of IGSCC in moderately sensitized (EPR = 20 $C \cdot cm^{-2}$) Type 304 SS specimens.[7] Results described in this report are from additional tests on these steels, including weldment specimens, in air and in water containing O_2, H_2O_2, and 0.1 ppm SO_4^{2-}, at several temperatures between 60 and 289°C.

Experimental Procedures

Cylindrical tensile specimens with a 6.35-mm diam. and a 36.0-mm gage length were fabricated from Types 316NG, 316L, and 304 SS. The chemical compositions of the materials used in these experiments are given in Table 1. Several tests were performed on specimens of sensitized Type 304 SS because this material exhibits higher susceptibility to SCC in oxygenated water. The experimental methods have been described in previous papers.[5,7,8] Crevice specimens were created by drilling two small-diameter (≈0.8-0.9 mm) through holes in the gage section of the specimens and placing a corresponding austenitic stainless steel pin in the top hole to form a tight crevice; the bottom hole was left open. Tests were carried to failure at strain rates of 1×10^{-5} and $2–3 \times 10^{-7}$ s^{-1} in air. and $2–3 \times 10^{-7}$ s^{-1} in water in small-diameter autoclaves with a once-through water system. The Type 316NG SS specimens were solution-annealed at 1050°C for 0.5 h and heat treated a 650°C for 24 b to simulate a worst-case weld treatment. which does not produce sensitization in low-carbon–content nuclear–grade material. The Type 316L SS base metal and weldment specimens were tested in the as–received condition without any heat treatment.

Table 1. Composition of Austenitic Stainless Steels (wt.%)

Alloy	Heat No.	Cr	Ni	Mo	Mn	Si	Cu	N	C	P	S	Fe
316NG	P91576	16.42	10.95	2.14	1.63	0.42	0.20	0.068	0.015	0.020	0.010	Bal
316NG	467958	17.14	12.74	2.43	1.51	0.64	0.16	0.069	0.020	0.029	0.008	Bal
316NG	D442604	17.29	12.85	2.52	1.66	0.46	0.08	0.100	0.014	0.018	0.002	Bal
316NG	D440104	17.91	13.25	2.48	1.75	0.49	0.01	0.098	0.015	0.011	0.002	Bal
316L	16650	16.50	10.39	2.09	1.78	0.43	0.19	0.540	0.018	0.026	0.013	Bal
316L[a]	4H3367	18.69	12.29	[b]	1.98	0.63	0.25	[b]	0.018	0.023	0.018	Bal
304	30956	18.70	8.00	0.44	1.54	0.48	0.19	0.100	0.060	0.019	0.007	Bal

[a]Type 316L SS filler metal for weld specimens.
[b]Not analyzed.

Water chemistry was established by bubbling a 20% O_2-80% N_2 gas mixture through deoxygenated/deionized feedwater (conductivity <0.2 μS/cm) contained in a 130–L stainless steel tank to produce a dissolved-O_2 concentration of –8.0 ppm. H_2O_2 (8.0 ppm) and H_2SO_4 (0.1 ppm) were added to the feedwater before sparging with the gas mixture to ensure adequate mixing. An external 0.1M KCl/AgCl/Ag reference electrode, a thermocouple, and Pt and Type 304 SS electrodes were located at the autoclave outlet to establish redox and open-circuit potential, respectively. The electrochemical potentials (ECPs) measured during the experiments were converted to the standard hydrogen electrode (SHE) scale by using thermocell and liquid junction potentials.[9]

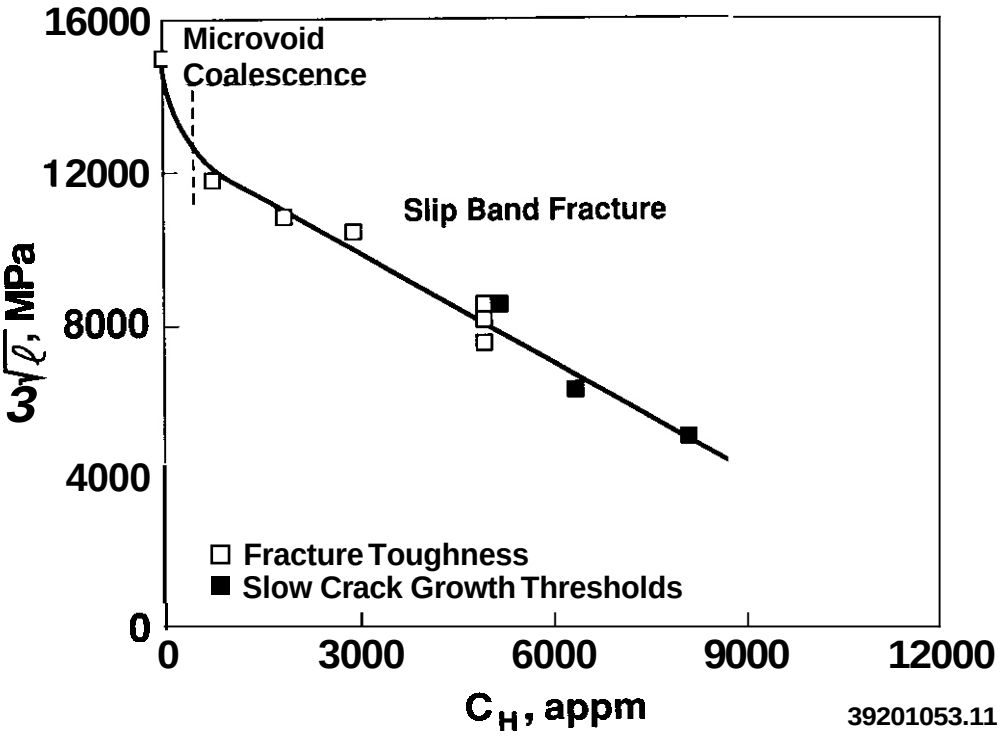

Figure 8. Fracture toughness and H-induced crack growth thresholds normalized by the square root of a characteristic microstructural distance versus near-crack-tip hydrogen concentration (13).

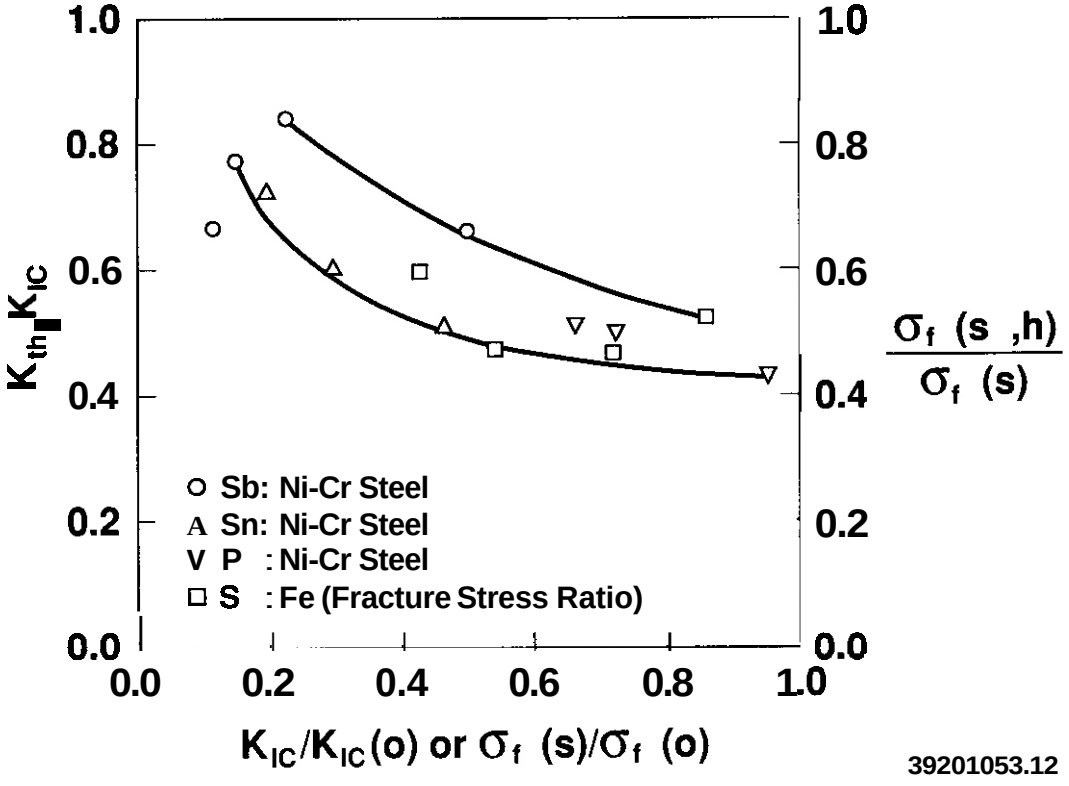

Figure 9. Subcritical crack growth threshold relative to the fracture toughness versus the normalized fracture toughness of fracture stress for a Ni-Cr steel or Fe (15). The s and h *in* σ_f(s,h) refer to the presence of grain boundary sulfur (s) and tests in hydrogen (h).

Tests provide information on time-to-failure. total strain, maximum stress, and fracture surface appearance. The load applied to each specimen was recorded continuously as a function of time, and an engineering-stress-versus-strain curve was produced for each specimen. Total elongation and reduction in area were determined by measuring the fractured specimen. The fracture surfaces were examined by both optical microscopy and **SEM** to determine the fractions of reduced cross-sectional areas with ductile. transgranular. and intergranular morphologies.[10,11]

Results and Analysis

Cracking susceptibility can be assessed from various parameters. Total elongation, reduction in area, and maximum stress are often used, as are fracture surface morphology and maximum crack length [either on the fracture surface or on the sectioned surface after test interruption). Because of the high SCC resistance of Type 316NG SS relative to that of sensitized Type 304 SS, it is difficult to quantify SCC behavior of Type 316NG SS in terms of crack growth rate[12] from SSRT results. ***An*** alternative, employed here, is evaluation of SCC susceptibility in terms of the ratio of the strain at failure ($\varepsilon_{env}/\varepsilon_{air}$) from companion tests on identical specimens in water and in air. Values of the strain ratio <1.0 indicate environmentally assisted cracking.

Results of SSRT tests at temperatures between 60 and 289°C on crevice and noncrevice specimens of Types 316NG 304 SS are presented in Tables 2–5. Some of the data have been reported **previously;**[5,7] recent work focused on effects of crevices on SCC of additional heats of Type 316NG SS, a larger temperature range **(60–289°C),** and baseline tests in air. Although some of the air tests were performed at a higher strain rate (e.g., **1×10^{-5} s^{-1}),** the yield and ultimate strengths. total elongation, reduction in area, and fracture morphology can be compared in the two environments to assess SCC susceptibility.

Table **2.** Influence of Temperature on SCC Susceptibility of Type 316NG SS Crevice Specimens Strained to Failure

								SSRT Parameters							
			Strain	Feedwater Chemistry[a]				Fail.	Yield	Max.	Total	Reduct.		Potentials (mV[SHE])	
Test	Heat	Temp.	Rate	H_2O_2	O_2	Cond.	pH at	Time	Stress	Stress	Elong.	In Area	Fracture		
No.	No.	(°C)	(s^{-1})	(ppm)	(ppm)	($\mu S \cdot cm^{-1}$)	25°C	(h)	(MPa)	(MPa)	(%)	(%)	Morphology[b]	304 SS	Pt
55	E91576	60	3×10^{-7}	air test				285	165	534	31	66	--	--	--
49	E91576	60	3×10^{-7}	0	7.4	0.91	5.67	287	156	518	31	64	--	433	483
68	P91576	95	1×10^{-5}	air test				8.2	194	514	29	--	--	--	--
42	P91576	95	3×10^{-7}	7.0	7.1	0.81	5.76	281	140	469	30	54	1.0 D	413	473
7	467958	95	1×10^{-5}	air test				5.8	272	478	21	59	0.9 D, 0.1 T	--	--
3	467958	95	3×10^{-7}	0	7.2	0.97	5.68	267	195	457	21	60	0.9 D, 0.1 T	346	449
56	D442604	95	2×10^{-7}	air test				417	161	516	31	69	--	--	--
57	D442604	95	2×10^{-7}	7.3	5.0	0.97	5.75	419	160	516	?a	68	--	380	365
53	D440104	95	3×10^{-7}	air test				275	169	519	30	69	--	--	--
59	D440104	95	3×10^{-7}	7.3	5.3	0.89	5.69	295	157	517	32	66	--	453	427
46	E91576	105	2×10^{-7}	air teat				401	150	424	29	57	0.9 D, 0.1 T	--	--
29	E91576	105	2×10^{-7}	6.1	7.9	0.90	5.72	400	151	424	29	60	1.0 D	489	392
69	467958	105	1×10^{-5}	air test				7.5	237	545	27	--	--		
30	467958	105	2×10^{-7}	5.3	7.6	0.94	5.73	358	191	463	28	61	1.0 D	499	414
19	P91576	150	1×10^{-5}	as test				7.2	156	400	26	62	0.9 D, 0.1 T	--	--
13	E91576	150	3×10^{-7}	5.7	7.0	0.92	5.80	252	137	400	27	61	0.9 D, 0.1 T	431	410
20	467958	150	1×10^{-5}	air test				7.0	204	435	25	63	0.9D, 0.1 T	--	--
14	467958	150	1×10^{-7}	7.0	6.9	0.92	5.71	661	177	441	24	59	0.9 D, 0.1T	418	380
53	P91576	289	2×10^{-7}	air test				403	119	462	29	64	--	--	--
c	P91576	289	2×10^{-7}	0	0.25	0.90	5.70	203	--	314	15	43	--	21	--

[a] Conductivity and pH were adjusted by addition of 0.1 ppm H_2SO_4.

[b] Ductile (D) and transgranular (T) in terms offractlon of cross-sectional area. Characterization of fracture surface morphologies is in accordance with illustrations and definitions in Refs. 10 and 11.

[c] Data from Ref. *8.*

Table 3. Influence of Temperature on SCC Susceptibility of Type 316NG SS Noncrevice Specimens Strained to Failure

Test No.	Heat NO.	Temp. (°C)	Strain Rate (s^{-1})	Feedwater Chemistry[a] H_2O_2 (ppm)	O_2 Ippml	Cond. (μS·cm^{-1})	pH at 25°C	SSRT Parameters: Fail. Time (h)	Yield Stress (MPa)	Max Stress (MPa)	Total Elong. (%)	Reduct. in Area (%)	Fracture Morph.[b]	Potential (mV[SHE]) 304 SS	Pt
54	P91576	60	3 x 10^{-7}	air test				681	163	488	74	79	--	--	--
52	P91576	60	3 x 10^{-7}	0	6.8	0.78	5.74	607	154	482	66	81		337	335
35	P91576	95	3 x 10^{-7}	air test				592	174	457	64	80	1.0D	--	--
9	P91576	95	3 x 10^{-7}	0	6.1	0.89	5.73	523	161	458	56	80	1.0D	372	441
10	P91576	95	3 x 10^{-7}	0	7.5	0.87	5.69	543	170	450	58	80	1.0 D	344	399
4	467958	95	1 x 10^{-4}	air test				1.5	312	535	52	82	1.0D	--	--
8	467958	95	3 x 10^{-7}	0	6.7	0.87	5.74	384	263	511	41	79	1.0 D	351	430
17	P91576	150	1 x 10^{-5}	air test				12.9	166	444	46	80	1.0D	--	--
11	P91576	150	3 x 10^{-7}	0	8.5	0.89	5.71	445	122	445	48	79	1.0D	324	360
15	P91576	150	3 x 10^{-7}	5.4	7.5	0.93	5.71	421	144	470	45	76	1.0D	433	411
18	467958	150	1 x 10^{-5}	air test				13.4	186	491	47	83	1.0D	--	--
12	467958	150	3 x 10^{-7}	0	8.6	0.89	5.72	437	164	488	47	81	1.0D	274	322
51	P91576	289	2 x 10^{-7}	air test				725	118	455	52	71	--	--	--
c	P51976	289	2 x 10^{-7}	0	0.25	0.91	5.70	474	--	461	34	44	--	2	--

[a]Conductivity and pH were adjusted by addition of 0.1 ppm H_2SO_4.

[b]Ductile (D) in terms of fraction of cross-sectional area. Characterization of fracture surface morphologies is in accordance with Refs. 10 and 11.

[c]Data from Ref. 8.

Table 4. Influence of Temperature on SCC Susceptibility of Sensitized Type 304 SS Crevice Specimensa Strained to Failure

Test No.	EPR (C·cm^{-2})	Temp. (°C)	strain Fate (s^{-1})	Feedwater Chemistry[b] H_2O_2 (ppm)	O_2 (ppm)	Cond. (μS·cm^{-1})	pH at 25°C	SSRT Parameters: Fail. Time (h)	Yield Stress (MPa)	Max. Stress (MPa)	Total Elong. (%)	Reduct. In Area (%)	Fracture Morph.[c]	Potential (mV[SHE]) 304 SS	Pt
70	20	52	1 x 10^{-5}	air test				8.6	262	592	31	--	--	--	--
27	20	52	3 x 10^{-7}	7.0	7.3	1.03	5.71	259	213	495	28	42	1.0 I	580	445
71	20	95	1 x 10^{-5}	air test				8.3	238	573	30	--	--	--	--
2[b]	3	95	3 x 10^{-7}	0	7.4	9.5	4.75	280	151	424	29	58	0.9D, 0.1T	394	549
23	20	95	3 x 10^{-7}	5.9	7.8	0.83	5.78	247	185	469	27	49	1.01	415	331
44	20	105	3 x 10^{-7}	air test				297	192	464	32	41	0.6D, 0.4I	--	--
31	20	105	2 x 10^{-7}	7.2	7.6	0.92	5.73	334	210	463	24	41	1.0 I	493	406
73	2	150	1 x 10^{-5}	air test				7.7	224	524	28	--	--	--	--
21	2	150	3 x 10^{-7}	6.0	7.3	0.95	5.63	249	159	426	27	61	0.9D, 0.1I	437	418
24	2	150	3 x 10^{-7}	6.0	7.6	0.94	5.79	173	170	368	19	42	0.9D, 0.1T	424	418
47	2	150	3 x 10^{-7}	8.0	8.0	0.91	5.86	268	161	455	29	67	--	186	209
72	20	150	1 x 10^{-5}	air test				7.8	222	537	28	--	--	--	--
22	20	150	3 x 10^{-7}	1.0	6.7	0.99	5.73	124	157	323	13	37	1.0I	426	417

[a]Specimens of Type 304 SS (Heat No. 309561 were solution-annealed at 1050°C for 0.5 h and heat treated at 700°C for 0.25 h plus 500°C for 24 h (EPR = 2 C·cm^{-2}) or 700°C for 12 h (20 C·cm^{-2}).

[b]Conductivity and pH were adjusted by addition of 0.1 ppm H_2SO_4, except for Test No. 2 with 1.0ppm H_2SO_4.

[c]Ductile (D), intergranular (I), and transgranular (T) In terms of fraction of crosssectional area. Characterization of fracture surface morphologies is in accordance with Refs. 10 and 11.

Table 5. Influence of Temperature on *SCC* Susceptibility of Sensitized Type **304** SS Noncrevice Specimens[a] Strained to Failure

Test No.	EPR (C·cm^{-2})	Temp. (°C)	Strain Rate	Feedwater Chemistry[b] H_2O_2 (ppm)	O_2 (ppm)	Cond. (μS·cm^{-1})	pH at 25°C	SSRT Parameters: Fail. Time (h)	Yield Stress (MPa)	Max Stress (MPa)	Total Elong. (%)	Reduct. In Area (%)	Fracture Morph.[c]	Potential (mV|SHE|) 304 SS	Pt
62	20	52	1 x 10^{-5}	air test				22.2	233	580	80	79	--	--	--
34	20	52	3 x 10^{-7}	6.3	6.7	0.89	5.76	799	212	569	86	78	0.7D, 0.31	557	431
63	20	95	1 x 10^{-5}	air test				19.5	194	521	70	80	--	--	--
25	20	95	3 x 10^{-7}	6.8	7.7	0.98	5.95	655	196	533	71	79	0.9D, 0.11	484	375
107[d]	2	140	1 x 10^{-6}	0	0.22	0.87	5.75	163	–	504	59	81	1.0D	221	378
64	20	150	1 x 10^{-5}	air test				15.1	190	494	55	79	--	--	--
26[b]	20	150	3 x 10^{-7}	7.1	7.6	8.4	4.82	518	163	511	56	74	0.9D, 0.11	520	475
48	2	150	3 x 10^{-7}	8.0	8.1	0.95	5.75	521	197	511	56	81	--	--	--
106[d]	a	165	1 x 10^{-6}	0	0.19	0.86	5.71	81	–	434	29	46	0.4D, 0.61	219	384
105[d]	2	190	1 x 10^{-6}	0	0.23	0.86	5.68	53	–	340	19	24	0.3D, 0.7I	199	327
65	2	225	1 x 10^{-5}	air test				14.2	160	496	51	82	--	--	--
103[d]	2	225	1 x 10^{-6}	0	0.22	0.88	5.76	50	–	317	18	26	0.3 D, 0.7I	170	285
102[d]	2	240	1 x 10^{-6}	0	0.22	0.87	5.73	56	–	339	20	19	0.4D, 0.61	148	265
66	2	255	1 x 10^{-5}	air test				14.6	159	511	52	78	--	--	--
104[d]	2	255	1 x 10^{-6}	0	0.20	0.90	5.78	61	–	358	22	30	0.3 D, 0.71	127	246
101[d]	2	270	1 x 10^{-6}	0	0.22	0.87	5.75	61	–	324	22	21	0.2D, 0.81	72	182
67	2	289	1 x 10^{-5}	air test				14.7	152	512	53	77	--	--	--
115[d]	2	289	1 x 10^{-6}	0	0.22	0.90	5.76	62	--	372	22	21	0.2D, 0.8I	29	--
17[d]	2	289	1 x 10^{-6}	0	0.18	0.90	5.80	49	--	315	18	10	0.1D, 0.91	19	--

[a]Specimens of Type 304 SS (Heat No. 30956) were solution-annealed at 1050°C for 0.5 h and heat treated at 700°C for 0.25 h plus 500°C for 24 h (EPR = 2 C·cm^{-2}) or 700°C lor 12 h (20 C cm^{-2}).

[b]Conductivity and pH were adjusted by addition of 0.1 ppm H_2SO_4, except for Test No. 26 with 1.0 ppm H_2SO_4.

[c]Ductile (D) and intergranular (I) in terms of fraction of cross-sectional area. Characterization of fracture surface morphologies is in accordance with Refs. 10 and 11.

[d]Data from Ref. 12.

The influence of crevice geometry on SCC susceptibility can also be determined from the above-mentioned parameters. Because the tests were performed at several strain rates, time-to-failure is not a useful parameter unless the comparison is based on identical specimens (crevice or noncrevice) at the same strain rate. Compared with noncrevice specimens, crevice specimens exhibit lower total elongation values both in water and air. The lower values are caused by the diametral holes in the in the gage length. In contrast to elongation behavior, the small holes act as a notch and fortuitously produce a degree of strengthening that offsets the reduced load-carrying capacity of the smaller cross-sectional area caused by the hole.[13] The lower total elongation of crevice compared with noncrevice specimens, and the similarity in the engineering-stress (based on a cross-sectional area without subtracting the area associated with the hole) versus engineering-strain curves up to the point of plastic instability (near the maximum stress) are shown in Fig. 1. For Type 316NG SS, there is relatively little variation in SSRT parameters from air to oxygenated water containing 100 ppb SO_4^{2-} at temperatures ≤150°C, even under crevice conditions. This is illustrated further by the stress-versus-strain curves in Fig. 2 for other heats of this steel at 95°C. In several instances, total elongation of the specimens in water was greater than in air (e.g., Fig. 2a).

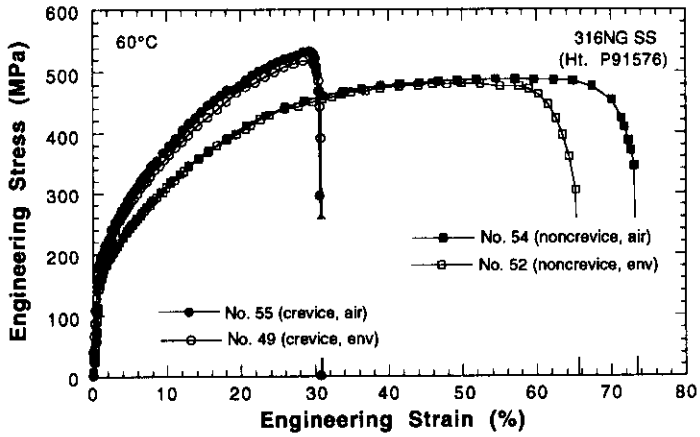

Figure 1. Engineering stress–strain curves for crevice and noncrevice specimens of Type 316NG SS (Heat No. P91576) in air and oxygenated water at 60°C

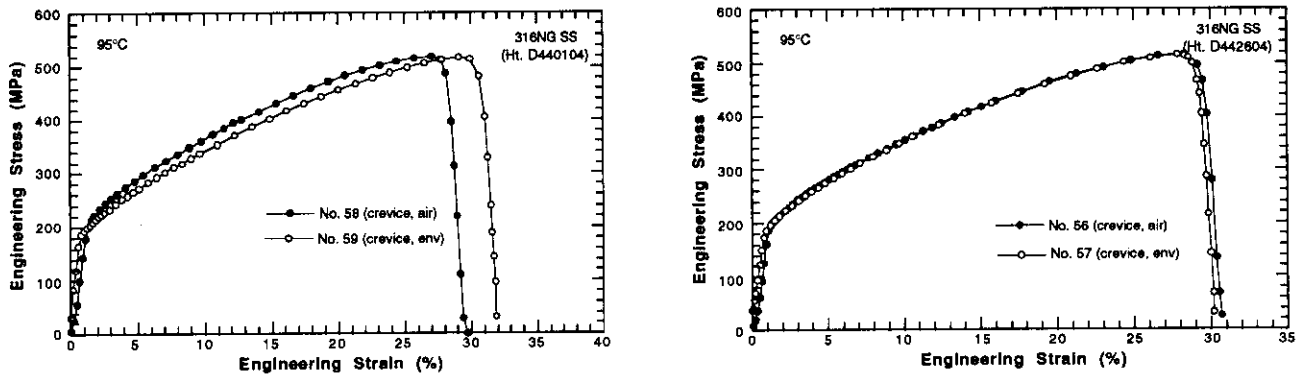

(a) (b)

Figure 2. Engineering stress–strain curves for crevice specimens of Type 316NG SS (Heat Nos. D440104 and D442604) in air and oxygenated water at 95°C.

To quantify SCC susceptibility of relatively resistant materials, parameters such as a stress or strain ratio have been explored[7,14,15] and met with limited success. In this approach, SSRT tests were conducted on identical specimens in air and water at low strain rates, but the tests were interrupted at plastic strains of 5–20%. A stress-ratio (SR) indicator of cracking susceptibility was defined as the ratio of the increase in stress after local yielding in the environment to the corresponding stress difference in an identical test in air, both computed at the same plastic strain. For crevice specimens, it can be defined as

$$SR_c = \frac{\sigma_{ec} - \sigma'_{as}/3}{\sigma_{ac} - \sigma'_{as}/3}, \quad (1)$$

where SR_c is the stress ratio for crevice specimens, σ_{ec} is the nominal stress of the crevice specimen in the aqueous environment at a specified plastic strain, σ_{ac} is the nominal stress of the crevice specimen in air, and σ'_{as} is the yield stress of the noncrevice specimen in air. Local plastic yielding is assumed to occur when the nominal stress equals $\sigma'_{as}/3$, because the stress concentration factor of the crevice specimen is ≈3. The SR for noncrevice specimens can be defined as

$$SR_{nc} = \sigma_{es} / \sigma_{as}, \quad (2)$$

where σ_{es} and σ_{as} are the nominal stresses of the noncrevice specimen in water and in air, respectively, at a specified plastic strain. A SR value of -1.0 is indicates no or low susceptibility to SCC.

Because small differences in the load–versus-elongation behavior of specimens in air and in water at small plastic strains were not reliable enough to quantify SCC susceptibility of the most resistant materials, SSRT tests were conducted to failure in this investigation. Total elongation at failure appears to be the most promising measure of SCC susceptibility. Consequently, the data in Tables 2–5 were analyzed on the basis of a strain–ratio parameter, namely, $S_r = \varepsilon_{env}/\varepsilon_{air}$ at failure for identical specimen geometries [crevice or noncrevice). Strain ratio values for different heats of Type 316NG SS and our reference heat of Type 304 SS for two levels of sensitization are shown in Tables 6 and 7 and the values are plotted as a function of temperature in Figs. 3 and 4, respectively. The results show that Type 316NG and lightly sensitized (EPR = 2 $C \cdot cm^{-2}$) Type 304 SS specimens are resistant to SCC in oxygenated water containing ~0.1 ppm SO_4^{2-} at temperatures <150°C, i.e., the S_r values are ≈1.0. At higher temperatures, the S_r values decrease significantly, indicating SCC. Moderately sensitized (EPR = 20 $C \cdot cm^{-2}$) Type 304 SS crevice specimens exhibit significant SCC susceptibility at a somewhat lower temperature compared to noncrevice specimens (Fig. 4). Noncrevice specimens of Type 316NG SS appear to exhibit greater SCC susceptibility than do crevice specimens at temperatures <150°C (Fig. 3), which is difficult to explain when compared with behavior at high temperatures. In almost all tests on crevice specimens, fracture occurred in the hole that contained the pin. which we attribute to the more aggressive water chemistry

Table 6. Influence of Temperature on SCC Susceptibility of Type 316NG SS Specimens in Oxygenated Water,[a] based on Strain Ratio ($\varepsilon_{env}/\varepsilon_{air}$) at Failure

Crevice SSRTs				Noncrevice SSRTs			
Test Nos.	Heat No.	Temp. (°C)	Strain Ratio	Test Nos.	Heat No.	Temp. (°C)	Strain Ratio
49/55	P91576	60	1.00	52/54	P91576	60	0.89
42/68	P91576	95	1.03	9/35	P91576	95	0.87
3/7	467958	95	1.00	10/35	P91576	95	0.91
57/56	D442604	95	0.97	8/4	467958	95	0.79
59/58	D440104	95	1.06	11/17	P91576	150	1.04
29/46	P91576	105	1.00	15/17	P91576	150	0.98
30/69	467958	105	0.96	12/18	467958	150	1.00
13/19	P91576	150	1.03	C/51	P91576	289	0.65
14/20	467958	150	0.96				
C/50	P91576	289	0.52				

[a] Conductivity and pH were adjusted by addition of 0.1 ppm H_2SO_4.

Results of initial SSRT tests at 95°C on the base metal and crevice and noncrevice weldment specimens of Type 316L SS with matching filler metal are shown in Table 8. The crevice specimen contained three small-diameter holes (with pins) in the base metal, in the weld heat–affected zone, and in the weld metal (Fig. 5). Both weld specimens fractured in the base metal, which is consistent with the behavior of noncrevice weldment specimens of Type 316NG SS in 289°C water where failure occurred in the base metal ~7–9 mm away from the weld heat–affected zone.[8] Comparison tests are being conducted in air at 95°C to assess the SCC resistance of the weld specimens.

Table 7. Influence of Temperature on SCC Susceptibility of Sensitized Type 304 SS Specimens[a] in Oxygenated Water,[b] based on Strain Ratio ($\varepsilon_{env}/\varepsilon_{air}$) at Failure

Crevice SSRTs				Noncrevice SSRTs			
Test Nos.	EPR ($C \cdot cm^{-2}$)	Temp. (°C)	Strain Ratio	Test Nos.	EPR ($C \cdot cm^{-2}$)	Temp. (°C)	Strain Ratio
27/70	20	52	0.91	34/62	20	52	1.07
2/71	3	95	0.97	25/63	20	95	1.01
23/71	20	95	0.90	107/64	2	140	1.07
31/44	20	105	0.75	26/64	20	150	1.02
21/73	2	150	0.96	48/64	2	150	1.02
24/73	2	150	0.68	106/64	2	165	0.53
47/73	2	150	1.03	105/64	2	190	0.35
22/72	20	150	0.46	103/65	2	225	0.35
				102/65	2	240	0.39
				104/66	2	255	0.42
				101/66	2	270	0.42
				115/67	2	289	0.41
				17/67	2	289	0.34

[a]Heat No. 30956.

[b]Conductivity and pH were adjusted by addition of 0.1 ppm H_2SO_4

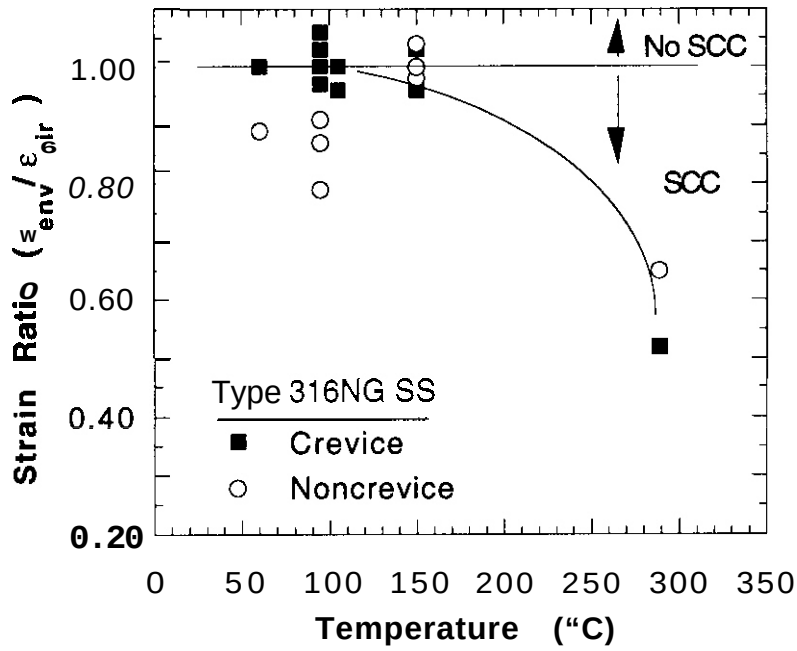

Figure 3. Strain ratio *at* failure for crevice and *non*-crevice *SSRT* specimens of Type *316NG SS* versus temperature.

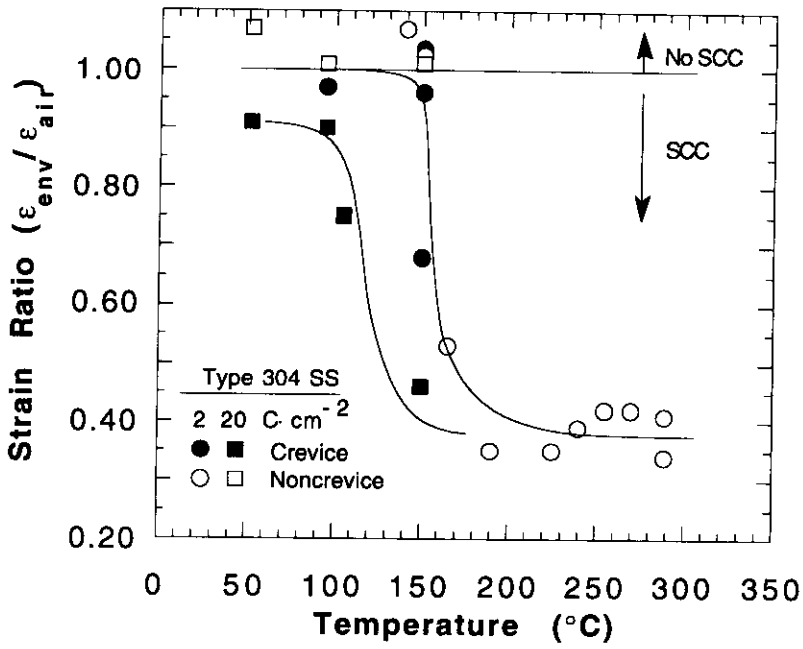

Figure 4. Strain ratio at failure for crevice and non-crevice SSRT specimens of sensitized Type 304 SS versus temperature.

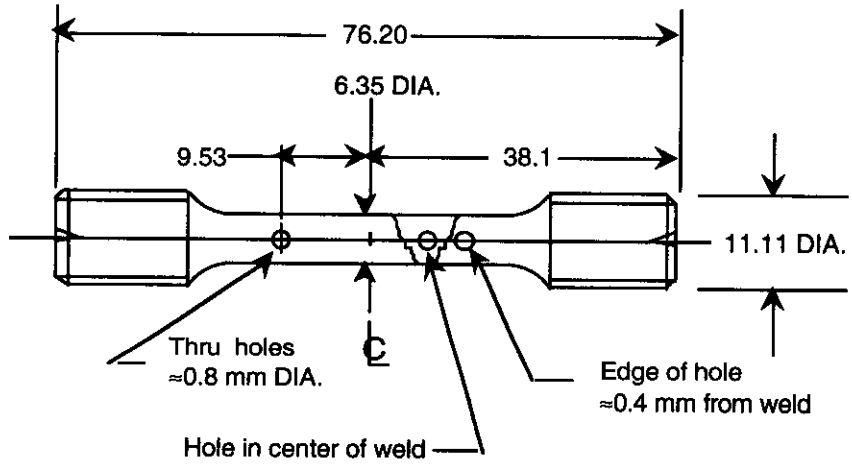

Figure 5. Weld specimen fabricated from gas-metal-arc welded plate of Type 316L SS with matching filler metal. Crevices formed by inserting tight-fitting SS pins into the holes.

Table 8. SCC Susceptibility of Type 316L SS Base Metal and Weld [Crevice and Noncrevice) Specimens Strained to Failure

Test No.	Heat No.	Temp. (°C)	Strain Rate (s^{-1})	Feedwater Chemistry[a] H_2O_2 (ppm)	O_2 (ppm)	Cond. ($\mu S \cdot cm^{-1}$)	pH at 25°C	SSRT Parameters Fail. Time (h)	Yield Stress (MPa)	Max. Stress (MPa)	Total Elong. (%)	Reduct. in Area (%)	Fracture Morphology[b]	Potentials (mV[SHE]) 304 SS	Pt
61	16650	95	3×10^{-7}	0	5.9	0.96	5.79	573	165	468	62	81	--	237	237
60	Weld[c]	95	3×10^{-7}	0	6.3	1.1	5.69	350	256	489	38	79	--	401	508
53	Weld[c,d]	95	3×10^{-7}	0	6.6	0.77	5.73	165	229	506	18	60	--	253	255

[a]Conductivity and pH were adjusted by addition of 0.1 ppm H_2SO_4.

[b]Not available at present.

[c]SSRT specimens were made from a gas-metal-arc weldment of Type 316L SS plate [Heat No. 166501 and filler metal [Heat No. 4H3367).

[d]Crevice specimen contained three small-diameter holes in the base metal. heat-affected zone. and In the weld metal with Type 316 SS plns Inserted Into them to produce tight crevices. Specimen failed In the base metal.

CONCLUSION

Type 316NG SS exhibits good resistance to SCC under crevice and noncrevice conditions in oxygenated water containing 50.1 ppm SO_4^{2-} at temperatures <150°C. This environment is representative of a nominal coolant chemistry for the ITER first wall/ blanket system, except for short-lived radical species from radiolysis of water.

FUTURE WORK

Additional SSRT tests will be conducted on crevice and noncrevice weldment specimens of Type 316NG SS in more aggressive water chemistries containing dissolved O_2, H_2O_2, and Cl^- to establish the margin of performance of the material under off-normal or poor lay-up water chemistry conditions at temperatures 5150°C. Several baseline tests will be performed in air to evaluate the SCC susceptibility from the strain-ratio parameter. Compact-tension specimens will be fabricated from several heats of Type 316NG SS for crack-growth-rate tests in simulated ITER water chemistries under cyclic loading conditions.

REFERENCES

1. D. L. Smith, Aqueous Corrosion Task for *ITER R&D*, U.S. Coordination Meeting, Argonne National Laboratory, August 6, 1990.

2. H. G. Khalak, Computer Simulation of Water Coolant Chemistry in a Fusion Reactor, Proc. 3rd National Conference on Undergraduate Research, April 27-29. 1989. University of North Carolina, Asheville. p. 287.

3. H. Khalak. A. B. Hull. and T. F. Kassner. Aqueous Stress Corrosion *of Austenitic* **Steels,** Sixth Fusion Reactor Materials Semiannual Progress Report for Period Ending March 31. 1989. DOE/ER-0313/6, *Oak* Ridge National Laboratory, p. 379.

4. A. Patel, A. B. Hull, and T. F. Kassner. Aqueous Stress Corrosion of Structural Materials, Seventh Fusion Reactor Materials Semiannual Progress Report for Period Ending September 30, 1989. DOE/ER-0313/7, *Oak* Ridge National Laboratory, p. 250.

5. A. B. Hull, M. R. Fox, J. W. Pascoe. and T. F. Kassner. Enuironmental Effects on Aqueous Stress Corrosion of Candidate Austenitic Steels for ITER Structural Applications. Ninth Fusion Reactor Materials Semiannual Progress Report for Period Ending September 30, 1990, DOE/ER-0313/9, Oak Ridge National Laboratory, p. 228.

6. A. B. Hull and T. F. Kassner. Aqueous Stress Corrosion of Candidate Austenitic Steels for ITER Structural Applications, Tenth Fusion Reactor Materials Semiannual Progress Report for Period Ending March 31, 1991, DOE/ER-0313/10, Oak Ridge National Laboratory, p. 241.

7. M. R. Fox. A. B. Hull. and T. F. Kassner, Stress Corrosion Cracking of Candidate Structural Materials under Simulated First-Wall/ Aqueous Coolant Environments. Fusion Technol.. **19,** 1619–1628 (1991).

6. P. S. Maiya, Plastic Strain, Enuironmental, and Creuice Effects on SCC Initiation and Propagation in Types 316NG and **304** Stainless Steel, Corrosion **45.** 915–924 (1969).

9. D. D. Macdonald, A. C. Scott, and P. Wentrcek. External Reference Electrodes for Use in High Temperature Aqueous Systems, J. Electrochem. Soc., **126.** 908–911 (1979).

10. H. D. Solomon, Transgranular. Granulated, and Intergranular Stress Corrosion Cracking In AISI 304 SS, Corrosion **40.** 493–506 (1984).

11. V. Kerlins, Modes of Fracture, Metals Handbook, 9th Ed.. **ASM,** Metals Park, OH (1987).

12. W. E. Ruther, W. K. Soppet. and T. F. Kassner. Effect of Temperature and Ionic Impurities at Very Low Concentrations on Stress Corrosion Cracking of AISI 304 Stainless Steel. Corrosion **44.** 791–799 (1988).

13. R. Hill, The Mathematical Theory of Plasticity, Oxford Press. UK, pp. 245–252 (1950).

14. P. S. Maiya, W. J. Shack, and T. F. Kassner. Stress Corrosion Cracking of Candidate Materials for Nuclear Waste Containers. Corrosion **46.** 954–963 (1990).

15. W. E. Ruther. T. F. Kassner. W. J. Shack, and W. K. Soppet, Environmentally Assisted Cracking of Austenitic Statnless Steels in Simulated NPR Water, Argonne National Laboratory, ANL/NPR-91/7 (February 1992).

CHARACTERIZATION OF RADIATION-INDUCED SEGREGATION IN AUSTENITIC STAINLESS STEELS USING ANALYTICAL ELECTRON MICROSCOPY AND SCANNING AUGER MICROPROBE TECHNIQUES — *G.* E. C. Bell. E. A. Kenik. and L. Heatherly. Jr. (Oak Ridge National Laboratory).

OBJECTIVE

To compare and contrast radiation-induced solute segregation measured in commercial and high purity heats of type *304* stainless steel (SS) using an analytical electron microscope (AEM) and scanning Auger microprobe (SAM).

SUMMARY

In this work. we characterized radiation induced grain-boundary segregation of commercial-purity (CP) and high-purity (HP) type *304* SS irradiated in a fission power reactor at 288°C to 2 x 10^{21} n/cm^2 (E > 1 MeV) or about 1 dpa using both high-resolution AEM and Auger electron spectroscopy (AES). Both AEM and AES showed strong nickel and silicon enrichment along with moderate chromium depletion at grain boundaries in the CP material. Chromium and nickel segregation, measured both by AEM and AES. were less in the HP material. No statistically significant minor element segregation was measurable with either AEM or AES. Good agreement between AEM segregation profiles measured perpendicular to grain boundaries and AES sputter-depth profile results as obtained.

PROGRESS AND STATUS

Introduction and Background

Irradiation-assisted stress corrosion cracking (IASCC) is considered one of the major environmental degradation mechanisms of austentitic SS in water-cooled nuclear power systems.[1-3] IASCC is a subset of intergranular stress corrosion cracking (IGSCC). IASCC has been observed in type *304* SS and other austentitic SS alloys, which have been exposed to a fast (E > 1 MeV) neutron fluence greater than about 5 x 10^{20} n/cm^2 in commercial boiling-water reactors (BWRs) and in test reactor experiments at BWR conditions (288°C). [ref. 11 IASCC has been manifested in the form of IGSCC.' It has been suggested that changes in grain-boundary composition caused by radiation induced segregation (RIS) play an important role in increasing the IASCC susceptibility of SS.[3-15] However. the precise mechanism of IASCC is yet unclear. Characterization of RIS profile is difficult because RIS profiles produced below 300°C in austenitic stainless steels are typically less than 5 nm in width on either side of a grain boundary.

IASCC may also be a degradation mechanism for water-cooled austentitic steels in fusion reactors.[16, 17] For fusion reactors, the RIS and IASCC characteristics of the materials will be different from those in light water reactors (LWRs) because of the harder neutron spectrum and higher neutron flux (viz., higher damage rate and lower helium production).[18] In this study, we examine the use of AEM and AES. two complimentary techniques, for characterizing RIS in austenitic SS materials.

AEM versus AES

AEM and AES are methods by which the microchemistry of a material near grain boundaries can he characterized. Both techniques have advantages and disadvantages. Examination of a sample by AEM gives accurate, absolute compositional profiles. by using energy dispersive X-ray (EDX) analysis or electron energy **loss** spectroscopy (EELS). of a few grain boundaries (two or three) on a very small length scale (~ 2 nm). AES is a surface analysis technique sampling only the first few layers of atoms. If a material can be fractured intergranularly without contamination of the fracture surfaces (e.g. via hydrogen charging and fracturing in vacuum), then the composition of a relatively large number of grain boundaries (10 to 20) can be characterized by AES. Compositional profiles as a function of distance from the grain boundary can be obtained in AES by controlled-ion sputtering of the fracture surface of the material and reanalyzing.

In contrast to AEM. it is difficult for AES to provide accurate. absolute compositional information without the use of standards of similar composition examined under similar experimental conditions. In order to make compositional determinations of alloys or mixtures of elements, correction for the mixture- (matrix) dependent parameters. such as the inelastic mean-free path, must be made. These corrections are not usually available, and comparison of Auger spectra with a standard alloy of similar, known composition is the only reliable method by which determinations of absolute composition can be made. For these reasons, AES data collected in the absence of a known composition standard are best represented in relative terms with the variation in ratios of one element or group of elements to another element or group of elements. For the materials examined here. ductile areas of the specimen are used as internal standards for the specimen and are assumed indicative of bulk composition. By comparing data from grain boundaries with that from ductile areas, variations in composition can be inferred.

Experimental

The two alloys investigated here were irradiated in different commercial BWRs at the same temperature. 288°C, nominally to the same fast neutron fluence of 2.0×10^{21} n/cm^2 ($E > 1$ MeV). or about 1 dpa. The HP material had a composition of Fe-18.58-9.44Ni-1.22Mn-0.017C-0.002P-0.003S-0.02Si-0.037N-0.0002B where the values shown are results of actual heat analysis in weight percent (wt %) and had been used as an absorbed tube in a control rod of a commercial BWR. The CP material had been used as sheath material on a control rod for a commercial BWR. Unfortunately. there was no heat analysis for the CP material. The CP material has a nominal composition of Fe-18Cr-8Ni-2Mn-0.08C_{max}-0.045P_{max}-0.03S_{max}-1Si_{max}, where the values shown are in wt %. Other CP type-304 alloys used for similar applications (i.e., control rod sheath material for BWR) have higher levels of silicon (0.5 wt %), phosphorus (0.03 wt %), sulfur (0.01wt %), and carbon (0.05 wt %), where the values in parentheses are typical values taken from one author's previous work,[19] as compared to the HP material. The materials and specimens were provided and fabricated by Or. A. J. Jacobs of General Electric Nuclear Energy as part of the International Cooperative Group on IASCC (ICG-IASCC) irradiated round-robin (IRR) analysis program. Standard 3-mm-diam x 0.25-mm-thick specimens were used for AEM and miniature "dog-bone"-shaped tensile specimens[19] were used for AES examination.

AES Analysis

Specimens were prepared by first electropolishing in a room-temperature, *60140%* concentrated phosphoric/sulfuric acid solution for 30 *s* at 7 V-DC. The specimen was then cathodically charged with hydrogen (~ *500* mA/cm^2) in a helium-deaerated 0.1 N sulfuric acid with 100 mg/ml sodium arsenite (added as a hydrogen recombination poison) solution at 70°C for a minimum of *24* h. During the charging, the specimen was periodically (about every *8* h) removed from the hydrogen-charging solution and eletropolished in the *60140%* phosphoric/sulfuric acid solution for 10 *s* at 7 V-DC to remove surface oxides. The use of deareated charging solutions and periodic electropolishing promotes hydrogen entry into the metal and IG fracture. After charging. the specimen was loaded into the tensile grips and transferred to the fracture and introduction system (FAIS) of the PHI 590 SAM (Fig. 1). In order to expose the grain boundaries for examination and minimize surface contamination, fracture of the specimen was induced at room temperature using a "slow strain rate" (SSR) [$<10^{-4}$ s^{-1}] tensile drive system with a vacuum of less than 10^{-7} torr. After fracture. one-half of the specimen was transferred to the ultra-high-vacuum ($< 10^{-10}$ torr) portion of the instrument for subsequent examination in both scanning electron and Auger electron modes. The perimeter of the specimens. both CP and HP. exhibited IG fracture while the central region had the appearance of ductile failure (Fig. 2). Regions with facetted. "smooth" planar surfaces were visually-identified as grain boundaries (GBs) while areas with evidence of microvoid coalescence during fracture were labeled as ductile. Spectra were collected from 0 to 1000 eV. The primary electron energy used during analysis of the surfaces was 5 keV with sample currents on the order of 10^{-6} A. Spectra were collected for 20 min on selected areas of ~ 200 mm^2 (magnification of 5000x). After analysis of the "as-fractured" (AF) surfaces, compositional depth profiling was accomplished by normal-incident sputtering of the sample with 5 keV argon ions with a total pressure of 5×10^{-5} torr pressure and total ion current of 25 mA and re-analyzing the previously identified grain boundary and ductile areas. Note that *60 s* of sputtering under these conditions typically removes approximately 1 nm of material from the surface. Sputtering and re-analysis continue until results from ductile and GB areas are similar, indicating that sputtering has removed the segregation zone. Raw Auger spectra were numerically smoothed and differentiated to

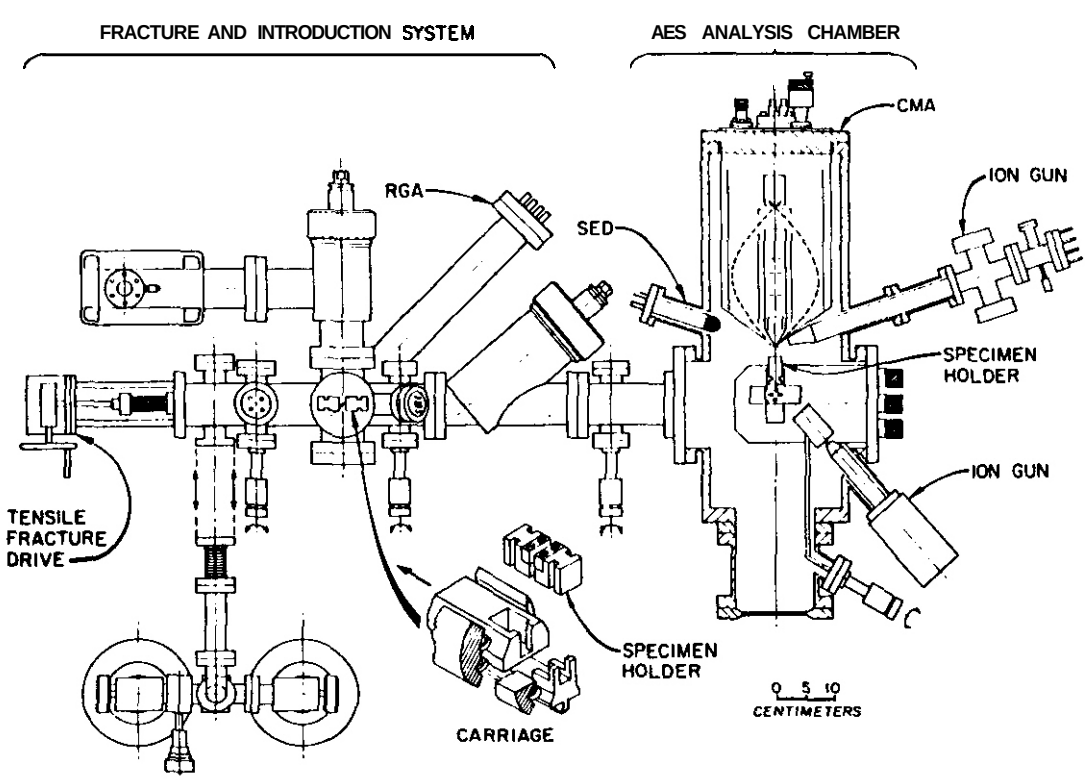

Fig. 1. Scanning Auger electron spectroscopy and fracture and introduction systems

accentuate the Auger peaks. Peak-to-peak heights of the 11 point smoothed and differentiated Auger spectra were measured for primary elemental Auger peaks with corresponding energies of Si (92 eV), P (120 eV), S (151 eV), Cl (180 eV), C (272 eV), O (510 eV), Cr (529 eV), Fe (703 eV), Ni (848 eV), and Na (980 eV). The measured peak-to peak heights were entered into a spreadsheet template (Microsoft Excel™) which corrected peak heights for elemental sensitivities, elemental overlap. and calculated the relevant compositional information and ratios.

AEM Analysis

AEM was performed on a Philips EM400T/field emission gun (FEG) in the scanning transmission electron microscopy (STEM) mode with a probe diameter of less than 2 nm. EDX analysis was performed perpendicular to each of two grain boundaries in each material. Details of the method of analysis have been given elsewhere.[20,21]

Results and Discussion

AES results from the AF surfaces are summarized in Fig.3. AF surfaces of the CP material showed depletion of chromium and enrichment of nickel [Fig. 3(*a*)] is shown by Ni/Cr ratios being greater at grain boundaries as compared to ductile areas. Ratios of the average Ni/Cr ratio for all grain boundaries analyzed to the average Ni/Cr ratio for all ductile areas analyzed were 2.2 ± 0.6, 1.13 ± 0.07, and 1.07 ± 0.02 for the AF. 60-and 120-s sputtered surfaces, respectively. indicating significant average segregation in the CP material. Similarly, silicon and phosphorous segregation were detectable for the CP material. Ratios of the average Si signal for all grain boundaries analyzed to the average Si signal for all ductile areas analyzed were 9.40 ± 3.77 for the AF surfaces. indicating strong Si segregation in the CP material. Phosphorous also showed significant segregation on the AF GBs with average ratio of phosphorous to sum of the metals (Fe+Cr+Ni) signal of more than 4.38 ± 1.58% at GBs and no statistically significant phosphorous signal in the ductile regions of the AF ductile and GR and ductile sputtered surfaces. No statistically significant segregation of sulfur was detected for the CP material. However, sulfur

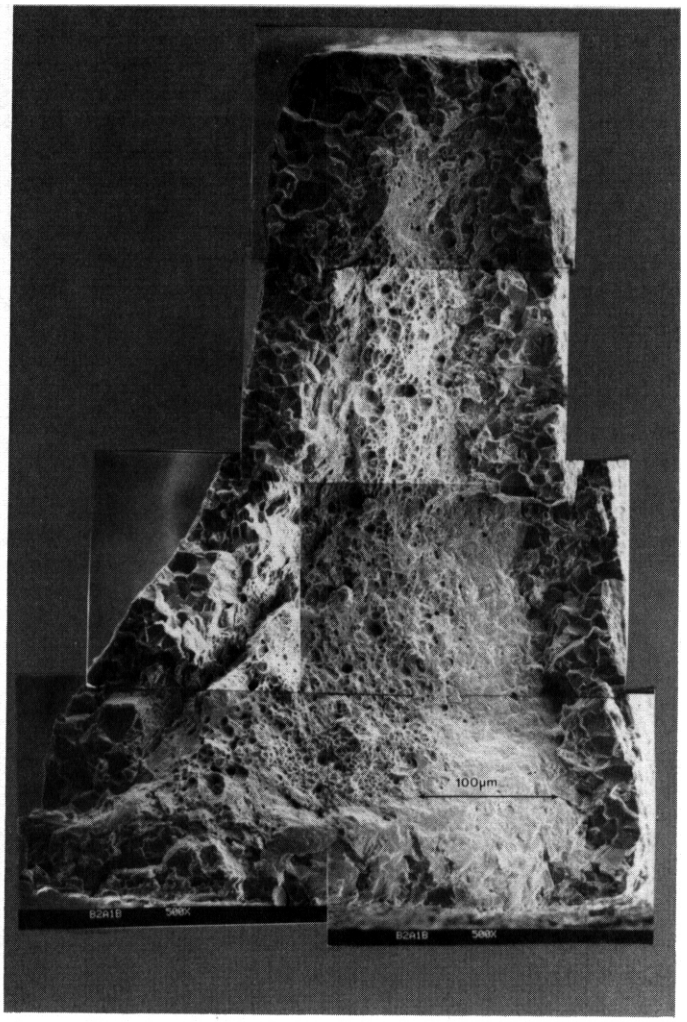

Fig. 2. Composite micrograph of typical fracture surface of HP material after hydrogen charging and fracturing in FAIS.

detection is difficult with AES due to continuous buildup of sulfur from contamination in the system. Only slight depletion of chromium and enrichment of nickel (Ni/Cr slightly greater for grain boundaries as compared to ductile areas) was detectable in the HP material [Fig. 3(*b*)]. Ratios of the average Ni/Cr ratio for all grain boundaries analyzed to the average Ni/Cr ratio for all ductile areas analyzed in the HP material were 1.19 ± 0.15 and 1.1 for the AF and 60-s sputtered surfaces. respectively. indicating less average segregation and a narrower segregation zone in the HP material. as compared to the CP materials. No statistically significant segregation of silicon. phosphorous or sulfur was detected for the HP material.

AEM results have been reported elsewhere[20,22] and are reproduced here for the purposes of comparison and the reader's convenience. Figures 4a and 4b illustrate the composition profiles measured near a grain boundary in the irradiated CP material. Similar profiles were observed for other boundaries. A very narrow (2.5 to 5-nm width) zone of RIS was observed at the boundary with fast-diffusing chromium exhibiting the widest profile. The grain boundary is depleted of chromium and iron by -4.5 and -3.5 at. %, respectively. whereas silicon, phosphorus, and nickel were enriched by approximately 3.0. 0.8, and 4.0 at. %. The average composition changes for the boundaries measured were 2.6 (Si). 0.6 (P), -4.8 (Cr), -2.8 (Fe), and 4.3 at. % (Ni), where positive values indicate enrichment at the boundary and negative values indicate depletion. No statistically significant segregation of sulfur was detected. Figures 4c and 4d illustrates composition profiles typical of grain boundaries in the HP material. A narrow (4 to 6 nm) width RIS zone is observed with chromium again exhibiting the widest profile. Though the measurements were

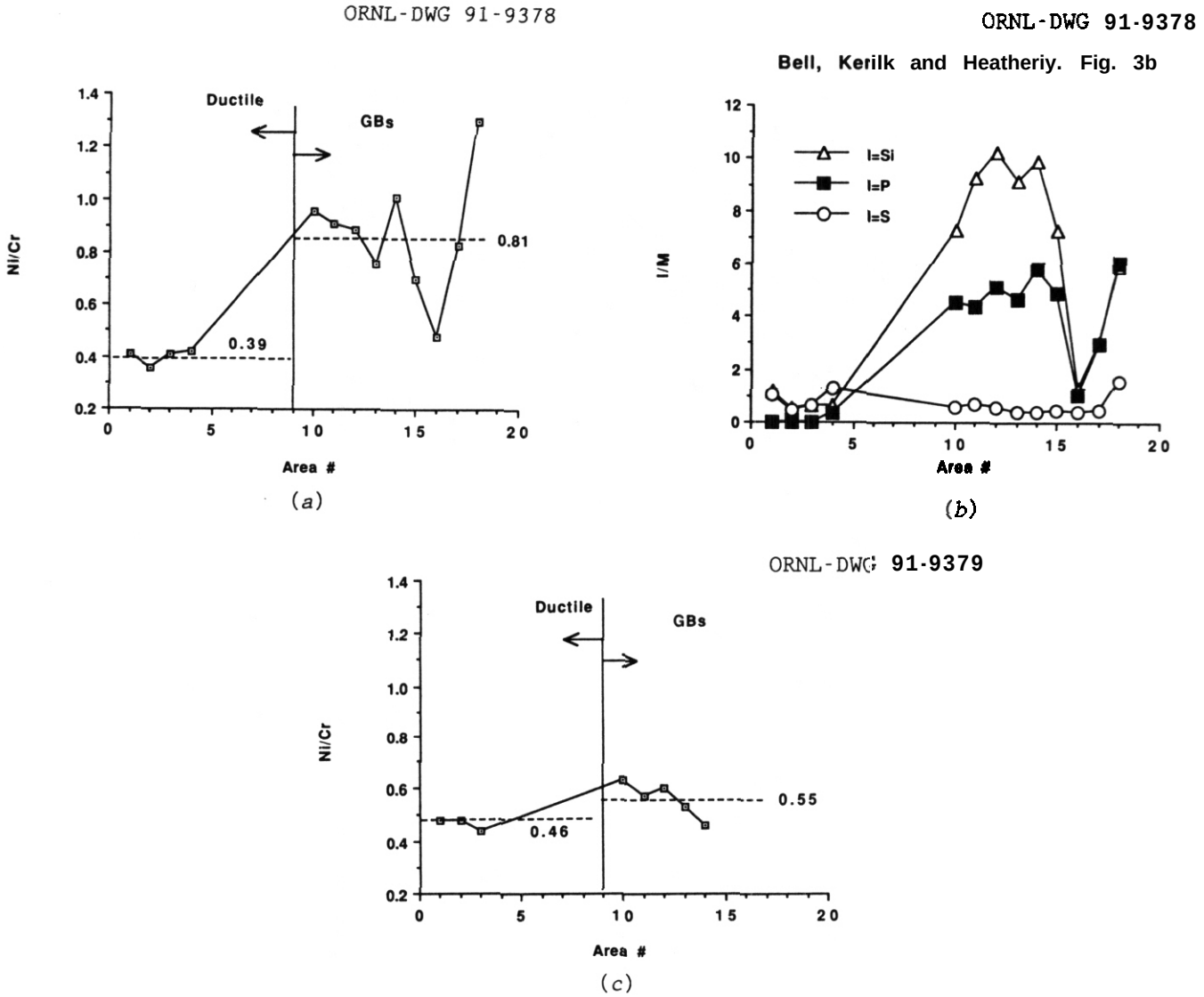

Fig. 3. AES results from AF surfaces of visually identified grain boundaries and ductile areas in type 304 SS irradiated to nominal fast nuetron fluence of 2 x 10^{25} m^{-2} (E > 1 MeV) at 288°C: (*a*) Ni/Cr for CP material, (*b*) Si, P, and S in CP material. (*c*) Ni/Cr for HP material.

performed in similar foil thicknesses and under similar experimental conditions, the HP material exhibits a lower degree of RIS to grain boundaries than does the CP material. No statistically significant segregation of silicon. phosphorus, or sulfur was detected. The average composition changes for the boundaries measured were 0.0 (Si). 0.0 (P), 0.0 (S), -1.7 (Cr), -0.9 (Fe), and 2.6 at. % (Ni), where positive values indicate enrichment at the boundary and negative values indicate depletion.

Good correlation was obtained using both techniques, particularly for Ni. Si. and Cr segregation. AEM gives better resolution absolute compositional and spatial resolution of the segregation of these elements while *AES* results show similar results only as trends in terms of ratios from sputter depth profiling. *AES* shows stronger segregation for light elements (silicon and phosphorous. in particular). This is because AEM results can be somewhat biased toward the matrix due to beam broadening and low elemental sensitivity of EDX toward elements with low Z numbers.

Other analyses in identical and similar materials have been performed. Shepherd23 of AERE Harwell examined both the HP and CP materials from the same BWR reactors and components irradiated to the same total fast fluence (2 x 10^{21} n/cm^2) at 288°C, using AEM with EDX under the ICG-IASCC IRR. AEM results from Shepherd agree well with the CP material: results presented here. In the case of the HP material, one of the two GBs investigated by Shepherd

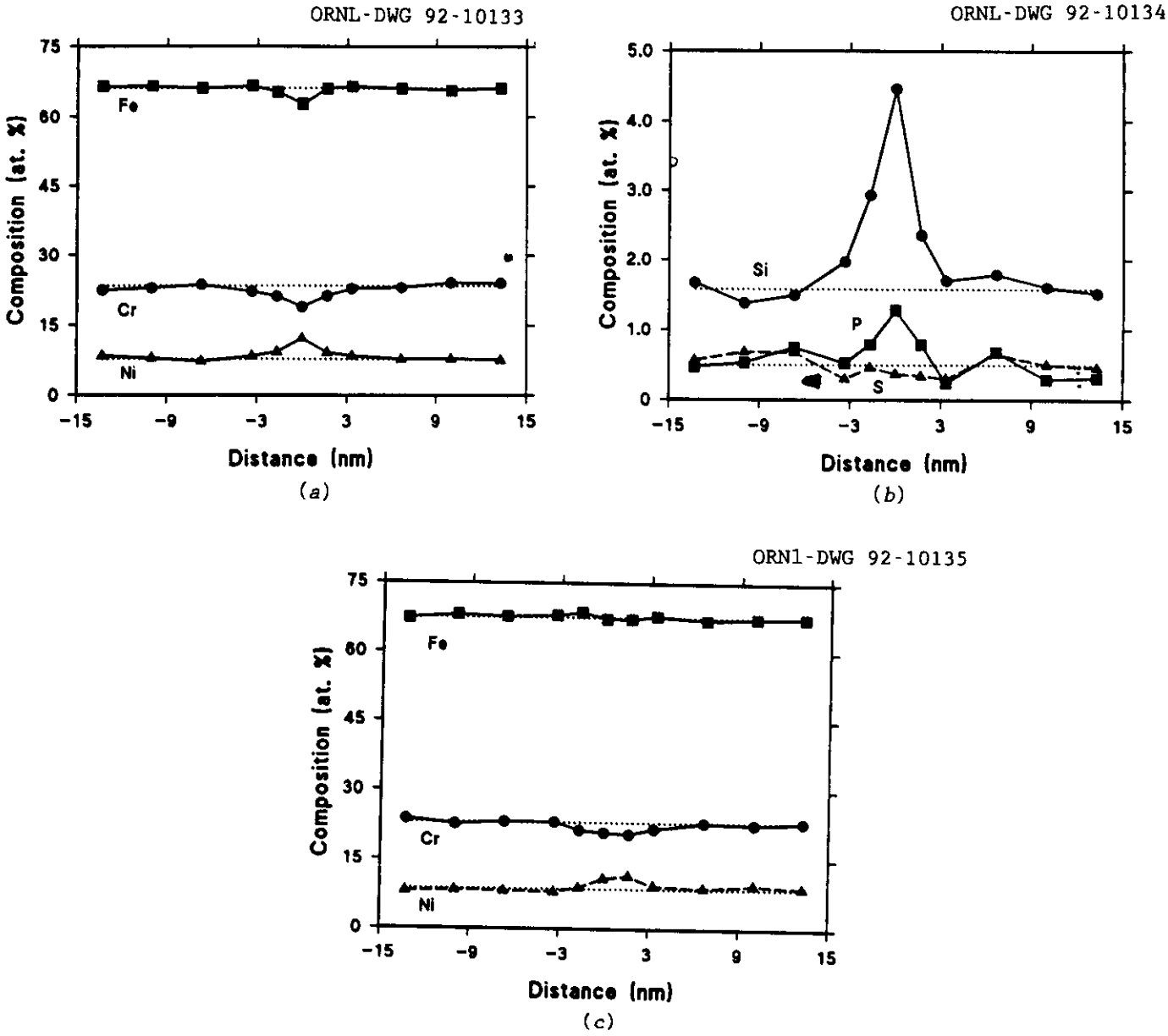

Fig. 4. AEM RIS profiles measured by X-ray microanalysis at grain boundaries of type 304 SS irradiated to nominal fast nuetron fluence of 2 x 10^{25} m^{-2} (E > 1 MeV) at 288°C:. (*a*) Fe, Ni, and Cr in CP material, (*b*) Si, P, and S in CP material, (*c*) Fe, Ni, and Cr for HP type 304 SS.

agreed with the ORNL AEM while analysis of the second boundary showed deep and narrow chromium depletion. No apparent reason for the difference in behavior between the two GBs xin the HP material has been established. AES analyses by Chung et. al.[24] on HP material from the same heat and irradiated to a lower fluence (1.25 x 10^{21} n/cm^2, E > 1 MeV) suggested that chromium and nickel segregation were stronger in HP materials, as compared to CP materials, and should therefore be more susceptible to IASCC. However, results from these analyses and similar analyses on other irradiated type 304 materials[25] by AEM and AES do not support the conclusions of ref. 24.

SUMMARY AND CONCLUSIONS

Radiation-induced grain boundary segregation in CP and HP type 304 SS irradiated in a fission power reactor at 288°C to 2 x 10^{21} n/cm^2 (E > 1 MeV) was characterized using both AEM and AES.

In general. HP materials showed less segregation as compared to the CP materials for irradiation conditions. Both AEM and AES showed strong enrichment in nickel, silicon. phosphorous, and depletion of chromium at grain boundaries in the CP material. AES indicated greater phosphorous and silicon segregation than did AEM. Both AEM and AES showed less enrichment of nickel and depletion of chromium in the high purity. When used as complimentary analyses methods. AEM and AES can provide important microchemical information for characterizing RIS in materials irradiated at low temperatures.

ACKNOWLEDGEMENTS

The authors thank Dr. Alvin J. Jacobs of General Electric Nuclear Energy for providing the materials and specimens. Dr. R. E. Clausing for his consultation regarding Auger results. and Ms. C. S. Lee for preparation of the manuscript. Research sponsored by the Office of Fusion Energy and the Division of Materials Science. U. S. Department of Energy under contract DE-AC05-84OR21400 with Martin Marietta Energy Systems. Inc.

REFERENCES

1. A. J. Jacobs. G. P. Wozadlo. "Availability Factor and Reliability Analysis." Proceedines of International Conference on Nuclear Power Plant Aging, American Society of Metals. Materials Park. Ohio. 1986. p. 173.

2. W. L. Clarke. A. J. Jacobs. "Materials in Nuclear Energy." Proceedines of International Conference. American Society for Metals. Metals Park. Ohio. 1982. p. 153

3. R. N. Duncan. Stainless Stee1 Failure Investigation Program. Final Summary Report, Report No. GEAP-5530. General Electric Nuclear Energy, 1968.

4. K. Fukuya. S. Nakahigashi. S. Ozaki, M. Terasawa, and S. Shima. Proceedines of the Third International Symposium on Environmental Degradation of Mater —— in Nuclear Power Systems-Water Reactors. The Metallurgical Society of AIME. Warrendale. Pennsylvania, 1987. p.665.

5. A. J. Jacobs, G. P. Wozadlo. N. Nakata. T. Yoshida. and I. Masaoka. Proceedings of the Third International Svmoosium on Environmental Degradation of Materials in Nuclear Power Svstems-Water Reactors. The Metallurgical Society of AIME. Warrendale. Pennsylvania. 1987.. p.683.

6. E. P. Simonen and R. H. Jones. Proceedines of the Third International Symposium on Environmental Degradation of Materials in Nuclear Power Systems-Water Reactors. The Metallurgical Society of AIME. Warrendale. Pennsylvania. 1987.. p.657.

7. H. Hanninen and Aho-Mantila. Proceedines of the Third International Symposium on Environmental Degradation of Materials in Nuclear Power Systems-Water Reactors. The Metallurgical Society of AIME. Warrendale. Pennsylvania. 1987. p.77.

8. F. Garzarolli. D. Alter, P. Dewes. and J. L. Nelson. Proceedings of the Third International Symposium on Environmental Degradation of Materials in Nuclear Power Systems-Water Reactors. The Metallurgical Society of AIME. Warrendale. Pennsylvania. 1987. p.657.

9. Aho-Mantila and H. Hanninen. "Materials for Nuclear Reactor Core Applications" Proceedines of International Conference. Vol. 1. British Nuclear Energy Society. London 1987. p. 349.

10 E. A. Kenik. Proc. Mater. Res. Soc. Symp. 62 (1986) 209.

11. D. I. R. Norris. C. Baker, and J. M. Titchmarsh. Radiation-Induced Sensitization of Stainless Steels, CEGB 1987, Proceedings of the Symposium held at Berkeley Nuclear Laboratories. Berkeley. California. September 23. 1986 (CEGB 1987). p. 86.

12. J. M. Perks. A. D. Marwick. C. A. English, Radiation-Induced Sensitization of Stainless Steels. CEBA 1987. Proceedings of the Symposium held at Berkeley Nuclear Laboratories. Berkeley. California. September 23. 1986. p. 15.

13. A. J. Jacobs. R. E. Clausing. L. Heatherly. and R. M. Kruger. Irradiation-Assisted Stress Corrosion Cracking and Grain Boundary Segregation n Heat-Treated Tvoe 304 SS. CONF-88063-3. Martin Marietta Energy Systems. Inc.. Oak Ridge Natl. Lab.. 1988.

14. P. L. Andresen. F. P. Ford. S. Murphy. and J. Perks. Proceedings of the Fourth International Symposium on Environmental Degradation of Materials in Nuclear Power Systems-Water Reactors. National Association of Corrosion Engineers. Houston. 1990.

15. C. Taylor, Radiation-Induced Sensitization of Stainless Steels, Proceedings of the Symposium held at Berkeley Nuclear Laboratories, Berkely. California, September 23. 1986. p. 60.

16. C. C. Baker, Fusion Technol. 15 (1989) 849.

17. R. H. Jones. Fusion Reactor Materials Semiannual Progress Report for the Period ending March 31. 1988. DOE/ER-0313/4, p.184.

18. S. Ohnuki. H. Takashi. R. Nagasaki. J. Nucl. Mater., 155-157 (1988) p. 823.

19. A. J. Jacobs. C. M. Shepherd. G. E. C. Bell, and G. P. Wozadlo. "High-Temperature Annealing as an IASCC Mitigation Technique." Proceeding of the Fifth International Symposium on Environmental Degradation of Materials in Nuclear Power Systems-Water Reactors, Monterey. California. August 25-29. 1991.

20. E. A. Kenik. "Radiation-Induced Segregation in Irradiated Type 304 Alloys for the ICG-IASCC Round Robin." Fusion Reactor Materials Semi-annual Report for the Period Ending March 31. 1991. DOE/ER-0313/10, U. S. DOE.

21. E. A. Kenik. "Materials Problem Solving with the Transmission Electron Microscope". Vol. 62. Eds. L. W. Hobbs. H. Westmacott. and D. B. Williams. Materials Research Society, Pittsburgh. 1986. p. 206.

22. E. A. Kenik. J. Nucl. Mater. 183 (in press)

23. C. M. Shepherd. Private Communication. April 1991.

24. H. M. Chung. W. E. Ruether. J. E. Sanecki. and T. F. Kassner. "Irradiation-Induced Sensitization and Stress Corrosion Cracking of Type 304 Stainless Steel Core-Internal Components." Proceedings of Fifth International Symposium on Environmental Degradation of Materials in Nuclear Power Systems: Water Reactors, Monterey. California. August 25-29. 1991..

25. A. J. Jacobs. Private Communication. October 1991.

ELECTROCHEMICAL AND MICROSTRUCTURAL CHARACTERIZATION OF AN AUSTENTITIC STAINLESS STEEL IRRADIATED BY HEAVY IONS ABOVE 600°C — G. E. C. Bell. E. A. Kenik (Oak Ridge National Laboratory) and T. Inazumi Japan Atomic Energy Research Institute.

OBJECTIVE

To investigate radiation-induced segregation (RIS) and sensitization using electrochemical methods and analytical electron microscopy (AEM).

SUMMARY

The electrochemical behavior and microstructural evolution of a solution-annealed, heavy-ion-irradiated. austenitic stainless steel (SS) have been investigated at temperatures above 600°C at doses of 1, 10 and 70 displacements per atom (dpa) with concurrent helium injection of 0.2 atomic parts per million He per dpa (appm-He/dpa). Changes in the electrochemical properties were measured by the single-loop electrochemical potentiokinetic reactivation (SL-EPR) technique using transmission electron microscopy (TEM) disk specimens. Microchemical analysis has also been performed on some duplicate specimens in an AEM.

Electrochemical results showed that the reactivation charge per unit etched area and Flade potential increased with increasing dose. In the case of the 70 dpa specimen. complete passivation of the specimen could not be obtained. AEM microanalysis showed changes in composition at both grain boundaries and faulted dislocation loops of chromium. iron. nickel. and silicon due to RIS.

PROGRESS AND STATUS

Introduction and Background

Heavy-ion irradiation (HII) is often used as a simulation technique for investigating RIS and the evolution of microstructures in materials during neutron irradiation.[1-6] Good simulations of neutron-irradiated segregation profiles near grain boundaries have been obtained6 using HII. Previously. we have reported the electrochemical and microstructural behavior of lower temperature (515°C) heavy-ion-irradiations[7] in which only radiation-induced sensitization (segregation) was present. In this research. we investigated the electrochemical and microstructural properties of higher temperature. heavy-ion-irradiated material in which both thermal and radiation induced changes in microchemical and electrochemical properties may occur (i.e., segregation. precipitation. and. thus, sensitization). Electrochemical properties were measured by the SL-EPR method of an austenitic stainless steel irradiated by heavy ions at temperatures between 651 and 693°C to doses of 1. 10 and 70 dpa and co-injected with 0.2 appm-He/dpa. The radiation-produced microstructure. segregation. and precipitation of some duplicate specimens have been examined by AEM.

Exoerimental

The material investigated was an experimental austenitic SS alloy designated LSlA with a composition of Fe-16.4Cr-13.7Ni-1.0Si-2.0Mn-1.7Mo-0.15Ti-0.08C percent by weight (wt %). LSlA is similar to a titanium-stabilized type 316 SS. The specimens were solution annealed at 1100°C for 1 h prior to irradiation. Specimen temperatures were measured during the irradiation. and all specimens were at their measured temperatures for ~ 4 h. Details of the specimen preparation for and HII conditions are given elsewhere.[2,4]

The electrochemical experiments were performed on 3-mm-diam TEM disk-type specimens. The experimental apparatus. procedures, and conditions have been described in detail elsewhere.[7-9] After SL-EPR testing of the damaged surface. thermal control SL-EPR data were

collected by removing the heavy-ion-damaged layer by electropolishing. The Flade potential. reactivation charge per unit tested specimen surface area. and reactivation charge per unit etch area of specimen surface area were calculated after completion of the SL-EPR test and surface examination using a Hitachi 8000 scanning electron microscope (SEM). The Flade potential was defined as the first inflection point of the applied potential versus measured current curve during the controlled cathodic scan. Since the potential scan rate is constant and applied potential is. therefore. proportional to time. the total reactivation charge was calculated by integrating the potential versus current curve from the initial passivating +200 mV versus saturated Calomel electrode (SCE) to free-corrosion potential measured during the potential scan.

Details of the AEM analysis[1] have been given elsewhere.

Results

The EPR results for the thermal control surfaces and heavy-ion-irradiated surfaces are shown in Fig. 1. along with the thermal and irradiation conditions of the surfaces and specimens. Figure 1 shows the SL-EPR curves for three heavy-ion-irradiated surfaces along with curves for solution-annealed material. which represent the pre-irradiation condition of the specimens, and typical thermal control surface results. The thermal control surface data shown were obtained by SL-EPR testing the 10 dpa specimen after the heavy-ion-damaged layer was removed by electropolishing. Results from other specimen (1 and 70 dpa) thermal control surfaces were similar. Peak current densities and reactivation charges per unit tested area for all specimens (thermal control and heavy-ion-irradiated) were similar. 5.0 to 5.4×10^4 mA (cm^{-2}-tested area) and 3.0 to 3.9×10^3 mC-(cm^{-2}-tested area). respectively. Differences in the SL-EPR results were obvious between the passivation potential (+200 mV versus SCE) and the Flade potential and in the etching that occurred during testing. SEM micrographs of the post-EPR test heavy-ion-irradiated surfaces are shown in Fig. 2. The solution-annealed specimen was not etched or pitted during the SL-EPR test and is not shown. Only grain-boundary etching was observed for the thermal control surfaces. and an example is shown in Fig. 2a. At 1 dpa. both grain-boundary and grain -face pitting/etching were observed [Fig. (2b)]. Grain-face pits were separated by smooth areas similar in appearance to the grain faces of thermal control material after EPR testing. We estimated that the pitting covers 40 to 60% of the surface of the grain. If we assume that 50% of the grain face is etched, we calculate a charge density of 6.45×10^3 mC-(cm^{-2}-etched area). At 10 dpa. grain-face etching spread over the entire face of the grain. and grain-boundary etching persisted [Fig. 2(c)]. At 70 dpa. measured currents at the passivation potential were high in comparison with other thermal control and heavy-ion surface data (Fig. 1). Grain-

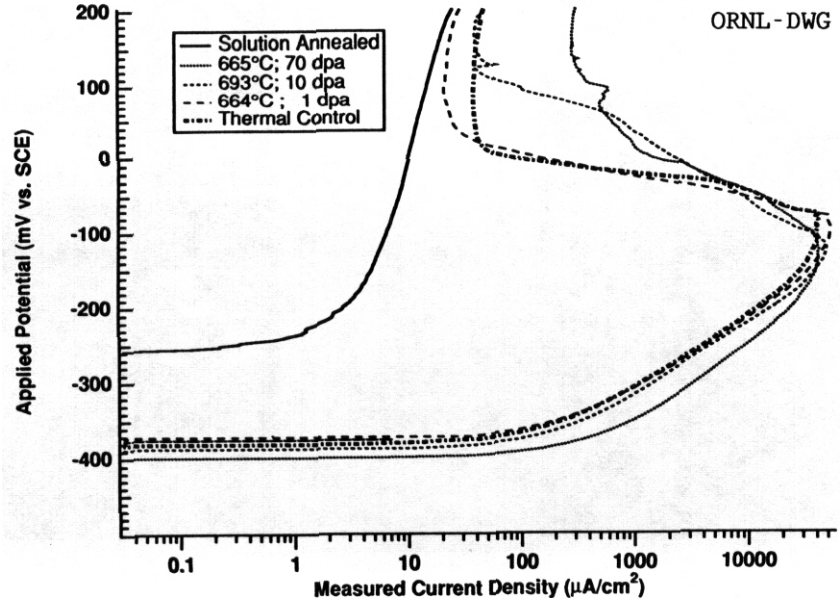

Fig. 1. SL-EPR results for heavy-ion-irradiated and thermal control surfaces of LS1A.

ORNL PHOTO 4654-92

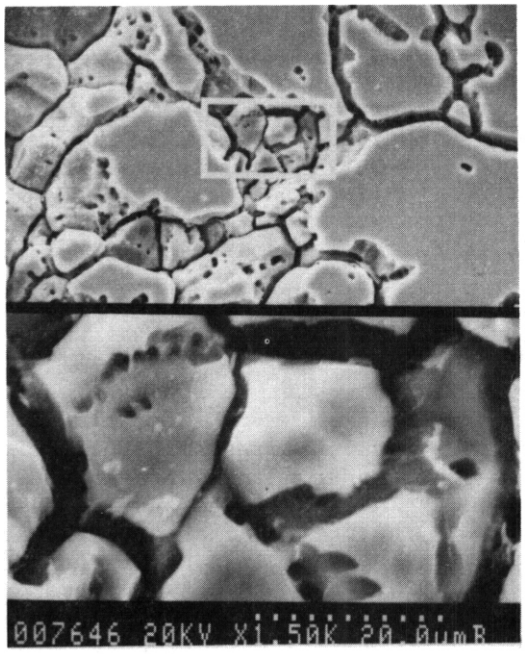

(a)

ORNL PHOTO 4655-92

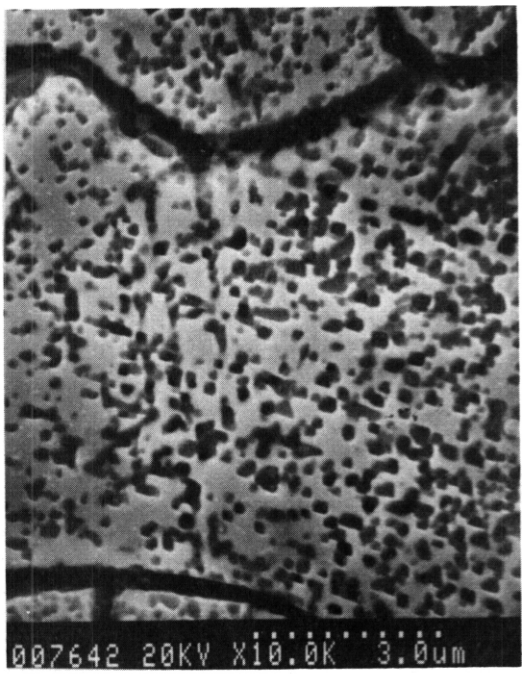

(b)

Fig. 2. SEM micrographs of Post-EPR test **LSlA** surfaces from Fig. 1: (a) thermal control surface. [Bottom magnification is 5x of top] (b) 1 dpa surface. (c) 10 dpa surface. and (d) 70 dpa surface [Bottom magnification is 5x of top]. Note the difference in magnification between micrographs.

(c)

ORNL PHOTO 4656-92

(d)

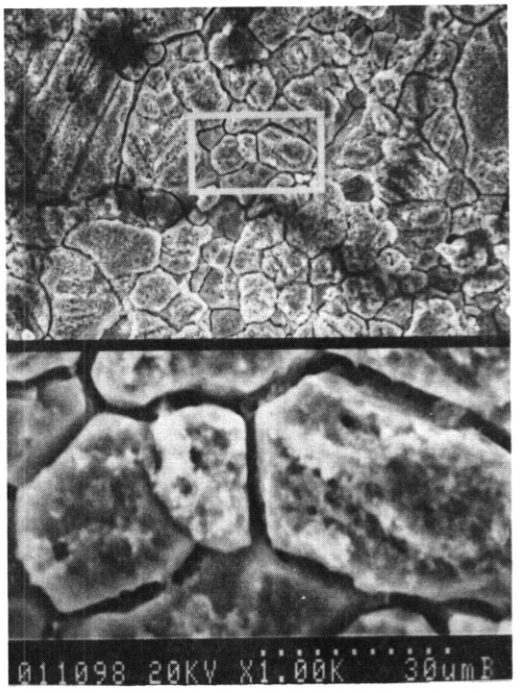

ORNL PHOTO 4657-92

boundary etching was present and grain-face etching increased further in intensity. The surface of the 70 dpa specimens had a very porous appearance [Figs. 2(d)]. The reactivation charges per unit etched area for the 10 and 70 dpa specimens were 3.34×10^3 and 3.90×10^3 mC·(cm^{-2}-etched area), respectively, the same as the value per unit test area because

ORNL-DWG 92-10132

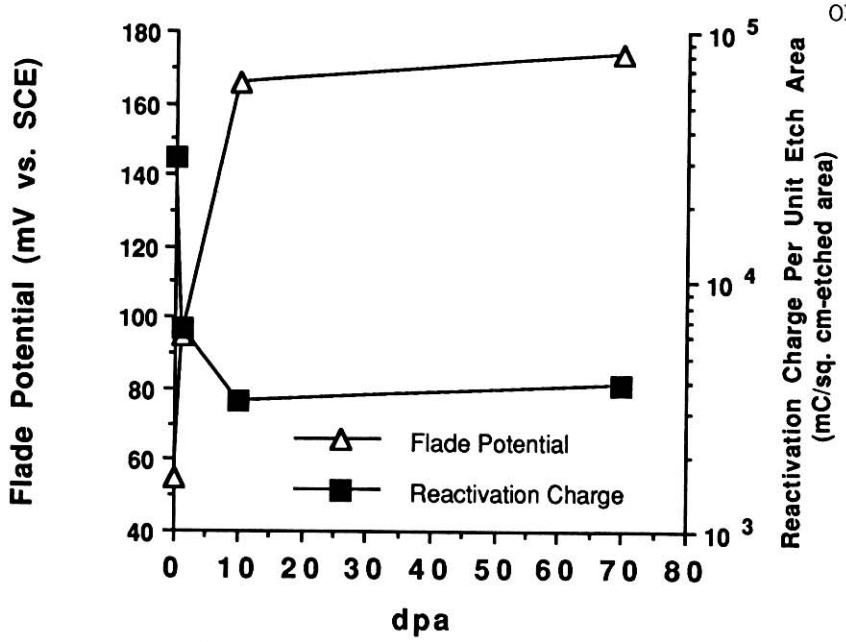

Fig. 3. Summary of SL-EPR results for heavy-ion-irradiated LS1A as a function of dose.

ORNL 9438-85

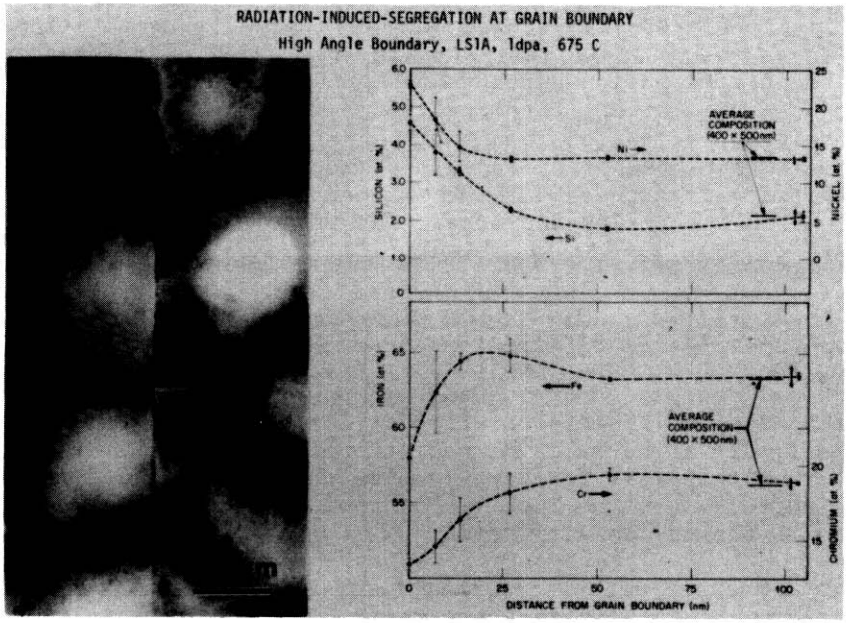

(*a*) (*b*)

Fig. 4. AEM results for 675°C, 1 dpa irradiation: (*a*) High angle grain boundary. Note: no precipitates at gain boundary. Arrows indicate position of AEM line scan. (*b*) Silicon, nickel, iron, and chromium profiles obtained. Error bars indicate standard deviation for multiple analyses.

etching occurred over the entire specimen surface. For thermal control surfaces. the calculated reactivation charge per unit grain-boundary area [(so-called P_a (ref. 9)] is the same as the reactivation charge per unit etched area because only the grain boundaries etched. The average P_a value for thermal control surfaces was 3.14 x 10^4 mC·(cm^2-GB). Similar P_a values, 2.66 x 10^4 mC·(cm^2-GB), were obtained for thermally aged control material (4 h @ 675°C). This indicates that the estimates of time at irradiation temperature were reasonable and that P_a values of this order are to be expected for thermally sensitized materials. Figure 3 summarizes the Flade potential and reactivation charge per unit of tested area results for the thermal control (0 dpa) and heavy-ion-irradiated specimens shown in Fig. 1. In general, the Flade potentials increased rapidly with increasing dose between 0 and 10 dpa and increase only slightly on further irradiation to 70 dpa. Reactivation charge per unit etched area decreased with irradiation to 10 dpa and then increased slightly between 10 and 70 dpa.

AEM results have been previously published elsewhere[1,5] and are reproduced here. Heavy-ion-irradiated (675°C, 1 dpa) grain boundaries did not exhibit chromium-rich precipitates (e.g., $M_{23}C_6$, M = Cr or Fe) [Fig. 4(*a*)] despite having been at temperature for more than 4 h and exhibiting grain-boundary etching during SL-EPR testing. Precipitation of nickel- and silicon-rich phases in the bulk and at grain boundaries in the alloy was observed even at 1 dpa and saturated between 10 and 70 dpa(ref.5). Figure 4b shows AEM data gathered using energy dispersive X-ray (EDX) analysis for iron. nickel. chromium. andsilicon of a high-angle grain boundary in LSlA irradiated by heavy ions at 675°C to 1 dpa. Depletion of molybdenum and manganese was also measured. Asymmetric and narrower profiles with high levels of segregation were measured face-on and edge-on to faulted dislocation loops.[1]

Discussion

The SL-EPR test method was developed to quantify the susceptibility of austenitic SS to intergranular stress corrosion cracking (IGSCC) in aqueous environments due to chromium depletion from thermal sensitization.[10] The SL-EPR method utilizes the fact that the passive film formed on the surface at passive potentials remains intact and is metastable at active (lower) potentials near room temperature in the test electrolyte. Any defect in the film (i.e., locally lower chromium content due to thermal precipitation of chromium-rich phases or RIS) will cause the film to break down in the region near the defect. This results in an increase in dissolution current and concurrent etching of the defect region. In the case of thermal sensitization. chromium-rich $M_{23}C_6$ carbides precipitate at grain boundaries and deplete only the region near the boundary of chromium. In the case of RIS, chromium is depleted at grain boundaries and other microstructural defects without precipitation of a chromium-rich phase via the inverse-Kirkendall effect.[1,6,11] Chromium depletion via RIS at grain boundaries and other microstructural defects has been previously detected by the SL-EPR method and by AEM for both neutron and heavy-ion-irradiated materials.[1,6,7,9,12]

Grain-boundary and grain-face etching due to RIS on SL-EPR-tested heavy-ion and neutron-irradiated surfaces have been previously reported.[7,9,12] Post-SL-EPR grain-boundary etching was evident at all doses and on the thermal control surfaces. However, chromium-rich phases were not present at grain boundaries of heavy-ion-irradiated material examined by AEM [e.g. Fig. 4(*a*)]. It appears that irradiation may suppress carbide precipitation at grain boundaries and that the grain-boundary etching observed after SL-EPR testing for heavy-ion-irradiated surfaces was the result of chromium depletion via RIS as shown in Fig. 4(*b*) and not due to thermal sensitization.

Flade potentials increased with increasing dose. This result is consistent with our previous heavy-ion-irradiated results on the same material at 515°C (ref. 7). Higher Flade potentials imply less stable passive films. The instability is due to compositional variations (i.e., chromium depletion) in the film. Concurrent with the increase in Flade potential was a decrease in reactivation charge per unit etched area due to irradiation and the appearance of grain-face etching. This result is also consistent with our previous data at lower temperatures.[7,9,12] These results (decreased passive film stability) indicate that the general corrosion rate of the material may be increased. Increased general corrosion can reduce the susceptibility to localized corrosion phenomena, such as intergranular (IG) or irradiation-assisted stress corrosion cracking (IASCC). because corrosion currents flow from both the grain boundaries and the grain faces and not just grain boundaries. Our results indicate that reactivation charges per unit etched specimen area were approximately one order of magnitude lower for heavy-ion-irradiated surfaces (grain face and grain-boundary etching) as compared to thermal control surfaces (grain-boundary etching only). It

may be possible that irradiated materials exhibiting grain-face attack during SL-EPR testing may be less susceptible to IGSCC and IASCC.[12,13]

SUMMARY AND CONCLUSIONS

The electrochemical and microstructural behavior of solution-annealed. heavy-ion-irradiated. austenitic SS (LS1A) has been investigated at temperatures above 600°C at doses of 1, 10, and 70 dpa. Significant changes in the electrochemical behavior of the specimens were observed as a function of dose. The following conclusions can be drawn from these results:

1. Both grain-face and grain-boundary etching were observed for heavy-ion-irradiated surfaces. AEM results indicated that chromium-rich phases were not present in the irradiated material. For heavy-ion-irradiated surfaces, grain-boundary etching was attributable to RIS and not to the precipitation of chromium-rich phases, despite the elevated temperature of the irradiation. It appears that irradiation may have suppressed the thermal precipiation of chromium-rich phases normally associated with thermal aging at these temperatures.

2. The Flade potential of LSlA increased with increasing radiation dose to 70 dpa indicating decreased passive film stability or thickness with increasing radiation dose. At 70 dpa. complete passivation was probably not obtained. Large changes occurred between 1 and 10 dpa with smaller, but detectable. changes occurring between 10 and 70 dpa.

3. Reactivation charge per unit etched area decreased rapidly between 0 and 10 dpa and then decreased slightly between 10 and 70 dpa. The presence of the grain-face etching and decreases in reactivation charge per unit etched area suggests that the susceptibility of materials exhibiting grain-face etching to localized attack (e.g., IASCC or IGSCC) may be reduced.

REFERENCES

1. E. A. Kenik, proc. Mater. Res. Soc. Symp., **62** (1986) 209.

2. E. A. Kenik. J. Nucl. Mater., 85 & 86 (1979) 659.

3. E. A. Kenik and E. Lee. in: Proceedings of the 41st Annual Meeting of Electron Microscopy Societv of America, Ed. G. W. Bailey, San Francisco Press, San Francisco. 1983. p. 234.

4. E. A. Kenik. Srr. Metall. 10 (1976) 733

5. E. H. Lee. A. F. Rowcliffe, and E. A. Kenik. J. Nucl. Mater. 83 (1979) 79.

6. C. M. Shepherd and T. M. Williams. Proceedings of the Fourth International Symposium on Environmental Degradation of Materials in Nuclear Power Systems-Water Reactors, Ed. D. Cubiccotti. National Association of Corrosion Engineers. Houston, 1990 p. 14.

7. G. E. C. Bell. T. Inazumi. E. A. Kenik. and T. Kondo. J. Nucl. Mater. (in press) (1992).

8. T. Inazumi. G. E. C. Bell. and K. Kiuchi, J. Nucl. Mater., 179-181 (1991) 619

9. T. Inazumi. G. E. C. Bell, E. A. Kenik. and K. Kiuchi. Corros. 46 (1990) 786.

10. W. E. Clarke, V. M. Romero. and J. C. Danko. Detection of Sensitization in Stainless Steel Usine Electrochemical Techniaues, Report No. GEAP21382, General Electric Nuclear Energy. 1976.

11. E. A. Kenik. J. Nucl. Mater. (in press)

12. T. Inazumi. G. E. C. Bell. P. J. Maziasz, and T. Kondo. (ICFRM-5), 1991

13. G. E. C. Bell. T. Tsukada. K. Shiba. and H. Nakajima. Fusion Reactor Materials Semiannual Progress Report for the Period Ending Septemb 30. 1991. DOE/ER-0313/11, U.S. DOE Report.

EFFECTS OF COMPOSITIONAL MODIFICATIONS ON THE SENSITIZATION BEHAVIOR OF FE-CR-MN STEELS — G. L. Edgemon (Georgia Institute of Technology), P. F. Tortorelli and G. E. C. Bell (Oak Ridge National Laboratory).

OBJECTIVE

The purpose of this task is to determine the corrosion susceptibility of reduced activation austenitic steels in aqueous environments for fusion applications involving water cooling and/or aqueous blankets.

SUMMARY

Fe-Cr-Mn steels may possibly be used in conjunction with aqueous blankets or coolants in a fusion device. Therefore, standard chemical immersion (modified Strauss) tests were conducted to characterize the effects of compositional modifications on the thermal sensitization behavior of these steels. A good correlation among weight losses, intergranular (IG) corrosion, and cracking was found. The most effective means of decreasing their susceptibility was through reduction of the carbon concentration of these steels to 0.1%. but the sensitization resistance of Fe-Cr-Mn-0.1C compositions was still inferior to type 304L and other similar stainless steels (SS). Alloying additions that form stable carbides did not have a very significant influence ON the sensitization behavior.

PROGRESS AND STATUS

Jntroduction

Good resistance to sensitization is required of any stainless steel (SS) being considered for use in fusion devices employing a liquid blanket and/or coolant. In aqueous environments, sensitized SS can be susceptible to intergranular stress corrosion cracking (IGSCC). Sensitization normally occurs when, upon heating at intermediate temperatures (500 to 700°C), chromium is depleted locally in areas around grain boundaries due to nucleation and growth of chromium-rich carbides. It can also be induced by radiation-induced segregation.[1-2]

While there is concern that Fe-Cr-Mn steels may present a safety problem due to release of volatile products under reactor accident conditions, they are attractive from waste management considerations because of their fast-induced radioactive decay characteristics compared to conventional Fe-Cr-Ni steels.3 It thus was of interest to investigate the thermal sensitization resistance of developmental Fe-Cr-Mn steels (see, for example, refs. 4-6 for potential use in aqueous environments of fusion devices. Standard chemical immersion tests and analytical electron microscopy (AEM) showed that developmental austenitic Fe-Mn-Cr steels based on Fe-20Mn-12Cr-0.25 (wt %) were extremely prone to thermal sensitization and, therefore, IG corrosion.7 Sensitization is exacerbated by higher carbon and lower chromium concentrations and. thus, the poor resistance of the previously examined developmental Fe-Mn-Cr alloys to thermally-induced chromium depletion and IG corrosion7 was not unexpected. (High carbon contents and relatively low levels of chromium are necessary to maintain austenite-stability in these steels because manganese is not as strong an austenite stabilizing element as nickel.[5]) The present study was undertaken to assess the sensitization behavior of two other classes of developmental Fe-Mn-Cr steels that included reduced carbon concentrations, higher chromium levels, and/or alloying additions that form more stable carbides than those of chromium.

Exoerimental Procedures

This sensitization study was mainly focused on Fe-Cr-Mn steels being developed by Oak Ridge National Laboratory (ORNL), but part of the effort was devoted to developmental Mn steels supplied by the Joint Research Centre (JRC), Ispra (courtesy of V. Coen).[8] The compositions of the steels are listed in Table 1. With the exception of 20Mn12CrWTiHC, the ORNL alloys had substantially less carbon than the 0.25 wt % carbon steels examined previously.' Susceptibility to sensitization and IG corrosion was evaluated using a variation of the modified $CuSO_4$ (Strauss) test, as defined per American Society for

Table 1. Compositions of Fe-Cr-Mn Steels Examined in this Study

Designation[a]	Concentration (wt%)						
	Mn	Cr	W	Ti	V	C	Other
20Mn12CrLC	20	12	–	–	–	0.1	–
20Mn12CrWTiLC	20	12	1	0.1	–	0.25	0.04P, 0.005 B
20Mn12CrWTiLC	20	12	1	0.1	–	0.1	–
20Mn12CrWTiLC	20	12	1	0.1	<0.1	0.1	–
20Mn14CrLC	20	12	–	–	–	0.1	–
18Mn13CrWNiLC	18	13.1	1.9	–	0.02	0.1	2 Ni. 0.2Si,0.04 N
17Mn10CrWHC	16.9	10.2	2.0	–	0.03	0.26	0.5 Si, 0.1 Ni. 0.08 N
11Mn12CrWVHC	10.6	12.4	1.4	–	0.6	0.3	0.2 Ni, 0.2 Si, 0.04 N
11Mn14CrWNiLC	11.3	13.6	1.4	–	0.6	0.1	2 Ni. 0.2 Si. 0.05 N
11Mn18CrWNiVLC	11.0	17.9	2.0	–	0.7	0.08	2.1 Ni. 0.35 Si. 0.05 N

[a] 20 Mn steels are ORNL developmental alloys: Rest are JRC. Ispra steels.

Testing and Materials (ASTM) Standard Practice A262E.[9] The test environment was a boiling. acidified $CuSO_4$ solution (100 mg of $CuSO_4$/L, 10% H_2SO_4), which accelerates IG corrosion of sensitized austenitic SS. AEM showed that the procedure adapted for use here was quite sensitive to chromium depletion at grain boundaries and thus was a good qualitative indicator of sensitiration.7 Normally, this type of corrosive attack is revealed by the cracking that occurs upon bending after exposure.9 but failure can occur at very low levels of stress for steels that are particularly susceptible.7 The specimens were not of the standard size for Strauss tests because of limited material availability. The dimensions of the ORNL steel specimens were 25 x 12 x 1 mm. while those cut from material provided by JRC. Ispra were disks 18 mm in diameter and 1- to 2- mm thick. The ORNL alloys were exposed in the acidified solution in two conditions: annealed (1150°C. 1 h in vacuum, water quenched) and aged (annealing followed by 650°C. 2 h in vacuum, water quenched). The JRC. Ispra specimens were tested only in the aged condition. Specimens were individually wrapped in copper wire and embedded in copper shot (per standard practice) prior to immersion in the solution The amount of solution per unit specimen surface area was nominally the same for all exposures. The duration of the exposures was limited to 8 h. which was sufficient to cause heavy IG corrosion of other Fe-Cr-Mn steels after aging, but not the sensitization of type 304L 55.7

After exposure. the specimens were examined visually and by optical and scanning electron microscopy (SEM). If not already broken during retrieval from the test bed, the specimens were bent and then checked for cracking. Maximum strains were on the order of 4%(ref. 9). In most cases. weight changes were also measured.

Results

Comparisons of weight changes after exposure to the $CuSO_4$ solution revealed that the aged Fe-Cr-Mn steels exhibited significantly higher weight losses than those in the annealed condition. This is clearly shown by the weight change data in Table 2. The

Table 2. Comparison of the effects of corrosion and stress on Fe-Cr-Mn steels

Designation	Condition	Wt. LO66 mg/cm$_2$	Surface Condition After 8h Immersion: No Stress[a]	Surface Condition After 8h Immersion: After Bending
20Mn12CrLC	Ann.	0.8	N	Some cracking
	Aged	–	–	Substantial cracking
	Aged	114	D	Fractured into pieces
	Aged	304	D*	–
20Mn12CrWTiHC	Ann.	–	N	No cracking
	Ann.	2.5	–	Some edge cracks
	Aged	–	–	Through thk. cracking
	Aged	24	B	–
	Aged	42	I	Fractured into pieces
20Mn12CrWTiLC	Ann.	*1*	N	No cracking
	Aged	6	I	Substantial cracking
	Aged	20	–	Substantial cracking
	Aged	123	D	Through thk. crakcing
20Mn12CrWTiVLC	Ann.	1	–	No cracking
	Ann.	1	–	No cracking
	Aged	1	–	Substantial cracking
	Aged	118	D	Fractured into pieces
20Mn14CrLC	Ann.	–	N	No cracking
	Aged	–	–	Substantial cracking
	Aged	4	N	Substantial cracking
	Aged	35	B	–
	Aged	50	B	–
17Mn10CrWHC	Aged	27	I	Fractured info pieces
	Aged	–	B	–
11Mn12CrWVHC	Aged	1	I	Substantial cracking
	Aged	1	–	Substantial cracking
18Mn13CrWNiLC	Aged	1	I	Fractured into pieces
11Mn14CrWNiLC	Aged	1	I	Mild cracking
	Aged	1	–	Substantial cracking

[a] B: Fractured during handling
N: No significant corrosion affects
D: Heavily dissolved
D*:Completely dissolved
I: Intergranular corrosion

annealed steels had consistently low weight losses (approximately 1 mg/cm^2), while the aged alloys showed a large variability. even among multiple specimens of the same composition. For every steel, however, the minimum weight loss of the aged specimens usually was at least an order of magnitude greater than that of the annealed ones. With the exception of the 17Mn10CrWHC steel, the weight losses of the aged JRC, Ispra steels were low (on the order of 1 mg/cm^2).

Examination of specimens exposed to the $CuSO_4$ solution revealed that most of the aged specimens had suffered some IG corrosion (see Table 2). In certain cases. IG cracks were also observed in the absence of applied stress. The steels showing the greatest tendency toward such cracking were the 20Mn12CrWTiHC steel [Fig. 1(*a*)] and *one* of the high carbon JRC steels (17Mn10CrWHC), but some cracks were also observed for steels with lower carbon concentrations [Fig. 1(*b*)]. The application of a stress (induced by simple bending) often led to substantial cracking of the aged specimens. The most severe cracking was noted for the 20Mn12CrWTiHC steel: bending produced through-thickness cracking of the aged steel, but cracks did not form when annealed specimens of this steel were similarly stressed (Fig. 2). Table *2* summarizes the results from examination of annealed and aged steels exposed to the $CuSO_4$ solution both in the presence and absence of applied stress. Note that cracking under stress was also observed for aged, low carbon Fe-Cr-Mn steels. An example of this is shown in Fig. 3 (20Mn14CrLC). For this steel, copper was deposited on the surface of an aged specimen during immersion in the solution, but the presence of the

ORNL PHOTO 4547-92

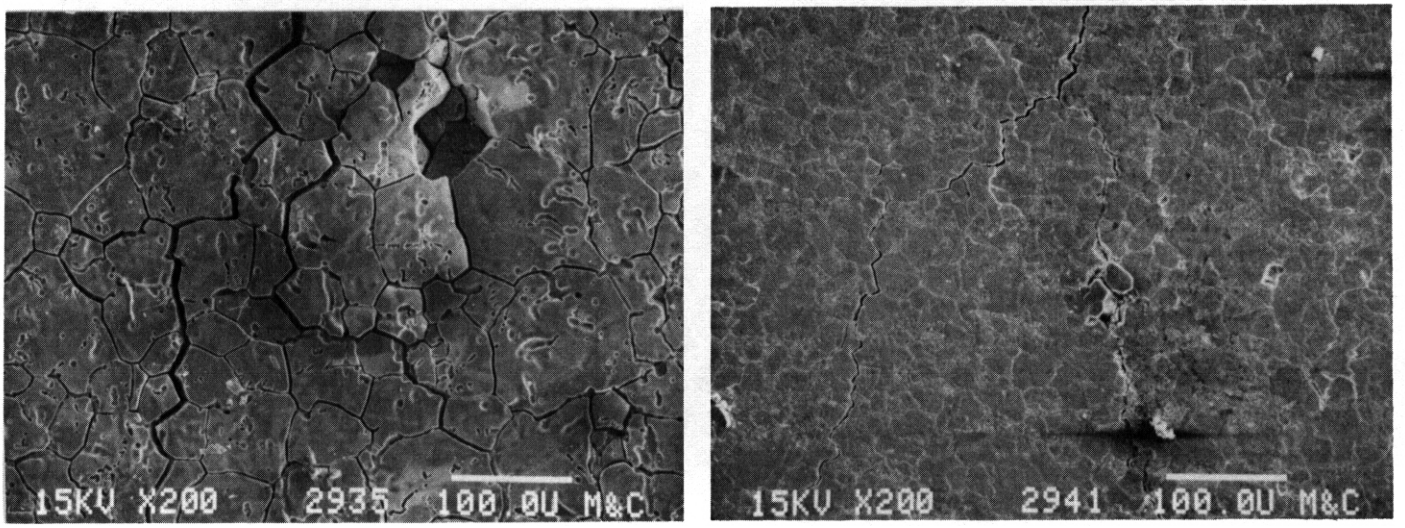

1. Aged Fe-Cr-Mn steels after exposure to $CuSO_4$ solution for 8 h, without subsequent applied stress: (*a*) 20Mn12CrWTiHC (*b*) 20Mn12CrWTiVLC.

ORNL PHOTO 4548-92

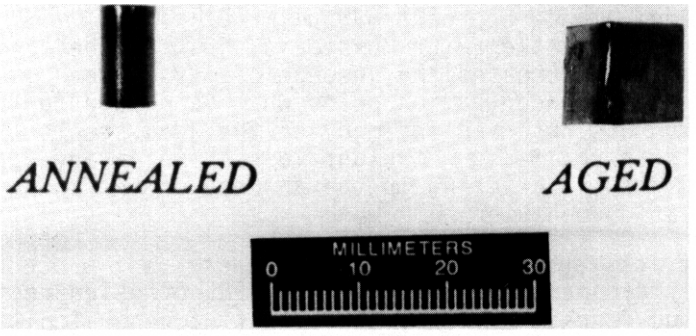

2. 20Mn12CrWTiHC after exposure to $CuSO_4$ solution for 8 h.

crystals did not appear to affect the IG cracking process. Two other aged specimens of this steel fractured into pieces during handling after exposure. This also occurred for one specimen each of aged 20MN12CrLC and 17Mn10CrWHC (see Table 2). Several other specimens, described as "fractured into pieces" in Table 2. disintegrated at very low applied stresses, that is. as soon as the bending force was initiated.

Discussion

The results from the $CuSO_4$ immersion tests indicate that the Fe-Mn-Cr steels of the present study are prone to sensitization. Despite significant variations in carbon contents and the presence of carbide-stabilizing elements (Ti, V. and W), all of the

ORNL PHOTO 4549-92

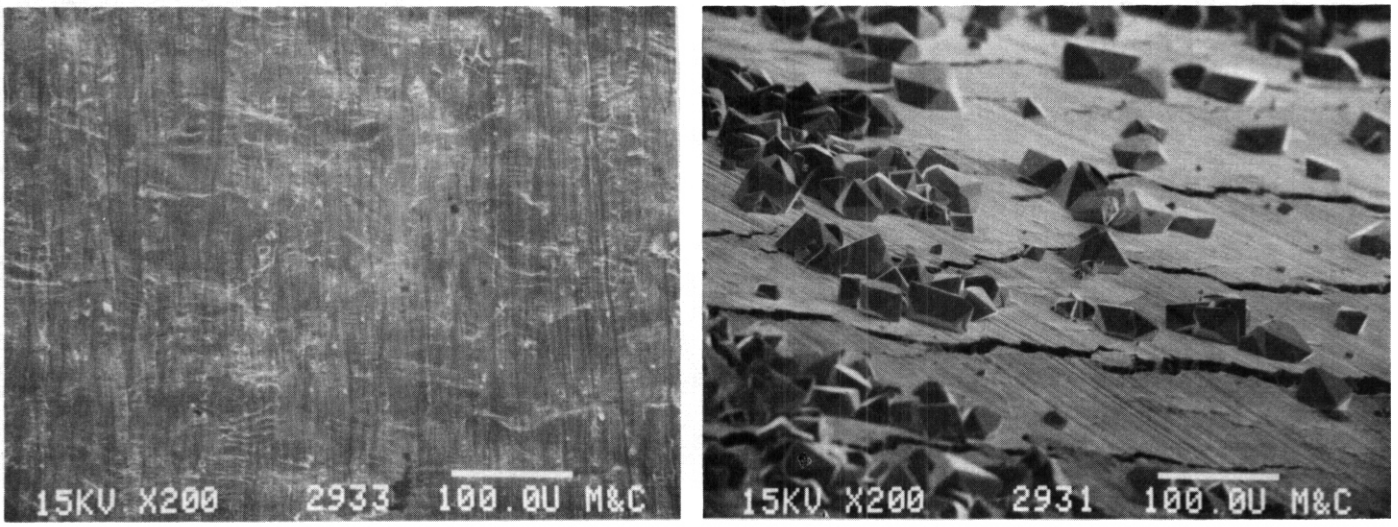

3. 20Mn14CrLC steel after exposure to $CuSO_4$ solution for 8 h and subsequent bending: (*a*) annealed (*b*) aged.

steels showed some susceptibility to thermal sensitization. The higher carbon-containing steels showed the worst overall cracking after exposure to the $CuSO_4$ solution, and no one composition with lower carbon concentration appeared to be definitively better than the rest. It should be noted that the Strauss test. albeit quite severe and very sensitive to chromium depletion at grain boundaries.' is only qualitative. With the exception of carbon, it may not differentiate among other alloying effects on sensitization for Fe-Cr-Mn steels. However, an SS that is known to be thermal sensitization-resistant. type 304L, typically does not crack after exposures up to 48 h.9 and after 8-h exposures, types 304. 304L, and 316L all were resistant.7 Therefore, the present results clearly demonstrate that the Fe-Cr-Mn steels are inferior to low-carbon versions of Fe-Cr-Ni SS. This finding is consistent with the chromium equivalence approach of Fullman.[10] Because of the relatively low chromium concentrations of the Fe-Cr-Mn steels, just a modest amount of chromium depletion at grain boundaries increases the susceptibility to corrosion in these regions by reducing the local chromium concentration below what is needed for protection (about 12 wt %). This IG corrosion was observed for many of the aged steels (see Fig. 3 and Table 2) and correlates well with the measured weight losses and observed cracking. The lack of significant weight losses and cracking in the absence of the aging treatment is consistent with known sensitization behavior.

While measurements of weight loss are not part of the Strauss test procedure, the present results indicate that they can be a good indicator of IG corrosion resistance for these steels because, without aging (sensitization). the amount of general dissolution is normally small. Because the major contribution to weight loss appears to be from dissolution in the chromium-depleted zones at grain boundaries, the smaller weight losses of most of the JRC steels are at least partially due to their larger grain size relative to the ORNL alloys.

The addition of elements (such as Ti) that form very stable carbides should decrease sensitization from chromium depletion by preferentially reacting with carbon during heat treatment and thus maintaining a higher effective chromium concentration (see. for example. ref. 10). As mentioned above, the results do not indicate a clear advantage for those steels containing such carbide-stabilizing elements. Vanadium and tungsten are not as strong MC formers as Ti and therefore are not as effective in reducing the amount of carbon available for reaction with Cr.[10,11] With respect to the JRC steels, it is possible that the presence of nitroaen (as an austenite stabilizer) mitiaated the effects of increased concentrations of chromium or stable carbide-formers by promoting the formation of CrN, which can also cause localized depletion of chromium.3 In all cases. the ability to obtain greater sensitization resistance by increasing the concentration of elements like titanium is limited by possible formation of brittle intermetallic phases.[3,7]

Despite the relatively poor response *of* the aged steels to exposures in the $CuSO_4$ solution, their general sensitization behavior was superior to the set of Fe-Cr-Mn steels previously evaluated.7 In the earlier study. all the steels contained 0.25% C and all failed after 8-h immersions by fracturing at low stress or crumbling when handled. Unlike the present experiments, none survived intact to the bending stage. In view of these prior results and the present data ON the high-carbon compositions. the lowering of the carbon concentration to 0.1% has improved the sensitization resistance of the Fe-Cr-Mn steels although, as discussed above, not to a level comparable to most Ni-stabilized SS.

SUMMARY AND CONCLUSIONS

The sensitization resistance of Fe-Cr-Mn steels was evaluated by a chemical immersion test previously shown to be effective in qualitatively characterizing chromium depletion at grain boundaries. A good correlation among weight loss, IG corrosion. and cracking was found.

Alloying additions that form stable carbides did not have a major influence on the sensitization behavior of these steels. The most effective means of decreasing their susceptibility was by reducing the carbon concentration to 0.1%. However. the sensitization resistance of Fe-Cr-Mn-0.1C steels appears to be significantly inferior to several Fe-Cr-Ni SS that are normally considered for applications where this phenomenon may be of concern.

ACKNOWLEDGEMENTS

This research was sponsored by the Office of Fusion Energy, U. S. Department of Energy, under contract DE-AC05-84OR21400 with Martin Marietta Energy Systems, Inc. The authors thank E. A. Kenik and R. L. Klueh for their reviews of the manuscript.

REFERENCES

1. D. I. R. Norris, Ed., Proceedings of the Symposium on Radiation-Induced Sensitization of Stainless Steels, Berkeley Nuclear Laboratory, Central Electricity Generating Board, Berkeley, California 1986.

2. T. Inazumi. G. E. C. Bell, E. A. Kenik. and K. Kiuchi, Corros. 46 (1990) 786.

3. E. Ruedl and T. Sasaki. J. Nucl. Mater. 122&123 (1984) 794.

4. R. L. Klueh. P. J. Masiasz. and E. H. Lee. Mater. Sci. and Eng. A102 (1988) 115.

5. R. L. Klueh and P. J. Masiasz. Mater. Sci. Eng. A127 (1990) 17.

6. G. J. Butterworth, J. Nucl. Mater. 179-181 (1991) 135.

7. G. E. C. Bell. P. F. Tortorelli, E. A. Kenik. and R. L. Klueh, J. Nucl. Mater. 179-181 (1991) 615.

8. G. Piatti. D. Boerman, and J. Heritier, Proceedings of the 15th Symposium on Fusion Technology, Vol. 2, Elsevier. Amsterdam, 1989. Vol. 2, p. 983.

9. Annual Book of ASTM Standards, Pt 10, American Society for Testing and Materials, Philadelphia, 1980.

10. R. L. Fullman, Acta Metall. 30 (1982) 1407

11. E. A. Kenik. P. J. Masiasz. and R. L. Klueh. Proceedings of the 47th Annual Meeting of the Electron Microscopy Society of America, San Francisco Press, San Francisco. 1989, p. 284.

LITHIUM PURIFICATION AT TEMPERATURES BELOW 500°C · G. E. C. Bell. (Oak Ridge National Laboratory)

OBJECTIVE

To investigate the potential of using chromium surfaces at temperatures below 500°C to remove nitrogen from lithium.

SUMMARY

A method for removal of nitrogen from liquid lithium has been investigated that allows nitrogen purification to be done at temperatures below 500°C. The method utilizes the formation of an insoluble. ternary compound on chromium-plated stainless steel surfaces to remove nitrogen. Capsule tests established the initial feasibility of the method and determined optimum warm-trapping parameters for a large-scale batch test. Favorable results from capsule tests were obtained with processing temperatures of 450°C and chromium surface area-to-lithium volume ratios greater than 100 m^{-1}. Nitrogen levels as low as 37 weight parts per million (wppm) were achieved in less than 30 h at 450°C by using a staged, large-scale batch process. When used in conjunction with conventional cold trapping. the method allows lithium purification to be done in a single. inexpensive vessel with a higher degree of safety. as compared to higher temperature methods (e.g., hot gettering).

PROGRESS AND STATUS

Introduction

Fusion reactor designs incorporating molten lithium will need to be concerned with lithium purity due to materials compatibility and resulting activation transport considerations.[1,2] Nonmetallic impurities in lithium, particularly nitrogen. can lead to increased materials compatibility problems and corrosion rates.[3-10] Lithium purification for nonmetallic and metallic elements is typically done in two stages as shown in Fig. 1. The lithium is first cold trapped.[11] It is held near its melting point (181°C) in a stainless steel container to allow precipitation of slightly soluble metallic and nonmetallic contaminants. Filtering and settling. then removes the precipitated impurities (O, C, Fe. Cr, Mo. etc.). Nitrogen has a relatively high solubility near the melting point[12,13] and cannot be removed by precipitation, settling, and filtering. Removal of nitrogen is typically done by hot gettering with zirconium at temperatures above 750°C.[14] Due to the elevated temperature and increased solubility of iron, nickel. and chromium at these temperatures. hot gettering requires the use of refractory metal container materials with low solubilities in lithium, such as titanium or molybdenum. to minimize contamination.[15,16]

In an effort to reduce the cost of purification and increase safety of the purification process, a method for removal of nitrogen from liquid lithium has been investigated that allows nitrogen purification to be done at temperatures below 500°C. Because the temperature of the method falls between cold trapping and hot gettering. the process has been dubbed "warm trapping." The method utilizes the formation of an insoluble. ternary compound, Li_9CrN_5, on chromium surfaces to remove nitrogen. The existence of lithium-metal-nitrogen compounds has been known for quite some time.[17] Calaway[18] and Barker et al.[19] investigated the reaction of chromium with dissolved nitrogen using resistivity methods. Barker et al. verified the reaction product as being Li_9CrN_5, which formed when nitrogen in solution was reacted with metallic chromium at 475°C. They further showed that the reaction product was insoluble in the lithium melt at this temperature. Barker. Frankham. and Moon[20] reported evidence of the formation of Li_9CrN_5 at nitrogen concentrations as low as 140 wppm-N. the detection limit of their resistivity apparatus at 475°C. Bell et al.[21] predicted equilibrium nitrogen concentrations in lithium exposed to steel at temperatures below 500°C to be less than 100 wppm-N. The impetus for investigating this method for purification came about by analysis of the lithium stream during normal processing of lithium [Fig. 1(*a*)] for use in thermal convection loops.[10] As shown in Fig. 2, both oxygen and nitrogen contents of the lithium were reduced in the cold trap, which operated at 205°C

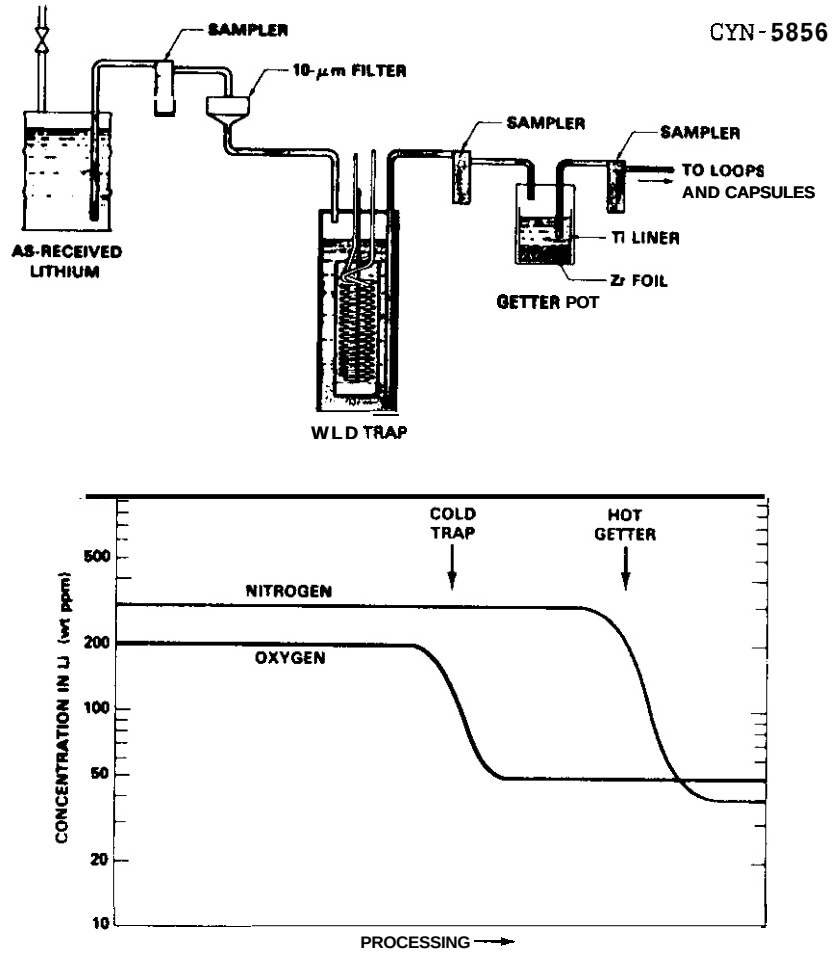

Fig. 1. (*a*) Typical purification system used for lithium and (*b*) "theoretical" chemical changes for system shown in (*a*).

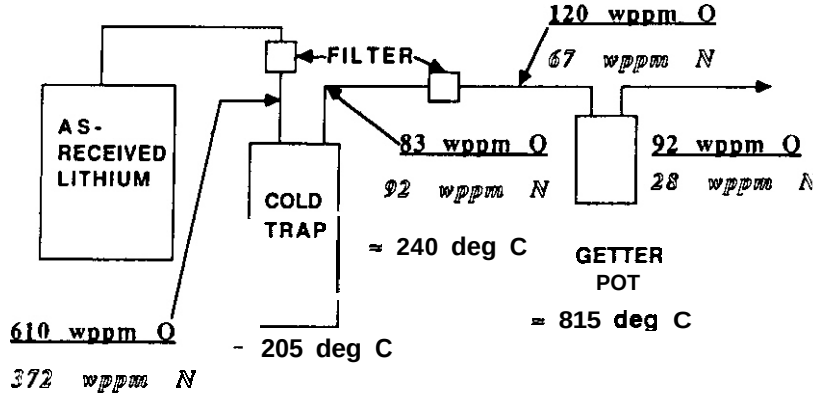

Fig. 2. Results of acutal analysis for batch of lithium purified using system shown in Fig. 1. Note that nitrogen content of lithium decreases during cold trapping and due to filtering with SS.

for more than 1800 h. Further, passing the lithium through a stainless steel (SS) filter (nominal 10-μm pore diameter and large chromium surface area to lithium volume. $\frac{SA^{Cr}}{V_{Li}}$) further reduced the nitrogen content of the transferred lithium prior to entering the hot-gettering vessel. In light of these results and with the helpful suggestions of Hubberstey,[22] an experimental program was undertaken to determine the feasibility of this method for lithium purification for nitrogen (< 50 wppm-N). Small-scale capsule tests (i5 to 20 g) were first used to determine the initial feasibility of the method and operating parameters for a large-scale batch test (15 to 20 kg). The large-scale batch test would determine the feasibility of the process on a larger. more reactor-relevant scale.

Experimental

Capsules were constructed from 25.4-mm OD X 1.65-mm wall X 152-mm-long type 304L SS tubes with trepan-welded end caps. Up to two specimens (19 X 76.2 X 1.5 mm), either bare-type 304L SS and 0.5-mm-thick chromium-plated type 304L SS, were enclosed in the tubes to obtain the desired $\frac{SA^{Cr}}{V_{Li}}$ for a particular capsule and to provide information about the effect of the reaction on the chromium metal surface. The capsules were assembled inside a recirculating. purified-argon atmosphere glove box. Impurity levels in the glove box were maintained below the limits of detection of the gas chromatography system used (< 2.5 vppm N_2, < 3.5 vppm O_2, and < 1 vppm H_2O @ 0.11 MPa). Sufficient lithium to half-fill the capsules at test temperatures was cut and weighed from cast sticks (0.015 to 0.020 kg). The lithium. reagent-grade (Alpha Products. 98.9% pure) lithium nitride (Li_3N) [-500 to 2100 wppm-N in Li], and specimens were inserted into the capsules. which were then welded shut. After welding. the capsules were heated to the desired temperature (350, 400. 450 ok 500°C) in air-tube furnaces with temperature controlled to ±5°C. The capsules were removed from the furnaces after either 500 or 1000 h and then cut open inside the glove box. The capsules were then heated in the glove box to about 230°C to melt and remove the lithium and disassemble the capsule. The specimens were removed and a sample of the lithium cast, cut. and sealed in a stop-cock-Pyrex transfer tube prior to analysis by the Analytical Chemistry Division of Oak Ridge National Laboratory (ORNL). Nitrogen analyses were performed by the micro-Kjdehal method.[23] The sampling and analytical errors for the capsule tests were estimated to be f30 wppm-N.

Because of the relatively low temperatures used, warm trapping can be done in SS vessels. Large-scale batch tests were performed in a modified cold trap as shown in Fig. 3. Modifications included chromium plating the cooling coil and installing chromium-plated SS between the outer wall and the thermal barrier to increase the chromium surface area for reaction. The $\frac{SA^{Cr}}{V_{Li}}$ of the modified cold trap was 0.8 ± 0.1 cm^{-1}. After assembling the system and leak checking. a 0.012 kg aliquot of reagent-grade (Alpha Products. 98.6% pure) Li_3N was added to the system before transferring the lithium into the cold/warm trap. Approximately 16 kg of lithium (372 wppm-N) was transferred from a 55-gal drum of lithium (part of a 95-kg lot purchased from Lithium Corporation of America) to the cold/warm trap. The calculated initial nitrogen content of the melt was 674 wppm-N. An argon overpressure of 0.15 MPa was established, and the vessel was heated to 450°C. This temperature was selected from data obtained in the capsule tests (see below). Compressed air was circulated through the inside of the cooling coils to produce a driving force for natural circulation and mixing in the cold/warm trap vessel. The melt was periodically sampled using "thief" *samplers*[23] through a I-in. ball valve access port located on the central standpipe of the vessel, The standpipe also allowed access for the periodic addition of chromium in the form of Ultrex-brand™, J. T. Baker Company chromium pellets or Fischer Scientific chromium metal "chunks" to increase chromium surface area in the warm trap. By transferring the lithium from the warm trap into a 10-1 staging pot with a $\frac{SA^{Cr}}{V_{Li}}$ value of 140 m^{-1}, additional chromium surface area could be utilized for nitrogen removal. In addition to micro-Kjdehal analysis of nitrogen. ion-coupled plasma spectroscopy (ICPS) was performed on select samples to determine if contamination was occurring due to warm trapping. The sample preparation procedure of Bauer[24] for ICPS analysis of lithium samples was followed.

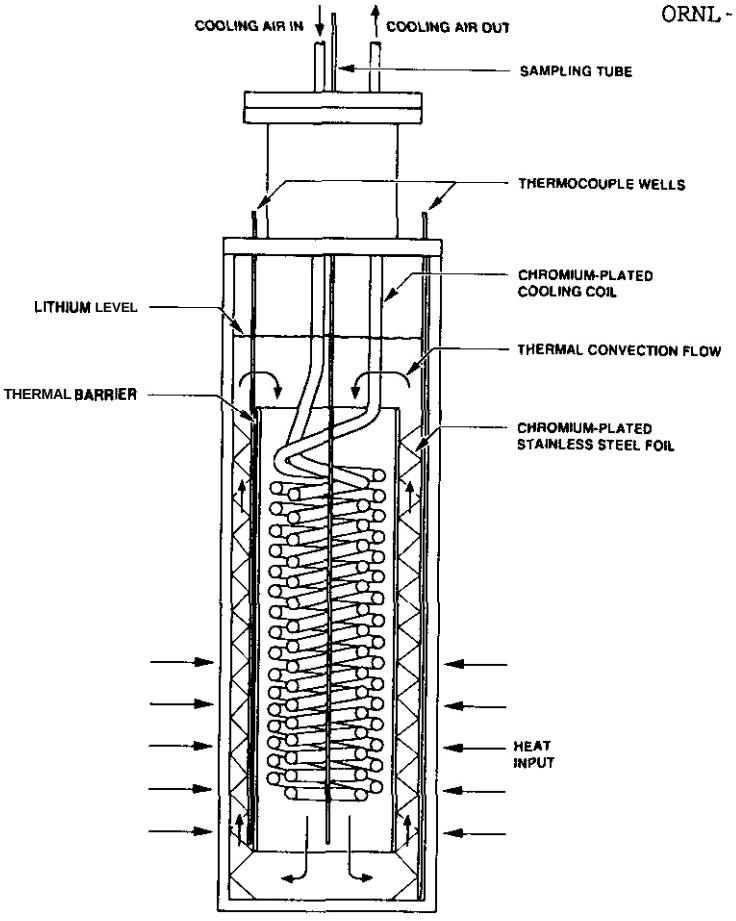

Fig. 3. Schematic of modified cold trap [11] used for large-scale batch tests.

Results and Discussion

Table 1 shows the results of the capsule tests. The method was successful in removing nitrogen from lithium at temperatures of *400* to 500°C with chromium-plated surfaces. Increasing the surface chromium activity by chromium plating increased nitrogen removal above 400°C. Chromium-plated specimens were uniformly attacked over the entire surface for surface area-to-volume ratios of 80 m^{-1}, indicating that the chromium surface product formed over the entire chromium surface. Weight changes for specimens (not shown) were consistent with nitrogen removal (i.e., higher weight loss occurred for higher nitrogen removal). Unplated type 304L SS did not remove nitrogen below 450°C. Nitrogen removal at 350°C was not achievable in 500 h for either plated or unplated surfaces. Increasing the temperature to 500°C for 500 h or the exposure time to 1000 h at 450°C did not significantly decrease final nitrogen concentrations. On the basis of these results. it was decided that the large-scale batch test would be conducted at 450°C with as large an $\frac{SA^{Cr}}{V_{Li}}$ as possible, within the space limitations of the the existing cold trap design."

Figure *4* shows the results of the large-scale batch test. The batch test was characterized by a large initial drop in nitrogen (~ 300 wppm-N) concentration followed by a gradual decrease in nitrogen content. Barker et al.[19] observed decreases in reaction rate in resistivity measurements and attributed the decrease to the formation of the insoluble reaction product Li_9CrN_5 on the surface of the chromium substrate, which inhibited further reaction of the nitrogen with the chromium. Due to space limitation within the modified cold trap. an initial $\frac{SA^{Cr}}{V_{Li}}$ of only ~ 80 m^{-1} could be obtained. This was apparently

Table 1. Results of Capsule Tests

Capsule ID (time)	$\frac{Cr SA}{LiV}$ (m-1)	Temperature	[N] i (wppm-N)	[N] f (wppm-N)
350U (500 h)	0	350°C	1652	1642
350P (500 h)	85	350°C	2091	2100
400U (500 h)	0	400°C	2104	2134
400P (500 h)	85	400°C	2139	1027
450U (500 h)	0	450°C	1972	1725
450P (500 h)	85	450°C	1829	421
450P2 (500 h)	100	450°C	1029	224
500P (500 h)	100	500°C	1073	300
4502P1 (500 h)	180	450°C	543	125
4502P2 (500 h)	180	450°C	885	138
4502P3 (500 h)	180	450°C	1675	164
4502P4 (1000 h)	180	450°C	1068	263

ORNL-DWG 92-10130

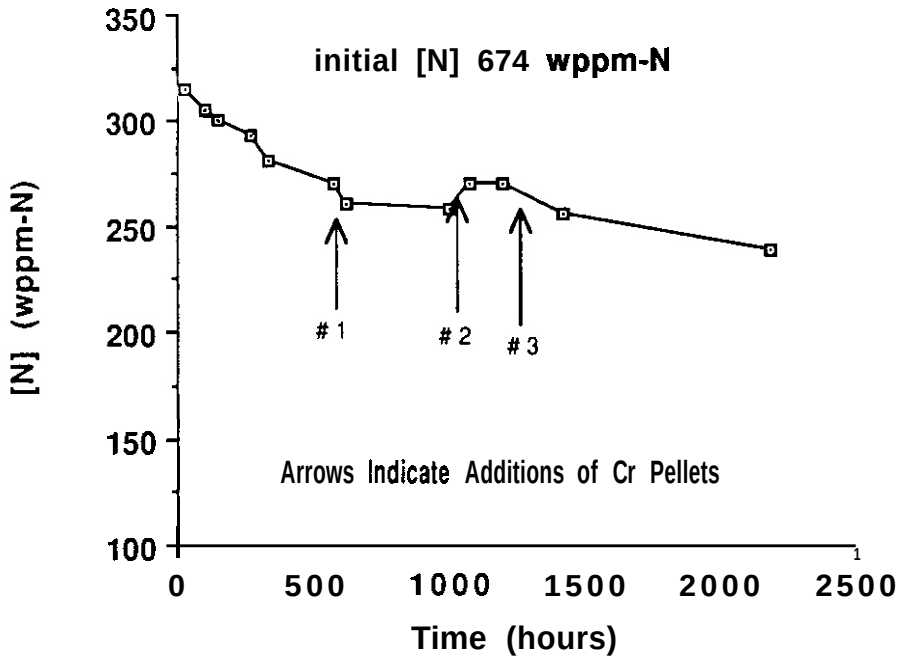

Fig. 4. Lithium concentration versus time in warm trap at 450°C to 2187 h with three additions of chromium "chunks" or pellets. Note that the calculated initial nitrogen concentration was 672 wppm-N.

insufficient to react all the initial dissolved nitrogen. Subsequent additions of chromium "chunks" and pellets to increase the $\frac{SA^{Cr}}{V_{Li}}$ had mixed results. The first addition (no. 1 of Fig. 4) of chromium "chunks" (0.28 kg @ 578 h) from Fischer Scientific Lot no. 796085 had the desired effect of causing an immediate drop in nitrogen concentration. The Fischer chromium "chunks" were shiny in appearance and probably provided a good, clean surface for the reaction to occur (thus. the drop in nitrogen content). The second (0.300 kg @ 1006 h) and third (0.270 kg @ 1205 h) additions of J. T. Baker Ultrex™ chromium pellets had either an adverse or no effect on the nitrogen content of the melt. The Ultrex™ pellets had a dull finish and although "pure" in terms of metallic elements and silicon, may have had a nitrogen surface contamination. The warm trap was operated at 450°C for 2187 h (239 wppm-N), at which point it was cooled to 250°C for 3000 h while the staging pot was built and preparations transfers of the lithium were made. The warm trap was then sampled and 7 L of lithium were then transferred through an in-line sampler into the staging pot. The staging pot was heated to 450°C and sampled after 30 h of operation. Results of the nitrogen analyses showed that the nitrogen concentration dropped from 252 wppm-N (average of sample taken from the warm trap and in-line sampler from transfer to staging pot) to 37 wppm-N in the staging pot after 30 h at 450°C.

It appears from the capsule and large-scale batch tests that the success of the warm trapping method at 450°C is dependent on providing sufficient chromium surface area for the reaction to occur on. Commercially available lithium typically contains on the order of 300 wppm-N [25] and, thus. $\frac{SA^{Cr}}{V_{Li}}$ values in excess of 140 m^{-1} would be required to process commercial-purity lithium to levels of nitrogen below 50 wppm-N.

ICPS analysis of samples taken from the warm trap at 333. 577. and 621 h showed a significant increase in nickel content of the lithium. as compared to hot-gettered lithium. which was below the detection limit of ICPS. This is probably due to prolonged contact of the melt with the stainless steel at relatively high temperatures (> 400°C). Warm trapping followed by cold trapping. in the same vessel. and filtration of the exit stream would theoretically remove this contamination.

CONCLUSIONS

A method for removal of nitrogen from liquid lithium has been investigated that allows purification to be done at temperatures below 500°C. The method utilizes the reaction of nitrogen dissolved in the lithium with chromium-plated SS surfaces to form an insoluble. ternary compound, Li_9CrN_5, and to remove nitrogen. Capsule tests were performed between 350 and 500°C. A large-scale batch test with staging was performed at 450°C. The following conclusions can be drawn:

1. Nitrogen removal from lithium using chromium surfaces is possible at temperatures above 400°C. The most favorable results from the capsule tests were obtained with processing temperatures of 450°C and chromium surface area-to-lithium volume ratios greater than 100 m^{-1}.

2. Nitrogen levels as low as 37 wppm were achieved in less than 30 h at 450°C by using a staged. large-batch process. The rate of nitrogen removal is primarily limited by the amount of chromium surface area provided for reaction to occur.

3. Contamination of the melt with elements from the SS. particularly nickel, can occur due to contact with SS at 450°C for prolonged periods of time. However. if warm trapping is followed with conventional cold trapping, metallic elements could be removed and lithium purification could be done in a single. inexpensive vessel with a higher degree of safety. as compared to hot gettering.

ACKNOWLEDGMENTS

The author expresses his appreciation to Dr. P. Hubberstey for his most insightful comment of October 1, 1987. which served as the impetus for this work: "Where did the nitrogen go?" Special thanks to Dr. P. F. Tortorelli for his discussions and collaboration on lithium purification and to Mr. E. E. Hoffman for his continued support of this research.

REFERENCES

1. A. C. Klein and W. F. Vogelsang. J. Nucl. Mater., **122 & 123 (1984) 1236.**

2. M. A. Abdou. Blanket Comparison and Selection Study, Report ANL/FPP-84-1, Argonne. National Laboratory. Argonne. Illinois. **1984.**

3. E. E. Hoffman. Corrosion of Materials by Lithium at Elevated Temperatures, ORNL/TM-**2674.** Martin Marietta Energy Systems, Inc., Oak Ridge Natl. Lab., **1959.**

4. P. Hubberstey. Liauid Metal Engineering and Technology, Vol. **2.** British Nuclear Energy Society, London, 1985. p.85.

5. M. G. Barker and S. A. Frankham. J. Nucl. Mater., **107 (1982) 218**

6. D. **L.** Smith and K. Natesan. Nucl. Technol. **22 (1974) 392.**

7. P. F. Tortorelli, J. Nucl. Mater., **155-157** (1988) 722.

8. J. H. DeVan, Ibid. **85 & 86 (1979) 249.**

9. P. Hubberstey and P. G. Roberts, Ibid **155-157 (1988) 694.**

10. G. E. Bell and M. A. Abdou. Fusion Nucl. Technol. **15** (1989) **315**

11. H. Bradley. R. B. Hand, E. E. Hoffman and T. P. Irwin. Report GESP-693. General Electric Company. 1971.

12. R. M. Yonco. E. Veleckis. and V. A. Maroni. J. Nucl. Mater. **57 (1975) 317.**

13. E. **E.** Hoffman. "Symposium on Newer Metals." ASTM Spec. Tech. Publ. **272 (1959). 195.**

14. H. U. Borgstedt. J. Nucl. Mater. **103 & 104 (1981) 693.**

15. H. **W.** Leavenworth and R. E. Cleary, Acta Metall. **9 (1961) 519.**

16. S. W. Strauss. J. L. White and B. F.Brown, Ibid. 6 (1958) **604**

17. V. R. Juza and J. Haug. Z. Anore. Allgem. Chem. **309 (1961) 276**

18. W. F. Calaway. Proceedines of 2nd International Conference on Liquid Metal Tech. in Energy Production. Richland. Washington. **1980 # 18.**

19. M. **G.** Barker, P. Hubberstey. A. T. Dadd. and S. A. Frankham. J. Nucl. Mater. **114 (1983) 143.**

20. M. G. Barker. S. **A.** Frankham, and N. J. Moon. Liauid Metal Tech. in Energy Production, **Vol. 2**, British Nuclear Energy Society, London, **1985** p. 77.

21. G. E. Bell, M. **A.** Abdou. and P. F. Tortorelli, Fusion Eng. Des. *8* (1989) **421.**

22. P. Hubberstey, Private Communication, October 1. **1987.**

23. G .E. Meadows and R. F Keough. J. Mater. Enerev Svst., **2 (1981) 44.**

24. D. **G.** Bauer. Kinetics of the Degradation of **316** Stainless Steel by Lithium. Ph.D. Thesis. University of Wisconsin-Madison. 1980.

25. T. C. Frianeza-Kullberg and D. J. Salmon. U. S. Patent No. **4,781,756.** November 1. **1988.**

7.0 SOLID BREEDER MATERIALS AND BERYLLIUM

IN-SITU TRITIUM RECOVERY FROM Li_2O IRRADIATED IN FAST NEUTRON FLUX - BEATRIX-II TEMPERATURE CHANGE SPECIMEN

O. D. Slagle and G. W. Hollenberg, Pacific Northwest Laboratory[a], T. Kurasawa, Japan Atomic Energy Research Institute, and R. A. Verrall, AECL Research

OBJECTIVE

To characterize the in situ tritium recovery behavior of Li_2O in the temperature range from 500 to 650°C during irradiation in a fast neutron flux.

SUMMARY

The BEATRIX-II irradiation experiment is an in-situ tritium release experiment to evaluate the stability and tritium release characteristics of Li_2O under fast neutron irradiation to extended burnups. A thin annular ring specimen capable of temperature changes was irradiated in Phase I of the experiment to a lithium burnup of 5%.

The primary emphasis of the test plan was to determine the effect and interrelationship of gas composition and temperature on the tritium recovery from Li_2O. Temperature changes in the range from 500 to 650°C resulted in a decreasing tritium inventory with increasing temperature and a series of specific temperature changes were carried out at intervals throughout the experiment to characterize the effect of burnup. Decreasing the amount of hydrogen in the sweep gas resulted in an increase in the tritium inventory in the Li_2O specimen. The tritium recovery during startup and shutdown was observed to be strongly influenced by the composition of the sweep gas.

PROGRESS AND STATUS

Introduction

The BEATRIX-II irradiation experiment is an in-situ tritium recovery experiment to evaluate the tritium release characteristics of Li_2O and to characterize its stability under fast neutron irradiation to extended burnups. This is an IEA sponsored experiment which is being carried out in the Materials Open Test Assembly of FFTF. The participants are Japan, Canada and the U.S. The in-situ tritium recovery experiment includes two specimens: a thin annular specimen capable of temperature changes and a larger temperature-gradient specimen. This paper will present the results for the temperature-change sample during Phase I of the experiment which consisted of 300 EFPD of operation equivalent to 5% lithium burnup.

Background

The design of the experiment and the operation of the system have been described previously.[1,2,3] BEATRIX-II Phase I consisted of three operational cycles: 85, 134 and 81 Effective Full Power Days (EFPD) of irradiation. During the first 85 EFPD of operation the tritium recovery rate from the temperature-change capsule was measured as a function of several environmental parameters: temperature, gas flow rate, and gas composition. The results of these tests have been described previously.[4,5] Temperature changes in the range from 500 to 650°C resulted in decreasing tritium inventory with increasing temperature. Lower gas flow rates resulted in slightly lower tritium recovery rates. Three different sweep gases were used: He with 0.1% H_2, He with 0.01% H_2 and pure He. Gas composition changes resulted in significantly larger changes in the tritium inventory than either flow rate or temperature changes and decreasing the amount of hydrogen in the sweep gas resulted in a decrease in the tritium recovery rate.

Experiment description

A description of the ring specimen and the irradiation conditions has been given previously.[3,4] The ring specimen is a thin-walled tube 8.9 cm long with an outer diameter of 1.84 cm and a wall thickness of 0.16 cm and a weight of 11.95 grams. Other characteristics of the specimen were: density - 80% TD, ^6Li enrichment - 61 at%, grain size ~5.5 microns and surface area - 600 cm^2/g.

The temperature is monitored/controlled by thermocouples located on the inner (hotter) surface of the specimen. The minimum achievable temperature of this surface was 550°C. The maximum temperature was chosen to be 100°C higher than this or 650°C. During irradiation at full power, the temperature difference across this specimen is calculated to be 40°C. The temperature of the specimen is controlled by changing the type of gas in the thermal-gap of the canister.',' Temperature changes occur in time periods less than 15 seconds. The total lithium burnup for the 300 EFPD irradiation was 5%.

'Pacific Northwest Laboratory is operated for the U.S. Department of Energy by Battelle Memorial Institute under Contract DE-AC06-76RLO 1830.

Results

During the first 85 EFPD cycle the test plan took a broad overview of the effect of all the parameters. During the remaining two operational cycles the primary emphasis of the test plan was on the effect and interrelationship of gas composition and temperature on the tritium recovery from Li_2O. In addition, a series of specific temperature changes were carried out at intervals throughout the experiment to characterize the effect of burnup.

Gas composition/temperature

The effect of gas composition on tritium recovery was measured by varying the gas composition between three different concentrations of hydrogen in the helium sweep gas: 0, 0.01%, and 0.1%. The temperature dependence of the gas composition dependence was studied by carrying out the gas composition changes at 550 and 650°C.

A series of gas changes were carried out in the order of: He-0.1%H_2, 2,4 or 8 days in He, 3 days in He-0.01%H_2, to He-0.1%H_2. An example of the effect of gas composition changes temperature on tritium recovery curves obtained during this series of gas changes is shown in Figure 1. For the two runs shown in Figure 1 the sequence of gas changes was from the reference gas of He-0.1%H_2, to helium for 8 days, to He-0.01% H_2 for 3 days, and then back to He-0.1%H_2. As seen previously,[4,5] decreasing the hydrogen concentration results in a sharp decrease in the tritium recovery rate followed by a slow recovery, while increasing the hydrogen concentration results in a tritium recovery peak. The tritium recovery gas composition changes were made at the temperatures of 550 and 650°C.

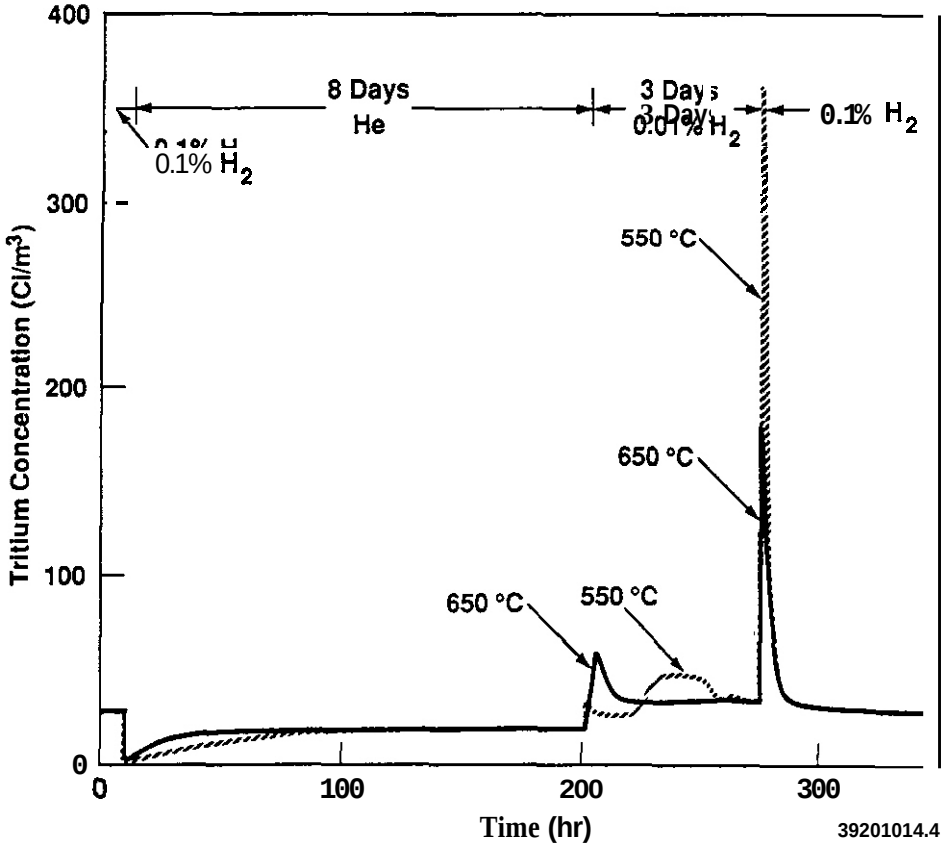

Fig. 1. Tritium concentration for a series of gas composition changes in the order of He-0.1%H_2, 8 days in He, 3 days in He-0.01%H_2, He-0.1%H_2 for temperatures of 550 and 650°C.

Gas changes from He to He-0.01% H_2 result in smaller initial recovery peaks at 550°C than at 650°C. In addition to the smaller initial recovery peak at 550°C, however, there is an additional delayed recovery peak which is much broader than the initial peak and extends over a time period on the order of a day. This suggests that at the lower temperature the tritium release from the specimen may come in two separate stages rather than the single event seen at the higher temperature.

The gas composition changes from He-0.01%H_2 to He-0.1% H_2 resulted in larger recovery peaks at 550°C than at 650°C. The larger peak at 550°C could result from residual tritium that was not released during the 3 days in He-0.01% H_2 because the specimen had not reached steady state at the lower temperature. Hence, the tritium inventory remained high in He-0.01% H for the specimen at the lower temperature and a larger change in inventory occurred when the gas composition was changed from He-0.01%H_2 to He-0.1%H_2. Alternatively, the differences in the tritium recovery peaks may indicate the sensitivity of the steady state tritium inventory in the different gas compositions to the temperature.

A more abbreviated series of gas changes were carried out in the order of: He-0.1%H_2, 2 days in He-0.01%H_2, 4 days in He, He-0.1%H_2. The tritium recovery curves at 550 and 650°C were very similar to each other, with decreasing recovery rates after the gas change transitions from He-0.1%H_2 to He-0.01%H_2 and from He-0.01%H_2 to He and with a tritium recovery peak for the transition from He to He-0.1%H_2. The primary difference is that at the higher temperature the recovery curves approached steady state faster and

the final recovery peaks for the transition from He to He-0.1% H_2 were sharper and occurred in a shorter time period.

Temperature/gas composition

The effect of temperature and temperature change on the tritium recovery rate was characterized using a sequence of temperature changes in the order of 650-600-550-600-650-550-650°C. The effect of sweep gas composition on the tritium recovery during this temperature sequence was studied in each of the three sweep gases: He-0.1%H_2, He-0.01%H_2 and He. Figure 2 compares recovery curves for a temperature change from 550 to 650°C in the three different sweep gases. The change in tritium inventory for He-0.1%H_2 is the smallest and the tritium recovery peak for this sweep gas consists of two peaks while the recovery curves for He and He-0.01%H_2 are single peaks that are similar to each other in shape and size. The double peak for He-0.1%H_2 is similar to that described previously.[4] The first peak is associated with the recovery of the reduced form, HT, and the second peak is associated with the oxidized form, HTO. This suggests that for the sweep gases containing lower concentrations of hydrogen the recovered tritium occurs predominately in the reduced form.

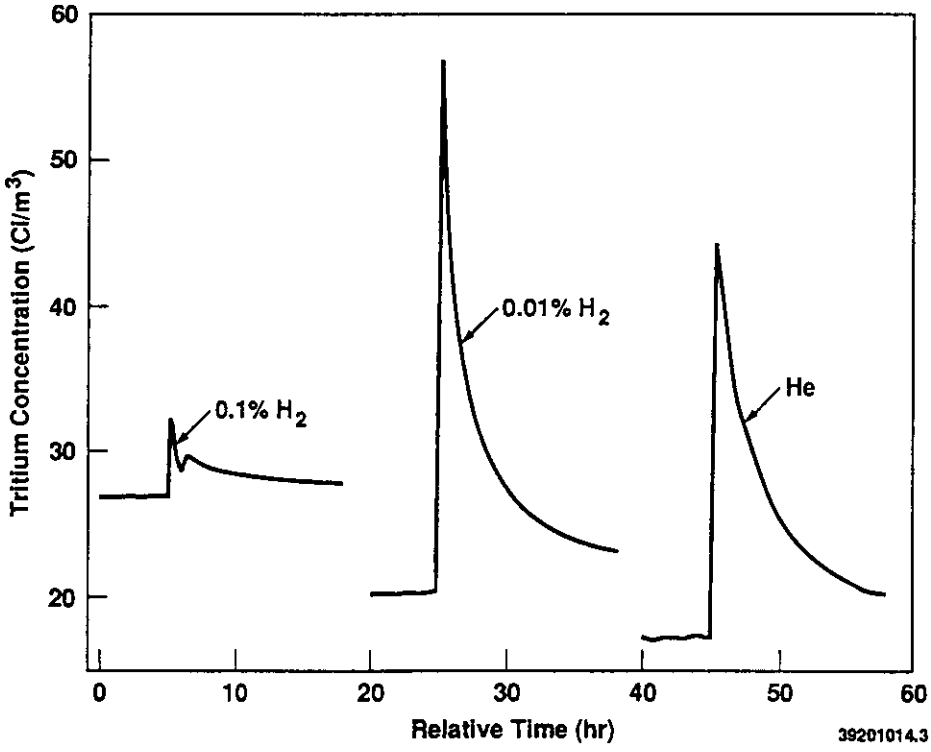

Fig. 2. Tritium concentration during temperature changes from 550 to 650°C in sweep gas compositions of He-0.1%H_2, He-0.01%H_2, and He.

Burnup effects

A series of temperature changes in the order of 650-600-550-650-550-650°C were carried out at different times in the experiment to characterize the effect of burnup in He-0.1% H_2. This was done after irradiation periods of 80, 215 and 290 EFPD. Figure 3 compares the tritium recovery curves measured during the final 550 to 650°C temperature change in the sequence as observed at the three different burnups. In general, it was found that early in the experiment a double peak was associated with a temperature change. This double peak transformed towards a single peak with increasing burnup. Since the first peak is due to the recovery of HT while the second is due to HTO, the observed change suggests that the amount of HTO recovered relative to amount of HT recovered, decreases with increasing burnup for a given temperature change. However, the observed change in peak shape may also be related to moisture reduction in the Li_2O specimen or in the tritium recovery system.

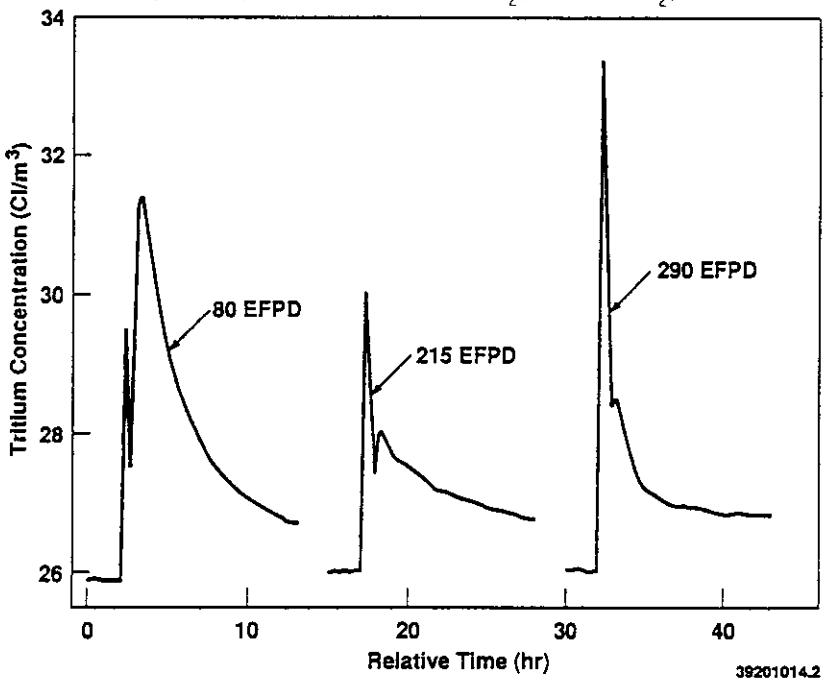

Fig. 3. Tritium concentration during temperature changes from 550 to 650°C after irradiation periods of 80, 215 and 290 EFPD.

Reactor shutdown and startup

Reactor shutdown and startup sequences provide opportunities to study the effect of changes in the

tritium generation rate and temperature on tritium recovery from the ring specimen. The effect of gas composition on the behavior of the specimen to a changing neutron flux was carried out during reactor startup and shutdown. Normally shutdowns/startups were carried out in the reference gas of He-0.1%H_2 but the effect of sweep gas composition on the behavior was studied by placing the specimen in helium sweep gas for two days prior to the shutdown of the second operational cycle and continuing the helium sweep gas through the startup of the third operational cycle.

During reactor startup/shutdown in reference gas, He-0.1% H_2, the observed tritium recovery curves are very similar to the temperature curves. This is as expected since the temperature is related directly to heat (tritium) generation and tritium recovery is related directly to tritium generation. However, using helium as a sweep gas during reactor shutdown was found to significantly affect the tritium recovery behavior observed. Figure 4 compares the recovered tritium during the reactor shutdowns in helium with the inner specimen temperature. As the neutron flux decreased, the specimen temperature and the recovered tritium both initially decreased as the tritium generation rate decreased, but later the recovered tritium concentration increased in direct contrast to the continual decrease in the generation rate. The increase in the tritium recovery with decreasing temperature first occurred between an inner specimen temperature of 500 and 475°C. This type of behavior continued until the an inner temperature of 350°C was reached.

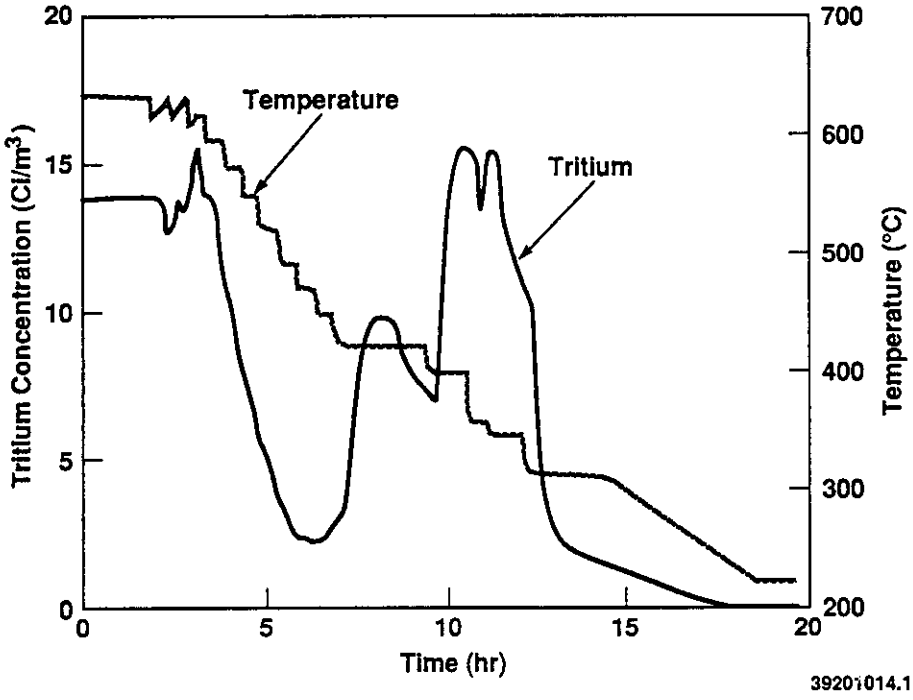

Fig. 4. Recovered tritium concentration and temperature of the ring specimen during a reactor shutdown in a helium sweep gas.

During reactor startup in helium, the tritium recovery behavior was also found to be different than observed for He-0.1% H2. Because the power increases during startup were in larger increments than those during shutdown, the change in behavior is not as distinctive. However, an increase in neutron flux and temperature at approximately 500 to 525°C resulted in a decrease in the recovered tritium. Above 525°C the tritium recovery rate increased with increasing neutron flux.

The anomalous tritium recovery behavior of the ring specimen during shutdown and startup in helium occurs in a temperature range on the order of the melting point of LiOH. In this temperature range the presence of LiOH is an important factor in determining the tritium inventory.[6,7] Two possible explanations for the present tritium recovery observations involve LiOH behavior and these are LiOH dissolution in Li_2O and the variation of the water vapor pressure over LiOH dissolved in Li_2O.

Because the moisture levels in the sweep gas are typically less than 0.1 Pa, it is expected that the amount of LiOH in the specimen remains below the solubility limit as the temperature is decreased. Therefore LiOH dissolution in Li_2O is not expected to be a factor in the tritium recovery.

An alternative explanation is associated with the water vapor pressure associated with LiOH dissolved in Li_2O. The results of a study by Norman and Hightower[8] indicate that for stable solid solutions of LiOH in Li_2O, i.e., less than the solubility limits, the water vapor pressure versus temperature curves exhibit a maximum in the temperature range below the two-phase boundary. That is, for a given amount of LiOH dissolved in Li_2O, at a temperature less than the two-phase boundary, a temperature decrease results in an increase in the equilibrium water vapor pressure. After reaching a maximum, a further decrease in temperature results in a decrease in the water vapor pressure. The observed peak in the tritium recovery curve during shutdown could then be associated with this peak in the water vapor pressure with decreasing temperature that results from the LiOH (or LiOT) dissolved in Li_2O. It is to be noted that the temperature at which this peak occurs increases with decreasing dissolved LiOH (LiOT).

Discussion

Changes in the specimen temperature either from changes in the thermal gap of the capsule (Figure 2) or from changes in neutron flux (Figure 4), produced larger changes in tritium inventory when the sweep gas was helium instead of He-0.1% H_2. In these data, the peak in the tritium recovery during shutdown occurs in the temperature region near 500°C and one explanation is that it is related to LiOH dissolved in Li_2O. In a previous paper,[5] a similar behavior was observed for the temperature-gradient specimen when shutdown occurred in He. However the recovery peak for the temperature gradient specimen was associated with much higher temperatures and the behavior was attributed to tritium/hydrogen dissolved in the lattice. One difference between helium sweep gas and He-0.1% H_2 sweep gas is the tritium/hydrogen ratio. A tritium concentration of 25 Ci/m^3 in He-0.1% H_2 is equivalent to a tritium/hydrogen ratio of approximately 1/100. In a helium sweep gas, where only trace amounts of hydrogen are present, the tritium/hydrogen rdtio becomes very large. If the Li_2O specimen is in equilibrium with the sweep gas it is expected that the same tritium/hydrogen ratio would be associated with tritium/hydrogen dissolved in the bulk of the material and with the tritium/hydrogen adsorbed on the surface. On this basis a larger tritium inventory is expected in a helium sweep gas and thus larger changes in the inventory are possible. This line of reasoning can only serve as a first approximation, however, since the total amount of tritium/hydrogen in the specimen would be expected to be less for lower hydrogen partial pressures such as in a helium sweep gas.

Sweep gas composition changes affected the tritium recovery significantly more than temperature change. This suggests that the interaction of gas and solid is more important than the thermally activated diffusion processes. Further definition of these processes will be the objective of future testing and analyses.

CONCLUSIONS

The results of the BEATRIX-II, Phase I irradiation experiment have provided an extensive data base on tritium recovery that gives insight into the in-situ tritium release characteristics of Li_2O for lithium burnups to 5%. The particular implications of the results are:

1. Decreasing the temperature directly affects the shape/size of the tritium recovery peaks observed during gas composition changes involving an increase in the hydrogen concentration and in several instances the lower temperatures gave delayed recovery peaks.

2. In general, reducing the amount of hydrogen in the helium sweep gas resulted in a larger change in tritium inventory during a given temperature transients and also resulted in a higher percentage of the recovered tritium being in the reduced form (HT).

3. The form of the tritium recovered, that is the amount of HT versus HTO, during a given temperature transient was found to change during the experiment. This could be due to burnup effects in the specimen but alternatively may result from changes in the tritium handling system such as lower surface moisture.

4. The tritium recovery during startup and shutdown was strongly influenced by the composition of the sweep gas.

FUTURE WORK

Post irradiation examination will be carried out to determine the actual tritium inventory of Li_2O at reference condition at the end of the experiment, the transport of Li_2O and the physical stability of the specimen during the irradiation. The next phase of the BEATRIX-II experiment (Phase II) includes a similarly configured ring specimen with a thinner wall and a higher density which results in a smaller temperature gradient across the specimen.

REFERENCES

1. G. W. Hollenberg, T. Kurasawa, H. Watanabe, S. E. Berk, I. J. Hastings, and D. E. Baker, Fusion Technology 15, 1349-1354 (1989).

2. R. J. Puigh, G. W. Hollenberg, T. Kurasawa, H. Watanabe, I. J. Hastings, J. M. Miller, S. E. Berk, R. E. Bauer, and D. E. Baker, In Proc. of the 15th Symposium on Fusion Technology, edited by AM Van Inger, A. Nigsen-Vis, and HP Kippel, pp 1282-1286, September 19-23, 1988, Utrecht, The Netherlands. Elsevier, Netherlands.

3. D. E. Baker, T. Kurasawa, J. M. Miller, and O. D. Slagle, Fusion Technolow 19, 1640-1645 (1991).

4. T. Kurasawa, O. D. Slagle, G. W. Hollenberg, and R. A. Verrall, Fusion Technology 19, 931-937 (1991).

5. T. Kurasawa, O. D. Slagle, G. W. Hollenberg, and R. A. Verrall, presented at the American Ceramic Society Meeting, April 28-May 2, 1991, Cincinnati, Ohio. PNL-SA-19029, Pacific Northwest Laboratory, Richland Washington.

6. M. C. Billone, C. C. Lin, H. Attaya, and Y. Gohar, Fusion Technology **19,** 976-983 (1991).

7. M. Tetenbaum and C. E. Johnson, J. Nucl. Mater. 126 (1984) 25.

8. J. H. Norman and G. R. Hightower, J. Nucl. Mater. 122 & 123 (1984) 913

8.0 CERAMICS

RADIATION-INDUCED CHANGES IN THE PHYSICAL PROPERTIES OF CERAMIC MATERIALS -- S.J. Zinkle (Oak Ridge National Laboratory) and E.R. Hodgson (EURATOM/CIEMAT Fusion Association, Madrid, Spain)

OBJECTIVE

The objective of this report is to review the effects of radiation on the electrical conductivity, loss tangent, and thermal conductivity of ceramics.

SUMMARY

The results from recent studies on radiation-induced changes in the electrical conductivity, loss tangent, and thermal conductivity of ceramics are reviewed, with particular emphasis on in-situ data obtained during irradiation. The in-situ measurements have found that the physical property degradation during irradiation is generally much more severe than indicated by post-irradiation measurements. In particular, permanent degradation in the electrical resistivity may occur after irradiation to damage levels of $< 10^{-3}$ displacements per atom (dpa) for temperatures near 450°C. This radiation-induced electrical degradation (RIED) is observed only if an electric field is applied during the irradiation.

PROGRESS AND STATUS

1. Introduction

It has become increasingly apparent in recent years that radiation-induced changes in the physical properties of ceramics will have a significant impact on the design of fusion reactors. Although ceramic components constitute only a small volume fraction of a fusion reactor plant (< 1%), virtually every aspect of the heating, control, and diagnostic measurement of the fusion plasma is dependent on the satisfactory performance of a ceramic material. The physical properties of importance for fusion ceramics include thermal conductivity, electrical conductivity and dielectric breakdown strength under dc or ac conditions, and the loss tangent at high frequencies. Table 1 summarizes the anticipated operating environments for insulating ceramics in a fusion reactor. The operating conditions span a wide range of flux, fluence, and electric fields. Of particular importance is the use of ceramics in various diagnostic components, where there is concern about possible decalibration of instruments due to gradual degradation in the electrical resistivity.

Table 1. Typical operating conditions for ceramics in the proposed ITER fusion reactor. Operating temperatures in a commercial fusion reactor will generally be higher.

Component	Electric Field (V/mm)	Irradiation Flux		Temperature, °C
		Displacive (dpa/s)	Ionizing (Gy/s)	
Diagnostics (magnetic coils, coaxial cables, insulators)	10-10,000	$\sim 10^{-8}$	~1000	100-350*
Active coil	~500	5×10^{-8}	125	~200
Divertor coil	~500	$<10^{-7}$	~1000	<200
1st wall current break	~20	$\sim 10^{-7}$	~3000	>300
Vacuum vessel current break	0.3	$<10^{-8}$	~200	100
Neutral beam insulators	~1000	$\sim 10^{-10}$	≤10	~50
RF windows (ICRH)	<1000	$<10^{-9}$	<100	<300
Ceramic breeder insulators	~500	$<10^{-7}$	~1000	~400

*Up to 1500°C for carbon tile diagnostics.

The topic of radiation effects in ceramics has been the subject of several previous reviews,[1-10] with recent emphasis given to fusion reactor applications.[3-10] Most of the studies on ceramics have concentrated on post-irradiation analyses of the microstructure, density, and strength changes, in a manner analagous to radiation effects studies on metals. It has generally been observed that irradiation causes a modest degradation in the structural and physical properties, although spectacular reductions were occasionally observed. In some cases, improvements in properties (e.g. higher electrical resistivity) were reported.

2. Mechanical Properties and Structural Changes

A rather extensive data base has been established on mechanical property and volumetric changes in ceramics following irradiation with fast neutron fluences up to about 3 x 10^{26} n/m^2 (~30 dpa).[1-10,13-15] These bulk measurements have been complemented by numerous transmission electron microscopy investigations (e.g., see reviews in refs. 8,16,17). The mechanical strength and Weibull modulus of ceramics are generally degraded by irradiation, with significant (> 20%) decreases typically occurring after doses > 1 dpa.[10,14] Substantial volumetric swelling also develops at comparable doses for elevated temperature irradiations, and anisotropic swelling in materials such as Al_2O_3 and BeO can produce microcracking and dramatic strength decreases.[1,2,8] Several studies have found that spectral differences between fusion and fission reactors may be significant.[18-20] In particular, the available evidence indicates that the increased concentration of transmutation products such as H, He, and C in a fusion environment will greatly enhance the amount of void swelling in swelling resistant ceramics such as $MgAl_2O_4$.[19,20]

3. Irradiation Effects on Physical Properties

Whereas radiation-induced volumetric changes and reduction in mechanical strength are significant in ceramics for damage levels > 1 dpa, substantial degradation in the physical properties may occur at damage levels < 10^{-3} dpa. In the following sections, the influence of irradiation on the electrical conductivity, loss tangent, and thermal conductivity is reviewed, with emphasis on the available in-situ data. Since the physical properties are sensitive to the concentrations of point defects and conduction electrons, it is natural to expect that these properties may be different during irradiation compared to the post-irradiation value.

3.1 Electrical Conductivity

For most insulator applications, the electrical conductivity during irradiation should be less than 10^{-4} S/m in order to prevent dielectric breakdown due to excessive joule heating. However, even for low power applications typical for many diagnostic components, it is desirable to keep $\sigma < 10^{-4}$ S/m to prevent instrument decalibration due to spurious leakage currents.

There is an extensive data base documenting the instantaneous increase in the electrical conductivity of insulating ceramics induced by exposure to ionizing radiation.[1,9,12,21-41] This radiation-induced conductivity (RIC) is due to the excitation of valence electrons into the conduction band, and has been observed during x-ray, gamma ray, electron, proton, and fission neutron irradiations. The electrical conductivity during irradiation is given by

$$\sigma = \sigma_o + KR^d \quad , \tag{1}$$

where σ_o is the conductivity in the absence of irradiation, and R is the ionizing dose rate. The value of the proportionality constant K has a strong material dependence, with typical values at room temperature ranging from 10^{-15} to 10^{-9} s/Gy-ohm-m for polymers and ceramics.[27,31,41,48] The value of the radiation dose rate exponent, d, is generally between 0.5 and 1.0, although supralinear values as high as 1.6 have been reported.[9,12,26,27,31,37,48] The value of the dose rate exponent is determined by the balance between production of conduction electrons by ionization, and trapping and recombination of electron-hole pairs. The general aspects of the observed RIC behavior can be explained by multitrap photoconductivity theory.[9,12,21,26,27,37]

Figure 1 shows a typical example of the temperature-dependent RIC of a ceramic insulator during exposure to ionizing radiation.[30] The electrical conductivity is weakly dependent on temperature at low temperatures (it may either decrease[11] or increase[23,26,30] with increasing temperature). From a technological perspective, it may be concluded that the RIC increases are significant ($\sigma \sim 10^{-7}$ S/m for a fusion-relevant irradiation flux) but can be accommodated with appropriate reactor designs.

Several studies have investigated the electrical conductivity of oxide ceramics during extended irradiation, with and without an applied electric field.[1,12,24-26,28,32-41] It is generally observed that the RIC decreases in specimens irradiated without an applied field,[1,26,33,40,41] which may be attributable to a buildup of electron traps produced by the displacement damage. On the other hand, recent work has shown that large, irreversible changes in the electrical conductivity may develop in oxide ceramics if an electric field is applied during irradiation.[12,28,32-36,39] This radiation-induced electrical degradation (RIED) develops

at moderate temperatures (300 to 550°C) after irradiation to damage levels of only 10^{-5} to 10^{-2} dpa, and occurs only if displacement damage and an electric field are simultaneously present. Figure 2 shows the typical fluence-dependent behavior of the electrical conductivity[12] of Al_2O_3. The base conductivity σ_o measured in the absence of radiation steadily increases with increasing dose and eventually becomes much larger than the initial RIC.

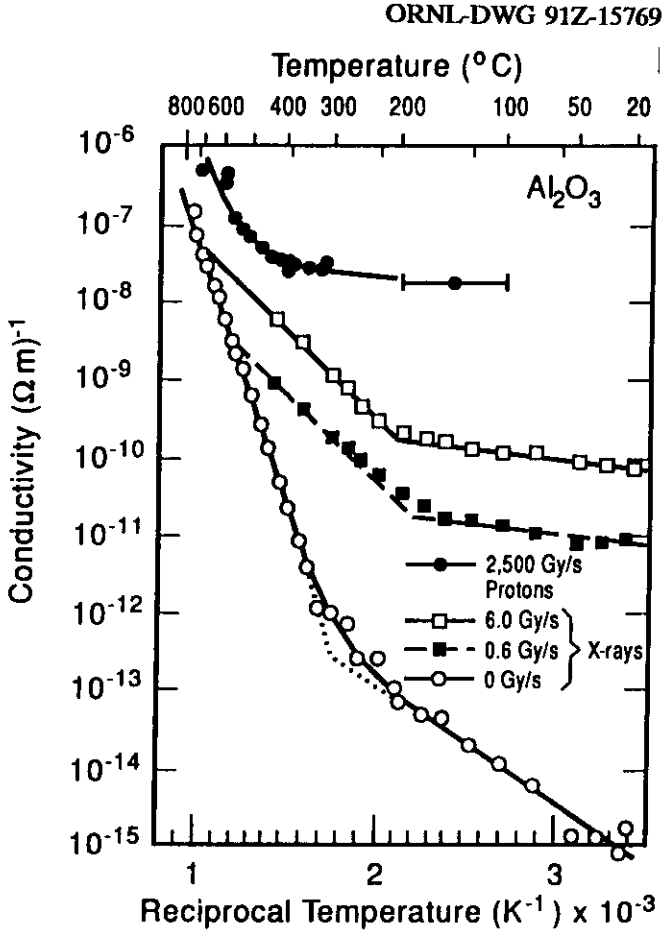

Fig. 1. Electrical conductivity of polycrystalline alumina vs. reciprocal temperature, with and without ionizing irradiation.[30]

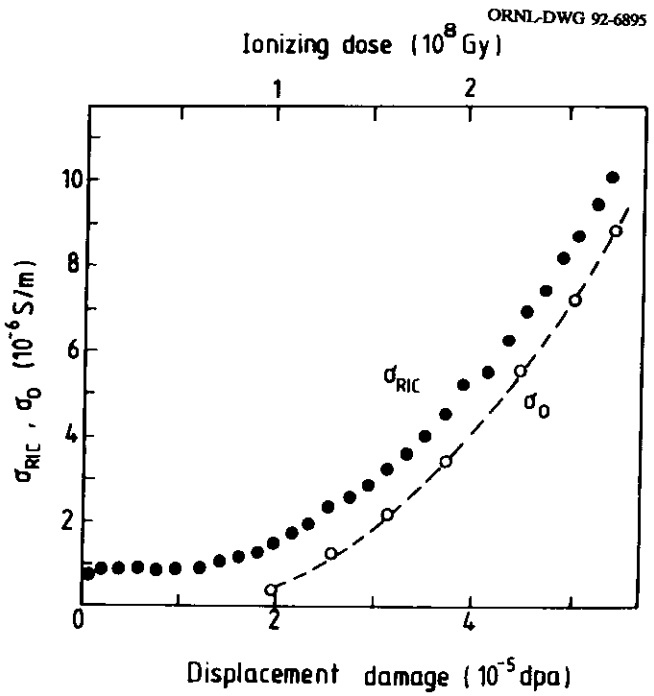

Fig. 2. Fluence-dependent behavior of the electrical conductivity measured in-situ during 1.8 MeV electron irradiation at 450°C with an applied dc electric field of 130 V/mm and an ionizing dose rate of 2800 Gy/s (ref. 12).

Figure 3 shows the base conductivity σ_o in Al_2O_3 after electron irradiation to a damage level of 4 x 10^{-5} dpa.[12,33]. The electrical conductivity of the specimen irradiated without an applied electric field was comparable to the nonirradiated condition, with an activation energy of ~1.5 eV. The specimen irradiated with an applied electric field showed a dramatic increase in the base conductivity and the activation energy was reduced to 0.18 eV, which suggests a change in the conduction mechanism. Pells[36] has made similar studies of RIED in Al_2O_3 and $MgAl_2O_4$ after proton irradiation with an applied field. The conductivity activation energy decreased in some cases to < 0.1 eV, which indicates the presence of electronic conductivity.

Significant degradation in the electrical resistivity of Al_2O_3 has been observed following electron irradiation even for electric fields as low as ~10 V/mm (refs. 34,35). However, an accelerated rate of degradation was observed if the electric field applied during the irradiation was above ~60 V/mm. In contrast to the well-known phenomenon of thermal-induced dielectric breakdown in non-irradiated ceramics,[42] RIED has been observed to be essentially identical for dc and ac fields for frequencies as high as 126 MHz (ref. 35). A comparable degradation rate has been observed for both single and polycrystals.[32]

The available data indicate that the severity of RIED may be strongly dependent on irradiation temperature and dose rate. Little or no degradation occurred in Al_2O_3 or Y_2O_3 for neutron doses of 0.01 to 0.1 dpa at temperatures of 700 to 1100°C with an applied field of ~40 V/mm (refs. 25,45) (the applied electric field strength was not given in ref. 25). No electrical degradation was observed in Al_2O_3 and $MgAl_2O_4$ during proton irradiation with an electric field of 500 V/mm to a damage level of ~10^{-3} dpa for irradiation temperatures less than 400 and 300°C, respectively, whereas substantial degradation occurred in both materials at 500°C.[36] Figure 4 shows the temperature-dependent base conductivity measured in Al_2O_3 following electron

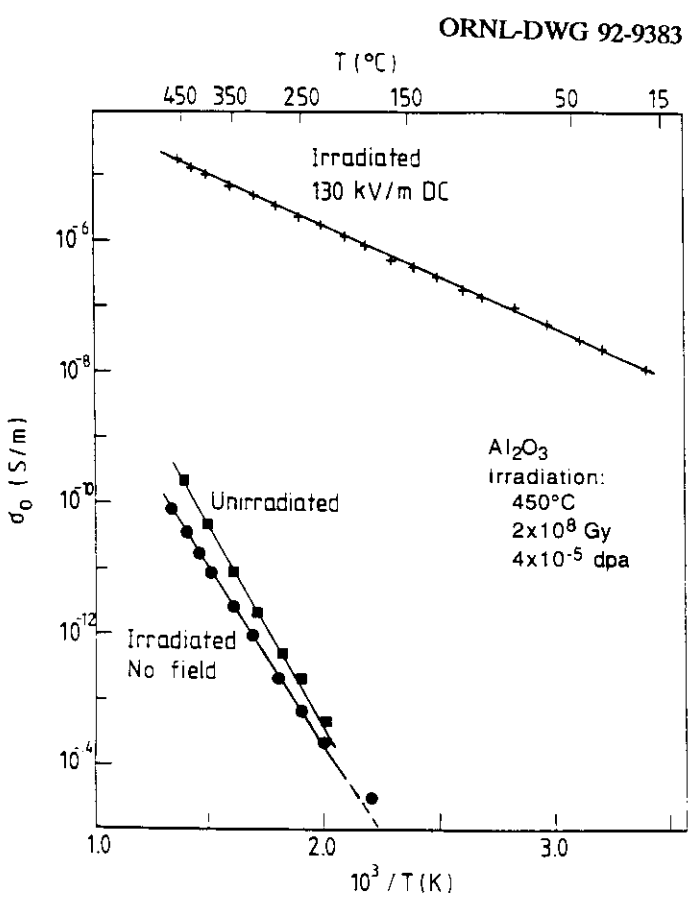

Fig. 3. Comparison of the postirradiation electrical conductivity of Al_2O_3 irradiated with 1.8 MeV electrons with and without an applied electric field (refs. 12,33, and unpubl. data).

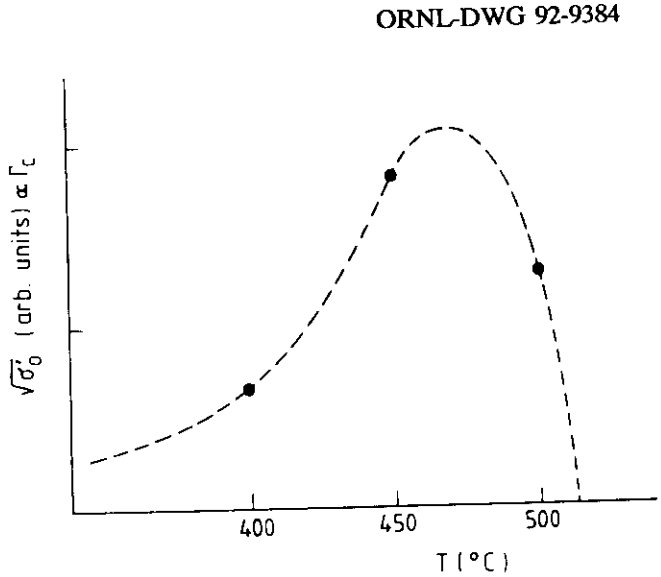

Fig. 4. Temperature dependence of radiation induced electrical degradation in Al_2O_3 after irradiation for 30 h with 1.8 MeV electrons with an applied electric field of 130 V/mm and a dose rate of 2800 Gy/s (refs. 32,33). The dashed curve shows the general theoretical temperature dependence for colloid formation (not a fit to the data).

irradiation to a damage level of 6 x 10^{-5} dpa with an applied electric field of 130 V/mm (refs. 32,33). The dashed curve shows the general temperature dependence predicted for the growth of colloids (metallic precipitates) in irradiated ionic crystals.[4,43,44] Colloid formation occurs in irradiated ionic materials as the result of clustering of anion vacancies (F centers), which produces microscopic regions containing only the complementary metal cations. The basic equations describing colloid aggregation are directly analogous to the chemical rate theory equations used to model void swelling in metals. Although it has not yet been directly shown that colloid formation is responsible for the observed RIED in oxide ceramics, the change in the activation energy for electrical conduction[12,33,36] and the flux dependence of RIED[32,33] support this mechanism.

A comparison of the RIED data obtained from different irradiation sources indicates that the irradiation spectrum may have some influence, although systematic trends are not apparent.[12,24,25,28,32-39,45] There are some indications that radiation fields that have high ratios of ionizing to displacive radiation (e.g., electrons and protons) produce an acceleration of the RIED compared to neutron irradiation. However, all of the available results indicate that a large, irreversible degradation of the electrical resistivity occurs in oxide ceramics at very low damage levels (10^{-5} to 10^{-2} dpa) at irradiation temperatures between 350 and 500°C when an electric field is applied during the irradiation.

3.2 Dielectric Properties at High Frequencies

The loss tangent (tan δ) is a measure of the amount of power absorbed in a dielectric material from an incident electromagnetic wave, which is of particular importance for the ceramic windows and feedthroughs associated with resonant frequency heating components for fusion reactors. The loss angle, δ, is related to the phase difference between the applied ac field and the resulting current. For an ideal loss-free dielectric, the current leads the voltage by 90° and the loss angle δ = 0 (ref. 46). Integration of the product of the current and voltage yields the power absorbed in low-loss dielectrics:

$$P = \omega \epsilon_0 \epsilon' \tan\delta E^2 \quad , \qquad (2)$$

where ω is the angular frequency of the ac electric field with rms amplitude E, and ϵ_0 and ϵ' are the free space and dielectric permittivities. According to fusion design analyses, the dielectric loss tangent for ion cyclotron (~100 MHz) and electron cyclotron (~100 GHz) resonance heating applications should be less than 10^{-3} and 10^{-6}, respectively.

The value of tan δ for low-loss dielectrics is dependent on temperature and frequency;[9,10,46-49] a typical value for a high-quality ceramic at room temperature is tan δ ~10^{-4}. The low value of tan δ required for electron cyclotron heating systems can only be achieved in present dielectrics by cooling to cryogenic temperatures. There are two major mechanisms responsible for energy losses in dielectrics:[*,**]

$$\tan\delta = \frac{\sigma}{\epsilon'\epsilon_0\omega} + \frac{\chi''}{\epsilon'} \qquad (3)$$

The first term represents electrical conductivity losses, which can be significant in ceramics during irradiation (cf. section 3.1) but becomes negligible for frequencies above ~100 MHz due to the inverse dependence on frequency.[40,46,48] The second term in Eq. 3 represents polarization losses, where χ'' is the imaginary part of the susceptibility.[**] Resonances in the polarization losses occur at frequencies corresponding to electron, ion, and defect jump polarizations?.[**] In practice, the widths of these resonances are very large due to a distribution of relaxation times, and tan δ varies slowly with frequency at frequencies relevant for plasma heating.[**]

As noted in previous reviews,[9,10] there have been relatively few studies of radiation-induced changes in the dielectric properties of ceramics. Most of these studies involved postirradiation measurements on specimens that were neutron irradiated at elevated temperatures. The post-irradiation data indicate that radiation-induced changes in the permittivity are generally very small (~1 to 5%), with either slight increases[13,48,50,52] or decreases[**] reported. The loss tangent was observed to increase in all irradiated materials studied, but the magnitude of the increase depended on the material, irradiation conditions, and measurement frequency.[9,10,13,41,48,50-53] The amount of increase was generally larger for the lower irradiation temperatures. Neutron irradiation to damage levels < 0.1 dpa at 70 to 200°C increased the loss tangent of Al_2O_3 by about a factor of three to ~10^{-3} for frequencies of 30 MHz to 35 GHz (refs. 48,52).

Several in-situ loss tangent measurements have been performed on ceramics during proton[40,41,54] or neutron[55,56] irradiation near room temperature at frequencies ranging from near dc to 10 GHz. Cryogenic in-situ tests at a frequency of 1 kHz have also been performed during neutron irradiation on organic dielectrics with relatively high loss factors?[**] These in-situ studies have found that large transient increases in the loss tangent may occur under certain conditions. Figure 5 shows the loss tangent of two ceramics measured in-situ at 100 MHz during pulsed neutron irradiation.[56] Most of the increase and subsequent decay of the loss tangent during the pulsed irradiation may be attributed to radiation-induced conductivity (cf. Eq. 3). At higher frequencies (1 to 10 GHz), where the electrical conductivity contribution to tan δ is reduced (Eq. 3), the loss tangent of a wide range of ceramics increased only slightly during pulsed neutron irradiation at a damage rate of ~10^{-5} dpa/s.[55]

Several studies have determined that significant annealing of the induced damage in ceramics may occur at room temperature.[40,41,53] For example, postirradiation measurements performed on a range of ceramics irradiated with protons to damage levels of ~2×10^{-2} dpa found that a substantial part of the loss tangent increase at 100 MHz was recovered within a matter of hours.[**] This indicates that postirradiation measurements of the loss tangent may be an underestimate of the in-situ value even at high frequencies where the in-situ electrical conductivity contribution is small.

Buckley and Agnew[54] have recently studied the effect of accumulated damage on the in-situ loss tangent of Al_2O_3. As shown in Fig. 6, the loss tangent showed a steady increase during proton irradiation at 300 K for damage levels greater than ~10^{-4} dpa. The value of tan δ as measured in-situ became unacceptably high (>10^{-3}) at damage levels on the order of 10^{-3} dpa. This degradation rate in the loss tangent is higher than postirradiation measurements would indicate, and may be due to the absence of postirradiation annealing effects.[**] Alternatively, the rapid degradation shown in Fig. 6 may also be associated with the ~10 V/mm electric field that was applied during the irradiation. The results of Hodgson[35] indicate that the application of even this small electrical field could cause significant degradation of the electrical properties over a wide frequency range. Additional in-situ measurements performed over a wide temperature range and in different irradiation spectra are needed to further examine this issue.

3.3 Thermal Conductivity

A high thermal conductivity is desirable to minimize the influence of thermal stresses in ceramic components during fusion reactor operation. The thermal conductivity of ceramic insulators is controlled by phonon scattering.[58,59] In contrast to metals, heat conduction in ceramics by electrons is negligible compared to the lattice heat conduction even during highly ionizing irradiation conditions which produce enhanced levels of conduction electrons (RIC). Numerous postirradiation

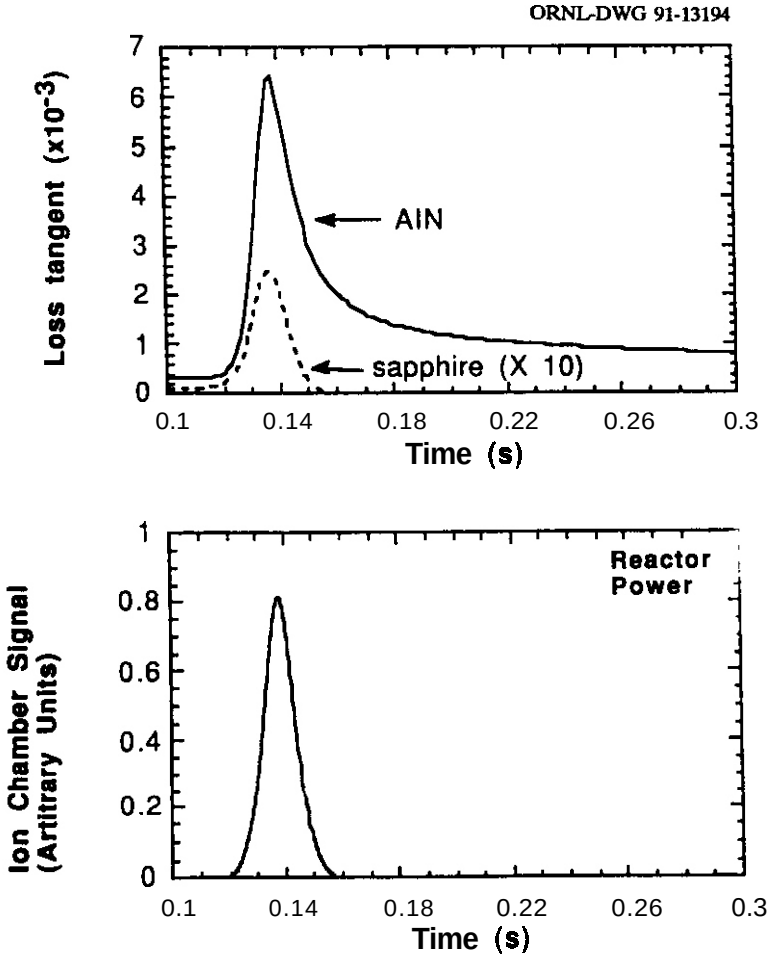

Fig. *5.* **Loss** tangent of **Al O,** and **AlN** at a frequency of 100 MHz measured in-situ during pulsed fission reactor irradiation at room temperature.' The reactor power pulse is shown on the same time scale. **The** peak ionizing and displacive radiation fields were *6* x 10^4 Gyls and 1.8 x 10^{-7} dpa/s, respectively.

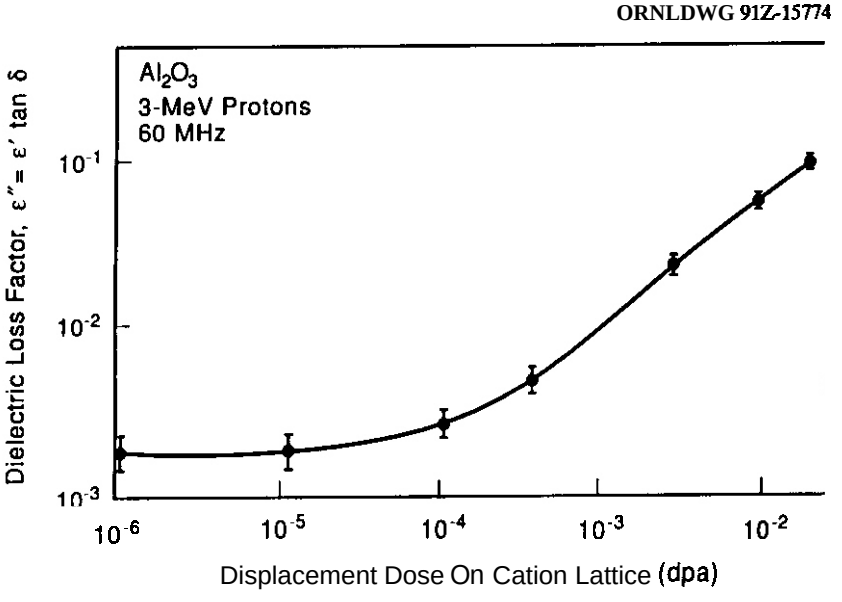

Fig. *6.* Dielectric loss factor of Polycrystalline Al_2O_3 at a frequency of 60 MHz measured in-situ during 3-MeV proton irradiation near room temperature.[54]

measurements performed on a wide range of ceramics have demonstrated that the thermal conductivity may he significantly degraded by neutron irradiation.[1,2,5,8,10,60-70] The thermal conductivity measured at room temperature is generally observed to saturate at 10 to 50% of the preirradiation value for damage levels greater than about 0.1 dpa. Irradiation and/or measurement at elevated temperatures produces proportionately less degradation in the thermal conductivity.

The radiation-induced decrease in the thermal conductivity is much more severe at low temperatures than at room temperature.[67,69,70] As shown in Fig. 7, the thermal conductivity of single crystal Al_2O_3 at cryogenic temperatures is initially very high (up to 15 times the room temperature copper value). However, neutron irradiation near −50 °C to a damage level of ~5 x 10^{-3} dpa reduced the peak conductivity to ~3% of its nonirradiated value.[67] The low-temperature in-situ data by McDonald[69] on irradiated BeO suggests that the rate of degradation shown in Fig. 7 would have been significantly faster if the irradiation was conducted at cryogenic temperature: Irradiation of BeO at 350 K[68] required 16 times higher fluence to produce the same thermal conductivity degradation observed after irradiation at 90 K.[69] McDonald also found that 25% of the thermal conductivity degradation in BeO irradiated at 90 K was recovered by isochronal annealing for 15 min at room temperature.

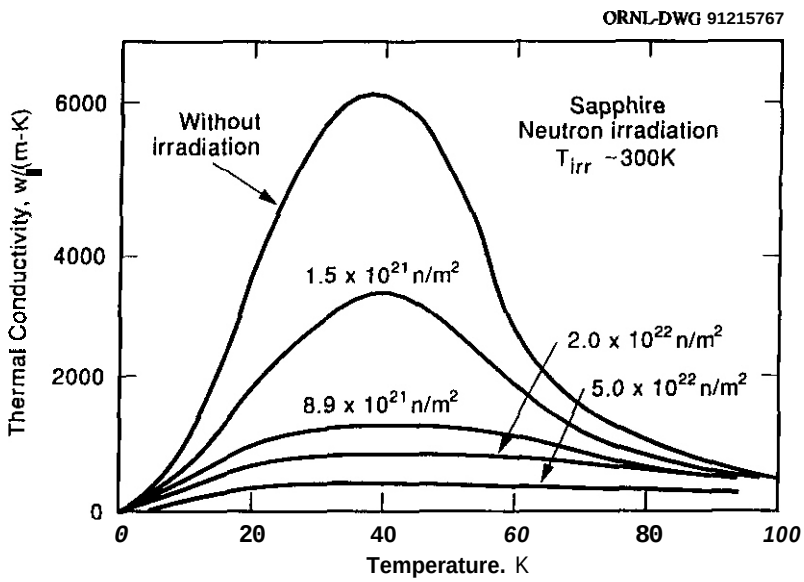

Fig. 7. Low-temperature thermal conductivity of single crystal Al_2O_3 measured after fission reactor irradiation." The irradiation temperature was not specified, but was presumably near 50°C (in-pile irradiation).

Although point defects are generally more important than extended defects in degrading the thermal conductivity of ceramics,[58,59] a recent analysis" indicates that the typical point defect supersaturation (heam-on vs. beam-off) during irradiation is not sufficient to produce significant instantaneous degradation. This analysis is supported by several low-flux (~10^{-10} dpa/s) in-situ neutron irradiation studies which did not detect any instantaneous changes in thermal conductivity as the irradiation source was turned on and off[24,69] On the other hand, there is clear evidence from in-situ" and postirradiation isochronal annealing[69] thermal conductivity measurements that postirradiation measurements may underestimate the degradation present during irradiation, due to point defect (and defect cluster) annealing effects that occur over an extended period of time. Keilholtz et al.[71] have also shown that the rate of thermal conductivity degradation in BeO measured in-situ during neutron irradiation at 920°C was flux-dependent. The rate of degradation was markedly slower for the lower flux irradiation, due to defect annealing that occurred during the irradiation.

4. Discussion

The available data suggest that there can he large in-situ physical property degradations in ceramics not observed in postirradiation measurements. Prompt effects associated with RIC can cause significant, albeit manageable, changes in a and tan 6. Further differences between extended in-situ irradiation and postirradiation properties can he attributed to two general effects. First, despite the refractory nature of ceramics, a substantial amount of the defects produced during irradiation may be annealed during postirradiation storage at room temperature prior to making measurements.[40,41,53,69] This thermal instability of radiation-induced defects also causes room and elevated temperature irradiations to yield smaller amounts of physical property degradation than what occurs during lower temperature irradiations.[9,10,52,61,64-72] Second, new radiation-induced processes such as RIED may be activated if the ceramic is irradiated under certain design-relevant conditions, e.g., with an applied electric field.[12,28,32-36,39]

These in-situ observations underscore the importance of performing irradiations and measuring property changes under conditions that closely resemble the anticipated operating environment. The combined effect of ionization, displacement damage, and an applied electric field (dc or ac) produces serious electrical degradation (RIED) in oxide ceramics, whereas this degradation does not occur if the electric field is absent. One particularly disconcerting aspect associated with RIED is that the degradation cannot he removed by high temperature annealing. Instead, the work by Pells" indicates that the degradation process may he further enhanced by postirradiation annealing. Most of the studies concerning the newly discovered phenomenon of RIED have utilized electrical conductivity measurements alone. It seems apparent that the other physical properties such as loss tangent and possibly thermal conductivity may also he further impaired by a similar process if an electric field is imposed during the irradiation.

The investigations of RIED have so far been limited to oxide ceramics. Due to their predominantly ionic bonding, oxides are more susceptible to colloid formation compared to ceramics with other types of bonding. It would certainly be worthwhile to extend the RIED investigations to insulating ceramics with predominantly covalent bonding, such as nitrides, to determine if a similar degradation occurs.

There are some indications that ceramics may be more sensitive than metals to irradiation spectrum differences, particularly with regard to the ionizing radiation component. For example, it has been demonstrated that the amount of volumetric swelling is reduced[74] and extended defect clusters do not form" in oxide ceramics if the irradiation field is highly ionizing. Similarly, the reduction in thermal conductivity in Al_2O_3 was apparently less for an irradiation with very high energy neutrons (LAMPF) compared to fission neutron irradiation.[64,66] Further work is needed to understand these spectrum effects before present-day irradiation results can be applied to fusion reactor designs.

5. Desien Guidelines

In general, postirradiation physical property data should not be considered appropriate for design purposes since it often is an undermeasure of the in situ property degradation. Recent in situ experiments have demonstrated that ceramics cannot be satisfactorily operated under certain experimental conditions. There is some urgency to solve these emerging challenges, in that a fusion reactor may become inoperative within a few weeks after initiation of D-T experiments due to electrical degradation of key ceramic components. Unacceptable degradation apparently develops at extremely small doses -- ~10^{-3} dpa depending on the temperature and dose rate, which corresponds in the first wall region to less than 1 h of full-power operation. This may be contrasted with structural degradation in metals and ceramics, which typically becomes of concern only after damage levels greater than 1 to 10 dpa. There does not appear to be a strong incentive for operating ceramics at cryogenic temperatures for damage levels $>10^{-3}$ dpa unless in situ anneals can be performed, due to the higher degradation rates in the thermal conductivity and loss tangent at low temperatures.

There are hopeful indications that catastrophic degradation of the physical properties of ceramics may be avoided by judicious choice of the operating temperature. The data presently available suggests that for first wall irradiation conditions the temperature range of 300 to 550°C should be avoided. Operation at lower or higher (up to 800 to 1000°C) temperatures may give acceptable performance. For ceramic applications in lower dose rate regimes such as near the vacuum vessel, colloid growth theory" would predict that the temperature range for serious degradation would shift to lower temperature. Obviously, considerable work is needed to confirm and theoretically comprehend the present results before firm guidelines can be established.

6. Conclusions

Recent in situ radiation effects studies have uncovered the existence of operational conditions in which unacceptable degradation of the physical properties of ceramics may occur at exceptionally low doses ($<10^{-3}$ dpa), due to a synergistic relation between ionization, displacement damage, and applied electric field. Postirradiation physical property data are often not indicative of the property values during irradiation, and generally should not be used for design purposes.

References

1. R.A. Wullaert et al., in Effects of Radiation on Materials and Components, Eds. J.F. Kircher and R.E. Bowman, (Reinhold Publ., New York, 1964) p. 277.
2. R.S. Wilks, J. Nucl. Mater. 26 (1968) 137.
3. Hj. Matzke, Rad. Effects 64 (1982) 3.
4. A.E. Hughes, Rad. Effects 97 (1986) 161.
5. F.W. Clinard, Jr., J. Nucl. Mater. 85&86 (1979) 393.
6. G.P. Pells, J. Nucl. Mater. 122&123 (1984) 1338.
7. J.L. Scott, F.W. Clinard, Jr., and F.W. Wiffen, J. Nucl. Mater. 133-134 (1985) 156.
8. F.W. Clinard, Jr. and L.W. Hobbs, in Physics of Radiation Effects in Crystals, Eds. R.A. Johnson and A.N. Orlov (Elsevier, Amsterdam, 1986) p. 387.
9. G.P. Pells, J. Nucl. Mater. 155-157 (1988) 67.
10. R. Heidinger, J. Nucl. Mater. 179-181 (1991) 64.
11. J.H. Crawford, Jr., Nucl. Instr. Meth. Phys. Res. B 1 (1984) 159.
12. E.R. Hodgson, Cryst. Latt. Def. Amorph. Mat. 18 (1989) 169.
13. W. Dienst, T. Fett, R. Heidinger, H.D. Rohrig and B. Schulz, J. Nucl. Mater. 174 (1990) 102.

14. W. Dienst, presented at the Fifth International Conference on Fusion Reactor Materials, Nov. **17-22, 1991,** Clearwater, Fla.; to be published in the proceedings.
15. T. Yano and T. Iseki, J. Nucl. Mater. 179-181 **(1991) 387.**
16. L.W. Hobbs, J. Amer. Cer. Soc. 62 **(1979) 267.**
17. C. Kinoshita, J. Nucl. Mater. 179-181 **(1991) 53;** idem, presented at the Fifth International Conference on Fusion Reactor Materials, Nov. **17-22, 1991;** to he published in the proceedings.
18. K. Tanimura, N. Itoh, and F.W. Clinard, J. Nucl. Mater. 183 **(1987) 182.**
19. S.J. Zinkle and S. Kojima, J. Nucl. Mater .179-181(1991) **395.**
20. G.P. Pells and M.J. Murphy, J. Nucl. Mater. 183 **(1991) 137.**
21. A. Rose, Phys. Rev. 97 **(1955) 322;** idem ibid., **1538.**
22. J.F. Fowler, Proc. Roy. Soc. London A 236 **(1956) 464.**
23. G.J. Dau and M.V. Davis, Nucl. Sci. Engr. 21 **(1965) 30.**
24. M.V. Davis, in Proc. Conf. on Nuclear Applications of Nonfissionable Ceramics, Eds. A. Boltax and J.H. Handwerk (Amer. Nucl. Soc., Hinsdale, IL, **1966)** p. **229.**
25. L.N. Grossman and A.I. Kaznoff, op.cit. ref. **24,** p. **421.**
26. R.W. Klaffky, B.H. Rose, A.N. Goland, and G.J. Dienes, Phys. Rev. B 21 **(1980) 3610;** also R.W. Klaffky, in Special Purpose Materials Semiann. Prog. Rep., DOE/ER-0048/1 **(1980) p.19.**
27. V.A.J. vanLint et al., Mechanisms of Radiation Effects in Electronic Materials, Vol. **1** (Wiley & Sans, New Yark, **1980).**
28. V.M. Ivanov et al., Inorganic Mater. 17 **(1981) 1203.**
29. O.B. Alekseevsii, S.A. Vorov'ev, R.G. Ziyakaev and V.V. Mameev, Sov. Atomic Energy 59, **2 (1986) 701.**
30. G.P. Pells, Rad. Effects 97 **(1986) 199.**
31. E.R. Hodgson and S. Clement, Rad. Effects 97 **(1986) 251;** idem, J. Nucl. Mater. 155-157 **(1988) 357.**
32. E.R. Hodgson, Rad. Eff. Def. Sol. 119-121 **(1991) 822.**
33. E.R. Hodgson, J. Nucl. Mater. 179-181 **(1991) 383.**
34. E.R. Hodgson, Nucl. **Instr.** Meth. B, in press.
35. E.R. Hodgson, presented at the Fifth International Conference on Fusion Reactor Materials, Nov. **17-22, 1991;** to be published in the proceedings.
36. G.P. Pells, J. Nucl. Mater. 184 **(1991) 177.**
37. G.P. Pells, J. Nucl. Mater. 184 **(1991) 183.**
38. T. Shikama, M. Narui, A. Ochiai, H. Kayano, and Y. Endo, 15th Int. Symp. on Effects of Radiation on Materials, Eds. R.E. Stoller et al., ASTM STP **1125,** in press.
39. T. Shikama, M. Narui, Y. Endo, T, Sagawa, and H. Kayano, presented at the Fifth International Conference on Fusion Reactor Materials, Nov. **17-22, 1991;** to he published in the proceedings.
40. E.H. Farnum, J.C. Kennedy, F.W. Clinard, and H.M. Frost, presented at the Fifth International Conference on Fusion Reactor Materials, Nov. **17-22, 1991;** to be published in the proceedings.
41. G.P. Pells et al., Harwell report AERE-R13222, Sept. **1988.**
42. K.L. Tsang, Y. Chen, and J.J. O'Dwyer, Phys. Rev. B 26 **(1982) 6909.**
43. **U.** Jain and A.B. Lidiard, Phil. Mag. 35 **(1977) 245.**
44. A.E. Hughes, Rad. Effects 74 **(1983) 57.**
45. **W.A.** Ranken, DOE Workshop on Electrical Breakdown of Insulating Ceramics in a High Radiation Field, Vail, CO, May, **1991, CONF-9105176,** p. **433.**
46. W.D. Kingery, H.K. Bowen and D.R. Uhlmann, Introduction to Ceramics, 2nd Ed. (Wiley-Interscience, New York, **1976)** p. **913.**
47. R. Heidinger, Int. J. Electronics 64 **(1988) 37.**
48. G.P. Pells and G.J. Hill, J. Nucl. Mater. 141-143 **(1986) 375.**
49. **G.S.** Perry, J. Mater. Sci. 1 (1966) **186.**
50. R. Heidinger, J. Nucl. Mater. 173 (1990) **243.**
51. H.M. Frost and F.W. Clinard, Jr. J. Nucl. Mater. 155-157 **(1988) 315.**
52. R. Heidinger and F. Koniger, J. Nucl. Mat. 155-157 **(1988) 344.**
53. S.N. Buckley and P. Agnew, J. Nucl. Mat. 155-157 **(1988) 361.**
54. S.N. Buckley and P. Agnew, in Microwave Processing of Materials II, Eds. W.B. Snyder, Jr. et al., MRS Symp. Proc. Vol. **189** (Mat. Res. Soc., Pittsburgh, PA, **1991)** p. **503.**
55. **D.** Edelson, R.E. Jaeger, and J.C. Williams, J. Amer. Cer. Sac. 52 **(1969) 359.**
56. R.E. Stoller, R.H. Goulding, and S.J. Zinkle, presented at the Fifth International Conference on Fusion Reactor Materials, Nov. **17-22, 1991;** to be published in the proceedings.
57. W.D. McMillan, R.L. Gause, E.E. Kerlin and J.E. Warwick, in Measurement of Dielectric Properties under Space Conditions, ASTM STP **420** (ASTM, Philadelphia, **1967)** p. **48.**
58. D.R. Flynn, in Proc. Symp. on Mechanical and Thermal Properties of Ceramics, Ed. J.B. Wachtman, Nat. Bureau Standards Special Publ. **303,** May **1969,** p. **63.**

59. P.G. Klemens, G.F. Hurley, and F.W. Clinard, Jr., in Proc. 2nd Top. Mtg. on Technology of Controlled Nuclear Fusion, Ed. G.L. Kulcinski, CONF-760935, 1976, p. 957.
60. F.W. Clinard, Jr., J. Mater. Energy Systems 6 (1984) 100; also G.F. Hurley and F.W. Clinard, in Special Purpose Materials Ann. Prog. Rep., DOE/ET-0095, 1979, p. 59.
61. R.J. Price, J. Nucl. Mater. 46 (1973) 268.
62. T. Yano and T. Iseki, J. Nucl. Mater. 179-181 (1991) 387.
63. Y. Fukushima, T. Yano, T. Marayuma, and T. Iseki, J. Nucl. Mater. 175 (1990) 203.
64. M. Rohde and B. Schulz, J. Nucl. Mater. 173 (1990) 289.
65. M. Rohde, J. Nucl. Mater. 182 (1991) 87.
66. M. Rohde and B. Schulz, 15th Int. Symp. on Effects of Radiation on Materials, Eds. R.E. Stoller et al., ASTM STP 1125 (ASTM, Philadelphia, in press).
67 R. Berman, E.L. Foster, and H.M. Rosenberg, in Report of the Bristol Conf. on Defects in Crystalline Solids (The Physical Society, London, 1955) p. 321.
68. A.W. Pryor, R.J. Tainsh and G.K. White, J. Nucl. Mater. 14 (1964) 208.
69. D.L. McDonald, Appl. Phys. Letters 2 (1963) 175.
70. B. Salce and A.M. deGoer, Conf. Digest on the Int. Conf. on Defects in Insulating Materials, Parma, 1988, p. 499.
71. G.W. Keilholtz, J.E. Lee, Jr. and R.E. Moore, J. Nucl. Mater. 11 (1964) 253.
72. K. Atobe and M. Nakagawa, Cryst. Latt. Def. 17 (1987) 229.
73. D.P. White, Semiann. Prog. Rep. on Fusion Reactor Materials, DOE/ER-0313/11, Sept. 1991, in press.
74. G.B. Krefft and E.P. EerNisse, J. Appl. Phys. 49 (1978) 2725.
75. S.J. Zinkle, submitted to J. Mater. Res.; also DOE/ER-0313/10, April, 1991, p. 302.

MATERIALS ISSUES IN OIAGNOSTIC SYSTEMS FOR BPX AND ITER -- F. W. Clinard, Jr. and E. H. Farnum (Los Alamos National Laboratory), 0. L. Griscom [Naval Research Laboratory), R. F. Mattas [Argonne National Laboratory), S. S. Medley [Princeton Plasma Physics Laboratory), F. W. Wiffen (U.S. Department of Energy), S. S. Wojtowicz [General Atomics), K. M. Young [Princeton Plasma Physics Laboratory) and S. J. Zinkle [Oak Ridge National Laboratory)

OBJECTIVE

The objective of this work is to summarize the critical materials requirements for diagnostic systems in next-step burning plasma devices and reactor-like machines. For the first device we have chosen the Burning Plasma Experiment (BPX), which is now defunct but whose design is well-developed; for the latter machine we discuss needs for the International Thermonuclear Experimental Reactor [ITER).

SUMMARY

Anticipated radiation fluxes in D-T burning machines such as BPX and ITER are intense, and accumulated damage levels are moderate to severe. Thus materials used in diagnostic systems may suffer significant degradation of electrical, optical, and structural properties, either from transient or permanent damage effects. Of particular concern are windows, optical fibers, reflectors, and insulators. However, materials design and modification based on results from an appropriate irradiation testing program, when combined with design optimization for location, shielding, and ease of replacement, should point the way to development of acceptable materials systems.

PROGRESS AND STATUS

Introduction

Magnetically-confined fusion devices require diagnostic facilities in order to analyze plasma performance and to control the plasma through feedback systems. All O-T burning machines will subject diagnostic materials to intense fluxes of displacive and ionizing radiation. For those machines, transient degradation of optical and electrical properties must be assessed. By end-of-life, materials near the first wall of BPX will have suffered moderate levels of permanent damage while damage in ITER will be severe; as a result, permanent degradation of both structural and electrical properties may be a significant issue. This report assesses the nature and extent of problems expected for four families of materials known to be useful for diagnostic systems: windows, optical fibers, reflector [mirrors) and insulators.

Irradiation Fluxes and Fluences

Neutron and gamma fluxes and fluences for BPX and for the physics and technology phases of ITER are shown in Table 1. Values are given both at the first wall and behind the cryostat; most diagnostics will be located at or between these two locations.

Table 1. Irradiation Fields in BPX and ITER

	BPX	ITER Physics Phase	ITER Technology Phase
First Wall			
Neutron flux (n/m^2s)	2.0×10^{19}	2.5×10^{18}	2.5×10^{18}
Neutron fluence (n/m^2)	2.0×10^{23}	2.0×10^{24}	2.0×10^{26}
Gamma flux (γ/m^2s)	8.0×10^{18}	2.0×10^{18}	2.0×10^{18}
Gamma fluence (Ylm^2)	8.0×10^{22}	1.6×10^{24}	1.6×10^{26}
Behind Cryostat			
Neutron flux [nlm^2s)	8.0×10^{17}	2.0×10^{9}	2.0×10^{9}
Neutron fluence (n/m^2)	8.0×10^{21}	1.5×10^{15}	1.8×10^{17}
Gamma flux (γ/m^2s)	3.0×10^{17}	1.0×10^{10}	1.0×10^{10}
Gamma fluence (γ/m^2)	3.0×10^{21}	7.5x1015	9.0×10^{17}

The ionizing energy represented by gamma irradiation must be converted to energy absorbed, in order to estimate the effect on materials parameters. A useful approximation for a low atomic number material such as Al_2O_3 is that $5x10^{18}$ fusion gamma/m^2 (of energy about 2 MeV) is equivalent to approximately 10^4 Gy of energy absorbed.

Windows

Candidate window materials for BPX and ITER will be subjected to radiation that can degrade transmission characteristics, induce luminescence, cause dimensional changes, and alter mechanical properties. Proposed candidate materials for windows are, according to Taylor [1]:

- crystalline quartz for the far infrared region;
- ZnSe for the infrared;
- fused silica for the visible and near ultraviolet;
- sapphire and MgF_2 for the ultraviolet.

The following discussion emphasizes the effect of dimensional changes in SiO_2, with optical damage in this material being discussed in the section on optical fibers.

Primak and co-workers [2-5] have shown that both fused silica and crystalline quartz change dimensions when irradiated with low fluences of fast neutrons or gamma rays at ambient temperature (Fig. 1). Small dimensional changes, on the order of $5x10^{-4}$, can result in high stress levels in window assemblies. This leads to the conclusion that fluence should be limited to about $5x10^{21}$ fusion nlm/m^2, unless windows can be periodically annealed or operated at temperatures greater than 300°C where radiation damage can continuously be removed. Larger dimensional changes could be tolerated if sliding seal assemblies can be developed.

Optical Fibers

Silica-based optical fibers are the leading candidates for diagnostic applications operating in the range 0.4-2.0 microns. These materials are mechanically viable, thermally stable, and less susceptible to radiation-induced attenuation than are other types of glasses. To preserve their mechanical and thermal characteristics, these fibers must be metal-coated rather than polymer-jacketed, but the technology to do this exists.

Figure 2 shows the spectral dependence of induced absorption in a commercial high-purity fused silica of low water content, after irradiation with 2 MeV electrons [6]. Also shown are Gaussian resolutions of several of the distinct color bands. The bands at 5.85 eV, 4.7 eV, and 2.0 eV result from defects that can be introduced by irradiation; these are, respectively, holes trapped at oxygen vacancies [7], interstitial oxygen molecules [8], and non-bridging oxygen [9].

In addition to the radiation-induced attenuation bands, there are also radiation-induced luminescence bands that may be excited either by the radiation itself or by light propagating in the fiber. In diagnostic applications, it is likely that the luminescence emisssions will have to be removed from the data stream by computer processing.

Reflectors

Reflectors are specified for use at wavelengths from 0.3 to 11 microns and 0.1 to 5 mm, at ternperatues up to 350°C. These diagnostic elements may be made of a variety of materials or materials combinations, depending on the wavelength to be reflected. Possibilities include:

- all metal, all ceramic, or all glass;
- ceramic with metal coating;
- ceramic or glass with dielectric coating;
- metal with dielectric coating;
- metal with metal coating.

Transient damage may be in the form of temporary luminescence or darkening. Permanent degradation could result from darkening, deposition of contamination layers, sputtering, microcracking, debonding, spalling, swelling, or structural damage. Many of the structural problems will be alleviated if metals systems are chosen: materials with sufficient ductility should be resistant to brittleness-related degradation mechanisms such as microcracking and spalling. Metals are of course also immune to luminescence and darkening effects.

Insulators

Bulk dielectrics will be used in a number of applications in fusion diagnostics, including magnetic probes, cables, and feedthroughs. The most severe environment is that for magnetic probes, whose operating conditions include:

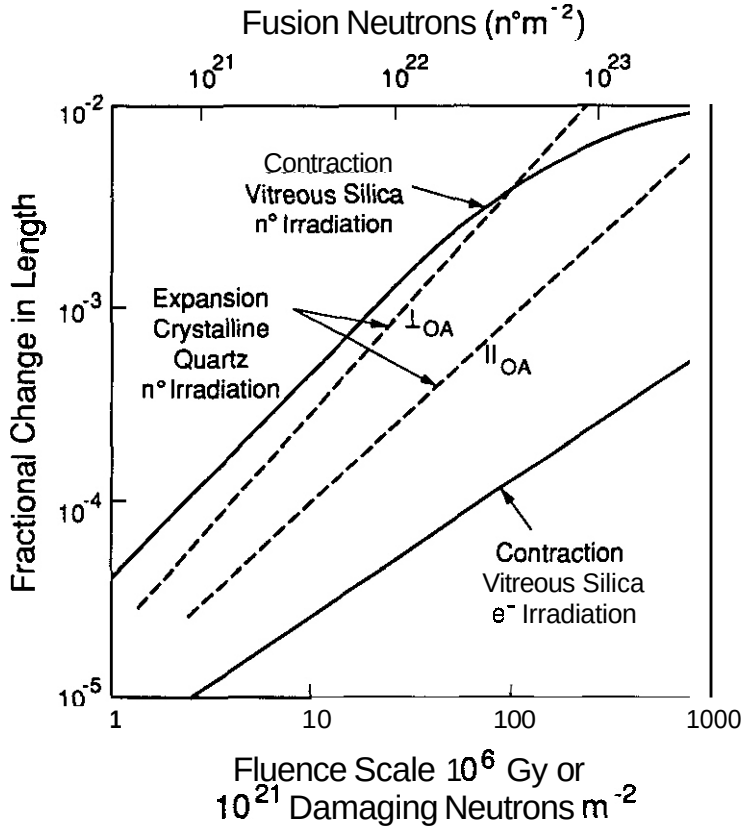

Figure 1. Fractional contraction of vitreous silica and expansion of crystalline quartz as a function of fluence of fission neutrons and ionization dose, at ambient temperature. The upper scale shows equivalent fluence of fusion neutrons. The term "OA" refers to optical axis. Refs. [1, 2, 4, 5].

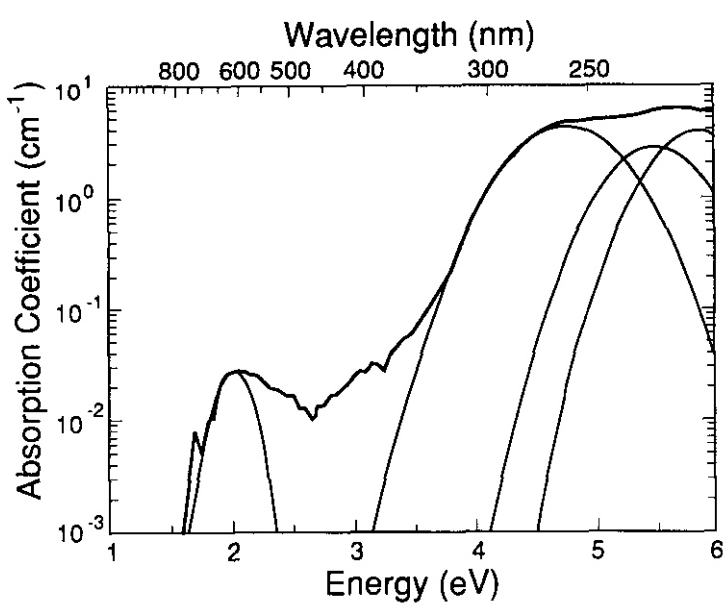

Figure 2. Optical absorption in Suprasil W2 fused silica after irradiation with 2 MeV electrons to 10 MGy. Ref. [6].

- frequencies from dc to 1 MHz;
- dc bias voltage from zero to 1000 V/mm, with higher voltage spikes during plasma disruption;
- temperatures up to 1200°C;
  vacuum, with possible tritium contamination;
- voltage transients during disruptions.

Degradation of these insulators can he permanent, as from neutron damage, or transient, for example as a result of absorption of ionizing energy during irradiation.

Transient increases in electrical conductivity as a result of absorption of ionizing energy can be dramatic: Farnum et al. [10] have observed an increase of four orders of magnitude in single-crystal Al_2O_3 during proton irradiation, as charge carriers are excited into conducting states. Much of the increase dissipates with time, as the concentration of point defects that can serve as trapping and recombination centers increases.

Recently, Hodgson [11] has identified another, possibly more serious problem: degradation of electrical and possibly even structural properties when insulators are irradiated while under an imposed electric field. This phenomenon, which is not well understood, is currently under study at several laboratories around the world.

Ceramics vary greatly in their sensitivity to structural damage. Silica-based materials can be permanently damaged by low doses such as those expected by end-of-life in HPX; an example is Macor machinable glass-ceramic [12], which suffers differential swelling as the crystalline and glassy phases expand and contract, respectively [13].

More conventional ceramics such as crystalline oxides and nitrides should not exhibit significant dimensional or strength changes at HPX neutron fluences. However, at the much higher doses characteristic of ITER some of these materials will show significant degradation. For example, Hickman [14] has shown that BeO loses 80% of its strength when irradiated at 100°C in a fission reactor to a fluence about fifty times less than that characteristic of the ITER lifetime first wall dose.

Cubic $MgAl_2O_4$ spinel can actually strengthen under high-dose fission neutron irradiation [15]. However, Zinkle and Kojima [16] have observed cavitation in grain boundaries of spinel at fusion-relevant He/dpa levels, demonstrating that the irradiation environment must be accurately simulated before final conclusions can be drawn as to performance of a candidate material for fusion applications.

Data Base for Materials in Diagnostic Systems

No comprehensive data base exists for radiation effects in diagnostic materials for fusion applications. However, assessments were made for the Joint European Torus (JET) in 1980 [17] and for the Diagnostics Hardening for Fusion Reactors Program in 1981 [18]. These reports contain extensive information on diagnostic materials and systems, as well as discussions of shielding and hardening techniques. An important goal of the ITER diagnostics program is to create an updated data base of radiation effects for that device.

FUTURE WORK

An expanded version of this progress report has been submitted for publication in the Journal of Nuclear Materials. Work on materials for ITER diagnostic systems is continuing, both within the United States and overseas.

REFERENCES

1. A. Taylor, Report on the Survivability of Diagnostic Windows for the CIT Reactor, Argonne National Laboratory, Fusion Power Program Internal Document (1988).

2. W. Primak and E. Edwards, Phys. Rev. 128 (1962) 2580

3. W. Primak, Radiation Damage in Diagnostic Window Materials for TFTR, Argonne National Laboratory Report ANLIFPPITM-146 (1981).

4. W. Primak, L. H. Fuchs and P. Day, J. Amer. Ceram. Soc. 38 (1955) 135.

5. W. Primak, Phys. Rev. 110 (1958) 1240.

6. E. J. Friebele, P. L. Higby and T. E. Tsai, Diffusion and Defect Data 53 (1987) 203.

7. O. L. Griscom, Nucl. Instr. and Meth. B1 (1984) 481.

8. K. Awazu and H. Kawazoe, J. Appl. Phys. 68 (1990) 3584.

9. Y. Hibino and H. Hanafusa. J. Appl. Phys. 60 (1986) 1797.

10. E. H. Farnum, J. C. Kennedy, F. W. Clinard and H. M. Frost, Radiation-Induced Conductivity in Alumina from 100 Hz to 10 MHz During Proton Radiation, J. Nucl. Mater. (in press).

11. E. R. Hodgson, J. Nucl. Mater. 179-181 (1991) 383

12. Macor is a product of Corning Glass Works, Corning, NY, USA.

13. W. A. Coghlan and F. W. Clinard, Jr., J. Nucl. Mater. 179-181 (1991) 391.

14. B. S. Hickman, in: Studies in Radiation Effects Series A, Physical and Chemical vol. 1, ed. G. J. Dienes (Gordon and Breach, New York, 1966) p.72.

15. G. F. Hurley, J. C. Kennedy, F. W. Clinard, Jr., R. A. Youngman and W. R. McDonell, J. Nucl. Mater. 103&104 (1981) 761.

16. S. J. Zinkle and S. Kojima, J. Nucl. Mater. 179-181 (1991) 395.

17. A. Holmes-Seidle, Radiation Effects in the Joint European Torus Experiment: Guidelines for Preliminary Design, Fulmer Research Laboratory Report R857/2 (1980).

18. J. F. Bauer, 8. A. Engholm, M. P. Hacker, I. Maya, P. H. Miller, W. E. Toffolo and S. S. Wojtowicz, Radiation Hardening of Diagnostics for Fusion Reactors, General Atomics Report GA-A16614 (December 1981).

OBSERVATION OF RADIATION-INDUCED CHANGES IN DIELECTRIC PROPERTIES IN CERAMIC INSULATORS

R. E. Stoller, R. H. Goulding, S. J. Zinkle, and D. A. Rasmussen (Oak Ridge National Laboratory)

OBJECTIVE

The objective of this work is to investigate the effects of radiation on the electrical properties of ceramic insulators in order to qualify them for use in ITER.

SUMMARY

Several experiments have been completed in which the dielectric properties of ceramic materials were measured during ionizing and displacive irradiation. The experimental matrix included single crystal sapphire, commercial-grade polycrystalline alumina, magnesium-aluminate spinel, silicon nitride, and aluminum nitride. These materials are candidates for use in a number of fusion reactor components. The measurements were made at 100 MHz using a capacitively-loaded resonant cavity. Essentially no effect of ionizing radiation alone was observed for damage rates up to about 5×10^5 Gy/h. However, pulsed fission reactor irradiation led to dramatic increases in the loss tangent. The fractional contributions of the ionizing and displacive fields to the total change observed during the neutron irradiations could not be unambiguously determined. The results of these experiments indicate that the use of post-irradiation measurements leads to an underestimate of the radiation-induced dielectric degradation that occurs in the radiation field.

PROGRESS AND STATUS

Introduction

Ceramic materials are specified for use in the fabrication of many components in current fusion reactor designs. Many of these applications rely on the high electrical resistivity that these materials typically exhibit. The applications for insulating ceramics range from simple dc voltage stand-offs to components in microwave heating systems that operate at high frequencies. The well-known phenomenon of radiation- induced conductivity (RIC) at dc or low frequency ac conditions,[1] and the recently discovered phenomenon of radiation induced electrical degradation (RIED)[2-5] give rise to some concern about whether the candidate materials will remain sufficiently insulating when exposed to a radiation field that is typical of their intended operating environment.

Both ion cyclotron resonance heating (ICRH) and electron cyclotron heating (ECH) have been proposed as major heating sources for machines such as the Burning Plasma Experiment (BPX) and the International Thermonuclear Experimental Reactor (ITER). For the components used in these heating systems, the critical dielectric parameter is the so-called loss tangent, since the radio frequency (rf) or microwave power absorbed in the ceramic is proportional to the loss tangent. The loss tangent, tan δ is defined as the ratio of the imaginary part (ε'') to the real part (ε') of the dielectric constant, tan $\delta = \varepsilon''/\varepsilon'$. The operating frequencies for ICRH and ECH systems are in the range of 100 MHz and 100 GHz, and they require loss tangents less than about 10^{-3} and 10^{-6}, respectively. Typical values for the loss tangent in unirradiated ceramics of interest to the fusion program are from 10^{-4} to 10^{-3} at room temperature. Thus, even in the absence of any radiation induced property degradation, the vacuum windows in ECH systems will require cooling to cryogenic temperatures to reduce the loss tangent.

Post-irradiation measurements have shown that ionizing and displacive radiation can either increase or decrease the value of the loss tangent [6-10] There is also some evidence that the amount of the increase is dependent on the neutron spectrum [6] However, there have been few relevant measurements of dielectric properties during irradiation[11] and the validity of post-irradiation measurements is called into question by data that hows significant levels of recovery in the loss tangent at room temperature following proton irradiation.[8] An example of this post-irradiation recovery for times from about 1 to 30 h is shown in Fig. 1 for spinel and 0.975% alumina.[8] While no change is observed in the alumina over this time period, the recovery is dramatic in the case of spinel. Because of these concerns, a workshop was recently sponsored by the International Energy Agency (IEA) to review the current understanding of radiation-induced

conductivity and dielectric property changes. The IEA workshop summary emphasized the need for in situ property measurement.[12]

In order to help address some of these concerns, a series of irradiation experiments have been conducted to measure the dielectric properties of candidate ceramic materials while they are exposed to either an ionizing irradiation field or a field that is both ionizing and displacive. Alumina, sapphire, and magnesium aluminate spinel were chosen for this initial work because they are prime candidates for use in ICRH and ECH heating systems. Silicon nitride and aluminum nitride were included in order to determine if covalently bonded materials exhibited behavior that was different from the more ionic materials. The sapphire was Crystal Systems White Hemlux with an (0001) orientation and the alumina was WESGO's AL-998 (0.998 purity). The spinel, aluminum nitride, and silicon nitride were obtained from CERCOM. A machinable, structural ceramic, Macor, was also included as part of an IEA round-robin experiment.[13] Similar measurements are underway using a somewhat different technique and a proton beam as an irradiation source.[14]

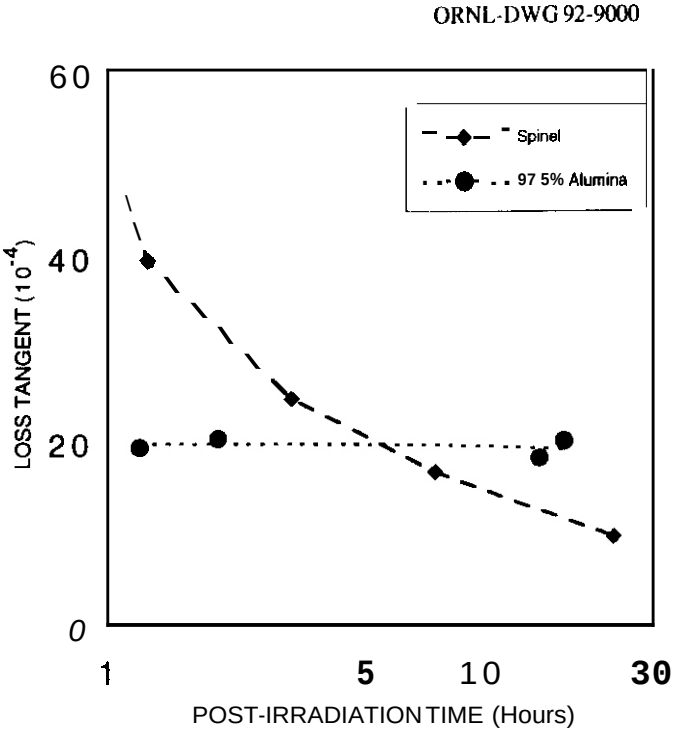

Fig. 1. Recovery of loss tangent at ambient temperature following proton irradiation[8].

Irradiation Facilities

the HFIR-GIF. The damage rate in the first experiment was ~1.25 x 10^5 Gy/h and for the second it was about 5.0 x 10^5 Gy/h. Gamma heating was monitored by a thermocouple brazed to the specimen chamber. A temperature of 73°C was measured at steady state at the lower damage rate. The steady state temperature exceeded 200°C at the higher damage rate. In order to prevent excessive heating, the cavity remained in the high field region only as long as was necessary to make the measurements. This kept the specimen temperature below about 100°C. Such low temperatures should have little effect on these materials, and the measurements were corrected to a common temperature of 30°C for comparison.

A TRIGA reactor at the University of

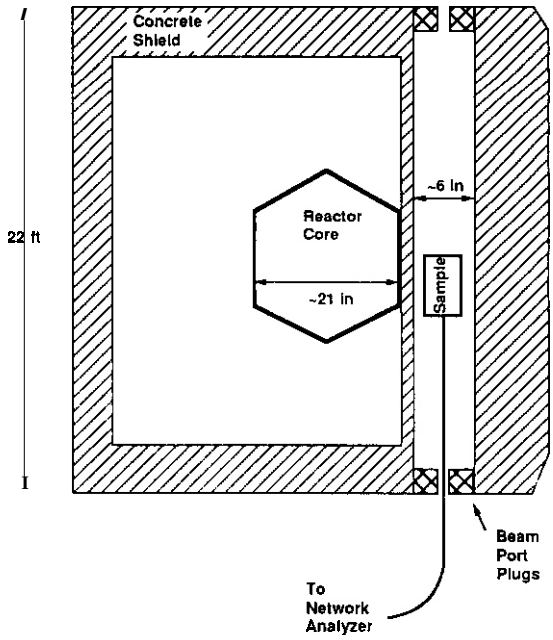

comparable to that expected in the ITER. The ionizing damage rate is somewhat higher. The maximum temperature due to gamma heating observed during the TRIGA irradiations was 33°C. The nominal peak damage rates are listed in Table 1, along with the value for the HFIR-GIF and the BPX values. Although it is unlikely that the BPX will be built, current irradiation parameters for the ITER are similar to those shown for BPX. The TRIGA parameters are given as a function of the reactivity insertions ($) that trigger the pulse. A positive reactivity of $1.00 is the amount required for the reactor to be critical on prompt neutrons alone.

Table 1. Typical radiation damage rates in various facilities

Facility	Ionizing Damage Rate (Gy/h)	Displacement Rate (dpa/s)
HFIR-GIF	up to 10^6	-none-
TRIGA:		
$1.50 pulse	1.3×10^7 (Al_2O_3)	1.3×10^{-8} (Ni)
$1.80 pulse	1.8×10^7	5.2×10^{-8}
$3.00 pulse	2.1×10^8	1.8×10^{-7}
BPX central cell:		
near first wall	3.7×10^7 (Si)	1.9×10^{-6} (Ni)
rear blanket	9.6×10^4	4.6×10^{-9}

The values listed in Table 1 are based on information obtained in discussions with the staff at each facility. The damage rate is material dependent; representative values are quoted for the materials indicated in parentheses. All of the values in Table 1 are approximate and more detailed dosimetry needs to be done to characterize both the anticipated fusion environment and test reactor environments. Additional radiation parameters of interest include the ratio of absorbed dose due to gamma rays to that due to neutrons (about 20 for the TRIGA and 1.0 for BPX), and the fraction of the neutron dose that leads to atomic displacements (about 0.1 in BPX). The need for accurate, detailed dosimetry is greater for understanding property changes in irradiated ceramics than it is for metals since ionizing radiation has little influence on the latter. For example, the ratio of ionizing to displacive radiation has been shown to influence dislocation loop formation in irradiated ceramics[15] and current indications are that the electrical properties will be more sensitive to the details of the irradiating particle spectrum than is microstructural evolution.

Experimental Method

The dielectric measurements were made using a capacitively loaded resonant cavity and a drawing of the cavity is reproduced in Fig. 3. The cavity method is well suited to measurement of the loss tangent because the power dissipation in the ceramic specimen is maximized relative to that dissipated in the balance of the experimental apparatus. In addition, losses in the feed line can be accounted for without the need for prior calibration, which would be extremely difficult to accomplish in situ. The loss tangent is measured by determining the cavity quality factor, Q, the ratio of the stored energy to the energy dissipated per rf field period. The loss tangent is given by the equation:

$$\tan\delta = \left[\frac{\beta\ell}{\sin(2\beta\ell)} + \frac{1}{2}\right]\left(\frac{1}{Q} + \frac{1}{Q_o}\right) , \qquad (1)$$

where: β is equal to the angular frequency divided by the speed of light, ℓ is the length of the coaxial cavity center conductor, Q is the quality factor with the ceramic in place, and Q_o is the quality factor at the same frequency when the ceramic is absent. Both of the Q values in Eq. (1) refer to the so-called "unloaded Q," for which only the energy stored and dissipated in the cavity itself are taken into account. They can be determined by measuring the ratio of the reflected to transmitted power as a function of frequency over a ~1 MHz range centered at the resonant frequency for the case of a tuned cavity. Relative changes in the dielectric constant can also be measured using the resonant cavity technique with an accuracy of $1/Q$, or less than 1% for the highest values of the loss tangent expected here.

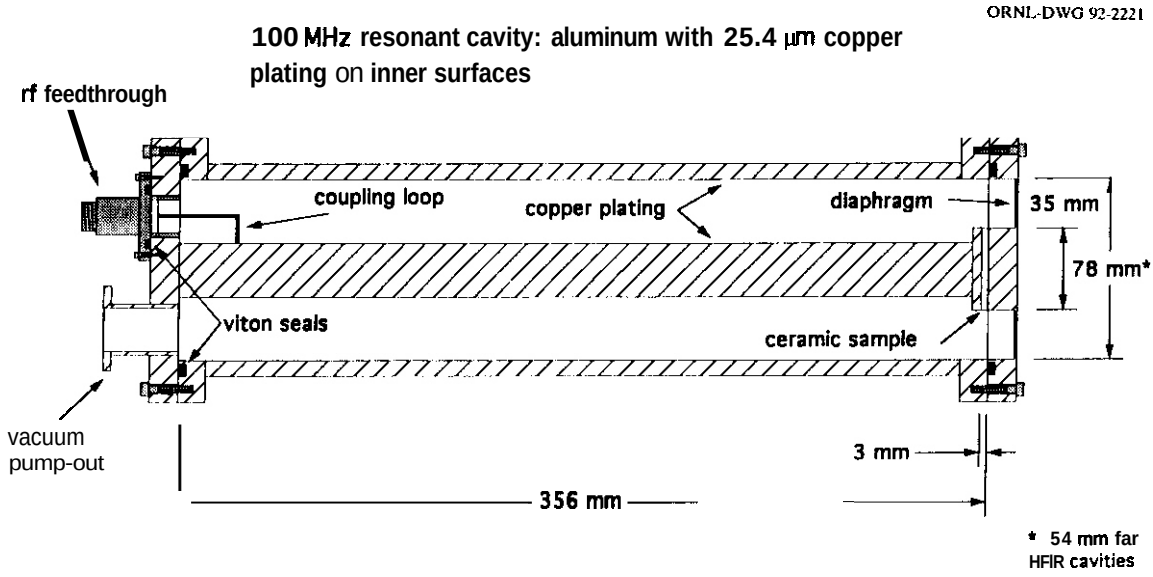

Fig. 3. Design of prototype resonant cavity for in situ dielectric measurements

These experiments utilized cavities that were sized to permit the measurement of the loss tangent at 100 MHz in the TEM mode. A copper cavity with the smaller of the diameters indicated in Fig. 3 was used for the HFIR measurements because this was the largest cavity that the dimensions of the HFIR-GIF would accommodate. This same cavity was also used in the initial TRIGA measurements to permit a direct comparison between the measurements obtained in the two facilities without introducing any uncertainties due to different cavities. However, a larger diameter cavity would yield a higher Q and hence improve the accuracy of the measurements. Therefore, the larger cavities were fabricated with an inside diameter of 78 mm since the TRIGA beam tube would accommodate this larger device. In order to minimize the induced radioactivity in the larger cavities, they were constructed of aluminum rather than copper. A layer of copper about 25.4 μm thick was plated onto the aluminum tubing to insure adequate electrical conductivity. Both the larger and the smaller cavities used the same disc-shaped specimens that were 35 mm in diameter and 3 mm thick. The larger cavities were also designed to permit them to be evacuated to determine whether there was any effect due to gas ionization in the cavity.

Two types of measurements were made. In the first, the voltage standing wave ratio (VSWR) was measured as a function of frequency near the resonant frequency. From these measurements, both the cavity Q and any shift in the resonant frequency can be calculated. This frequency sweep requires about 25 ms to complete. In the case of pulsed TRIGA irradiation, these measurements were only conducted for pulse reactivity insertions of $1.80 or less so that the sweep could be completed while the reactor power was above the pulse half-maximum. The second measurement was the time-dependence of the cavity input impedance. From this, the time dependent cavity Q and resonant frequency shift could be calculated. The loss tangent was obtained from the Q values and the real part of the dielectric constant (e') was obtained from the resonant frequency shifts for both types of measurements.

Experimental Results and Discussion

The results of measurements in the HFIR-GIF indicated that purely ionizing radiation did not increase the loss tangent in either single or polycrystalline alumina (0.995 purity) at a dose rate ~1.25 x 10^5 Gy/h up to a maximum exposure of 3.75 x 10^5 Gy. A small change in the cavity Q was observed at the higher damage rate of 5.0 x 10^5 Gy/h. This change in Q appeared to be due to the formation of a weakly ionized plasma in the cavity. The measured Q was dependent on the residual gas pressure in the cavity, with a peak value near 20 Pa. Subsequent modeling of the experiment appears to indicate that gas ionization, rather than a change in the specimen loss tangent, was responsible for the change in Q [ref. 16].

Pulsed neutron irradiation in the TRIGA reactor gave rise to dramatic changes in the cavity Q. The loss tangent increased as the reactor power (hence atomic displacement rate) increased during the pulse as shown for a 0.998 alumina sample in Fig. 4. In the case of alumina, the degree of increase was observed to scale with specimen purity in a way that was consistent with previous post-irradiation measurements, i.e., the higher the material purity, the greater the increase in loss tangent. All of the materials tested exhibited similar behavior. Typical results for a displacement rate of 5.2 x 10^{-8} dpa/s are shown in Fig. 5 for a range of materials. Although the sapphire has the lowest loss tangent in the unirradiated condition, it is more sensitive to radiation than the polycrystalline alumina or spinel. The covalent materials, aluminum and silicon nitride, exhibited much higher losses in the unirradiated condition than the more ionic ceramics. The aluminum nitride appeared to be much more sensitive to radiation than silicon nitride.

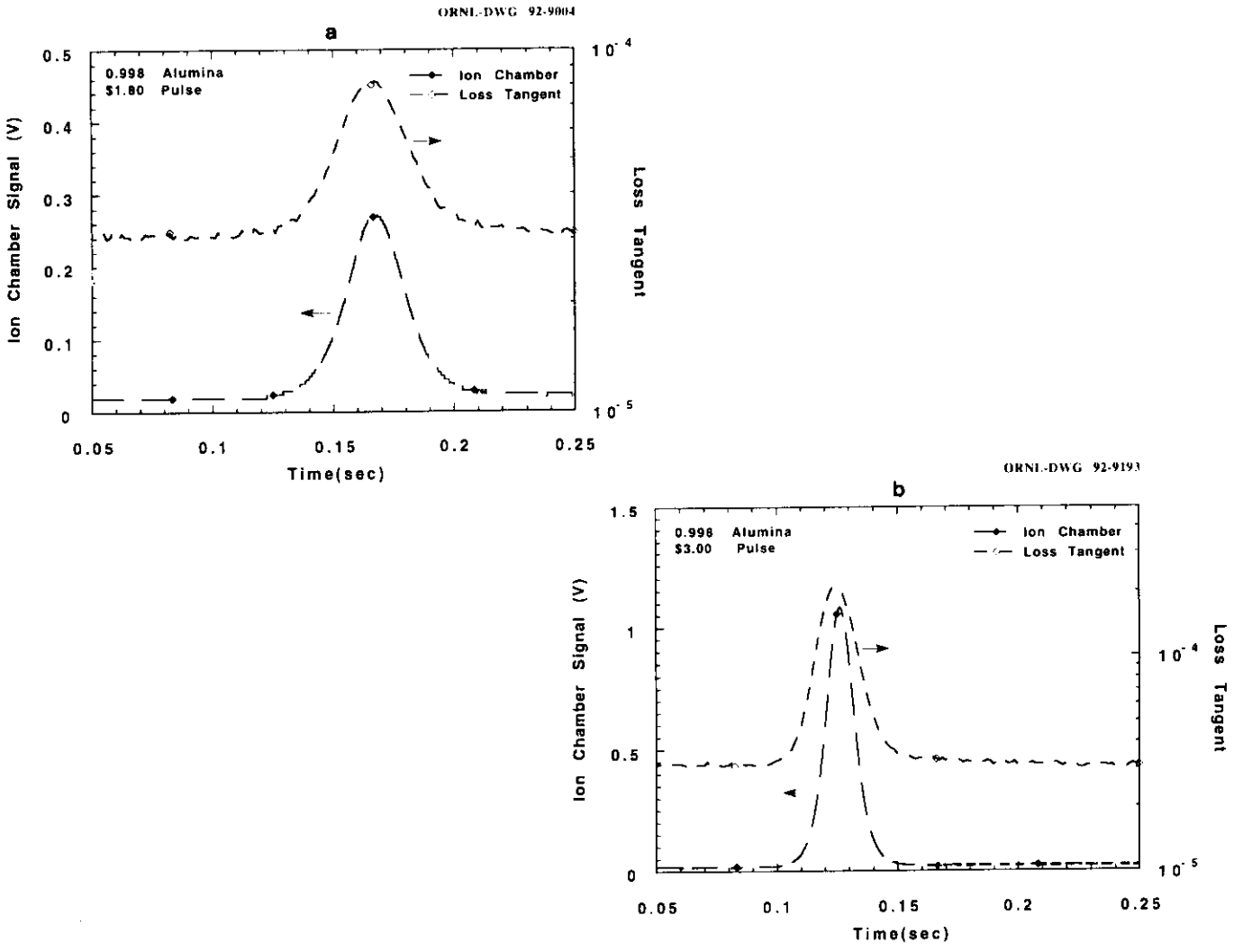

Fig. 4. Time scan comparing typical loss tangent measurements and the output from the TRIGA ionization chamber during a $1.80 pulse (a) and a $3 pulse (b). Reactor power is proportional to the signal from the ionization chamber.

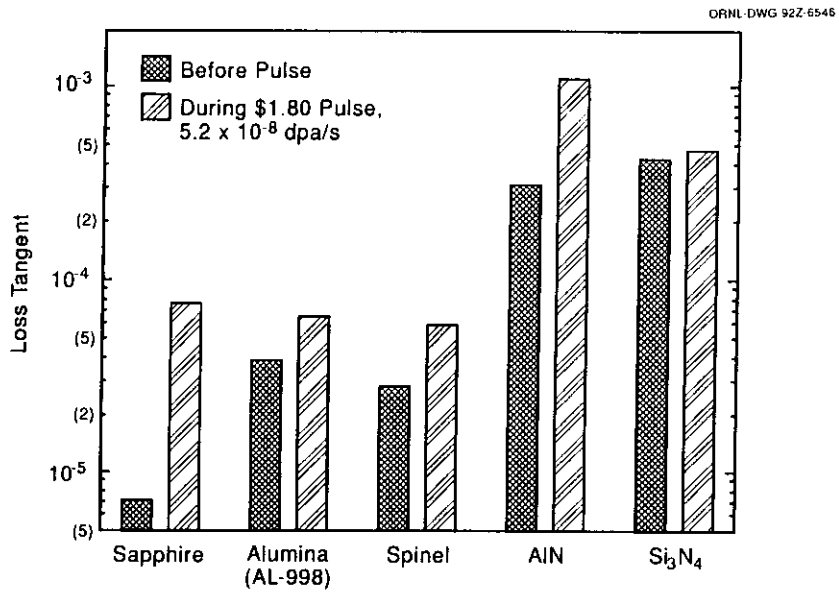

Fig. 5. Typical values of the radiation-induced changes in the loss tangent measured during a $1.80 TRIGA pulse, ~$5.2 \times 10^{-8}$ dpa/s.

The observed change in loss tangent increased with the displacement rate as shown in Fig. 6. The sapphire again appears to be more sensitive to changes in the displacement rate than alumina or spinel. This is significant because the low loss tangent of unirradiated sapphire has led it to be a leading candidate for applications that require low loss. However, its loss tangent exceeds that of alumina at displacement rates greater than about 1×10^{-7} dpa/s. If the reactor power dependence observed in Fig. 6 persists up to the highest displacement rate expected in ITER (~2×10^{-6} dpa/s), the room temperature loss tangent of sapphire would be near the maximum that is believed to be tolerable in current designs, even for ICRH heating systems. It is also important to point out that this change was observed during the first reactor pulse when the total displacement dose is essentially zero (<2×10^{-9} dpa). In addition, the data shown in Fig. 7 indicates the possibility of a weak, fluence-dependent degradation of the loss tangent in specimens that were exposed to multiple pulses. RIED[2-5] could lead to even greater losses as the exposure increases. Thus, basing material selection on unirradiated properties alone could lead to premature failure of reactor components and systems.

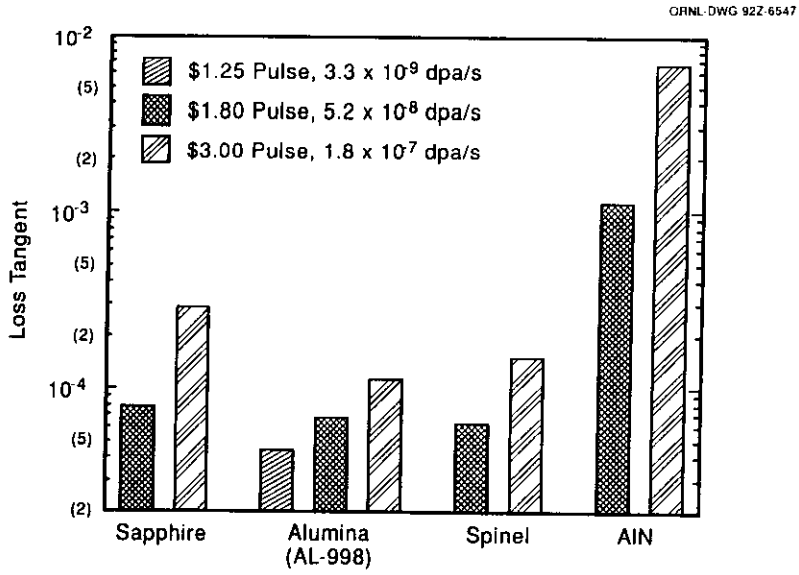

Fig. 6. Effect of damage rate on the measured value of the loss tangent under pulsed neutron irradiation.

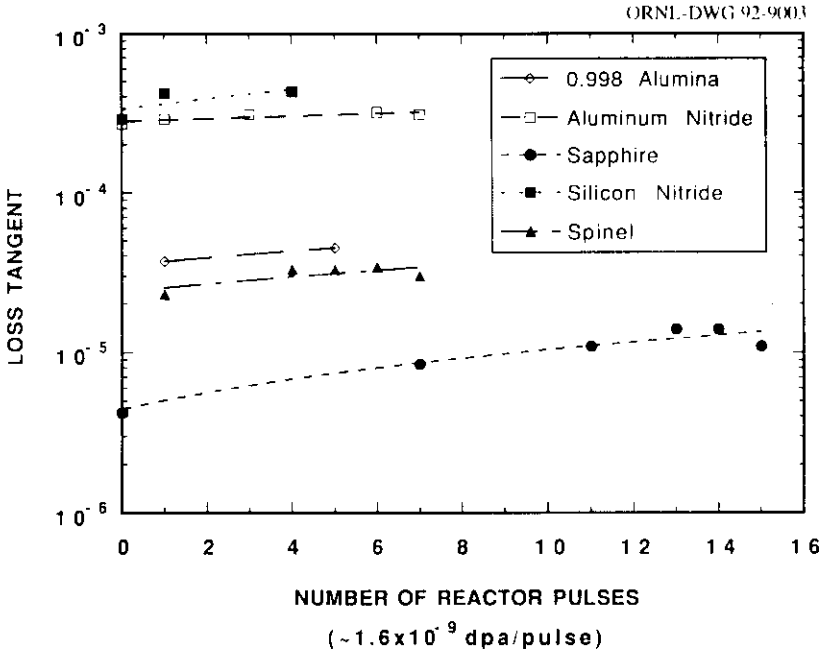

Fig. 7. Fluence dependence of loss tangent for specimens exposed to multiple pulses.

Summary

A significant influence of neutron irradiation has been observed on the dielectric properties of several common ceramic materials. The relative increase in the loss tangent measured in situ at about 10^{-9} dpa was already equal to or greater than that observed in post-irradiation measurements on material irradiated with either protons or neutrons to a total dose of 0.01 to 0.1 dpa.[7,8] Two experimental issues remain unresolved at this time. The first issue is the ionization of residual gas in the cavity. This ionization would lead to the formation of a plasma. If the plasma density was sufficiently high, the electrical conductivity of the plasma would affect the measured Q values. Additional experiments are planned that will permit lower pressures to be obtained. However, as shown in Fig. 8, current measurements

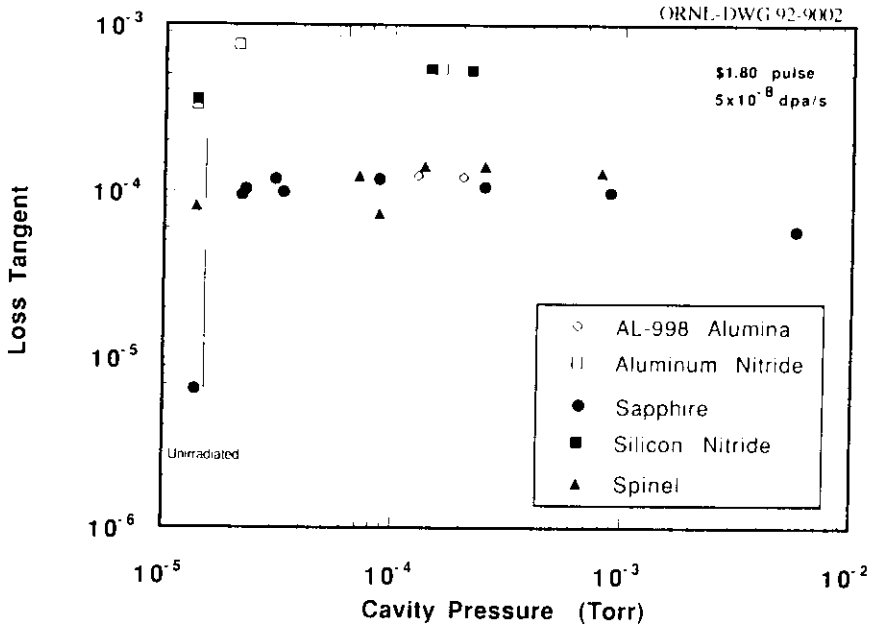

Fig. 8. Influence of residual cavity pressure on the measured loss tangent.

over a range of pressures, using either air or helium, indicate that plasma effects do not contribute to the measured cavity Q for pressures below about 10 m-torr. This result is consistent with theoretical modeling of the experiments.[16] Secondly, the fact that the ionizing dose rate in the TRIGA was about 10 to 100 times higher than in the HFIR-GIF precludes a firm conclusion regarding the relative importance of ionization and displacement damage. Preliminary analysis of these experiments indicates that an ionization-induced RIC effect could be responsible for a large fraction of the loss tangent changes that have been observed. Further experiments are planned in the TRIGA to resolve this question, in which lead shielding will be used to selectively reduce the ionizing damage rate. However, the ionizing and displacive damage rates in the TRIGA experiments were within the range that is expected for ITER. Thus, the increases in the loss tangent observed in these initial experiments are directly relevant, and they highlight the need for a careful experimental program to qualify ceramics for use as insulators in fusion reactors.

REFERENCES

1. R. W. Klaffky, B. H. Rose, A. N. Goland, and G. J. Dienes, Phys. Rev. *B* 21 (1980) 3610-3634.

2. E. R. Hodgson, *J.* Nucl. Mater. 179-181 (1991) 383-386.

3. G. P. Pells, *J.* Nucl. Mater. 184 (1991) 177-182.

4. T. Shikama, "Electrical Conductivity of Single Crystal Alumina Under Neutron and Gamma-ray Irradiation," Effects of Radiation on Materials, ASTM STP 1125, R. E. Stoller, A. S. Kumar, and D. S. Gelles, Eds, American Society of Testing and Materials, Philadelphia, in press.

5. S. J. Zinkle and E. R. Hodgson, "Radiation-Induced Changes in the Physical Properties of Ceramic Materials," presented at the Fifth International Conference on Fusion Reactor Materials, November, 1991, to be published in *J.* Nucl. Mater.

6. J. L. Scott, F. W. Clinard, Jr. and F. W. Wiffen, *J.* Nucl. Mater. 133 & 134 (1985) 156-163.

7. G. P. Pells and G. J. Hill, *J.* Nucl. Mater. 141-143 (1986) 375-381

8. S. N. Buckley and P. Agnew, *J.* Nucl. Mater. 155-157 (1988) 361-365.

9. G. P. Pells, *J.* Nucl. Mater. 155-157 (1988) 67-76.

10. H. M. Frost, "Millimeter-Wave Properties of Neutron-Irradiated Ceramics for RF-Window MFE Applications," Eighth Annual Progress Report On Special Purpose Materials for Magnetically Confined Fusion Reactors, DOE/ER-0113/5, National Technical Information Service, Springfield, Virginia, March, 1986, pp. 11-16.

11. D. Edelson, R. E. Jaeger, and J. C. Williams, *J.* Amer. Cer. *Soc.* 52 (1969) 359-362.

12. F. W. Clinard, Jr., "IEA Workshop on In-Situ Measurements of Electrical Properties of Irradiated Ceramics," Fusion Reactor Materials, Semiannual Progress Report. Sept. 30, 1990, DOE/ER-0313/9, USOOE, Office of Fusion Energy, pp. 291-294.

13. G. P. Pells, R. Heidinger, A. Ibarra-Sanchez, H. Ohno, and R. H. Goulding, "An Intercomparison of Techniques for Measuring Dielectric Permitivity and Loss over a Wide Frequency Range," presented at the Fifth International Conference on Fusion Reactor Materials, November, 1991, to be published in *J.* Nucl. Mater.

14. E. H. Farnum, J. C. Kennedy, F. W. Clinard, and H. M. Frost, "Radiation-induced Conductivity in Alumina from 100 Hz to 10 MHz During Proton Irradiation," presented at the Fifth International Conference on Fusion Reactor Materials, November, 1991, to be published in *J.* Nucl. Mater.

15. S. J. Zinkle, "Microstructural Changes in Oxide Ceramics Following Light Ion Irradiation," Fusion Reactor Materials, Semiannual Progress Report, March 31, 1991, DOE/ER-0313/10, USDOE, Office of Fusion Energy, pp. 302-309.

16. R. H. Goulding, R. E. Stoller, and S. J. Zinkle, to be published.

MEASUREMENT OF ELECTRICAL AND OPTICAL PROPERTIES OF DIELECTRIC MATERIALS DURING NEUTRON IRRADIATION --
E. H. Farnum, F. W. Clinard, Jr., J. C. Kennedy III, W. F. Sommer and W. P. Unruh (Los Alamos National Laboratory)

OBJECTIVE

The objective of this experiment is to determine the extent of degradation of electrical and optical properties of candidate dielectric materials during neutron irradiation. The goals are to identify promising dielectrics for ITER and other fusion machines, characterize mechanisms of degradation, and establish the basis for optimization of candidate materials.

SUMMARY

An in-situ neutron irradiation experiment will be carried out at Los Alamos National Laboratory during the summer of 1992, to assess behavior of electrical insulators and optical fibers during neutron irradiation. Testing will be carried out at the Los Alamos Spallation Radiation Effects Facility (LASREF). Experiments include measurement of ac and dc electrical properties of Al_2O_3 at 300, 400, and 500°C, with applied electric fields up to 2000 V/cm. Additional measurements will be carried out on MgO-insulated instrumentation cables. Tests on optical fibers include attenuation, fluorescence, and reflectance measurements, at ambient temperature and moderate to intense neutron fluxes. Results will be applied to identification and improvement of candidate materials for ITER and other fusion devices.

PROGRESS AND STATUS

Introduction

The prospect of radiation-induced degradation of electrical insulators and optical materials is of concern for ITER and other D-T burning fusion devices. Difficulties can be anticipated for many applications, with perhaps the greatest concern being that for radiation-sensitive diagnostic components

Radiation damage effects in dielectric materials can be divided into two categories: permanent and transient. The first, which is primarily fluence-related, includes such properties as swelling and strength change and can for the most part be studied by post-irradiation examination. Examples of transient effects are changes in electrical conductivity and dielectric breakdown strength, and fluorescence. The studies described here focus primarily on transient changes, although some properties to be measured such as dielectric breakdown, optical absorption and reflectance are also affected by accumulated dose.

Transient degradation can pose a serious threat to the integrity of insulators. Klaffky et al. [1] have measured orders-of-magnitude increases in electrical conductivity of Al_2O_3 under electron irradiation, and Hodgson [2] has shown that simultaneous application of radiation and an electric field can over a period of time cause significant permanent as well as transient degradation. Farnum et al. [3] have demonstrated that proton irradiation induces large immediate increases of conductivity in Al_2O_3, but that these are subsequently reduced by accumulation of displacement damage; the latter effect is attributed to trapping and recombination of electronic charge carriers by those defects. In similar tests, optical fibers have been shown to suffer large increases in absorption at relatively low fluxes [4] and fluences [5].

It is important to keep the following considerations in mind when dealing with transient effects:

- degradation can occur immediately upon application of the radiation field, and can therefore pose a threat to fusion devices early in their operation;
- changes in electrical and optical properties can be brought about by ionizing as well as displacive radiation;
- tests of such effects must be conducted during, as well as after, irradiation.

Planned Experiments

The LASREF irradiation experiment, which is scheduled for the summer of 1992, has five parts:

1) AC conductivity in alumina and sapphire. This is a collaborative study with T. Shikama of Tohoku University. Samples will be subjected to an applied field of 2000 V/cm, and will be tested at frequencies from 100 Hz to 1 MHz. Test temperatures for this and the following two experiments are 300, 400, and 500°C.

2) DC conductivity in alumina. This study will be carried out in collaboration with R. Stoller, ORNL. Applied fields will be 500 V/cm and 1500 V/cm.

3) AC and DC conductivity in MgO-insulated, stainless-steel sheathed cables. Applied field will be 1000 Vlcm.

4) Absorption, reflectance, and fluorescence in SiO_2-based optical fibers. This is a collaborative effort with D. Griscom, NRL and P. O'Roarke, SRL. The fibers are metal-clad, radiation-resistant commercial Droducts. and will be tested at ambient temoerature (60°C) and four fluxes. Both low-OH and hioh-OH pure silica core fibers will be studied.

5) Miscellaneous samples. A variety of diagnostic materials will be irradiated at ambient temperature for post-irradiation examination.

Following irradiation, selected samples will be examined by optical and electron microscopy to determine the extent of microscopic alteration. Of special importance is determination of changes in those samples tested under imposed electric fields, since Hodgson [6] has reported formation of defect aggregates under these conditions that may play a role in radiation-induced degradation of electrical properties.

Neutron Source

Irradiations will be carried out at the Los Alamos Spallation Radiation Effects Facility (LASREF), which is located at the beam stop area of the Los Alamos Meson Physics Facility (LAMPF). LAMPF is an 800 MeV proton accelerator, the beam of which is stopped in a water-cooled copper cylinder. High-energy spallation neutrons are produced by nuclear processes, and samples placed around the beam stop are bombarded by these neutrons. The irradiation volume at high flux is large (10 x 20 x 40 cm), allowing ample room for multiple-capsule in-situ tests. The neutron flux at LASREF is pulsed, with beam on for 0.5-0.8 ms during an 8.3 ms cycle.

Irradiation parameters for this LASREF test include:

- neutron energy spectrum: fusion-like, with high-energy tail;
- average neutron flux in high-flux region: 5×10^{17} nlm^{2}s;
- average neutron flux during beam-on period: 8×10^{18} nlm^{2}s;
- fluence for 1000-2000 h exposure: $2\text{-}4 \times 10^{24}$ nlm^2;
- approximate damage level for Al_2O_3 after 1000 h: 0.2 dpa;
- average gamma flux in high-flux region: 1×10^2 Gyls (E ≈ 2 MeV);
- ambient temperature: ≈60°C
- furnace atmosphere: Ar/6% N_2 gas at 130 kPa

FUTURE WORK

A series of in-situ tests at LASREF andlor other irradiation sources will follow this study. The goals of that future work are to determine in more detail the extent of degradation of electrical and optical properties of these and other candidate materials, and to establish a level of understanding sufficient to allow optimization of those materials.

REFERENCES

1. R. W. Klaffky, B. H. Rose, A. N. Goland, and G. J. Dienes, Phys. Rev. 821 (1980) 3610.
2. E. R. Hodgson, J. Nucl. Mater. 179-181 (1991) 383.
3. E. H. Farnum, J. C. Kennedy, F. W. Clinard and H. M. Frost, J. Nucl. Mater. (in press)
4. E. J. Friebele, C. G. Askins and M. E. Gingerich, Appl. Opt. 23 (1984) 4202
5. J. K. Partin, "Fiber Optics in High-Dose Radiation Fields", SPIE Proceedings on Radiation Effects in Optical Materials, Vol. 541, p. 97 (1985).
6. E. R. Hodgson, "Radiation-Enhanced Electrical Breakdown in Fusion Insulators", DOE Task Force Meeting on Electrical Breakdown of Insulating Ceramics in a High Radiation Field, U.S. Department of Energy Report CONF-9105176, p. 1 (1991).

THE EFFECT OF PHONON SCATTERING BY ALUMINUM PRECIPITATES AND VOIDS ON THE THERMAL CONDUCTIVITY OF Al_2O_3 -- D. P. White (Oak Ridge National Laboratoly)

OBJECTIVE

This work is intended lo provide information on the changes expected in the thermal conductivity of alumina due to phonon scattering by aluminum precipitates and voids.

SUMMARY

Recent calculations' on the effect of vacancies and conduction band electrons on the thermal conductivity of Al_2O_3 have shown that large decreases in the conductivity may be expected due to the scattering of phonons by vacancies in material exposed to displacive radiation. This work has been extended to include the effects of aluminum precipitates and voids on the lattice thermal conductivity. The change in the thermal conductivity due to these extended defects is presented.

PROGRESS AND STATUS

Introduction

The thermal conductivity of a ceramic is given by[2]

$$K=\frac{1}{3}\int S(\omega)\, v^2\, \tau(\omega)\, d\omega \quad , \tag{1}$$

where $S(\omega)$ is the specific heat per unit volume due to lattice modes of frequency $\omega d\omega$, v is the phonon velocity, and $\tau(\omega)$ is the phonon relaxation time. The reciprocal relaxation time is additively composed of the reciprocal relaxation time for each interaction separately so that, $1/\tau(\omega) = \sum 1/\tau_\alpha(\omega)$, where $\tau_\alpha(\omega)$ denotes the relaxation time for the interaction of type *a*.

Extended Defects

The reciprocal relaxation time due to intrinsic 3-phonon scattering is of the form[3,4]

$$\frac{1}{\tau_i}(\omega,T) = BT\omega^2 \quad , \tag{2}$$

where *T* is the temperature and *B* is a material dependent parameter. The reciprocal relaxation time for extended three dimensional defects is of the form[5-7]

$$\frac{1}{\tau_x} = NAv = \frac{3}{4}\, v\, \frac{x}{r} = C \tag{3}$$

where N is the number density of defects, A is their cross sectional area, x is the volume fraction of defects, and r is their radius. Substituting these forms for the relaxation time into equation 1 it is found that at high temperatures

($T \geq \frac{\theta}{3}$, where θ is the Debye temperature) that the fractional reduction in the thermal conductivity due to scattering by the extended defects is.

$$\frac{\delta K_x}{K_i} = \frac{\omega_x}{\omega_D} \tan^{-1}\left(\frac{\omega_D}{\omega_x} \right), \tag{4}$$

where K_i is the intrinsic thermal conductivity, ω_D is the Debye frequency, and $\omega_x = (C/B)^{1/2}$. Substituting equation *2* into equation 1 the parameter B may be expressed in terms of the intrinsic thermal conductivity as,

$$B = \frac{K_B \omega_D}{K_i 2\pi^2 v}, \tag{5}$$

where K_B is the Boltzmann constant.

Fractional Change in Thermal Conductivity

The fractional change in the thermal conductivity of alumina due to the scattering of phonons by extended defects can now be calculated using equation **4.** The Debye frequency is given by $\omega_D = (6\pi^2/\Omega)^{1/3}$, where Ω is the volume per atom ($\Omega = 8.5 \times 10^{-30}$ m^3)[8] thus $\omega_D = 1.34 \times 10^{14}$ s^{-1}. Taking the phonon velocity to be[9] $v = 7 \times 10^3$ m/s it is found that,

$$\frac{\delta K_x}{K_i} = 4.674\times10^{-6} \left(\frac{K_i\, x}{r}\right)^{1/2} \tan^{-1}\left[2.139\times10^{5} \left(\frac{r}{K_i\, x}\right)^{1/2} \right]. \tag{6}$$

Thus given the intrinsic conductivity, the volume fraction of defects and their radius the change in the thermal conductivity may be calculated. At 400 K, K_i = 26.4 W/m-K (Ref. **10).** Using this value the fractional change in the thermal conductivity due to phonon scattering by 10nm diameter defects at 400 K is plotted versus the volume fraction of defects in Figure 1. As an example, a 1% volume concentration of such defects would result in a **5.2%** fractional decrease in the thermal conductivity, and a **10%** concentration would result in a **15.7%** decrease.

Combined Vacancy and Extended Defect Scattering

Any material which has evolved extended voids and precipitates as a result of exposure to radiation will retain some fraction of the vacancies as individual point defects. Thus any reduction in the thermal conductivity due to extended defects will be accompanied by a reduction due to vacancy scattering.

The fractional reduction in the thermal conductivity due to point defects is[1,6,11]

$$\frac{\delta K_p}{K_i} = 1 - \frac{\omega_0}{\omega_D} \tan^{-1}\left(\frac{\omega_D}{\omega_0} \right), \tag{7}$$

where $\omega_0 = (B/A)^{1/2}$, where A appears in the point defect relaxation time as $1/\tau_p = A\,\omega^4$ and is proportional to the defect concentration, and B is given in equation **5.** For vacancies'

$$\frac{\delta K_v}{K_i} = 1 - \frac{0.2049}{(K_i C_v)^{1/2}} \tan^{-1}\left(\frac{(K_i C_v)^{1/2}}{0.2049} \right) \tag{8}$$

where C_v is the vacancy concentration per atom. The fractional reduction in the thermal conductivity at **400** K versus vacancy concentration is plotted in Figure 2. In this case a **0.1%** vacancy concentration leads to a **15%** reduction and a 1% concentration leads to a **52%** reduction. If $\omega_x << \omega_0$ then the reductions are additive. Thus for a sample with a 10% volume concentration of extended defects with a diameter of 10nm and a 0.1% atom concentration of vacancies at 400 K $\omega_x = 1.44\times10^{13}$ s^{-1} and $\omega_0 = 1.69\times10^{14}$ s^{-1} and a total reduction of **15.7+ 15 = 30.7%** would result.

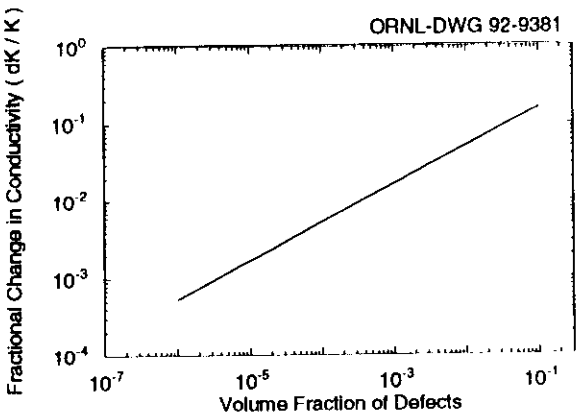

Figure 1: Fractional change in the lattice thermal conductivity versus the volume concentration of 10 nm diameter defects, at 400 K

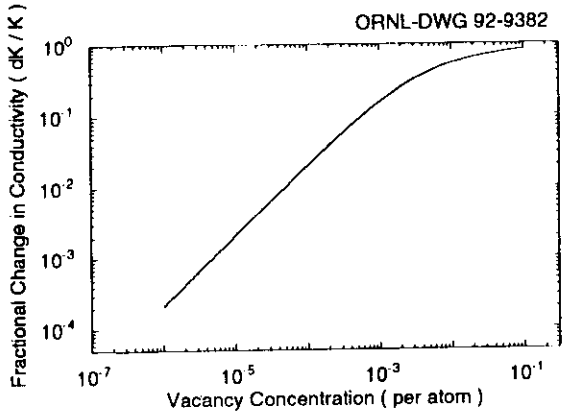

Figure 2: Fractional change in the lattice thermal conductivity versus the vacancy concentration, at 400 K

Application to Experiment

Pells and Shikama[12] studied void and aluminum precipitate formation in 1MeV electron irradiated alumina. The results of this work can be used to predict the resulting reduction in the thermal conductivity. For example, Table 1 gives the typical defect concentrations found in a sample irradiated at 1130 K to 124MC/m^2 = 6.2 dpa. Given K_i = 6.94 W/m-K at 1130 K (Ref. 10) and using the defect parameters given in Table 1, $\omega_x = 6.2632\times10^{8}[6.94(.056/3.5\times10^{-9} + .029/8.5\times10^{-9})]^{1/2} = 7.27\times10^{12}$ s^{-1}, and $\delta K_x/K_i$ = 8.2% from equation 4.

Assuming a 0.1% vacancy concentration $\delta K_v/K_i$ = 5% and assuming a 1% vacancy concentration $\delta K_v/K_i$ = 29%. This would produce a total reduction of 13.2% and 37.2%, respectively, in the thermal conductivity for the two cases.

Table 1: Defect Type, Size, and Concentration

Defect Type	Most Probable Diameter ($\times 10^{-9}$ m)	Volume %
Void	7	5.6
Al Precipitate	17	2.9

DISCUSSION AND CONCLUSIONS

The scattering of phonons by extended 3 dimensional defects can lead to large reductions in the thermal conductivity of alumina. It has been shown that at 400 K a 10% concentration of 10 nm diameter defects leads to a 15.7% reduction in the thermal conductivity. A predicted decrease of 8.2% due to scattering of phonons by extended defects was found for experimentally determined defect concentrations at 1130 K. If these same concentrations of defects were present at lower temperatures a larger fractional decrease would be expected. For example, using the data from Table 1 a fractional decrease of $\delta K_x/K_i$ = 15.5% would result at 400 K.

FUTURE WORK

A calculation of the effect of the higher thermal conductivity of the aluminum precipitates on the overall thermal conductivity is planned. It is also planned to extend the calculations of this work and reference 1 to low temperatures in order to predict the changes in the thermal conductivity at liquid nitrogen temperatures.

REFERENCES

1. D.P. White, DOE/ER-0313/11, 277, (1991).
2. P.G. Klemens, in *Thermal Conductivity*, ed.. R.P. Tye, vol. 1, p. 1, Academic Press, London, (1969).
3. P.G. Klemens, Proc. Roy. Soc. (London). A208, 108, (1951).
4. P.G. Klemens, in *Solid* State Physics, eds. F. Seitz and D. Turnbull, Academic Press, New *York,* vol. 7, (1958).
5. D.P. While, Doctoral dissertation. The University of Connecticut, Storrs, CT, (1991).
6. P.G. Klemens, Nucl. Inst. Meth. Phy. Res., B1, 204, (1984).
7. D.P. White, and P.G. Klemens, J. Appl. Phys., vol. 71, 4258. (1992).
8. W.E. Lee, and K.P.D. Lagerlof, J. Elec. Micros. Tech., 2,247, (1985).
9. A.M. deGoer, J. Phys (Paris), 30,389, (1969).
10. Y.S. Touloukian, and C.Y. Ho eds.. *Thermophysical* Properties of *Matter vol.* 2, IFI/Plenum, New York-Washington, (1970).
11. P.G. Klemens, Phys. Rev., 119. no. 2.507, (1960)
12. G.P. Pells, and T. Shikama, Phil. Mag. A, vol. 48, 779, (1983)

IN-WAVEGUIDE MEASUREMENTS OF MMW DIELECTRIC PROPERTIES OF CERAMIC MATERIAIS FOR THE US FUSION REACTOR MATERIALS RESEARCH PROGRAM—James C. Kennedy. III, Eugene F Farnum, and Frank W. Chard, Jr., Los Alamos National Laboratory

OBJECTIVE

The objective of this project is to obtain accurate measurements of dielectric properties of candidate ceramic insulating materials for fusion reactors, including some materials that have been identified as standards in the US Fusion Reactor Materials Research Program.

SUMMARY

As part of an International Energy Agency (IEA) collaboration, a set of round-robin materials was purchased for comparing dielectric measurements at laboratories in the United Kingdom (UK), Spain, Germany, US, and Japan. P. Pells at Aldermasten, UK, purchased MACOR 9658. a glass-mica composite, and Roger Stoller,[1] from Oak Ridge National Laboratory, purchased WESGO AL-300 and AL-995, polycrystalline alumina standards. We obtained some of each of these materials for making these measurements. Our results have been shared with the other IEA partners, and P. Pells is preparing a summary document.

We used the millimeter wave apparatus described below and elsewhere in detail[2,3] to measure the dielectric properties of these materials at 90 to 100 GHz at room temperature. The nomina1 purity of AL-300 was 0.967; the nominal purity of AL-995 was 0.995.

Our method was to measure the power transmission coefficient. We used computerized data reduction techniques to compute k (the dielectric constant) and tan6 (the loss tangent) directly from transmission maxima and their corresponding frequencies; to verify this method, we applied the same technique to theoretically derived channel spectra that were obtained by solving exactly the complex transmission coefficient? given k and tanδ.

The alumina material with a lower level of purity resulted in higher loss but lower dielectric constant. We obtained dielectric constants that were higher for all the materials than manufacturer-reported values taken at lower frequencies. In addition, we obtained higher dielectric constant values than those found by other investigators at 100 GHz for AL-995[5,6] and MACOR.' Tanδ values were in good agreement with those of other investigators obtained by free-space methods[6] and dispersive Fourier-transform techniques[5] in the same frequency range.

PROGRESS AND STATUS

Experiments

Generally, an IMPAT diode generates millimeter waves that are swept from 90 to 100 GHz. A WR-10 waveguide with dimensions of 2.54 x 1.27 mm holds a snugly fitting ceramic bar. Isolators on either side of the waveguide section reduce undesired multiple reflections. High-directivity directional couplers extract a signal, and the signal's amplitude is measured by square-law detectors. The signal is displayed logarithmically as a power channel spectrum of transmission loss versus frequency. A computer arithmetically averages the channel spectra obtained over several frequency sweeps and stores the averages for later data reduction. Calibrations include amplitude normalization, frequency correction of the IMPAT diode to true frequency values, and detector linearity checks.

We ground one sample of each material to waveguide dimensions; the vertical dimensions of the samples were within 0.0015 cm and the horizontal dimensions were within 0.0025 cm. Samples for the alumina were nominally 5 cm in length the MACOR samples were 3 cm long. Generally, a longer sample provides more transmission peaks, thereby improving the data reduction statistics. In addition, higher attenuation in a low-loss sample improves the accuracy of the relative measurements. Samples were measured in each of four possible orientations in the waveguide.

Direct computation of k and tan6 from the theoretically generated channel spectra given by equation (1) using the above equations gives values typically within 0.5% of the input values of k and tan6 used in generating the theoretical spectra.

Results

Experimental Data

Material	k	Tanδ
AL-300	9.74(± 0.05)	1.3×10^{-3} ($\pm 0.1\times10^{-3}$)
AL-995	9.88(± 0.04)	5.7×10^{-4} ($\pm 0.5\times10^{-4}$)
MACOR	6.94(± 0.01)	1.26×10^{-2} ($\pm 0.01\times10^{-2}$)

Others' Prior Results (100 GHz)

Material	k	Tanδ	Ref.
WESGO AL-995	9.60	6×10^{-4}	5
WESGO AL-995	9.58	4.9×10^{-4}	7
MACOR	5.67	1.5×10^{-2}	5

Manufacturer Values

Material	Frequency	k	Tanδ	Density
AL-300	8.5 GHz	9.32	4.0×10^{-4}	3.76
AL-995	8.5 GHz	9.61	1.4×10^{-4}	3.86
MACOR	8.6 GHz	5.68	7.0×10^{-3}	2.52

Discussion

Dielectric constant values for insulating ceramics are generally frequency-independent through the microwave and millimeter-wave regions. The reason we obtained higher values for the dielectric constant than the values obtained by other investigators is not fully understood, although it is known[3] that dielectric constant values determined from amplitude measurements are less accurate than values determined from phase measurements. Conversely, loss tangent values determined from amplitude measurements are considerably more accurate than values obtained from phase measurements. However, the magnitude of the error in k from amplitude measurements is expected to be on the order of tanδ, a value that is Considerably less than difference observed by other investigators.

Data Reduction

The complex transmission coefficient (T) of a material of arbitrary loss nnd of thickness *d* in the direction of wave propagation in a waveguide is given by:[4]

$$T = te^{-jt'} = (4\sqrt{a}\, e^{-j\beta d}) / (\sqrt{a} + 1)2 - (\sqrt{a} - 1)2\, e-2jOd \qquad (1)$$

where

$$\beta = 2\pi \sqrt{(k - p)} / \lambda$$

For a waveguide propagating a TE-wave with cutoff wavelength λ_c and the E vector polarized perpendicular to the plane of incidence,

$$a = (k - p) / (1 - p); \quad p = (\lambda / \lambda_c)^2$$

For tan6 > 0, k = k (1 – jtanδ).

The above complex equations are transcendental and simultaneous and may be solved graphically or by iterative substitution. When tan6 is < 0.1, **k** can **be** found to a good approximation from |T|2. This value of **k** is then substituted in equation (1) and the quadratic solved for tanδ. The resulting tan6 value **can** be used to get a more accurate value of k. Although this numerical iterative procedure has not been fully computer-coded at this time, we confirmed these results by using a second method. A graphically implemented iterative procedure that generates the theoretical channel spectra and minimizes differences between the observed transmission maxima gave values close to those computed directly from the magnitude of the transmission maxima and the corresponding frequency.

The direct computation of k and tan6 (when tan6 < 0.1) is performed by adapting equations for the free space situation[3,7] to the waveguide situation:[3,8]

$$k = (Nc / 2df_N)2 - p$$

$$\tan 6 = -\ln (A_N) [2(k - p) / Nxkl \quad , \text{and}$$

$$A_N = (1/2) \{[(1 - a^2)^2 / a^4 \, |T|^2 + 4/a^2]^{1/2} - (1 - a^2) / a^2 \, |T|\}$$

where

$$a = [(k - p) / (1 - p)]^{1/2} - 1 / [(k - p) / (1 - p)]^{1/2} + 1 \, ,$$

c = speed of light,

N = number of observed transmission maxima,

f_N = frequency interval between the first and last transmission maxima, and

|T| = magnitude of the complex transmission coefficient.

Measurement errors, such as an error caused by a gap between the material and the top of the wide dimension (here less than 0.0015 cm), would result in slightly higher values of k and tanδ. Conversely, wall losses tend to lower values for k and tanδ. The reported data is not corrected for gap errors or wall losses; we are currently evaluating the overall effect of these errors.

The relationship between dielectric constant values for AL-300 and AL-995 is as expected; the lower value for AL-300 corresponds to the material's lower density. Dielectric constants for ceramics at room temperature are primarily determined by density, and to a lesser extent by impurities. Conversely, tanδ is primarily determined by the presence of impurities and high-loss secondary phases.[6]

Our tan6 values for MACOR are similar to those obtained at the same frequencies by other investigators[5] who used dispersive Fourier-transform spectroscopy to measure the refractive index and the absorption coefficient. The absorption coefficient of MACOR has been observed[g] to have a power law dependence on the frequency at measured frequencies above 100 GHz. Extending the assumption of a power law dependence to lower frequencies would explain why our tan6 values for MACOR at 100 GHz are higher than the manufacturer-reported values taken at lower frequencies.

Our obtained tan6 values for alumina at 100 GHz that are higher than manufacturer-reported values at lower frequencies is expected because tan6 in alumina has also been observed to have a power-law dependence on frequency.[6] Our tan6 values are in good agreement with those obtained by other investigators at 100 GHz[5,6] for AL-995. Obtaining higher tan6 values for AL-300 is consistent with the material's higher impurity levels.

Correlating dielectric properties with chemical and microstructural properties is fundamental to understanding the loss mechanisms involved in insulating ceramic materials. If the ceramic materials measured are to be used as standards, then an in-depth chemical and microstructural analysis should be undertaken to enable such correlations and allow for meaningful comparison of results among investigators.

REFERENCES

1. R.E. Stoller, "Ceramics for Fusion Program Research Materials Inventory." in 'Fusion Reactor Materials Semiannual Progress Report for the Period Ending March 31, 1990," US Department of Energy Office of Fusion Energy Report (August 1990), p. 299.

2. H.M. Frost, "Facility for Measuring Microwave Properties of Radiation-Damaged Ceramics for RF Windows and other Fusion Applications," in "Seventh Annual Progress Report on Special Purpose Materials for Magnetically Confined Fusion Reactors," US Department of Energy Report DOE/ER-0113/4 (May 1985), pp. 29-32.

3. H.M. Frost, "Millimeter-Wave Properties of Neutron Irradiated Ceramics for RF-Window MFE Applications," in "Eighth Annual Progress Report on Special Purpose Materials for Magnetically Confined Fusion Reactors," US Department of Energy Report DOE/ER-0113/5 (March 1986), pp. 11-16.

4. R.M. Redheffer. "Measurement of Dielectric Constants," in "Technique of Microwave Measurements," C.G. Montgomery, Ed., Massachusetts Institute of Technology Radiation Lab Series (1947), Vol. 11. pp. 561-676.

5. M.N. Afsar and K.J. Button, ***Digest of Millimeter and Submillimeter Wave Materials Information and Measurements*** (Cambridge: Massachusetts Institute of Technology, 1983).

6. W.W. Ho, "Millimeter Wave Dielectric Property Measurement of Gyrotron Window Materials," in "Technical Report for the Period January 1983- October 1984," Oak Ridge National Laboratory Report ORNL/SUB/83-51926/2, Rockwell International Science Center (April 1985).

7. W.W. Ho, "Millimeter Wave Dielectric Property Measurement of Gyrotron Window Materials," in "Technical Report for the Period January 1983- February 1984," Oak Ridge National Laboratory Report ORNL/SUB/83-51926/1, Rockwell International Science Center (April 1984).

8. H.M. Frost, "Improved Computation of Dielectric Constants Measured by In-Waveguide Techniques," in "Fusion Reactor Materials Semiannual Progress Report for the Period Ending September 30, 1987," US Department of Energy Office of Fusion Energy Report DOE/ER-0313/3 (March 1988), pp. 297-298.

9. J.R. Birch, "Optical Constants of Some Commercial Microwave Materials Between 90 and 1200 GHz," *IEEE Proceedings* **130,** H, 5, 327-330 (August 1983).

DISTRIBUTION

1–17. Argonne National Laboratory, 9700 South Cass Avenue, Argonne, IL 60439

M. C. Billone	P. A. Finn	R. F. Mattas
P. E. Blackburn	A. K. Fisher	L. A. Neimark
O. K. Chopra	A. B. Hull	D. L. Smith
H. M. Chung	C. E. Johnson	S. W. Tam
R. G. Clennner	F. Kassner	H. Wiedersich
D. R. Diercks	B. A. Loomis	

18. Argonne National Laboratory, EBR-II Division, Reactor Materials Section, P.O. Box 2528, Idaho Falls, ID 83403-2528
D. L. Porter

19. Auburn University, Department of Mechanical Engineering, 201 Ross Hall, Auburn, AL 36849
B. A. Chin

20–34. Battelle-Pacific Northwest Laboratory, P. O. Box 999, Richland, WA 99352

M. D. Freshley	M. L. Hamilton	B. D. Shipp
F. A. Garner (5)	H. L. Heinisch	O. D. Slagle
D. S. Gelles	G. W. Hollenberg	J. L. Straalsund
L. R. Greenwood	R. H. Jones	

35. Carnegie Institute of Technology, Carnegie-Mellon University, Schenley Park, Pittsburgh, PA 15213
W. M. Garrison, Jr.

36. Department of Energy, Richland Operations Office, Federal Bldg., MS A590, Richland, WA 99352
Paul Pak

37. EG&G Idaho, Inc., Fusion Safety Program, P.O. Box 1625, Idaho Falls, ID 83415-3523
D. F. Holland

38. GE Astrospace Division, San Jose Operations, 6835 via Deloro, P.O. Box 530954, San Jose, CA 95153-5354
Mike Kangilaski

39–42. General Atomics, P.O. Box 85608, San Diego, CA 92138

J. Baur	D. I. Roberts
T. A. Lechtenberg	K. R. Schultz

43. General Dynamics Corporation, 5001 Kearny Villa Road, San Diego, CA 92138
T. L. Cookson

44. Georgia Institute of Technolow, School of Textile Engineering, Atlanta, GA 30332
O. S. Tucker

45. Grand Canyon University, Department of Natural Science, 3300 W. Camelback Rd., Phoenix, AZ 85017
W. A. Coghlan

46–48. Lawrence Livermore National Laboratory, P.O. Box 808, Livermore, CA 94550

E.C.N. Dalder	J. Perkins
M. Guinan	

49–57. Los Alamos National Laboratory, P.O. Box 1663, Los Alamos, NM 87545

J. L. Anderson	E. H. Farnum	C. D. Kise
L. D. Caudill	H. M. Frost	R. Liepens
F. W. Clinard	G. Hurley	T. Zocco

58. Manlabs, Inc., 231 Erie Street, Cambridge, MA 02139
D. Tognarelli

59. Massachusetts Institute of Technology, Department of Metallurgy and Materials Science, Cambridge, MA 02139
L. W. Hobbs

60–61. Massachusetts Institute of Technology, Room 13-4069, Cambridge, MA 02139

N. J. Grant	K. C. Russell

62–63. Massachusetts Institute of Technology, Plasma Fusion Center Headquarters, Cambridge, MA 02139
H. D. Becker
D. B. Montgomery

64. McDonnell-Douglas Missile Systems Company, Mail Code 306 4204, P.O. Box 516, St. Louis, MO 63166
J. W. Davis

65–67. National Institute of Standards and Technology, Boulder, CO 80302
F. R. Fickett
R. P. Reed
H. I. McHenry

68. National Materials Advisory Board, 2101 Constitution Avenue, Washington, DC 20418
K. M. Zwilsky

69. Naval Research Laboratory, Washington, DC 20375
J. A. Sprague

70–111. Oak Ridge National Laboratory, P.O. Box 2008, Oak Ridge, TN 37831

Central Research Library	T. D. Burchell	T. K. Roche
Document Reference Section	R. H. Goulding	A. F. Rowcliffe (10)
Laboratory Records Department (2)	M. L. Grossbeck	R. L. Senn
Laboratory Records—RC	E. A. Kenik	J. Sheffield
Patent Section	R. L. Klueh	L. Snead
D. J. Alexander	Eal Lee	R. E. Stoller
C. C. Baker	A. W. Longest	K. R. Thoms
G.E.C. Bell	L. K. Mansur	P. F. Tortorelli
J. Bentley	P. J. Maziasz	D. P. White
E. E. Bloom	J. E. Pawel	S. J. Zinkle
	T. C. Reuther	R. Yamada

112. Oregon Graduate Institute. Oept. of Materials Science & Engineering, 19600 N.W. Von Neumann Drive, Beaverton, OR 97006
J. M. McCarthy

113115. Princeton University, Princeton Plasma Physics Laboratory, P.O. Box 451, Princeton, NJ 08540
C. Bushnell
Long-Poe Ku
H. Furth

116. Reactor Materials Technology, 212 Baywood Ave., Pittsburgh, PA 15228
A. Boltax

117–118. Rensselaer Polytechnic Institute, Troy, NY 12181
D. Steiner
David Duquette

119. Rockwell International Corporation, NA02, Rocketdyne Division, 6633 Canoga Avenue, Canoga Park, CA 91304
D. W. Kneff

120–121. Sandia National Laboratories, P.O. Box 5800. Albuquerque, NM 87185-5800
M. J. Davis
W. B. Gauster

122–123. Sandia National Laboratories, Livermore Division 8316, Livermore, CA 94550
W. Bauer
W. G. Wolfer

124. San Diego State University, Mechanical Engineering Dept., San Diego, CA 92182-0191
L. D. Thompson

125–126. University of California, Department of Chemical and Nuclear Engineering, Santa Barbara, CA 93106
G. E. Lucas
G. R. Odette

127–129. University of California, Department of Chemical, Nuclear and Thermal Engineering, Los Angeles, CA 90024
M. A. Abdou
N. M. Ghoniem
R. W. Conn

130. University of Michigan, Department of Nuclear Engineering, Ann Arbor, MI 48109
T. Kammash

131. University of Missouri, Department of Nuclear Engineering, Rolla, MO 65401
A. Kumar

132—133. University of Wisconsin, Nuclear Engineering Dept., 1600 Johnson Drive, Madison, WI 53706
J. E. Alanchard
G. L. Kulcinski

134—139. Westinghouse Hanford Company. P. O. Box 1970. Richland. WA 99352
H. R. Brager
A. M. Ermi
G. D. Johnson
F. M. Mann
R. J. Puigh
R. L. Simons

140-142. Hokkaido University, Faculty of Engineering, Kita 13, Nishi 8, Kita-ku, Sapporo 060, Japan
Heischichiro Takahashi
Somei Ohnuki
Akira Okada

143-146. Japan Atomic Energy Research Institute, Tokai Research Establishment, Tokai-mura, Naka-gun, Ibaraki-ken 319-11, Japan
Tatsuo Kondo
Akimichi Hishinuma (3)

147. Kyushu University, Department of Nuclear Engineering, Faculty of Engineering, Kyushu University 36, Hakozaki, Fukuoka 812, Japan
C. Kinoshita

148. Kyushu University, Research Institute for Applied Mechanics, 6-1, Kasuga-Koen, Kasuga-Shi, Fukuoka-Ken 816, Japan
Takeo Muroga

149-150. Muroran Institute of Technology, Department of Metallurgical Engineering, 27-1 Mizumoto-cho, Muroran 050, Japan
Toshihei Misawa
Akihiko Kimura

151. Nagoya University, Department of Nuclear Engineering, Furo-Cho, Chikusa-ku, Nagoya 464-01, Japan
Michio Kiritani

152-153. Nagoya University, Institute of Plasma Physics, Furo-Cho, Chikusa-ku, Nagoya 464-01, Japan
Akira Miyahara
Chusei Namba

154-155. National Institute for Fusion Science, Furo-cho, Chikusa-ku, Nagoya 464-01, Japan
Osamu Motojima
Nobuaki Noda

156. National Research Institute for Metals, 1-2-1, Sengen, Tsukuba-shi, Ibaraki 305, Japan
Fujio Abe

157-158. National Research Institute for Metals, Tsukuba Branch, Sengen, Tsukuba-shi, Ibaraki-ken 305, Japan
Josei Nagakawa
Haruki Shiraishi

159. Osaka University, Department of Nuclear Engineering, 2-1 Yamadaoka, Suita, Osaka 565, Japan
Tetuo Tanabe

160. PNC Oarai, 4002 Narita, Oarai, Ibaraki 311-13, Japan
Itaru Shibasaki

161. Science University of Tokyo, Department of Materials Science & Technology, 2641 Yamazaki Noda City, Chiba Prefecture 278 Japan
Naohira Igata

162. Tohoku University, Institute for Materials Research, Katahira 2-1-1, Sendai 980, Japan
Hideki Matsui

163. Tohoku University, Institute for Materials Research, Oarai Branch, Oarai, Ibaraki 311-13, Japan
Tatsuo Shikama

164. Tohoku University, Institute for Materials Research, Orai Branch, Oarai, Higashi-Ibaraki-gun, Ibaraki-ken 311-13, Japan
Hideo Kayano

165. Tohoku University, Department of Nuclear Engineering, Tohoku University, Aoba, Aramaki, Sendai 980, Japan
Katsunori Abe

166–167. University of Tokyo, Department of Nuclear Engineering, 3-1, Hongo 7-Chome, Bunkyo-ku, Tokyo 113 Japan
Shiori Ishino (2)

168–169. University of Tokyo, Department of Materials Science, 3-1, Hongo 7-Chome, Runkyo-ku, Tokyo 113, Japan
Akira Kohyama Yutaka Kohno

170. University of Tokyo, Nuclear Engineering Research Institute, 3-1, Hongo 7-Chome, Bunkyo-ku, Tokyo 113, Japan
Naoto Sekimura

171. Commission of European Communities, Directorate-General for Research Science and Education, Fusion Programme RUE De La Loi 200, B-1049 Brussels, Belgium
J. Darvas

172-173. Chalk River Nuclear Laboratories, Atomic Energy of Canada, Ltd., Chalk River, Ontario KOJ 1JO, Canada
I. J. Hastings D. P. Jackson

174. Southwestern Institute of Physics, P.O. Box 432, Chenedu 610041, Sichuan, P. R. China
J. P. Qian

175. Institute of Atomic Energy, Academia Sinica. P.O. Box 215-51, Beijing, P.R. China
J. Yu

176. Riso National Laboratory, Materials Department, P.O. Box 49, OK-4000, Roskilde, Denmark
B. N. Singh

177. Centre d'Etudes Nucleaires, Saclay, DLPC/SPCM, Commissariat a 1'Energie Atomique. 91191 Gif-Sur-Yvette, Cedex, France
N. Roux

178. Commission for European Communities, Joint Research Centre, I.A.M. Ispra Establishment 21020 Ispra (Varese), Italy
P. Schiller

179. EURATOM/CIEMAT Fusion Association, Avenida Complutense 22, 28040, Madrid, Spain
E. R. Hodgson

180. Paul Scherrer Institute, CH-5232 Villigen, Wuerenlingen PSI, Switzerland
M. Victoria

181. Harwell Laboratory, B393, Radiation Damage Department, Oxfordshire, OX11 ORA, United Kingdom
C. A. English

182. Metallurgical and Nuclear Consultant, 9A Cumnor Rise Road, Cumnor Hill, Oxford OX2 9HD, United Kingdom
D. R. Harries

183. Culham Laboratory, U.K. Atomic Energy Authority, D5/117, Abingdon, Oxon OX14 3DB, United Kingdom
G. J. Butterworth

184. Hahn-Meitner-Institut fur Kernforschung Berlin, Glienicker Str. 100, D-1000 Berlin 39, Germany
H. J. Wollenberger

185. Institut fur Festkorperforschung der Kernforschungsanlage, 0-5170 Julich 1, Postfach 1913, Germany
H. Ullmaier

186-187. Kernforschungszentrum Karlsruhe, Postfach 3640, 75 Karlsruhe 1, Germany
M. Dalle-Donne (INR) K. Ehrlich (IMF-II)

188. A.A. Raikov Institute of Metallurgy, USSR Academy of Sciences, Leninsky Prospect 49, Moscow, USSR
L. I. Ivanov

189. CRISM "Prometey," Naberezhnava r. Monastyrick 1, 193167, Leningrad, Leningrad, USSR
V. V. Rybin

190. D.V. Efremov Institute of Electro-Physical Apparatus, 189631, Leningrad, USSR
Yu. G. Prokofiev

191. Institute of Power Engineering, 218 M. Krasnosel's Kaji St., 107113 Moscow, USSR
G. M. Kalinin

192. Kharkov Physical-Technical Institute, Kharkov, Academishen, 1, Moscow, USSR
I. M. Neckludov

193. V. I. Lenin Research Institute of Atomic Reactors, 433510 Dimitrovgrad-10, Ulyanovsk Region, USSR
V. K. Shamardin

194. Department of Energy, DOE Oak Ridge Field Office, P.O. Box 2008, Oak Ridge, TN 37831-6269
Assistant Manager for Energy Research and Development

195. Department of Energy, DOE Oak Ridge Field Office, P. O. Box 2008, Oak Ridge, TN 37831-6269
S. D. Frey

196. Department of Energy, Office of Basic Energy Sciences, Washington, DC 20585
J. B. Darby

197–202. Department of Energy, Office of Fusion Energy, Washington, DC 20585
S. E. Berk
M. M. Cohen
N. A. Davies
R. J. Dowling
R. E. Price
F. W. Wiffen

203-252. Department of Energy, Office of Scientific and Technical Information, Office of Information Services, P.O. Box 62, Oak Ridge, TN 37831
For distribution as shown in DOE/TIC-4500, Distribution Categories UC-423 (Magnetic Fusion Reactor Materials) and UC-424 (Magnetic Fusion Energy Systems)